Publication Date (Web): September 11, 2015 | doi: 10.1021/bk-2015-1194.fw001

Advances in CO_2 Capture, Sequestration, and Conversion

In Advances in CO2 Capture, Sequestration, and Conversion; He, et al.;
ACS Symposium Series; American Chemical Society: Washington, DC, 2015.

Publication Date (Web): September 11, 2015 | doi: 10.1021/bk-2015-1194.fw001

In Advances in CO2 Capture, Sequestration, and Conversion; He, et al.;
ACS Symposium Series; American Chemical Society: Washington, DC, 2015.

ACS SYMPOSIUM SERIES **1194**

Advances in CO_2 Capture, Sequestration, and Conversion

Fangming Jin, Editor
Shanghai Jiao Tong University
Shanghai, China

Liang-Nian He, Editor
Nankai University
Tianjin, P. R. China

Yun Hang Hu, Editor
Michigan Technological University
Houghton, Michigan

Publication Date (Web): September 11, 2015 | doi: 10.1021/bk-2015-1194.fw001

Sponsored by the
ACS Division of Energy and Fuels

American Chemical Society, Washington, DC

Distributed in print by Oxford University Press

Library of Congress Cataloging-in-Publication Data

Advances in CO2 capture, sequestration, and conversion / Fangming Jin, editor, Shanghai Jiao Tong University, Shanghai, China, Liang-Nian He, editor, Nankai University, Tianjin, P. R. China, Yun Hang Hu, editor, Michigan Technological University, Houghton, Michigan ; sponsored by the ACS Division of Energy and Fuels.
pages cm. -- (ACS symposium series ; 1194)
Includes bibliographical references and index.
ISBN 978-0-8412-3088-0 (alk. paper) -- ISBN 978-0-8412-3085-9 (alk. paper) 1. Carbon sequestration. 2. Carbon dioxide mitigation. I. Jin, Fangming, editor. II. He, Liang-Nian, editor. III. Hu, Yun Hang, editor. IV. American Chemical Society. Division of Energy and Fuels V. Title: Advances in carbon dioxide capture, sequestration, and conversion.
SD387.C37A325 2015
577′.144--dc23

2015030792

The paper used in this publication meets the minimum requirements of American National Standard for Information Sciences—Permanence of Paper for Printed Library Materials, ANSI Z39.48n1984.

Distributed in print by Oxford University Press

PRINTED IN THE UNITED STATES OF AMERICA

Publication Date (Web): September 11, 2015 | doi: 10.1021/bk-2015-1194.fw001

Foreword

The ACS Symposium Series was first published in 1974 to provide a mechanism for publishing symposia quickly in book form. The purpose of the series is to publish timely, comprehensive books developed from the ACS sponsored symposia based on current scientific research. Occasionally, books are developed from symposia sponsored by other organizations when the topic is of keen interest to the chemistry audience.

Before agreeing to publish a book, the proposed table of contents is reviewed for appropriate and comprehensive coverage and for interest to the audience. Some papers may be excluded to better focus the book; others may be added to provide comprehensiveness. When appropriate, overview or introductory chapters are added. Drafts of chapters are peer-reviewed prior to final acceptance or rejection, and manuscripts are prepared in camera-ready format.

As a rule, only original research papers and original review papers are included in the volumes. Verbatim reproductions of previous published papers are not accepted.

ACS Books Department

Publication Date (Web): September 11, 2015 | doi: 10.1021/bk-2015-1194.fw001

Publication Date (Web): September 11, 2015 | doi: 10.1021/bk-2015-1194.pr001

Preface

The earth's sustainable development is threatened by the energy exhaustion and rising atmospheric concentrations of CO_2 linked to global warming. One of the causes of the energy crisis and the increased atmospheric CO_2 content could be the imbalance between the rapid consumption of fossil fuels due to anthropogenic activities and the slow formation of fossil fuels. An efficient method for counteracting the imbalance in the carbon cycle and keeping sustainable development should involve CO_2 utilization and conversion. To further promote research and development in CO_2 areas, and to foster professional collaboration among researchers, we organized a symposium on "Materials and Technologies for CO_2 Capture, Sequestration, and Conversion" as a part of the 246th American Chemical Society National Meeting, which took place September 8-12, 2013 in Indianapolis, IN (USA). This symposium was sponsored by the ACS Division of Energy and Fuels. This book was developed on this symposium.

This book brings together recent advances in CO_2 capture, sequestration, and conversion and consists of 14 peer-reviewed chapters, with emphasis on the photocatalytic conversion of CO_2, chemical fixation of CO_2, and CO_2 reforming of methane. It also includes novel methods of CO_2 reduction, such as selective hydrogenation in supercritical carbon dioxide and hydrothermal reduction of CO_2, and the recent advances in CO_2 capture and storage.

All chapters were written by scientists and researchers who are experts in their own fields. Most of those chapters were developed from ACS articles presented at the symposium, and others were from invited contributors in the related research areas. This book is very useful for researchers and engineers in CO_2 utilization and conversion.

We would like to thank all the authors of the chapters for their contributions to the ACS book and the ACS symposium, along with all of the peer reviewers for their efforts in evaluating the manuscripts to improve the quality of those chapters. We also wish to thank the ACS Division of Energy and Fuels and ACS Books for the opportunities to organize the symposium and to publish this book, respectively. Thanks as well to Tim Marney and Anne Brenner of ACS Books for their great efforts in the peer-review process and production of this book.

In Advances in CO2 Capture, Sequestration, and Conversion; He, et al.;
ACS Symposium Series; American Chemical Society: Washington, DC, 2015.

Fangming Jin
School of Environmental Science & Engineering
Shanghai Jiao Tong University
Visiting Professor, Tohoku University, Japan
Fellow, Graduate School of Environmental Studies, Tohoku University, Japan
800 Dongchuan Road, Shanghai 200240, China
+86-21-021-54742283 (telephone)
+86-21-021-54742283 (fax)
fmjin@sjtu.edu.cn (e-mail)

Liang-Nian He
Institute of Elemento-Organic Chemistry
State Key Lab of Elemento-Organic Chemistry, Nankai University
Tianjin 200071, P. R. China
+86 22 2350 3878 (telephone)
+86 22 2350 3878 (fax)
heln@nankai.edu.cn (e-mail)

Yun Hang Hu
Department of Materials Science and Engineering
Michigan Technological University
Houghton, Michigan 49931, United States
906-4872261 (telephone)
yunhangh@mtu.edu (e-mail)

Publication Date (Web): September 11, 2015 | doi: 10.1021/bk-2015-1194.pr001

Publication Date (Web): September 11, 2015 | doi: 10.1021/bk-2015-1194.ot001

Editors' Biographies

Fangming Jin

Dr. Fangming Jin is a Distinguished Professor at Shanghai Jiao Tong University. She received her Ph.D. from Tohoku University in Japan. After that she became an assistant professor and then an associate professor at Tohoku University in Japan. In 2007, she returned to China and became a Professor at Tongji University and also a Chair Professor sponsored by the Chang Jiang Scholar Program (administered by the Ministry of Education of the People's Republic of China). In 2010 she moved to Tohoku University (Japan) as a professor, and then in 2011, she moved back to Shanghai Jiao Tong University and got an honor of "Recruitment Program of Global Experts" Talents in Shanghai. Her research centers on the conversion of CO_2 and biomass into fuels and chemicals, in order to explore a potentially useful technology for improvement in the carbon cycle by mimicking nature. She has authored more than 200 scientific publications, including peer-reviewed papers, patents, books, and book chapters. Prof. Jin is also a Visiting Professor at Tohoku University, a Fellow of the Graduate School of Environmental Studies at Tohoku University, and a Visiting scientist at RIKEN, Japan.

Liang-Nian He

Prof. Liang-Nian He received his Ph.D. from Nankai University in 1996 under the guidance of academician Ru-Yu Chen. He then worked as a Chinese postdoctoral fellow with academician Ren-Xi Zhuo at Wuhan University. He worked as a Postdoctoral Research Associate at the National Institute of Advanced Science and Technology (Japan) from 1999 to 2003 before joining Nankai University in April of 2003. In 2009, He was selected as a "Chutian Scholar" Professor. Now Professor He is a Professor of Chemistry at Nankai University, a Fellow of the Royal Society of Chemistry (FRSC, from 2011), he became one of the Most Cited Chinese Researchers (Elsevier) in 2014, "the top 1% of highly cited authors in RSC journals in 2014," and got a "Nature Science" award by the Tianjin government in 2015. Prof. He has over 150 scientific publications and eight patents. He also has edited 12 books and chapters and delivered more than 50 invited lectures at international/national conferences, universities, and research organizations.

Now He also serves as a Series Editor of "Green Chemistry and Sustainable Technology" (Springer) and on the Advisory Board of the new book Series published by CRC Press "Green Syntheses." He is also a member of the Editorial Boards for "Journal of CO_2 Utilization," "Sustainable Chemical

In Advances in CO2 Capture, Sequestration, and Conversion; He, et al.;
ACS Symposium Series; American Chemical Society: Washington, DC, 2015.

Processes," "Current Organic Synthesis," "Current Chemical Research," "The Open Organic Chemistry Journal," "The Open Catalysis Journal," "Reports in Organic Chemistry," and "Current Catalysis" as well as an associate Editor of "Sustainable Development" (in Chinese) and a member of the Ionic Liquids Professional Committee and Chinese Fine Chemical Committee. In addition, he serves as a referee for leading journals in the fields of chemistry, green chemistry, catalysis, and environmental science.

Prof. He's current research interests cover green synthetic chemistry, CO_2 chemistry (CO_2 activation and its chemical transformation into fuels/value-added chemicals), catalysis in green solvents and biomass conversion (castor-related energy), and green technology related to desulfurization.

Publication Date (Web): September 11, 2015 | doi: 10.1021/bk-2015-1194.ot001

Yun Hang Hu

Dr. Yun Hang Hu is the chair of the Energy and Fuels Division of the American Chemical Society (ACS), the president of the Hydrogen Storage Division of the International Association of Hydrogen Energy (IAHE), a fellow of American Association for the Advancement of Science (AAAS), a fellow of Royal Society of Chemistry (RSC), and the inaugural Charles and Carroll McArthur Chair Professor at Michigan Technological University. He received his Ph.D. in physical chemistry from Xiamen University. His main research interests include nanomaterials, clean fuels, hydrogen storage materials, CO_2 conversion, catalysis, quantum chemistry calculations, and solar energy. He has published more than 120 papers in prestigious journals with more than 4000 citations. He was an organizer and chair for more than 30 international symposia, an editor for three ACS books, and an editorial board member for nine international journals.

Publication Date (Web): September 11, 2015 | doi: 10.1021/bk-2015-1194.ch001

Chapter 1

Recent Advances (2012–2015) in the Photocatalytic Conversion of Carbon Dioxide to Fuels Using Solar Energy: Feasibilty for a New Energy

Yasuo Izumi*

Department of Chemistry, Graduate School of Science, Chiba University, Yayoi 1-33, Inage-ku, Chiba 263-8522, Japan
***E-mail: yizumi@faculty.chiba-u.jp**

In this chapter, recent advances in photocatalytic CO_2 conversion with water and/or other reductants are reviewed for the publications between 2012 and 2015. Quantitative comparisons were made for the reaction rates in μmol h^{-1} g_{cat}^{-1} to acertain the progress of this field although the rates depends on photocatalyst conditions and reaction conditions (temperature, pressure, and photon wavelength and flux). TiO_2 photoproduced methane or CO from CO_2 and water at rates of 0.1–17 μmol h^{-1} g_{cat}^{-1} depending on the crystalline phase, crystalline face, and the defects. By depositing as minimal thin TiO_2 film, the rates increased to 50–240 μmol h^{-1} g_{cat}^{-1}. Gaseous water was preferred rather than liquid water for methane/CO formation as compared to water photoreduction to H_2. Pt, Pd, Au, Rh, Ag, Ni, Cu, Au_3Cu alloy, I, MgO, RuO_2, graphene, g-C_3N_4, Cu-containing dyes, and Cu-containing metal-organic frameworks (MOFs) were effective to assist the CO_2 photoreduction using TiO_2 to methane (or CO, methanol, ethane) at rates of 1.4–160 μmol h^{-1} g_{cat}^{-1}. Metals of greater work function were preferred. By depositing as minimal thin photocatalyst film, the rates increased to 32–2200 μmol h^{-1} g_{cat}^{-1}. The importance of crystal face of TiO_2 nanofiber was suggested. As for semiconductors other than TiO_2, ZnO, Zn_6Ti layered double hydroxide (LDH), Mg_3In LDH, $KTaO_3$, $In(OH)_3$, graphene, graphene oxide, g-C_3N_4, CoTe, ZnO,

In Advances in CO2 Capture, Sequestration, and Conversion; He, et al.;
ACS Symposium Series; American Chemical Society: Washington, DC, 2015.

ZnTe, $SrTiO_3$, $ZnGa_2O_4$, Zn_2GeO_4, Zr–Co–Ir oxides, Nb_2O_5, $HNbO_3$, $NaNbO_3$, $InNbO_4$, NiO, Co_3O_4, Cu_2O, AgBr, carbon nanotube, and the composites of these were reported to form methane, CO, methanol, acetaldehyde from CO_2 and water at rates of 0.15–300 μmol h^{-1} g_{cat}^{-1} that were comparable to rates using promoted TiO_2. The band energy designs comprising appropriate conduction band for CO_2 reduction and valence band for water oxidation were made progresses in these semiconductors and semiconductor junctions in the three years. If H_2 was used as a reductant, Ni/SiO_2-Al_2O_3 formed methane at 423 K under pressurized $CO_2 + H_2$ at a rate of 55 mmol h^{-1} g_{cat}^{-1}. This rate was not enabled by heating the system under dark, suggesting photoactivated reaction followed by thermally-assisted reaction(s) via Ni–H species. As pure photocatalytic reactions from $CO_2 + H_2$, methanol formation rates were improved up to 0.30 μmol h^{-1} g_{cat}^{-1} by the doping of Ag/Au nanoparticles, $[Cu(OH)_4]^{2-}$ anions, and Cu-containing dyes to Zn–Ga LDH. Furthermore, sacrificial reductants, e.g. hydrazine, Na_2SO_3, methanol, triethanol amine, and triethyamine, were also utilized to form CO, formate, and methanol at rates of 20–2400 μmol h^{-1} g_{cat}^{-1} using semiconductor or MOF photocatalysts. Finally, similar to the integrated system of semiconductor photocatalyst for water oxidation and metal complex/enzyme catalyst for CO_2 (photo)reduction, two semiconductors (WO_3, Zn–Cu–Ga LDH) were combined on both side of proton-conducting polymer to form methanol at a rate of 0.05 μmol h^{-1} g_{cat}^{-1} from CO_2 and moisture. These promotion of photoconversion rates of CO_2 and new photocatalysts found in these three years have indicated the way beyond for a new energy.

Publication Date (Web): September 11, 2015 | doi: 10.1021/bk-2015-1194.ch001

Introduction

To enable carbon neutral cycle in modern industrial society, CO_2 conversion into fuels utilizing natural (sustainable) energy is one of the ideal methods. Carbon monoxide, methane, methanol, acetaldehyde, and ethane obtained from CO_2 are attractive products because they can be easily intergrated into the existing fuel and chemical technology. Although various review articles have been published dealing with the conversion of solar energy into fuels (*1*, *2*) and the conversion of CO_2 into fuels (*3*–*8*) until 2012, the researches and developments are more intensive during 2012 and 2015 for the target of CO_2 reduction into fuels that enables carbon neutral and suppresses the anthropogenic increase of CO_2 concentrations in the atmosphere.

In this chapter, recent advance based on various intensive researches between 2012 and 2015 in the CO_2 photoconversion into fuels is reviewed in hope for a new energy. Similar to previous review for studies before early 2012 (*4*), the scope

In Advances in CO2 Capture, Sequestration, and Conversion; He, et al.;
ACS Symposium Series; American Chemical Society: Washington, DC, 2015.

of this chapter is limited to semiconductor photocatalysis for the conversion of CO_2. Especially, some orders of increase for the CO_2 conversion rates and new photocatalysts are focused.

Photon Energy Conversion of CO_2 to Fuels with Water

1. TiO_2 Photocatalysts

1.1. Difference of Crystal Phases

The CH_4 formation rate was 0.19 μmol h^{-1} g_{cat}^{-1} in atomospheric pressure of CO_2 and moisture using TiO_2 (*9*). Under similar reaction conditions using some crystal phases of TiO_2, the CO formation rates were in the order

anatase (3.3 μmol h^{-1} g_{cat}^{-1}) > brookite (1.5 μmol h^{-1} g_{cat}^{-1}) > rutile (0.82 μmol h^{-1} g_{cat}^{-1}) (Table 1).[10] (1)

If the TiO_2 photocatalysts were preheated at 483 K in a flow of helium to make defects, the CO formation rates were in the order

brookite (17 μmol h^{-1} g_{cat}^{-1}) > anatase (10 μmol h^{-1} g_{cat}^{-1}) > rutile (4.0 μmol h^{-1} g_{cat}^{-1}) (2).

The order did not change if minor methane formation was added to the CO formation (Table 1). The binding of CO_2 on Ti^{3+} sites and the reduction of the bound CO_2^- species by O-defect sites were suggested (*10*).

$$CO_2 + Ti^{3+} \rightarrow Ti^{4+}–CO_2^- \quad (3)$$

$$CO_2^- + H^+ + e^- \rightarrow CO + OH^- \quad (4)$$

$$CO_2^- + Ti^{3+}–V_O–Ti^{4+} \rightarrow CO + Ti^{4+}–O^{2-}–Ti^{4+} \quad (5)$$

The activity order reported in reference (*11*) was consistent with equation 1. Furthermore, the anatase:brookite phase ratio was varied by changing the amout of urea used during the TiO_2 synthesis. The improved photoconversion of CO_2 suggested heterojunction effects of two crystalline phases.

anatase (75%)-brookite (25%) > P25 (anatase 80%, rutile 20%) > anatase > brookite (6)[11]

In Advances in CO2 Capture, Sequestration, and Conversion; He, et al.;
ACS Symposium Series; American Chemical Society: Washington, DC, 2015.

Publication Date (Web): September 11, 2015 | doi: 10.1021/bk-2015-1194.ch001

Publication Date (Web): September 11, 2015 | doi: 10.1021/bk-2015-1194.ch001

Table 1. Reported CO_2 Photoreduction Catalysts, Reaction Conditions, and the Formation Rates in Water/with Moisture Using TiO_2

Photocatalyst		*Reactants*		*T (K)*	*Light source*	*Reactor*	*Major product {formation rate ($\mu mol\ h^{-1}\ g_{cat}^{-1}$)}*	*Ref*
Brand name	*Amount (mg)*	*CO_2*	*H_2O*					
P25	10	Atmosph. *P*	Atmosph. *P*	Room *T*	100W Hg	Closed	CH_4 (0.19)	(*9*)
TiO_2 (anatase)	100	99 kPa	2.3 kPa		150 W solar simulator	Stainless steel, Flow	CO (3.3)	(*10*)
TiO_2 (rutile)							CO (0.82)	(*10*)
TiO_2 (brookite)							CO (1.5)	(*10*)
Defective TiO_2 (anatase)[a]							CO (10.4), CH_4 (2.5)	(*10*)
Defective TiO_2 (rutile)[a]							CO (4.0)	(*10*)
Defective TiO_2 (brookite)[a]							CO (17.0), CH_4 (1.9)	(*10*)
TiO_2 (anatase)	100	Atmosph. *P*	Saturated		150 W solar simulator	Stainless steel	CO (1.2)	(*11*)
TiO_2 (atatase:brookite =3:1							CO (2.1)	(*11*)
TiO_2 (brookite)							CO (0.7)	(*11*)
TiO_2 (anatase) {010}	100	101 kPa	Liq (1 mL)	293	300 W Hg	Pyrex	CH_4 (1.2)	(*12*)

Publication Date (Web): September 11, 2015 | doi: 10.1021/bk-2015-1194.ch001

Photocatalyst		*Reactants*		*T (K)*	*Light source*	*Reactor*	*Major product {formation rate ($\mu mol\ h^{-1}\ g_{cat}^{-1}$)}*	*Ref*
Brand name	*Amount (mg)*	*CO_2*	*H_2O*					
TiO_2 (anatase) {101}							CH_4 (0.74)	(*12*)
TiO_2 (anatase) {001}							CH_4 (0.19)	(*12*)
TiO_2 (anatase) {001}:{101} =11:89	100						CH_4 (0.15)	(*13*)
TiO_2 (anatase) {001}:{101} =58:42							CH_4 (1.4)	(*13*)
TiO_2 (anatase){001}: {101}=83:17							CH_4 (0.55)	(*13*)
P25	20	200 kPa	12.3 kPa	323	100 W Xe	Stainless steel	CO (1.2), CH_4 (0.38)	(*15*)
P25	20	200 kPa	Liq (4 mL)	323	100 W Xe	Stainless steel	CO (0.80), CH_4 (0.11)	(*15*)
TiO_2 (anatase)	500	Saturated	Liq (1 L)	303	UV lamp	Pyrex	CH_4 (11)	(*18*)
TiO_2 nanofiber	5	Atmosph. *P*	Satur. *P*		500 W Xe		CO (12), CH_4 (6)	(*20*)
TiO_2 (anatase)	Film	Atmosph. *P*	Satur. *P*	Room *T*	400 W Xe	Stainless steel, Flow	CO (240)	(*26*)

Continued on next page.

Publication Date (Web): September 11, 2015 | doi: 10.1021/bk-2015-1194.ch001

Table 1. (Continued). Reported CO_2 Photoreduction Catalysts, Reaction Conditions, and the Formation Rates in Water/with Moisture Using TiO_2

Photocatalyst		*Reactants*		*T (K)*	*Light source*	*Reactor*	*Major product {formation rate ($\mu mol\ h^{-1}\ g_{cat}^{-1}$)}*	*Ref*
Brand name	*Amount (mg)*	*CO_2*	*H_2O*					
P25	1.25 cm^2 Film	190 kPa	Satur. *P*	<333	1000W Xe	Aluminum	CH_4 (50)	(*27*)
TiO_2	100						CH_4 (0.52)	(*29*)

[a] Heated at 493 K for 90 min in a flow of He.

Publication Date (Web): September 11, 2015 | doi: 10.1021/bk-2015-1194.ch001

1.2. Difference of Crystal Facets

The reactivity order for facets in the CO_2 photoreduction to methane using anatase TiO_2 was reported

$$\{0\ 1\ 0\} > \{1\ 0\ 1\} > \{0\ 0\ 1\} \qquad (7)\ (\text{Table 1}).^{12}$$

The ratio of exposed {0 0 1} face versus thermodynamically stable {1 0 1} face was progressively varied between 11:89 and 83:17 for anatase TiO_2 utilizing the F^- as stabilizing agent for the {0 0 1} face (*13*). The conduction band (CB) and valence band (VB) for {0 0 1} face were calculated to position at slightly negative energy, thereby photoexcited electrons and holes move to {1 0 1} and {0 0 1} faces, respectively, similar to normal heterojunction of two kinds of semiconductors (Figure 1). The rates of CO_2 photoreduction to methane reached the maxium when the exposed face ratio of 58:41 (1.4 μmol h^{-1} g_{cat}^{-1}; Table 1).

Related to the study, hollow anatase TiO_2 dominating {1 0 1} face was synthesized and the methane formation rate using TiO_2 doped with 1 wt% RuO_2 was by a factor of 1.5 higher than general hollow anatase TiO_2 (Table 2) (*14*).

1.3. Difference of Reactant Water Phases

The photoreduction CO_2 (200 kPa) with gaseous water (12.3 kPa) and liquid water was compared (Figure 2) (*15*). Total formation rates of CO and methane using TiO_2 were improved by a factor of 1.7 with gaseous water (1.6 μmol h^{-1} g_{cat}^{-1}) rather than with liquid water.

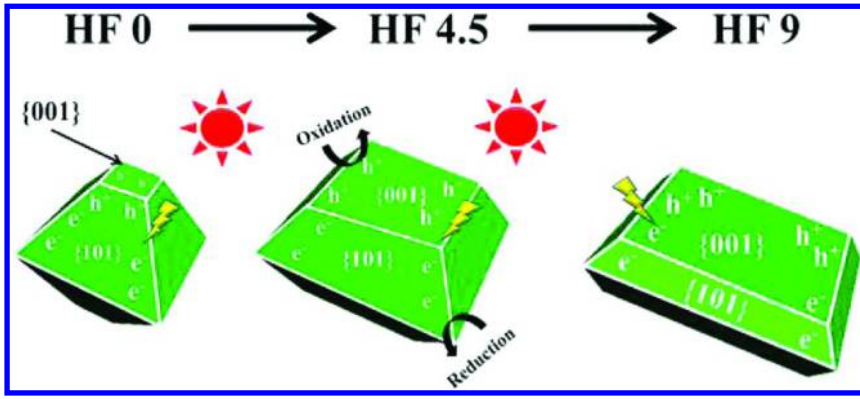

Figure 1. The control of {001} and {101} exposed face ratio for anatase TiO_2 for photocatalytic CO_2 reduction (13). Reproduced from reference listing (13). Copyright 2014, ACS.

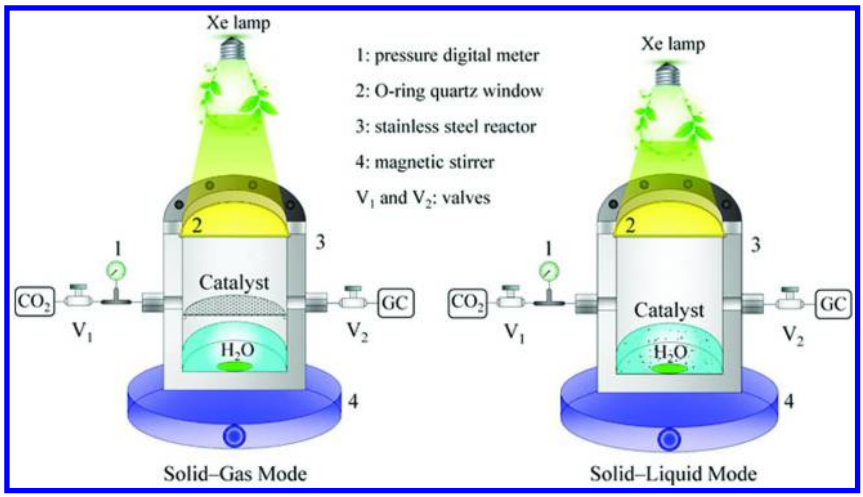

Figure 2. Reactors used for photocatalytic reduction of CO_2 with H_2O. Left: TiO_2 under moisture, right: TiO_2 immersed in liquid water. The distance between the Xe lamp and the catalyst was adjusted to be the same for the two reaction modes (15). Reproduced from reference listing (15). Copyright 2014, ACS.

2. Metal-Loaded TiO_2 Photocatalysts

2.1. Comparisions of Metal

The photoreduction CO_2 (200 kPa) with gaseous water (12.3 kPa) and liquid water was compared (Figure 2) (*15*). The improvement of total photoreduction rates of CO_2 using Pt-TiO_2 was by a factor of 2.9 (6.3 μmol h^{-1} g_{cat}^{-1}) (Table 2). This improvement was greater compared to the case for TiO_2 (Table 1). The comparison between solid–gas and solid–liquid interface reactions was also made for CO_2 photoreduction over layered double hydroxide (LDH) photocatalyst (*16*). The major pathways were CO_2 reduction to methanol and proton reductions to H_2, respectively.

Total photo-formation rates of methane and CO from CO_2 and gaseous water were in the order:

> Pt-TiO_2 (6.3 μmol h^{-1} g_{cat}^{-1}) > Pd-TiO_2 (5.4 μmol h^{-1} g_{cat}^{-1}) > Au-TiO_2 (4.6 μmol h^{-1} g_{cat}^{-1}) > Rh-TiO_2 (4.1 μmol h^{-1} g_{cat}^{-1}) > Ag-TiO_2 (3.8 μmol h^{-1} g_{cat}^{-1}) (Table 2)[15] (8)

following the order of work function (WF)

> Pt (5.12–5.93 eV) > Pd (5.22–5.6 eV) > Au (5.31–5.47 eV) > Rh (4.98 eV) > Ag (4.52–4.74 eV).[17] (9)

The selectivity for CO_2 photoreduction as compared to H_2O photoreduction to H_2 was 56% using TiO_2, but it decreased to 39–45% by the addition of Pt, Pd, Au, Rh, and Ag because the trapped electrons on these metals thermodynamically preferred to transfer to protons [$E° = 0 – 0.0591 \times$ pH V, versus standard hydrogen electrode (SHE)] rather than both CO_2 and protons ($E° = -0.32 – 0.0591 \times$ pH V, versus SHE) (*16*).

Solvothermal synthesis of anatase TiO_2 with Ni ions was done and the band gap slightly decreased from 3.16 eV for TiO_2 to 3.00 eV for Ni-TiO_2. Accordingly, photocatalytic production rate of methane from CO_2 increased from 11 (TiO_2) to 14 μmol h^{-1} g_{cat}^{-1} (Ni-TiO_2; Table 2) (*18*). Ni-TiO_2 prepared via sol–gel method, coated on monoliths, and threaded with quartz plate photocatalytically converted CO_2 into methanol at a rate of 20 μmol h^{-1} g_{cat}^{-1} (Table 2) (*19*). The reduction of CO_2 on TiO_2 and oxidation of water on NiO were assumed utilizing the p–n heterojunction.

The effects of Au and Pt loading on TiO_2 were also tested by preparing nanofiber TiO_2 by electrospinning by appling 15 kV between needle for sample precursors and collector (*20*). Under atmospheric pressure of CO_2 saturated with moisture irradiated by UV-visible light, the TiO_2 nanofiber formed CO and minor methane (Table 1). The selectivity changed to form major methane by the loading of Au (62 μmol h^{-1} g_{cat}^{-1}) and Pt (84 μmol h^{-1} g_{cat}^{-1}). The generation rate of mehane further improved to 110 μmol h^{-1} g_{cat}^{-1} using Au(0.25 atomic%)-Pt(0.75%)-TiO_2 nanofiber (Table 2). Au was metallic state whereas Pt was Pt^0, Pt^{2+}, and Pt^{4+} states in these photocatalysts. Electron trap effect due to greater WF for Pt and surface plasmon resonance (SPR) effect at 540–590 nm for Au worked synergetically in the Au(0.25 atomic%)-Pt(0.75%)-TiO_2 nanofiber. The relatively higher formation rates compared to reference (*15*) would be the difference of amount of photocatalyst used (5 mg (*20*) versus 20 mg (*15*)).

Doubly doping of Cu(0.1%) and I(10%) to TiO_2 was effective to photoconvert CO_2 into CO at a rate of 12 μmol h^{-1} g_{cat}^{-1} in comparison to that (0.7 μmol h^{-1} g_{cat}^{-1}) using undoped TiO_2 (Table 2) (*21*). Double-walled TiO_2 nanotube promoted Cu and Pt with the ratio 1:2 showed good hydrocarbon generation rates of 154–164 μmol h^{-1} g_{cat}^{-1} in pressurized CO_2 conditions (Table 2) (*22*).

The combination of graphene and TiO_2 was reported to effectively form ethane at a formation rate of 17 μmol h^{-1} g_{cat}^{-1} (*23*) and CO at a formation rate of 8.9 μmol h^{-1} g_{cat}^{-1} (*24*) from CO_2 and water (Table 2). Nitrogen-doped TiO_2 was combined with graphitic carbon nitride (g-C_3N_4) (*25*). The assembly prepared from urea and $Ti(OH)_4$ with the molar ratio of 7:3 at 853 K was the best to form CO at a rate of 12 μmol h^{-1} g_{cat}^{-1} (Table 2). While graphene is regarded as a media to shuttle electrons from TiO_2 (*23*), g-C_3N_4 (CB minimum: −1.12 V versus SHE) was considered as electron donor to TiO_2 (*25*).

Publication Date (Web): September 11, 2015 | doi: 10.1021/bk-2015-1194.ch001

Publication Date (Web): September 11, 2015 | doi: 10.1021/bk-2015-1194.ch001

Table 2. Reported CO_2 Photoreduction Catalysts, Reaction Conditions, and the Formation Rates in Water/with Moisture Using Metal, Metal Oxide, or Other Additive-Loaded TiO_2

Photocatalyst		*Reactants*		*T (K)*	*Light source*	*Reactor*	*Major product {formation rate ($\mu mol\ h^{-1}\ g_{cat}^{-1}$)}*	*Ref*
Brand name[a]	*Amount (mg)*	*CO_2*	*H_2O*					
RuO_2-hollow TiO_2 {101} major	100	60 kPa		Satur. *P*	300 W Xe	Teflon lined Stainless	CH_4 (1.7)	(*14*)
Pt(0.5%)-P25	20	200 kPa	12.3 kPa	323	100 W Xe	Stainless steel	CH_4 (5.2), CO (1.1)	(*15*)
Pd(0.5%)-P25							CH_4 (4.3), CO (1.1)	(*15*)
Au(0.5%)-P25							CH_4 (3.1), CO (1.5)	(*15*)
Rh(0.5%)-P25							CH_4 (3.5), CO (0.62)	(*15*)
Ag(0.5%)-P25							CH_4 (2.1), CO (1.7)	(*15*)
MgO(1.0%)-Pt(0.5%)-P25							CH_4 (11), CO (0.03)	(*15*)
Pt(0.5%)-P25	20	200 kPa	Liq (4 mL)	323	100 W Xe	Stainless steel	CH_4 (1.4), CO (0.76)	(*15*)
Ni-TiO_2 (anatase)	500	Saturated	Liq (1 L)	303	UV lamp	Pyrex	CH_4 (14)	(*18*)
Ni(1.5%)-TiO_2 monolith	200	Atmosph. *P*	Satur. *P*		200 W Hg	Pyrex	CH_3OH (20)	(*19*)
Au(1%[b])-TiO_2 nanofiber	5	Atmosph. *P*	Satur. *P*		500 W Xe		CH_4 (62), CO (40)	(*20*)

Publication Date (Web): September 11, 2015 | doi: 10.1021/bk-2015-1194.ch001

Photocatalyst		*Reactants*		*T (K)*	*Light source*	*Reactor*	*Major product {formation rate ($\mu mol\ h^{-1}\ g_{cat}^{-1}$)}*	*Ref*
Brand name[a]	*Amount (mg)*	*CO_2*	*H_2O*					
Pt(1%[b])-TiO_2 nanofiber	5						CH_4 (84), CO (16)	(*20*)
Au(0.25%[b])-Pt(0.75%[b])-TiO_2 nanofiber	5						CH_4 (110), CO (54)	(*20*)
Cu(0.1%)-I(10%)-TiO_2	100	Atmosph. *P*	Satur. *P*		450 W Xe (λ>400 nm)		CO (12)	(*21*)
Cu-Pt_2/TiO_2 Nanotube	6.7	99.9%	Satur. *P*	Solar Simulator, AM1.5	High *P* cell	CH_4 (120)	CO (12)	(*22*)
		1.0%	Satur. *P*				CH_4 (160)	(*22*)
graphene(2%)-TiO_2	100	Atmosph. *P*	Liq (0.4 mL)		300 W Xe arc	Glass	C_2H_6 (17), CH_4 (8.0)	(*23*)
graphene-TiO_2	10	Atmosph. *P*	Liq (0.4 mL)		300 W Xe arc		CO (8.9)	(*24*)
g-C_3N_4-N-TiO_2	100	Atmosph. *P*	Satur. *P*	303	300 W Xe arc	Teflon	CO (12)	(*25*)
Pt(0.21%[b])-TiO_2	Film	Atmosph. *P*	Satur. *P*	Room *T*	400 W Xe	Stainless steel, Flow	CH_4 (420)	(*26*)
Pt(0.94%[b])-TiO_2							CH_4 (1400)	(*26*)

Continued on next page.

Publication Date (Web): September 11, 2015 | doi: 10.1021/bk-2015-1194.ch001

Table 2. (Continued). Reported CO_2 Photoreduction Catalysts, Reaction Conditions, and the Formation Rates in Water/with Moisture Using Metal, Metal Oxide, or Other Additive-Loaded TiO_2

Photocatalyst		*Reactants*		*T (K)*	*Light source*	*Reactor*	*Major product {formation rate ($\mu mol\ h^{-1}\ g_{cat}^{-1}$)}*	*Ref*
Brand name[a]	*Amount (mg)*	*CO_2*	*H_2O*					
Pt(1.3%[b])-TiO_2							CH_4 (630)	(*26*)
Pt(2.5%[b])-TiO_2							CH_4 (63)	(*26*)
Au(1.5%)-P25	50	190 kPa	Satur. *P*	<333	1000W Xe	Aluminum	CH_4 (32)	(*27*)
Au(0.5%)-Cu(1%)-P25	50						CH_4 (44)	(*27*)
	25				125 W HP Hg		none	(*27*)
	25				150 W Xe (λ>400 nm)		CH_4 (0.89)	(*27*)
Cu(1.5%)-P25	50						CH_4 (40)	(*27*)
Au(1.5%)-P25	0.6 (1.25 cm^2)						CH_4 (210)	(*27*)
Au(0.5%)-Cu(1%)-P25							CH_4 (2200)	(*27*)
Cu(1.5%)-P25							CH_4 (280)	(*27*)
$Cu(bpy)_2$-P25	100	Gas	Gas		λ>400 nm		CH_4 (0.3)	(*28*)

Publication Date (Web): September 11, 2015 | doi: 10.1021/bk-2015-1194.ch001

Photocatalyst		*Reactants*		*T (K)*	*Light source*	*Reactor*	*Major product {formation rate ($\mu mol\ h^{-1}\ g_{cat}^{-1}$)}*	*Ref*
Brand name[a]	*Amount (mg)*	*CO_2*	*H_2O*					
$Cu_3(btc)_2$-core|TiO_2-shell	300	150 kPa	Liq (5 mL) not immersed	313	300 W Xe arc (λ>400 nm)	Stainless steel	CH_4 (2.6)	(*29*)
$Cu_3(btc)_2$	200						none	(*29*)

[a] The loading ratio is weight % except for [b]. [b] Atomic %.

2.2. Effective Thin Layer Photocatalysts

The CO_2 reduction rates using moisture and Pt-supported TiO_2 were improved by the deposition of photocatalyst thin layer (*26*). Ti(*i*-OC_3H_7)$_4$ was bubbled by N_2 gas and deposited on indium tin oxide (ITO)-coated glass maintained at 773 K. Then, platinum was sputtered on the TiO_2 film. Based on the images of field-emission scanning electron microscopy (FE-SEM), the TiO_2 film comprised single crystal rods grown on the glass with a typical column diameter of 250 nm and height of 1.5 μm and possessing an orientation of anatase {1 1 2} plane (Figure 3).

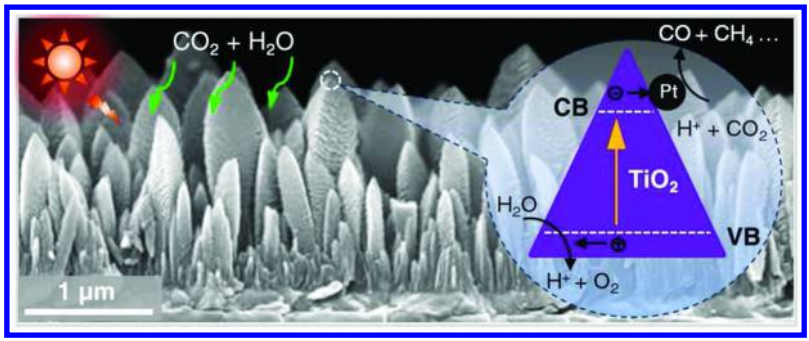

Figure 3. FE-SEM image of thin Pt-TiO_2 film deposited from Ti(i-OC_3H_7)$_4$ and Pt sputtering (26). Reproduced from reference listing (26). Copyright 2012, ACS.

Due to the high dispersion, the TiO_2 film produced CO at higher rate per unit amout of photocatalyst: 240 μmol h^{-1} g_{cat}^{-1} from CO_2 and moisture (Table 1). When the Pt atomic % was 0.21, 0.94, 1.3, and 2.5, the average Pt particle size was 0.63, 1.0, 1.3, and 1.9 nm, respectively. By the doping of Pt, the selectivity changed from CO to CH_4. This selectivity change was ascribed that sufficient electrons were accumulated in Pt and thermodynamically stable CH_4 was produced rather than CO. The CH_4 formation rates were maximal at 0.94 atomic % of Pt. By checking the TiO_2 surface coverage of Pt nanoparticles, the increase of methane formation rates until 0.94 atomic % of Pt was ascribed to the increased number of effective Pt sites. The decrease above 0.94 atomic % of Pt was ascribed to particle size effects of Pt. Namely, the reduction potential for Pt nanoparticles is similar to the CB of TiO_2 (≈0 V versus SHE) and electrons excited in CB of TiO_2 would shift to Pt (Figure 4, middle). In contrast, when the Pt nanoparticle size increase at the higher loading, the potential shift to +1.21 V versus SHE as the WF of Pt is 5.65 eV, thereby both electrons and holes tend to shift to Pt and recombine (Figure 4, right) (*26*).

The CO_2 reduction using moisture and metal-supported TiO_2 was further improved irradiated by 1000 W-Xe lamp, pressurized reactor cell (190 kPa of CO_2), and also the deposition of photocatalyst thin layer (0.6 mg per 1.25 cm^2) (*27*). Using sequentially-deposited and hydrogen-reduced (@673 K) Au(0.5 wt%)-Cu(1.0 wt%)-TiO_2 photocatalyst, methane was formed at a rate of 2200 μmol h^{-1} g_{cat}^{-1} (Table 2). In comparison to the performance of Au(1.5 wt%)-TiO_2 and Cu(1.5 wt%)-TiO_2 photocatalysts (210–280 μmol h^{-1} g_{cat}^{-1}), Au–Cu alloy phase detected in high-resolution transmission electron microscopy (HR-TEM) seemed to be specifically effective. The role of hydrogen-reduced Ti^{3+} sites was also suggested to donate electrons to CO_2.

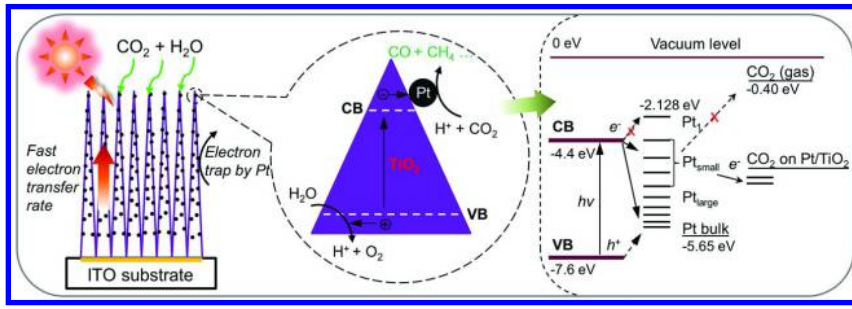

Figure 4. CO_2 photoreduciton mechanism using Pt-TiO_2 nanostructured film. The photogenerated electrons move fast inside the highly-oriented TiO_2 single crystals and flow to the Pt nanoparticles, where the reduction reaction occurs to convert CO_2 into CO or CH_4 (middle) (26). Reproduced from reference listing (26). Copyright 2012, ACS.

Using 125-W high-pressure Hg and 150-W Xe lamps (with cutoff filter of λ > 400 nm) for ultraviolet (UV) and visible irradiations, respectively, for Au-Cu-TiO_2 photocatalyst, no product and methane only were formed, respectively (Table 2) (*27*). Thus, SPR (the wavelength 570–580 nm) effect of Au in visible light region was suggested to transfer the hot electrons to Cu sites (Figure 5). Carbene pathway was proposed based on Fourier transform infrared (FTIR) rather than formaldehyde pathway (Scheme 1) (*5*).

Publication Date (Web): September 11, 2015 | doi: 10.1021/bk-2015-1194.ch001

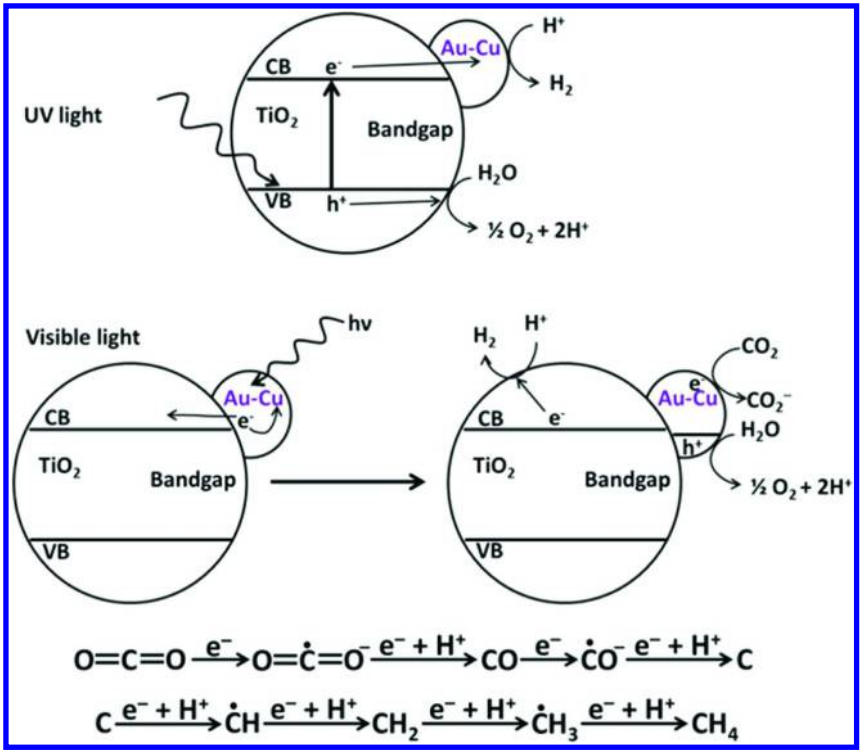

Figure 5. Proposed photocatalytic reaction mechanism of CO_2 reduction with moisture using Au(0.5 wt%)-Cu(1.0 wt%)-TiO_2 photocatalyst (27). Reproduced from reference listing (27). Copyright 2014, ACS.

Publication Date (Web): September 11, 2015 | doi: 10.1021/bk-2015-1194.ch001

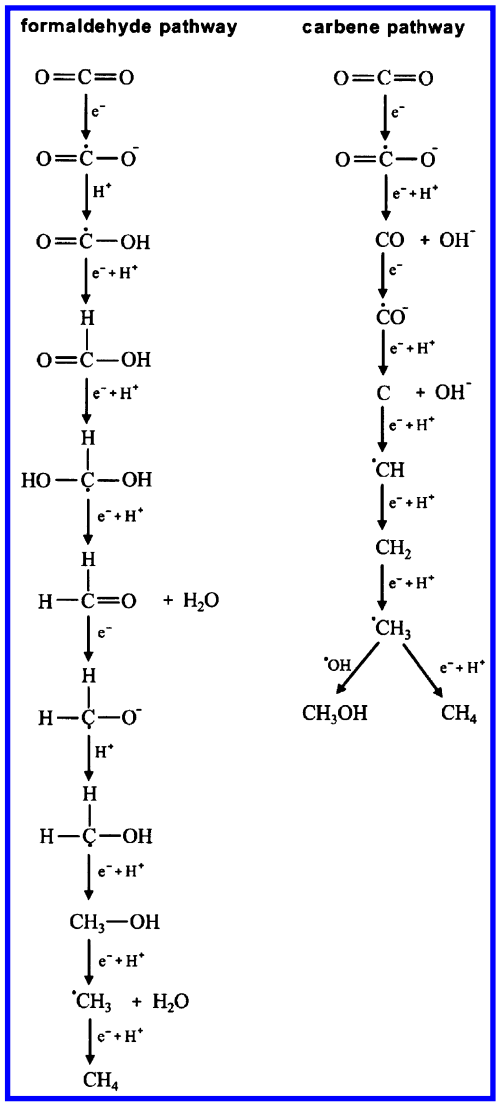

Scheme 1. Two proposed mechanisms for the photoreduction of CO_2 to methane: formaldehyde (left) and carbine pathways (right) (5). Reproduced from reference listing (15). Copyright 2013, John Wiley and Sons.

Publication Date (Web): September 11, 2015 | doi: 10.1021/bk-2015-1194.ch001

3. Metal Oxide or Metal-Organic Framework (MOF)-Loaded TiO_2 Photocatalysts

The Pt-TiO_2 photocatalyst in previous section was further doped with MgO (*15*). It became methane selective and total formation rate of methane and CO (11 μmol h^{-1} g_{cat}^{-1}) increased by a factor of 1.8 compared to that using Pt-TiO_2 (Table 2). Doped MgO layer would help CO_2 chemisorption over the catalyst and improve the selectivity for CO_2 reduction versus proton reduction. The Cu bipyridyl (bpy) dye to TiO_2 also promoted the photoreduction of CO_2 to methane at a rate of 0.3 μmol h^{-1} g_{cat}^{-1} (Table 2) (*28*).

The assembly of TiO_2 with MOF was also reported (*29*). $Cu_3(btc)_2$ (btc = benzene-1,3,5-tricarboxylate) microcrystals synthesized in the presence of polyvinylpyrrolidone were mixed with tetrabutyl titanate in ethanol and then in HF aqueous solution. By heating at 453 K for 12 h, anatase-phase TiO_2 shells of mean thickness of ~200 nm over the $Cu_3(btc)_2$ cores were formed (Figure 6).

Methane was formed using $Cu_3(btc)_2$-core|TiO_2-shell from CO_2 and water irradiated by visible light (λ > 400 nm) at a rate of 2.6 μmol h^{-1} g_{cat}^{-1}, much higher than than the sum of rates using each component (0.52 and ~0 μmol h^{-1} g_{cat}^{-1}; Tables 1, 2). Exclusive selectivity to methane rather than H_2 was also claimed, probably due to high electron density in the core-shell structure for the eight electron reduction to methane. A 1-ps build-up time in the transient absorption (TA) spectroscopy for the $Cu_3(btc)_2$-core|TiO_2-shell suggested electron transfer/relaxation from CB of TiO_2 to the interface state with $Cu_3(btc)_2$ (*29*).

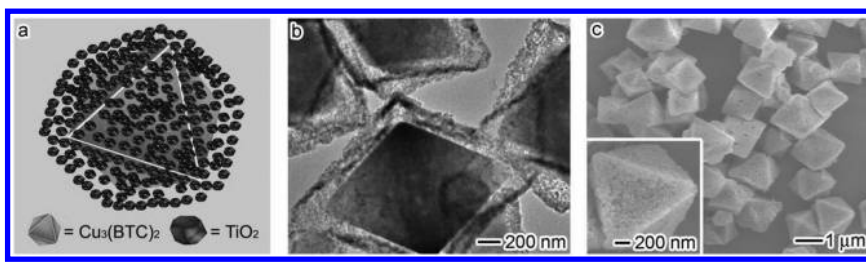

Figure 6. (a) Core–shell structure, (b) TEM, and (c) SEM images of $Cu_3(btc)_2$@TiO_2 (29). Reproduced from reference listing (29). Copyright 2014, John Wiley and Sons.

4. Semiconductor Photocatalysts Other Than TiO_2

4.1. Photocatalysts Comprising Single Compound

4.1.1. Metal Oxides and Hydroxides

By the irradiation of deep UV light at 185 nm from Hg lamp and using the synthetic quartz windows for the reactor (Figure 7), CO_2 (9.6 kPa) was converted into CH_4 with saturated moisture at a rate of 2.1 μmol h^{-1} for 13.9 h *in the absence of catalyst* (Table 3). It was suggested that water photolysis was the exclusive

In Advances in CO2 Capture, Sequestration, and Conversion; He, et al.;
ACS Symposium Series; American Chemical Society: Washington, DC, 2015.

hydrogen source for the CO_2 conversion (see *Photon energy conversion of CO_2 to fuels with hydrogen or sacrificial reducing agents, section 1*). The conversion of CO_2 was accelerated (7.7 μmol h^{-1}; Table 3) in the presence of Zn_6Ti LDH (100 mg), but the addition of MgO, TiO_2, CeO_2, or HY-zeolite rather reduced the photocomversion rates of CO_2 (*30*).

A series of LDHs of $[Ni_3M^{III}(OH)_8]_2CO_3{\cdot}mH_2O$, $[Mg_3M^{III}(OH)_8]_2CO_3{\cdot}mH_2O$, and $[Zn_3M^{III}(OH)_8]_2CO_3{\cdot}mH_2O$ (M^{III} = Al, Ga, and In) was tested for CO_2 photoreduction in water (*31*). $[Mg_3M^{III}(OH)_8]_2CO_3{\cdot}mH_2O$ was relatively active, e. g. $[Mg_3In(OH)_8]_2CO_3{\cdot}mH_2O$ produced CO and O_2 at the formation rates of 3.2 and 17 μmol h^{-1} g_{cat}^{-1}, respectively (Table 3). $[Mg_3M^{III}(OH)_8]_2CO_3{\cdot}mH_2O$ was selective to form hydrogen whereas $[Ni_3M^{III}(OH)_8]_2CO_3{\cdot}mH_2O$ was relatively selective to CO formation. The affinity of the surface with CO_2 may be related.

Hexagonal nanoplate-textured micro-octahedron Zn_2SnO_4 as large as a few microns was synthesized and tested for CO_2 photoreduciton with 0.4 mL of water (*32*). Due to its small (quantum) size, the band gap was relative wide (3.87 eV) in which the VB maximum at 2.7 eV and CB minimum at −1.17 eV. The methane formation rate increased from 4.8 to 35 ppm h^{-1} g_{cat}^{-1} by loading of 1 wt% of Pt and 1 wt% of RuO_2 to nanoplate-textured micro-octahedron Zn_2SnO_4. $KTaO_3$ photocatalytically reduced CO_2 with water irradiated by Xe arc lamp to form CO at a rate of 0.34 μmol h^{-1} g_{cat}^{-1} (Table 3) (*33*).

Mesoporous $In(OH)_3$ photoproduced methane from CO_2 and water at a rate of 0.8 μmol h^{-1} g_{cat}^{-1} (Table 3). The rate was by 20 times greater thant that using $In(OH)_3$ without mesoporous structure due to the difference of specific surface area and pore volume (*34*). Monoclinic $Bi_6Mo_2O_{15}$ sub-nanowires photocatalyzed CO_2 to methane and the rate was maximal by the preheating at 1073 K. Surface oxygen vacancy created by the heating was considered as an electron trap (*35*).

Figure 7. Left: Photoreactor composed by 185 nm-Hg lamp (1), synthetic quartz windows (2), and gas chamber (3). Right: Upper view showing the shallow bed of the photocatalyst placed in the photoreactor (30). Reproduced from reference listing (30). Copyright 2012, ACS.

Publication Date (Web): September 11, 2015 | doi: 10.1021/bk-2015-1194.ch001

Publication Date (Web): September 11, 2015 | doi: 10.1021/bk-2015-1194.ch001

Table 3. Reported CO_2 Photoreduction Catalysts, Reaction Conditions, and the Formation Rates in Water/with Moisture Using Semiconductor Photocatalysts Other Than TiO_2

Photocatalyst		*Reactants*		*T (K)*	*Light source*	*Reactor*	*Major product {formation rate ($\mu mol\ h^{-1}\ g_{cat}^{-1}$)}*	*Ref*
Brand name	*Amount (mg)*	*CO_2*	*H_2O*					
No catalyst	—	9.6 kPa	Satur. *P*	338	Hg (185, 254 nm)	Quartz	CH_4 (2.1[a])	(*30*)
KY-zeolite	500						CH_4 (3.1)	(*30*)
Zn_6Ce LDH	500						CH_4 (4.3)	(*30*)
Zn_6Ti LDH	500						CH_4 (3.3)	(*30*)
Zn_6Ti LDH	100						CH_4 (77)	(*30*)
Mg_3In LDH	100	500 μmol	Liq (4 mL)		200 W Hg-Xe	Quartz	CO (3.2)	(*31*)
$KTaO_3$	100	Atmosph. *P*	Liq (6 mL)	300 W Xe arc	Borosilicate	CO (0.34)	(*33*)	
Pt(0.5 %)-$In(OH)_3$	200	80 kPa	Liq (2–3 mL)		300 W Xe arc	Circulated	CH_4 (0.8)	(*34*)
Graphene Oxide	200	101 kPa	Satur. *P*	298	300 W halogen	Stainless	CH_3OH (0.17)	(*36*)
g-C_3N_4 (bulk)	20	60 kPa	Liq (0.1 mL)		300 W Xe	Teflon-lined	CH_3CHO (3.9)	(*37*)
g-C_3N_4 (nanosheet)							CH_4 (4.8)	(*37*)
CoTe	—	124 kPa	Satur. *P*	288	300 W Xe (λ > 420 nm)	Quartz	CH_4 (5.0)	(*38*)

Publication Date (Web): September 11, 2015 | doi: 10.1021/bk-2015-1194.ch001

Photocatalyst		*Reactants*		*T (K)*	*Light source*	*Reactor*	*Major product {formation rate ($\mu mol\ h^{-1}\ g_{cat}^{-1}$)}*	*Ref*
Brand name	*Amount (mg)*	*CO_2*	*H_2O*					
ZnTe(3.4%)-ZnO	10	Saturated	Liq (80 mL)	288	300 W Xe arc ($\lambda > 420$ nm)	Quartz	CH_4 (44)	(*39*)
ZnTe(25%)-$SrTiO_3$	20	Atmosph. *P*	Satur. *P*		300 W Xe arc ($\lambda > 420$ nm)	Quartz	CH_4 (2.4)	(*40*)
$ZnGa_2O_4$	100	Atmosph. *P*	Liq (0.4 mL)		300 W Xe arc	Glass	CH_4 (0.26)	(*41*)
$ZnGa_2O_4$:Zn_2GeO_4 (4.5:1)	100						CH_4 (3.9)	(*41*)
Zr-Co-Ir-SBA-15	5	101 kPa	13 Pa		355 nm laser		CO (1.7)	(*45*)
Pt(0.5%)-c-$NaNbO_3$	100	80 kPa	Satur. *P*		300 W Xe arc	Pyrex	CH_4 (4.9), CO (0.82)	(*46*)
Pt(0.5%)-o-$NaNbO_3$	100						CH_4 (2.5)	(*46*)
Pt(0.4%)-Nb_2O_5	100	89 kPa	12 kPa	333	350 W Xe	Quartz	CH_4 (0.15)	(*47*)
Pt(0.4%)-HNb_3O_8	100						CH_4 (0.47)	(*47*)
Pt(0.4%)-SiO_2-HNb_3O_8	100						CH_4 (2.9)	(*47*)
Pt(0.4%)-SiO_2 pillar-HNb_3O_8	100	81 kPa	20 kPa				CH_4 (3.8)	(*47*)

Continued on next page.

Publication Date (Web): September 11, 2015 | doi: 10.1021/bk-2015-1194.ch001

Table 3. (Continued). Reported CO_2 Photoreduction Catalysts, Reaction Conditions, and the Formation Rates in Water/with Moisture Using Semiconductor Photocatalysts Other Than TiO_2

Photocatalyst		*Reactants*		*T (K)*	*Light source*	*Reactor*	*Major product {formation rate ($\mu mol\ h^{-1}\ g_{cat}^{-1}$)}*	*Ref*
Brand name	*Amount (mg)*	*CO_2*	*H_2O*					
$InNbO_4$	140	Saturated	0.2M $KHCO_3$		500 W halogen	Pyrex	CH_3OH (1.4)	(*48*)
NiO(0.5%)-$InNbO_4$	140						CH_3OH (1.6)	(*48*)
Co_3O_4(1.0%)-$InNbO_4$	140						CH_3OH (1.5)	(*48*)
Pt-o-$NaNbO_3$	50	Atmosph. *P*	Liq (4 mL)		300 W Xe arc (λ > 420 nm)	Pyrex vessel	none	(*49*)
Pt-g-C_3N_4							CH_4 (0.8)	(*49*)
Pt-g-C_3N_4/o-$NaNbO_3$							CH_4 (6.4)	(*49*)
ZnO-g-C_3N_4	10	400 kPa	Liq (4 mL)	353	500 W Xe (λ > 420 nm)	Stainless steel	CO (29)	(*50*)
Pt(0.5%)-red P-g-C_3N_4	20	Atmosph. *P*	Liq (0.2 mL)		500 W Xe arc		CH_4 (300)	(*51*)
g-C_3N_4							CH_4 (0.26)	(*52*)
graphene (15%)-g-C_3N_4							CH_4 (0.59)	(*52*)

Publication Date (Web): September 11, 2015 | doi: 10.1021/bk-2015-1194.ch001

Photocatalyst		*Reactants*		*T (K)*	*Light source*	*Reactor*	*Major product {formation rate ($\mu mol\ h^{-1}\ g_{cat}^{-1}$)}*	*Ref*
Brand name	*Amount (mg)*	*CO_2*	*H_2O*					
RGO(0.5%)-Cu_2O	500	Atmosph. *P*	Liq (3 mL)		150 W Xe	Glass	CO (0.43)	(*53*)
Ag/AgBr/ CNT	500	7.5 MPa	0.2M $KHCO_3$ (100 mL)		150 W Xe (λ > 420 nm)	Stainless steel	CH_4 (30), CH_3OH (18), CO (8.0)	(*54*)

[a] μmol of CH_4 h^{-1}.

Publication Date (Web): September 11, 2015 | doi: 10.1021/bk-2015-1194.ch001

4.1.2. Carbon-Related Materials

Graphene oxide (GO) with lateral dimension of several micrometers and thickness of 1–3 nm was exfoliated from graphite in acids and tested for CO_2 reduction with moisture irradiated by UV–visible light (*36*). The methanol formation rate (0.17 μmol h^{-1} g_{cat}^{-1}) was by a factor of 5.8 higher compared to one using TiO_2 under the reaction conditions (Table 3). The CB minimum estimated for GO (−0.79 V versus SHE) would bend to nearly close to reduction potential from CO_2 to methanol (−0.38 V versus SHE) if the GO with electron-drawing oxygenated functional groups was p-type semiconductor.

Bulk g-C_3N_4 with the Bruanuer–Emmett–Teller surface area (S_{BET}) of 50 m^2 g^{-1} was compared to g-C_3N_4 nanosheet with S_{BET} of 306 m^2 g^{-1} (*37*). Clear difference of selectivity to acetaldehyde and methane (−0.24 V) was observed and one of the major reasons was the difference of band gap (BG), 2.77 and 2.97 eV, respectively. More negative electron potential for the latter sample was considered to effectively reduce CO_2 via glyoxal to acetaldehyde and then to methane (*5*).

4.1.3. Other Materials

As one of the metal calcogenide compounds, the CB of hydrothermally-synthesized CoTe positioned at relatively negative potential and the BG was 2.05 eV. The methane formation rate using CoTe was 5.0 μmol h^{-1} g_{cat}^{-1} (Table 3) (*38*).

4.2. Assembled Photocatalysts

4.2.1. Zn, Cu-Containing Compounds

The doping of high-potential ZnTe to ZnO was reported (*39*). The BG of ZnTe was 2.2 eV and the CB minimum was at −1.8 V versus SHE. Due to the excited electrons to CB of ZnO and holes remained at VB of ZnTe, methane was formed irradiated by visible light ($\lambda > 420$ nm). ZnTe was a sensitizer for visible light, but the reason of quite high formation rate (44 μmol h^{-1} g_{cat}^{-1}; Table 3) from CO_2 to methane via electron transfer from CB of ZnO is not known and control reaction tests are needed. High-potential ZnTe was also combined with $SrTiO_3$ and formed methane from CO_2 and moisture (Table 3) (*40*).

The performance of CO_2 photoreduction to methane using cubic spinel $ZnGa_2O_4$ was improved by mixing pseudo cubic inverse spinel Zn_2GeO_4 from 0.26 to 3.9 μmol h^{-1} g_{cat}^{-1} (Table 3) (*41*). One of the reasons was suggested to be the reduction of band gap from 4.45 to 4.18 eV to utilize wider spectrum of light (*42*).

Zn-doped (100)-oriented p-GaP was utilized for CO_2 photoreduction with water irradiated by a laser light at 532 nm. To prevent the photocorrosion of GaP, atomic layer deposition of Ti choloride and water vapor was performed to

create 1–10 nm-thick TiO_2 layers over GaP (*43*). Methanol was formed on the GaP photoelectrode covered with 5 nm-thick TiO_2 at a rate of 1.2 μmol h^{-1} cm_{cat}^{-2} at the applied voltage of −0.5 V (versus SHE) in 0.5 M NaCl and 10 mM pyridine solution. Thin TiO_2 layer seemed not just the passivation layer to transmit the light at 532 nm, but also to serve to form p–n junction for charge separation (*43*).

Cu_2O electrodeposited on CuO nanorods perpendicularly grown on Cu foil photoreduced CO_2 in CO_2-saturated 0.1 M Na_2SO_4 aqueous solution at the electric potential smaller than 0.37 V (versus SHE) irradiated by simulated AM 1.5 light. The geometry of CuO nanorod and Cu_2O shell should facilitate charge separation irradiated by light and CO_2 reduction on CuO (*44*).

4.2.2. Zr, Co, Ir-Containing Compounds

Stepwise synthesis of photoreduction sites of CO_2 and photooxidation sites of water in single sample was reported. Zirconocene dichloride was reacted with an ordered mesoporous SiO_2, SBA-15, to form Zr-SBA-15 (*45*). The Co precursor preferably reacted with Zr–OH group to form links of Zr^{IV}–O–Co^{II} in Zr(1.1 mol%)-Co(0.7 mol%)-SBA-15. Ir^{III} acetylacetonate was photodeposited on Zr-Co-SBA-15, but not on Zr-SBA-15 and Co-SBA-15, suggesting electron transfer by the irradiation of 355 nm laser light from Co to Zr (Zr^{III}–O–Co^{III}) coupled with the electron transfer from Ir to Co ($Ir^{III}\cdots$O–$Co^{II} \rightarrow Ir^{IV}$–O–$Co^{II}$). Though the Ir^{IV}–O–Co^{II} link may be lost upon calcination later than the electrodeposition, Zr^{IV}–O–Co^{II} and IrO_x nanocluster were formed in the vicinity over SBA-15.

The CO formation at a rate of 1.7 μmol h^{-1} g_{cat}^{-1} under 101 kPa of CO_2 and 13 Pa of water irradiated by laser at 355 nm (127 mW cm^{-2}; Table 3) was ascribed to water oxidation on IrO_x nanocluster and the resultant electron transfer to neighboring Co^{II} and then to Zr^{IV} (*45*). Spectroscopic insight for the interaction of Zr^{III} and CO_2 would be expected.

4.2.3 Nb-Containing Compounds

Two phases of perovskite-type $NaNbO_3$ doped with 0.5 wt% of Pt were tested (Table 3) (*46*). One is cubic $NaNbO_3$ (c-$NaNbO_3$) and the other is more common orthorhombic $NaNbO_3$ (o-$NaNbO_3$). The Pt-c-$NaNbO_3$ photocatalyst produced major methane (4.9 μmol h^{-1} g_{cat}^{-1}) and minor CO (0.82 μmol h^{-1} g_{cat}^{-1}) from gaseous CO_2 and moisture, and the methane formation rate was by a factor 2.0 greater compared to that using Pt-o-$NaNbO_3$. Two reasons of the difference was suggested to be (1) minor difference of band gap value and (2) homogeneous frontier orbital [highest occupied molecular orbital (MO), lowest unoccupied MO] distribution in *x*, *y*, *z*-direction for c-$NaNbO_3$ versus the distorted distribution in *z*-direction for o-$NaNbO_3$.

Pt-photodeposited layered HNb_3O_8 was superior to Pt-photodeposited layered KNb_3O_8 for CO_2 photoreduction at 333 K (*47*). The methane formation rates were improved to 3.8 μmol h^{-1} g_{cat}^{-1} when the moisture pressure increased from 12 to

In Advances in CO2 Capture, Sequestration, and Conversion; He, et al.;
ACS Symposium Series; American Chemical Society: Washington, DC, 2015.

20 kPa and also SiO_2 pillared between the layers of HNb_3O_8 (Table 3). However, not O_2 or H_2 was detected in the study, suggesting incomplete photocatalytic cycle.

For $InNbO_4$, the doping of NiO (0.5%) or Co_3O_4 (1.0%) slightly promoted the methanol photoformation (1.6–1.5 μmol h^{-1} g_{cat}^{-1}) from CO_2 compared to unpromoted one (1.4 μmol h^{-1} g_{cat}^{-1}; Table 3) (*48*).

4.2.4 C-Containing Compounds

o-$NaNbO_3$ nanowire was combined with polymeric g-C_3N_4 (*49*). Methane was photogenerated using Pt-g-C_3N_4/$NaNbO_3$ at a rate of 6.4 μmol h^{-1} g_{cat}^{-1} higher by a factor of 8 compard to that using Pt-g-C_3N_4 (Table 3). Pt-o-$NaNbO_3$ was inert in the conditions. The advantage of Pt-g-C_3N_4/$NaNbO_3$ was ascribed to the chage separation at the heterojunction of p-type g-C_3N_4 to attract holes and n-type $NaNbO_3$ to attract excited electrons.

g-C_3N_4 was also combined with ZnO (*50*) and red-P (*51*) to form heterojunction and converted CO_2 into major CO and major methane at rates of 29 and 300 μmol h^{-1} g_{cat}^{-1}, respectively. The reason of quite high methane formation rate using red-P-g-C_3N_4 is unclear and control reaction tests are needed.

The disadvantages, low electric conductivity and rapid recombination of photogenerated electrons and holes, of 2-dimensional(D) g-C_3N_4 for photocatalysis were solved by assembling graphene with g-C_3N_4 (*52*). The electrons at N 2p was photoexcited to C 2p (CB: −1.42 V versus SHE) in g-C_3N_4 and could move to conducting network graphene (Fermi level: −0.08 V versus SHE). Thus, CO_2 photoreduction rate into methane was boosted from 0.26 μmol h^{-1} g_{cat}^{-1} (g-C_3N_4) to 0.59 μmol h^{-1} g_{cat}^{-1} for graphene (15 wt%)-g-C_3N_4 assembly (Table 3).

Cu_2O assembled with 0.5 wt% of reduced graphene oxide (RGO) was also reported. CO was produced from CO_2 and water at a rate of 0.43 μmol h^{-1} g_{cat}^{-1} (Table 3) (*53*). Similar to reference 44, negative potential of CB for Cu_2O (−1.44 V versus SHE, pH 0) should be advantageous for electron donation toward CO_2-derived species.

A part of Ag^+ of AgBr/carbon nanotube (CNT) was photoreduced to form Ag/AgBr/CNT (*54*). The photocatalyst was immersed in weak alkaline solution pressurized with 7.5 MPa of CO_2. Methane, methanol, and CO were formed at a total formation rate of 56 μmol h^{-1} g_{cat}^{-1} (Table 3). Longer CNT was preferable than shorter one probably due to better charge separation efficiency.

Photon Energy Conversion of CO_2 to Fuels with Hydrogen or Sacrificial Reducing Agents

1. Photon Energy Conversion of CO_2 to Fuels with Hydrogen

If oxidation of water produces O_2, protons, and electrons, utilizing natural light, photon energy conversion of CO_2 to fuels with hydrogen (H atom equivalent to a proton and an electron) is also important as a latter half cycle of artificial photosynthesis (*4*).

In Advances in CO2 Capture, Sequestration, and Conversion; He, et al.;
ACS Symposium Series; American Chemical Society: Washington, DC, 2015.

Publication Date (Web): September 11, 2015 | doi: 10.1021/bk-2015-1194.ch001

Publication Date (Web): September 11, 2015 | doi: 10.1021/bk-2015-1194.ch001

By the irradiation of deep UV light at 185 nm from Hg lamp and using synthetic quartz windows for the reactor, CO_2 (9.6 kPa) was converted into major CH_4 and minor CO with H_2 (45 kPa) at a rate of 4.5 μmol h^{-1} for 82 h *in the absence of catalyst* (Table 4) (*30*). This rate was faster than the photolysis of CO_2 with water (*see Photon energy conversion of CO_2 to fuels with water, section 4.1.1*; Table 3). Light of 185 nm was confirmed to be responsible for the photolysis of CO_2 rather than light of 254 nm from the Hg lamp.

High conversion of CO_2 with H_2 was reported using Ni/SiO_2-Al_2O_3 in similar reactor to Figure 7 at a methane formation rate of 55 mmol h^{-1} g_{cat}^{-1} (Table 4) (*55*). By the effects of high-power solar simulator and heat of reaction for CO_2 hydrogenation to methane (165 kJ mol^{-1}), the temperature reached 423 K and gas pressure would be some hundreds kPa. Control experiment at 453 K in dark formed methane at significantly lower rate of 8.9 μmol h^{-1} g_{cat}^{-1}. Thus, the photocatalytic reduction was photoactivated and accompanied by thermal catalytic step(s). Ni/SiO_2-Al_2O_3 when UV light was filtered showed similar activity to NiO irradiated by UV-visible light (13 mmol h^{-1} g_{cat}^{-1}; Table 4). The performance irradiated under UV-visible light was in the order

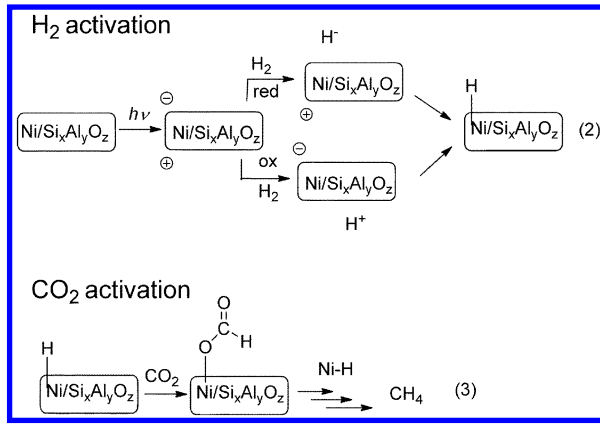

Scheme 2. Proposed reaction mechanism of photocatalytic CO_2 reduction with H_2 presumably assisted by later thermal catalytic step(s) using Ni/SiO_2-Al_2O_3 (55). Reproduced from reference listing (55). Copyright 2014, ACS.

Ni/SiO_2-Al_2O_3 > NiO (BG 3.5 eV) > Fe_2O_3 (BG 2.2 eV) > CoO (BG 2.6 eV) (10).

It was difficult to find the direct relationship between the reactivity and BG values or the conduction band level. Instead, formation of active Ni–H species was proposed by reducing/oxidizing H_2 to H^-/H^+ and reacting with Ni^+/Ni^-, respectively (Scheme 2) (*55*).

Publication Date (Web): September 11, 2015 | doi: 10.1021/bk-2015-1194.ch001

Table 4. Reported CO_2 Photoreduction Catalysts, Reaction Conditions, and the Formation Rates Using Various Semiconductors with Hydrogen

Photocatalyst		*Reactants*		*T (K)*	*Light source*	*Reactor*	*Major product {formation rate ($\mu mol\ h^{-1}\ g_{cat}^{-1}$)}*	*Ref*
Brand name	*Amount (mg)*	*CO_2*	*H_2*					
No catalyst	—	9.6 kPa	45 kPa	338 K	Hg (185, 254 nm)	Quartz	CH_4 (4.5[a])	(*30*)
Ni/SiO_2-Al_2O_3	250	3.7 mmol	17 mmol	<423	Solar simulator (AM1.5 filter)	Aluminum	CH_4 (55 000)	(*55*)
NiO							CH_4 (13 000)	(*55*)
Fe_2O_3							CO (7 200)	(*55*)
CoO							CO (2 500), CH_4 (1 600)	(*55*)
Ni/SiO_2-Al_2O_3	250	3.7 mmol	17 mmol		Solar simulator (λ > 420 nm)	Aluminum	CH_4 (13 000)	(*55*)
NiO							CH_4 (210), CO (170)	(*55*)
$Zn_3Ga\|CO_3$ LDH	100	2.3 kPa	21.7 kPa	<313	500 W Xe arc	Pyrex	CO (0.08), CH_3OH (0.05)	(*56*)
Ag(0.36%)-$Zn_3Ga\|CO_3$ LDH	100	2.3 kPa	21.7 kPa	<313	500 W Xe arc	Pyrex	CH_3OH (0.12), CO (0.10)	(*57*)
Au(4.1%)-$Zn_3Ga\|CO_3$ LDH	100	2.3 kPa	21.7 kPa	<313	500 W Xe arc	Pyrex	CO (0.20), CH_3OH (0.03)	(*57*)

Publication Date (Web): September 11, 2015 | doi: 10.1021/bk-2015-1194.ch001

Photocatalyst		*Reactants*		*T (K)*	*Light source*	*Reactor*	*Major product {formation rate ($\mu mol\ h^{-1}\ g_{cat}^{-1}$)}*	*Ref*
Brand name	*Amount (mg)*	*CO_2*	*H_2*					
CuPcTs-$Zn_3Ga|CO_3$ LDH	100	2.3 kPa	21.7 kPa	<313	500 W Xe arc	Pyrex	CO (0.11), CH_3OH (0.096)	(*58*)
$Zn_3Ga|Cu(OH)_4$ LDH	100	2.3 kPa	21.7 kPa	<313	500 W Xe arc	Pyrex	CH_3OH (0.30), CO (0.13)	(*60*)

[a] μmol of CH_4 h^{-1}.

Publication Date (Web): September 11, 2015 | doi: 10.1021/bk-2015-1194.ch001

A LDH $[Zn_3Ga(OH)_8]_2CO_3 \cdot mH_2O$ (m~4; Zn_3Ga) exhibited direct electronic transition and the BG value was 5.6 eV (*56*). This wide-BG LDH was combined with SPR of Ag and Au nanoparticles (Scheme 3) (*57*). The SPR peaks appeared in visible light region centered at 411 and 555 nm, respectively. By the irradiation of UV-visible light, the total formation rates of CO and methanol using Zn_3Ga LDH (0.13 μmol h^{-1} g_{cat}^{-1}) increased to 0.22 μmol h^{-1} g_{cat}^{-1} using Ag/Zn_3Ga LDH and to 0.23 μmol h^{-1} g_{cat}^{-1} using Au/Zn_3Ga LDH. The selectivity to methanol was also improved from 39 to 54 mol% (Table 4) by the doping of Ag, whereas the Au dope led to selective CO formation (13 mol%).

Ag/Zn_3Ga LDH and Cu phthalocyanine tetrasulfonate (PcTs)-doped Zn_3Ga LDH were active irradiated by visible light (λ > 420 nm; total formation rate 0.12 and 0.15 μmol h^{-1} g_{cat}^{-1}, respectively) (*57*, *58*). The mechanism could be explained by the electron shift due to SPR in Ag to wide-BG Zn_3Ga LDH then to CO_2-derived species (Scheme 3, right) and electron shift from wide-band gap Zn_3Ga LDH to LUMO of CuPcTs then to CO_2-derived species (Scheme 4). Conversely, as the WF of Au was larger than that for Ag (*17*), the electrons could not be supplied to the CB of LDH (Scheme 3, left). Thus, Au worked as electron trap from LDH irradiated by UV light and SPR in Au was ineffective for CO_2 photoreduction (*57*). The electron flows originating from SPR were in consistent with charge transfer mechanism reviewed previously (*59*).

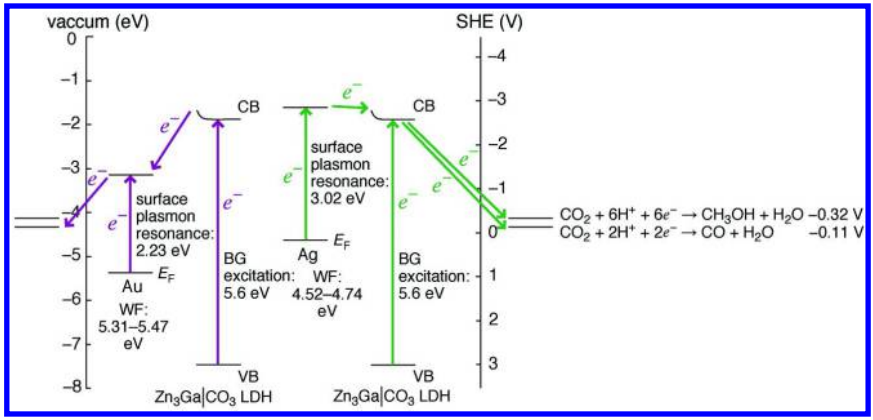

Scheme 3. The energy diagram and proposed electron flows in Ag/Zn_3Ga LDH (right) and Au/Zn_3Ga LDH (left) (57). Reproduced from reference listing (57). Copyright 2015, Elsevier.

Publication Date (Web): September 11, 2015 | doi: 10.1021/bk-2015-1194.ch001

The CO_2 photoreduction ability of $[Zn_{1.5}Cu_{1.5}Ga(OH)_8]_2CO_3{\cdot}mH_2O$ (Figure 8A) was also improved by the interlayer anion substitution by $[Cu(OH)_4]^{2-}$for CO_3^{2-} (Figure 8B) (*60*). Especially, methanol formation rates increased from 0.05 to 0.30 μmol h^{-1} g_{cat}^{-1} by the anion substitution (Table 4). X-ray absorption near-edge structure (XANES) was applied to monitor the diffusion of photogenerated electrons to active Cu^{II} sites as the 1s-3d pre-edge peak intensity (*61*). Electron diffusion to Cu sites was an order of magnitude faster in the direction of the cationic layers of $[Zn_{1.5}Cu_{1.5}Ga(OH)_8]_2CO_3{\cdot}mH_2O$ (580 μmol h^{-1} g_{cat}^{-1}; Figure 8A) than in the perpendicular direction to interlayer $[Cu(OH)_4]^{2-}$ in $[Zn_3Ga(OH)_8]_2[Cu(OH)_4]{\cdot}mH_2O$ (36 μmol h^{-1} g_{cat}^{-1}; Figure 8B) (*61*, *62*). With the information of FTIR, selective methanol formation mechanism via hydrogen carbonate (bicarbonate) and step-by-step reduction with proton and electron was proposed using $[Zn_3Ga(OH)_8]_2[Cu(OH)_4]{\cdot}mH_2O$ LDH (Scheme 5).

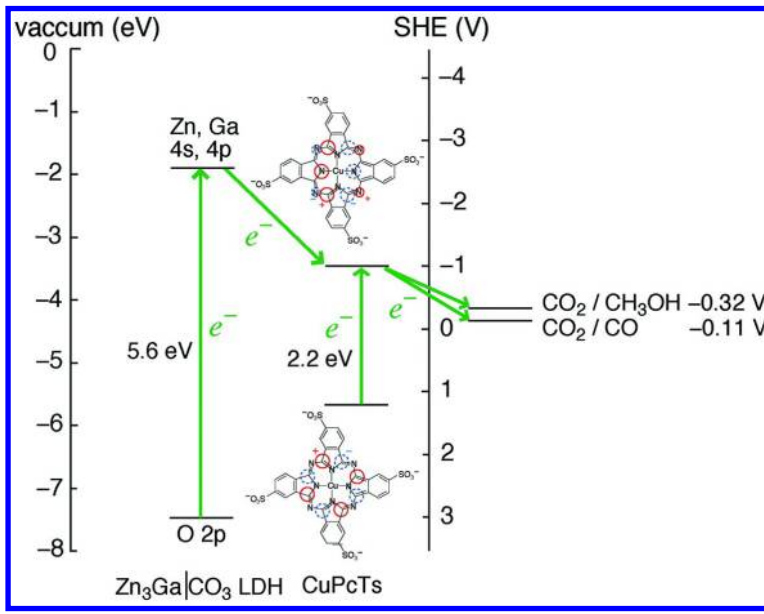

Scheme 4. The energy diagram and proposed electron flows in CuPcTs/Zn_3Ga LDH.

In Advances in CO2 Capture, Sequestration, and Conversion; He, et al.;
ACS Symposium Series; American Chemical Society: Washington, DC, 2015.

Publication Date (Web): September 11, 2015 | doi: 10.1021/bk-2015-1194.ch001

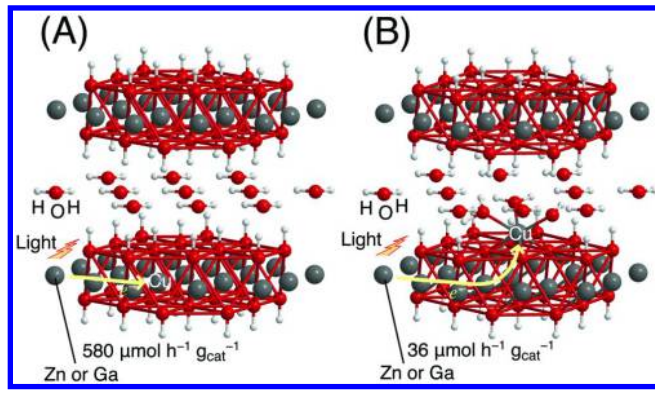

Figure 8. Structure of $[Zn_{1.5}Cu_{1.5}Ga(OH)_8]_2CO_3{\cdot}mH_2O$ ***(A)*** *and structure of $[Zn_3Ga(OH)_8]_2[Cu(OH)_4]{\cdot}mH_2O$* ***(B)****. Interlayer carbonates are not drawn in (A) for clarity (62). Reproduced from reference listing (62). Copyright 2014, High-Energy Accelerator Research Organization.*

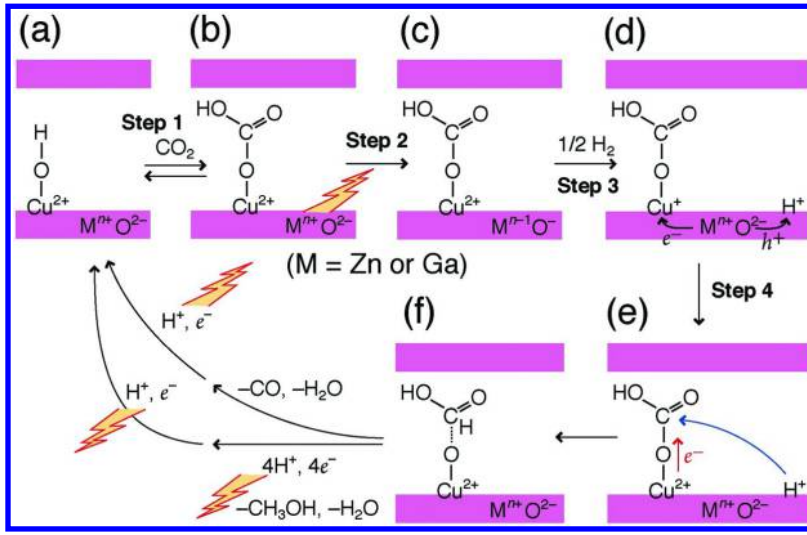

Scheme 5. Proposed photocatalytic cycle of CO_2 reduction to methanol or CO using LDH catalysts comprising Zn, Ga, and interlayer Cu sites (61). Reproduced from reference listing (61). Copyright 2014, Elsevier.

2. Photon Energy Conversion of CO_2 to Fuels with Other Sacrificial Reducing Agents than H_2

CO_2 photoreduction into major CO using Au_3Cu alloy on $SrTiO_3/TiO_2$ nanotubes and hydrous hydrazine was reported at a formation rate of 730 μmol h^{-1} g_{cat}^{-1} (Table 5) (*63*). Cuboid Cu_2O powder was superior (20 ppm h^{-1} g_{cat}^{-1}) to octahedral Cu_2O for CO_2 photoreduction to CO in water and the rate was by several times enhanced by the addition of 0.25 wt% of RuO_x using Na_2SO_3 as sacrificial reducing agent (*64*).

In Advances in CO2 Capture, Sequestration, and Conversion; He, et al.;
ACS Symposium Series; American Chemical Society: Washington, DC, 2015.

Na_2SO_3 was also used as sacrificial reducing agent, and the CO_2 pressure to water suspension of Au-TiO_2 was raised to 1.0 MPa at 298 K. The methane generation rate increased to 20 μmol h^{-1} g_{cat}^{-1} (Table 5) (*65*). Methanol was used as sacrificial reducing agent, and the generation rates of methyl formate from CO_2 was in the order using hexagonal $ZnIn_2S_4$ > cubic $ZnIn_2S_4$ > microspheric $ZnIn_2S_4$ (Table 5) (*66*).

The progress of MOF as photocatalysts for CO_2 reduction was fast in these three years. MIL-101(Fe) comprising Fe_3O clusters linked by terephthalates to form quasi-spherical cages produced formate at a rate of 150 μmol h^{-1} g_{cat}^{-1} in the presence of triethanol amine (TEOA) as reducing agent from dissolved CO_2 in acetonitrile irradiated by visible light ($420 < \lambda < 800$ nm; Table 5) (*67*). MIL-53(Fe) comprising chains of hydroxy corner-sharing FeO_6 octahedra linked by terephthalates to form 1D pores and MIL-88(Fe) comprising oxo-centered Fe_3O clusters linked by terephthalates to form 3D porous network were less active (74–23 μmol h^{-1} g_{cat}^{-1}) compared to MIL-101(Fe) (Table 5). The electron transfer from O^{2-} to Fe^{3+} irradiated by visible light was proposed as the first step for the CO_2 reduction.

When 2-aminoterephthalic acid was used for the syntheses of MOF's above, the generation rates of formate were improved to 450–75 μmol h^{-1} g_{cat}^{-1} compared to MIL's unfunctionalized by the amine group (150–23 μmol h^{-1} g_{cat}^{-1}; Table 5). Amine group significantly extended the UV absorption edge toward visible region, and proposed to create second electron transfer pass from NH_2 to Fe-O center. The flat band position for MIL-101(Fe), MIL-53(Fe), and MIL-88(Fe) were −0.52, −0.70, and −0.48 V, respectively, versus SHE. The values were clearly more negative than the reduction potential of CO_2 to formate (−0.28 V), however, the order of photocatalysis

$$\text{MIL-101(Fe)} > \text{MIL-53(Fe)} > \text{MIL-88(Fe)} \qquad (11)$$

was not correlated to the flat band potential (*67*).

A combination of Zn-containing MOF (called ZIF-8) and Zn_2GeO_4 was reported (*68*). In aqueous solution with 0.1 M Na_2SO_3 aqueous solution saturated with CO_2, methanol was photogenerated at a rate of 0.22 μmol h^{-1} g_{cat}^{-1} (Table 5). A Co-containing MOF, Co-ZIF-9, was tested with the aid of CdS photocatalyst and sacrificial reductant, TEOA irradiated by visible light (*69*). CO was formed at a rate of 2400 μmol h^{-1} g_{cat}^{-1} (Table 5). Co ions in ZIF-9 was suggested to received excited electrons in CdS.

5,10,15,20-Tetrakis(4-carboxyphenyl)porphyrin coordinated to Al^{3+} to form MOF. The methanol formation rate from CO_2 utilizing triethylamine (TEA; 38 ppm h^{-1} g_{cat}^{-1}) was improved by introducing Cu^{2+} to the porphyrin in the MOF (260 ppm h^{-1} g_{cat}^{-1}; Table 5) (*70*). The surface of GO was carboxylated and was functionalized with $–CH_2–COCl$ and then reacted with Co phthalocyanine tetrasulfonamide (*71*). Sensitization by CoPc and transferred electrons to GO were suggested to reduce CO_2 into methanol at a rate of 79 μmol h^{-1} g_{cat}^{-1} compared to 39 μmol h^{-1} g_{cat}^{-1} using unsensitized GO by using TEA as sacrificial reductant (Table 5).

Publication Date (Web): September 11, 2015 | doi: 10.1021/bk-2015-1194.ch001

In Advances in CO2 Capture, Sequestration, and Conversion; He, et al.;
ACS Symposium Series; American Chemical Society: Washington, DC, 2015.

Publication Date (Web): September 11, 2015 | doi: 10.1021/bk-2015-1194.ch001

Table 5. Reported CO_2 Photoreduction Catalysts, Reaction Conditions, and the Formation Rates with Sacrificial Reducing Agents

Photocatalyst		*Reactants*		*T (K)*	*Light source*	*Reactor*	*Major product {formation rate ($\mu mol\ h^{-1}\ g_{cat}^{-1}$)}*	*Ref*
Brand name	*Amount (mg)*	*CO_2*	*Reducing agent*					
$Au_3Cu/SrTiO_3/TiO_2$	5	33.7 kPa	$N_2H_4 \cdot H_2O$		300 W Xe		CO (730)	(*63*)
Cu_2O	500	Saturated	0.7 M Na_2SO_3		300 W Xe ($\lambda >$ 350 nm)	Glass	CO	(*64*)
Au(0.1%)-TiO_2	500	1.0 MPa	Na_2SO_3	298	125 W Hg	High *P* cell	CH_4 (20)	(*65*)
hex-$ZnIn_2S_4$	10	Saturated	CH_3OH	298	250 W Hg		MF (190)	(*66*)
cub-$ZnIn_2S_4$							MF (160)	
sph-$ZnIn_2S_4$							MF (50)	
MIL-101(Fe)	50	Saturated in CH_3CN	TEOA		300 W Xe (420 $< \lambda <$ 800 nm)	Flask	HCO_2^- (150)	(*67*)
MIL-53(Fe)							HCO_2^- (74)	(*67*)
MIL-88(Fe)							HCO_2^- (23)	(*67*)
NH_2-MIL-101(Fe)							HCO_2^- (450)	(*67*)
NH_2-MIL-53(Fe)							HCO_2^- (120)	(*67*)
NH_2-MIL-88(Fe)							HCO_2^- (75)	(*67*)

Publication Date (Web): September 11, 2015 | doi: 10.1021/bk-2015-1194.ch001

Photocatalyst		*Reactants*		*T (K)*	*Light source*	*Reactor*	*Major product {formation rate (μmol h^{-1} g_{cat}^{-1})}*	*Ref*
Brand name	*Amount (mg)*	*CO_2*	*Reducing agent*					
Zn_2GeO_4-ZIF-8	200	Saturated	Liq (100 mL), 0.1 M Na_2SO_3		500 W Xe arc		CH_3OH (0.22)	(*68*)
CdS-Co-ZIF-9 20, 1		101 kPa	TEOA (1 mL)	303	300 W Xe (λ > 420 nm)		CO (2400)	(*69*)
Al–porphyrin MOF	30	Atmosph. *P*	TEA (1 mL)	278	300 W Xe (λ > 420 nm)		CH_3OH	(*70*)
Al–Cu-porphyrin MOF							CH_3OH	(*70*)
GO	100		TEA (10 mL)		20 W white cold LED	Borosil	CH_3OH (39)	(*71*)
CoPc-GO							CH_3OH (79)	(*71*)

Photon Energy Conversion of CO_2 to Fuels Using Combination System with Photooxidation Catalysts

Although the homogeneous photocatalysts and enzymes for CO_2 reduction are out of scope of this chapter that is limiting to semiconductor photocatalysts, several studies were reported/reviewed to combine homogeneous complex or enzyme for CO_2 photoreduction with semiconductor photocatalyst, e.g. Ru bpy-like complex with Ag/TaON (*72*, *73*).

The phenomena of photocatalytic oxidation of water and photocatalytic reduction of CO_2 were combined using a cell (Figure 9A), in which the two photocatalysts, WO_3 and $[Zn_{1.5}Cu_{1.5}Ga(OH)_8]_2[Cu(OH)_4]\cdot mH_2O$ LDH, were separated by a polymer electrolyte (PE) film (Figure 9B) (*16*). WO_3 was used for the photooxidation of water, whereas Zn–Cu–Ga LDH was used for the photoreduction of CO_2. Protons and electrons, which were formed on WO_3 under the flow of moisture (solid–gas interface mode; Figure 9B), were used on Zn–Cu–Ga LDH instead of reactant H_2 in *Photon energy conversion of CO_2 to fuels with hydrogen or sacrificial reducing agent, section 1* (*56–58*, *60*). For this process, photocatalysts pressed on both sides of the PE film were irradiated by UV–visible light through quartz windows and through the space in carbon electrode plates set for both gas flow and light transmission. Methanol was the major product on LDH at a formation rate of 0.045 μmol h^{-1} g_{cat}^{-1} under the flow of CO_2 (Table 6). This rate accounted for 68–100% of photocurrents between the two redox photoelectrodes.

In comparison, liquid-type another cell, which consisted of WO_3 and LDH immersed in acidic solutions, with the PE film distinguishing the two compartments was reported (Figure 9C). The photocurrent from LDH to WO_3 was increased by 2.4–3.4 times in comparison to gas–solid mode cell (Figure 9B) tested under similar conditions. However, major product from LDH was H_2 at a formation rate of 0.67 μmol h^{-1} g_{cat}^{-1}. The difference of phase of water (moisture in panel B, liquid in panel C; Figure 9) directed the selectivity to methanol (equation 12) versus H_2 (equation 13) (*16*). This trend of phase difference was in consistent with that found for metal-loaded TiO_2 (*Photon energy conversion of CO_2 to fuels with water, section 2.1*) (*15*).

$$CO_2 + 6H^+ + 6e^- \rightarrow CH_3OH + H_2O \quad (12)$$

$$2H^+ + 2e^- \rightarrow H_2 \quad (13)$$

Using a similar tandem twin reactor separated by PE film, CO_2 conversion to methanol was also reported at rates of 1.6–1.8 μmol h^{-1} g_{cat}^{-1} using WO_3 on photoanode and Pt(1 wt%)-$CuAlGaO_4$ and/or Pt(0.8 %)-$SrTiO_3$:Rh on photocathode (*74*). A clear difference to reference 16 was the photocatalysts were not mounted on electrode and redox mediator (Fe^{3+} in anode and Fe^{2+} in cathode) was used. However, it is not certain whether electrons or Fe^{2+} would transfer through the PE film.

In Advances in CO2 Capture, Sequestration, and Conversion; He, et al.;
ACS Symposium Series; American Chemical Society: Washington, DC, 2015.

Publication Date (Web): September 11, 2015 | doi: 10.1021/bk-2015-1194.ch001

Publication Date (Web): September 11, 2015 | doi: 10.1021/bk-2015-1194.ch001

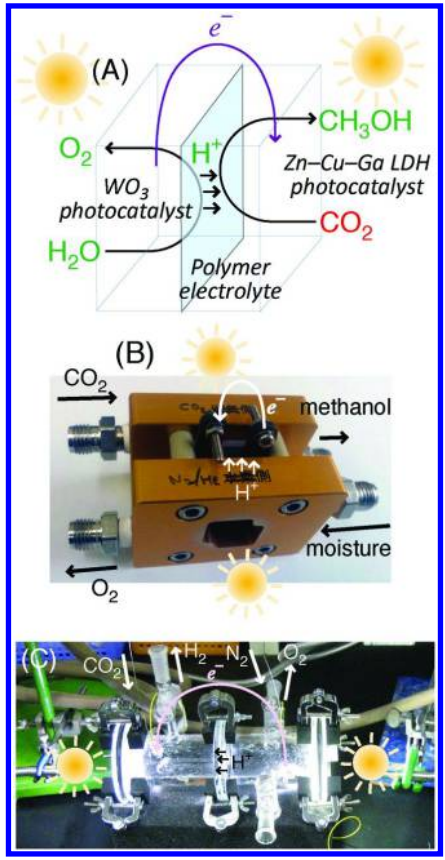

Figure 9. The reaction path in photofuel cell (A), cell-1 to flow moisture to WO_3 (B, front) and to circulate CO_2 to LDH (B, back), and cell-2 to flow N_2 to WO_3 (C, right) and CO_2 to LDH (C, left) immersed in HCl solutions (16). Reproduced from reference listing (16). Copyright, 2014, The Royal Society of Chemistry.

Publication Date (Web): September 11, 2015 | doi: 10.1021/bk-2015-1194.ch001

Table 6. Reported CO_2 Photoreduction Catalysts, Reaction Conditions, and the Formation Rates Combined with Photooxidation Catalysts

Photocatalyst		*Reactants*		*T (K)*	*Light source*	*Reactor*	*Major product {formation rate ($\mu mol\ h^{-1}\ g_{cat}^{-1}$)}*	*Ref*
Brand name	*Amount (mg)*	*CO_2*	*H_2O*					
anode:								
WO_3	95	(Ne/N_2)	Satur. *P*	< 315	500 W Xe arc	PEFC		(*16*)
cathode:								
$Zn_{1.5}Cu_{1.5}Ga\|Cu(OH)_4$	45	3.5 kPa					CH_3OH (0.045)	
anode:								
WO_3	300	(Ar)	225 mL (Fe^{3+}: 2mM)		300 W Xe	Twin R separated by PE		(*74*)
cathode:								
Pt(1 %)-$CuAlGaO_4$	300	Saturated	(Fe^{2+}: 2mM)				CH_3OH (1.8)	
anode:								
WO_3	300							(*74*)
cathode:								
Pt(1 %)-$CuAlGaO_4$,	150						CH_3OH (1.6)	
Pt(0.8 %)-$SrTiO_3$:Rh	150							

Concluding Remarks

Recent advances in photocatalytic CO_2 conversion with water and/or other reductants in these three years were reviewed in comparison to classic studied prior to 2012 (*4*) using TiO_2 (*75–81*), ZnO (*81*), CdS (*81*), GaP (*81*), SiC (*81*), WO_3 (*81*), Zn_2GeO_4 (*82*), Bi_2WO_6 (*83*), HNb_3O_8 (*84*), $CuGa_{1-x}Fe_xO_2$ (*85*), $A^{II}La_4Ti_4O_{15}$ (*86*), $[Zn_{1.5}Cu_{1.5}Ga(OH)_8]_2CO_3{\cdot}mH_2O$ (*56*, *60*), ZrO_2 (*87*), GaP (*81*, *88*), GaAs (*88*, *89*), and InP (*89*). Starting from CO_2 and water, methane or CO formation using TiO_2 was improved to 0.1–17 μmol h^{-1} g_{cat}^{-1} by choosing approperiate crystalline phase (brookite or anatase), crystalline face, and the defects. Metals, e.g. Pt, Pd, Au, Rh, Ag, Ni, Cu, Au_3Cu alloy, I, MgO, RuO_2, graphene, g-C_3N_4, Cu-containing dyes, and Cu-containing MOFs were effective to assist TiO_2 to form methane, CO, methanol, or ethane at rates of 1.4–160 μmol h^{-1} g_{cat}^{-1} and further to 32–2200 μmol h^{-1} g_{cat}^{-1} if minimal thin photocatalyst film was well deposited.

Semiconductors, e.g. ZnO, Zn_6Ti LDH, Mg_3In LDH, $KTaO_3$, graphene, GO, g-C_3N_4, CoTe, TiO_2-coated p-GaP, Zn_2SnO_4, ZnO, ZnTe, $SrTiO_3$, $ZnGa_2O_4$, Zn_2GeO_4, Zr–Co–Ir oxides, Nb_2O_5, $HNbO_3$, $NaNbO_3$, KNb_3O_8, $InNbO_4$, NiO, Co_3O_4, Cu_2O, and their assemblies were effective to photogenerate methane, CO, methanol, acetaldehyde at rates of 0.15–300 μmol h^{-1} g_{cat}^{-1} in good competition with promoted TiO_2.

If H_2 was used, new photoactivation of CO_2 followed by thermal assisted reaction(s) was reported using Ni/SiO_2-Al_2O_3 to produce methane at 423 K under pressurized $CO_2 + H_2$ at a rate of 55 mmol h^{-1} g_{cat}^{-1} presumably via Ni–H species. As pure photocatalytic reaction, methanol formation rates were improved up to 0.30 μmol h^{-1} g_{cat}^{-1} by the doping of Ag/Au nanoparticles, $[Cu(OH)_4]^{2-}$ anions, and Cu-containing dyes to Zn–Ga LDH. The combination of two semiconductors (WO_3, Zn–Cu–Ga LDH) were reported to from methanol at a rate of 0.05 μmol h^{-1} g_{cat}^{-1} from CO_2 and gaseous water.

In this chapter, the improvement of CO_2 conversion and new materials for the photoreduction were focused, and the importance of wavelength (deep UV, UV, and visible light) and flux of incident light, temperature, and form (powder, nanofiber, and/or film) of photocatalysts, pressure of reactants, were critical to determine the photoconversion of CO_2 for the stage of new energy application levels. To enable the optimum reaction and photocatalyst conditions, the importance of reactor cell (*30*, *55*) was also suggested.

However, reaction mechanisms of CO_2 activation, e.g. via glyoxal (*9*), via O-defect to form CO (equations 3–5) (*10*), multiple-step formaldehyde pathway (*5*), mutiple-step carbene pathway (*5*, *27*), via metal–H active species (*55*), and via hydrogen carbonate (bicarbonate) (*56*, *61*), are still in debate. To clarify the mechanism and responsible sites, spectroscopic studies, e.g. FTIR (*27*, *45*, *61*, *67*, *70*), diffuse reflectance infrared Fourier transform (*10*), electron paramagnetic resonance (*9*, *67*), FE-SEM (*22*, *26*, *49*, *57*), HR-TEM (*20*, *26*, *27*, *46*, *47*, *49*, *54*), photoluminescence (*15*), action (in-profile) spectrum (*55*, *57*, *58*), time-resolved TA (*26*, *29*, *55*), valence X-ray photoelectron (*35*, *39*, *49*), XANES (*57*, *61*), EXAFS (*90*), and density functional theory calculations (*9*, *13*, *29*, *34*, *46*) are inevitable.

Publication Date (Web): September 11, 2015 | doi: 10.1021/bk-2015-1194.ch001

In Advances in CO2 Capture, Sequestration, and Conversion; He, et al.;
ACS Symposium Series; American Chemical Society: Washington, DC, 2015.

Publication Date (Web): September 11, 2015 | doi: 10.1021/bk-2015-1194.ch001

Acknowledgments

The authors are grateful for the financial supports from the Grant-in-Aid for Scientific Research C (26410204, 22550117) from Japan Science Promotion Agency, the Feasibility Study Stage of A-STEP (Proposal Nos. AS262Z00159L, AS251Z00906L, AS231Z01459C) from the Japan Science and Technology Agency, the Iwatani Naoji Foundation, Asahi Glass Foundation, the Promotion Section of Technology Innovation, Daikin Industries, and approval of the Photon Factory Proposal Review Committee for X-ray measurements (2014G631, 2011G033, 2009G552) for research related to this chapter.

References

1. Lewis, N.; Nocera, D. G. Powering the Planet: Chemical Challenges in Solar Energy Utilization. *Proc. Nat. Acad. Sci.* **2006**, *103*, 15729–15735.
2. Bolton, J. R. Solar Photoproduction of Hydrogen: A Review. *Solar Ener.* **1996**, *57*, 37–50.
3. Aresta, M.; Dibenedetto, A.; Angelini, A. Catalysis for the Valorization of Exhaust Carbon: from CO_2 to Chemicals, Materials, and Fuels. Technological Use of CO_2. *Chem. Rev.* **2014**, *114*, 1709–1742.
4. Izumi, Y. Recent Advances in the Photocatalytic Conversion of Carbon Dioxide to Fuels with Water and/or Hydrogen Using Solar Energy and Beyond. *Coord. Chem. Rev.* **2013**, *257*, 171–186.
5. Habisreutinger, S. N.; Schmidt-Mende, L.; Stolarczyk, J. K. Photocatalytic Reduction of CO_2 on TiO_2 and Other Semiconductors. *Angew. Chem., Int. Ed.* **2013**, *52*, 7372–7408.
6. Smestad, G. P.; Steinfeld, A. Review: Photochemical and Thermochemical Production of Solar Fuels from H_2O and CO_2 Using Metal Oxide Catalysts. *Ind. Eng. Chem. Res.* **2012**, *51*, 11828–11840.
7. Roy, S. C.; Varghese, O. K.; Paulose, M.; Grimes, C. A. Toward Solar Fuels: Photocatalytic Conversion of Carbon Dioxide to Hydrocarbons. *ACS Nano* **2010**, *4*, 1259–1278.
8. Indrakanti, V. P.; Kubicki, J. D.; Schobert, H. H. Photoinduced Activation of CO_2 on Ti-based Heterogeneous Catalysts: Current State, Chemical Physics-based Insights and Outlook. *Ener. Environ. Sci.* **2009**, *2*, 745–758.
9. Dimitrijevic, N. M.; Vijayan, B. K.; Poluektov, O. G.; Rajh, T.; Gray, K. A.; He, H.; Zapol, P. Role of Water and Carbonates in Photocatalytic Transformation of CO_2 to CH_4 on Titania. *J. Am. Chem. Soc.* **2011**, *133*, 3964–3971.
10. Liu, L.; Zhao, H.; Andino, J. M.; Li, Y. Photocatalytic CO_2 Reduction with H_2O on TiO_2 Nanocrystals: Comparison of Anatase, Rutile, and Brookite Polymorphs and Exploration of Surface Chemistry. *ACS Catal.* **2012**, *2*, 1817–1828.
11. Zhao, H.; Liu, L.; Andino; Li, Y. Bicrystalline TiO_2 with Controllable anatase–Brookite Phase Content for Enhanced CO_2 Photoreduction to Fuels. *J. Mater. Chem. A* **2013**, *1*, 8209–8216.

12. Ye, L.; Mao, J.; Peng, T.; Zan, L.; Zhang, Y. Opposite Photocatalytic Activity Orders of Low-Index Facets of Anatase TiO_2 for Liquid Phase Dye Degradation and Gaseous Phase CO_2 Photoreduction. *Phys. Chem. Chem. Phys.* **2014**, *16*, 15675–15680.
13. Yu, J.; Low, J.; Xiao, W.; Zhou, P.; Jaroniec, M. Enhanced Photocatalytic CO_2-Reduction Activity of Anatase TiO_2 by Coexposed {001} and {101} Facets. *J. Am. Chem. Soc.* **2014**, *136*, 8839–8842.
14. Jiao, W.; Wang, L.; Liu, G.; Lu, G. Q.; Cheng, H. M. Hollow Anatase TiO_2 Single Crystals and Mesocrystals with Dominant {101} Facets for Improved Photocatalysis Activity and Tuned Reaction Preference. *ACS Catal.* **2012**, *2*, 1854–1859.
15. Xie, S.; Wang, Y.; Zhang, Q.; Deng, W.; Wang, Y. MgO- and Pt-Promoted TiO_2 as an Efficient Photocatalyst for the Preferential Reduction of Carbon Dioxide in the Presence of Water. *ACS Catal.* **2014**, *4*, 3644–3653.
16. Morikawa, M.; Ogura, Y.; Ahmed, N.; Kawamura, S.; Mikami, G.; Okamoto, S.; Izumi, Y. Photocatalytic Conversion of Carbon Dioxide into Methanol in Reverse Fuel Cells with Tungsten Oxide and Layered Double Hydroxide Photocatalysts for Solar Fuel Generation. *Catal. Sci. Technol.* **2014**, *4*, 1644–1651.
17. Weast, R. C. *CRC Handbook of Chemistry and Physics*; CRC Press: Boca Raton, FL, 2001; vol. 82; pp 12−130.
18. Kwak, B. S.; Vignesh, K.; Park, N. K.; Ryu, H. J.; Baek, J. I.; Kang, M. Methane Formation from Photoreduction of CO_2 with Water Using TiO_2 Including Ni Ingredient. *Fuel* **2015**, *143*, 570–576.
19. Ola, O.; Maroto-Valer, M. M. Role of Catalyst Carriers in CO_2 Photoreduction over Nanocrystalline Nickel Loaded TiO_2-based Photocatalysts. *J. Catal.* **2014**, *309*, 300–308.
20. Zhang, Z.; Wang, Z.; Cao, S. W.; Xue, C. Au/Pt Nanoparticle-Decorated TiO_2 Nanofibers with Plasmon-Enhanced Photocatalytic Activities for Solar-to-Fuel Conversion. *J. Phys. Chem. C* **2013**, *117*, 25939–25947.
21. Zhang, Q.; Gao, T.; Andino, J. M.; Lio, Y. Copper and Iodine Co-modified TiO_2 nanoparticles for Improved Activity of CO_2 Photoreduction with Water Vapor. *Appl. Catal. B* **2012**, *123/124*, 257–264.
22. Zhang, X.; Han, F.; Shi, B.; Farsinezhad, S.; Dechaine, G. P.; Shankar, K. Photocatalytic Conversion of Diluted CO_2 into Light Hydrocarbons Using Periodically Modulated Multiwalled Nanotube Arrays. *Angew. Chem., Int. Ed.* **2012**, *51*, 12732–12735.
23. Tu, W.; Zhou, Y.; Liu, Q.; Yan, S.; Bao, S.; Wang, X.; Xiao, M.; Zou, Z. An In Situ Simultaneous Reduction-Hydrolysis Technique for Fabrication of TiO_2-Graphene 2D Sandwich-Like Hybrid Nanosheet: Graphene-Promoted Selectivity of Photocatalytic-Driven Hydrogenation and Coupling of CO_2 into Methane and Ethane. *Adv. Funct. Mater.* **2013**, *23*, 1743–1749.
24. Tu, W.; Zhou, Y.; Liu, Q.; Tian, Z.; Gao, J.; Chen, X.; Zhang, H.; Liu, J.; Zou, Z. Robust Hollow Spheres Consisting of Alternating Titania Nanosheets and Graphene Nanosheets with High Photocatalytic Activity for CO_2 Conversion into Renewable Fuels. *Adv. Func. Mater.* **2012**, *22*, 1215–1221.

Publication Date (Web): September 11, 2015 | doi: 10.1021/bk-2015-1194.ch001

25. Zhou, S.; Liu, Y.; Li, J.; Wang, Y.; Jiang, G.; Zhao, Z.; Wang, D.; Duan, A.; Liu, J.; Wei, Y. Facile In Situ Synthesis of Graphitic Carbon Nitride (g-C_3N_4)-N-TiO_2 Heterojunction as an Efficient Photocatalyst for the Selective Photoreduction of CO_2 to CO. *Appl. Catal., B* **2014**, *158/159*, 20–29.
26. Wang, W. N.; An, W. J.; Ramalingam, B.; Mukherjee, S.; Niedzwiedzki, D. M.; Gangopadhyay, S.; Biswas, P. Size and Structure Matter: Enhanced CO_2 Photoreduction Efficiency by Size-Resolved Ultrafine Pt Nanoparticles on TiO_2 Single Crystals. *J. Am. Chem. Soc.* **2012**, *134*, 11276–11281.
27. Neaţu, Ş.; Maciá-Agulló, J. A.; Concepción, P.; Garcia, H. Gold–Copper Nanoalloys Supported on TiO_2 as Photocatalysts for CO_2 Reduction by Water. *J. Am. Chem. Soc.* **2014**, *136*, 15969–15976.
28. Yuan, Y. J.; Yu, Z. T.; Zhang, J. Y.; Zou, Z. G. A Copper(I) Dye-Sensitised TiO_2-Based System for Efficient Light Harvesting and Photoconversion of CO_2 into Hydrocarbon Fuel. *Dalton Trans.* **2012**, *41*, 9594–9597.
29. Li, R.; Hu, J.; Deng, M.; Wang, H.; Wang, X.; Hu, Y.; Jiang, H. L.; Jiang, J.; Zhang, Q.; Xie, Y.; Xiong, Y. Integration of an Inorganic Semiconductor with a Metal–Organic Framework: A Platform for Enhanced Gaseous Photocatalytic Reactions. *Adv. Mater.* **2014**, *26*, 4783–4788.
30. Sastre, F.; Corma, A.; García, H. 185 nm Photoreduction of CO_2 to Methane by Water. Influence of the Presence of a Basic Catalyst. *J. Am. Chem. Soc.* **2012**, *134*, 14137–14141.
31. Teramura, K.; Iguchi, S.; Mizuno, Y.; Shishido, T.; Tanaka, T. Photocatalytic Conversion of CO_2 in Water over Layered Double Hydroxides. *Angew. Chem. Int. Ed.* **2012**, *51*, 8008–8011.
32. Li, Z.; Zhou, Y.; Zhang, J.; Tu, W.; Liu, Q.; Yu, T.; Zou, Z. Hexagonal Nanoplate-Textured Micro-Octahedron Zn_2SnO_4: Combined Effects toward Enhanced Efficiencies of Dye-Sensitized Solar Cell and Photoreduction of CO_2 into Hydrocarbon Fuels. *Crys. Growth Des.* **2012**, *12*, 1476–1481.
33. Li, K.; Handoko, A. D.; Khraisheh, M.; Tang, J. Photocatalytic Reduction of CO_2 and Protons Using Water as an Electron Donor over Potassium Tantalate Nanoflakes. *Nanoscale* **2014**, *6*, 9767–9773.
34. Guo, J.; Ouyang, S.; Kako, T.; Ye, J. Mesoporous $In(OH)_3$ for Photoreduction of CO_2 into Renewable Hydrocarbon Fuels. *Appl. Surf. Sci.* **2013**, *280*, 418–423.
35. Li, P.; Zhou, Y.; Tu, W.; Wang, R.; Zhang, C.; Liu, Q.; Li, H.; Li, Z.; Dai, H.; Wang, J.; Yan, S.; Zou, Z. Synthesis of $Bi_6Mo_2O_{15}$ Sub-Microwires via a Molten Salt Method and Enhancing the Photocatalytic Reduction of CO_2 into Solar Fuel through Tuning the Surface Oxide Vacancies by Simple Post-Heating Treatment. *Crys. Eng. Commun.* **2013**, *15*, 9855–9858.
36. Hsu, H. C.; Shown, I.; Wei, H. Y.; Chang, Y. C.; Du, H. Y.; Lin, Y. G.; Tseng, C. A.; Wang, C. H.; Chen, L. C.; Lin, Y. C. Graphene Oxide as a Promising Photocatalyst for CO_2 to Methanol Conversion. *Nanoscale* **2013**, *5*, 262–268.
37. Niu, P.; Yang, Y.; Yu, J. C.; Liu, G.; Cheng, H. M. Switching the Selectivity of the Photoreduction Reaction of Carbon Dioxide by Controlling the Band Structure of a g-C_3N_4 Photocatalyst. *Chem. Commun.* **2014**, *50*, 10837–10840.

38. Khan, M. S.; Ashiq, M. N.; Ehsan, M. F.; He, T.; Ijaz, S. Controlled Synthesis of Cobalt Telluride Superstructures for the Visible Light Photo-conversion of Carbon Dioxide into Methane. *Appl. Catal., A* **2014**, *487*, 202–209.
39. Ehsan, M. F.; He, T. In Situ Synthesis of ZnO/ZnTe Common Cation Heterostructure and Its Visible-Light Photocatalytic Reduction of CO_2 into CH_4. *Appl. Catal., B* **2015**, *166/167*, 345–352.
40. Ehsan, M. F.; Ashiq, M. N.; Bi, F.; Palanisamy, S.; He, T. Preparation and Characterization of $SrTiO_3$-ZnTe Nanocomposites for the Visible-Light Photoconversion of Carbon Dioxide to Methane. *RSC Adv.* **2014**, *4*, 48411–48418.
41. Yan, S.; Wang, J.; Gao, H.; Wang, N.; Yu, H.; Li, Z.; Zhou, Y.; Zou, Z. Zinc Gallogermanate Solid Solution: A Novel Photocatalyst for Efficiently Converting CO_2 into Solar Fuels. *Adv. Funct. Mater.* **2013**, *23*, 1839–1845.
42. Blankenship, R. E.; Tiede, D. M.; Barber, J.; Brudvig, G. W.; Fleming, G.; Ghirardi, M.; Gunner, M. R.; Junge, W.; Kramer, D. M.; Melis, A.; Moore, T. A.; Moser, C. C.; Nocera, D. G.; Nozik, A. J.; Ort, D. R.; Parson, W. W.; Prince, R. C.; Sayre, R. T. Comparing Photosynthetic and Photovoltaic Efficiencies and Recognizing the Potential for Improvement. *Science* **2011**, *332*, 805–809.
43. Zeng, G.; Qiu, J.; Li, Z.; Pavaskar, P.; Cronin, S. B. CO_2 Reduction to Methanol on TiO_2-Passivated GaP Photoctalysts. *ACS Catal.* **2014**, *4*, 3512–3516.
44. Ghadimkhani, G.; de Tacconi, N. R.; Chanmanee, W.; Janaky, C.; Rajeshwar, K. Efficent Solar Photoelectrosynthesis of Methanol from Carbon Dioxide Using Hybrid CuO–Cu_2O Semiconductor Nanorod Arrays. *Chem. Commun.* **2013**, *49*, 1297–1299.
45. Kim, W.; Yuan, G.; McClure, B. A.; Frei, H. Light Induced Carbon Dioxide Reduction by Water at Binuclear $ZrOCo^{II}$ Unit Coupled to Ir Oxide Nanocluster Catalyst. *J. Am. Chem. Soc.* **2014**, *136*, 11034–11042.
46. Li, P.; Ouyang, S.; Xi, G.; Kako, T.; Ye, J. The Effects of Crystal Structure and Electronic Structure on Photocatalytic H_2 Evolution and CO_2 Reduction over Two Phases of Perovskite-Structured $NaNbO_3$. *J. Phys. Chem. C* **2012**, *116*, 7621–7628.
47. Li, X.; Li, W.; Zhuang, Z.; Zhong, Y.; Li, Q.; Wang, L. Photocatalytic Reduction of Carbon Dioxide to Methane over SiO_2-Pillared HNb_3O_8. *J. Phys. Chem. C* **2012**, *116*, 16047–16053.
48. Lee, D. S.; Chen, H. J.; Chen, Y. W. Photocatalytic Reduction of Carbon Dioxide with Water Using $InNbO_4$ Catalyst with NiO and Co_3O_4 Cocatalysts. *J. Phys. Chem. Solid* **2012**, *73*, 661–669.
49. Shi, H.; Chen, G.; Zhang, C.; Zou, Z. Polymeric g-C_3N_4 Coupled with $NaNbO_3$ Nanowires toward Enhanced Photocatalytic Reduction of CO_2 into Renewable Fuel. *ACS Catal.* **2014**, *4*, 3637–3643.
50. He, Y.; Wang, Y.; Zhang, L.; Teng, B.; Fan, M. High-Efficiency Conversion of CO_2 to Fuel over ZnO/g-C_3N_4 Photocatalyst. *Appl. Catal., B* **2015**, *168/169*, 1–8.

Publication Date (Web): September 11, 2015 | doi: 10.1021/bk-2015-1194.ch001

51. Yuan, Y. P.; Cao, S. W.; Liao, Y. S.; Yin, L. S.; Xue, C. Red Phosphor/g-C_3N_4 Heterojunction with Enhanced Photocatalytic Activities for Solar Fuel Production. *Appl. Catal., B* **2013**, *140/141*, 164–168.
52. Ong, W. J.; Tan, L. L.; Chai, S. P.; Yong, S. T. Graphene Oxide as a Structure-Directing Agent for the Two-Dimensional Interface Engineering of Sandwich-Like Graphene–g-C_3N_4 Hybrid Nanostructures with Enhanced Visible-Light Photoreduction of CO_2 to Methane. *Chem. Commun.* **2015**, *51*, 858–861.
53. An, X.; Li, K.; Tang, J. Cu_2O/Reduced Graphene Oxide Composites for the Photocatalytic Conversion of CO_2. *ChemSusChem* **2014**, *7*, 1086–1093.
54. Asi, M. A.; Zhu, L.; He, C.; Sharma, V. K.; Shu, D.; Li, S.; Yang, J.; Xiong, Y. Visible-Light-Harvesting Reduction of CO_2 to Chemical Fuels with Plasmonic Ag@AgBr/CNT Nanocomposites. *Catal. Today* **2013**, *216*, 268–275.
55. Sastre, F.; Puga, A. V.; Liu, L.; Corma, A.; García, H. Complete Photocatalytic Reduction of CO_2 to Methane by H_2 under Solar Light Irradiation. *J. Am. Chem. Soc.* **2014**, *136*, 6798–6801.
56. Ahmed, N.; Shibata, Y.; Taniguchi, T.; Izumi, Y. Photocatalytic Conversion of Carbon Dixoide into Methanol Using Zinc–Copper–M(III) (M = Aluminum, Gallium) Layered Double Hydroxides. *J. Catal.* **2011**, *279*, 123–135.
57. Kawamura, S.; Puscasu, M. C.; Yoshida, Y.; Izumi, Y.; Carja, G. Tailoring Assemblies of Plasmonic Silver/Gold and Zinc–Gallium Layered Double Hydroxides for Photocatalytic Conversion of Carbon Dioxide Using UV–Visible Light. *Appl. Catal. A* **2015**DOI:10.1016/apcata.2014.12.042.
58. Kawamura, S.; Ahmed, N.; Morikawa, M.; Mikami, G.; Carja, G.; Izumi, Y. Photocatalytic Conversion of Carbon Dioxide Using Zn–Cu–Al or Ga Layered Double Hydroxides: Cu in Contact with Gaseous Reactant is Needed for Methanol Generation. *Oil Gas Sci. Technol.* **2015**May5in press.
59. Hou, W.; Cronin, S. B. A Review of Surface Plasmon Resonance-Enhanced Photocatalysis. *Adv. Funct. Mater.* **2013**, *23*, 1612–1619.
60. Ahmed, N.; Morikawa, M.; Izumi, Y. Photocatalytic Conversion of Carbon Dioxide into Methanol Using Optimized Layered Double Hydroxide Catalysts. *Catal. Today* **2012**, *185*, 263–269.
61. Morikawa, M.; Ahmed, N.; Yoshida, Y.; Izumi, Y. Photoconversion of Carbon Dioxide in Zinc–Copper–Gallium Layered Double Hydroxides: The Kinetics to Hydrogen Carbonate and Further to CO/Methanol. *Appl. Catal., B* **2014**, *144*, 561–569.
62. Izumi, Y.; Kawamura, S.; Morikawa, M.; Naveed, A. Monitoring of Electron Flow in Layered Double Hydroxides to Photoreduce Carbon Dioxide into Fuels; Photon Factory Activity Report 2013 (Highlights); 2014; Vol. 31A, pp 36−37. , *31A*, 36–37.
63. Kang, Q.; Wang, T.; Li, P.; Liu, L.; Chang, K.; Li, M.; Ye, J. Photocatalytic Reduction of Carbon Dioxide by Hydrous Hydrazine over Au–Cu Alloy Nanoparticles Supported on $SrTiO_3/TiO_2$ Coaxial Nanotube Arrays. *Angew. Chem. Int. Ed.* **2015**, *54*, 841–845.

64. Handoko, A. D.; Tang, J. Controllable Proton and CO_2 Photoreduction over Cu_2O with Various Morphologies. *Int. J. Hydrogen Energy* **2013**, *38*, 13017–13022.
65. Rossetti, I.; Villa, A.; Pirola, C.; Prati, L.; Ramis, G. A Novel High-Pressure Photoreactor for CO_2 Photoconversion to Fuels. *RSC Adv.* **2014**, *4*, 28883–28885.
66. Chen, J.; Xin, F.; Yin, X.; Xiang, T.; Wang, Y. *RSC Adv.* **2015**, *5*, 3833–3839.
67. Wang, D.; Huang, R.; Liu, W.; Sun, D.; Li, Z. Fe-Based MOFs for Photocatalytic CO_2 Reduction: Role of Coordination Unsaturated Sites and Dual Excitation Pathways. *ACS Catal.* **2014**, *4*, 4254–4260.
68. Liu, Q.; Low, Z. X.; Li, L.; Razmjou, A.; Wang, K.; Yao, J.; Wang, H. ZIF-8/Zn_2GeO_4 Nanorods with an Enhanced CO_2 Adsorption Property in an Aqueous Medium for Photocatalytic Synthesis of Liquid Fuel. *J. Mater. Chem. A* **2013**, *1*, 11563–11569.
69. Wang, S.; Wang, X. Photocatalytic CO_2 Reduction by CdS Promoted with a Zeolitic Imidazolate Framework. *Appl. Catal., B* **2015**, *162*, 494–500.
70. Liu, Y.; Yang, Y.; Sun, Q.; Wang, Z.; Huang, B.; Dai, Y.; Qin, X.; Zhang, X. Chemical Adsorption Enhanced CO_2 Capture and Photoreduction over a Copper Porpyrin Based Metal Organic Framework. *ACS Appl. Mater. Interfaces* **2013**, *5*, 7654–7658.
71. Kumar, P.; Kumar, A.; Sreedhar, B.; Sain, B.; Ray, S. S.; Jain, S. L. Cobalt Phthalocyanine Immobilized on Graphene Oxide: An Efficient Visible-Active Catalyst for the Photoreduction of Carbon Dixoide. *Chem. Eur. J.* **2014**, *20*, 6154–6161.
72. Sekizawa, K.; Maeda, K.; Domen, K.; Koide, K.; Ishitani, O. Artificial Z-Scheme Constructed with a Supramolecular Metal Complex asd Semiconductor for the Photocatalytic Reduction of CO_2. *J. Am. Chem. Soc.* **2013**, *135*, 4596–4599.
73. Windle, C. D.; Perutz, R. N. Advances in Molecular Photocatalytic and Electrocatalytic CO_2 Reduction. *Coord. Chem. Rev.* **2012**, *256*, 2562–2570.
74. Lee, W. H.; Liao, C. H.; Tsai, M. F.; Huang, C. W.; Wu, J. C. S. A Novel Twin Reactor for CO_2 Photoreduction to Minic Artifial Photosynthesis. *Appl. Catal., B* **2013**, *132/133*, 445–451.
75. Yui, T.; Kan, A.; Saitoh, C.; Koide, K.; Ibusuki, T.; Ishitani, O. Photochemical Reduction of CO_2 Using TiO_2: Effects of Organic Adsorbates on TiO_2 and Deposition of Pd onto TiO_2. *ACS Appl. Mater. Interfaces* **2011**, *3*, 2594–2600.
76. Yang, C. C.; Yu, Y. H.; van der Linden, B.; Wu, J. C. S.; Mul, G. Artificial Photosynthesis over Crystalline TiO_2-Based Catalysts: Fact or Fiction? *J. Am. Chem. Soc.* **2010**, *132*, 8398–8406.
77. Varghese, O. K.; Paulose, M.; LaTempa, T. J.; Grimes, C. A. High-Rate Solar Photocatalytic Conversion of CO_2 and Water Vapor to Hydrocarbon Fuels. *Nano Lett.* **2009**, *9*, 731–737.
78. Tseng, I. H.; Chang, W. C.; Wu, J. C. S. Photoreduction of CO_2 Using Sol-Gel Derived Titania and Titania-Supported Catalysts. *Appl. Catal., B* **2002**, *37*, 37–48.

Publication Date (Web): September 11, 2015 | doi: 10.1021/bk-2015-1194.ch001

79. Kaneco, S.; Kurimoto, H.; Shimizu, Y.; Ohta, K.; Mizuno, T. Photocatalytic Reduction of CO_2 Using TiO_2 Powders in Supercritical Fluid CO_2. *Energy* **1999**, *24*, 21–30.
80. Anpo, M; Yamashita, H.; Ichihashi, Y.; Fujii, Y.; Honda, M. Photocatalytic Reduction of CO_2 with H_2O on Titanium Oxides Anchored within Micropores of Zeolites: Effects of the Structure of the Active Sites and the Addition of Pt. *J. Phys. Chem. B* **1997**, *101*, 2632–2636.
81. Inoue, T.; Fujishima, A.; Konishi, S.; Honda, K. Photoelectrocatalytic Reduction of Carbon Dioxide in Aqueous Suspensions of Semiconductor Powders. *Nature* **1979**, *277*, 637–638.
82. Liu, Q.; Zhou, Y.; Kou, J.; Chen, X.; Tian, Z.; Gao, J.; Yan, S.; Zou, Z. High-Yield Synthesis of Ultralong and Ultrathin Zn_2GeO_4 Nanoribbons toward Improved Photocatalytic Reduction of CO_2 into Renewable Hydrocarbon Fuel. *J. Am. Chem. Soc.* **2010**, *132*, 14385–14387.
83. Zhou, Y.; Tian, Z.; Zhao, Z.; Liu, Q.; Kou, J.; Chen, X.; Gao, J.; Yan, S.; Zou, Z. High-Yield Synthesis of Untrathin and Uniform Bi_2WO_6 Square Nanoplates Benefitting from Photocatalytic Reduction of CO_2 into Renewable Hydrocarbon Fuel under Visible Light. *ACS Appl. Mater. Interfaces* **2011**, *3*, 3594–3601.
84. Li, X.; Pan, H.; Li, W.; Zhuang, Z. Photocatalytic Reduction of CO_2 to Methane over HNb_3O_8 Nanobelts. *Appl. Catal., A* **2012**, *413/414*, 103–108.
85. Lekse, J. W.; Underwood, M. K.; Lewis, J. P.; Matranga, C. C. Synthesis, Characterization, Electronic Structure, and Photocatalytic Behavior of $CuGaO_2$ and $CuGa_{1-x}Fe_xO_2$ (x = 0.05, 0.10, 0.15, 0.20) Delafossites. *J. Phys. Chem. C* **2012**, *116*, 1865–1872.
86. Iizuka, K.; Wato, T.; Miseki, Y.; Saito, K.; Kudo, A. Photocatalytic Reduction of Carbon Dioxide over Ag Cocatalyst-Loaded $ALa_4Ti_4O_{15}$ (A = Ca, Sr, and Ba) Using Water as a Reducing Reagent. *J. Am. Chem. Soc.* **2011**, *133*, 20863–20868.
87. Kohno, Y.; Tanaka, T.; Funabiki, T.; Yoshida, S. Photoreduction of Carbon Dioxide with Hydrogen over ZrO_2. *Chem. Commun.* **1997**, 841–842.
88. Aurian-Biajeni, B.; Halmann, M.; Manassen, J. Electrochemical Measurement on the Photoelectrochemical Reduction of Aqueous Carbon Dioxide on p-Gallium Phosphide and p-Gallium Arsenide Semiconductor Electrodes. *Solar Energy Mater.* **1983**, *8*, 425–440.
89. Canfield, D.; Frese, K. W., Jr Reduction of Carbon Dixoide to Methanol on n- and p-GaAs and p-InP. Effect of Crystal Face, Electrolyte and Current Density. *J. Electrochem. Soc.* **1983**, *130*, 1772–1773.
90. Izumi, Y.; Itoi, T.; Peng, S.; Oka, K.; Shibata, Y. Site Structure and Photocatalytic Role of Sulfur or Nitrogen-Doped Titanium Oxide with Uniform Mesopores under Visible Light. *J. Phys. Chem. C* **2009**, *113*, 6706–6718.

Publication Date (Web): September 11, 2015 | doi: 10.1021/bk-2015-1194.ch001

Publication Date (Web): September 11, 2015 | doi: 10.1021/bk-2015-1194.ch002

Chapter 2

Transition Metal-Promoted CO_2 Conversion under Mild Reaction Conditions

Qing-Wen Song and Liang-Nian He*

State Key Laboratory and Institute of Elemento-Organic Chemistry, Collaborative Innovation Center of Chemical Science and Engineering (Tianjin), Nankai University, Tianjin 300071, P. R. China
***E-mail: heln@nankai.edu.cn**

Carbon dioxide can be regarded as an inexpensive, abundant sustainable feedstock for producing value-added chemicals. Therefore, development of efficacious processes using CO_2 as chemical feedstock under mild conditions particularly low CO_2 pressure (ideally at 1 bar) could be still highly desirable. Accordingly, only if we understand the underlying principles of CO_2 activation can the goal of using CO_2 as an environmentally friendly and economically feasible source of carbon under mild reaction conditions be achieved. In this regard, transition metal catalysis based on CO_2 activation for efficient chemical transformation of CO_2 with outstanding selectivities is appealing from a standpoint of sustainable chemistry. In this context, great efforts have been devoted to constructing C-N and C-O bond on the basis of selecting high-energy starting materials and CO_2 activation through molecular catalysis to overcome its thermodynamic stability and kinetic inertness. The aim of this chapter is to draw attention to the chemical fixation of CO_2 with propargylic alcohols or propargylmines to *a*-alkylene cyclic carbonates, *β*-oxoalkylcarbamates and 2-oxazolidinones through various transition metal catalysis. This is an attractive strategy to utilize CO_2 to produce useful products. A thorough overview of the catalytic utilization of CO_2 with propargylic alcohols with gaining insights into the reaction mechanism is also presented.

In Advances in CO2 Capture, Sequestration, and Conversion; He, et al.;
ACS Symposium Series; American Chemical Society: Washington, DC, 2015.

Carbon Dioxide Chemistry

With increasing awareness of the elevated CO_2 levels in the atmosphere, there has been great effort placed into the development of strategies towards its potential use as an inexpensive and abundant C_1 building block since it is nontoxic, noncorrosive, non-flammable, and renewable (*1–3*). However, only a small proportion of the total abundance of CO_2 is currently being consumed by chemical industry due to its low reactivity as a result of its high thermodynamic stability and kinetic inertness (*4–7*). As expected, large numbers of metal catalytic systems sprang up thanks to the unique advantages associated with high reactivity and selectivity towards CO_2 conversion.

Much importantly, chemical utilization of CO_2 as green carbonyl source holds great promise as an alternative to conventional phosgene processes in organic synthesis. In particular, catalytic formation of C-N and C-O bond from CO_2 would be important in both industry and academia because such processes offer economical and environmental advantages such as perfect atom efficiency and formation of water as only by-product (*5*). To overcome the intrinsic inactivity of CO_2, highly reactive reagents are usually investigated to couple with CO_2. Accordingly, the introduction of various nucleophiles is a primary consideration (*8*). Notably, these nitrogen or oxygen-containing nucleophiles exhibit much better reactivity than general carbon nucleophiles, which are commonly limited with organolithium and Grignard reagents, phenolates in classic C–C bond formation via CO_2 activation. In the past decades, many publications have appeared, focusing on incorporation of CO_2 into propargylic alcohols to generate *a*-alkyldine cyclic carbonates, 2-oxazolidinones and/or β-oxoalkylcarbamates in the presence of amines. Through great progress has been made, high CO_2 pressure and reaction temperature are usually required for performing the reaction efficiently. In other words, chemical transformation of CO_2 at atmospheric pressure and room temperature still remains a great challenge. As expected, further enhanced reactivity and selectivity could depend on the transition-metal catalysis which could be capable of activating the carbon-carbon triple bond of propargylic alcohols on the basis of mechanistic understanding on a molecular level.

The purpose of this review is to feature recent advances on metal-promoted incorporation of CO_2 as both carbon and oxygen source into propargylic alcohols/amines through carbonylative or carboxylative cyclization under milder reaction conditions particular low pressure in the production of carbonyl-containing heterocycles including cyclic carbonates, 2-oxazolidinones or β-oxoalkylcarbamates. We believe that this type of reactions will open new avenues in the field of upgrading use of CO_2 from waste to sustainable chemical feedstock in organic synthesis. This review will stimulate further interest in research that may lead to the development of complementary strategies.

Publication Date (Web): September 11, 2015 | doi: 10.1021/bk-2015-1194.ch002

In Advances in CO2 Capture, Sequestration, and Conversion; He, et al.;
ACS Symposium Series; American Chemical Society: Washington, DC, 2015.

Publication Date (Web): September 11, 2015 | doi: 10.1021/bk-2015-1194.ch002

Synthesis of *a*-Alkylidene Cyclic Carbonates from Propargylic Alcohols and CO_2

The catalytic carboxylative cyclization of propargylic alcohols with CO_2 holds great promise for direct incorporating CO_2 into high value-added chemicals as depicted in Scheme 1; that is, α-alkylidene cyclic carbonate, an important framework in natural products with potential bioactivities (*9*) and a broad range of applications as intermediates in organic synthesis (*10–12*). To date, several metal-free catalytic systems, such as tertiary phosphine (*13*, *14*), N-heterocyclic carbene (NHC)/CO_2 adduct (*15*), bicyclic guanidine (*16*), N-heterocyclic olefin/CO_2 adduct (*17*), and alkoxide-functionalized imidazolium betaine/CO_2 adduct (*18*) have been developed for the preparation of α-alkylidene cyclic carbonates. However, higher CO_2 pressure and reaction temperature are usually required for performing the reaction efficiently. In this regard, further enhanced reactivity and selectivity could depend on the transition-metal catalysis. Therefore, efforts to convert CO_2 to useful chemicals will inevitably rely on its activation through molecular catalysts, particularly transition-metal catalysts on the basis of mechanistic understanding at a molecular level.

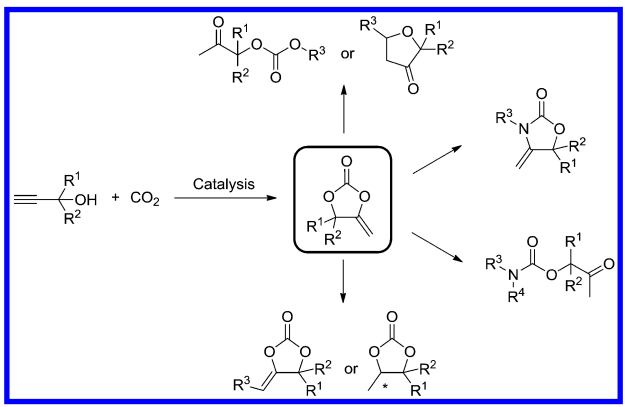

Scheme 1. Incorporation of CO_2 into α-alkylidene cyclic carbonates and their derivatives.

In early years, several catalytic systems such as Ru (*19*), Co (*20*), Pd (*21*), Cu (*22*) were founded to synthesize *a*-alkylidene cyclic carbonates from propargylic alcohols and CO_2. However, those procedures pose a number of drawbacks, in particular, using complicated catalysts, requirement of higher CO_2 pressure, strict avoidance of moisture and air. To be delighted, these problems can be overcome through rational design of robust metal catalytic system.

Recent years, a number of novel effective catalytic systems well up. Ionic liquids (ILs) have some very attractive properties, such as being non-volatile, non-flammable, and having high thermal stabilities and excellent solubility in both organic and inorganic substances (*23*). Additionally, catalytic reactions have been widely studied using ILs as solvents and/or catalysts. Deng and co-workers pioneered the use of effective CuCl/[BMIm][$PhSO_3$] catalytic system with high selectivity (IL media, 2 mol% copper catalyst, 120 °C, 1.0 MPa, 8 h) (Scheme 2)

In Advances in CO2 Capture, Sequestration, and Conversion; He, et al.;
ACS Symposium Series; American Chemical Society: Washington, DC, 2015.

(*24*). In this system, ILs as a novel reaction medium could promote the reaction smoothly and be easily recovered and reused after completing the reaction. Notably, direct distillation of cyclic carbonates from the reaction mixture after the reaction, the copper catalyst immobilized in ILs could be reused 3 times without losing activity.

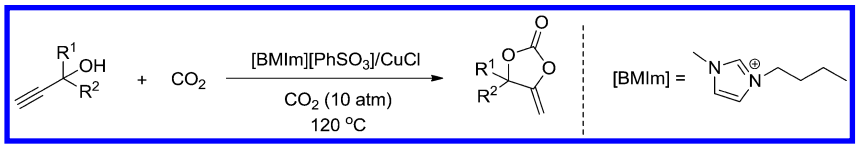

Scheme 2. CuCl/[BMIm][PhSO$_3$]-promoted carboxylative cyclization of propargylic alcohols and CO$_2$.

The reaction between CO_2 and propargylic alcohols catalyzed by AgOAc in 1-ethyl-3-methylimidazolium diethylphosphate ([EMIM][(EtO)$_2$PO$_2$]) was conducted at 30 °C under 4 MPa CO_2 developed by Han group (*25*). [EMIM][(EtO)$_2$PO$_2$] acted as both base and solvent in the reaction. Moreover, the AgOAc/[EMIM][(EtO)$_2$PO$_2$] catalytic system could be reused three times without considerable loss of the activity.

Herein, task-specific basic ILs have displayed superior performance for CO_2 conversion through carboxylative cyclization of propargylic alcohols with CO_2. Recently, our group developed a two-component catalytic system of 1-butyl-2-methyl-3-methylimidazolium halogen ([BMMIM]X, X = Cl or Br) in combination with basic silver compounds (AgOAc, Ag_2CO_3 or Ag_2O), which was able to promote CO_2 conversion in the synthesis of α-methylene cyclic carbonate from 2-methyl-3-butyn-2-ol with CO_2 as shown in Scheme 3 (*26*). Using catalytic loading of [BMMIM]Br/AgOAc (2 mol% [BMMIM]Br, 1 mol% AgOAc), up to 96% yield of product was obtained under CO_2 balloon at 60 °C for 12 h. In this reaction, acetate anion/halogen anion acts as Lewis base and silver/imidazolium cation performs as Lewis acid.

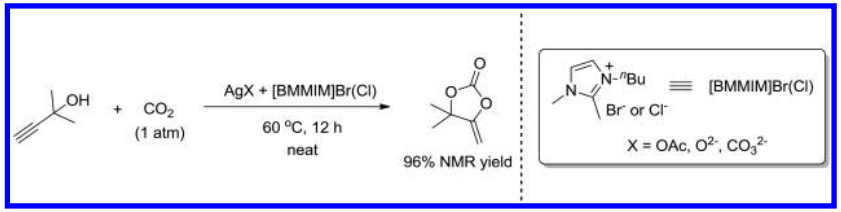

Scheme 3. [Ag]/ILs-catalyzed carboxylative cyclization of propargylic alcohols and CO$_2$.

Supercritical carbon dioxide (scCO_2) as a reactant and promising reaction medium has recently received much attention, not only because of its benign character, but also greatly improving the catalytic activity and the product selectivity (*27*). Jiang and co-workers (*28*) presented a heterogeneous polymer-supported catalyst containing cuprous iodide and amino functions promoted cyclization of propargylic alcohols with CO_2 to α-alkylidene cyclic

Publication Date (Web): September 11, 2015 | doi: 10.1021/bk-2015-1194.ch002

carbonates under supercritical conditions (8 mol% catalyst, 40 °C, 14 MPa, 24 h) (Scheme 4). The bifunctional polymer containing organic base and Lewis acid was demonstrated to be effective and reusable catalyst.

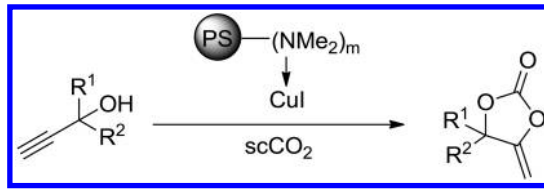

Scheme 4. Carboxylative cyclization of propargylic alcohols with $scCO_2$ catalyzed by DMAM-PS-CuI.

Polystyrene-supported N-heterocyclic carbene-silver complexes [PS-NHC-Ag(I)] was confirmed to be an effective catalyst with high activity and and selectively yielding the corresponding *α*-alkylidene cyclic carbonates in good yields under mild conditions (2 mol% catalyst, 40 °C, 5 MPa, 24 h) (Scheme 5) (*29*). NHC, as a strong nucleophile behaving basic feature, could promoted the cyclization in combination with silver. More importantly, the supported catalysts could be separated easily from the products and reused up to 15 times without loss of their high catalytic activity, showing excellent stability.

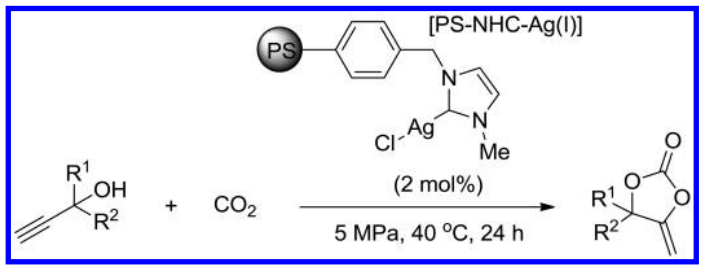

Scheme 5. Synthesis of various cyclic carbonates catalyzed by polystyrene-supported NHC-Ag.

Recently, our group (*30*) described a sustainable and cost-competitive catalytic process promoted by Ag_2WO_4/Ph_3P system for efficient chemical fixation of CO_2 to produce *α*-alkylidene cyclic carbonates as illuminated in Scheme 6. Such CO_2 fixation protocol proceeded smoothly with only 1 mol% of Ag_2WO_4 and 2 mol% PPh_3 as well as atmospheric CO_2 at room temperature under solvent-free conditions, featuring environmentally benign and low energy-consumption manner along with easy operating procedure. Importantly, the catalytic system is not sensitive to air and moisture. In addition, dual activation for both propargylic substrate and CO_2 by Ag_2WO_4/Ph_3P was also characterized by NMR technique (see Figure 1 for ^{13}C NMR), which based on the cooperative catalytic mechanism by silver cation and tungstate anion.

In Advances in CO2 Capture, Sequestration, and Conversion; He, et al.;
ACS Symposium Series; American Chemical Society: Washington, DC, 2015.

Publication Date (Web): September 11, 2015 | doi: 10.1021/bk-2015-1194.ch002

Publication Date (Web): September 11, 2015 | doi: 10.1021/bk-2015-1194.ch002

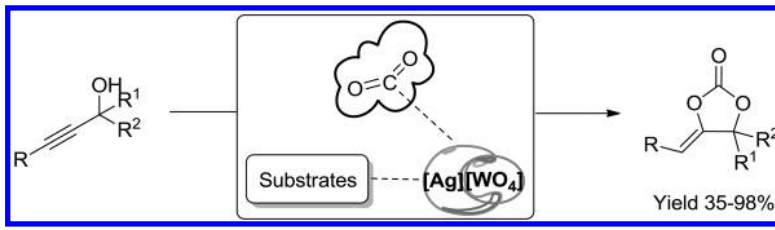

Scheme 6. Ag_2WO_4/Ph_3P-promoted fixation of CO_2.

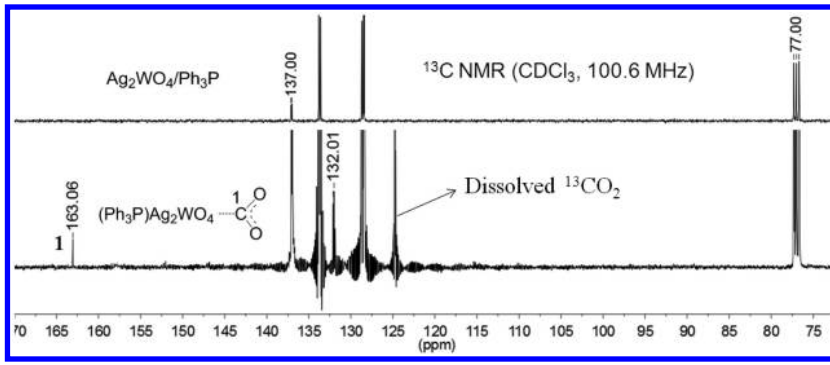

Figure 1. ^{13}C NMR investigation for CO_2 activation by Ag_2WO_4/Ph_3P.

Terminal propargylic alcohols and internal propargylic alcohols have different reactivity which is related to the substituent at the position of terminal alkyne. One of the most effective catalytic systems could be Ag(I)/1,8-diazabicyclo[5.4.0]undec-7-ene (DBU) system (*31*) for the cyclization reaction of CO_2 with internal propargylic alcohols (Scheme 7, Base **A**). The combined use of a catalytic amount of silver acetate and a stoichiometric amount of DBU efficiently promoted the reaction under mild reaction conditions (room temperature and 1-10 atm CO_2) into a wide range of internal propargylic alcohols to afford the corresponding cyclic carbonates in high yields. Moreover, all the cyclic carbonates were found to be single isomers. Additionally, when the chiral Schiff base ligand was used (Scheme 7, Base **B**) instead of DBU (*32*), enantioselective chemical CO_2 incorporation into various bispropargylic alcohols was achieved by the combined use of a catalytic amount of silver acetate.

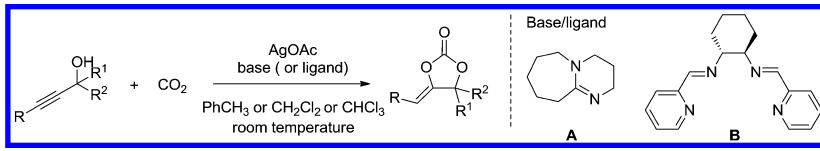

Scheme 7. Proposed mechanism of CO_2 incorporation into propargylic alcohols.

In Advances in CO2 Capture, Sequestration, and Conversion; He, et al.;
ACS Symposium Series; American Chemical Society: Washington, DC, 2015.

Mechanistic Consideration on Carboxylative Cyclization of Propargylic Alcohols with CO_2

The strategy to produce *α*-alkylidene cyclic carbonates is fundamentally based on the cyclization of the propargylic carbonate species $HC{\equiv}CCH_2OCO_2$– into the corresponding *a*-alkylidene cyclic carbonate (*16*, *19*, *20*, *28*, *30*, *31*). The propargylic alcohols initially reacted with CO_2 to generate the carbonate intermediate in the presence of large amount of organic base (Scheme 8). Then, an intramolecular ring-closing reaction would then proceed at the alkyne, which would be activated by the metal species to afford the corresponding cyclic carbonate with the release of the catalyst. The activation of the alkyne by the metal complex was proposed to be crucial to promote the present reaction in the literature (*31*).

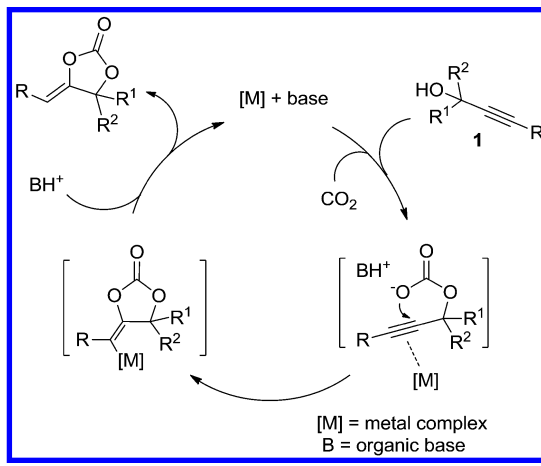

Scheme 8. Plausible mechanism for the transition-metal-catalyzed carboxylic reaction of propargylic alcohols and CO_2.

In the process of our recent study, we found that higher CO_2 pressure or additional energy is eventually inevitable for getting desired yield, despite nice selectivities can be reached with the transition-metal catalysis in most of previous reports. Generally, alkylcarbonic intermediates **I** involving in the two-component "metal-base"-catalyzed reaction of propargylic alcohols and CO_2 was brought forward in previous work. We made judgments that higher CO_2 pressure and temperature still be indispensable due to the strong interaction between base-H^+ and $HC{\equiv}CC(R^1R^2)OCO_2^-$ which limits the O-nucleophilicity of alkylcarbonic anion (**I**) based on the understanding and analysis of reaction mechanism. As previous reported, bulky cation, e.g. in K_2CO_3/crown ether (*33*) could enhance the catalytic roles of anion (e.g. enhanced O-nucleophilicity and basicity).

In Advances in CO2 Capture, Sequestration, and Conversion; He, et al.;
ACS Symposium Series; American Chemical Society: Washington, DC, 2015.

Publication Date (Web): September 11, 2015 | doi: 10.1021/bk-2015-1194.ch002

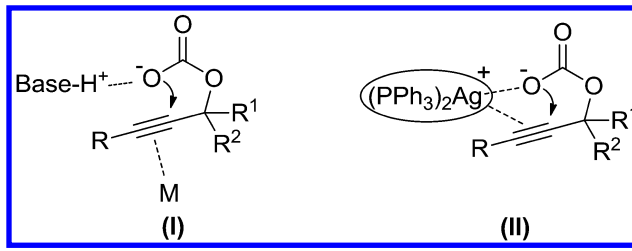

*Scheme 9. Activation mode by two-component catalyst system (**I**) and well-defined bifunctional metal complex (**II**).*

Publication Date (Web): September 11, 2015 | doi: 10.1021/bk-2015-1194.ch002

Recently, based on the well-developed silver-promoted chemical fixation of CO_2 at ambient conditions, mechanistic insights into the bifunctional silver-catalyzed carboxylative cyclization were further explored (*34*). The single-component basic silver complex (e.g. $[(PPh_3)_2Ag]_2CO_3$) (*35*). could perform excellent catalytic roles via the intermediate generated with the aid of $[(PPh_3)_2Ag]_2CO_3$ (Scheme 9, **II**). Presumably, intermediate **II**, bulky $[(Ph_3P)_2Ag(I)]$ can enhance O-nucleophilicity of alkylcarbonic anion, activate C≡C triple bond to facilitate subsequent attack through an intramolecular mode, rendering the reaction to efficiently perform at ambient conditions. On the basis of understanding and insight into the reaction mechanism at molecule level, we put forward the postulate that the ideal catalytic system would be a kind of bifunctional ones with both Lewis acid and Lewis base sites in combination with another key bulkier counterions cation compatibly.

Based on this assumption, a few experiments on reaction of propargylic alcohols with $^{13}CO_2$ were designed and monitored by using NMR technique to elucidate the catalytic role of $[(Ph_3P)_2Ag]_2CO_3$. Results revealed that the silver complex could effective activate CO_2 and propargylic alcohol i.e. OH group and C≡C bond.

Density functional theory (DFT) calculations were also performed in order to gain a deeper insight into the reaction and activation mode **I** and **II** as shown in Scheme 9. As illustrated in various parameters including electron charge of oxygen atom, stabilization energy and relative activation energy in comparison with that of **I**, the DFT results supported the effective activation model **II**.

To further confirm the catalytic conversion of CO_2 to cyclic carbonate at this study, $^{13}C_{carbonyl}$-labelled experiment was performed (Scheme 10). The presence of $^{13}C_{carbonyl}$-labelled *a*-methylidene cyclic carbonate verified successful CO_2 conversion.

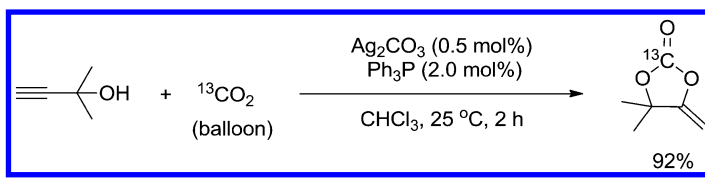

Scheme 10. $^{13}C_{carbonyl}$-labeled experiment.

In Advances in CO2 Capture, Sequestration, and Conversion; He, et al.;
ACS Symposium Series; American Chemical Society: Washington, DC, 2015.

Without using Lewis acid in the catalytic system, we (*36*) designed and prepared the ammonium tertiary phosphate catalyst, aiming to use for activating CO_2 and nucleophilic substrate due to its strong nucleophilicity and basicity to further support our postulate on ingenious interreaction model on a molecular level during the reaction (Scheme 11). Gratifyingly, up to 96% yield of *a*-methylidene cyclic carbonate was obtained by employing 1 mol% of $(^nBu_4N)_3PO_4$ under atmospheric pressure of CO_2 at 60 °C for 12 h. Phosphate anion (HPO_4^{2-}) bearing negative charge after trapping one proton leads to the evitable interaction with carboxylate anion. Additionally, bulkyl cation can enhance the O-nucleophilicity of carboxylate anion via the steric effect.

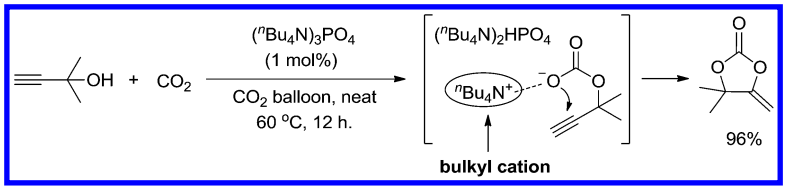

Scheme 11. Elaborately designed experiment on $(^nBu_4N)_3PO_4$-catalyzed carboxylic reaction in the absence of any metal.

In summary, efficient protocols to generate *a*-alkyldine cyclic carbonates has been well-developed in which CO_2 has been utilized as a carboxylating reagent through the metal-promoted carboxylative cyclization of propargylic alcohols. The metal-promoted procedure offers salient advantages and features: (1) it generally requires no organic solvent; (2) the catalytic system is very effective under mild conditions; (3) excellent yields, region-, and chemoselectivity towards the target products are obtained; (4) simple work-up procedure is required.

Reaction of CO_2 with Propargylamines

Synthesis of *a*-alkylidene oxazolidinones through carboxylative cyclization of propargylic amines and CO_2 is regarded as one of the most attractive synthetic methods. These heterocyclics are useful intermediates for further preparation of functional carbamates or oxazolidinones. As a consequence, great efforts have been made to accelerate this carboxylative cyclization through transition-metal catalysis including Cu (*37*), Ru (*38*), Pd (*39*, *40*), Ag (*41*, *42*), Au (*43*), basic species like guanidine derivatives (*44–47*), basic alumina (*48*), and (*t*-BuOI) (*49*) or using electrochemical method (*50*) (Scheme 12). This strategy is fundamentally based on the cyclization of the propargylic carbonate species into the corresponding *a*-alkylidene cyclic carbonate in the presence of metal catalyst.

Publication Date (Web): September 11, 2015 | doi: 10.1021/bk-2015-1194.ch002

In Advances in CO2 Capture, Sequestration, and Conversion; He, et al.;
ACS Symposium Series; American Chemical Society: Washington, DC, 2015.

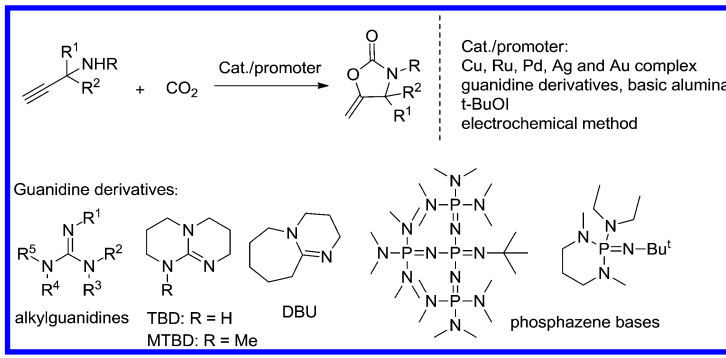

Scheme 12. Various catalytic systems for the preparation of oxazolidines from propargylic amines and CO_2.

Silver salts have been demonstrated to be one of the most efficient catalysts for the preparation of oxazolidinones from CO_2 and propargylic amines (*41*). This procedure could be successfully applied to various terminal and internal *N*-substituted and *N*-unsubstituted propargylic amines to afford the corresponding 1,3-oxazolidin-2-ones in high to excellent yield at ambient reaction conditions (2 mol % AgOAc, 0.1 MPa CO_2, 25 °C, 12 h). In the ring-closing reaction, silver catalyst capable of activating the alkyne is the key step which avoids the additional energy input. And free propargylic amine could work as a base to assist with the carbamate formation as shown in Scheme 13.

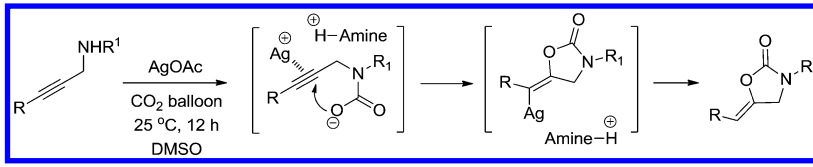

Scheme 13. The AgOAc-promoted carboxylative cyclization of propargylic amines and CO_2.

In general, high CO_2 pressure is required for CO_2 conversion. Therefore, the fixation of atmospheric CO_2 thus represents an attractive research area in both organic and green chemistry and still faces great challenge. Yoshida and coworkers developed a methodology for the synthesis of oxazolidinones by the fixation of CO_2 from the air with propargylic amines (*42*). The efficient process has been achieved by using the silver/DBU dual-catalyst system. Atmospheric CO_2 is initially trapped by DBU to form the DBU–CO_2 adduct *in situ*, and thus reacts with the silver-coordinated propargylic amine (Scheme 14). Then, intramolecular 5-exo-cyclization followed by proto-demetallation produces the oxazolidinone with regeneration of the silver complex and DBU. As a result, the reaction afforded a variety of substituted oxazolidinones in good yields, and the process provided an alternative practical protocol for the utilization of air as a source of CO_2.

In Advances in CO2 Capture, Sequestration, and Conversion; He, et al.;
ACS Symposium Series; American Chemical Society: Washington, DC, 2015.

Publication Date (Web): September 11, 2015 | doi: 10.1021/bk-2015-1194.ch002

Publication Date (Web): September 11, 2015 | doi: 10.1021/bk-2015-1194.ch002

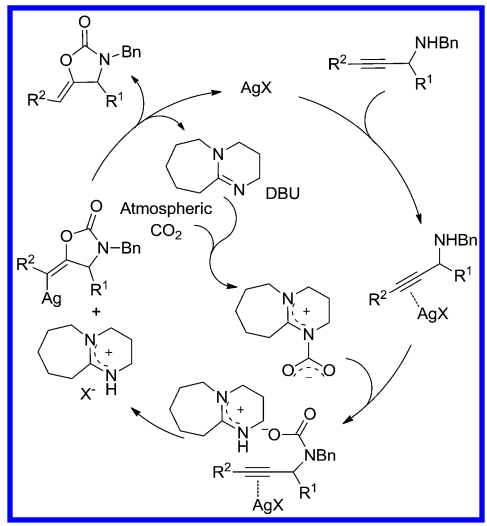

Scheme 14. Proposed reaction mechanism for the [Ag]/DBU dual-activated fixation of atmospheric CO_2.

Recently, Ikariya group (*43*) described the NHC-Au(I) complexes-promoted carboxylative cyclization of a range of propargylic amines to afford (Z)-5-alkylidene-1,3-oxazolidin-2-ones in methanol under mild conditions (0.5-1 atm CO_2, 40 °C, 16-91% yield). The highly active catalyst permits CO_2 transformation under a mixed gas atmosphere containing CO or H_2. The chlorogold(I) precursor can form a catalytically active cationic species via facile dissociation of the anionic ligand in a polar methanol medium as depicted in Scheme 15. The alkyne moiety of propargylic carbamate formed through a spontaneous carboxylation of the amine substrate is activated by the cationic Au(I) center. The carbamate anion attacks nucleophilically on the triple bond in an *anti* fashion to generate the corresponding neutral alkenylgold intermediate, followed by proto-demetallation with liberation of the urethane product.

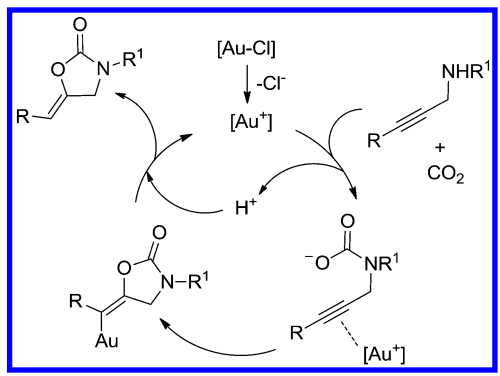

Scheme 15. Proposed mechanism for the NHC-Au complexes-catalyzed carboxylative cyclization of propargylic amines and CO_2.

In Advances in CO2 Capture, Sequestration, and Conversion; He, et al.;
ACS Symposium Series; American Chemical Society: Washington, DC, 2015.

Moreover, they successfully identified the key alkenylgold(I) intermediate from a stoichiometric reaction of Au(OH)(IPr) and 1-methylamino-2-butyne in THF (Scheme 16). In this reaction, the methanol would pose two unique advantages: (1) promoting the formation of catalytically active cationic gold species; and (2) facilitating proto-demetallation especially with regard to the CO_2-mediated acceleration due to in situ generation of methylcarbonic acid in the product-releasing step.

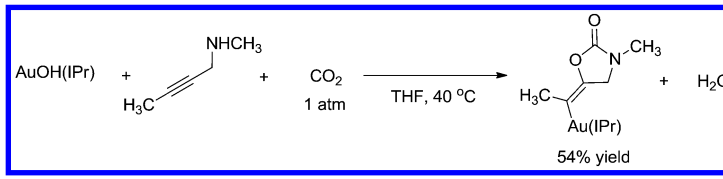

Scheme 16. Formation of the alkenylgold(I) complex.

Allenes have the similar reactivity to alkynes. Therefore, 2,3-allenic amines can also react with CO_2 to form 5-vinyl-1,3-oxazolidin-2-ones (*51*, *52*). Takao Ikariya *et al*. (*51*) first accomplished the Pd-catalyzed cyclic urethane synthesis via intramolecular addition of carbamic acids across the carbon-carbon double bond in allenic substrates. The dense CO_2 proved to be crucial for smooth CO_2 fixation.

The catalytic reaction is likely initiated by the oxidative addition of the carbamic acid generated from the allenic amine and CO_2, which is responsible for the formation of hydridopalladium species. The allene moiety inserts into the Pd-H bond to give an η^3-allylpalladium intermediate, and the following reductive elimination would afford the cyclization product as described in Scheme 17.

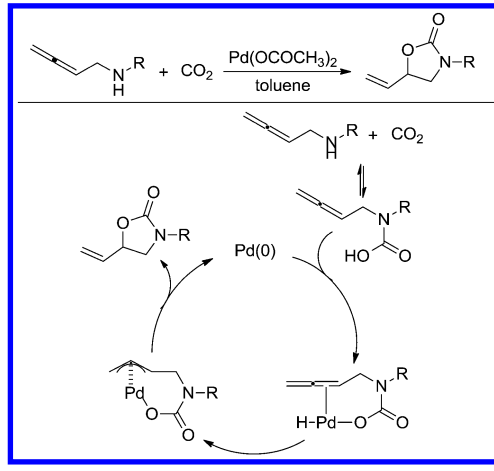

Scheme 17. Proposed mechanism for the Pd-catalyzed reaction of allenic amines with CO_2.

In Advances in CO2 Capture, Sequestration, and Conversion; He, et al.;
ACS Symposium Series; American Chemical Society: Washington, DC, 2015.

Publication Date (Web): September 11, 2015 | doi: 10.1021/bk-2015-1194.ch002

Publication Date (Web): September 11, 2015 | doi: 10.1021/bk-2015-1194.ch002

Recycling of Intramolecular-Produced CO_2 Molecule into Valuable Chemicals

In traditional decarboxylation reactions, CO_2 is produced as a co-product, which are disadvantageous from an economic point of view. However, there are few reports on the recycling of this in situ-formed CO_2 molecule. Delightedly, in recent years, more and more attention has been paid to converting the CO_2 molecule produced intramolecularly into value-added chemicals.

In 2001, Ihara and co-worker (*53*) reported a novel synthesis of cyclic carbonates by Pd-catalyzed domino reaction of 4-methoxycarbonyloxy-2-butyn-1-ols with phenols (Scheme 18). This protocol enables the efficient construction of cyclic carbonates in a one-pot process with recycling of the CO_2 molecule. It is the precursory example of efficient re-fixation of the CO_2 molecule from a decarboxylation reaction featuring as convenient and environmentally friendly procedure.

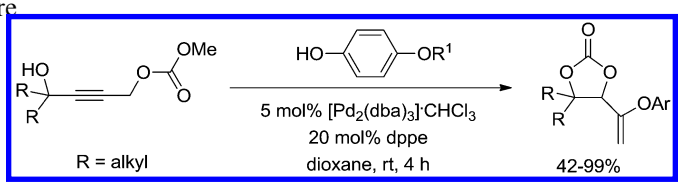

Scheme 18. Domino reactions of various propargylic carbonates with substituted phenols.

A plausible mechanism is shown in Scheme 19. In the presence of the palladium catalyst, the propargylic carbonate **A** would undergo elimination of CO_2 to give the allenylpalladium methoxide **B**, which would be subject to nucleophilic attack by phenols to give the π-allylpalladium complex **D** through the intermediate **C**. Finally, **D** would re-fix CO_2 to afford the carbonate species **E**, which would subsequently cyclize to produce the aryloxy-substituted cyclic carbonate.

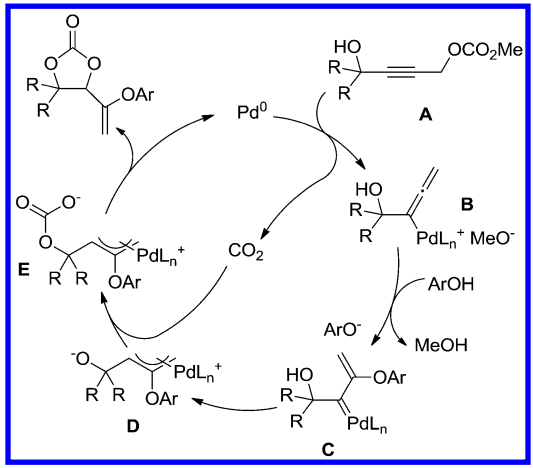

Scheme 19. Possible reaction mechanism of the domino reaction.

In Advances in CO2 Capture, Sequestration, and Conversion; He, et al.;
ACS Symposium Series; American Chemical Society: Washington, DC, 2015.

Additional typical example of one-pot process with recycling of the CO_2 molecule is the synthesis of oxazolidin-2-ones via copper(I)-catalyzed tandem cyclization of propiolic acid, primary amine and aldehyde (*54*) (Scheme 20). This is an efficient approach for the synthesis of oxa-zolidin-2-one under mild reaction conditions and the procedure is applicable to a broad scope of aldehydes, primary amines and propiolic acids. The reaction is mainly through the decarboxylative and carboxylative cyclization procedure.

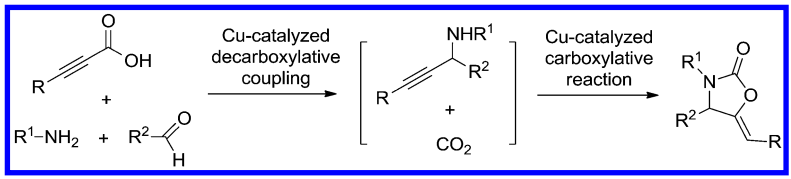

Scheme 20. Cu(I)-catalyzed tandem cyclization of propiolic acid, primary amine and aldehyde.

Firstly, propiolic acid undergoes a Cu(I)-catalyzed decarboxylation affording copper acetylide and CO_2 (Scheme 21). Then the copper acetylide attacks the *in situ* formed imine resulting in the formation of the intermediate propargylic amine. Finanlly, a Cu(I)-catalyzed addition of CO_2 released from the propiolic acid to propargylic amine gives the desired product via a Cu(I)-catalyzed cyclization carboxylation.

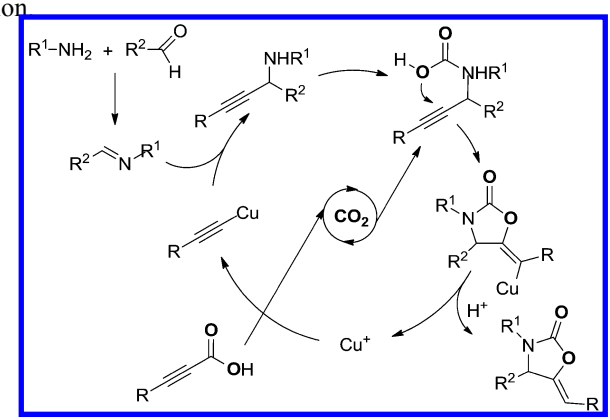

Scheme 21. Proposed mechanism of Cu(I)-catalyzed three-component reaction of propiolic acid, primary amine and aldehyde.

Synthesis of Oxazolidinones Derivatives from Propargylic Alcohols, Primary Amines, and CO_2

Oxazolidinones are important heterocyclic compounds, and meanwhile they can be used as chiral synthons or chiral auxiliaries in asymmetric syntheses. In addition, they usually acts as necessary moiety in pharmaceutical chemistry due to significant antibacterial properties (*55*) Thus, synthesis of this heterocyclic system is of much interest, and a number of procedures have been developed (*56–60*). A

In Advances in CO2 Capture, Sequestration, and Conversion; He, et al.;
ACS Symposium Series; American Chemical Society: Washington, DC, 2015.

Publication Date (Web): September 11, 2015 | doi: 10.1021/bk-2015-1194.ch002

method in which CO_2 has been utilized as a substrate is through the cyclization of easily available propargylic alcohols and primary amines to generate functional oxazolidinones bearing exocyclic alkenes (5-methylene-1,3-oxazolidin-2-ones or *a*-methylene oxazolidinones), which could allow further transformation of the 1,3-oxazolin-2-one and the preparation of synthetically useful derivatives. This route offers economical and environmental advantages such as high atom efficiency and water as only by-product.

To date, several metal-free systems, such as tertiary phosphine (*61*), organic bases (*16*), and ILs (*62*) have been developed for the preparation of 5-methylene-1,3-oxazolidin-2-ones. However, high CO_2 pressure and reaction temperature (5-14 MPa CO_2, 100-140 °C) are usually required for performing the reaction efficiently. In this regard, further enhanced reactivity and selectivity could depend on the transition-metal catalysis including Cu (*63–65*), and Ag (*30*, *34*, *36*, *66*).

In 2005, Deng group (*63*) developed a CuCl/[BMIm]BF_4 system for the three-component reaction under relatively mild conditions (2.5 MPa CO_2, 100 °C, 10 h). Therefore, several 5-methylene-1,3-oxazolidin-2-ones were prepared in excellent yields. Moreover, IL as well as CuCl catalyst can be recovered and reused three times without appreciable loss of activity. This methodology offers significant improvements with regard to yield of products, simplicity in operation, cost efficiency, and green aspects avoiding toxic or expensive reagents.

Later, Jiang and coworkers (*64*) developed an efficient and eco-friendly Cu-promoted process to synthesize 4-methyleneoxazolidin-2-ones and 4-methyloxazol-2-ones in $scCO_2$ as shown in Scheme 22. CO_2 was employed not only as reaction medium, but also as starting material. This is the first example for the synthesis of 4-methyloxazol-2-ones from secondary propargylic alcohols with high yield. By using CuCl as catalyst, 4-methylene-1,3-oxazolidin-2-ones could be prepared via the cycloadditon reaction of propargylic alcohols with primary amines with atmospheric CO_2 at 60 °C without any additional solvent (*65*). This methodology affords an ecofriendly, mild, and easy approach to chemical fixation of CO_2.

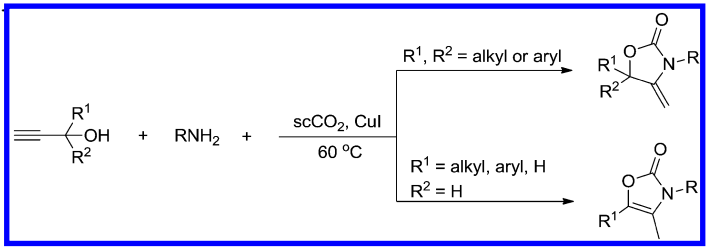

Scheme 22. CuI-catalyzed three-component reaction of propargylic alcohols, primary amines and $scCO_2$.

Afterwards, they (*66*) also reported the silver-catalyzed synthesis of 4-alkylidene-1,3-oxazolidin-2-ones through the reaction of internal propargylic alcohols in $scCO_2$. The catalytic system was effective for various alcohols, but invalid for internal propargylic alcohols with alkyl group at terminal site as illustrated in Scheme 23.

In Advances in CO2 Capture, Sequestration, and Conversion; He, et al.;
ACS Symposium Series; American Chemical Society: Washington, DC, 2015.

Publication Date (Web): September 11, 2015 | doi: 10.1021/bk-2015-1194.ch002

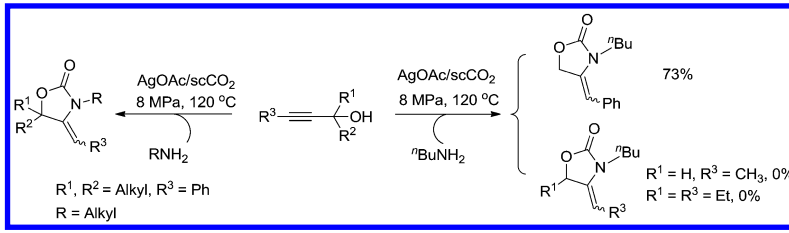

Scheme 23. AgOAc-catalyzed three-component reaction of propargylic alcohols, primary amines and $scCO_2$.

Recently, the successful transformation of propargylic alcohols to α-alkylidene cyclic carbonates through CO_2 fixation at ambient conditions prompted us to expand potential application of this functional Ag_2WO_4/Ph_3P system to synthesis of α-alkylidene oxazolidinones *via* the three-component reaction of propargylic alcohols, primary amines and CO_2 under mild conditions (*30*) (Scheme 24). Pleasingly, the transformation was performed smoothly with a variety of propargylic alcohols and primary amines in the presence of 0.5 MPa CO_2 at 50 °C for 12 h.

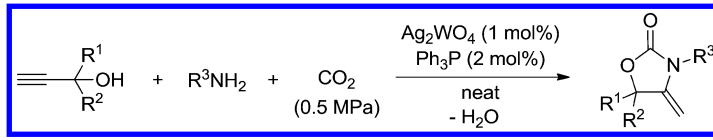

Scheme 24. Ag_2WO_4/Ph_3P-promoted three-component reaction of propargylic alcohols, primary amines and $scCO_2$.

The mechanism of three-component reaction *via* a tandem aminolysis of α-alkylidene cyclic carbonates/intramolecular cyclization was generally described as depicted in Scheme 25.

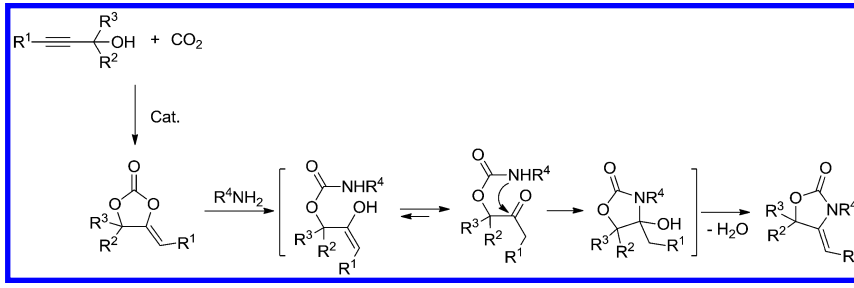

Scheme 25. Proposed mechanism for the three-component reaction of propargylic alcohols, primary amines and CO_2.

The three-component assembly of aldehydes, alkynes, and amines is well known as an A3 coupling reaction, which has been extensively and intensively studied because of its wide use in pharmaceutical chemistry and synthetic organic chemistry (*67*, *68*). Li *et al.* (*69*) developed an efficient CuI-catalyzed

In Advances in CO2 Capture, Sequestration, and Conversion; He, et al.;
ACS Symposium Series; American Chemical Society: Washington, DC, 2015.

Publication Date (Web): September 11, 2015 | doi: 10.1021/bk-2015-1194.ch002

four-component, tandem A3-coupling/carboxylative cyclization between aldehydes, aliphatic amines, terminal alkynes, and CO_2 under atmospheric pressure for the synthesis of important oxazolidinone products (Scheme 26). It is a rare example in which CO_2 acts as both a promoter and substrate for the tandem A3-coupling/carboxylative cyclization reaction. Remarkably, the copper is regarded as twice activation of the alkyne in A3-coupling and carboxylative cyclization procedure.

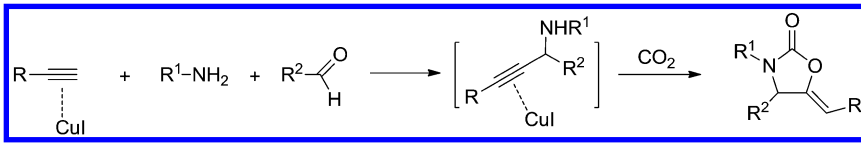

Scheme 26. Copper-catalyzed four-component coupling between aldehydes, amines, alkynes and CO_2.

Ketones are much less reactive than aldehydes for both steric and electronic reasons. Recently, it has been reported that ketones could be coupled with alkynes, amines and CO_2 catalyzed by $CuI/SnCl_2$ to provide the oxazolidinones in DMSO at 70 °C (*70*). Experiment results show steric hindrance has an extreme effect on the four-component coupling and aliphatic ketones, basic primary amines, and aryl alkynes are good substrates.

Synthesis of *β*-Oxopropylcarbamates from Propargylic Alcohols, Secondary Amines, and CO_2

One of the most promising examples of CO_2 fixation is the three-component reaction of propargyl alcohols, secondary amines and CO_2 to access *β*-oxopropylcarbamates (Scheme 27), which stands for an important class of carbamate compounds in agriculture and pharmacology, as useful intermediates in organic synthesis and as protective groups of an amine function in peptide chemistry (*71*). In this context, early reported catalytic systems include metal complex of Ru (*72*, *73*), Fe (*74*), Cu (*22*), which most gave only moderate yield even in the high CO_2 pressure (≥3 MPa) with the aid of the additional heat (≥70 °C). Recently, AgOAc/DBU was found to be an effective catalytic system for the *β*-oxopropylcarbamates synthesis under 2 MPa CO_2 at 90 °C (*75*). Without using catalyst, excess amines (2 equiv.) combined with much higher CO_2 pressure (14 MPa) and reaction temperature (130 °C) are needed to gain satisfied yield (*76*). Moreover, bicyclic guanidines (*16*) have been developed for the synthesis of *β*-oxopropylcarbamates from propargyl alcohols, secondary amines and CO_2 under supercritical conditions (up to 82% GC yield at 100 °C). Despite well-established synthetic protocols, effective methodologies using CO_2 as a feedstock under atmospheric pressure with low energy input are still challenging.

Publication Date (Web): September 11, 2015 | doi: 10.1021/bk-2015-1194.ch002

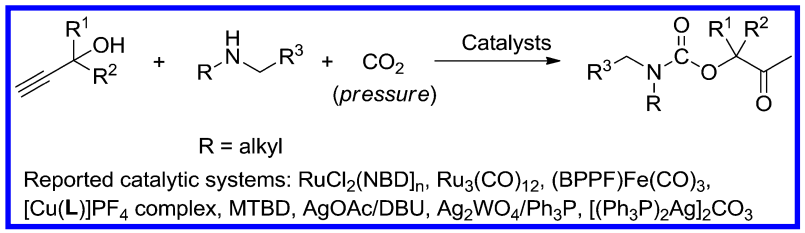

Scheme 27. Various catalytic systems on three-component reaction of propargylic alcohols, secondary amines and CO_2.

In the course of our continuing efforts in developing silver-catalyzed carboxylative cyclization of propargylic alcohols and CO_2 under atmospheric pressure (*30*, *34*), we have discovered that a silver catalyst combined with PPh_3 ligand could promote the generation of the silver propargylic carbonate intermediate, and the resulting intermediates could further undergo a subsequent attack through an intramolecular mode to produce the α-alkylidene cyclic carbonates (Scheme 28). We hypothesized that chemical transformation of three-component reaction of propargylic alcohols, secondary amines and CO_2 could be achieved by using silver complexes as catalysts. Subsequently, we disclosed the first catalytic protocol utilization atmospheric pressure of CO_2 for the synthesis of β-oxopropylcarbamates directly from propargylic alcohols and secondary amines at 30 °C, revealing an unprecedented reactivity for silver complex under mild conditions.

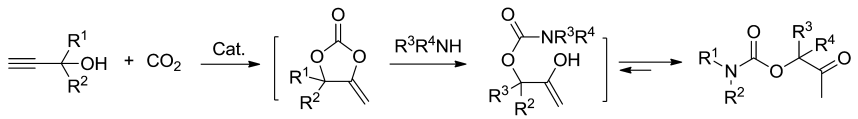

Scheme 28. Proposed mechanism for the three-component reaction of propargylic alcohols, secondary amines, and CO_2.

Conclusions

CO_2 fixation and conversion hold great promise for recycling CO_2 into value-added products due to the great potential of CO_2 as sustainable and renewable C_1 feedstock. Great efforts and wonderful progress have been made on CO_2 as a C_1 feedstock in synthetic chemistry for producing bulk chemicals, fuels, and materials. In this regard, we particularly presented the transition metal-promoted CO_2 conversion under mild conditions for the synthesis of specialized/commodity chemicals based on the carboxylative cyclization of propargylic alcohols, propargylic amines and their derivatives. There remain many challenges to be overcome, such as reaction control and reactivity enhancement, and opportunities to be explored further on the topic of CO_2 in synthetic chemistry, especially in terms of functionalization of CO_2 through CO_2 activation by using metal catalytic systems. We hope this presentation will

In Advances in CO2 Capture, Sequestration, and Conversion; He, et al.;
ACS Symposium Series; American Chemical Society: Washington, DC, 2015.

Publication Date (Web): September 11, 2015 | doi: 10.1021/bk-2015-1194.ch002

provoke further interest in academic research and industrial development that may lead to the development of CO_2 as an environmentally benign C_1 feedstock for organic synthesis.

Acknowledgments

We are grateful to the National Natural Sciences Foundation of China, Specialized Research Fund for the Doctoral Program of Higher Education (project 20130031110013), MOE Innovation Team (IRT13022) of China for financial support.

Publication Date (Web): September 11, 2015 | doi: 10.1021/bk-2015-1194.ch002

References

1. Abelson, P. H. Limiting atmospheric CO_2. *Science* **2000**, *289*, 1293–1293.
2. Aresta, M.; Dibenedetto, A. Utilisation of CO_2 as a chemical feedstock: opportunities and challenges. *Dalton Trans.* **2007**, 2975–2992.
3. He, L.-N.; Wang, J.-Q.; Wang, J.-L. Carbon dioxide chemistry: examples and challenges in chemical utilization of carbon dioxide. *Pure Appl. Chem.* **2009**, *81*, 2069–2080.
4. Sakakura, T.; Choi, J.-C.; Yasuda, H. Transformation of carbon dioxide. *Chem. Rev.* **2007**, *107*, 2365–2387.
5. Yang, Z.-Z.; He, L.-N.; Gao, J.; Liu, A.-H.; Yu, B. Carbon dioxide utilization with C-N bond formation: carbon dioxide capture and subsequent conversion. *Energy Environ. Sci.* **2012**, *5*, 6602–6639.
6. Huang, K.; Sun, C.-L.; Shi, Z.-J. Transition-metal-catalyzed C–C bond formation through the fixation of carbon dioxide. *Chem. Soc. Rev.* **2011**, *40*, 2435–2452.
7. Aresta, M.; Dibenedetto, A.; Angelini, A. Catalysis for the valorization of exhaust carbon: from CO_2 to chemicals, materials, and fuels. technological use of CO_2. *Chem. Rev.* **2014**, *114*, 1709–1742.
8. Yu, B.; He, L.-N. Upgrading incorporation of carbon dioxide into heterocycles. *ChemSusChem* **2015**, *8*, 52–62.
9. Zhang, H.; Liu, H. B.; Yue, J. M. Organic carbonates from natural sources. *Chem. Rev.* **2014**, *114*, 883–898.
10. Ohe, K.; Matsuda, H.; Ishihara, T.; Ogoshi, S.; Chatani, N.; Murai, S. Palladiun-catalyzed reaction of 5-methylene-1,3-dioxolan-2ones-A new access to and reactivity of oxatrimethylenemethane palladium. *J. Org. Chem.* **1993**, *58*, 1173–1177.
11. Ohe, K.; Matsuda, H.; Morimoto, T.; Ogoshi, S.; Chatani, N.; Murai, S. Nucleophilic-substitution at the central allyl carbon-atom of a (pi-allyl)palladium complex. *J. Am. Chem. Soc.* **1994**, *116*, 4125–4126.
12. Besse, V.; Camara, F.; Voirin, C.; Auvergne, R.; Caillol, S.; Boutevin, B. Synthesis and applications of unsaturated cyclocarbonates. *Polym. Chem.* **2013**, *4*, 4545–4561.

13. Fournier, J.; Bruneau, C.; Dixneuf, P. H. Phosphine catalyzed synthesis of unsaturated cyclic carbonates from carbon dioxide and propargylic alcohols. *Tetrahedron Lett.* **1989**, *30*, 3981–3982.
14. Kayaki, Y.; Yamamoto, M.; Ikariya, T. Stereoselective formation of alpha-alkylidene cyclic carbonates via carboxylative cyclization of propargyl alcohols in supercritical carbon dioxide. *J. Org. Chem.* **2007**, *72*, 647–649.
15. Kayaki, Y.; Yamamoto, M.; Ikariya, T. N-Heterocyclic carbenes as efficient organocatalysts for CO_2 fixation reactions. *Angew. Chem., Int. Ed.* **2009**, *48*, 4194–4197.
16. Cà, N. D.; Gabriele, B.; Ruffolo, G.; Veltri, L.; Zanetta, T.; Costa, M. Effective guanidine-catalyzed synthesis of carbonate and carbamate derivatives from propargyl alcohols in Supercritical carbon dioxide. *Adv. Synth. Catal.* **2011**, *353*, 133–146.
17. Wang, Y. B.; Wang, Y. M.; Zhang, W. Z.; Lu, X. B. Fast CO_2 sequestration, activation, and catalytic transformation using N-Heterocyclic Olefins. *J. Am. Chem. Soc.* **2013**, *135*, 11996–12003.
18. Wang, Y. B.; Sun, D. S.; Zhou, H.; Zhang, W. Z.; Lu, X. B. Alkoxide-functionalized imidazolium betaines for CO_2 activation and catalytic transformation. *Green Chem.* **2014**, *16*, 2266–2272.
19. Bruneau, C.; Dixneuf, P. H. Catalytic incorporation of CO_2 into organic substrates: Synthesis of unsaturated carbamates, carbonates and ureas. *J. Mol. Catal.* **1992**, *74*, 97–107.
20. Inoue, Y.; Ishikawa, J.; Taniguchi, M. M. Reaction of enohexopyranoside acetates with lithium dimethylcuppate (I) and its application to synthesis of Prelog-Djerssi lactone. *Bull. Chem. Soc. Jpn.* **1987**, *60*, 1204–1206.
21. Iritani, K.; Yanagihara, N.; Utimoto, K. Carboxylative coupling of propargylic alcohols with allyl chloride. *J. Org. Chem.* **1986**, *51*, 5499–5501.
22. Kim, H.-S.; Kim, J.-W.; Kwon, S.-C.; Shim, S.-C.; Kim, T.-J. Catalytic formation of carbamates and cyclic carbonates by copper complex of 2,5,19,22-tetraaza[6,6](1,1′)ferrocenophane-1,5-diene X-ray crystal structure of $[Cu(I)]PF_6$. *J. Organomet. Chem.* **1997**, *545–546*, 337–344.
23. Welton, T. Room-temperature ionic liquids. solvents for synthesis and catalysis. *Chem. Rev* **1999**, *99*, 2071–2084.
24. Gu, Y. L.; Shi, F.; Deng, Y. Q. Ionic liquid as an efficient promoting medium for fixation of CO_2: clean synthesis of α-methylene cyclic carbonates from CO_2 and propargyl alcohols catalyzed by metal salts under mild conditions. *J. Org. Chem.* **2004**, *69*, 391–394.
25. Shi, J. H.; Song, J. L.; Zhang, B. B.; Ma, J.; Zhang, P.; Wu, T. B.; Han, B. X. Efficient synthesis of α-alkylidene cyclic carbonate from CO_2 and propargylic alcohols in ionic liquids under mild conditions. *Sci. China Chem.* **2014**, *44*, 146–152.
26. Our study results showed that basic silver salts combination with imidazole salts were good catalytic system for the synthesis of α-methylene cyclic carbonates through the carboxylative cyclization of terminal propargyl alcohols with CO_2.

Publication Date (Web): September 11, 2015 | doi: 10.1021/bk-2015-1194.ch002

27. Jiang, H. F. Transition metal-catalyzed organic reactions in supercritical carbon dioxide. *Curr. Org. Chem* **2005**, *9*, 289–297.
28. Jiang, H. F.; Wang, A Z.; Liu, H. L.; Qi, C. R. Reusable polymer-supported amine-copper catalyst for the formation of α-alkylidene cyclic carbonates in supercritical carbon dioxide. *Eur. J. Org. Chem.* **2008**, *2008*, 2309–2312.
29. Tang, X. D.; Qi, C. R.; He, H. T.; Jiang, H. F.; Ren, Y. W.; Yuan, G. Q. Polystyrene-supported *N*-heterocyclic carbene–silver complexes as robust and efficient catalysts for the reaction of carbon dioxide and propargylic alcohols. *Adv. Synth. Catal.* **2013**, *355*, 2019–2028.
30. Song, Q. W.; Yu, B.; Li, X. D.; Ma, R.; Diao, Z. F.; Li, R. G.; Li, W.; He, L. N. Efficient chemical fixation of CO_2 promoted by bifunctional Ag_2WO_4/Ph_3P system. *Green Chem.* **2014**, *16*, 1633–1638.
31. Yamada, W.; Sugawara, Y.; Cheng, H. M.; Ikeno, T.; Yamada, T. Silver-catalyzed incorporation of carbon dioxide into propargylic alcohols. *Eur. J. Org. Chem.* **2007**, *2007*, 2604–2607.
32. Yoshida, S.; Fukui, K.; Kikuchi, S.; Yamada, T. Silver-Catalyzed enantioselective carbon dioxide incorporation into bispropargylic alcohols. *J. Am. Chem. Soc.* **2010**, *132*, 4072–4073.
33. Uemura, K.; Kawaguchi, T.; Takayama, H.; Nakamura, A.; Inoue, Y. Preparation of alkylidene cyclic carbonates via cyclization of propargylic carbonates. *J. Mol. Catal. A Chem.* **1999**, *139*, 1–9.
34. Song, Q.-W.; Chen, W.-Q.; Ma, R.; Yu, A.; Li, Q.-Y.; Chang, Y.; He, L.-N. Bifunctional silver(I) complex-catalyzed CO_2 conversion at ambient conditions: Synthesis of α-methylene cyclic car-bonates and derivatives. *ChemSusChem* **2015**DOI:10.1002/cssc.201402921.
35. G. Bowmaker, A.; Effendy; Hanna, J. V.; Healy, P. C.; King, S. P.; Pettinari, C.; Skelton, B. W.; White, A. H. Solution and mechanochemical syntheses, and spectroscopic and structural studies in thesilver(I) (bi-)carbonate: triphenylphosphine system. *Dalton Trans.* **2011**, *40*, 7210–7218.
36. Song, Q.-W.; He, L.-N. Bifunctional silver (I) catalysis for upgrading CO_2. *Prepr. Pap.-Am. Chem. Soc., Div. Energy Fuels.* **2014**, *59*, 299–300.
37. Dimroth, P.; Pasedach, H. DE Pat. 1164411, 1964.
38. Mitsudo, T.; Hori, Y.; Yamakawa, Y.; Watanabe, Y. Ruthenium catalyzed selective synthesis of enol carbamates by fixation of carbon dioxide. *Tetrahedron Lett.* **1987**, *28*, 4417–4418.
39. Bacchi, A.; Chiusoli, G. P.; Costa, M.; Gabriele, B.; Righi, C.; Salerno, G. Palladium-catalysed sequential carboxylation–alkoxycarbonylation of acetylenic amines. *Chem. Commun.* **1997**, *33*, 1209–1210.
40. Shi, M.; Shen, Y.-M. Transition-metal-catalyzed reactions of propargylamine with carbon dioxide and carbon disulfide. *J. Org. Chem.* **2002**, *67*, 16–21.
41. Yoshida, S.; Fukui, K.; Kikuchi, S.; Yamada, T. Silver-catalyzed preparation of oxazolidinones from carbon dioxide and propargylic amines. *Chem. Lett.* **2009**, *38*, 786–787.
42. Yoshida, M.; Mizuguchi, T.; Shishido, K. Synthesis of oxazolidinones by efficient fixation of atmospheric CO_2 with propargylic amines by using

a silver/1,8-diazabicyclo[5.4.0]undec-7-ene (DBU) dual-catalyst system. *Chem. Eur. J.* **2012**, *18*, 15578–15581.
43. Hase, S.; Kayaki, Y.; Ikariya, T. NHC–Gold(I) complexes as effective catalysts for the carboxylative cyclization of propargylamines with carbon dioxide. *Organometallics* **2013**, *32*, 5285–5288.
44. Costa, M.; Chiusoli, G. P.; Rizzardi, M. Base-catalysed direct introduction of carbon dioxide into acetylenic amines. *Chem. Commun.* **1996**, *32*, 1699–1700.
45. Costa, M.; Chiusoli, G. P.; Taffurelli, D.; Dalmonego, G. Superbase catalysis of oxazolidin-2-one ring formation from carbon dioxide and prop-2-yn-1-amines under homogeneous or heterogenous conditions. *J. Chem. Soc., Perkin Trans. 1* **1998** (9), 1541–1546.
46. Yoshida, M.; Komatsuzaki, Y.; Ihara, M. Synthesis of 5-vinylideneoxazolidin-2-ones by DBU-mediated CO_2-fixation reaction of 4-(benzylamino)-2-butynyl carbonates and benzoates. *Org. Lett.* **2008**, *10*, 2083–2086.
47. Kayaki, Y.; Yamamoto, M.; Suzuki, T.; Ikariya, T. Carboxylative cyclization of propargylamines with supercritical carbon dioxide. *Green Chem.* **2006**, *8*, 1019–1021.
48. Maggi, R.; Bertolotti, C.; Orlandini, E.; Oro, C.; Sartori, G.; Selva, M. Synthesis of oxazolidinones in supercritical CO_2 under heterogeneous catalysis. *Tetrahedron Lett.* **2007**, *48*, 2131–2134.
49. Takeda, Y.; Okumura, S.; Tone, S.; Sasaki, I.; Minakata, S. Cyclizative atmospheric CO_2 fixation by unsaturated amines with *t*-BuOI leading to cyclic carbamates. *Org. Lett.* **2012**, *14*, 4874–4877.
50. Feroci, M.; Orsini, M.; Sotgiu, G.; Rossi, L.; Inesi, A. Electrochemically promoted C-N bond formation from acetylenic amines and CO_2. synthesis of 5-methylene-1,3-oxazolidin-2-ones. *J. Org. Chem.* **2005**, *70*, 7795–7798.
51. Kayaki, Y.; Mori, N.; Ikariya, T. Palladium-catalyzed carboxylative cyclization of α-allenyl amines in dense carbon dioxide. *Tetrahedron Lett.* **2009**, *50*, 6491–6493.
52. Li, S. H.; Ye, J. T.; Yuan, W. M.; Ma, S. M. Highly regioselective three-component palladium-catalyzed synthesis of 5-vinyloxazolidin-2-ones from 2,3-allenyl amines, organic iodides, and carbon dioxide. *Tetrahedron* **2013**, *69*, 10450–10456.
53. Yoshida, M.; Ihara, M. Palladium-catalyzed domino reaction of 4-methoxycarbonyloxy-2-butyn-1-ols with phenols: a novel synthetic method for cyclic carbonates with recycling of CO_2. *Angew. Chem., Int. Ed.* **2001**, *40*, 616–619.
54. Feng, H. D.; Ermolat'ev, D. S.; Song, G. H.; Van der Eycken, E. V. Synthesis of oazolidin-2-ones via a cpper(I)-ctalyzed tndem dcarboxylative/ crboxylative cclization of a popiolic Acid, a pimary aine and an adehyde. *Adv. Synth. Catal.* **2012**, *354*, 505–509.
55. Dyen, M. E.; Swern, D. 2-Oxazolidones. *Chem. Rev.* **1967**, *67*, 197–246.
56. Miller, A. W.; Nguyen, S. T. (Salen)chromium(III)/DMAP: an efficient catalyst system for the selective synthesis of 5-substituted oxazolidinones from carbon dioxide and aziridines. *Org. Lett.* **2004**, *6*, 2301–2304.

Publication Date (Web): September 11, 2015 | doi: 10.1021/bk-2015-1194.ch002

57. Liu, J. M.; Peng, X. G.; Liu, J. H.; Zheng, S. Z.; Sun, W.; Xia, C. G. Synthesis of 2-oxazolidinones by salen-co-complexes catalyzed oxidative carbonylation of β-amino alcohols. *Tetrahedron Lett.* **2007**, *48*, 929–932.
58. Bhanage, B. M.; Fujita, S.; Ikushima, Y.; Arai, M. Synthesis of cyclic ureas and urethanes from alkylene diamines and amino alcohols with pressurized carbon dioxide in the absence of catalysts. *Green Chem.* **2003**, *5*, 340–342.
59. Kong, D. L.; He, L. N.; Wang, J. Q. Facile synthesis of oxazolidinones catalyzed by *n*-Bu_4NBr_3/*n*-Bu_4NBr directly from olefins, chloramine-T and carbon dioxide. *Catal. Commun.* **2010**, *11*, 992–995.
60. Du, Y.; Wu, Y.; Liu, A.-H.; He, L.-N. Quaternary ammonium bromide functionalized- polyethylene glycol: A highly efficient and recyclable catalyst for selective synthesis of 5-aryl oxazolidinones from carbon dioxide and aziridines under solvent-free conditions. *J. Org. Chem.* **2008**, *73*, 4709–4712.
61. Fournier, J.; Bruneau, C.; Dixneuf, P. H. A simple synthesis of oxazolidinones in one step from carbon dioxide. *Tetrahedron Lett.* **1990**, *31*, 1721–1722.
62. Zhang, Q. H.; Shi, F.; Gu, Y. L.; Yang, J.; Deng, Y. Q. Efficient and eco-friendly process for the synthesis of *N*-substituted 4-methylene-2-oxazolidinones in ionic liquids. *Tetrahedron Lett.* **2005**, *46*, 5907–5911.
63. Gu, Y. L.; Zhang, Q. H.; Duan, Z. Y.; Zhang, J.; Zhang, S. G.; Deng, Y. Q. Ionic liquid as an efficient promoting medium for fixation of carbon dioxide: a clean method for the synthesis of 5-methylene-1,3-oxazolidin-2-ones from propargylic alcohols, amines, and carbon dioxide catalyzed by Cu(I) under mild conditions. *J. Org. Chem.* **2005**, *70*, 7376–7380.
64. Jiang, H. F.; Zhao, J. W.; Wang, A. Z. An efficient and eco-friendly process for the conversion of carbon dioxide into oxazolones and oxazolidinones under supercritical conditions. *Synthesis* **2008** (5), 763–769.
65. Xu, J. X.; Zhao, J. W.; Jia, Z. B.; Zhang, J. H. Facile and mild process for chemical fixation of CO_2 to 4-methylene-1,3-oxazolidin-2-ones under solvent-free conditions. *Synth. Commun.* **2011**, *41*, 858–863.
66. Jiang, H.-F.; Zhao, J.-W. Silver-catalyzed activation of internal propargylic alcohols in supercritical carbon dioxide: efficient and eco-friendly synthesis of 4-alkylidene-1,3-oxazolidin-2-ones. *Tetrahedron Lett.* **2009**, *50*, 60–62.
67. Herrerias, C. I.; Yao, X. Q.; Li, Z. P.; Li, C. J. Reactions of C-H bonds in water. *Chem. Rev.* **2007**, *107*, 2546–2562.
68. Li, C. J. The development of catalytic nucleophilic additions of terminal alkynes in water. *Acc. Chem. Res* **2010**, *43*, 581–590.
69. Yoo, W. J.; Li, C. J. Copper-catalyzed four-component coupling between aldehydes, amines, alkynes, and carbon dioxide. *Adv. Synth. Catal.* **2008**, *350*, 1503–1506.
70. Zhao, J. W.; Huang, H. W.; Qi, C. R.; Jiang, H. F. CuI/$SnCl_2$ co-catalyzed four-component reaction of ketones, amines, alkynes, and carbon dioxide. *Eur. J. Org. Chem.* **2012**, *2012*, 5665–5667.
71. Adams, P.; Baron, F. A. Esters of carbamic acid. *Chem. Rev.* **1965**, *65*, 567–602.

Publication Date (Web): September 11, 2015 | doi: 10.1021/bk-2015-1194.ch002

72. Bruncau, C.; Dixncuf, P. H. Catalytic synthesis of O-β-oxoalkylcarbamates. *Tetrahedron Lett.* **1987**, *28*, 2005–2008.
73. Sasaki, Y.; Dixneuf, P. H. Ruthenium-catalyzed reaction of carbon dioxide, amine, and acetylenic alcohol. *J. Org. Chem.* **1987**, *52*, 4389–4391.
74. Kim, T. J.; Kwon, K.-H.; Kwon, S.-C.; Baeg, J.-O.; Shim, S.-C. Iron complexes of 1,1′-bis(diphenylphosphino)ferrocene (BPPF) as efficient catalysts in the synthesis of carbamates. X-ray crystal structure of (BPPF)Fe(CO)$_3$. *J. Organomet. Chem.* **1990**, *389*, 205–217.
75. Qi, C. R.; Huang, L. B.; Jiang, H. F. Efficient synthesis of β-oxoalkyl carbamates from carbon dioxide, internal propargylic alcohols, and secondary amines catalyzed by silver salts and DBU. *Synthesis* **2010** (9), 1433–1440.
76. Qi, C. R.; Jiang, H. F. Efficient synthesis of β-oxopropylcarbamates in compressed CO_2 without any additional catalyst and solvent. *Green Chem.* **2007**, *9*, 1284–1286.

Publication Date (Web): September 11, 2015 | doi: 10.1021/bk-2015-1194.ch002

Publication Date (Web): September 11, 2015 | doi: 10.1021/bk-2015-1194.ch003

Chapter 3

CO_2 Chemistry in SCUT Group: New Methods for Conversion of Carbon Dioxide into Organic Compounds

Chaorong Qi and Huanfeng Jiang*

School of Chemistry and Chemical Engineering,
South China University of Technology,
Guangzhou 510640, P. R. China
***E-mail: jianghf@scut.edu.cn**

This paper reviews our recent work on the conversion of carbon dioxide (CO_2) into useful organic compounds. Many new methods have been developed for the efficient synthesis of cyclic carbonates, oxazolidinones, carbamates and carboxylic acids using CO_2 as the raw material. $ScCO_2$ or compressed CO_2 provides a platform for successfully performing the catalytic reactions with epoxides/aziridines, propargylic alcohols and amines, leading to environmentally friendly processes for the synthesis of a wide range of important heteroatom-containing compounds. CO_2 was further proved to be a powerful and versatile building block in the synthesis of 3(2*H*)-furanones and α-hydroxy ketones, although in these cases only one of the oxygen atoms of CO_2 was incorporated into the final products. Electrochemical methods for the conversion of CO_2, including the electrochemical oxidative carboxylation of alkenes and electrochemical carboxylations of unsaturated hydrocarbons (alkenes and alkynes) with CO_2, will also be discussed with special emphasis placed on the mechanistic aspects.

In Advances in CO2 Capture, Sequestration, and Conversion; He, et al.;
ACS Symposium Series; American Chemical Society: Washington, DC, 2015.

Publication Date (Web): September 11, 2015 | doi: 10.1021/bk-2015-1194.ch003

Introduction

Carbon dioxide (CO_2) is a greenhouse gas. Due to human CO_2 emissions, the level of CO_2 in the atmosphere has been rising extensively during and after the industrial revolution, which began in 1850. This has caused serious environmental problems, including global warming and climate changes. Therefore, the capture, utilization and storage of CO_2 have drawn much public attention (*1–6*). Chemical fixation of CO_2 into value-added organic chemicals is of great interest from the viewpoints of protection of the environment as well as the utilization of C_1 resources (*7–11*). Although CO_2 is abundant, readily available and renewable, the relative thermodynamic stability and high oxidation state of the linear molecule limit its widespread use in chemical reaction as a raw material, and its transformation often requires reaction with high-energy starting materials or electroreductive processes. By far the development of efficient and eco-friendly processes for chemical fixation of CO_2 remains a significant challenge.

This paper reviews our recent work in the conversion of carbon dioxide into useful organic compounds, including the catalytic reactions and electrochemical reactions of CO_2 with different substrates. Many efficient and eco-friendly catalytic systems have been developed for the fixation of CO_2 with epoxides/aziridines, propargylic alcohols and amines. Moreover, several novel reactions have also been developed for the synthesis of carbamates, oxazolidinones, 3(*2H*)-furanones and α-hydroxy ketones. The electrochemical reactions of CO_2 including the electrochemical oxidative carboxylation of alkenes and electrochemical carboxylations of unsaturated hydrocarbons with CO_2 were investigated with inexpensive and easily available metals as electrolyte materials.

Catalytic Reactions

Reaction with Epoxides or Aziridines

One promising methodology in chemical fixation of CO_2 is to efficiently convert CO_2 to the five-membered heterocycles such as cyclic carbonates or oxazolidinones. The resulting cyclic carbonates are excellent aprotic solvents, pharmaceutical and fine chemical intermediates, precursors for polycarbonate materials, intermediates in organic synthesis (*12–16*). Oxazolidinones are also important heterocyclic compounds showing a large application as intermediates and chiral auxiliaries in organic synthesis (*17–21*).

The cycloaddition of CO_2 with epoxides or aziridines is known to be catalyzed by alkali metal salts (*22–24*), organic bases (*25*, *26*), metal oxides (*27*, *28*), transition metal complexes (*29–35*), supported quaternary ammonium and phosphonium salts (*36–40*), Although the addition of CO_2 with epoxides or aziridines to produce five-membered heterocycles has been studied extensively, there is continuing motivation for developing efficient catalysts for chemical fixation of CO_2 which would ideally carboxylate both epoxides and aziridines.

In early 2007, we reported our initial results using naturally occurring amino acids as catalyst for this transformation (*41*). In this study, the coupling reaction of CO_2 with propylene oxide catalyzed by L-phenylalanine was chosen as the

In Advances in CO2 Capture, Sequestration, and Conversion; He, et al.;
ACS Symposium Series; American Chemical Society: Washington, DC, 2015.

model reaction and was first investigated. The best reaction conditions were as follows: propylene oxide (20 mmol), dichloromethane (1 mL), catalyst (0.6 mol%); CO_2 pressure: 6 MPa; reaction temperature: 130 °C; time: 48 h. Under the optimized conditions, all of the monosubstituted terminal epoxides surveyed could be transformed to the corresponding cyclic carbonates as a sole product in good to excellent yield. Cyclohexene oxide reacted with CO_2 to yield the *cis*-cyclic carbonate cyclohexyl-1,3-dioxolan-2-one in 36% yield, and the lower yield could be attributed to the effect of high steric hindrance of cyclohexene epoxide (Scheme 1).

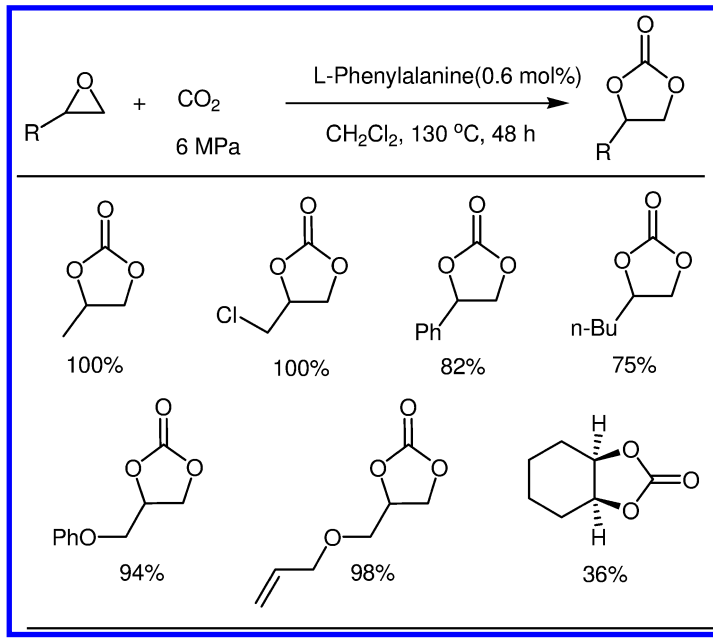

Scheme 1. Synthesis of Cyclic Carbonate from CO_2 and Epoxides Catalyzed by L-Phenylalanine.

A catalytic cycle for the coupling reaction of CO_2 with cyclohexene oxide using amino acids as catalyst is postulated in Scheme 2, in which the cooperation of the Lewis acid activation of the ammonium group and the nucleophilic attack of the carboxylate ion (Lewis base) on the epoxide were proposed as a key activation factor for this transformation. Initially, a cyclohexene oxide molecule (**1**) coordinates to the $-NH_3^+$ group of an amino acid to form an active intermediate **2**, which then undergoes a nucleophilic attack by the carboxylate ion of another amino acid on the methine carbon of the cyclohexene oxide to yield a oxy anion species **3**, which finally reacts with CO_2 to afford the *cis*-cyclohexene carbonate product **5** *via* intermediate **4**.

In Advances in CO2 Capture, Sequestration, and Conversion; He, et al.;
ACS Symposium Series; American Chemical Society: Washington, DC, 2015.

Publication Date (Web): September 11, 2015 | doi: 10.1021/bk-2015-1194.ch003

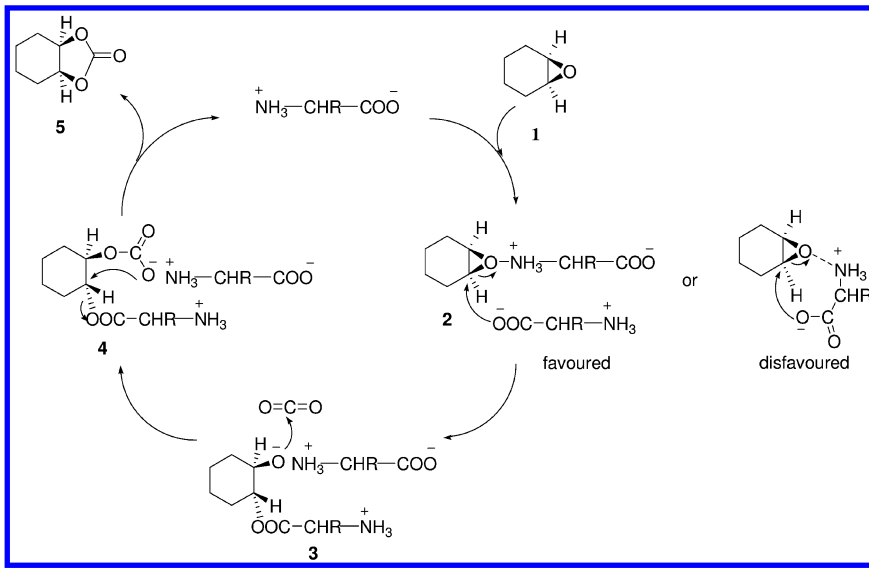

Scheme 2. Proposed Mechanism for the Coupling of Cyclohexene Oxide with CO_2 Catalyzed by α-Amino Acids.

Further study showed that by using amino acids as catalysts, the reaction of CO_2 and epoxides could be carried out in supercritical carbon dioxide in the absence of any organic solvents, and L-histidine exhibited the highest catalytic activity under supercritical conditions (*42*). More importantly, this catalytic system could be successfully extended to the coupling reaction of CO_2 with aziridines (*43*). As seen in Table 1, at 8 MPa of CO_2 pressure and 110 °C, various monosubstituted aziridines underwent the cycloaddition with CO_2 in the presence of L-histidine (0.6 mol%), affording the corresponding oxazolidinones in moderate to excellent yields (54-99%) and high levels of regioselectivity (87:13 to 100:0). 5-Substituted products were obtained as the major isomer. Due to the self-oligomerization, 2-phenylaziridine and 1-methyl-2-phenylaziridine afforded relatively low yields of the desired products. The product regioselectivity mainly depends on the substituent group at the nitrogen atom. Increasing steric hindrance of *N*-substituted group R leads to an enhancement of the regioselectivity of the product. Aziridines with either an electron-donating group or an electron-withdrawing group on the C-1-aryl group could react with CO_2 and give oxazolidinones in high yield and regioselectivity.

Publication Date (Web): September 11, 2015 | doi: 10.1021/bk-2015-1194.ch003

Table 1. Synthesis of Oxazolinones from CO_2 and Aziridines

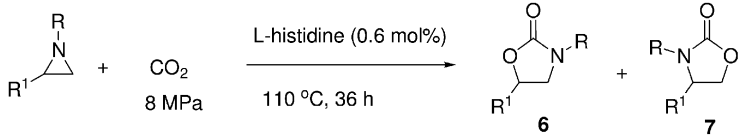

Substrate	Conversion/yield (%)	Molar ratio of 6:7
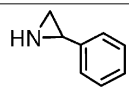	>99/54	87:13
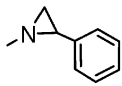	>99/79	94:6
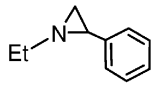	>99/97	98:2
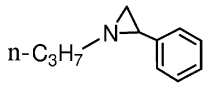	>99/99	93:7
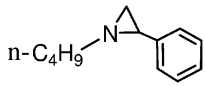	>99/97	95:5
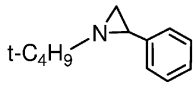	45/42	100:0
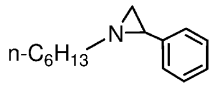	>99/97	99.5:0.5
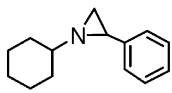	>99/95	98:2
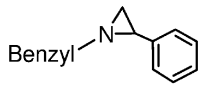	>99/96	100:0
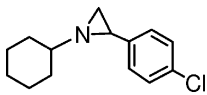	>99/94	99:1
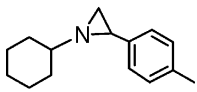	>99/96	99:1
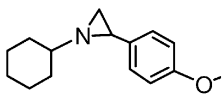	>99/92	100:0

Publication Date (Web): September 11, 2015 | doi: 10.1021/bk-2015-1194.ch003

A mechanism was proposed to account for the regioselective formation of 5-substituted oxazolidinones as the major product in this transformation (Scheme 3).

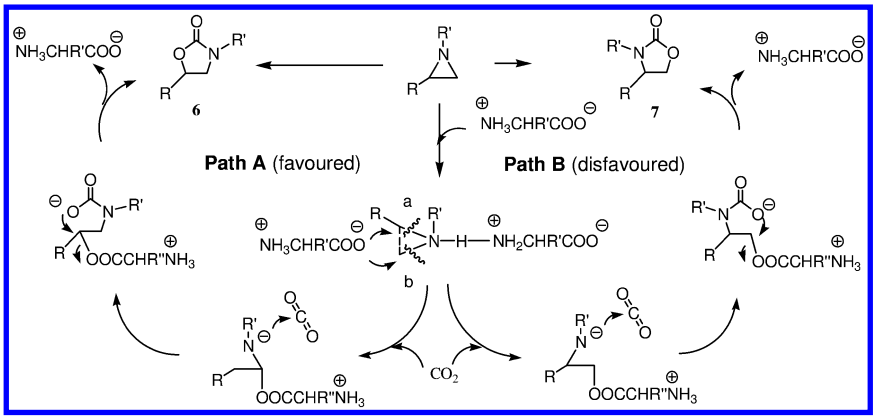

Scheme 3. Proposed Mechanism for the Coupling of CO_2 and Aziridines Catalyzed by α-Amino Acids.

Once having established that the small organic molecules α-amino acids are highly efficient catalysts for the coupling of CO_2 with epoxides or aziridines, we further envisioned that functionalized polystyrene, with α-amino acids as a catalytically active species being covalently grafted onto polystyrene, could be utilized as an active and recyclable heterogeneous catalyst for the reaction of CO_2 with epoxides or aziridines. Four new polystyrene-supported amino acids catalysts were then synthesized and their structures were shown in Scheme 4. After careful catalyst characterization through IR, SEM, TGA/DSC and elemental analysis, we studied the catalytic activity of these catalysts towards the carboxylation of epoxides and aziridines with CO_2. To our delight, these catalysts showed higher catalytic activity than the small molecule analogues for the carboxylation of epoxides and aziridines with CO_2 under supercritical conditions. Furthermore, they could be easily separated from the product just by simple filtration and reused up to 5 times without loss of their high efficacy (*44*).

Publication Date (Web): September 11, 2015 | doi: 10.1021/bk-2015-1194.ch003

Publication Date (Web): September 11, 2015 | doi: 10.1021/bk-2015-1194.ch003

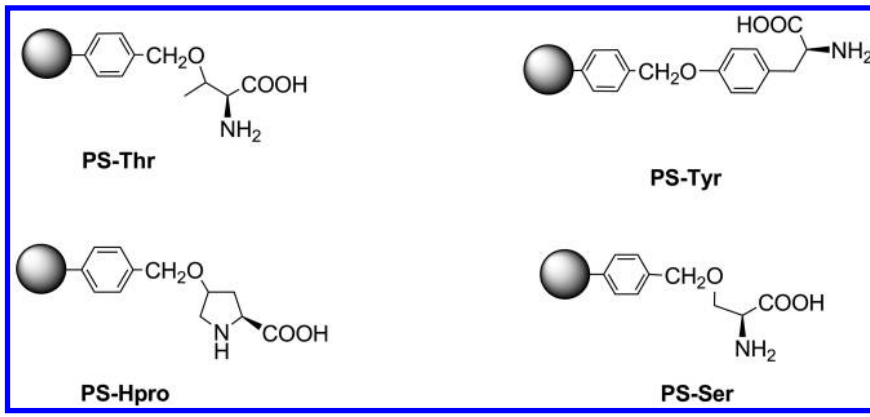

Scheme 4. Structures of the Four Cross-Linked-Polystyrene-Supported Amino Acids.

Metal–organic framework (MOF) heterogeneous catalysts have recently attracted much attention for the conversion of carbon dioxide into cyclic carbonate due to their excellent properties such as extremely large surface areas and well-ordered porous structures. However, these studies mainly rely on the intrinsic catalytic activity of the metal-connecting points, such as weak Lewis acidity (*45*, *46*), whereas introducing well-defined metal complexes into MOF structures is a more rational strategy to develop more efficient heterogeneous catalysts. Recently, with the use of dicarboxylfunctionalized nickel salphen complex **8** as bridging metalloligand, we successfully synthesized a novel 3D MOF, which could be used as a self-supported heterogeneous catalyst for the coupling of CO_2 with epoxides in the presence of quaternary ammonium salts (*47*). This is the first example showing that a M(salen)-based MOF material is efficient both as a CO_2 adsorbent and as a recycle catalyst for CO_2 conversion. Inspired by this work, asymmertic cycloaddition of CO_2 with racemic propylene oxide has also been achieved under relatively mild conditions by using a chiral MOF (CMOF) as heterogeneous catalyst, which contains chiral Ni(saldpen) [saldpen =(R,R)-N,N′-bis-(salicylidine)diphenylethylenediamine] complex **9** as bridging metalloligand (*48*).

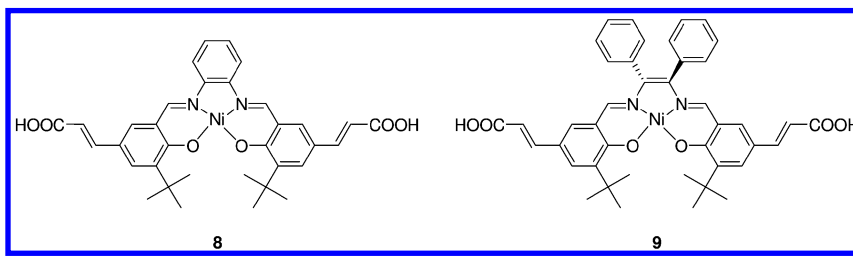

In Advances in CO2 Capture, Sequestration, and Conversion; He, et al.;
ACS Symposium Series; American Chemical Society: Washington, DC, 2015.

Reaction with Propargylic Alcohols

The cyclization of CO_2 with propargylic alcohols is also an atom-economic route to α-alkylidene cyclic carbonates, which are versatile intermediate in organic synthesis. Many transition metals as well as organic compunds, including Cu (*49*, *50*), Co (*51*), Ag (*52–55*), tertiary phosphanes (*56*, *57*), *N*-heterocyclic carbenes (*58*), tert-butyl hypoiodite (*59*), functionalized imidazolium betaines (*60*), and N-heterocyclic olefins (*61*), have been investigated for the reaction. However, in most cases, the reactions have been accomplished under homogeneous catalytic conditions and the catalysts could not able to be recycled.

In 2008, we reported the use of (dimethylamino)methyl-polystyrene-supported copper(I) iodide (DMAM-PS-CuI) (10) as an efficient and environmentally benign heterogeneous catalyst for the reaction of CO_2 and propargyl alcohols under supercritical conditions (*62*). In this study, the reaction of 2-methylbut-3-yn-2-ol and CO_2 was chosen as model reaction to test the catalytic activity of DMAM-PS-CuI. Under 14 MPa of CO_2 at 40 °C, the reaction proceeded smoothly and gave the product in almost quantitative yield in the presence of 8 mol% of DMAM-PS-CuI. For comparison, a yield of 77% was obtained with CuI alone as the catalyst and Et_3N as base under the same conditions, which shows that the Cu^I catalytic activity is significantly enhanced by fixing it to the polymer-supported base. Following this test, recycling experiment for the same reaction was carried out and the results showed that the supported catalyst could recycle up to five times albeit with obvious decrease of yield. By ICP analysis we suggested that leaching of Cu combined with physical destruction of the polymer matrix by stirring might be responsible for the decline of yield. Under the optimized reaction conditions, various aliphatic-substituted secondary and tertiary terminal propargylic alcohols were allowed to react with CO_2 and afforded the corresponding products in good to high yields with excellent selectivity (Scheme 5). When primary and internal propargylic alcohols were used as substrates, the desired products were not detected, which indicates that the present methodology could be specific to aliphatic-substituted secondary and tertiary terminal propargylic alcohols.

A plausible mechanism for the reaction is postulated in Scheme 6. Firstly, carbonate intermediate **11** is formed from the reaction of propargylic alcohol and CO_2 activated by the amine group of DMAM-PS-CuI. Then the cyclization of intermediate **11** takes place with the assistance of CuI to yield the cyclic carbonate **13** through intermediate **12**, along with the release of the catalyst **10**.

Publication Date (Web): September 11, 2015 | doi: 10.1021/bk-2015-1194.ch003

In Advances in CO2 Capture, Sequestration, and Conversion; He, et al.;
ACS Symposium Series; American Chemical Society: Washington, DC, 2015.

Publication Date (Web): September 11, 2015 | doi: 10.1021/bk-2015-1194.ch003

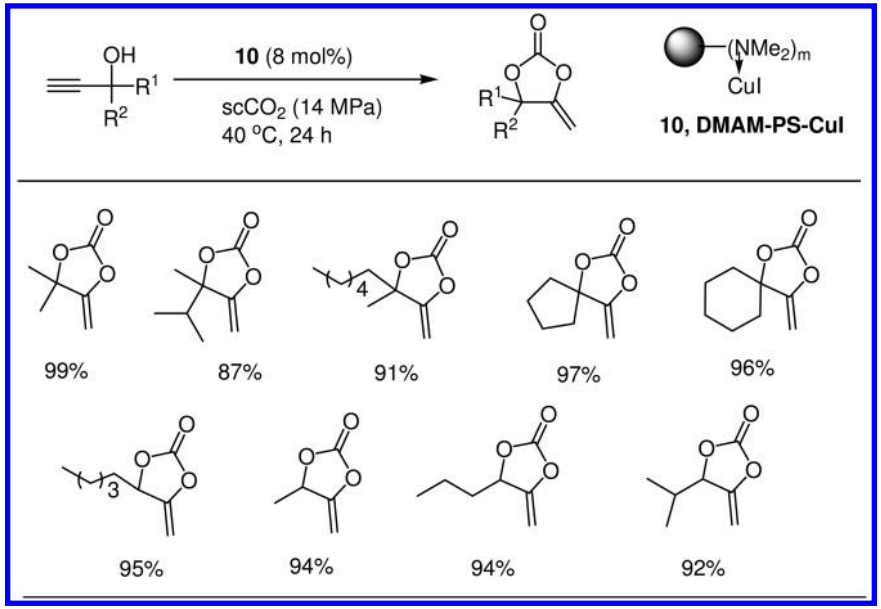

Scheme 5. Synthesis of α-Methylene Cyclic Carbonates from Propargylic Alcohols with $ScCO_2$ Catalyzed by DMAM-PS-CuI.

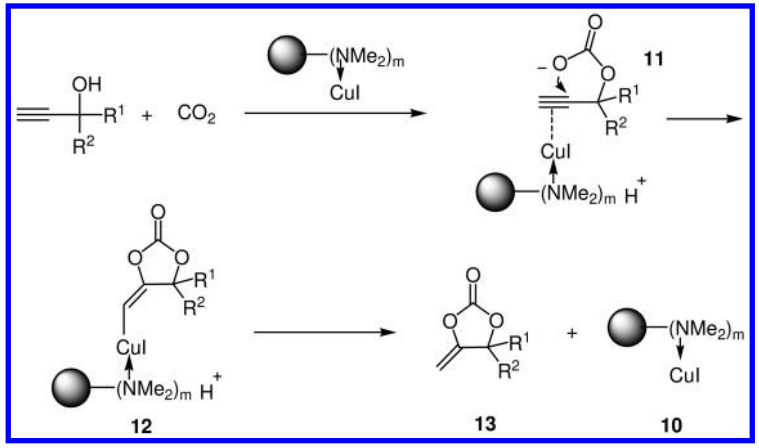

Scheme 6. Proposed Mechanism for CO_2 Incorporation into Propargylic Alcohols Catalyzed by DMAM-PS-CuI.

In Advances in CO2 Capture, Sequestration, and Conversion; He, et al.;
ACS Symposium Series; American Chemical Society: Washington, DC, 2015.

Publication Date (Web): September 11, 2015 | doi: 10.1021/bk-2015-1194.ch003

Subsequently, in order to develop more robust heterogenous catalysts, we synthesized a polystyrene-supported N-heterocyclic carbene–copper complex [PS-NHC-Cu(I), **14**] and three polystyrene-supported N-heterocyclic carbene–silver complexes [PS-NHC-Ag(I), **15**] catalyst and then investigated their catalytic activity for the reaction of propargylic alcohols and carbon dioxide.

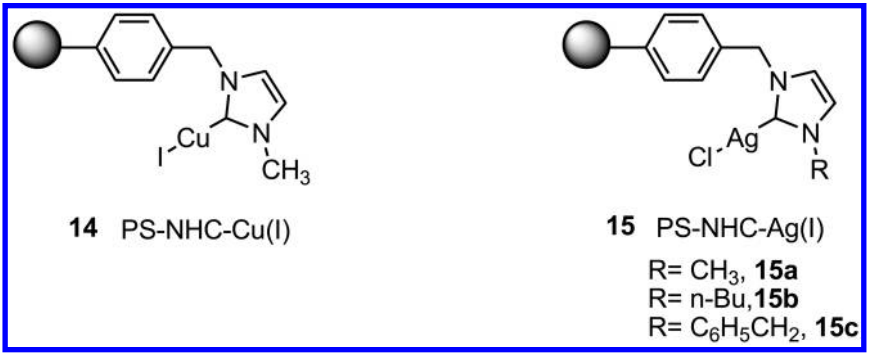

Although PS-NHC-Cu(I) (**14**) showed no catalytic activity to the reaction, PS-NHC-Ag(I) (**15**) exhibited high activity and selectivity for the transformation. For example, with 2 mol% **15a** as the catalyst under 5 MPa of CO_2, a variety of terminal propargylic alcohols could be transformed into the corresponding *α*-alkylidene cyclic carbonates in high to excellent yields (Scheme 7). It is noteworthy that the supported catalysts showed excellent stability and could be reused up to 15 times without loss of their high catalytic activity (*63*).

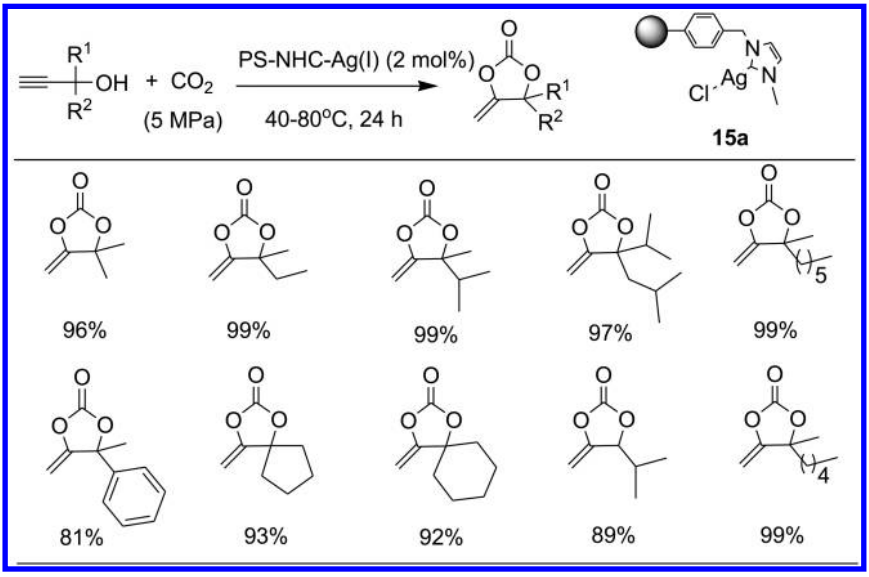

Scheme 7. Synthesis of α-Methylene Cyclic Carbonates from Propargylic Alcohols and CO_2 Catalyzed by PS-NHC-Ag(I).

In Advances in CO2 Capture, Sequestration, and Conversion; He, et al.;
ACS Symposium Series; American Chemical Society: Washington, DC, 2015.

Reaction with Propargylic Alcohols and Secondary Amines

Organic carbamates are compounds of great interest because of their growing application in agriculture, pharmacology and as useful intermediates in organic synthesis. The classical method for the synthesis of carbamates involves the use of highly toxic phosgene as starting material which may cause serious environmental pollution and safety problems (*64*).

One-pot three-component coupling reaction of propargylic alcohols, secondary amines and CO_2 is a promising route to β-oxoalkylcarbamates. Pioneering work has been carried out by Dixneuf and co-workers, who used ruthenium(II) complexes as catalysts (*65*, *66*). Although subsequently other catalysts such as iron complexes (*67*), lanthanide chlorides (*68*), and copper(I) complexes (*49*, *69*) have been developed for this reaction, their catalytic activity and/or selectivity remained low, and large amount of solvent were required.

In 2007, we reported a simple, efficient and environmentally benign methodology for the synthesis of β-oxopropylcarbamates (*70*). As shown in Scheme 8, a series of secondary amines such as diethyl amine, pyrrolidine and morpholine could undergo the three-component assembly with various terminal propargyl alcohols in the absence of any additional catalyst and organic solvent just by heating in compressed CO_2 at 130 °C. The corresponding β-oxopropylcarbamates were afforded in moderate to high yields. It should be noted that secondary amine was supposed to act not only as a reaction reagent but as an active catalyst in this reaction. Recently, He and co-worker reported the synthesis of β-oxopropylcarbamates under solvent-free conditions with the use of a combination of Ag_2WO_4 and Ph_3P as catalytic system (*55*).

Although the three-component coupling reaction of terminal propargylic alcohols, secondary amines and CO_2 proceeded smoothly under metal-free conditions, internal propargylic alcohols failed to go through such an assembly. With the goal of broadening the scope of the reaction, we further examined other catalytic systems with different transition metal catalysts. After the systematic investigation, we finally found that the combination of silver acetate and DBU is a highly active catalytic system to convert an extensive variety of internal propargylic alcohols into the corresponding β-oxoalkyl carbamates in high yields (Scheme 9) (*71*).

Publication Date (Web): September 11, 2015 | doi: 10.1021/bk-2015-1194.ch003

In Advances in CO2 Capture, Sequestration, and Conversion; He, et al.;
ACS Symposium Series; American Chemical Society: Washington, DC, 2015.

Publication Date (Web): September 11, 2015 | doi: 10.1021/bk-2015-1194.ch003

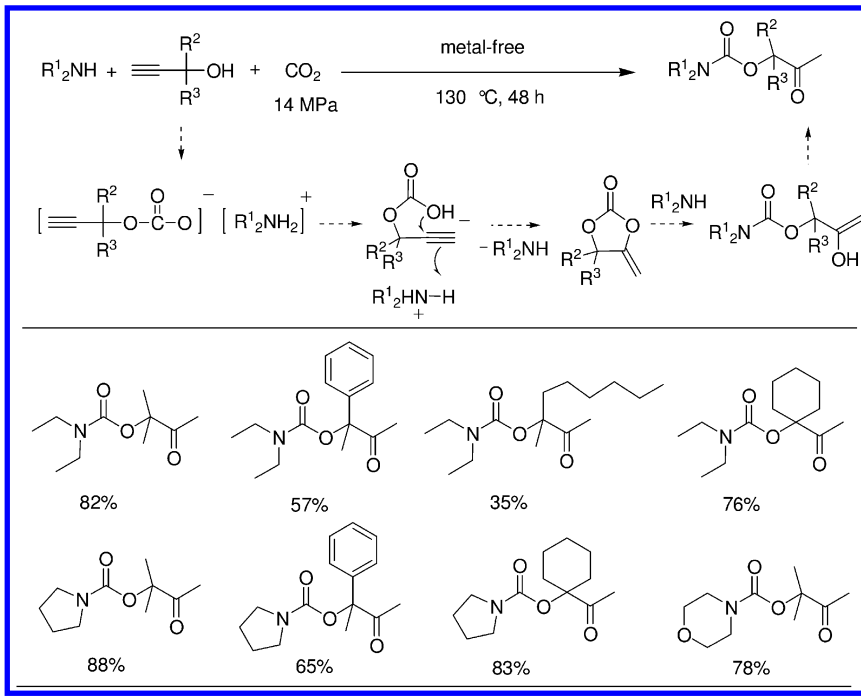

Scheme 8. Synthesis of β-Oxoalkylcarbamates from CO_2, Secondary Amines, and Propargyl alcohols.

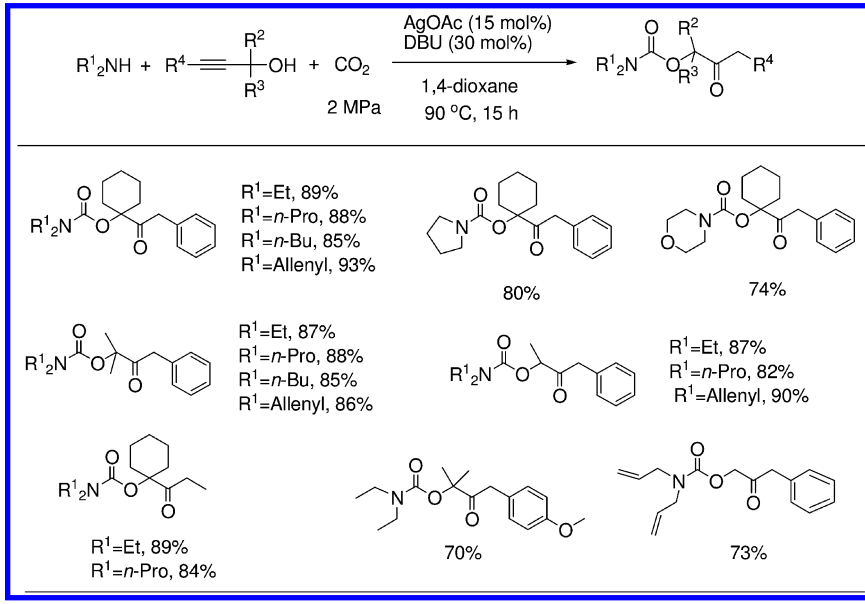

Scheme 9. Synthesis of β-Oxoalkyl Carbamates from CO_2, Internal Propargylic Alcohols, and Secondary Amines Catalyzed by AgOAc/DBU.

In Advances in CO2 Capture, Sequestration, and Conversion; He, et al.;
ACS Symposium Series; American Chemical Society: Washington, DC, 2015.

Publication Date (Web): September 11, 2015 | doi: 10.1021/bk-2015-1194.ch003

Reaction with Amines and *N*-Tosylhydrazones

Recently, *N*-tosylhydrazones have been extensively used as valuable building blocks to construct versatile molecules via transition-metal-catalyzed or metal-free cross coupling reactions (*72–74*). However, *N*-tosylhydrazones have never been used for the fixation of carbon dioxide. We first developed a base-promoted three-component coupling reaction of CO_2, amines and *N*-tosylhydrazones under transition-metal free conditions, which provides an efficient route to carbamates (*75*). As seen in Scheme 10, with the use of K_2CO_3 as the base in a mixed MeCN/H_2O (15:1) solvent system, a range of carbamates could be prepared from various amines and *N*-tosylhydrazones. However, *N*-tosylhydrazones derived from aliphatic ketones or aldehydes and aniline could not undergo the transformation.

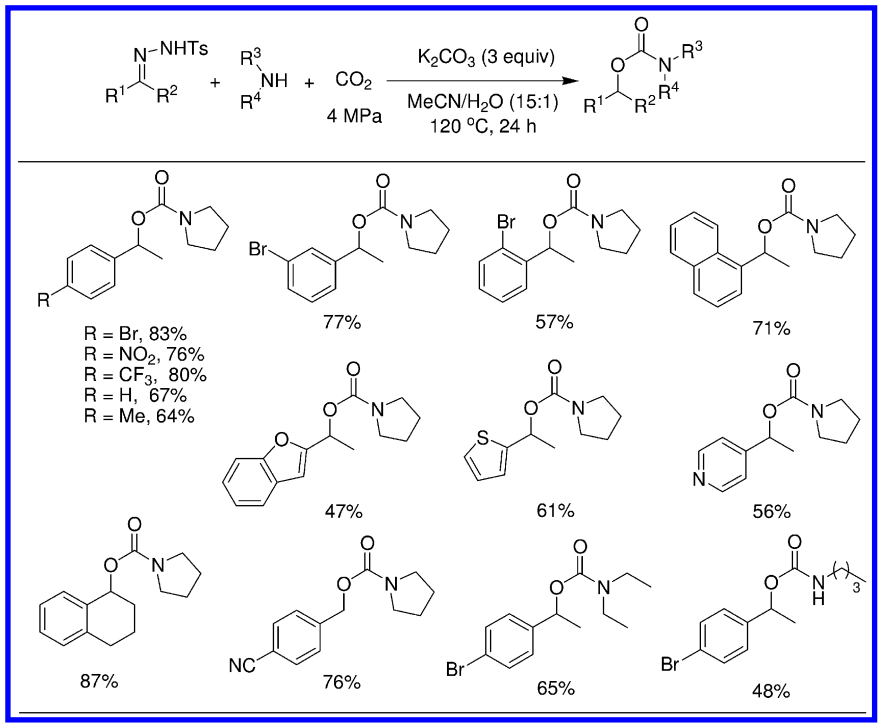

Scheme 10. Synthesis of Carbamates from a Variety of Amines and N-Tosylhydrazones

It is interesting to find that when the reaction was carried out with *N*-tosylhydrazone **16** as substrate, two regioisomers **17** and **18** were isolated in 43% and 14% yield, respectively, indicating that the reaction may proceed through the formation of an allylic carbocation intermediate. On the basis of this observation and the results of control experiments and deuterium-labeling experiments, we proposed a plausible mechanism for this transformation (Scheme 11). First of all, *N*-tosylhydrazone **16** undergoes thermal decomposition in the

In Advances in CO2 Capture, Sequestration, and Conversion; He, et al.;
ACS Symposium Series; American Chemical Society: Washington, DC, 2015.

presence of base to provide diazo component **19**, which could be protonated by carbonic acid formed from water and CO_2 to yield a diazonium ion **20**. After the generation of an allylic carbocation species **21**, the nucleophilic attack of carbamate anion, generated in situ from the reaction of the amine with CO_2, will takes place to afford the desired product **17** and **18**.

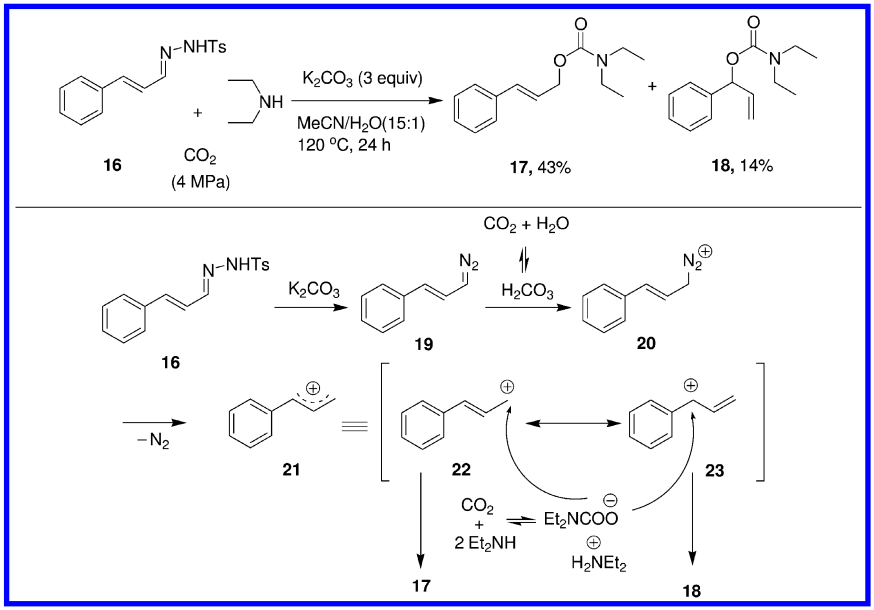

*Scheme 11. Proposed reaction mechanism of the coupling of CO_2, Et_2NH, and N-tosylhydrazone **16**.*

Reaction with Propargylic Alcohols and Primary Amines

The three-component reaction of propargylic alcohols, primary amines, and CO_2 is an attractive method for the synthesis of oxazolidinones. Although many catalytic systems have been developed for the reaction, they usually suffered from harsh conditions, poor yields and use of hazardous and expensive catalysts (*76–78*). In 2008, we first reported the results of the investigation of the three-component reaction under supercritical conditions (*79*). When terminal tertiary propargylic alcohols were employed to react with aliphatic primary amines at 60 °C under 8 MPa of CO_2 for 24 h, the corresponding 4-methylene oxazolidin-2-ones were obtained in good to high yields in the presence of copper(I) iodide (5 mol%) (Scheme 12). The steric hindrance of the sustituents on the primary amines affected the cycloaddition significantly. When tert-butylamine or aromatic primary amines such as 2-pyridylamine were used as the coupling partner, no desired products were detected under the standard conditions.

In Advances in CO2 Capture, Sequestration, and Conversion; He, et al.;
ACS Symposium Series; American Chemical Society: Washington, DC, 2015.

Publication Date (Web): September 11, 2015 | doi: 10.1021/bk-2015-1194.ch003

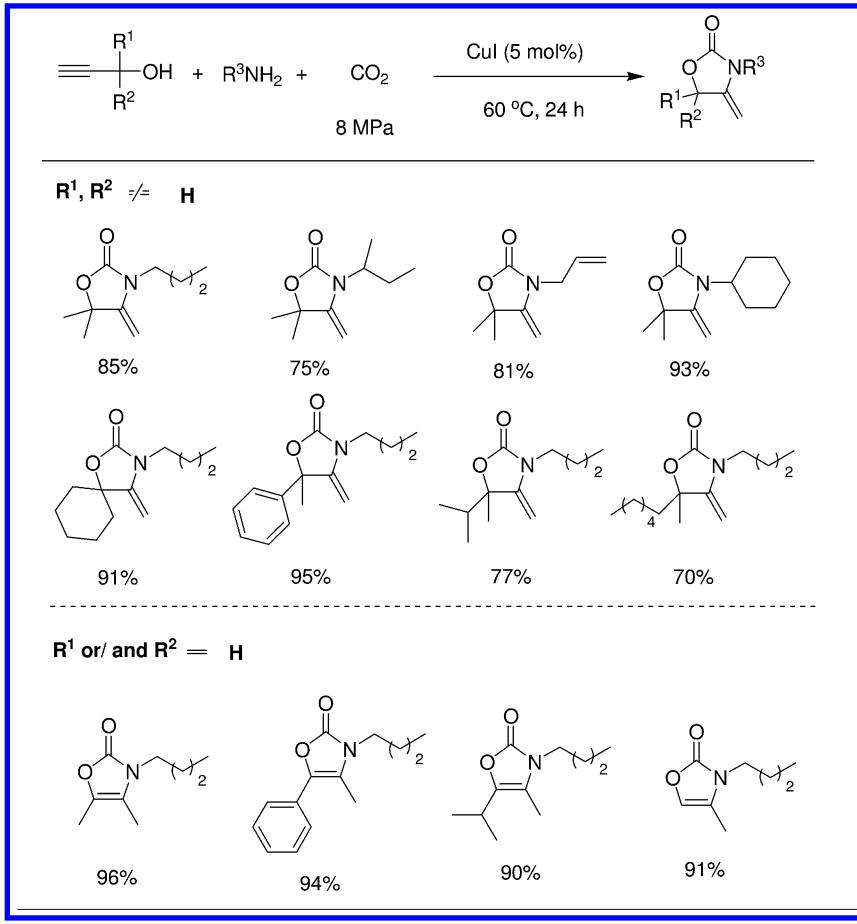

Scheme 12. The reaction of CO_2, Terminal Propargylic Alcohols, and Primary Amines Catalyzed by CuI.

Unexpectedly and interestingly, terminal secondary and primary propargylic alcohols provided 4-methyloxazol-2-ones as the sole products under the same reaction conditions. This was quite different from the previously reported processes in which only tertiary propargylic alcohols could react with primary amines and CO_2 yielding 4-methyleneoxazolidin-2-ones (*77*, *78*). Although it is not clear why this happen, we suggest that $scCO_2$ as reaction medium might play an important role in the reaction. This might be due to the reason that $scCO_2$ could facilitate the formation of reaction intermediates.

In Advances in CO2 Capture, Sequestration, and Conversion; He, et al.;
ACS Symposium Series; American Chemical Society: Washington, DC, 2015.

Publication Date (Web): September 11, 2015 | doi: 10.1021/bk-2015-1194.ch003

A proposed mechanism is illustrated in Scheme 13. Cyclic carbonates **24** was initially formed form the reaction of propargyl alcohols and $scCO_2$ catalyzed by CuI/amine, which then undergo aminolysis to give the 2-oxoalkyl carbamate **25**, followed by intramolecular cyclization to yield the key intermediate **26**. The regioselectivity derives from alternative elimination via **26**: the 4-hydroxy group is eliminated together with 5-H to form conjugated oxazolones **28** if there is a hydrogen atom in the 5-position; if not, 4-hydroxy is eliminated with hydrogen atom of 4-methyl to afford the oxazolidinones **27**.

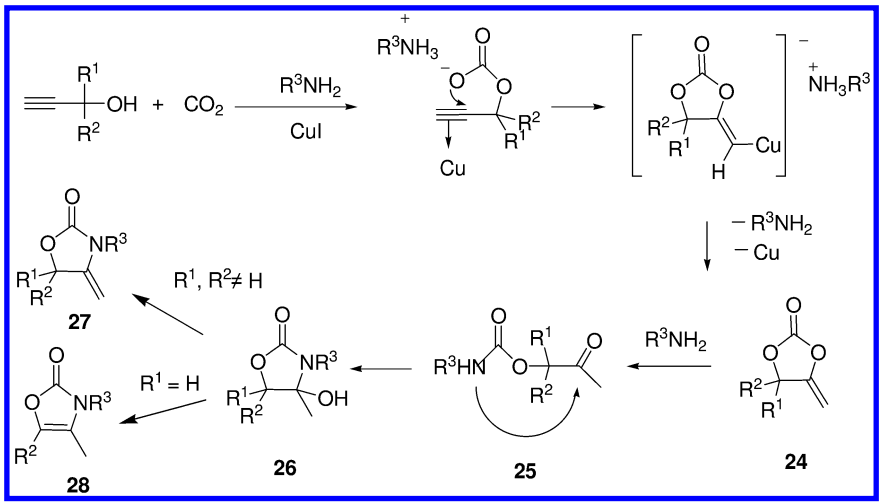

Scheme 13. Proposed Mechanism for the Reaction of Propargylic Alcohols with Amines and $scCO_2$.

In comparison with terminal propargylic alcohols, internal propargylic ones were less reactive. They needed more active catalyst and higher reaction temperature to work. By rising the temperature to 120 °C and replacing the CuI with silver acetate, internal proparylic alcohols could be activated to react with primary amines and CO_2 to yield the corresponding oxazolidinones in good to high yields under supercritical conditions (Scheme 14). The silver-catalyzed reaction mechanism was proposed to be similar to that of the Cu(I)-catalyzed process descried above (*80*).

In Advances in CO2 Capture, Sequestration, and Conversion; He, et al.;
ACS Symposium Series; American Chemical Society: Washington, DC, 2015.

Publication Date (Web): September 11, 2015 | doi: 10.1021/bk-2015-1194.ch003

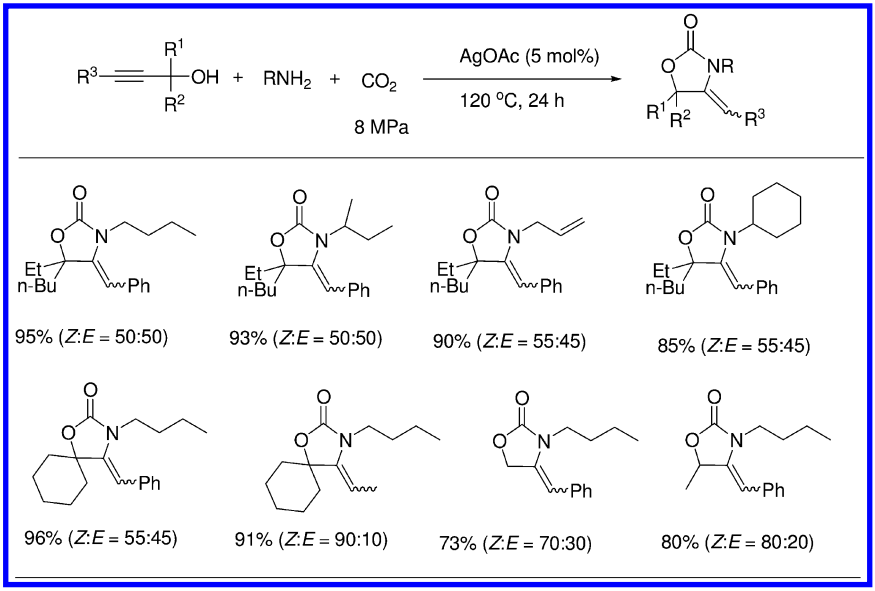

Scheme 14. Synthesis of 4-Alkylene-1,3-Oxazolidin-2-ones from Internal Propargylic Alcohols and Primary Amines in scCO$_2$ Catalyzed by Silver Acetate.

Publication Date (Web): September 11, 2015 | doi: 10.1021/bk-2015-1194.ch003

Reaction with Ketones, Primary Amines, and Alkynes

The carboxylative cyclization of propargylic amines with CO_2 is an alternative route to oxazolidinones, which can be performed under catalytic or catalyst-free conditions (*81–85*). Since propargylic amines can be synthesis through a A^3-coupling reaction of aldehydes, amines and alkynes (*86–88*), it is reasonable to envision that oxazolidinones can be synthesized via a four-component, tandem A^3-coupling/carboxylative cyclization between aldehydes, amines, terminal alkynes, and CO_2. Li and co-worker first reported such an approach by using CuI as catalyst under an atmospheric pressure of CO_2 (*89*). However, in their study, ketones were not examined for the transformation, which may be due to their poor reactivity. We found that by employing a combination of CuI and $SnCl_2$ as a catalyst system at higher CO_2 pressure (1.5 MPa), various aliphatic ketones could smoothly undergo the four-component reaction to furnish the corresponding products (Scheme 15) (*90*).

In Advances in CO2 Capture, Sequestration, and Conversion; He, et al.;
ACS Symposium Series; American Chemical Society: Washington, DC, 2015.

Publication Date (Web): September 11, 2015 | doi: 10.1021/bk-2015-1194.ch003

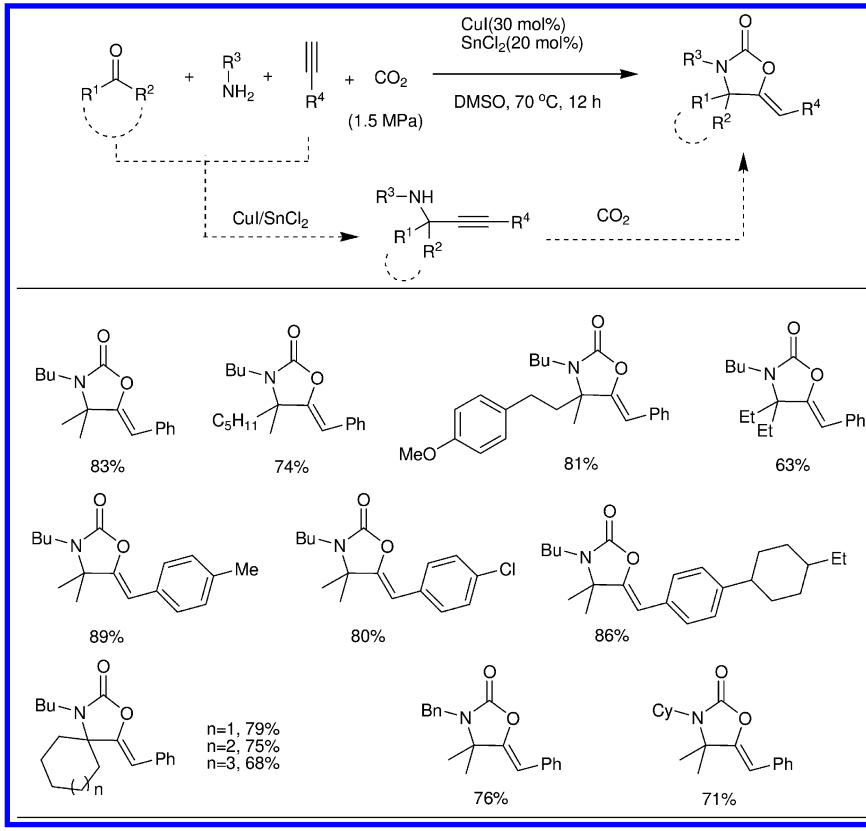

Scheme 15. Synthesis of Oxazolidinones via CuI/$SnCl_2$ Co-Catalyzed Four-Component Coupling of Various ketones, Amines, Alkynes, and CO_2.

Reaction with Primary Amines, and Alkynes

1,3-Oxazolidin-2-ones could also be produced from alkynes, amines, and CO_2. As can be seen from Scheme 16, by using copper (I) iodide as catalyst at 90 °C under 2 MPa of CO_2 pressure, various terminal aryl alkynes could react with aliphatic primary amine and CO_2 to yield the desired oxazolidinones in good to high yields under the solvent-free conditions. However, 4-nitrophenylacetylene and aliphatic alkyne failed to furnish the desired 1,3-oxazolidin-2-ones (*91*).

The reaction was proposed to proceed through a tandem process (Scheme 16). Firstly, two alkyne molecules react with one amine molecule via a copper-catalyzed tandem anti-markovnikov hydroamination and alkyne addition to furnish a propargylamine intermediate, which then undergoes the cycloadditon with CO_2 to afford the product 5-arylidene-1,3-oxazolidin-2-one.

In Advances in CO2 Capture, Sequestration, and Conversion; He, et al.;
ACS Symposium Series; American Chemical Society: Washington, DC, 2015.

Publication Date (Web): September 11, 2015 | doi: 10.1021/bk-2015-1194.ch003

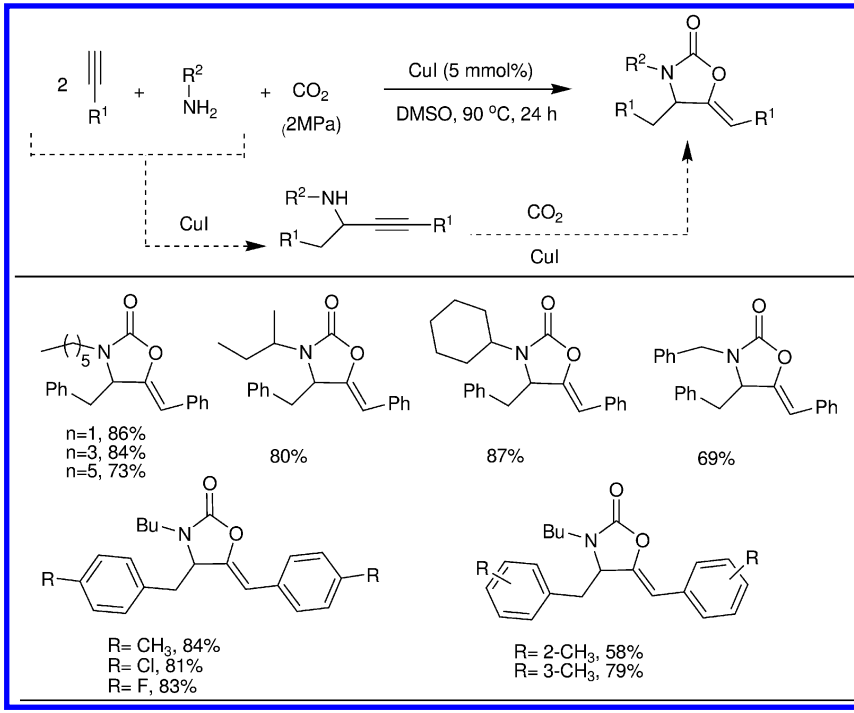

Scheme 16. CuI Catalyzed Synthesis of 1,3-Oxazolidin-2-ones from Alkynes, Amines, and CO_2.

Reaction with Propargylic Alcohols and Nitriles

The 3(*2H*)-furanones have attracted tremendous interest in biologically active natural product research and synthetic chemistry (*92–97*). Although many approaches to substituted 3(*2H*)-furanones have been developed (*93–96*, *98–107*), most of them suffer from limited substrate scope or the lack of readily available precursors and the synthetic procedures are usually tedious.

During the course of our continuing investigations on the reaction between propargylic alcohols and CO_2, we developed a novel and efficient method for the synthesis of highly substituted 3(*2H*)-furanones from CO_2, propargylic alcohols and nitriles (Scheme 17) (*108*). It is important to note that, in contrast to the reactions discussed above, in which the whole CO_2 molecule is incorporated into the final products, only one of the oxygen atoms of CO_2 is found to be incorporated into the product in this transformation.

A domino process is proposed in Scheme 18. Firstly, the cycloaddition of CO_2 to the propargylic alcohol in the presence of the copper salt and DBU generates the *Z*-alkylidene cyclic carbonate **29**, followed by the hydrolysis to yield the intermediate **30**. Then, the nucleophilic attack of **30** on the nitrile promoted by copper gives the intermediate **31**, which can be converted to the ester **32** in the presence of water. Subsequent intramolecular Claisen condensation of **32** provides **33** which eventually affords the product **34** *via* dehydration.

In Advances in CO2 Capture, Sequestration, and Conversion; He, et al.;
ACS Symposium Series; American Chemical Society: Washington, DC, 2015.

Publication Date (Web): September 11, 2015 | doi: 10.1021/bk-2015-1194.ch003

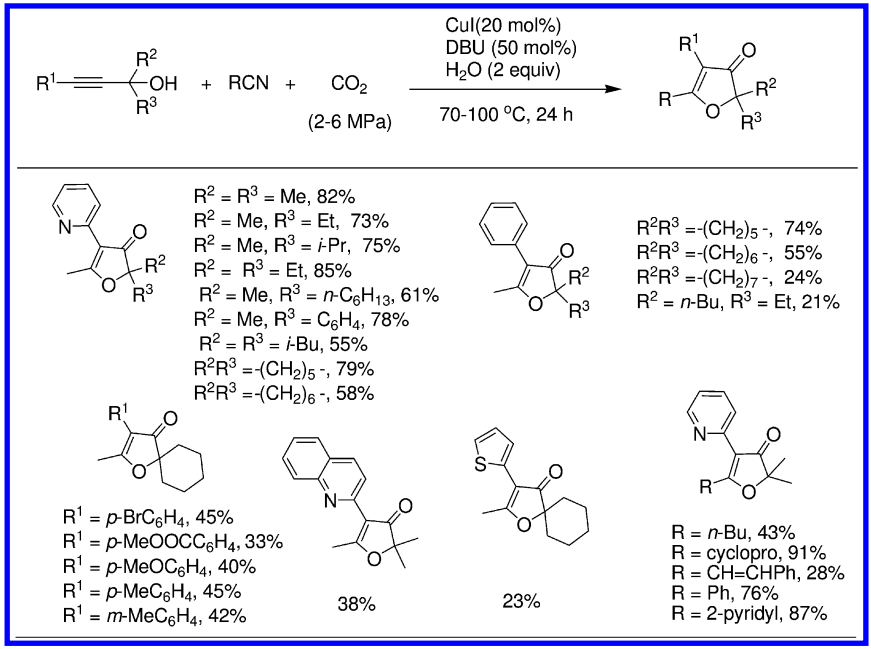

Scheme 17. Synthesis of 3(2H)-Furanones from CO_2 and Nitriles and Propargylic Alcohols.

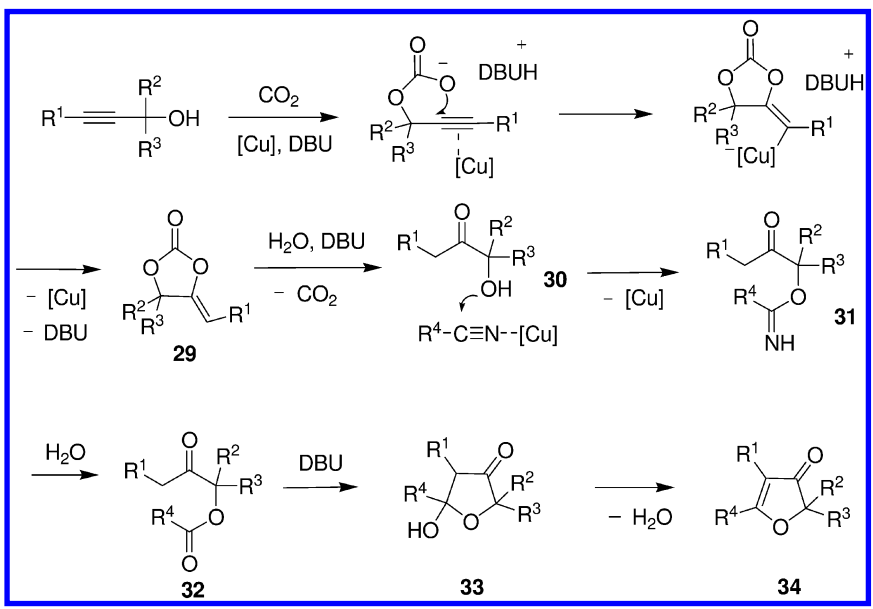

Scheme 18. Plausible Reaction Mechanism for the Synthesis of 3(2H)-Furanones from CO_2, Nitriles, and Propargylic Alcohols

In Advances in CO2 Capture, Sequestration, and Conversion; He, et al.;
ACS Symposium Series; American Chemical Society: Washington, DC, 2015.

Publication Date (Web): September 11, 2015 | doi: 10.1021/bk-2015-1194.ch003

The steps from **29** to **30** and from **30** to **34** were confirmed by the control experiments (eq 1). Moreover, when the transformation was performed in the presence of H_2O^{18}, the ^{18}O-labeled product was not detected (eq 2), indicating that the oxygen atom of the carbonyl group of the product originated from carbon dioxide.

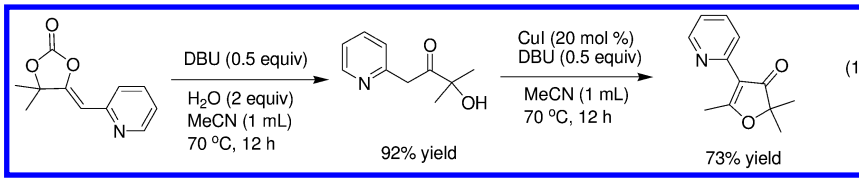

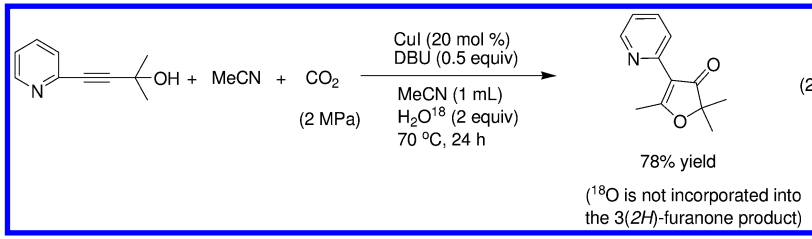

More interestingly, diyne alcohols could also afford substituted 3(*2H*)-furanones when treating them in a mix-solvent of MeCN/Et_3N under 2 MPa of CO_2 pressure in the absence of CuI (Scheme 19) (*109*). However, in this transformation, MeCN acted only as a solvent and did not react with the substrates. It was also proved by control experiments that the oxygen atom of the carbonyl group in the product results from carbon dioxide, and the other oxygen atom originate from diyne alcohol rather than from water.

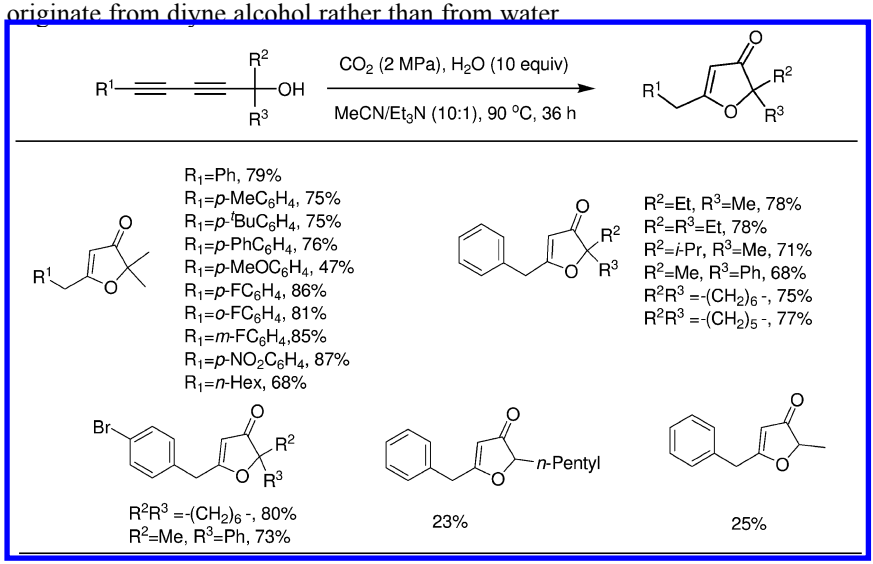

Scheme 19. Synthesis of 3(2H)-Furanones from Diyne Alcohols and CO_2.

In Advances in CO2 Capture, Sequestration, and Conversion; He, et al.;
ACS Symposium Series; American Chemical Society: Washington, DC, 2015.

Publication Date (Web): September 11, 2015 | doi: 10.1021/bk-2015-1194.ch003

Reaction with Propargylic Alcohols and Water

α-Hydroxy ketones are versatile building blocks for different syntheses (*110–112*). Conventional method for accessing such compounds is based on the hydration of propargylic alcohols using toxic mercury salts as catalyst, which can easily have a detrimental influence on the environment. During the investigation of the synthesis of 3(*2H*)-furanones from propargylic alcohols and nitriles (*108*), α-hydroxy ketones was selectively formed when silver salt was used as catalsyst. After intensive optimization of the reaction conditions, we successfully established a facile and efficient method to synthesize tertiary α-hydroxy ketones via a tandem incorporation of CO_2 into propargylic alcohols/hydrolysis process. As can be seen from Scheme 20, with the use of AgOAc/DBU as catalyst system in mixed solvent MeCN/H_2O (10:3) under CO_2 atmosphere (2 MPa), various tertiary propargylic alcohols could readily undergo hydration to afford the corresponding α-hydroxy ketones in moderate to excellent yields. Importantly, the hydration exhibits complete regioselectivity and high functional group tolerance (*113*).

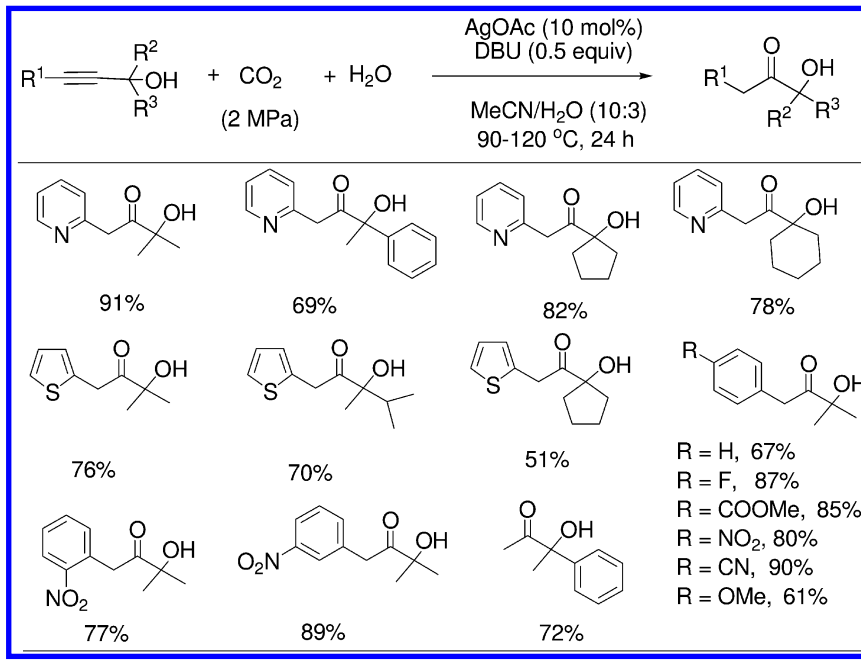

Scheme 20. Synthesis of Various α-Hydroxy Ketones.

Electrochemical Reactions

Electrochemical Reaction with Alkenes

The direct synthesis of cyclic carbonates from alkenes instead of epoxides through a one-pot oxidative carboxylation is a promising strategy for the fixation of CO_2, because alkenes are cheaper and more easily available in comparison with epoxides. Many catalytic system have been successfully investigated for

In Advances in CO2 Capture, Sequestration, and Conversion; He, et al.;
ACS Symposium Series; American Chemical Society: Washington, DC, 2015.

such a transformation (*114–116*). But some drawbacks still exist such as the need for stoichiometric hazardous oxidants or highly reactive catalysts, low yield and selectivity. Electrochemical method could provide an alternative solution to these problems. We recently developed a new and efficient electrochemical route to directly convert CO_2 and olefins into cyclic carbonates under very mild conditions without the need for sacrificial metal anodes, dangerous oxidants or expensive catalysts. As can be seen from Scheme 21, with NH_4I as the supporting electrolyte and graphite as the inert anode, a wide range of olefins could be smoothly transformed to cyclic carbonates in good to excellent yields at room temperature within 3 hours under 0.5 MPa of CO_2. It is noteworthy that the electrochemical process is compatible with a variety of functional groups, including halogen, CN, NO_2, OMe, NH_2 and OH groups (*117*).

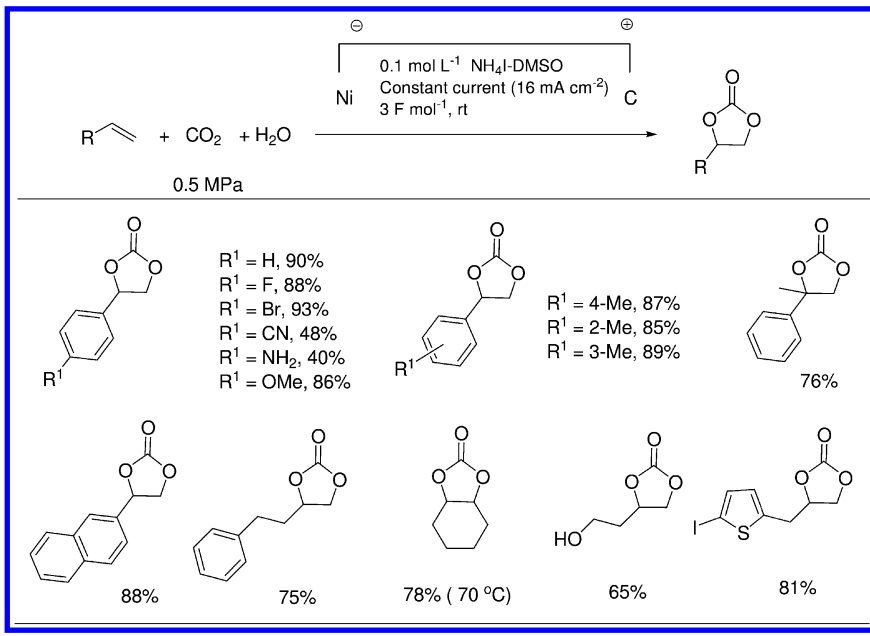

Scheme 21. Electrochemical Route to Cyclic Carbonates from Alkenes, CO_2, and Water.

Mechanism investigation concluded that the synergistic action of I_2 and NH_3, which are generated in situ at the anode and cathode, respectively, plays a key role in this process (Scheme 22). Initially I_2 reacts with olefins and water to give intermediate iodohydrin, which then react with CO_2 under the assistance of NH_3, followed by an intramolecular cyclization to give the product cyclic carbonates. During the electrolysis, I^- and NH_4^+ ions are recyclable, so the transformation only consumes electrons besides substrates.

In Advances in CO2 Capture, Sequestration, and Conversion; He, et al.;
ACS Symposium Series; American Chemical Society: Washington, DC, 2015.

Publication Date (Web): September 11, 2015 | doi: 10.1021/bk-2015-1194.ch003

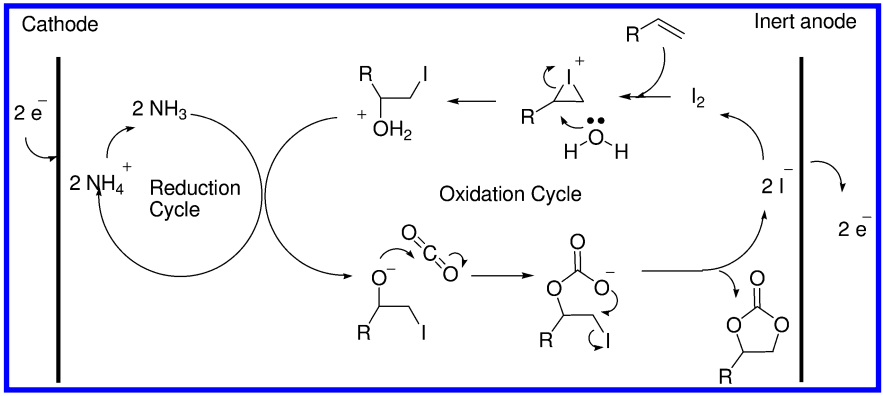

Scheme 22. Proposed Mechanism of the Electrochemical Route to Cyclic Carbonates.

Publication Date (Web): September 11, 2015 | doi: 10.1021/bk-2015-1194.ch003

Electrochemical Reaction with Aryl-Substituted Alkenes

2-Arylsuccinic acids are valuable compounds which are used as anti-tumor agents or as synthetic intermediates for the production of macromolecular materials (*118*). Many electrochemical routes to 2-arylsuccinic acids using CO_2 as a raw material have been developed, however, they usually suffer from the low yield and selectivity, the need of expensive electrodes, or the requirement of additional catalysts (*119–123*). We have successfully achieved the electrochemical dicarboxylation of aryl-substituted alkenes with CO_2 using non-noble metals as the electrode without the addition of any catalysts (*124*).

After a systematic investigation, the efficient electrochemical dicarboxylation of styrene with CO_2 was accomplished in a undivided cell with Ni as cathode and Al as anode containing n-Bu_4NBr-DMF as the supporting electrolyte with a constant current (10 mA cm^{-2}), affording 2-phenylsuccinic acid in 87% yield under 4 MPa pressure of CO_2 at room temperature in the absence of additional catalysts (eq 3). Other aryl-substituted alkenes could also afford the corresponding dicarboxylic acids in moderate to good yields (50-85%) and high selectivity (98%) under the optimized reaction conditions. Noted that, 1-phenylcyclohexene, which did not work in the previously reported nickel complex-catalyzed electrochemical carboxylation (*121*), could be converted into 1-phenylcyclohexane-1,2-dicarboxylic acid in 50% yield in our reaction system.

In Advances in CO2 Capture, Sequestration, and Conversion; He, et al.;
ACS Symposium Series; American Chemical Society: Washington, DC, 2015.

Publication Date (Web): September 11, 2015 | doi: 10.1021/bk-2015-1194.ch003

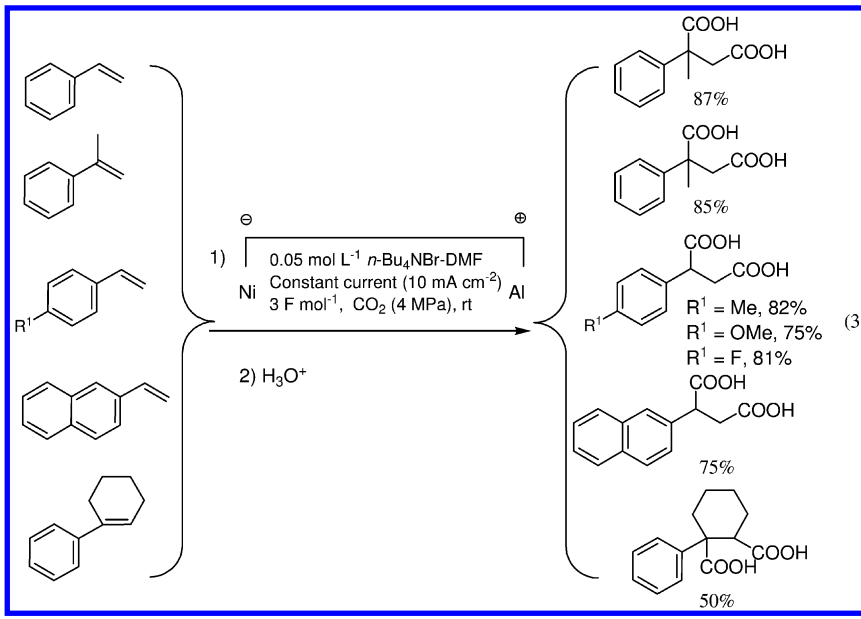

Interestingly, when 4-chlorostyrene and (*E*)-β-bromostyrene used as substrates, the insertion of CO_2 into the C-Cl/C-Br bond instead of the C=C double bond was occurred and related carboxylic acids 35 and 36 were obtained in 61% and 70% yields, respectively, which showed that the C-Cl or C-Br bond is easier reduced (or cleaved) than the C=C double bond or C-F bond (eq 4-5).

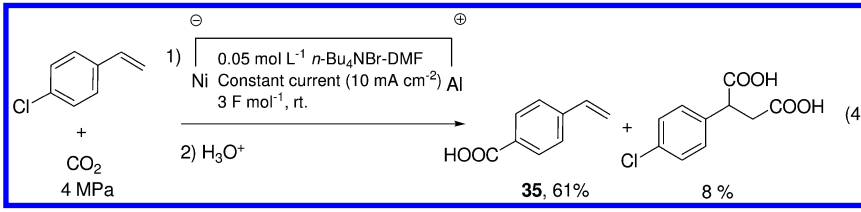

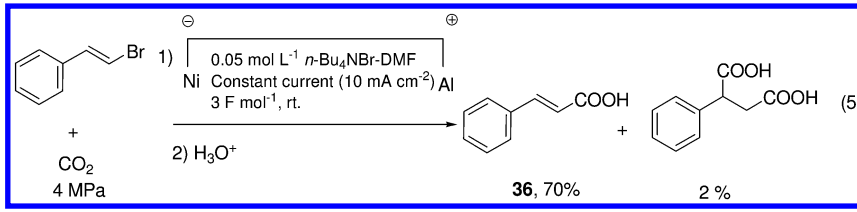

A possible mechanism for the electrochemical reaction of styrene and CO_2 is outlined in Scheme 23. Firstly, CO_2 is reduced to its radical anion, which then attacks styrene to give carboxylate radical anion **37**. Alternatively, a one-electron reduction of styrene generates its radical anion, which will also react with CO_2 to afford intermediate **37**. Further reaction of **37** with CO_2 radical anion gives a dicarboxylate anion **38**, which will be captured by Al^{3+} ions generated at the anodic Al metal to form stable aluminum carboxylate **39**. Finally, treatment of the metal carboxylate with acid gives dicarboxylic acid **40**.

In Advances in CO2 Capture, Sequestration, and Conversion; He, et al.;
ACS Symposium Series; American Chemical Society: Washington, DC, 2015.

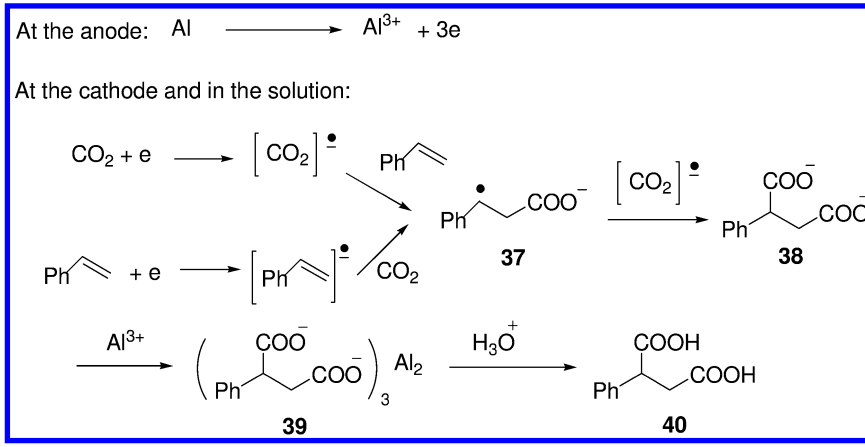

Scheme 23. Electrochemical Reaction Mechanism of Styrene with CO_2.

Electrochemical Reaction with Arylacetylenes

The electrochemical dicarboxylation of arylacetylenes with carbon dioxide has also been studied using Ni as the cathode and Al as the anode in an undivided cell (*125*). With *n*-Bu_4NBr-DMF as the supporting electrolyte at a constant current under CO_2 pressure of 3 MPa and room temperature, various arylacetylenes gave aryl-maleic anhydrides **41** in good yield and selectivity, along with a small amount of 2-arylsuccinic acids **42** as a byproduct under dry conditions (Scheme 24).

Interestingly, the ratio of **41** to **42** was found to be dependent on the amount of water present in the electrolyte solution. For example, in the case of the electrochemical reation of phenylacetylene, when a small amount of water (from 0 to 0.30 g) was added to electrolyte solution, the yield of **41a** dramatically decreased from 89% to 3% while the yield of **42a** increased from 4% to 90% (Scheme 25). These results indicated that the presence of water in the electrolysis system could provide protons to make phenylacetylene easily be reduced into styrene, which will subsequently undergo electrochemical dicarboxylation with CO_2 to give the saturated phenylsuccinic acids **42a** (*124*).

Moreover, further investigation on this transformation showed that when adding catalytic amount of some common metal salts into the electrolysis system, different results would be observed (*126*). In the presence of 10 mol% of CuI, phenylacetylene underwent the electrocarboxylation with CO_2 and gave 43 and 44 as the products instead of 41a and 42a in high total isolated yield .Other metal salts such as $FeCl_3$, $CuCl_2$ also resulted in the same products but with lower yields (Scheme 26). Although the role of the metal salts in this transformation is not known yet, the results of the CV behavior of phenylacetylene and CO_2 in the presence or absence of CuI indicated that CuI might activate CO_2 by means of coordination with them.

In Advances in CO2 Capture, Sequestration, and Conversion; He, et al.;
ACS Symposium Series; American Chemical Society: Washington, DC, 2015.

Publication Date (Web): September 11, 2015 | doi: 10.1021/bk-2015-1194.ch003

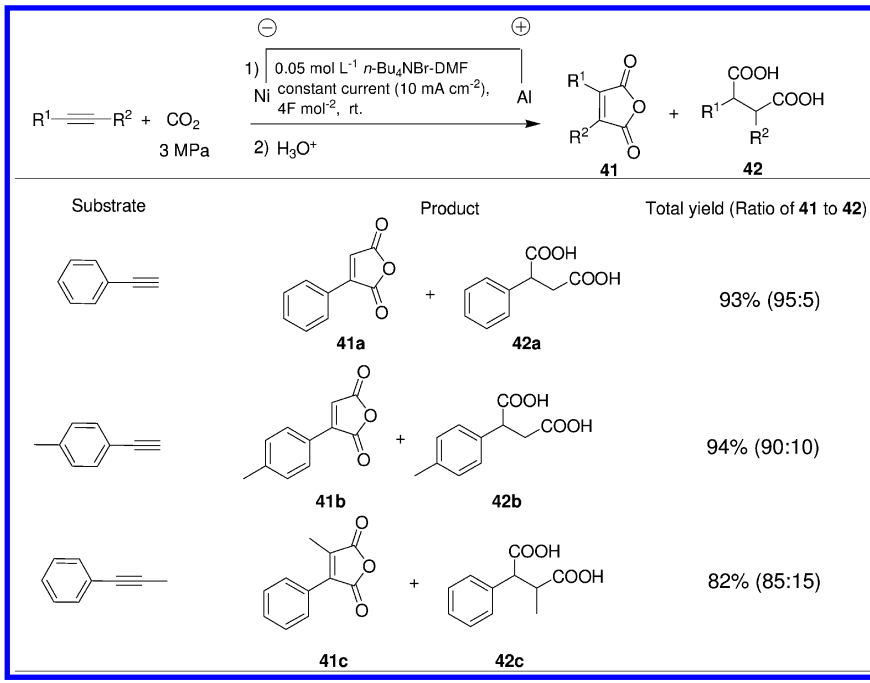

Scheme 24. Electrochemical Dicarboxylation of Phenylacetylene Derivatives with CO_2.

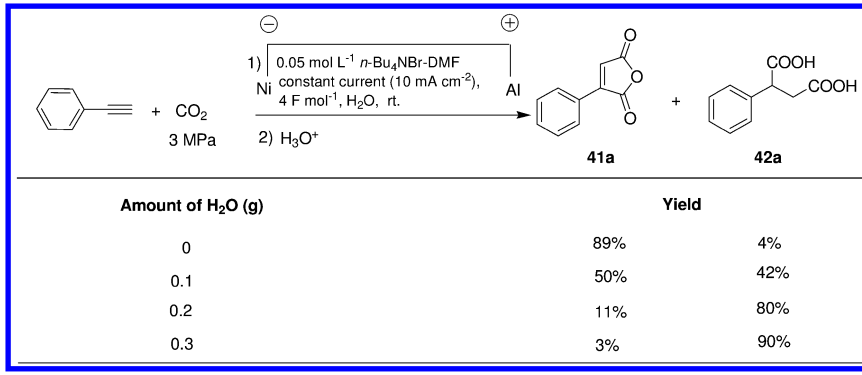

Amount of H_2O (g)	Yield	
0	89%	4%
0.1	50%	42%
0.2	11%	80%
0.3	3%	90%

Scheme 25. Influence of H_2O on the Electrocarboxylation of Phenylacetylene with CO_2.

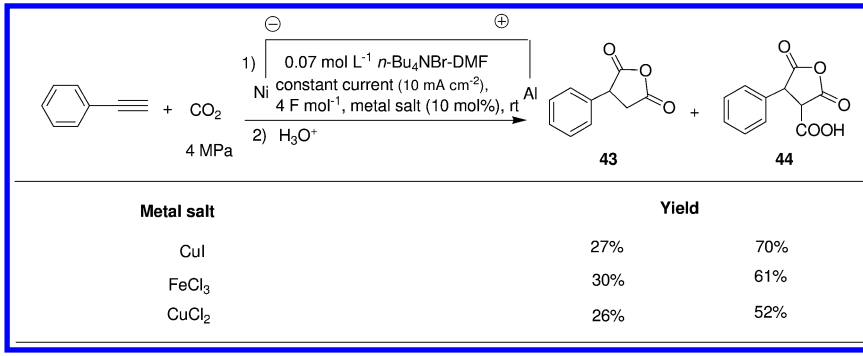

Metal salt	Yield	
CuI	27%	70%
$FeCl_3$	30%	61%
$CuCl_2$	26%	52%

Scheme 26. Effect of Various Metal Salt Catalysts on the Electrocarboxylation of Phenylacetylene with CO_2.

Electrochemical Reaction with Dienes

The electrocarboxylation of 1,3-butadiene aimed at synthesizing adipic acid (*127*, *128*), one of the most important industrial chemicals, has been one of the most important research topics in the synthetic electroorganic chemistry for more than 30 years (*129*). However, the electrochemical reaction between CO_2 and 1,3-butadiene often led to the generation of a complicated mixture containing 3-pentenoic acid, 4-pentenoic acid, 2-ethylsuccinic acid and 3-hexene-1,6-dioic acid (*130*). Therefore, it is still necessary to exploit an efficient electrochemical route for the synthesis of 3-hexene-1,6-dioic acid from 1,3-butadiene and CO_2.

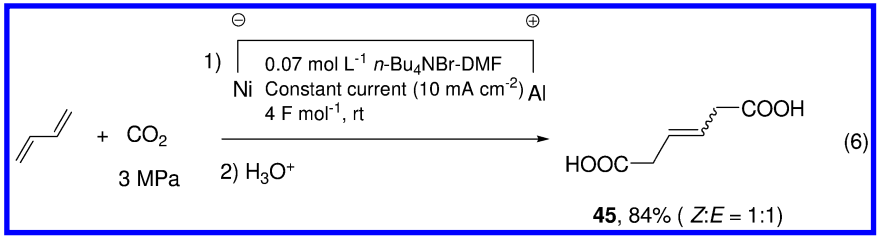

Encouraged by the successful carboxylation of arylacetylenes or aryl-substituted alkenes with CO_2, we further investigate the feasibility of the electrochemical route for the synthesis of 3-hexene-1,6-dioic acid, a precursor of adipic acid, using 1,3-butadiene and CO_2 as raw materials in the absence of additional catalysts. Fortunately, 3-hecene-1,6-dioic acid (45, 1:1 mixture of *Z* and *E* isomers) was obtained in 84% yield under the optimum conditions (Ni cathode and Al anode, *n*-Bu_4NBr-DMF as electrolyte, the electricity 4 F mol^{-1} of starting substrates, CO_2 pressure 3 MPa) (eq 6) (*131*). With Metal Al as a sacrificial anode, Several other cathode materials were also investigated. Ag, Zn and Pt cathodes afforded 3-hecene-1,6-dioic acid in very low yields (5%, 10%, and 22%, respectively), while Cu and stainless steel cathodes could also give the product in good yields (59% and 71%, respectively). Under the optimum

In Advances in CO2 Capture, Sequestration, and Conversion; He, et al.;
ACS Symposium Series; American Chemical Society: Washington, DC, 2015.

Publication Date (Web): September 11, 2015 | doi: 10.1021/bk-2015-1194.ch003

conditions, other 1,3-dienes substrates could also undergo the electrochemical carboxylation smoothly and gave 1,4-addition products in good to excellent yields with high regioselectivities. Cyclohexadiene could be also converted into the corresponding dicarboxylic acids in 70% yield (eq 7).

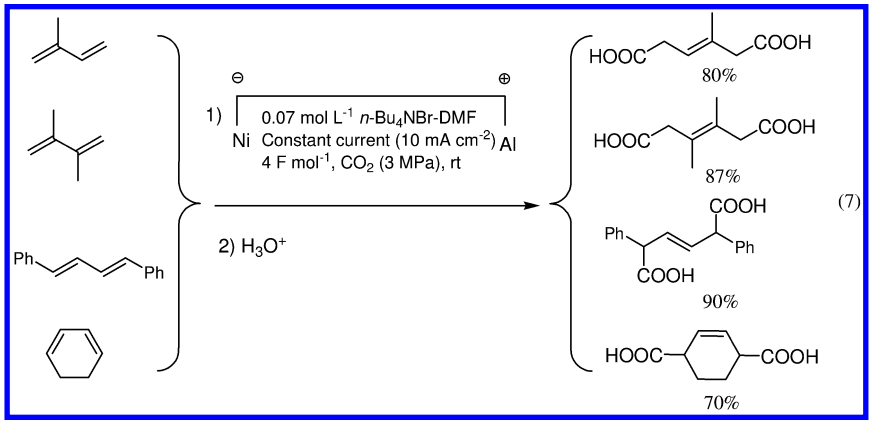

(7)

Conclusions

In conclusion, we have developed many new methods for the efficient synthesis of cyclic carbonates, oxazolidinones, carbamates and carboxylic acids using CO_2 as the raw material. $ScCO_2$ or compressed CO_2 provides a platform for performing the catalytic reactions with epoxides/aziridines, propargylic alcohols and amines. They could not only facilitate the easy separation of the product, but also showed a positive effect on the production in all the cases. Especially, by using the strategy of heterogeneous catalysis in $scCO_2$, the environmentally friendly processes for the fixation of CO_2 have been achieved. In this sense, more efficient and robust heterogeneous catalysts are needed to be developed. Our research also uncovers that CO_2 could be used for the synthesis of the highly substituted 3(*2H*)-furanones and *α*-hydroxy ketones, which opens up new routes to these compounds which are difficult to be synthesized by using classic methods. On the other hand, electrochemical carboxylations of unsaturated hydrocarbons by CO_2 to many useful carboxylic acid derivatives with inexpensive and easily available metal as electrolyte materials such as Ni and Al at mild conditions have also been achieved. For example, the synthesis of industrial important raw material adipic acid from CO_2 and 1,3-butadiene is proved to be feasible via the two-step electrochemical route. However, there are still many limitation needed to be circumvented, such as the low current efficiency. Besides, due to the complexity of the electrolysis systems, the mechanism of these transformation in most cases are uncertain and thus need to be studied in more detail in order to develop more facile routes for the reduction of CO_2.

Publication Date (Web): September 11, 2015 | doi: 10.1021/bk-2015-1194.ch003

In Advances in CO2 Capture, Sequestration, and Conversion; He, et al.;
ACS Symposium Series; American Chemical Society: Washington, DC, 2015.

References

1. Sumida, K.; Rogow, D. L.; Mason, J. A.; McDonald, T. M.; Bloch, E. D.; Herm, Z. R.; Bae, T.-H.; Long, J. R. Carbon Dioxide Capture in Metal–Organic Frameworks. *Chem. Rev.* **2012**, *112*, 724–781.
2. He, M.; Sun, Y.; Han, B. Green Carbon Science: Scientific Basis for Integrating Carbon Resource Processing, Utilization, and Recycling. *Angew. Chem., Int. Ed.* **2013**, *52*, 9620–9633.
3. Beckman, E. J. Green chemical processing using CO_2. *Ind. Eng. Chem. Res.* **2003**, *42*, 1598–1602.
4. Sakakura, T.; Choi, J. C.; Yasuda, H. Transformation of Carbon Dioxide. *Chem. Rev.* **2007**, *107*, 2365–2387.
5. Hunt, A. J.; Sin, E. H. K.; Marriott, R.; Clark, J. H. Generation, Capture, and Utilization of Industrial Carbon Dioxide. *ChemSusChem* **2010**, *3*, 306–322.
6. D'Alessandro, D. M.; Smit, B.; Long, J. R. Carbon Dioxide Capture: Prospects for New Materials. *Angew. Chem., Int. Ed.* **2010**, *49*, 6058–6082.
7. Sakakura, T.; Choi, J.-C.; Yasuda, H. Transformation of Carbon Dioxide. *Chem. Rev.* **2007**, *107*, 2365–2387.
8. Cokoja, M.; Bruckmeier, C.; Reger, B.; Herrmann, W. A.; Kühn, F. E. Transformation of Carbon Dioxide with Homogeneous Transition-Metal Catalysts: A Molecular Solution to a Global Challenge? *Angew. Chem., Int. Ed.* **2011**, *50*, 8510–8537.
9. Mikkelsen, M.; Jørgensen, M.; Krebs, F. C. The Teraton Challenge: A Review of Fixation and Transformation of Carbon Dioxide. *Energy Environ. Sci.* **2010**, *3*, 43–81.
10. Wang, W.; Wang, S.; Ma, X.; Gong, J. Recent Advances in Catalytic Hydrogenation of Carbon Dioxide. *Chem. Soc. Rev.* **2011**, *40*, 3703–3727.
11. Huang, K.; Sun, C.-L.; Shi, Z.-J. Transition-Metal-Catalyzed C–C Bond Formation through the Fixation of Carbon Dioxide. *Chem. Soc. Rev.* **2011**, *40*, 2435–2452.
12. Bayardon, J.; Holz, J.; Schaffner, B.; Andrushko, V.; Verekin, S.; Preetz, A.; Borner, A. *Angew. Chem., Int. Ed.* **2007**, *46*, 5971–5974.
13. Shaikh, A. A. G.; Sivaram, S. Organic Carbonates. *Chem. Rev.* **1996**, *96*, 951–976.
14. Biggadike, K.; Angell, R. M.; Burgess, C. M.; Farrell, R. M.; Hancock, A. P.; Harker, A. J.; Irving, W. R.; Ioannou, C.; Procopiou, P. A.; Shaw, R. E.; Solanke, Y. E; Singh, O. M. P.; Snowden, M. A.; Stubbs, R. J.; Walton, S.; Weston, H. E. Selective Plasma Hydrolysis of Glucocorticoid γ-Lactones and Cyclic Carbonates by the Enzyme Paraoxanase: An Ideal Plasma Inactivation Mechanism. *J. Med. Chem.* **2000**, *43*, 19–21.
15. Matsumoto, K.; Fuwa, S.; Kitajima, H. Enzyme-Mediated Enantioselective Hydrolysis of Cyclic Carbonates. *Tetrahedron Lett.* **1995**, *36*, 6499–6502.
16. Takata, T.; Furusho, Y.; Murakawa, K.; Endo, T.; Matsuoka, H.; Hirasa, T.; Matsuo, J.; Sisido, M. Optically Active Poly(aryl carbonates) Consisting of Axially Chiral Units. Chiral Binaphthyl Group Induced Helical Polymer. *J. Am. Chem. Soc.* **1998**, *120*, 4530–4531.

Publication Date (Web): September 11, 2015 | doi: 10.1021/bk-2015-1194.ch003

17. Cacchi, S.; Fabrizi, G.; Goggiamani, A.; Zappia, G. 3-Aryl-2-oxazolidinones through the Palladium-Catalyzed N-arylation of 2-Oxazolidinones. *Org. Lett.* **2001**, *3*, 2539–2541.
18. Sim, T. B.; Kang, S. H.; Lee, K. S.; Lee, W. K. A Novel Synthesis of 5-Functionalized Oxazolidin-2-ones from Enantiomerically Pure 2-Substituted N-[(R)-(+)-α-methylbenzyl]aziridines. *J. Org. Chem.* **2003**, *68*, 104–108.
19. Aurelio, L.; Brownlee, R. T. C.; Hughus, A. B. Synthetic Preparation of N-Methyl-α-amino Acids. *Chem. Rev.* **2004**, *104*, 5823–5846.
20. Makhtar, T. M.; Wright, G. D. Streptogramins, Oxazolidinones, and Other Inhibitors of Bacterial Protein Synthesis. *Chem. Rev.* **2005**, *105*, 529–542.
21. Andreou, T.; Costa, A. M.; Esteban, L.; Gonzalez, L.; Mas, G.; Vilarrasa, J. Synthesis of (−)-Amphidinolide K Fragment C9−C22. *Org. Lett.* **2005**, *7*, 4083–4086.
22. Ako, T.; Fukai, T.; Sahashi, R. Cycloaddition of Oxirane Group with Carbon Dioxide in the Supercritical Homogeneous State. *Ind. Eng. Chem. Res.* **2002**, *41*, 5353–5358.
23. Song, J.; Zhang, Z.; Huan, B.; Hu, S.; Li, W.; Xie, Y. Synthesis of Cyclic Carbonates from Epoxides and CO_2 Catalyzed by Potassium Halide in the Presence of β-Cyclodextrin. *Green Chem.* **2008**, *10*, 1337–1341.
24. Hancock, M. T.; Pinhas, A. R. A Convenient and Inexpensive Conversion of an Aziridine to an Oxazolidinone. *Tetrahedron Lett.* **2003**, *44*, 5457–5460.
25. Shen, Y. M.; Duan, W. L.; Shi, M. Chemical Fixation of Carbon Dioxide Co-Catalyzed by a Combination of Schiff Bases or Phenols and Organic Bases. *Eur. J. Org. Chem.* **2004**, *14*, 3080–3089.
26. Sun, J.; Cheng, W.; Yang, Z.; Wang, J.; Xu, T.; Xin, J.; Zhang, S. Superbase/Cellulose: An Environmentally Benign Catalyst for Chemical Fixation of Carbon Dioxide into Cyclic Carbonates. *Green Chem.* **2014**, *16*, 3071–3078.
27. Yano, T.; Matsui, H.; Koike, T.; Ishigure, H.; Fujihara, H.; Yoshihara, M.; Maeshima, T. Magnsium Oxide-Catalysed Reaction of Carbon Dioxide with an Epoxide with Retention of Stereochemistry. *Chem. Commun.* **1997**, *12*, 1129–1130.
28. Yamaguchi, K.; Ebitani, K.; Yoshida, T.; Yoshida, H.; Kaneda, K. Mg-Al Mixed Oxides as Highly Active Acid-base Catalysts for Cycloaddition of Carbon Dioxide to Epoxides. *J. Am. Chem. Soc.* **1999**, *121*, 4526–4527.
29. Paddock, R. L.; Nguyen, S. T. Chemical CO_2 Fixation: Cr(III) Salen Complexes as Highly Efficient Catalysts for the Coupling of CO_2 and Epoxides. *J. Am. Chem. Soc.* **2001**, *123*, 11498–11499.
30. Jing, H.; Edulji, S. K.; Gibbs, J. M.; Stern, C. L.; Zhou, H. Y.; Nguyen, S. T. (Salen)Tin Complexes: Syntheses, Catalytic Activity in the Formation of Propylene Carbonate form CO_2 and Propylene Oxide. *Inorg. Chem.* **2004**, *43*, 4315–4327.
31. Miller, A. W.; Nuguyen, S. T. (Salen)chromium(III)/DMAP: an Efficient Catalyst System for the Selective Synthesis of 5-Substituted Oxazolidinones from Carbon Dioxide and Aziridines. *Org. Lett.* **2004**, *6*, 2301–2304.
32. Yan, P.; Jing, H. Catalytic Asymmetric Cycloaddition of Carbon Dioxide and Propylene Oxide Using Novel Chiral Polymers of BINOL-Salen- Cobalt(III) Salts. *Adv. Synth. Catal.* **2009**, *351*, 1325–1332.

Publication Date (Web): September 11, 2015 | doi: 10.1021/bk-2015-1194.ch003

33. Clegg, W.; Harrington, R. W.; North, M.; Pasquale, R. Cyclic Carbonate Synthesis Catalysed by Bimetallic Aluminium–Salen Complexes. *Chem. Eur. J.* **2010**, *16*, 6828–6843.
34. Fontana, F.; Chen, C. C.; Aggarwal, V. K. Palladium-Catalyzed Insertion of CO_2 into Vinylaziridines: New Route to 5-Vinyloxazolidinones. *Org. Lett.* **2011**, *13*, 3454–3457.
35. Ren, W.-M.; Liu, Y.; Lu, X.-B. Bifunctional Aluminum Catalyst for CO_2 Fixation: Regioselective Ring Opening of Three-Membered Heterocyclic Compounds. *J. Org. Chem.* **2014**, *79*, 9771–9777.
36. Xie, Y.; Zhang, Z.; Jiang, T.; He, J.; Han, B.; Wu, T.; Ding, K. CO_2 Cycloaddition Reactions Catalyzed by an Ionic Liquid Grafted onto a Highly Cross-Linked Polymer Matrix. *Angew. Chem. Int. Ed.* **2007**, *46*, 7255–7258.
37. Sakai, T; Tsutsumi, Y.; Ema, T. Highly Active and Robust Organic–Inorganic Hybrid Catalyst for the Synthesis of Cyclic Carbonates from Carbon Dioxide and Epoxides. *Green Chem.* **2008**, *10*, 337–341.
38. Du, Y.; Wu, Y.; Liu, A. H.; He, L. N. Quaternary Ammonium Bromide Functionalized Polyethylene Glycol: A Highly Efficient and Recyclable Catalyst for Selective Synthesis of 5-Aryl-2-oxazolidinones from Carbon Dioxide and Aziridines Under Solvent-Free Conditions. *J. Org. Chem.* **2008**, *73*, 4709–4712.
39. Yang, Z.-Z.; Li, Y.-N.; Wei, Y.-Y.; He, L.-N. Protic Onium Salts-catalyzed Synthesis of 5-Aryl-2-oxazolidinones from Aziridines and CO_2 under Mild Conditions. *Green Chem.* **2011**, *13*, 2351–2353.
40. Seo, U. R.; Chung, Y. K. Poly(4-vinylimidazolium)s/Diazabicyclo [5.4.0]undec- 7-ene/Zinc(II) Bromide-Catalyzed Cycloaddition of Carbon Dioxide to Epoxides. *Adv. Synth. Catal.* **2014**, *356*, 1955–1961.
41. Qi, C.; Jiang, H.; Wang, Z.; Zou, B.; Yang, S. Naturally Occurring α-Amino Acid Catalyzed Coupling of Carbon Dioxide with Epoxides to Afford Cyclic Carbonates. *Synlett* **2007**, 255–258.
42. Qi, C. R.; Jiang, H. F. Histidine-Catalyzed Synthesis of Cyclic Carbonates in Supercritical Carbon Dioxide. *Sci. China Chem.* **2010**, *53*, 1566–1570.
43. Jiang, H. F.; Ye, J. W.; Qi, C. R.; Huang, L. B. Naturally Occurring α-Amino Acid: A Simple and Inexpensive Catalyst for the Selective Synthesis of 5-Aryl-2-oxazolidinones from Carbon Dioxide and Aziridines under Solvent-Free Conditions. *Tetrahedron Lett.* **2010**, *51*, 928–932.
44. Qi, C.; Ye, J.; Zeng, W.; Jiang, H. Polystyrene-Supported Amino Acids as Efficient Catalyst for Chemical Fixation of Carbon Dioxide. *Adv. Synth. Catal.* **2010**, *352*, 1925–1933.
45. Song, J.; Zhang, Z.; Hu, S.; Wu, T.; Jiang, T.; Han, B. MOF-5/n-Bu_4NBr: An Efficient Catalyst System for the Synthesis of Cyclic Carbonates from Epoxides and CO_2 under Mild Conditions. *Green Chem.* **2009**, *11*, 1031–1036.
46. Miralda, C. M.; Macias, E. E.; Zhu, M.; Ratnasamy, P.; Carreon, M. A. Zeolitic Imidazole Framework-8 Catalysts in the Conversion of CO_2 to Chloropropene Carbonate. *ACS Catal.* **2012**, *2*, 180–183.

Publication Date (Web): September 11, 2015 | doi: 10.1021/bk-2015-1194.ch003

47. Ren, Y.; Shi, Y.; Chen, J.; Yang, S.; Qi, C.; Jiang, H. Ni(salphen)-Based Metal–Organic Framework for the Synthesis of Cyclic Carbonates by Cycloaddition of CO_2 to Epoxides. *RSC Adv.* **2013**, *3*, 2167–2170.
48. Ren, Y.; Cheng, X.; Yang, S.; Qi, C.; Jiang, H.; Mao, Q. A Chiral Mixed Metal–Organic Framework Based on a Ni(saldpen) Metalloligand: Synthesis, Characterization and Catalytic Performances. *Dalton Trans.* **2013**, *42*, 9930–9937.
49. Kim, H. S.; Kim, J. W.; Kwon, S. C.; Shim, S. C.; Kim, T. J. Catalytic Formation of Carbamates and Cyclic Carbonates by Copper Complex of 2,5,19,22-Tetraaza[6,6](1,1′)ferrocenophane-1,5-diene X-ray Crystal Structure of $[Cu(1)]PF_6$. *J. Organomet. Chem.* **1997**, *545–546*, 337–344.
50. Gu, Y.; Shi, F.; Deng, Y. Ionic Liquid as an Efficient Promoting Medium for Fixation of CO_2: Clean Synthesis of α-Methylene Cyclic Carbonates from CO_2 and Propargyl Alcohols Catalyzed by Metal Salts under Mild Conditions. *J. Org. Chem.* **2004**, *69*, 391–394.
51. Inoue, Y.; Ishikawa, J.; Taniguchi, M.; Hashimoto, H. Cobaltocene-Catalyzed Reaction of Carbon Dioxide with Propargyl Alcohols. *Bull. Chem. Soc. Jpn.* **1987**, *60*, 1204–1206.
52. Yamada, W.; Sugawara, Y.; Cheng, H. M.; Ikeno, T.; Yamada, T. Silver-Catalyzed Incorporation of Carbon Dioxide into Propargylic Alcohols. *Eur. J. Org. Chem.* **2007**, 2604–2607.
53. Kiuchi, S.; Yoshida, S.; Sugawara, Y.; Yamada, W.; Cheng, H. M.; Fukui, K.; Sekine, K.; Iwakura, I.; Ikeno, T.; Yamada, T. Silver-Catalyzed Carbon Dioxide Incorporation and Rearrangement on Propargylic Derivatives. *Bull. Chem. Soc. Jpn.* **2011**, *84*, 698–717.
54. Yoshida, S.; Fukui, K.; Kikuchi, S.; Yamada, T. Silver-Catalyzed Enantioselective Carbon Dioxide Incorporation into Bispropargylic Alcohols. *J. Am. Chem. Soc.* **2010**, *132*, 4072–4073.
55. Song, Q.-W.; Yu, B.; Li, X.-D.; Ma, R.; Diao, Z.-F.; Li, R.-G.; Li, W.; He, L.-N. Efficient Chemical Fixation of CO_2 Promoted by a Bifunctional Ag_2WO_4/Ph_3P System. *Green Chem.* **2014**, *16*, 1633–1638.
56. Fournler, J.; Bruneau, C.; Dixneuf, P. H. Phosphine Catalysed Synthesis of Unsaturated Cyclic Carbonates from Carbon Dioxide and Propargylic Alcohols. *Tetrahedron Lett.* **1989**, *30*, 3981–3982.
57. Kayaki, Y.; Yamamoto, M.; Ikariya, T. Stereoselective Formation of α-Alkylidene Cyclic Carbonates via Carboxylative Cyclization of Propargyl Alcohols in Supercritical Carbon Dioxide. *J. Org. Chem.* **2007**, *72*, 647–649.
58. Kayaki, Y.; Yamamoto, M.; Ikariya, T. N-Heterocyclic Carbenes as Efficient Organocatalysts for CO_2 Fixation Reactions. *Angew. Chem. Int. Ed.* **2009**, *48*, 4194–4197.
59. Minakata, S.; Sasaki, I.; Ide, T. Atmospheric CO_2 Fixation by Unsaturated Alcohols Using tBuOI under Neutral Conditions. *Angew. Chem., Int. Ed.* **2010**, *49*, 1309–1311.
60. Wang, Y.-B.; Sun, D.-S.; Zhou, H.; Zhang, W.-Z.; Lu, X.-B. Alkoxide-Functionalized Imidazolium Betaines for CO_2 Activation and Catalytic Transformation. *Green Chem.* **2014**, *16*, 2266–2272.

In Advances in CO2 Capture, Sequestration, and Conversion; He, et al.;
ACS Symposium Series; American Chemical Society: Washington, DC, 2015.

Publication Date (Web): September 11, 2015 | doi: 10.1021/bk-2015-1194.ch003

61. Wang, Y.-B.; Wang, Y.-M.; Zhang, W.-Z.; Lu, X.-B. Fast CO_2 Sequestration, Activation, and Catalytic Transformation Using N-Heterocyclic Olefins. *J. Am. Chem. Soc.* **2013**, *135*, 11996–12003.
62. Jiang, H. F.; Wang, A. Z.; Liu, H. L.; Qi, C. R. Reusable Polymer-Supported Amine-Copper Catalyst for the Formation of α-Alkylidene Cyclic Carbonates in Supercritical Carbon Dioxide. *Eur. J. Org. Chem.* **2008**, *13*, 2309–2312.
63. Tang, X.; Qi, C.; He, H.; Jiang, H.; Ren, Y.; Yuan, G. Polystyrene-Supported N-Heterocyclic Carbene–Silver Complexes as Robust and Efficient Catalysts for the Reaction of Carbon Dioxide and Propargylic Alcohols. *Adv. Synth. Catal.* **2013**, *355*, 2019–2028.
64. Adams, P.; Baron, F. A. Esters of Carbamic Acid. *Chem. Rev.* **1965**, *65*, 567–602.
65. Sasaki, Y.; Dixneuf, P. H. Ruthenium-Catalyzed Reaction of Carbon Dioxide, Amine, and Acetylenic Alcohol. *J. Org. Chem.* **1987**, *52*, 4389–4391.
66. Burncau, C.; Dixneuf, P. H. Catalytic Synthesis of O-β-oxoalkylcarbamates. *Tetrahedron Lett.* **1987**, *28*, 2005–2008.
67. Kim, T. J.; Kwon, K. H.; Kwon, S. C.; Baeg, J. O.; Shim, S. C.; Lee, D. H. Iron Complexes of 1,1′-Bis(diphenylphosphino)ferrocene (BPPF) as Efficient Catalysts in the Synthesis of Carbamates. X-ray Crystal Structure of (BPPF)$Fe(CO)_3$. *J. Organomet. Chem.* **1990**, *389*, 205–217.
68. Shim, S. C.; Baeq, J. O.; Doh, C. H.; Youn, Y. Z.; Kim, T. J. Synthesis of Carbamates from Amines, Acetylenic Alcohols, and Carbon Dioxide Using a Lanthanide Catalyst. *Bull. Korean Chem. Soc.* **1990**, *11*, 467–468.
69. Kwon, S. C.; Cho, C. S.; Shim, S. C.; Kim, T. J. Catalytic Formation of Cyclic Carbonates and Carbamates by $[Cu(1)](BF_4)_2$ (1 = 2,5,19,22-Tetraaza[6,6](1,1′) ferrocenophane-1,5-diene). *Bull. Korean Chem. Soc.* **1999**, *20*, 103–105.
70. Qi, C. R.; Jiang, H. F. Efficient Synthesis of β-Oxopropylcarbamates in Compressed CO_2 without Any Additional Catalyst and Solvent. *Green Chem.* **2007**, *9*, 1284–1286.
71. Qi, C.; Huang, L.; Jiang, H. Efficient Synthesis of β-Oxoalkyl Carbamates from Carbon Dioxide, Internal Propargylic Alcohols, and Secondary Amines Catalyzed by Silver Salts and DBU. *Synthesis* **2010**, *9*, 1433–1440.
72. Xiao, Q.; Zhang, Y.; Wang, J. Diazo Compounds and N-Tosylhydrazones: Novel Cross-Coupling Partners in Transition-Metal-Catalyzed Reactions. *Acc. Chem. Res.* **2013**, *46*, 236–247.
73. Barluenga, J.; Valdés, C. Tosylhydrazones: New Uses for Classic Reagents in Palladium-Catalyzed Cross-Coupling and Metal-Free Reactions. *Angew. Chem. Int. Ed.* **2011**, *50*, 7486–7500.
74. Shao, Z.; Zhang, H. N-Tosylhydrazones: Versatile Reagents for Metal-Catalyzed and Metal-Free Cross-Coupling Reactions. *Chem. Soc. Rev.* **2012**, *41*, 560–572.
75. Xiong, W.; Qi, C.; He, H.; Ouyang, L.; Zhang, M.; Jiang, H. Base-Promoted Coupling of Carbon Dioxide, Amines, and N-Tosylhydrazones: A Novel and Versatile Approach to Carbamates. *Angew. Chem. Int. Ed.* **2015**, *54*, 3084–3087.

Publication Date (Web): September 11, 2015 | doi: 10.1021/bk-2015-1194.ch003

76. Fournier, J.; Bruneau, C.; Dixneuf, P. H. A Simple Synthesis of Oxazolidinones in One Step from Carbon Dioxide. *Tetrahedron Lett.* **1990**, *31*, 1721–1722.
77. Gu, Y.; Zhang, Q.; Duan, Z.; Zhang, J.; Zhang, S.; Deng, Y. Ionic Liquid as an Efficient Promoting Medium for Fixation of Carbon Dioxide: A Clean Method for the Synthesis of 5-Methylene-1,3-oxazolidin-2-ones from Propargylic Alcohols, Amines and Carbon Dioxide Catalyzed by Cu(I) under Mild Conditions. *J. Org. Chem.* **2005**, *70*, 7376–7380.
78. Zhang, Q.; Shi, F.; Gu, Y.; Yang, J.; Deng, Y. Efficient and Eco-Friendly Process for the Synthesis of N-Substituted 4-Methylene-2-oxazolidinones in Ionic Liquids. *Tetrahedron Lett.* **2005**, *46*, 5907–5911.
79. Jiang, H.; Zhao, J.; Wang, A. An Efficient and Eco-Friendly Process for the Conversion of Carbon Dioxide into Oxazolones and Oxazolidinones under Supercritical Conditions. *Synthesis* **2008**, *5*, 763–769.
80. Jiang, H. F.; Zhao, J. W. Silver-Catalyzed Activation of Internal Propargylic Alcohols in Supercritical Carbon Dioxide: Efficient and Eco-Friendly Synthesis of 4-Alkylidene-1,3-oxazolidin-2-ones. *Tetrahedron Lett.* **2009**, *50*, 60–62.
81. Shi, M.; Shen, Y.-M. Transition-Metal-Catalyzed Reactions of Propargylamine with Carbon Dioxide and Carbon Disulfide. *J. Org. Chem.* **2002**, *67*, 16–21.
82. Kayaki, Y.; Yamamoto, M.; Suzuki, T.; Ikariya, T. Carboxylative Cyclization of Propargylamines with Supercritical Carbon Dioxide. *Green Chem.* **2006**, *8*, 1019–1021.
83. Yoshida, M.; Mizuguchi, T.; Shishido, K. Synthesis of Oxazolidinones by Efficient Fixation of Atmospheric CO_2 with Propargylic Amines by using a Silver/1,8-DiazabicycloACHTUNGTRENUNG[5.4.0]undec-7-ene(DBU) Dual-Catalyst System. *Chem. Eur. J.* **2012**, *18*, 15578–15581.
84. Costa, M.; Chiusoli, G. P.; Rizzardi, M. Base-Catalysed Direct Introduction of Carbon Dioxide into Acetylenic Amines. *Chem. Commun.* **1996**, 1699–1700.
85. Takeda, Y.; Okumura, S.; Tone, S.; Sasaki, I.; Minakata, S. Cyclizative Atmospheric CO_2 Fixation by Unsaturated Amines with t-BuOI Leading to Cyclic Carbamates. *Org. Lett.* **2012**, *14*, 4874–4877.
86. Yao, X.; Li, C.-J. Phosphine-Triggered Complete Chemo-Switch: From Efficient Aldehyde−Alkyne−Amine Coupling to Efficient Aldehyde−Alkyne Coupling in Water. *Org. Lett.* **2005**, *7*, 4395–4398.
87. Lo, V. K.-Y.; Liu, Y.; Wong, M.-K.; Che, C.-M. Gold(III) Salen Complex-Catalyzed Synthesis of Propargylamines via a Three-Component Coupling Reaction. *Org. Lett.* **2006**, *8*, 1529–1532.
88. Gommermann, N.; Knochel, P. Practical Highly Enantioselective Synthesis of Propargylamines through a Copper-Catalyzed One-Pot Three-Component Condensation Reaction. *Chem Eur. J.* **2006**, *12*, 4380–4392.
89. Yoo, W.-J.; Li, C.-J. Copper-Catalyzed Four-Component Coupling between Aldehydes, Amines, Alkynes, and Carbon Dioxide. *Adv. Synth. Catal.* **2008**, *350*, 1503–1506.

Publication Date (Web): September 11, 2015 | doi: 10.1021/bk-2015-1194.ch003

90. Zhao, J.; Huang, H.; Qi, C.; Jiang, H. CuI/$SnCl_2$ Co-Catalyzed Four-Component Reaction of Ketones, Amines, Alkynes, and Carbon Dioxide. *Eur. J. Org. Chem.* **2012**, 5665–5667.
91. Zhao, J.; Jiang, H. Copper (I) Catalyzed Synthesis of 1,3-oxazolidin-2-ones From Alkynes, Amines, and Carbon Dioxide under Solvent-Free Conditions. *Tetrahedron Lett.* **2012**, *53*, 6999–7002.
92. Smith, A. B., III; Guaciaro, M. A.; Schow, S. R.; Wovkulich, P. M.; Todu, B. H.; Hall, T. W. A Strategy for the Total Synthesis of Jatrophone: Synthesis of Normethyljatrophone. *J. Am. Chem. Soc.* **1981**, *103*, 219–222.
93. Jerris, P. J.; Smith, A. B., III Synthesis and Configurational Assignment of Geiparvarin: A Novel Antitumor Agent. *J. Org. Chem.* **1981**, *46*, 577–585.
94. Smith, A. B., III; Levenberg, P. A.; Jerris, P. J.; Scarborough, R. M., Jr; Wovkulich, P. M. Synthesis and Reactions of Simple 3(*2H*)-Furanones. *J. Am. Chem. Soc.* **1981**, *103*, 1501–1513.
95. Manfredini, S.; Baraldi, P. G.; Bazzanini, R. B.; Guarneri, M.; Simoni, D.; Balzarini, J.; De Clercq, E. Geiparvarin Analogs. 4.1. Synthesis and Cytostatic Activity of Geiparvarin Analogs Bearing a Carbamate Moiety or a Furocoumarin Fragment on the Alkenyl Side Chain. *J. Med. Chem.* **1994**, *37*, 2401–2405.
96. Chimichi, S.; Boccalini, M.; Cosimelli, B.; Viola, G.; Vedaldi, D.; Dall'Acqua, F. New Geiparvarin Analogues from 7-(2-Oxoethoxy)coumarins as Efficient in Vitro Antitumoral Agents. *Tetrahedron Lett.* **2002**, *43*, 7473–7476.
97. Stierle, A. A.; Stierle, D. B.; Patacini, B. The Berkeleyamides, Amides from the Acid Lake Fungus Penicillum Rubrum. *J. Nat. Prod.* **2008**, *71*, 856–860.
98. Langer, P.; Krummel, T. Chemo- and Regioselective Synthesis of Functionalized 3(*2H*)-Furanones by the First Cyclization Reactions of 1,3-Bis(trimethylsiloxy)buta-1,3-dienes with α-Chlorocarboxylic Acid Chlorides. *Chem. Commun.* **2000**, *11*, 967–968.
99. Langer, P.; Krummel, T. Chemo-, Regio-, and Stereoselective Cyclizations of 1,3-Bis(trimethylsilyloxy)-1,3-butadienes with α-Chloroacetic Acid Chlorides and α-Chloroacetic Acetals. *Chem. Eur. J.* **2001**, *7*, 1720–1727.
100. Winkler, J. D.; Oh, K.; Asselin, S. M. Synthesis of Highly Functionalized Furanones via Aldol Reaction of 3-Silyloxyfurans. *Org. Lett.* **2005**, *7*, 387–389.
101. Kato, K.; Nouchi, H.; Ishikura, K.; Takaishi, S.; Motodate, S.; Tanaka, H.; Okudaira, K.; Mochida, T.; Nishigaki, R.; Shigenobu, K.; Akita, H. A Facile Access to Spiro Furanone Skeleton Based on Pd(II)-mediated Cyclization–Carbonylation of Propargylic Esters. *Tetrahedron* **2006**, *62*, 2545–2554.
102. Trofimov, B. A.; Shemyakina, O. A.; Mal'kina, A. G.; Ushakov, I. A.; Kazheva, O. N.; Alexandrov, G. G.; Dyachenko, O. A. A Domino Reaction of α,β-Acetylenic γ-Hydroxy Nitriles with Arenecarboxylic Acids: An Unexpected Facile Shortcut to 4-Cyano-3(*2H*)-Furanones. *Org. Lett.* **2010**, *12*, 3200–3203.
103. Poonoth, M.; Krause, N. Cycloisomerization of Bifunctionalized Allenes: Synthesis of 3(2*H*)-Furanones in Water. *J. Org. Chem.* **2011**, *76*, 1934–1936.

Publication Date (Web): September 11, 2015 | doi: 10.1021/bk-2015-1194.ch003

104. Liu, Y.; Liu, M.; Guo, S.; Tu, H.; Zhou, Y.; Gao, H. Gold-Catalyzed Highly Efficient Access to 3(2*H*)-Furanones from 2-Oxo-3-butynoates and Related Compounds. *Org. Lett.* **2006**, *8*, 3445–3448.
105. Kirsch, S. F.; Binder, J. T.; Liébert, C.; Menz, H. Gold(III)- and Platinum(II)-Catalyzed Domino Reaction Consisting of Heterocyclization and 1,2-Migration: Efficient Synthesis of Highly Substituted 3(2H)-Furanones. *Angew. Chem. Int. Ed.* **2006**, *45*, 5878–5880.
106. Reiter, M.; Turner, H.; Mills-Webb, R.; Gouverneur, V. Palladium-Catalyzed Oxidative Cyclizations: Synthesis of Dihydropyranones and Furanones. *J. Org. Chem.* **2005**, *70*, 8478–8485.
107. Marson, C. M.; Edaan, E.; Morrell, J. M.; Coles, S. J.; Hursthouse, M. B.; Davies, D. T. A Catalytic Asymmetric Protocol for the Enantioselective Synthesis of 3(*2H*)-Furanones. *Chem. Commun.* **2007**, *24*, 2494–2496.
108. Egi, M.; Azechi, K.; Saneto, M.; Shimizu, K.; Akai, S. Cationic Gold(I)-Catalyzed Intramolecular Cyclization of γ-Hydroxyalkynones into 3(2*H*)-Furanones. *J. Org. Chem.* **2010**, *75*, 2123–2126.
109. Qi, C.; Jiang, H.; Huang, L.; Yuan, G.; Ren, Y. Carbon Dioxide Triggered and Copper-Catalyzed Domino Reaction: Efficient Construction of Highly Substituted 3(2*H*)-Furanones from Nitriles and Propargylic Alcohols. *Org. Lett.* **2011**, *13*, 5520–5523.
110. Yuan, G.; He, Z.; Zheng, J.; Chen, Z.; Huang, H.; Shi, D.; Qi, C.; Jiang, H. Carbon Dioxide-Mediated Synthesis of 3(2*H*)-Furanones from Diyne Alcohols. *Tetrahedron Lett.* **2011**, *52*, 5956–5959.
111. Somers, P. K.; Wandless, T. J.; Schreiber, S. L. *J. Am. Chem. Soc.* **1991**, *113*, 8045–8056.
112. Palomo, C.; González, A.; García, J. M.; Landa, C.; Oiarbide, M.; Rodríguez, S.; Linden, A. *Angew. Chem., Int. Ed.* **1998**, *37*, 180–182.
113. Palomo, C.; Oiarbide, M.; Aizpurua, J. M.; González, A.; García, J. M.; Landa, C.; Odriozola, I.; Linden, A. *J. Org. Chem.* **1999**, *64*, 8193–8200.
114. He, H.; Qi, C.; Hu, X.; Guan, Y.; Jiang, H. Efficient Synthesis of Tertiary α-Hydroxy Ketones through CO_2-Promoted Regioselective Hydration of Propargylic Alcohols. *Green Chem.* **2014**, *16*, 3729–373.
115. Chen, F.; Dong, T.; Xu, T.; Li, X.; Hu, C. Direct Synthesis of Cyclic Carbonates from Olefins and CO_2 Catalyzed by a $MoO_2(acac)_2$-Quaternary Ammonium Salt System. *Green Chem.* **2011**, *13*, 2518–2524.
116. Wang, J.; Wang, J.; He, L.; Dou, X.; Wu, F. A CO_2/H_2O_2-Tunable Reaction: Direct Conversion of Styrene into Styrene Carbonate Catalyzed by Sodium Phosphotungstate/n-Bu_4NBr. *Green Chem.* **2008**, *10*, 1218–1223.
117. Eghbali, N.; Li, C. Conversion of Carbon Dioxide and Olefins into Cyclic Carbonates in Water. *Green Chem.* **2007**, *9*, 213–215.
118. Gao, X.; Yuan, G.; Chen, H.; Jiang, H.; Li, Y.; Qi, C. Efficient Conversion of CO_2 with Olefins into Cyclic Carbonates via a Synergistic Action of I_2 and Base Electrochemically Generated in Situ. *Electrochem. Commun.* **2013**, *34*, 242–245.
119. Noji, M.; Suzuki, K.; Tashiro, T.; Suzuki, M.; Harada, K.; Masuda, K.; Kidani, Y. Syntheses and Antitumor Activities of

Publication Date (Web): September 11, 2015 | doi: 10.1021/bk-2015-1194.ch003

1R,2R-Cyclohexanediamine Pt(II) Complexes Containing Dicarboxylates. *Chem. Pharm. Bull.* **1987**, *35*, 221–228.
120. Filardo, G.; Gambino, S.; Silvestri, G.; Gennaro, A.; Vianello, E. Electrocarboxylation of Styrene through Homogeneous Redox Catalysis. *J. Electroanal. Chem.* **1984**, *177*, 303–309.
121. Gambino, S.; Gennaro, A.; Filardo, G.; Silvestri, G.; Vianello, E. Electrochemical Carboxylation of Styrene. *J. Electroanal. Chem.* **1987**, *134*, 2172–2175.
122. Dérien, S.; Clinet, J. C.; Duñach, E.; Périchon, J. Electrochemical Incorporation of Carbon Dioxide into Alkenes by Nickel Complexes. *Tetrahedron* **1992**, *48*, 5235–5248.
123. Ballivet-Tkatchenko, D.; Jean-Claude, F.; Tanji, J. Electrocatalytic Reduction of CO_2 for the Selective Carboxylation of Olefins. *Appl. Organometal. Chem.* **2000**, *14*, 847–849.
124. Senboku, H.; Komatsu, H.; Fujimura, Y.; Tokuda, M. Efficient Electrochemical Dicarboxylation of Phenyl-substituted Alkenes: Synthesis of 1-Phenyl-1,2-alkanedicarboxylic Acids. *Synlett* **2001**, 418–420.
125. Yuan, G. Q.; Jiang, H. F.; Lin, C.; Liao, S. J. Efficient Electrochemical Synthesis of 2-Arylsuccinic Acids from CO_2 and Aryl-Substituted Alkenes with Nickel as Cathode. *Electrochim. Acta* **2008**, *53*, 2170–2176.
126. Yuan, G. Q.; Jiang, H. F.; Lin, C. Efficient Electrochemical Dicarboxylations of Arylacetylenes with Carbon Dioxide Using Nickel as Cathode. *Tetrahedron* **2008**, *64*, 5866–5872.
127. Li, C.; Yuan, G.; Jiang, H. Electrocarboxylation of Alkynes with Carbon Dioxide in the Presence of Metal Salt Catalysts. *Chin. J. Chem.* **2010**, *28*, 1685–1689.
128. Engels, R.; Smitt, C. J.; Van Tolborg, W. J. M. Reactions at the Counter Electrode in Electroreductions under Aprotic Conditions in One-Compartment Cells. *Angew. Chem., Int. Ed.* **1983**, *22*, 492–493.
129. Pletcher, D.; Girault, J. T. The Influence of Cell Design and Electrolysis Parameters on the Cathodic Coupling of Butadiene and Carbon Dioxide in Acetonitrile. I. Undivided Parallel Plate Configurations. *J. Appl. Electrochem.* **1986**, *16*, 791–802.
130. Grinberg, V. A.; Koch, T. A.; Mazin, V. M.; Mysov, E. I.; Sterlin, S. R. Electrochemical Reduction of CO_2 in the Presence of 1,3-Butadiene Using a Hydrogen Anode in a Nonaqueous Medium. *Russ. Chem. Bull.* **1999**, *48*, 294–299.
131. Bringmann, J.; Dinjus, E. Electrochemical Synthesis of Carboxylic Acids from Alkenes Using Various Nickel-Organic Mediators: CO_2 as C1-Synthon. *Appl. Organomet. Chem.* **2001**, *15*, 135–140.
132. Li, C. H.; Yuan, G. Q.; Ji, X. C.; Wang, X. J.; Ye, J. S.; Jiang, H. F. Highly Regioselective Electrochemical Synthesis of Dioic Acids from Dienes and Carbon Dioxide. *Electrochim. Acta* **2011**, *56*, 1529–1534.

Publication Date (Web): September 11, 2015 | doi: 10.1021/bk-2015-1194.ch003

Publication Date (Web): September 11, 2015 | doi: 10.1021/bk-2015-1194.ch004

Chapter 4

Application of Diverse Hydrogen Sources to Methanol Synthesis from CO_2

Dezhang Ren, Zhiyuan Song, Jun Fu, and Zhibao Huo*

School of Environmental Science and Engineering, Shanghai Jiao Tong University, 800 Dongchuan Road, Shanghai 200240, China
***E-mail: hzb410@sjtu.edu.cn**

In recent years, carbon dioxide (CO_2) hydrogenation to methanol is attracting interest because of its abundance, low cost, nontoxicity and high potential as a renewable source. However, this method involving both high-purity gaseous hydrogen and hydrogen storage is considered as an energy-intensive process. Thus, development of other hydrogen donors systems is highly essential. The propose of this review is to discuss recent advances and future possibilities for the development of other hydrogen sources for methanol production from CO_2. Several hydrogen sources including organosilane, borane derivatives, $LiAlH_4$, water, NADH and ascorbic acid are discussed. Compared with hydrogenation of CO_2 with gaseous hydrogen, these hydrogen sources exhibit high safety, easy handling, etc features.

In Advances in CO2 Capture, Sequestration, and Conversion; He, et al.;
ACS Symposium Series; American Chemical Society: Washington, DC, 2015.

Publication Date (Web): September 11, 2015 | doi: 10.1021/bk-2015-1194.ch004

Introduction

Carbon dioxide (CO_2) as a common greenhouse gas is considered as a primary contributor to climate change and global warming, for the CO_2 concentration in the atmosphere is rising rapidly during the last decades. Hence, the strategies and measures of dealing with CO_2 emissions were attracted much attention from scientists, government officials to folks. Fossil energy effective utilization, carbon dioxide capture & storage (CCS) and carbon dioxide capture & utilization (CCU) are three mainstream directions of reduction of CO_2 emissions. CCU is a promising way which focused on using CO_2 as a feedstock on industrial production, for CO_2 is non-toxic, inexpensive and abundant carbon sources (C1 building block). Hydrogenation of CO_2 into methanol is an important pathway of CCU technology. Methanol as an important fuel and industrial product can be used for various fields. Methanol not only can be used as antifreeze, solvent and fuel, but convenient for storage and transportation for its low corrosive and liquid phase. Synthesis of methanol from CO_2 *via* appropriate ways is a novel strategy in the context of global warming and energy crisis. Industrialized production of methanol using syngas ($CO + H_2$) as main feedstock, which synthetized from natural gas, catalyzed by $Cu/ZnO/Al_2O_3$ under high temperature and pressure condition. Although CO_2 is an important reactant in the syngas process for methanol production (*1*), natural gas is a fossil energy resource, directly conversion of CO_2 to methanol is still a greener alternative way. The conversion process require hydrogen donors. H_2 as a common hydrogen source in the catalytic process of methanol production from CO_2 has been studied for many years (*2*, *3*). There has been significant work on this field. However, there are several safe risks should be faced due to its gas phase and flammable characters in the course of H_2 transportation and application. Therefore, the exploitation of other hydrogen sources to replace H_2 for reduction of CO_2 to methanol is a good choice. Herein, advances of methanol synthesis from CO_2 with several hydrogen sources such as organosilane (R_3SiH), borane, $LiAlH_4$, water, etc are introduced.

Conversion of CO_2 into Methanol with Organosilane as Hydrogen Source

Organosilane with reducing group Si-H can be used as hydride donor in inorganic and organic chemistry reaction, such as metal salts reduction, H_2 production with the strong Brønsted acids added and hydrogenation of organic compounds under appropriate conditions. More detail information can refer the review published from L. Larson and L. Fry, in which a series hydrogenation of organic reactions using organosilane were summarized (*4*). For the area of CO_2 reduction, Koinuma and co-workers reported the hydrosilylation of CO_2 catalyzed by ruthenium and palladium complexes with diethylmethylsilane ($HSiMeEt_2$) as reductant in 1981. The main product diethylmethylsilyl formate ($HCO_2SiMeEt_2$) was obtained (*5*). Several research groups developed different catalysts in similar orgainosilane system to produce formoxysilanes and methane from CO_2 (*6*, *7*). In order to obtain methanol or methoxide, Eisenberg and Eisenshmid attempted to reduce CO_2 in alkylsilanes (Me_2SiH_2, Et_2SiH_2, Me_3SiH)

In Advances in CO2 Capture, Sequestration, and Conversion; He, et al.;
ACS Symposium Series; American Chemical Society: Washington, DC, 2015.

system using Ir complexes as catalyst. Methoxide was gained after a long time of reaction under mild condition (Scheme 1). After investigated by $^{13}CO_2$-labed experiment, the possible intermediates, formates, acetals, were detected. The formation of Si-O bonds during the reaction were considered to facilitate the reductions (*8*). As mentioned above, transition metal complexes are the preferred catalysts to active CO_2 in orgainosilane system. Interestingly, some nucleophilic metal-free organocatalysts such as *N*-heterocyclic carbenes and trityl borate $[Ph_3C][B(C_6F_5)_4]$ show similar effect when introduced into alkylsianes system to catalytic reduce CO_2 to methanol (Scheme 1) (*9*, *10*), and quantum mechanical calculations were used to discuss the reduction mechanism (*10*, *11*).

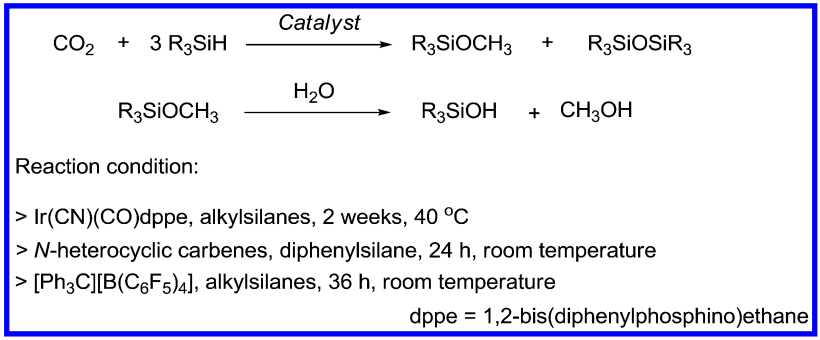

Scheme 1. Methanol production from CO_2 and organosliane (8–10).

Conversion of CO_2 into Methanol with Borane Derivative as Hydrogen Source

Similar to organosliane, borane derivatives were applied as reduce reagents in CO_2 reduction. Frustrated Lewis pairs (FLPs) systems including AlX_3 (X=Cl or Br) and $PMes_3$ (Mes=2,4,6-$C_6H_2Me_3$) were introduced to convert CO_2 to methanol using ammonia borane (H_3NBH_3) as hydrogen donor. The formation of MeO-Al bonds was considered as a driving force to facilitate the methanol production (*12*). Considering the stoichiometric amounts of FLPs were used in the reaction, more efficient nickel pincer hydride complex ((2,6-$C_6H_3(OP^tBu_2)_2$)Ni = [Ni]H) was developed for catalytic conversion of CO_2 using catecholborane (HBcat) as hydrogen donor (Scheme 2) (*13*). The computational mechanistic study was given by the same research group to understand the Ni-HBcat catalytic system (*14*). Similar to sliane system, metal-free organocatalyts can also be use to active CO_2. Metal-free phosphine-borane organocatalyst was applied to convert CO_2 to methanol, several borane complexes were prepared as hydroboranes, such as catecholborane, pinacolborane, 9-borabicyclo[3.3.1]nonane, $BH_3{\cdot}SMe_2$ and $BH_3{\cdot}$THF for offering hydrogen donors to the reaction system (*15*). Most of silane or borane reduction systems were conducted under mild conditions, some recent published results showed high yield, TON and TOF for methanol production (*9*, *16*).

In Advances in CO2 Capture, Sequestration, and Conversion; He, et al.;
ACS Symposium Series; American Chemical Society: Washington, DC, 2015.

Publication Date (Web): September 11, 2015 | doi: 10.1021/bk-2015-1194.ch004

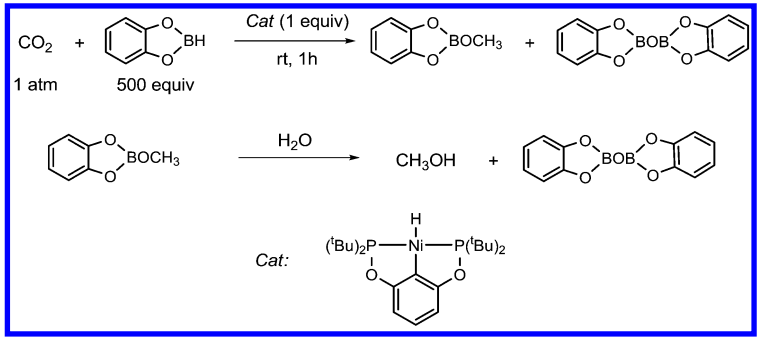

Scheme 2. Methanol production from CO_2 and HBcat.

Conversion of CO_2 into Methanol with $LiAlH_4$ as Hydrogen Source

Lithium aluminium hydride ($LiAlH_4$) is a common reducing agent in organic reaction discovered in 1947 (*17*). The application of $LiAlH_4$ on methanol production from CO_2 was reported in 1948. The dried CO_2 was introduced into stoichiometric excess $LiAlH_4$ with diethyl carbitol as solvent, then a certain amount of *n*-butylcarbitol was added to decompose the excess $LiAlH_4$ and produce methanol. The highest yield of methanol is 81% (Scheme 3) (*18*).

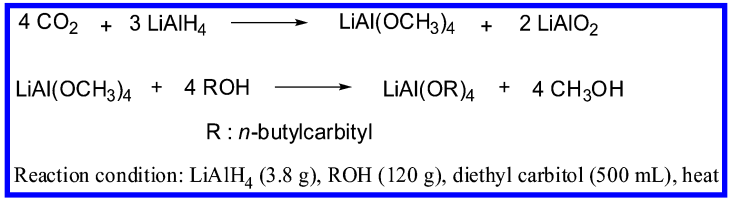

Scheme 3. Methanol production from CO_2, $LiAlH_4$ and n-butylcarbitol.

In radiopharmaceutical chemistry, synthesis of [^{11}C]methanol from [^{11}C]CO_2 with $LiAlH_4$ as reductant in THF is a common method. The drawbacks of this system stated by Roeda and co-workers is that [^{11}C]formate as an intermediate during the reducing process was always detected, which considered as a loss in that field (*19*).

Conversion of CO_2 into Methanol Using Water as Hydrogen Source

Water is a widespread and abundant renewable resource, which can be easily obtained in nature. It is a necessities of daily life and widely used in industry, agriculture and other fields. For chemistry industry, water is a green solvent and hydrogen source. In this part, we will introduce two approaches using water as hydrogen donor to transfer CO_2 to methanol.

In Advances in CO2 Capture, Sequestration, and Conversion; He, et al.;
ACS Symposium Series; American Chemical Society: Washington, DC, 2015.

Publication Date (Web): September 11, 2015 | doi: 10.1021/bk-2015-1194.ch004

Photoelecrocatalytic Reduction of CO_2 in Water

The phenomenon of photocatalytic water splitting was discovered in 1972 (*20*). From this starting point, photocatalysis as a new subject was established and developed boomingly in short time. For the area of CO_2 reduction, Inoue and co-workers first attempted the photocatalytic reduction of CO_2 in water, which generated formic acid, formaldehyde, methanol and methane, using semiconductors such as WO_3, TiO_2, ZnO, CdS, GaP and SiC in 1979 (*21*). The possible pathway of methanol formation is described *via* semiconductor mechanism (Scheme 4).

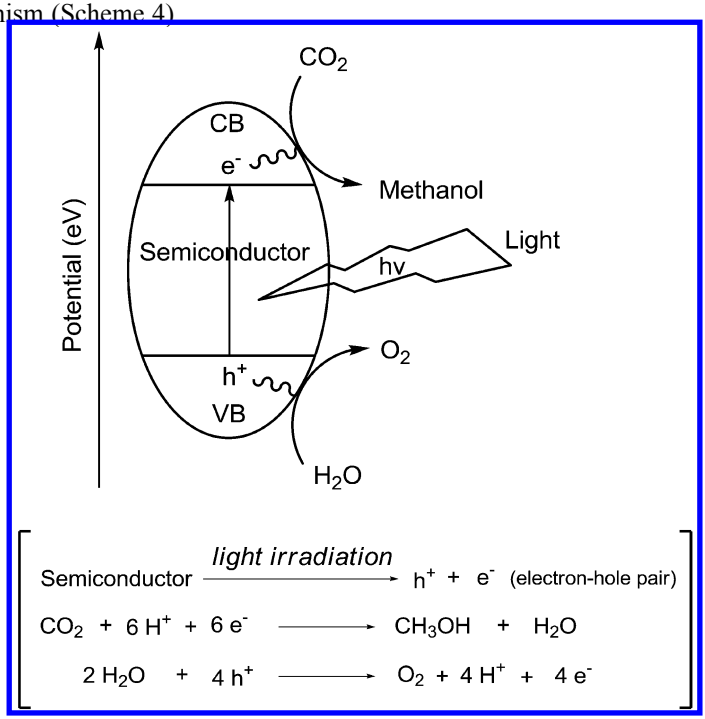

Scheme 4. Proposed semiconductor mechanism of methanol production from CO_2.

TiO_2 is one of the promising material for its photocatalytic properties. However, some challenges still exist not only in the area of CO_2 photocatalytic reduction, but also in water splitting. Firstly, TiO_2 cannot directly effective utilize the light having wavelength longer than 387 nm which is the boundary between ultraviolet and visible light (*22*). Unfortunately, ultraviolet light only occupy 2-5% sunlight spectrum (*23*). The measures of extension of Ti-based semiconductor's photo-response to whole sunlight region is important. Secondly, the formation of photo-generated electrons and holes on the surface of TiO_2 after irradiated by light play a crucial role for the reduction of CO_2. Recombination of these electrons and holes lead TiO_2 to lose effectiveness. Hence, keeping enough lifetime of the electrons and holes after they were generated and separated is also a key point of photocatalysis system (*24*).

In Advances in CO2 Capture, Sequestration, and Conversion; He, et al.;
ACS Symposium Series; American Chemical Society: Washington, DC, 2015.

Publication Date (Web): September 11, 2015 | doi: 10.1021/bk-2015-1194.ch004

Recently, several approaches focused on these challenges. In order to develop light-harvesting strategies for extending TiO_2 application effectiveness, transition metal complexes with organic ligands are considered as efficient and stable light-harvesting center on TiO_2. Ma and co-workers modified the TiO_2 nanotubes (TNT) by Zn(II)/Cu(II)/Co(II)-porphyrin-Ru(II) polypyridly complexes. The best yield of methanol production from CO_2 was 746 μmol L^{-1} g^{-1}cat catalyzed by Zn(II)porphyrin-Ru(II) polypyridly complexes modified TNT (*25*). Doping metal or nonmetal elements into TiO_2 is another way to improve TiO_2 photocatalytic activity (*26*). The doping elements provide new energy levels into the band gap of TiO_2, which can be considered as empty or occupied orbitals inserted between conduction band (CB) and valence band (VB) (*24*). For example, C/N-TiO_2 nanoparticles were synthesized for photocatalytic reduction of CO_2 to methanol. The good photoactivity of catalyst was maintained due to the doping of C and N into the TiO_2 nanoparticles. The highest yield of methanol was 0.478 μmol g^{-1} h^{-1} (*26*). Luo and co-workers prepared Cu and Ce co-doped TiO_2 catalysts using the equivalent-volume incipient wetness impregnation method. The Cu/Ce-TiO_2 catalysts with good light-harvesting abilities and highly photoactivities for reduction of CO_2. 180.3 μmol g^{-1}cat of methanol was obtained under the optimal condition. Calculation results shown that the existence of Ce into the TiO_2 facilitate the formation of photo-generated electrons and holes, and the role of Cu on the TiO_2 surface was to offer channels for photoelectrons to inhabit the electron/hole recombination, which will be discussed below (*27*). In general, the efficient of light harvesting of transition metal organic complexes are greater than inorganic ions doping (*25*). In order to avoid the recombination of photoelectrons and holes, the concept of electron traps was introduced into the design of photocatalyst. Various transition metals, such as Pt, Pd and Cu were loaded onto TiO_2 surface, which offering electron trapping sites to keep long lifetime of electrons and holes (*28*). The heterojunction between TiO_2 (n-type semiconductor) and NiO (p-type semiconductor) can effectively prolong the lifetime of electrons/holes in photogeneration of methanol from CO_2 (*23*). The heterojunction formed between TiO_2 and $FeTiO_3$ was introduced for methanol formation, authors believed $FeTiO_3$ loaded onto TiO_2 not only narrowed band gap of the system, but also offered enough lifetime to holes, because of VB of $FeTiO_3$ is lower than that of TiO_2, and electrons can transfer from TiO_2 to $FeTiO_3$ (*28*).

In addition to Ti-based material, other semiconductors also can be used to photocatalytic transform CO_2 to methanol. The same challenging tasks as TiO_2 mentioned above were faced to deal. $InTaO_4$ was studied for photoreduction of CO_2 by Pan and Chen, they synthesized $InTaO_4$ and loaded Ni onto the $InTaO_4$ suface. The NiO/$InTaO_4$ was formed by calcined in air at first. After that the solid powder was carried out a reduction-oxidation pretreatment to form a Ni-NiO core-shell structure on the $InTaO_4$ surface. The highest yield of methanol was 1.394 μmol h^{-1} g^{-1}, and the increasing the amount of NiO and the reduction-oxidation pretreatment had a positive effect on $InTaO_4$ activities (*29*). SiC with strong reduction photoelectrons, for its much negative potential of conduction band, can be used to photoreduction of CO_2 (*30*). Li and co-workers prepared a Cu_2O/SiC nanoparticles photocatalyst, in which Cu_2O was considered as a good selectivity for methanol formation, to use for reduction of CO_2 into

Publication Date (Web): September 11, 2015 | doi: 10.1021/bk-2015-1194.ch004

methanol. The highest yield of methanol was 191 μmol g^{-1} using Cu_2O/SiC photocatalyst, which is much higher than that of 153 μmol g^{-1} using only SiC under visible light irradiation (*30*). A research group from the University of Texas at Arlington designed one kind of hybrid CuO-Cu_2O semiconductor nanorod arrays for photogeneration of methanol from CO_2. The nanorod arrays were synthesized *via* a oxidation-electrodeposition hybrid process on Cu substrates (*31*). Bi-based oxides have been studied in the area of photocatalysis for many years, which showed low toxicity and good light-harvesting activities. Peng and co-workers synthesized a lamellar structure $BiVO_4$ under surfactant-assisted hydrothermal condition for photosynthesis of methanol from CO_2 in NaOH solution. The concentration of NaOH played a crucial role in the photoreduction system because it controlled the CO_2 solubility and the amount of OH^- which considered as hole-scavenger to facilitate the separation of photoelectrons and holes. The stable property of $BiVO_4$ is excellent proved by repeated experiments (*32*). Huang and co-workers synthesized a hollow microspheres structure of Bi_2WO_6 which displayed great photocatalytic activity and methanol selectivity for photoreduction CO_2. The comparative experiments illustrated that the CO_2 conversion efficiency of hollow microspheres structure is much better than that of bulk powder (*33*).

Publication Date (Web): September 11, 2015 | doi: 10.1021/bk-2015-1194.ch004

Reduction of CO_2 with Zero-Valent Metals in Water

In adition to photoelectrocatalytic directly utilization of H_2O as hydrogen donors for reduction of CO_2, replacement of hydrogen from H_2O by oxidation of active zero-valent metals in aqueous system for catalytic synthesis of methanol from CO_2 is an alternative way. An interesting study was given by Guan and co-workers, they developed a zero-valent Fe-based aqueous CO_2 reduction system. H_2 (5808.1 μmol g^{-1}) and a trace amount of CH_4 (0.63 μmol g^{-1}) were detected using Fe^0 powder as reductant under the reaction condition (95 kPa CO_2, 5 mL H_2O, room temperature, 20 h). Under the similar reaction conditions, using Fe^0-Cu-K-Al modified from Fe^0 showed higher catalytic activity, 61.63 μmol g^{-1} of CH_3OH was obtained (Scheme 5), other products such as H_2 (4776.3 μmol g^{-1}), CH_4 (29.73 μmol g^{-1}), C_3H_8 (57.34 μmol g^{-1}) and C_2H_5OH (78.68 μmol g^{-1}) were detected. The dissolved CO_2 formed to carbonic acid was considered to facilitate the Fe^0 oxidation and hydrogen production. And introducing elements of K and Cu into zero-valent Fe promoted the production of methanol and other organic compounds (*34*).

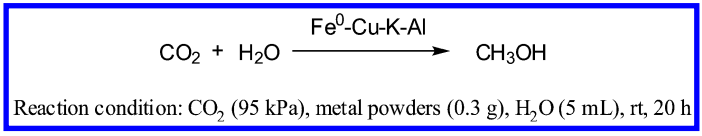

Scheme 5. Reduction of CO_2 with H_2O using Fe-based composites.

In Advances in CO2 Capture, Sequestration, and Conversion; He, et al.;
ACS Symposium Series; American Chemical Society: Washington, DC, 2015.

Recently, Jin's group dedicated to hydrothermal conversion of CO_2 to value-added chemicals using metals powder as reducing reagent (*35*–*37*). In their methanol production study, Cu and Zn were used as catalyst and reductant respectively, $NaHCO_3$ was used as the CO_2 source for easy handling purpose (Scheme 6). The highest yield of methanol was 11.4% under 350 °C for 3 h. XRD results showed Zn was converted to ZnO and Cu remained unchanged (*38*). The hydrogen obtained from reaction between H_2O and inexpensive zero-valent metal for CO_2 reduction is a promising strategy (*35*, *36*). In addition, the metal oxides produced from the oxidation reaction also can be reduced to metal by green energy (*37*, *39*), which forms a sustainable reaction cycle.

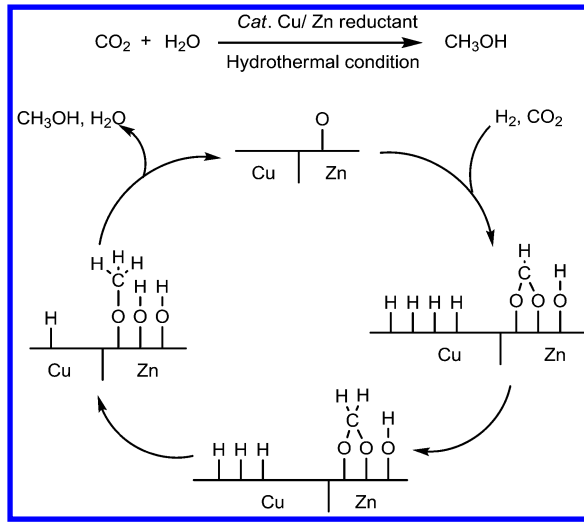

Scheme 6. Proposed mechanism of methanol production from CO_2 on hydrothermal condition.

Enzyme-Catalyzed Conversion of CO_2 to Methanol with Reduced Nicotinamide Adenine Dinucleotide (NADH) as Hydrogen Source

Obert and Dave first reported an integrated enzymatic system for the synthesis of methanol from CO_2. Three dehydrogenases, such as formate dehydrogenase ($F_{ate}DH$), formaldehyde dehydrogenase ($F_{ald}DH$), alcohol dehydrogenase (ADH) were used as catalysts, and NADH was used as hydrogen donor. The whole reaction process can be separated three steps: CO_2 was reduced to formate, then the formate was reduced to formaldehyde, finally the formaldehyde was reduced to methanol, and each step was catalyzed by corresponding enzyme. Three dehydrogenases were encapsulated into a porous silica sol-gel matrix for keeping the concentration of reactants in matrix to enhance the reaction process (*40*). Several groups followed this research and modified the enzymatic reduction system to aviod some drawbacks. In recent years, Jiang's group published

In Advances in CO2 Capture, Sequestration, and Conversion; He, et al.;
ACS Symposium Series; American Chemical Society: Washington, DC, 2015.

Publication Date (Web): September 11, 2015 | doi: 10.1021/bk-2015-1194.ch004

two papers focused on encapsulation process. They prepared an alginate-silica (ALG-SiO_2) composite as enzyme carrier which effectively promoted the methanol formation and stabilized the activity of enzymes, compared with previous research (*41*). In order to seek more pH stable, mechanical strength and biocompatibility materials than silica, they chose Ti-based composite and synthesized the titania nanoparticles *via* a facile way and immobilized the dehydrogenases into these nanoparticles, it also showed great catalytic activity for methanol formation (*42*). More recently, the problem of NADH regeneration was increasingly attracted the attention of scientists, for NADH is an expensive consumable in the above reduction systems. Utilization of photochemical or chemical methods to in situ reduce NAD^+ to NADH, and thereby drive the CO_2 reduction system is a greener strategy (Scheme 7). Sodium dithionite (SDT) was used as reducer for regenerating NADH by Dibenedetto and co-workers. However, SDT accelerated the deactivation of enzymes. Hence, authors designed a novel two compartments reactor to avoid the deactivation. The first compartment was used to reduce NAD^+ to NADH by SDT, the regenerated solution was transferred by a plug into the second compartment which performed the reduction of CO_2, the solution from the second compartment would be inputted the first one again and formed a reaction cycle (*43*). Similar works given by a research group from France used phosphite as hydrogen donor to regenerate NADH (*44*). The attempt to photoregenerate NADH by Dibenedetto and co-workers was that they used transition metal compounds (ZnS, Ru/ZnS) as photocatalysts to perform the reduction of NAD^+ under visible light irradiation. But in this case, different from this chapter part (Photoelecrocatalytic reduction of CO_2 in water), the hydrogen source offered for NAD^+ reduction was acquired from bioglycerol (*43*).

Publication Date (Web): September 11, 2015 | doi: 10.1021/bk-2015-1194.ch004

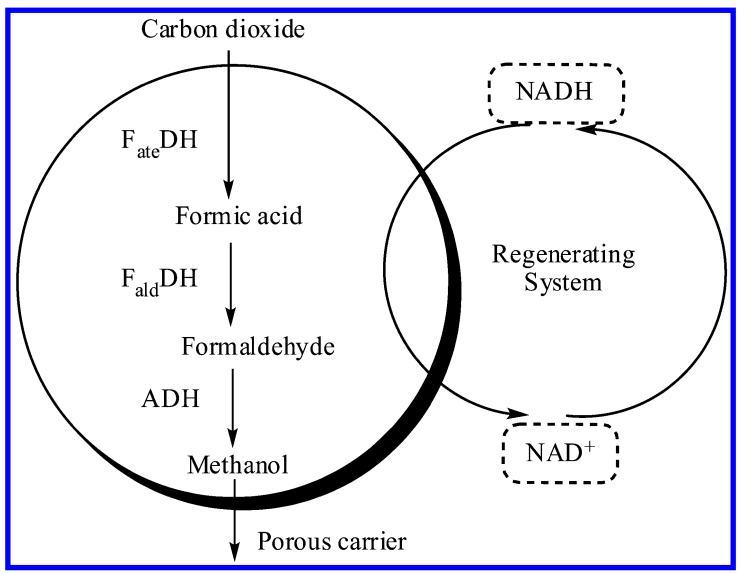

Scheme 7. Enzymatic conversion of CO_2 to methanol with a NADH regenerating system.

In Advances in CO2 Capture, Sequestration, and Conversion; He, et al.;
ACS Symposium Series; American Chemical Society: Washington, DC, 2015.

Conversion of CO_2 into Methanol with Other Hydrogen Sources

Besides the common hydrogen donors mentioned above, ascorbic acid was also used as reductants for the synthesis of methanol from CO_2. Photoreduction of CO_2 into methanol with H_2O as hydrogen source has been introduced in this chapter part (Photoelecrocatalytic reduction of CO_2 in water). Here, MacDonnell and co-workers added ascorbic acid as reducer and combined Ru(II) trisphenanthroline, pyridine as catalysts to develop an aqueous homogeneous photochemical system for transformation of CO_2 to formate and methanol (Scheme 8). Pyridine showed great catalytic ability in the presence of Ru(II) trisphenanthroline (*45*). A Kazakstan's research team detected methanol and other organic compounds formation from the interaction between CO_2 and propylene using Rh-Co/Al_2O_3 as catalyst (*46*). However, it is difficult to determine the carbon source (from CO_2 or propylene) in these methanol synthesis.

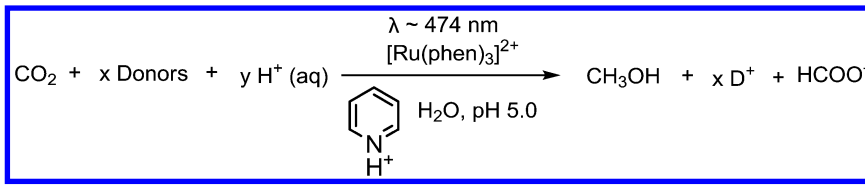

Scheme 8. Reduction of CO_2 with Ru(II) trisphenanthroline, pyridine as catalysts.

Conclusion

In the chapter, we have reviewed some methods for the synthesis of methanol from CO_2 with different hydrogen sources. Utilization of these hydrogen sources for CO_2 reduction are superior to that of gaseous hydrogen in some respects including safety, convenience of handling, etc. Based on the above consideration, we briefly introduced several inorganic and organic hydrogen sources for transforming CO_2 to methanol. Although these approaches show large differences in efficiency and evaluation systems, and exist many problems of their own. Nevertheless, these explorations give new ideas and encourage scientists to develop higher efficient and greener ways to reduce CO_2 to methanol. Further research should focus on seeking new high efficient hydrogen sources and enhancing the research on mechanism of these systems. With the advances made in materials science, it should be possible today to prepare efficient catalysts for the development of hydrogen sources for CO_2 reduction to methanol.

Acknowledgments

The authors gratefully acknowledge the financial support from the National Natural Science Foundation of China (No. 21277091). The State Key Program of National Natural Science Foundation of China (No. 21436007). Key Basic Research Projects of Science and Technology Commission of Shanghai (14JC1403100). The Program for Professor of Special Appointment (Eastern

In Advances in CO2 Capture, Sequestration, and Conversion; He, et al.;
ACS Symposium Series; American Chemical Society: Washington, DC, 2015.

Publication Date (Web): September 11, 2015 | doi: 10.1021/bk-2015-1194.ch004

Scholar) at Shanghai Institutions of Higher Learning (ZXDF160002). The Project-sponsored by SRF for ROCS, SEM (BG1600002).

References

1. Behrens, M.; Studt, F.; Kasatkin, I.; Kuhl, S.; Havecker, M.; Abild-Pedersen, F.; Zander, S.; Girgsdies, F.; Kurr, P.; Kniep, B. L.; Tovar, M.; Fischer, R. W.; Norskov, J. K.; Schlogl, R. The active site of methanol synthesis over $Cu/ZnO/Al_2O_3$ industrial catalysts. *Science* **2012**, *336*, 893–897.
2. Liao, F.; Huang, Y.; Ge, J.; Zheng, W.; Tedsree, K.; Collier, P.; Hong, X.; Tsang, S. C. Morphology-dependent interactions of ZnO with Cu nanoparticles at the materials' interface in selective hydrogenation of CO_2 to CH_3OH. *Angew. Chem., Int. Ed.* **2011**, *50*, 2162–2165.
3. Rezayee, N. M.; Huff, C. A.; Sanford, M. S. Tandem amine and ruthenium-catalyzed hydrogenation of CO to methanol. *J. Am. Chem. Soc.* **2015**, *137*, 1028–1031.
4. Larson, G. L.; Fry, J. L. *Ionic and Organometallic-Catalyzed Organosilane Reductions*; Wiley, 2008.
5. Koinuma, H.; Kawakami, F.; Kato, H.; Hirai, H. Hydrosilylation of carbon dioxide catalysed by ruthenium complexes. *J. Chem. Soc., Chem. Commun.* **1981**, 213–214.
6. Jansen, A.; Görls, H.; Pitter, S. trans-$[RuIICl(MeCN)_5][RuIII\text{-}Cl_4(MeCN)_2]$: A reactive intermediate in the homogeneous catalyzed hydrosilylation of carbon dioxide. *Organometallics* **2000**, *19*, 135–138.
7. Park, S.; Bezier, D.; Brookhart, M. An efficient iridium catalyst for reduction of carbon dioxide to methane with trialkylsilanes. *J. Am. Chem. Soc.* **2012**, *134*, 11404–11407.
8. Eisenschmid, T. C.; Eisenberg, R. The iridium complex catalyzed reduction of carbon dioxide to methoxide by alkylsilanes. *Organometallics* **1989**, *8*, 1822–1824.
9. Riduan, S. N.; Zhang, Y.; Ying, J. Y. Conversion of carbon dioxide into methanol with silanes over N-heterocyclic carbene catalysts. *Angew. Chem., Int. Ed.* **2009**, *48*, 3322–3325.
10. Schafer, A.; Saak, W.; Haase, D.; Muller, T. Silyl cation mediated conversion of CO_2 into benzoic acid, formic acid, and methanol. *Angew. Chem., Int. Ed.* **2012**, *51*, 2981–2984.
11. Riduan, S. N.; Ying, J. Y.; Zhang, Y. G. Mechanistic insights into the reduction of carbon dioxide with silanes over *N*-heterocyclic carbene catalysts. *ChemCatChem* **2013**, *5*, 1490–1496.
12. Menard, G.; Stephan, D. W. Room temperature reduction of CO_2 to methanol by Al-based frustrated Lewis pairs and ammonia borane. *J. Am. Chem. Soc.* **2010**, *132*, 1796–1797.
13. Chakraborty, S.; Zhang, J.; Krause, J. A.; Guan, H. An efficient nickel catalyst for the reduction of carbon dioxide with a borane. *J. Am. Chem. Soc.* **2010**, *132*, 8872–8873.

In Advances in CO2 Capture, Sequestration, and Conversion; He, et al.;
ACS Symposium Series; American Chemical Society: Washington, DC, 2015.

14. Huang, F.; Zhang, C.; Jiang, J.; Wang, Z. X.; Guan, H. How does the nickel pincer complex catalyze the conversion of CO_2 to a methanol derivative? A computational mechanistic study. *Inorg. Chem.* **2011**, *50*, 3816–3825.
15. Courtemanche, M. A.; Legare, M. A.; Maron, L.; Fontaine, F. G. A highly active phosphine-borane organocatalyst for the reduction of CO_2 to methanol using hydroboranes. *J. Am. Chem. Soc.* **2013**, *135*, 9326–9329.
16. Deglmann, P.; Ember, E.; Hofmann, P.; Pitter, S.; Walter, O. Experimental and theoretical investigations on the catalytic hydrosilylation of carbon dioxide with ruthenium nitrile complexes. *Chemistry* **2007**, *13*, 2864–2879.
17. Finholt, A. E.; Bond, A. C.; Schlesinger, H. I. Lithium aluminum hydride, aluminum hydride and lithium gallium hydride, and some of their applications in organic and inorganic chemistry. *J. Am. Chem. Soc.* **1947**, *69*, 1199–1203.
18. Nystrom, R. F.; Yanko, W. H.; Brown, W. Reduction of carbon dioxide to methanol by lithium aluminum hydride. *J. Am. Chem. Soc.* **1948**, *70*, 441–441.
19. Roeda, D.; Dollé, F. [^{11}C]Methanol production by a fast and mild aqueous-phase reduction of [^{11}C]formic acid with samarium diiodide. *J. Labelled Comp. Radiopharm.* **2006**, *49*, 295–304.
20. Fujishima, A.; Honda, K. Electrochemical photolysis of water at a semiconductor electrode. *Nature* **1972**, *238*, 37–38.
21. Inoue, T.; Fujishima, A.; Konishi, S.; Honda, K. Photoelectrocatalytic reduction of carbon dioxide in aqueous suspensions of semiconductor powders. *Nature* **1979**, *277*, 637–638.
22. Wang, J.; Ji, G.; Liu, Y.; Gondal, M. A.; Chang, X. Cu_2O/TiO_2 heterostructure nanotube arrays prepared by an electrodeposition method exhibiting enhanced photocatalytic activity for CO_2 reduction to methanol. *Catal. Commun.* **2014**, *46*, 17–21.
23. Ola, O.; Mercedes Maroto-Valer, M. Role of catalyst carriers in CO_2 photoreduction over nanocrystalline nickel loaded TiO_2-based photocatalysts. *J. Catal.* **2014**, *309*, 300–308.
24. Neatu, S.; Macia-Agullo, J. A.; Garcia, H. Solar light photocatalytic CO_2 reduction: General considerations and selected bench-mark photocatalysts. *Int. J. Mol. Sci.* **2014**, *15*, 5246–5262.
25. Wang, C.; Ma, X.-X.; Li, J.; Xu, L.; Zhang, F.-x. Reduction of CO_2 aqueous solution by using photosensitized-TiO_2 nanotube catalysts modified by supramolecular metalloporphyrins-ruthenium(II) polypyridyl complexes. *J. Mol. Catal. A: Chem.* **2012**, *363-364*, 108–114.
26. Truong, Q. D.; Le, T. H.; Liu, J.-Y.; Chung, C.-C.; Ling, Y.-C. Synthesis of TiO_2 nanoparticles using novel titanium oxalate complex towards visible light-driven photocatalytic reduction of CO_2 to CH_3OH. *Appl. Catal., A* **2012**, *437-438*, 28–35.
27. Luo, D. M.; Bi, Y.; Kan, W.; Zhang, N.; Hong, S. G. Copper and cerium co-doped titanium dioxide on catalytic photo reduction of carbon dioxide with water: Experimental and theoretical studies. *J. Mol. Struct.* **2011**, *994*, 325–331.

Publication Date (Web): September 11, 2015 | doi: 10.1021/bk-2015-1194.ch004

28. Truong, Q. D.; Liu, J.-Y.; Chung, C.-C.; Ling, Y.-C. Photocatalytic reduction of CO_2 on $FeTiO_3/TiO_2$ photocatalyst. *Catal. Commun.* **2012**, *19*, 85–89.
29. Pan, P.-W.; Chen, Y.-W. Photocatalytic reduction of carbon dioxide on NiO/$InTaO_4$ under visible light irradiation. *Catal. Commun.* **2007**, *8*, 1546–1549.
30. Li, H.; Lei, Y.; Huang, Y.; Fang, Y.; Xu, Y.; Zhu, L.; Li, X. Photocatalytic reduction of carbon dioxide to methanol by Cu_2O/SiC nanocrystallite under visible light irradiation. *J. Nat. Gas Chem.* **2011**, *20*, 145–150.
31. Ghadimkhani, G.; de Tacconi, N. R.; Chanmanee, W.; Janaky, C.; Rajeshwar, K. Efficient solar photoelectrosynthesis of methanol from carbon dioxide using hybrid CuO-Cu_2O semiconductor nanorod arrays. *Chem. Commun.* **2013**, *49*, 1297–1299.
32. Mao, J.; Peng, T.; Zhang, X.; Li, K.; Zan, L. Selective methanol production from photocatalytic reduction of CO_2 on $BiVO_4$ under visible light irradiation. *Catal. Commun.* **2012**, *28*, 38–41.
33. Cheng, H.; Huang, B.; Liu, Y.; Wang, Z.; Qin, X.; Zhang, X.; Dai, Y. An anion exchange approach to Bi_2WO_6 hollow microspheres with efficient visible light photocatalytic reduction of CO_2 to methanol. *Chem. Commun.* **2012**, *48*, 9729–9731.
34. Guan, G.; Kida, T.; Ma, T.; Kimura, K.; Abe, E.; Yoshida, A. Reduction of aqueous CO_2 at ambient temperature using zero-valent iron-based composites. *Green Chem.* **2003**, *5*, 630–634.
35. Lyu, L.; Zeng, X.; Yun, J.; Wei, F.; Jin, F. No catalyst addition and highly efficient dissociation of H_2O for the reduction of CO_2 to formic acid with Mn. *Environ. Sci. Technol.* **2014**, *48*, 6003–6009.
36. Jin, F.; Zeng, X.; Liu, J.; Jin, Y.; Wang, L.; Zhong, H.; Yao, G.; Huo, Z. Highly efficient and autocatalytic H_2O dissociation for CO_2 reduction into formic acid with zinc. *Sci. Rep.* **2014**, *4*, 4503.
37. Jin, F. M.; Gao, Y.; Jin, Y. J.; Zhang, Y. L.; Cao, J. L.; Wei, Z.; Smith, R. L. High-yield reduction of carbon dioxide into formic acid by zero-valent metal/metal oxide redox cycles. *Energy Environ. Sci.* **2011**, *4*, 881–884.
38. Huo, Z. B.; Hu, M. B.; Zeng, X.; Yun, J.; Jin, F. M. Catalytic reduction of carbon dioxide into methanol over copper under hydrothermal conditions. *Catal. Today* **2012**, *194*, 25–29.
39. Service, R. F. Solar fuels. Sunlight in your tank. *Science* **2009**, *326*, 1472–1475.
40. Obert, R.; Dave, B. C. Enzymatic conversion of carbon dioxide to methanol: Enhanced methanol production in silica sol−gel matrices. *J. Am. Chem. Soc.* **1999**, *121*, 12192–12193.
41. Xu, S.-w.; Lu, Y.; Li, J.; Jiang, Z.-y.; Wu, H. Efficient conversion of CO_2 to methanol catalyzed by three dehydrogenases co-encapsulated in an alginate-silica (ALG-SiO_2) hybrid gel. *Ind. Eng. Chem. Res.* **2006**, *45*, 4567–4573.
42. Sun, Q.; Jiang, Y.; Jiang, Z.; Zhang, L.; Sun, X.; Li, J. Green and efficient conversion of CO_2 to methanol by biomimetic coimmobilization of three dehydrogenases in protamine-templated titania. *Ind. Eng. Chem. Res.* **2009**, *48*, 4210–4215.
43. Dibenedetto, A.; Stufano, P.; Macyk, W.; Baran, T.; Fragale, C.; Costa, M.; Aresta, M. Hybrid technologies for an enhanced carbon recycling based

Publication Date (Web): September 11, 2015 | doi: 10.1021/bk-2015-1194.ch004

on the enzymatic reduction of CO_2 to methanol in water: Chemical and photochemical NADH regeneration. *ChemSusChem* **2012**, *5*, 373–378.
44. Cazelles, R.; Drone, J.; Fajula, F.; Ersen, O.; Moldovan, S.; Galarneau, A. Reduction of CO_2 to methanol by a polyenzymatic system encapsulated in phospholipids-silica nanocapsules. *New J. Chem.* **2013**, *37*, 3721–3730.
45. Boston, D. J.; Xu, C.; Armstrong, D. W.; MacDonnell, F. M. Photochemical reduction of carbon dioxide to methanol and formate in a homogeneous system with pyridinium catalysts. *J. Am. Chem. Soc.* **2013**, *135*, 16252–16255.
46. Shapovalova, L. B.; Zakumbaeva, G. D.; Gabdrakipov, A. V.; Shlygina, I. A.; Zhurtbaeva, A. A. Interaction between CO_2 and propylene over Rh-Co/Al_2O_3 catalysts. *Appl. Organomet. Chem.* **2000**, *14*, 853–856.

Publication Date (Web): September 11, 2015 | doi: 10.1021/bk-2015-1194.ch004

Publication Date (Web): September 11, 2015 | doi: 10.1021/bk-2015-1194.ch005

Chapter 5

A Basic Quantum Chemical Review on the Activation of CO_2

Shinichiro Nakamura,[*,1] Makoto Hatakeyama,[1] Yuanqing Wang,[1] Koji Ogata,[1] and Katsushi Fujii[1,2]

[1]RIKEN Research Cluster for Innovation, Nakamura Lab., Wako, Saitama 351-0198, Japan
[2]Research Center for Advanced Science and Technology, University of Tokyo, Tokyo 153-8904, Japan
[*]E-mail: snakamura@riken.jp

The basic quantum chemical review of CO_2 activation is presented. The molecular properties are discussed, describing the single molecule of CO_2, its geometry, wave functions, charges, and spectroscopic properties of vibrational frequencies, in vacuum and solutions. An answer to "*What is the activation of CO_2?*" from the quantum chemical viewpoint is presented. Finally, the discussion will attempt to bridge these quantum chemical features and experimental facts.

Introduction

The activation of CO_2 is one of the most important subjects to which contemporary researchers in science and technology are expected to contribute, since CO_2 reduction will eventually become an inevitable challenge which must be overcome from the viewpoints of environmental problems as well as renewable energy problems. This short review presents a basic quantum chemical discussion on CO_2 activation, in an attempt to provide a bridge between elemental quantum chemistry and the frontier of experimental researches. We hope that the ideas put forward will serve as hints for future designs in studies on CO_2 as useful chemical resources. First, we will start by describing the single molecule of CO_2, its geometry, wave functions, charges, and spectroscopic properties of vibrational frequencies, in vacuum and solutions. Secondly, we will present an answer to "*What is the activation of CO_2?*" from the quantum chemical viewpoint. That

In Advances in CO2 Capture, Sequestration, and Conversion; He, et al.;
ACS Symposium Series; American Chemical Society: Washington, DC, 2015.

is, the quantitative differences in CO_2 molecular properties in the ground state relative to the activated states. The third discussion will attempt to bridge these quantum chemical features and experimental facts. We believe that the link from such quantum chemical viewpoints to important experiments is of critical importance for future design. Finally, we will describe future prospects by citing three recently reported experimental works.

What is CO_2?

The CO_2 molecule is known to be one of the most stable and familiar chemicals in everyday life. It is generated as one of the last products from many chemical reactions such as burning of carbon-containing materials or metabolism in biological systems. Its basic chemical and thermodynamic properties are described in standard textbooks as well as in hand books (*1–4*). Important molecular properties are summarized in Table 1. An obvious but important fact is that the molecule has no dipole moment in the ground state and the dielectric constant is almost 1.0 (almost the same as that of vacuum). This indicates that the molecule is in itself very inert. Notice that this molecule still absorbs the light due to CO bond stretching and bending motions.

Table 1. Molecular Properties of Carbon Dioxide

Molecular Properties		References
Molecular weight	44.0098 g/mol	[1]
Density	1.976 g/L (gas at 0 ℃ and 760 mm Hg); 0.914 g/L (liquid at 0 ℃ and 34.3 atm); 1.512 g/L (solid at -56.6 ℃)	[2]
Point group	$D_{\infty h}$	[1]
Diploe moment	0 D	[3]
Dielectric constant	1.000922 (gas)	[3]
Sublimation point	-78.4 ℃	[4]
Melting Point	-56.56 ℃ (triple point)	[4]
Vapor pressure	760 mm Hg at -78.2 ℃	[3]
Viscosity	0.0147 $mN \cdot s \cdot m^{-2}$ (gas)	[3]
Solubility in water	0.614×10^{-3} mole fraction at 25 ℃ and 100 kPa CO_2 partial pressure	[4]
Acidity(pKa of H_2CO_3)	$pK_{a1} = 6.35$, $pK_{a1} = 10.33$ at 25 ℃	[4]
Enthalpy, $\Delta_f H^o\,(298.15\,K)$	-393.522 $kJ \cdot mol^{-1}$	[3]
Heat capacity, C_p^o	37.129 $J \cdot K^{-1} \cdot mol^{-1}$	[3]
Entropy, $S^o\,(298.15K)$	213.795 $J \cdot K^{-1} \cdot mol^{-1}$	[3]

Publication Date (Web): September 11, 2015 | doi: 10.1021/bk-2015-1194.ch005

Publication Date (Web): September 11, 2015 | doi: 10.1021/bk-2015-1194.ch005

Figure 1 shows the representative frontier (HOMO and LUMO) molecular orbitals (MOs) of CO_2. The MOs are the most popular basic information obtained by molecular orbital calculations. The MOs shown in Figure 1 are not experimentally observable physical quantities. Nevertheless, they are used frequently as tools to understand and examine molecules, as already fully demonstrated, especially in organic and organometallic chemistry (*5*). The MOs are considered to be one of the most figurative images expressed by molecules, at least in the eyes of molecular scientists. Throughout this paper, the calculations are carried out by Gaussian 09, Rev B (*6*, *7*). The solvent effect is obtained by the PCM method (*6*, *7*).

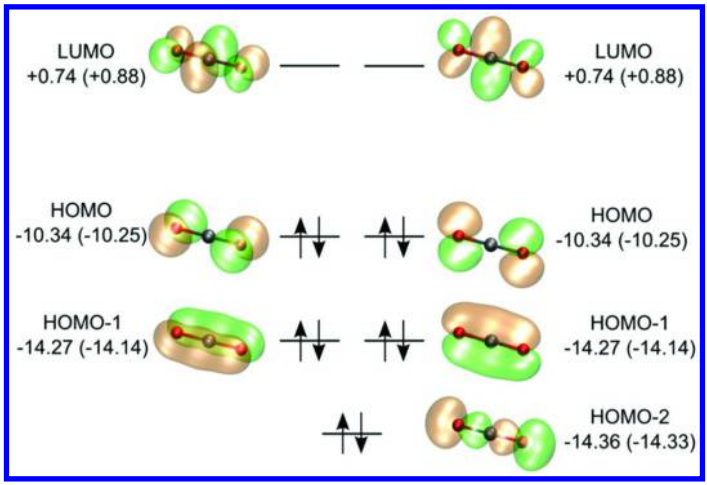

Figure 1. Frontier molecular orbitals for ground state CO_2. The unit of orbital energy is eV in vacuum (in water, PCM). The calculations are carried out by B3LYP/cc-pVTZ.

It is noteworthy that the two highest occupied orbitals (HOMO) and two lowest unoccupied orbitals (LUMO) are both degenerated in energy. Therefore, in principle, the molecule has four electrons with the same energy level which are ready to be released. It also has four unoccupied sites to which four electrons can transfer. It is a matter of course, if one of the four electrons is released or transferred, in which case the degeneracy will be immediately broken. For this reason, the transfer of four electrons to or from the outside of the molecule does not occur simultaneous. However, suffice it to say, there are seldom organic molecules having such properties, since it is neither an inorganic transition metal complex nor a solid state. Interestingly, these degenerated frontier orbitals of CO_2 (Figure 1) show somewhat similar topological features with the d-orbitals (two HOMOs) and f-orbitals (two LUMOs) of transition metals and lanthanoids, respectively.

The representative spectroscopic properties of gas phase molecules such as UV absorption wavelengths, IR absorption (*8*, *9*), Raman scattering, NMR chemical shifts of carbon, are shown in literatures (*3*, *4*). Among of these, from the molecular activation point of view, an exceptional property of this molecule

should be emphasized. This molecule has a unique quantum property, Fermi Resonance (*10*). The Fermi resonance is the shifting of the energies and intensities of absorption bands in an infrared or Raman spectrum. It is the consequence of quantum mechanical mixing. The energy level of anti-symmetric CO stretching modes is located very close to the energy level of overtone bending modes. This implies a strategy for the activation of the molecule, which is unique in CO_2. As one guiding principle, it is possible to take advantage of the fact that the overtone bending motions can couple with the stretching motions.

Although the properties of CO_2 in condensed solid (dry ice), in liquid, and in the supercritical phase are also important and closely related to the current subject, these are out of the scope of this review.

Publication Date (Web): September 11, 2015 | doi: 10.1021/bk-2015-1194.ch005

What is CO_2 Activation?

The activation of molecule is to increase the degree of reactivity in the molecule. Therefore, it can be measured by the difference in molecular properties relative to those in the most stable ground state. From a conventional molecular structural point of view, it is possible to state that CO_2 activation consists of three types: (i) bending of the OCO angle from 180 degrees, (ii) elongation of the CO bond at least, one of two CO bonds, and (iii) polarization of the charge on C and O, including the charge transfer to or from the outside. As a matter of fact, these three are almost always coupled with each other. Figure 2 shows the schematic illustration of the three types.

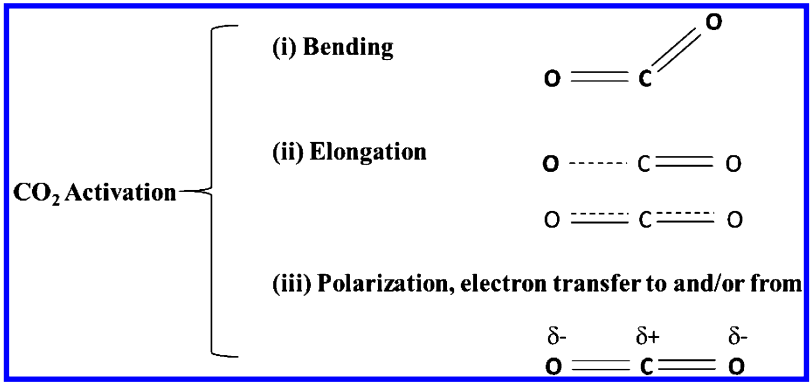

Figure 2. Three types of CO_2 activations.

The examples for the first type of CO_2 activation through the bending of the OCO angle are available in crystal data especially in transition metal complexes (*11*, *12*). Nine modes of the coordination are listed by D.H.Gibson (*11*), as shown in Figure 3. In this review, many instructive examples are collected with very useful descriptions of each of the coordination. As for the coordination to mononuclear metal centers, the oxygen-end on type (M..O=C=O) is also known only by spectroscopic evidences (*12*, *13*).

In Advances in CO2 Capture, Sequestration, and Conversion; He, et al.;
ACS Symposium Series; American Chemical Society: Washington, DC, 2015.

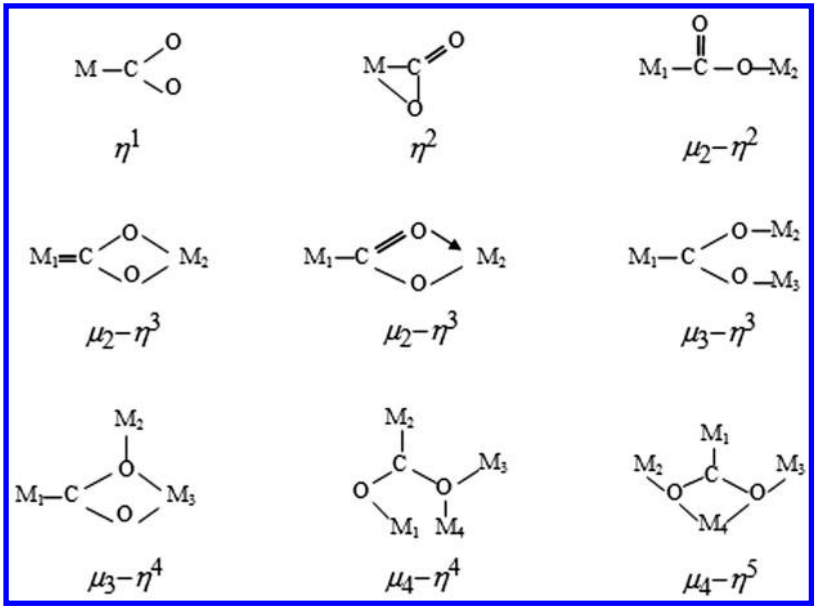

Figure 3. Nine modes of coordination. (see ref (9)).

One significant role of theoretical studies is to provide a clear picture (interpretation) that is not available by experimental approaches. Walsh Diagram (*14*) is one such example. Figure 4 shows an important part of the Walsh Diagram. The diagram clearly shows how the molecule can be activated by its geometrical modification (bending). This schematic diagram displays the energy level of the molecular orbitals as a function of the OCO angle. The most stable state is the linear shape which is shown on the right side of the picture. As the angle decreases, the frontier orbitals change their energy levels, followed by the orbital topological mixture of each other. It is known that when the angle becomes close to 90 degrees (not shown), the orbitals energies of HOMO and LUMO become almost the same value. That is, the molecule is so activated that theoretically electron absorption and extraction are both possible without barrier.

In order to provide concrete examples for inducing bending activation, we carried out the calculations using experimental X-ray structures (*15*, *16*). As shown in Figures 5 and 6, the calculated IR frequencies show shifts that reflect the geometry of OCO angle bending, compared with non-coordinated molecules (experimental values are 667.0 (bending),1285.4 (symmetric stretching), 2349.0 (asymmetric stretching) and 1388.2 (Fermi Resonance) in cm^{-1}, (*6*)). These shifts of IR frequencies are, in fact, a result of activation through coordination.

In order to study the second and third types of the activation (Figure 2), we carried out geometry optimization for the neutral, cationic, and anionic states of the CO_2 molecule in vacuum as well as in various solvents. The results are shown in Table 2. It should be noted that the absolute values are not available by any experimental method, neither for charges on atoms nor for (orbital) energies. On the other hand, they are available through theoretical calculations within the limitation of adopted approximation. To calculate the charges, Mulliken's

In Advances in CO2 Capture, Sequestration, and Conversion; He, et al.;
ACS Symposium Series; American Chemical Society: Washington, DC, 2015.

Publication Date (Web): September 11, 2015 | doi: 10.1021/bk-2015-1194.ch005

population analysis (*17*, *18*) and Natural Bond Orbital (MBO) approximation (*17*, *18*) are commonly used in many theoretical studies.

The elongation of the CO bond can be induced, only slightly, by the environment such as solvent, whereas the charges on atoms are considerably modified by the solvent polarities. For example, the charge on oxygen is more negative in water than in hexane or vacuum. Note that the anionic state of CO_2 is not linear, showing that the bending geometry is the most stable structure in vacuum as well as in various solvents (~134 degree, Table 2). By contrast, the neutral and cationic CO_2 molecule show the linear structure. They are confirmed as minimum by frequency analysis.

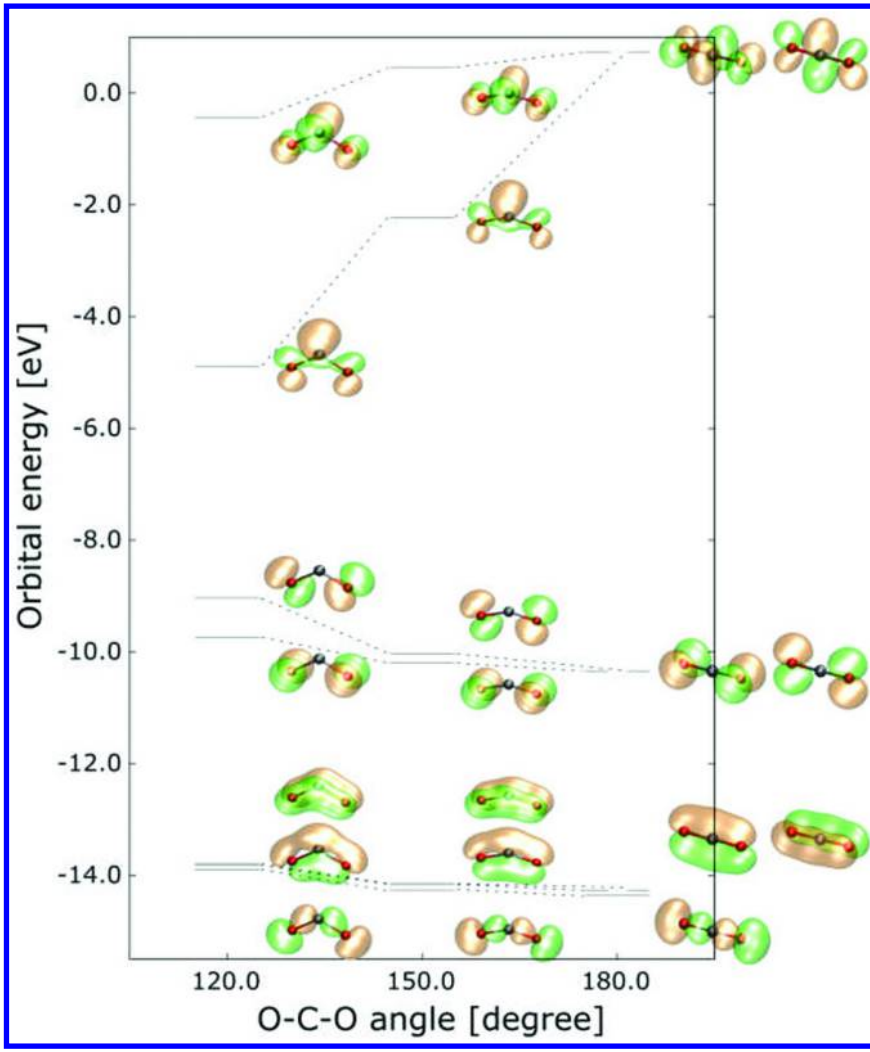

Figure 4. Important part of Walsh diagram, calculated by DFT-B3LYP/cc-pVTZ in vacuum.

Publication Date (Web): September 11, 2015 | doi: 10.1021/bk-2015-1194.ch005

Publication Date (Web): September 11, 2015 | doi: 10.1021/bk-2015-1194.ch005

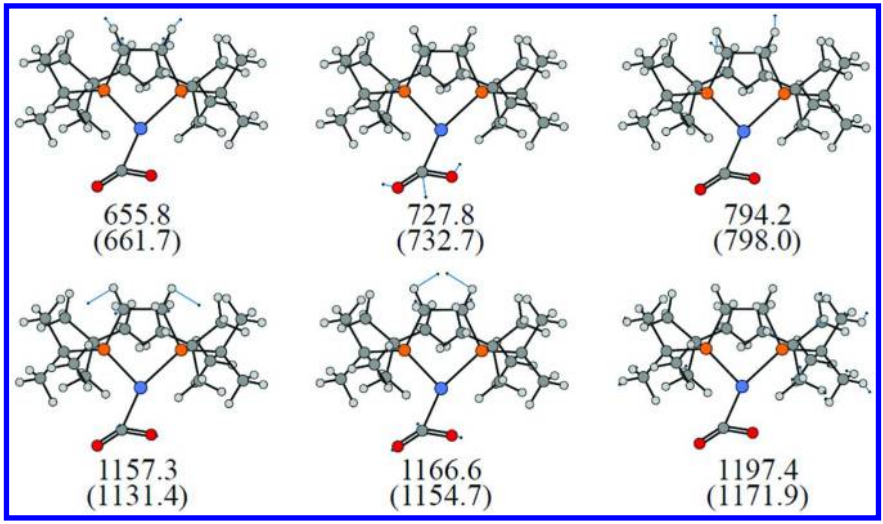

Figure 5. CO_2 activation through coordination, calculated frequencies, and normal modes for 1,2-bis(di-tert-butylphosphino)ethane)Ni(II)(η^2-CO_2) (15), in vacuum (in water, PCM).

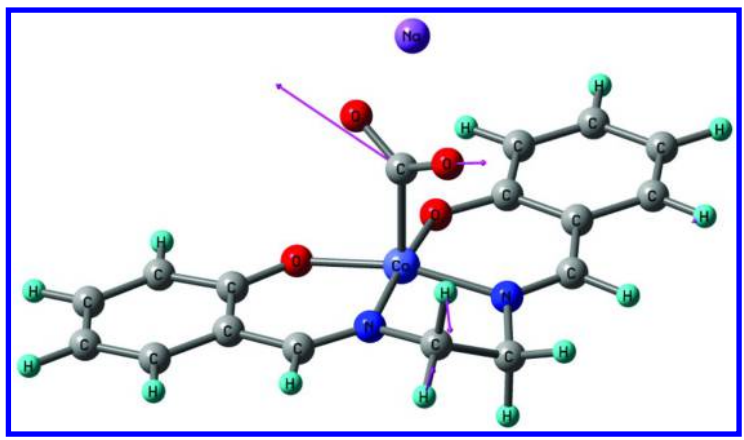

Figure 6. In (N,N'-ethylene-bis(salicylideneaminato))Co(II)(h^1-CO_2)$Na^{\pm 0}$ CO_2 activations through coordination (16), Binding energies ΔG[kcal/mol] are -23.7 (B3LYP in vacuum) and -9.0 (B3LYP+PCM in water)= -9.0, energies of the C=O stretching [cm^{-1}] are 1284.5, 1594.0 (B3LYPA in vacuum) and 1261.4, 1609.5 (B3LYP+PCM in water).

Publication Date (Web): September 11, 2015 | doi: 10.1021/bk-2015-1194.ch005

Table 2. Calculated Geometries (in Å and degree), and Charges (Mulliken's population and NBO charge) for the Neutral, Cationic, and Anionic States of CO_2, in Vacuum, and in Various Solvents (by PCM method)

	B3LYP/cc-pVTZ						
	PCM	*L_C-O*	*A_O-C-O*	*Mulliken_C*	*Mulliken_O*	*NBO_C*	*NBO_O*
neutral_CO2	vacuum	1.160	180.0	0.368	-0.184	0.984	-0.492
	water	1.160	180.0	0.407	-0.203	1.005	-0.502
	methanol	1.160	180.0	0.405	-0.203	1.004	-0.502
	acetonitrile	1.160	180.0	0.406	-0.203	1.004	-0.502
	n-Hexane	1.160	180.0	0.382	-0.191	0.991	-0.496
cation_CO2	vacuum	1.172	180.0	0.545	0.227	0.985	0.008
	water	1.170	180.0	0.587	0.206	1.015	-0.007
	methanol	1.170	180.0	0.586	0.207	1.014	-0.007
	acetonitrile	1.170	180.0	0.586	0.207	1.014	-0.007
	n-Hexane	1.171	180.0	0.560	0.220	0.996	0.002
anion_CO2	vacuum	1.240	134.7	-0.133	-0.433	0.505	-0.753
	water	1.238	134.4	-0.119	-0.440	0.513	-0.756
	methanol	1.238	134.4	-0.120	-0.440	0.512	-0.756
	acetonitrile	1.238	134.4	-0.120	-0.440	0.512	-0.756
	n-Hexane	1.239	134.6	-0.128	-0.436	0.507	-0.754

Making a Bridge to Experimental Studies

We believe that in the future, experimental breakthroughs will be made when successful links are made between abundantly reported promising experimental data (*19–21*) and basic quantum chemical knowledge. We must remember two facts. The first is that only the approximate solutions of the basic equation are available. The second is that the calculations are always on the model. Therefore, the most significant contribution from the computational science to the experimental scientists is a conceptual stimulus rather than the results of accurate numerical calculations. This is discussed below for the sake of this link.

The CO_2 reduction is often discussed as multi electron processes, such as 8e- to CH_4 and 6e- to C_2H_4. However, almost no *elemental reactions* include the many-body process. Instead, the majority of the chemical reactions consist of a two-body event. The elemental process of electron transfer can apparently include multi-electron process, because the electrode participates in the event. There are pioneering works which show the situation depending on the conditions of concentration, concurrent protonation, and diffusion (*22*, *23*).

The quantum chemical study is powerful for such processes. The breakdown of complicated overall reactions into elemental reactions is indispensable. Since the reactions on the electrode occur together with the reconstruction of the inner Helmholtz layer, one of the most serious challenges is to combine quantum chemical studies with first-principles studies to understand events of liquid-solid interface on electrodes. The remarkable breakthrough is reported, where a simulation scheme for performing first-principles molecular dynamics at a constant electrode potential is presented, opening the way for a more realistic modeling of voltage-driven devices. The system is allowed to exchange electrons with a reservoir at fixed potential, and dynamical equations for the total electronic charge are derived by using the potential energy of the extended system (*24*).

Taking into account this problem, the theoretical study of electrochemical CO_2 activation is thus a very important future subject. To resolve it straightforwardly, recent methodological approaches proposed by M. Otani et al. seem promising (*25–27*). On the other hand, there is an excellent experimental review by Y. Hori (*28*) in which we can find the detailed descriptions for various activations of CO_2. Especially critical are the various forms of CO_2 activation in water (CO_2, HCO_3-, H_2CO_3, and CO_3^{2-}). They appear with clear pH dependency, which is still difficult for calculations to include correctly from statistical point of view.

At the end of this short review, we cite one recent review paper concerning the computational approach of the subject which covers almost all of the recent important computational studies (*29*). Finally we cite three remarkable experimental examples. Understanding these results on a molecular level will pave new ways in this research area. The first one is that ionic liquid can be a good catalyst for CO_2 reduction, where the CO_2 anion radical is suggested to be an important intermediate (*30–32*). The second is the excited-state acid-base mechanism in nanoscale reaction environment (*33*). The third is a very novel photochemical example where the irradiation of a long wavelength breaks the CO bond by the so called *dressed photon phonon* (*34*). Theoretical studies are awaited for these three.

In Advances in CO2 Capture, Sequestration, and Conversion; He, et al.;
ACS Symposium Series; American Chemical Society: Washington, DC, 2015.

Publication Date (Web): September 11, 2015 | doi: 10.1021/bk-2015-1194.ch005

References

1. Chase, M. W., Jr. *NIST-JANAF Thermochemical Tables 4th Edition Monograph 9 (Part I and Part II)*; American Institute of Physics: New York; 1998, p 643.
2. O'Neil, M. J. *The Merck Index - An Encyclopedia of Chemicals, Drugs, and Biologicals*; Whitehouse Station, NJ: Merck and Co., Inc., 2006; p 293.
3. James G. S. *Lange's Handbook of Chemistry*, 16th ed.; McGraw-Hill Professional: New York, 2005.
4. Lide, D. R. *CRC Handbook of Chemistry and Physics*, Internet Version 2005; CRC Press: Boca Raton, FL, 2005.
5. Albright T. A.; Burdett, J. K.; Whangbo, M-H. *Orbital Interaction in Chemistry*; John Wiley & Sons, Inc.: New York, 2013.
6. Frisch, M. J.; Trucks, G. W.; Schlegel, H. B.; Scuseria, G. E.; Robb, M. A.; Cheeseman, J. R.; Scalmani, G.; Barone, V.; Mennucci, B.; Petersson, G. A.; Nakatsuji, H.; Caricato, M.; Li, X.; Hratchian, H. P.; Izmaylov, A. F.; Bloino, J.; Zheng, G.; Sonnenberg, J. L.; Hada, M.; Ehara, M.; Toyota, K.; Fukuda, R.; Hasegawa, J.; Ishida, M.; Nakajima, T.; Honda, Y.; Kitao, O.; Nakai, H.; Vreven, T.; Montgomery, Jr., J. A.; Peralta, J. E.; Ogliaro, F.; Bearpark, M. J.; Heyd, J.; Brothers, E. N.; Kudin, K. N.; Staroverov, V. N.; Kobayashi, R.; Normand, J.; Raghavachari, K.; Rendell, A. P.; Burant, J. C.; Iyengar, S. S.; Tomasi, J.; Cossi, M.; Rega, N.; Millam, N. J.; Klene, M.; Knox, J. E.; Cross, J. B.; Bakken, V.; Adamo, C.; Jaramillo, J.; Gomperts, R.; Stratmann, R. E.; Yazyev, O.; Austin, A. J.; Cammi, R.; Pomelli, C.; Ochterski, J. W.; Martin, R. L.; Morokuma, K.; Zakrzewski, V. G.; Voth, G. A.; Salvador, P.; Dannenberg, J. J.; Dapprich, S.; Daniels, A. D.; Farkas, Ö.; Foresman, J. B.; Ortiz, J. V.; Cioslowski, J.; Fox, D. J. *Gaussian 09*; Gaussian, Inc.: Wallingford, CT, 2009.
7. Tomashi, J.; Mennucci, B.; Cammi, R. Quantum mechanical continuum solvation models. *Chem. Rev.* **2005**, *105*, 2999–3093.
8. Shimanouchi, T. *Tables of Molecular Vibrational Frequencies*, Consolidated Volume 1; NSRDS NBS-39, Washington, DC, 1972; p 39.
9. Coblentz Society, Inc. Evaluated Infrared Reference Spectra. In *NIST Chemistry WebBook*; NIST Standard Reference Database Number 69; Linstrom, P. J., Mallard, W. G., Eds.; National Institute of Standards and Technology: Gaithersburg, MD. http://webbook.nist.gov (accessed March 10, 2015).
10. Nakamoto K. *Infrared and Raman Spectra of Inorganic and Coordination Compounds: Theory and Applications in Inorganic Chemistry (Volume A)*; John Wiley & Sons, Inc.: New York, 1997
11. Gibson, D. H. The organometallic chemistry of carbon dioxide. *Chem.Rev.* **1996**, *96*, 2063–2095.
12. Gibson, D. H. Carbon dioxide coordination chemistry: metal complexes and surface-bound species. What relationships? *Coord. Chem. Rev.* **1999**, *186*, 335.
13. Jessop, P. G.; Ikariya, T.; Noyori, R. Homogeneous hydrogenation of carbon dioxide. *Chem. Rev.* **1995**, *95*, 259–272.

Publication Date (Web): September 11, 2015 | doi: 10.1021/bk-2015-1194.ch005

14. Freund, H. J.; Roberts, M. W. Surface chemistry of carbon dioxide. *Surf. Sci. Rep.* **1996**, *25*, 225–273.
15. Anderson, J. S.; IIuc, V. M.; Hillhouse, G. L. Reactions of CO_2 and CS_2 with 1,2-bis(di-tert-butylphosphino)ethane complexes of nickel(0) and nickel(I). *Inorg. Chem.* **2010**, *49*, 10203–10207.
16. Gambarotta, S.; Arena, F.; Floriani, C.; Zanazzi, P. F. J. Carbon dioxide fixation: bifunctional complexes containing acidic and basic sites working as reversible carriers. *J. Am. Chem. Soc.* **1982**, *104*, 5082–5092.
17. Mulliken, R. S. Electronic population analysis on LCAO–MO molecular wave functions. I. *J. Chem. Phys.* **1955**, *23*, 1833–1840.
18. Reed, A. E.; Ewinstock, R. B.; Weihold, F. Natural population analysis. *J. Chem. Phys.* **1985**, *83*, 735–746.
19. Federsel, C.; Jackstell, R.; Beller, M. State-of-the-art catalysts for hydrogenation of carbon dioxide. *Angew. Chem., Int. Ed.* **2010**, *49*, 6254–6257.
20. *Carbon Dioxide as Chemical Feedstock*; Aresta, M., Ed.; Wiley-VCH: Weinheim, 2010.
21. Sakakura, T.; Choi, J.-C.; Yasuda, H. Transformation of carbon dioxide. *Chem. Rev.* **2007**, *107*, 2365–2387 and references therein.
22. Wawzonek, S; Latinene, H. A. The reduction of unsaturated hydrocarbons at the dropping mercury electrode.11. Aromatic polynuclear hydrocarbons. *J. Am. Chem. Soc.* **1942**, *64*, 2365–2368.
23. Fujihira, M.; Suzuki, H.; Hayano, S. The protonation of aromatic hydrocarbon radical anions III. Elucidation of electrode process of aromatic hydrocarbon reduction. *J. Electroanal.Chem.* **1971**, *30*, 393–407.
24. Bonnet, N.; Morishita, T.; Sugino, O.; Otani, M. First-principles molecular dynamics at a constant electrode potential. *Phys. Rev. Lett.* **2012**, *109*, 266101.
25. Otani, M.; Sugino, O. First-principles calculations of charged surfaces and interfaces: A plane-wave nonrepeated slab approach. *Phys. Rev. B* **2006**, *73*, 115407.
26. Sugino, O.; Hamada, I.; Otani, M.; Morikawa, Y.; Okamoto, Y.; Ikeshoji, T. First-principles molecular dynamics simulation of biased electrode/solution interface. *Surf. Sci.* **2007**, *601*, 5237.
27. Otani, M.; Hamada, I.; Sugino, O.; Morikawa, Y.; Okamoto, Y.; Ikeshoji, T. Electrode dynamics from first principles. *J. Phys. Soc. Jpn.* **2008**, *77*, 024802.
28. Hori, Y. In *Modern Aspects of Electrochemistry*; Vayenas, C., White, R., Gamboa-Aldeco, M., Eds.; Springer: New York, 2008; Vol. 42, pp 89−189.
29. Cheng, D.; Negreiros, F. R.; Aprà, E.; Fortunelli, A. Computational approaches to the chemical conversion of carbon dioxide. *ChemSusChem* **2013**, *6*, 944–965and references therein.
30. Rosen, B. A.; Salehi-Khojin, A.; Thorson, M. R.; Zhu, W.; Whipple, D. T.; Kenis, P. J. A.; Masel, R. I. Ionic liquid-mediated selective conversion of CO_2 to CO at low overpotentials. *Science* **2011**, *334*, 643.
31. Rosen, B. A.; Haan, J. L.; Mukherjee, P.; Braunschweig, B.; Zhu, W.; Salehi-Khojin, A.; Dlott, D. D.; Masel, R. I. In situ spectroscopic examination

Publication Date (Web): September 11, 2015 | doi: 10.1021/bk-2015-1194.ch005

of a low overpotential pathway for carbon dioxide conversion to carbon monoxide. *J.Phys. Chem. C* **2012**, *116*, 15307.
32. Rosen, B. A.; Zhu, W.; Kaul, G.; Salehi-Khojin, A.; Masel, R. I. Water enhancement of CO_2 conversion on silver in 1-ethyl-3-methylimidazolium tetrafluoroborate. *J. Electrochem. Soc.* **2013**, *160*, H138.
33. Look, E. G.; Gafney, H. D. Photocatalyzed conversion of CO_2 to CH_4: An excited-state acid–base mechanism. *J. Phys. Chem. A* **2013**, *117*, 12268–12279.
34. Tanjeem, N.; Kawazoe, T.; Yatsui, T. CO_2 phonon mode renormalization using phonon-assisted energy up-conversion. *Sci. Rep.* **2013**, *3*, 3341.

Publication Date (Web): September 11, 2015 | doi: 10.1021/bk-2015-1194.ch005

Publication Date (Web): September 11, 2015 | doi: 10.1021/bk-2015-1194.ch006

Chapter 6

Influence of Zirconia Phase on the Performance of Ni/ZrO_2 for Carbon Dioxide Reforming of Methane

Xiaoping Zhang,[1,2] Qingde Zhang,[1] Noritatsu Tsubaki,[3] Yisheng Tan,[1] and Yizhuo Han*[,1]

[1]State Key Laboratory of Coal Conversion, Institute of Coal Chemistry, Chinese Academy of Sciences, Taiyuan 030001, China
[2]University of Chinese Academy of Sciences, Beijing 100039, China
[3]Department of Applied Chemistry, University of Toyama, Toyama 930-8555, Japan
***E-mail: hanyz@sxicc.ac.cn**

The influence of crystal phase of zirconia on the performance of Ni/ZrO_2 catalysts for dry reforming of methane was investigated. Ni/ZrO_2 catalysts were prepared by incipient-wetness impregnation method with 5% Ni loading, using amorphous, monoclinic, and tetragonal ZrO_2 as supports. The catalysts were characterized by N_2 adsorption–desorption, X-ray diffraction (XRD), temperature-programmed reduction with hydrogen (H_2-TPR), temperature-programmed oxidation with O_2 and hydrogenation (O_2-TPO/TPH), temperature-programmed oxidation with CO_2 (CO_2-TPO) and transmission electron microscopy (TEM). Ni nanoparticles supported on amorphous ZrO_2 (Ni/am-ZrO_2) exhibited higher activity and better stability, which was suggested to be closely associated with the higher Ni dispersion due to the presence of mesoporous amorphous ZrO_2. In contrast, Ni/t-ZrO_2 and Ni/m-ZrO_2 suffered a continuous decline of activity during 50 h of TOS, related to the sintering of Ni and carbon deposition. Additionally, it was found that both Ni particle size and the crystal phase of zirconia strongly influenced the nature of deposited carbon. The coke deposited on Ni/t-ZrO_2 displayed the highest formation rate and the lowest activity towards O_2 and CO_2, while

In Advances in CO2 Capture, Sequestration, and Conversion; He, et al.;
ACS Symposium Series; American Chemical Society: Washington, DC, 2015.

significant deactivation was observed on Ni/m-ZrO_2 owing to the encapsulating carbon. The stability of catalysts was significantly influenced by the carbon morphology.

Introduction

Carbon dioxide reforming of methane (DRM) is receiving renewed interest for the production of syngas due to both environmental and economic concerns (*1*). The process consumes both methane and carbon dioxide—two major greenhouse gases that cause global warming. Syngas produced by this process with low H_2/CO ratio is more desirable for Fischer-Tropsch (F-T) synthesis and oxosynthesis. Although noble metals exhibit superior performance for this reaction, Ni based catalysts have been comprehensively investigated due to their high activity and lower cost. However, Ni based catalysts always suffer from serious carbon deposition, leading to the catalyst deactivation (*2*).

During dry reforming of methane, carbon deposition mainly originates from methane decomposition (1) and Boudouard reaction (2).

$$CH_4 \rightarrow C + 2H_2 \qquad \Delta H^0_{298} = 75KJ/mol \tag{1}$$

$$2CO \rightarrow C + CO_2 \qquad \Delta H^0_{298} = -171KJ/mol \tag{2}$$

It is well known that carbon deposition is significantly suppressed on catalysts with small Ni particles (*3*, *4*). The formation of carbon deposition needs bigger active ensemble size. Hou et al. (*3*) suggested that the enhanced activity and high coke resistance were observed on the Ni catalyst with the highest Ni dispersion for the combined CO_2 reforming and partial oxidation of methane. Studies have shown that the dispersion of Ni is significantly influenced by the nature of support (*5*). Furthermore, supports with strong Lewis basicity, such as ZrO_2, MgO and La_2O_3, can greatly improve the carbon deposition resistance (*6*–*9*). The strong basicity promotes the chemisorption of CO_2, which can react with carbon species to form CO. In addition, studies demonstrated that metal–support interaction, catalyst morphology and promoters also strongly affect the formation of carbon (*2*).

Zirconia is widely investigated as a catalytic support or promoter in dry reforming of methane because of its moderate acidity and basicity, high thermal stability, and surface oxygen mobility (*10*, *11*). It was reported (*10*) that coke accumulation on Pt/ZrO_2 was greatly suppressed because of the lack of a significant concentration of strong Lewis acid sites. In particular, the crystal phase of zirconia was found to exert great influence on the catalytic performance. Campa et al. (*12*) reported that Rh supported on the tetragonal zirconia is far more active and selective than Rh supported on the monoclinic zirconia for partial oxidation of methane. The more covalent character of the Zr–O bond and more oxygen defective structure of m-ZrO_2 exert negative influence on Rh dispersion. Furthermore, the ability of CO_2 activation, which is essential to remove the surface carbon species, is closely related to the crystal phase of ZrO_2 due to the presence of different active sites (*13*–*15*). However, few literatures have reported

Publication Date (Web): September 11, 2015 | doi: 10.1021/bk-2015-1194.ch006

In Advances in CO2 Capture, Sequestration, and Conversion; He, et al.;
ACS Symposium Series; American Chemical Society: Washington, DC, 2015.

on the effect of the amorphous, monoclinic or tetragonal phase on the catalytic performance of Ni/ZrO_2 catalysts in DRM reaction.

In the present work, we studied the influence of crystal phase of zirconia over the activity and stability on Ni/ZrO_2 catalysts in DRM reaction. Additionally, the nature of deposited carbon was investigated by temperature-programmed surface reaction (TPSR) and transmission electron microscopy (TEM).

Experimental

Catalyst Preparation

The amorphous ZrO_2 (am-ZrO_2), tetragonal zirconia (t-ZrO_2) and monoclinic zirconia (m-ZrO_2) were prepared by several methods described below.

Amorphous ZrO_2 (am-ZrO_2) was prepared by a combined precipitation and reflux digestion method adapted from a method reported elsewhere (*16*). First, stoichiometric quantities of pluronic P123 ($EO_{20}PO_{70}EO_{20}$, Sigma–Aldrich) and $ZrOCl_2 \cdot 8H_2O$ were dissolved in deionized water with vigorous stirring. The resulting solution was heated to 80 °C. An aqueous solution of 10 wt% KOH was added dropwise to pH=11. The obtained slurry was digested at 100 °C for 240 h. Subsequently, the precipitate was filtered, thoroughly washed with deionized water several times, and dried at 110 °C for 12 h. Finally, the resulting product was calcined at 700 °C for 4 h with a ramp of 1 °C/min under air atmosphere.

The tetragonal zirconia (t-ZrO_2) was prepared by similar precipitation method as described above. But ammonia (30 wt%) was adopted as the precipitant and the solution was digested at 100 °C for 36 h.

The monoclinic zirconia (m-ZrO_2) was prepared using a hydrothermal method. First, 400 ml of 0.2M $ZrOCl_2 \cdot 8H_2O$ was added dropwise to 500 ml of 2M NaOH with vigorous stirring. Then the mixture was transferred to teflon-lined stainless autoclave and treated at 180 °C for 48 h. After cooling to room temperature, the final product was filtered and thoroughly washed with deionized water. The product was dried at 110 °C for 10 h and then calcined at 700 °C for 4 h in the air.

The Ni/ZrO_2 catalysts were prepared by incipient wetness impregnation. A aqueous solution of $Ni(NO_3)_2 \cdot 6H_2O$ was added dropwise to the support to obtain 5 wt% Ni content. The obtained material was dried at 110 °C for 10 h and then calcined at 700 °C for 4 h.

Catalyst Evaluation

The catalyst performance was evaluated in a quartz micro-reactor with an inner diameter of 8 mm. Typically, 0.5g catalyst diluted with 1.5g quartz sand (20-40 meshes) was placed in the middle of the reactor. Prior to the reaction, the sample was reduced in a 10% H_2/Ar mixture at 750 °C for 1 h. Then reactant gas mixture without any dilution was introduced with the total flow rate of 200 mL/min ($CH_4/CO_2 = 1$). The gaseous products were analyzed by an on-line gas chromatograph (GC) equipped with a TCD detector.

Publication Date (Web): September 11, 2015 | doi: 10.1021/bk-2015-1194.ch006

In Advances in CO2 Capture, Sequestration, and Conversion; He, et al.;
ACS Symposium Series; American Chemical Society: Washington, DC, 2015.

Publication Date (Web): September 11, 2015 | doi: 10.1021/bk-2015-1194.ch006

Catalyst Characterization

The N_2 adsorption isotherms were measured at -196 °C on a static volumetric instrument (TriStar 3000). The specific surface areas were calculated via the BET method and the pore size distributions were estimated by the BJH method using the desorption branch.

H_2 temperature-programmed reduction (H_2-TPR) was carried out on tp-5080 automated chemisorption analyzer. Prior to the reduction, samples were pretreated at 500 °C for 1 h in flowing argon, and then cooled down to 100 °C. Tests were conducted by introducing a 10% H_2/Ar (35 mL/min) mixture gas at a heating rate of 5°C /min from 100 °C to 800 °C. The consumption of H_2 in the reactant stream was analyzed online by a gas chromatograph with a thermal conductivity detector (TCD).

Hydrogen pulse chemisorption experiments were performed at 40 °C with a tp-5080 automated chemisorption analyzer, assuming that the adsorption stoichiometry is H/Ni = 1.

The X-ray diffraction (XRD) analysis was performed using Rigaku MiniFlex II X-ray diffractometer, using Cu Kα radiation (40 kV, 40 mA, $\lambda = 0.15418$ nm). The scanning range of 2θ was between 20–80.0°, with a scanning rate of 4°/min.

The amount of carbon deposited on the surface of spent catalyst was determined by TG performed on Rigaku TG-8120.

Temperature-programmed oxidation with O_2 (O_2-TPO), temperature-programmed hydrogenation (TPH), and temperature-programmed oxidation with CO_2 (CO_2-TPO) were performed in a fixed-bed reactor in order to characterize the reactivity of surface carbons on catalysts. The sample (~100 mg) was first loaded in a quartz tube. Then, a 10% O_2/Ar (50 mL/min) mixed gas was introduced for the O_2-TPO experiment. The temperature was increased at a rate of 5 °C/min from 100 to 800 °C. For TPH and CO_2-TPO measurements, the samples were exposed to a stream of 10% H_2/Ar or 10% CO_2/Ar, respectively. The outlet products were monitored online by a mass spectrometer (Pfeiffer OmniStar).

The morphologies of catalysts were observed using a JEOL-JEM-2100F transmission electron microscope operating at 200 kV.

Results and Discussion

XRD Analysis

The XRD patterns of ZrO_2 supports and the reduced Ni/ZrO_2 catalysts are shown in Figure 1. The am-ZrO_2 sample displayed a broad peak at 2θ ~30°, corresponding to the amorphous crystal phase. The characteristic diffraction peaks of tetragonal crystal phase at 2θ = 30.3°, 35.3°, 50.4° and 60.2° were observed on t-ZrO_2. The m-ZrO_2 was defined as monoclinic crystal phase due to the presence of characteristic diffraction patterns at 2θ = 28.2° and 31.5°. For all Ni/ZrO_2 catalysts, characteristic diffraction peak of Ni at 2θ = 44.5° was additionally observed. The impregnation of nickel reduced at 750 °C had no influence on crystal phase of ZrO_2.

In Advances in CO2 Capture, Sequestration, and Conversion; He, et al.;
ACS Symposium Series; American Chemical Society: Washington, DC, 2015.

Publication Date (Web): September 11, 2015 | doi: 10.1021/bk-2015-1194.ch006

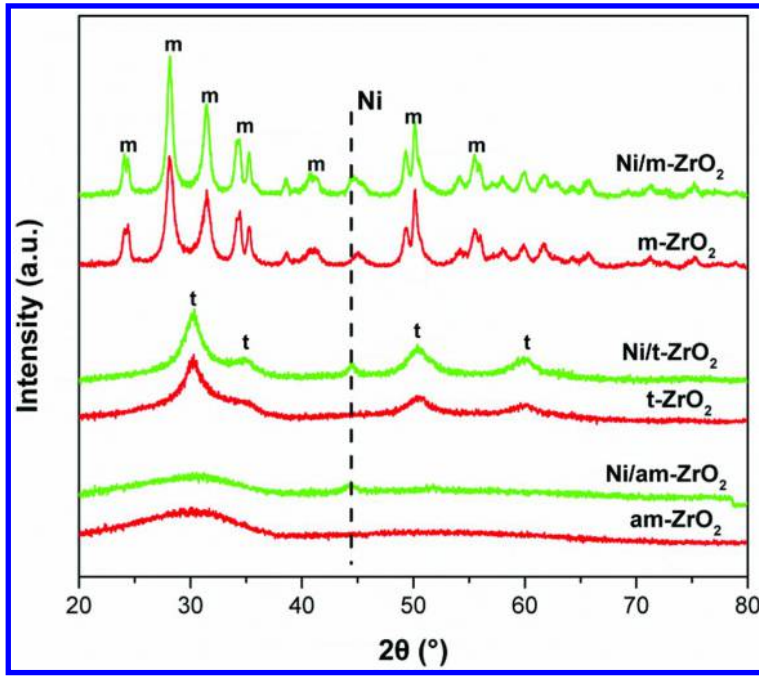

Figure 1. XRD patterns of ZrO_2 polymorphs and the reduced Ni/ZrO_2 samples.

Textural Properties

The N_2 adsorption–desorption isotherms and pore-size distribution of Ni/ZrO_2 samples are shown in Figure 2. Although the mesoporous structure was evidenced by the presence of hysteresis loops for all Ni/ZrO_2 catalysts, the pore structures were quite different. The Ni/am-ZrO_2 sample displayed type IV isotherms and H2-shaped hysteresis loops, implying the presence of typical worm-like mesoporous structure which could be confirmed by the TEM images. The larger hysteresis loop in Ni/am-ZrO_2 implied a larger pore size distribution. A similar pattern was observed on Ni/t-ZrO_2 with a H2 hysteresis loop in the relative pressure range of 0.55–1.0, suggesting a uniform inter-particle or irregular tube-like porosity. In addition, the average pore size of Ni/am-ZrO_2 (13 nm) was larger than that of Ni/t-ZrO_2 (8 nm). In contrast, the hysteresis loop on Ni/m-ZrO_2 became very small and shifted to higher relative pressure, which suggested the biggest pore size and a poorly defined mesoporous structure.

The surface area, pore volume, and pore diameter of the samples are listed in Table 1. Although both am-ZrO_2 and t-ZrO_2 displayed nearly the same surface area, the pore volume and the average pore diameter of am-ZrO_2 were much larger than that of t-ZrO_2, which promoted the dispersion of Ni and facilitated the transport of reactant gas. For all Ni/ZrO_2 catalysts, the surface areas and the pore volumes decreased slightly due to the introduction of nickel. It is worth noting that an obvious decrease of pore volume and shrinkage of pore diameter can be observed after the introduction of Ni to am-ZrO_2. This is probably suggested

that most Ni particles were incorporated into pores of am-ZrO_2 matrix due to the enlargement of pore volume and pore diameter. As a comparison, the Ni/m-ZrO_2 exhibited much lower surface area and smaller pore volume, which always lead to the poor dispersion of active metals.

Table 1. Textural Properties of ZrO_2 and Ni/ZrO_2 Samples

Samples	*Specific surface area (m^2g^{-1})*	*Pore volume (cm^3g^{-1})*	*Average pore diameter (nm)*	*Isotherm type*
am-ZrO_2	241	1.35	18	
Ni/am-ZrO_2	206	0.84	13	IV H2
m-ZrO_2	21	0.14	25	
Ni/m-ZrO_2	17	0.12	28	IV H3
t-ZrO_2	259	0.64	8	
Ni/t-ZrO_2	214	0.51	8	IV H2

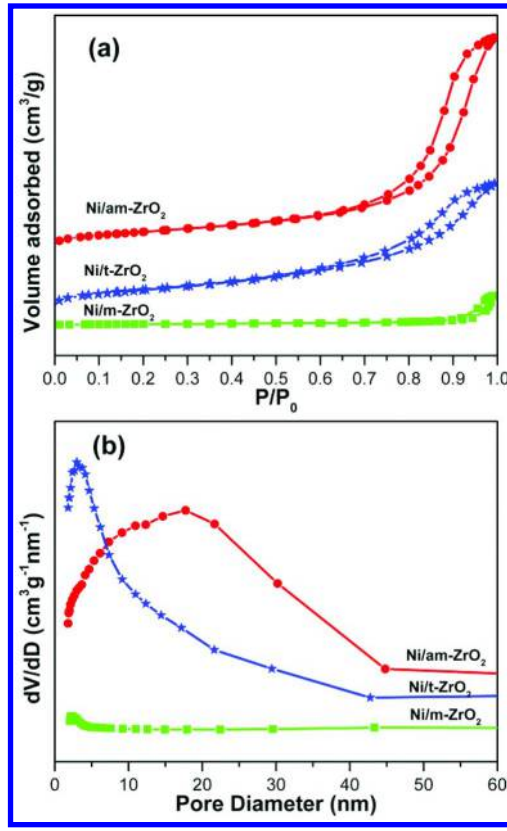

Figure 2. (a) N_2 isotherms and (b) BJH pore-size distributions of the reduced Ni/ZrO_2 samples.

In Advances in CO2 Capture, Sequestration, and Conversion; He, et al.;
ACS Symposium Series; American Chemical Society: Washington, DC, 2015.

Publication Date (Web): September 11, 2015 | doi: 10.1021/bk-2015-1194.ch006

Publication Date (Web): September 11, 2015 | doi: 10.1021/bk-2015-1194.ch006

H_2-TPR Experiment

Figure 3 shows the H_2-TPR profiles of Ni/ZrO_2 catalysts. It can be found that the reducibility of NiO was significantly influenced by crystal phase as well as the pore structure of ZrO_2. Ni/m-ZrO_2 displayed an intensive peak at 513 °C, which was attributed to the reduction of NiO exhibiting weak interaction with the support. It also exhibited a shoulder at 267 °C, which was assigned to the reduction of bulk NiO particles. The poorly defined mesoporous structure and the low surface area of m-ZrO_2 might contribute to the poor dispersion of Ni and the weak interaction of Ni-ZrO_2. In case of Ni/t-ZrO_2, there were three reduction peaks, which related to the different interaction between Ni and ZrO_2. The small peak at 357 °C was corresponding to the reduction of the highly dispersed NiO. The reduction peak located at 440 °C was associated to NiO interacted weakly with support and the intense peak at 682 °C was ascribed to the reduction of NiO interacted strongly with ZrO_2. The higher reduction temperature of NiO on Ni/t-ZrO_2 suggested the strong interaction of Ni and ZrO_2, which could be related to the effect of nano-sized ZrO_2 particles observed by TEM (Figure 4e). Similar profile was observed for Ni/am-ZrO_2 with an additional peak at 485 °C. Compared to Ni/t-ZrO_2, Ni/am-ZrO_2 was more reducible, evidenced by the presence of intense reduction peak at lower temperature (632 °C). It can be suggested that the larger pore size and the abundant surface oxygen species of am-ZrO_2 sample facilitate the reduction of Nickel oxide species at lower temperatures (*17*, *18*).

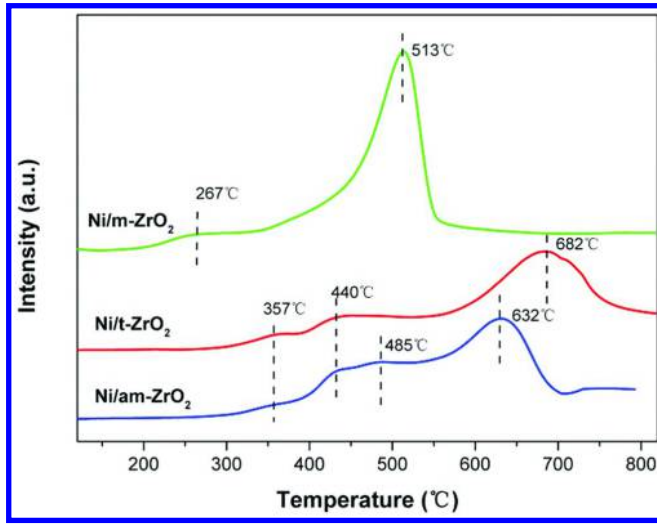

Figure 3. H_2-TPR profiles of Ni/ZrO_2 catalysts.

In Advances in CO2 Capture, Sequestration, and Conversion; He, et al.;
ACS Symposium Series; American Chemical Society: Washington, DC, 2015.

Table 2. Physicochemical Properties, Stability, and Coking Rate of Ni/ZrO_2 Catalysts

Catalysts	*Ni particle size[a] (nm)*		*Dispersion[b] (%)*	*Stability[c] (%)*	*Coking rate[d] ($mg/g_{cat}·h$)*
	reduced	*spent*			
Ni/am-ZrO_2	10.8	11.2	8.3	100	0.15
Ni/m-ZrO_2	15.3	18.1	6.4	55.9	0.41
Ni/t-ZrO_2	13.4	14.9	7.1	90.2	0.99

[a] Calculated using Scherrer formula on the (111) peak of Ni. [b] Ni dispersion was calculated from H_2 chemisorption results. [c] Ratio of final CH_4 conversion to initial CH_4 conversion. [d] Coke deposition was quantified by thermogravimetry.

Publication Date (Web): September 11, 2015 | doi: 10.1021/bk-2015-1194.ch006

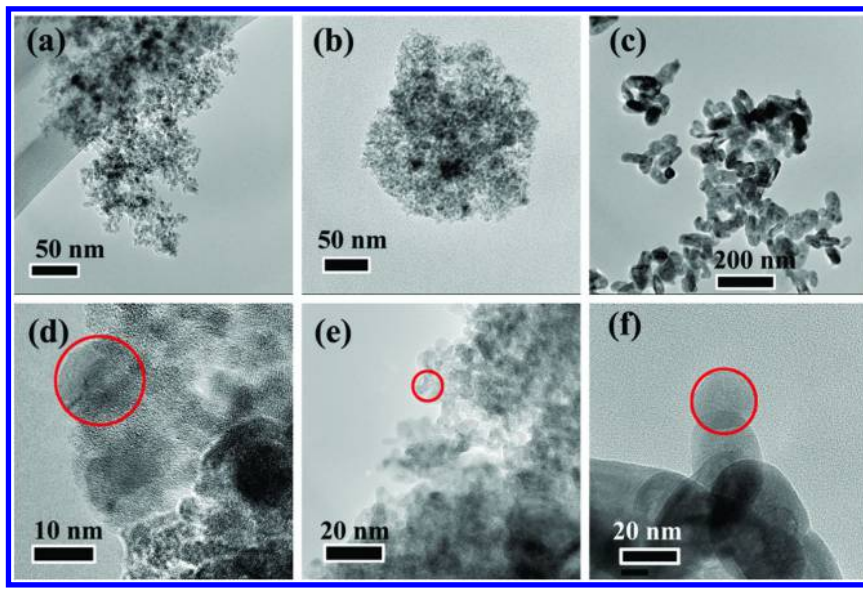

Figure 4. TEM images of (a, d) Ni/am-ZrO_2, (b, e) Ni/t-ZrO_2 and (c, f) Ni/m-ZrO_2; the encircled portion are Ni particles.

In Advances in CO2 Capture, Sequestration, and Conversion; He, et al.;
ACS Symposium Series; American Chemical Society: Washington, DC, 2015.

Morphology Analysis

The TEM images of the reduced Ni/ZrO_2 catalysts are shown in Figure 4. It is obvious that Ni/am-ZrO_2 exhibited a disordered structure of amorphous zirconia with numerous worm-like pores (Figure 4a). Nickel nanoparticles with sizes of ~10 nm were uniformly distributed within the amorphous ZrO_2 (Figure 4d). For Ni/t-ZrO_2, the support featured small uniform spherical particles with sizes ranging from 3 to 7 nm (Figure 4b, e). In contrast to conventional supported catalyst, nano-sized Ni particles were supported on or surrounded by comparably sized ZrO_2 particles. Therefore, it is difficult to accurately determine the distribution of the Ni particles because of the overlap between the Ni and ZrO_2 particles. In consistent with the results of N_2 adsorption isotherms, Ni/t-ZrO_2 exhibited an interparticle porosity with small pore size. As observed, Ni/m-ZrO_2 displayed the irregular ZrO_2 particles with size up to 40×100 nm (Figure 4c). It is obvious that the aggregated Ni particles resulted in the poor distribution of the particles within the ZrO_2 matrix. In addition, there appeared irregular channels in the bulk of the ZrO_2 particles. However, Ni particles were located on the surface of support rather than entered into the mesopore channels, which contributed to the less contact area and weak interaction of Ni-ZrO_2 (Figure 4f).

Catalytic Performance

The conversions of CH_4 and CO_2, as well as H_2/CO ratios of various catalysts in the dry reforming of methane reaction at 750 °C are shown in Figure 5. It can be seen that Ni/t-ZrO_2 exhibited higher initial methane conversion than that of Ni/am-ZrO_2. This may be related to the strong interaction between the nickel metal and the support evidenced by the results of H_2-TPR, leading to the higher CH_4 dissociation rate on Ni/t-ZrO_2 (*12*). However, the methane conversion on Ni/t-ZrO_2 decreased continuously with time on-stream, losing 9.8% of its initial CH_4 activity. In contrast, the Ni/am-ZrO_2 catalyst displayed a slightly low initial activity. But the CH_4 conversion remained stable during TOS of 50 h and no catalyst deactivation was observed. It can be concluded that the particular structure of mesoporous amorphous ZrO_2 facilitated the dispersion of Ni and suppressed the sintering of Ni. Furthermore, the formation of smaller particle size inhibited carbon deposition, contributing to the superior stability of Ni/am-ZrO_2 catalyst. Ni/m-ZrO_2 exhibited quite low initial activity and suffered significant deactivation, probably due mainly to the weak interaction between Ni and ZrO_2 and the poor dispersion of Ni.

Figure 5b shows that the conversions of CO_2 were higher than that of CH_4 over all Ni/ZrO_2 catalyst. This could be attributed to the involvement of the reverse water gas shift (RWGS) reaction (*19*). The H_2/CO ratios as a function of time on stream are shown in Figure 5c. For Ni/t-ZrO_2 and Ni/m-ZrO_2, the H_2/CO ratio decreased owing to the increasing occurrence of RWGS and the decreasing activity of methane reforming.

Publication Date (Web): September 11, 2015 | doi: 10.1021/bk-2015-1194.ch006

In Advances in CO2 Capture, Sequestration, and Conversion; He, et al.;
ACS Symposium Series; American Chemical Society: Washington, DC, 2015.

Publication Date (Web): September 11, 2015 | doi: 10.1021/bk-2015-1194.ch006

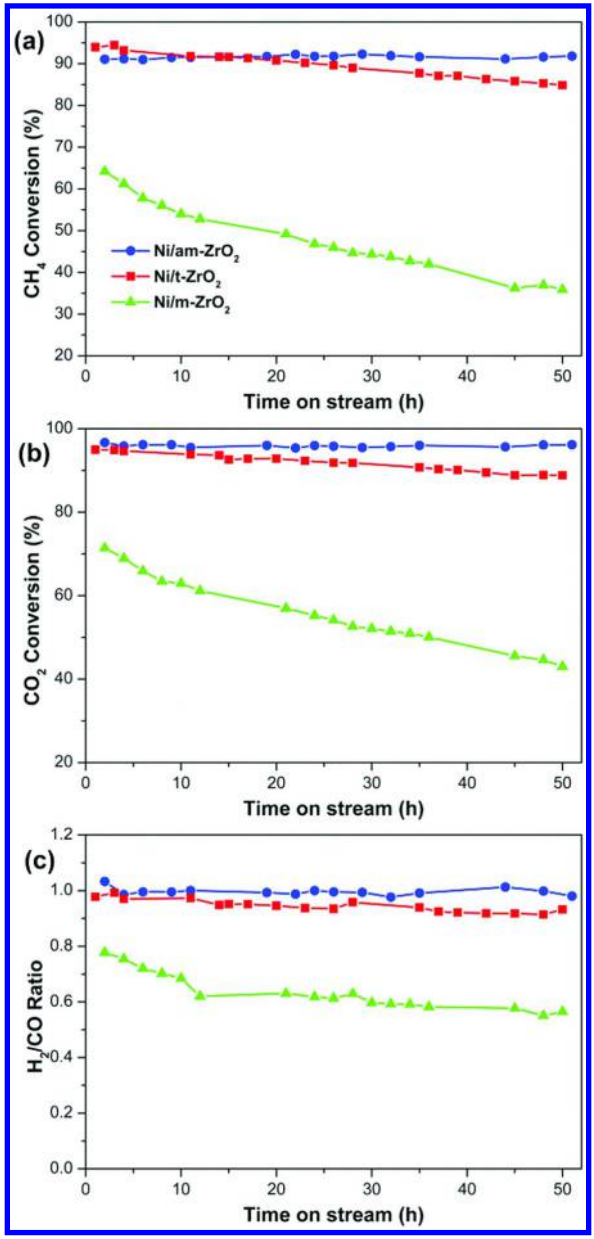

Figure 5. Dependence of catalytic performance of the reduced Ni/ZrO_2 catalysts on reaction time. (a) CH_4 conversion, (b) CO_2 conversion ,(c) H_2/CO ratio. Reaction conditions: T = 750 °C, CH_4/CO_2 = 1, GHSV = 24 000 mL/(g·h).

Publication Date (Web): September 11, 2015 | doi: 10.1021/bk-2015-1194.ch006

Deactivation Analysis

Ni supported catalysts for carbon dioxide reforming of methane always suffer from serious deactivation mainly due to both the sintering of Ni and carbon deposition. In order to further study the influence of crystal phase of ZrO_2 on the deactivation of Ni/ZrO_2 catalysts, the spent catalysts were characterized by XRD, TG, O_2-TPO, TPH, CO_2-TPO, and TEM.

Figure 6 showed the XRD patterns of spent catalysts. The average size of the Ni particles was calculated by Scherrer equation (Table 2). It can be seen that the sintering of Ni particles was inhibited due to the mesoporous amorphous structure of Ni/am-ZrO_2 catalyst (*20*). In case of Ni/t-ZrO_2, Ni particles did not undergo considerable degree of sintering probably due to the strong interaction between Ni and ZrO_2. In contrast, the aggregation of Ni particles was observed on the spent Ni/m-ZrO_2 catalyst. This can be ascribed to the weak metal–support interaction and the poor porosity.

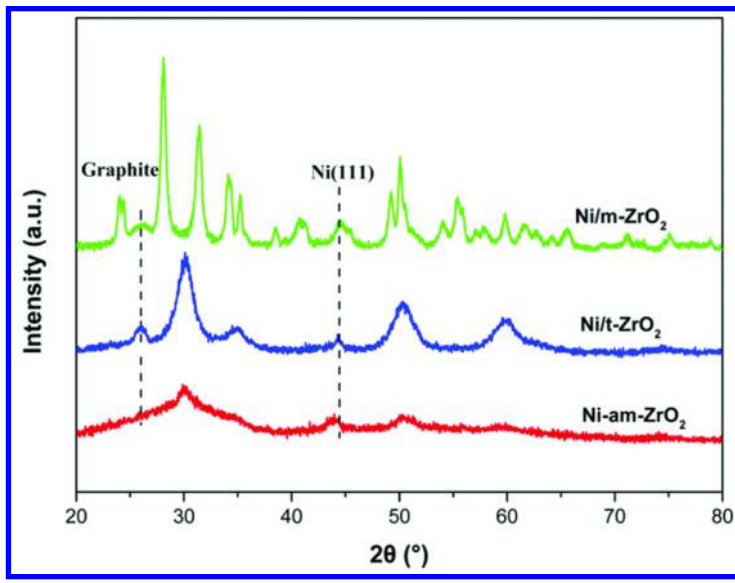

Figure 6. XRD patterns of spent Ni/ZrO_2 catalysts.

There appeared obvious diffraction peak at 2θ = 26° over Ni/m-ZrO_2 and Ni/t-ZrO_2 samples, illustrating the formation of graphitic carbon. However, no diffraction peaks of graphitic carbon were observed on Ni/am-ZrO_2, implying the superior coke resistance.

Carbon deposition is the significant reason for the deactivation of Ni based catalysts in carbon dioxide reforming of methane. Table 2 shows the rate of carbon deposition on the catalysts, evaluated by TG analysis. The amount of carbon deposition decreased in the following sequence: Ni/t-ZrO_2 > Ni/m-ZrO_2 > Ni/am-ZrO_2. Only trace amount of coke was observed on Ni/am-ZrO_2 with a coking rate of 0.15 mg/g_{cat}·h, which was in agreement with the superior stable catalytic

In Advances in CO2 Capture, Sequestration, and Conversion; He, et al.;
ACS Symposium Series; American Chemical Society: Washington, DC, 2015.

Publication Date (Web): September 11, 2015 | doi: 10.1021/bk-2015-1194.ch006

performance during TOS of 50 h. It has been reported that nickel particle size plays a crucial role on carbon deposition for dry reforming of methane. Catalysts with large Ni particle size favor the formation of carbon while small Ni particle size contributes to the enhanced coke resistance (*21*). Therefore, Ni/am-ZrO_2 exhibited the highest coke resistance due to the high dispersion of Ni nanoparticles. While the aggregation of Ni over Ni/t-ZrO_2 and Ni/m-ZrO_2 was favorable to the carbon accumulation.

Although Ni/t-ZrO_2 showed the highest carbon deposition rate (0.99 $mg/g_{cat}{\cdot}h$), it displayed a lower deactivation rate than Ni/m-ZrO_2. Therefore, there was no direct relationship between the coking rate and the deactivation rate.

O_2-TPO experiments were conducted to investigate the type of coke species (Figure 7). There was a very broad asymmetric peak between 400 and 700 °C over the Ni/m-ZrO_2 catalyst, implying two types of carbon species.

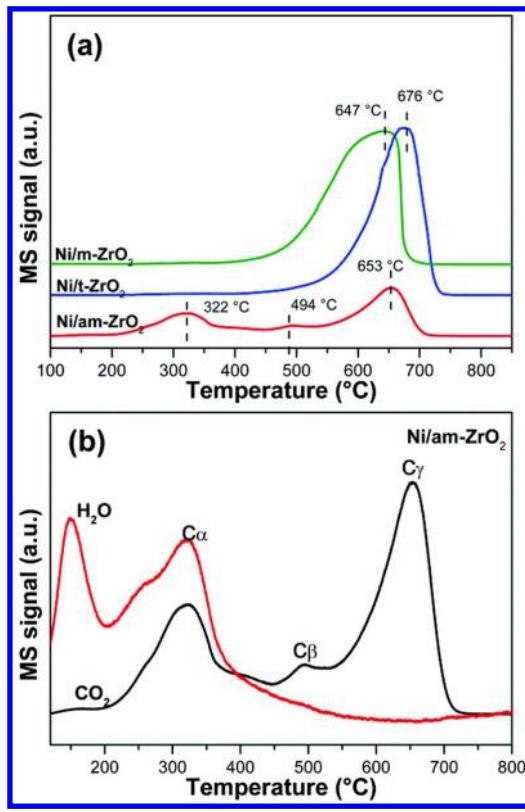

Figure 7. O_2-TPO profiles of the spent catalysts.

Wang et al. suggested that the peak between 350 and 500 °C can be designated as Cβ and the peak above 550 °C can be attributed to the oxidation of Cγ (*22*). Therefore, carbon deposited on Ni/m-ZrO_2 could be mainly attributed to relatively inert Cγ, with minor Cβ. The O_2-TPO profile of Ni/t-ZrO_2 was similar to that of Ni/m-ZrO_2. However, the CO_2 peak on Ni/t-ZrO_2 shifted to a much higher temperature (676 °C), illustrating a higher crystallization degree of

In Advances in CO2 Capture, Sequestration, and Conversion; He, et al.;
ACS Symposium Series; American Chemical Society: Washington, DC, 2015.

carbon species. For Ni/am-ZrO_2, three peaks centered at 322, 494 and 653 °C were present. The first peak at 322 °C was attributed to amorphous polymeric Cα species (*23*), which is considered as important intermediates. The Cα species are the product of methane decomposition and can be further converted to syngas (*24*). The second peak at 494 °C was ascribed to the formation of small amount of less active graphitic carbon species (Cβ). The peak at 653 °C could be related to inert graphitic Cγ species with the lowest reactivity.

Figure 7b shows the CO_2 and H_2O responses obtained during the O_2-TPO experiment of Ni/am-ZrO_2. Two peaks of H_2O responses were observed. The peak at 148 °C might be related to the desorption of OH and adsorbed H_2O. It is worth noting that the peak at 320 °C exhibited almost identical profile compared with that of CO_2 responses associated to Cα. Therefore, the Cα species can be ascribed to CH_x species due to the simultaneous formation of water. The CH_x species resulted from dehydrogenation of methane are considered as important intermediates for the formation of synthesis gas.

Publication Date (Web): September 11, 2015 | doi: 10.1021/bk-2015-1194.ch006

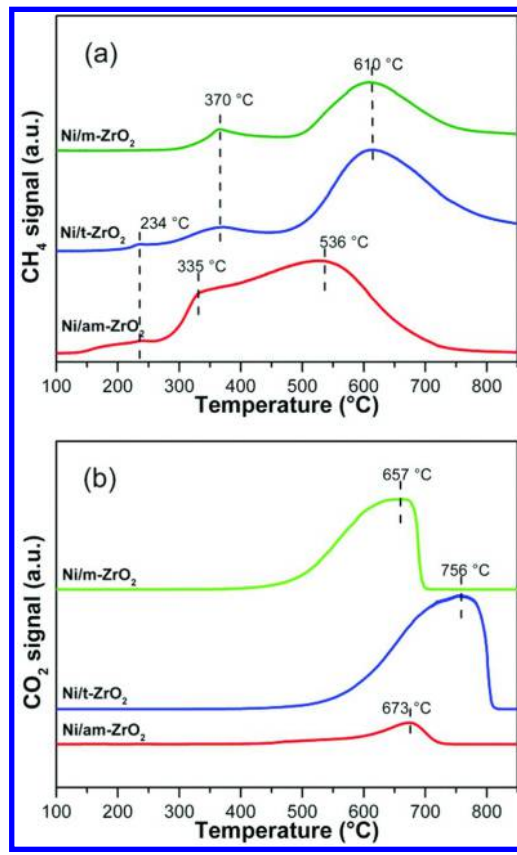

Figure 8. (a) TPH profiles of spent catalysts, (b) O_2-TPO profiles of spent catalysts, conducted after TPH on the same samples.

In Advances in CO2 Capture, Sequestration, and Conversion; He, et al.;
ACS Symposium Series; American Chemical Society: Washington, DC, 2015.

To further investigate the carbon deposits, TPH was applied. All Ni/ZrO_2 catalysts displayed two main CH_4 release peaks (Figure 8a). For Ni/am-ZrO_2, the small peak at 335 °C was attributed to Cα and the major peak at 536 °C was attributed to Cβ. Similar carbon species were also identified for Ni/t-ZrO_2 and Ni/m-ZrO_2 catalysts. Moreover, both peaks shifted to much higher temperature (370 and 610 °C, respectively), illustrating the less active surface carbon species over Ni/t-ZrO_2 and Ni/m-ZrO_2. O_2-TPO was conducted on the catalyst samples after TPH test, in order to analyze the carbon that could not be hydrogenated (Figure 8b). Ni/am-ZrO_2 exhibited only one peak at around 673 °C associated with Cγ species, suggesting that both Cα and Cβ can be eliminated by hydrogen. However, the inert Cγ species can not be removed by H_2 below 850 °C. For Ni/t-ZrO_2 and Ni/m-ZrO_2, a very broad asymmetric peak indicated that two types of carbon species remained. This suggested that carbon deposition on these two catalysts showed higher resistant to hydrogenation than that on Ni/am-ZrO_2.

Publication Date (Web): September 11, 2015 | doi: 10.1021/bk-2015-1194.ch006

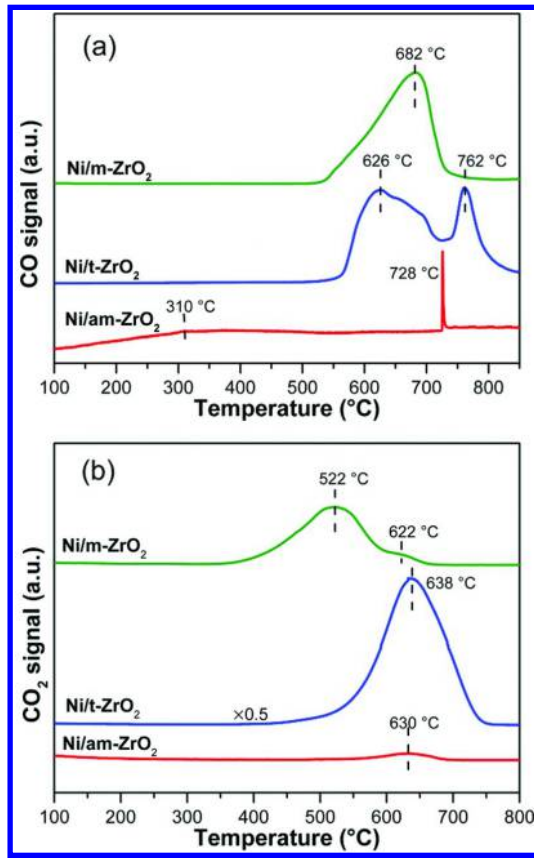

Figure 9. (a) CO_2-TPO profiles of spent catalysts, (b) O_2-TPO profiles of spent catalysts, conducted after CO_2-TPO on the same samples.

CO_2-TPO experiments were conducted to evaluate the activity of deposited carbon under reaction conditions. Figure 9a shows a broad peak at 310 °C and a sharp peak at 728 °C on Ni/am-ZrO_2 ascribed to active CH_x (Cα) and inert coke species (Cβ and Cγ), respectively. Only one peak at 682 °C was observed on Ni/m-ZrO_2, while two main peaks at 626 and 762 °C can be found on Ni/t-ZrO_2. It is worth noting that only a part of coke species on Ni/t-ZrO_2 can be removed by CO_2 under reaction temperature (750 °C) due to the presence of oxidation peak at higher temperature (762 °C). The differences of CO_2-TPO profiles between these Ni/ZrO_2 catalysts might be related to the nature of deposited carbon as well as the structure of ZrO_2. O_2-TPO experiment was also performed following CO_2-TPO treatment (Figure 9b), in order to study the inertness of deposited carbon to oxidation by CO_2. It is worth noting that only small amount of carbon remained on the surface of Ni/am-ZrO_2 after CO_2-TPO treatment, implying the high activity of coke towards oxidation by CO_2. This was consistent with the low coking rate and the superior stability of the Ni/am-ZrO_2 catalyst. For Ni/m-ZrO_2, the O_2-TPO profile showed a main peak at 522 °C with a shoulder at 622 °C, which can be identified as Cβ and Cγ respectively. Compared with O_2-TPO profile without the treatment of CO_2-TPO, it can be speculated that Cγ species were easier to be eliminated by CO_2 than Cβ on Ni/m-ZrO_2. This may be related to the morphology and location of carbon species (*25*). For Ni/t-ZrO_2, similar peak can be observed on O_2-TPO profiles before and after the treatment of CO_2-TPO, indicating the presence of the same carbon species after the oxidation of CO_2.The larger peak at 638 °C illustrated that carbon species on Ni/t-ZrO_2 was less active to CO_2, which was in consistent with the results of CO_2-TPO (Figure 9a).

The morphology of deposited carbon on the spent catalysts was analyzed by TEM. Figure 10 displayed three types of deposited carbon: graphite ribbons (Figure 10d), encapsulating carbon (Figure 10e) and multi-walled carbon nanotubes (MWCNTs) (Figure 10f). The most species observed on Ni/m-ZrO_2 were graphite ribbons and encapsulating carbon, in spite of the presence of MWCNTs (Figure 10a). In contrast, MWCNTs were the dominant carbon species while graphite ribbons and encapsulating carbon were detected to a lesser extent on Ni/t-ZrO_2 (Figure 10b). According to the results of O_2-TPO, the temperature of coke oxidation on Ni/t-ZrO_2 was higher than that on Ni/m-ZrO_2, indicating that MWCNTs were less active than other carbon species (*26*). It can also be found that carbon deposited on Ni/t-ZrO_2 displayed high oxidation-resistant to CO_2 under reaction conditions. However, no obvious relationship between the activity of carbon species and the deactivation rate was observed. Therefore, the morphology of deposited carbon should be considered. As reported, encapsulating carbon is responsible for the deactivation of the catalyst while MWCNTs exert low influence on catalytic activity (*26*, *27*). Therefore, the encapsulating carbon species observed on Ni/m-ZrO_2 were corresponding to its significant deactivation.

Figure 10c shows that no obvious MWCNTs or encapsulating carbon species existed on the Ni/am-ZrO_2 catalyst. This indicated that carbon deposition was greatly suppressed, leading to the superior stability of the catalyst.

Publication Date (Web): September 11, 2015 | doi: 10.1021/bk-2015-1194.ch006

Publication Date (Web): September 11, 2015 | doi: 10.1021/bk-2015-1194.ch006

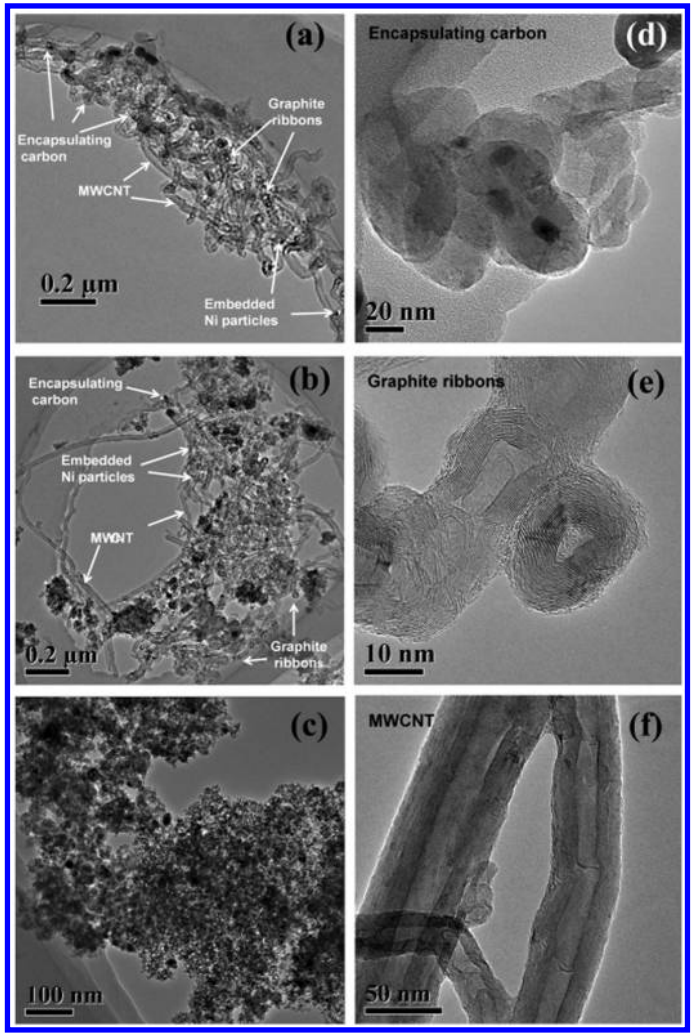

Figure 10. TEM micrographs of spent catalysts: (a) Ni/m-ZrO_2, (b) Ni/t-ZrO_2, (c) Ni/am-ZrO_2, (d) graphite ribbons, (e) encapsulating carbon, (f) MWCNTs.

Conclusions

The performance of Ni/ZrO_2 catalysts for dry reforming of methane depended strongly on the phase of ZrO_2. The Ni/am-ZrO_2 feathering a disordered mesoporous structure of amorphous zirconia showed superior stability than Ni/t-ZrO_2 and Ni/m-ZrO_2. The activity and stability of the catalyst were closely associated with the dispersion of Ni, which was strongly influenced by the crystal phase of ZrO_2. The mesoporous amorphous ZrO_2 was favorable to the homogeneous dispersion of Ni, leading to the high activity and the enhanced coke resistance.

The comparison between the deactivation of various Ni/ZrO_2 catalysts suggested that the morphology, species and reactivity of deposited carbon strongly depended on the particle size of Ni as well as the crystal phase of zirconia. It was found that the deactivation of catalyst was mainly determined by carbon morphology rather than coking rate. Ni nanoparticles supported on am-ZrO_2 exhibited superior stability for DRM reaction due to the higher reactivity of the deposited carbon. The significant deactivation of Ni/m-ZrO_2 was attributed to the presence of the encapsulating carbon, which covered the active Ni sites. MWCNTs appearing on the surface of Ni/t-ZrO_2 showed limited influence on the stability of Ni/t-ZrO_2, in spite of its low activity.

Publication Date (Web): September 11, 2015 | doi: 10.1021/bk-2015-1194.ch006

Acknowledgments

The authors are grateful for financial support from the Key Project of Energy Base of the Chinese Academy of Science (Contract No. 08YCA71921) and the International S&T Cooperation Project of Shanxi Province, China (Contract No. 2008081012).

References

1. Fan, M. S.; Abdullah, A. Z.; Bhatia, S. Catalytic technology for carbon dioxide reforming of methane to synthesis gas. *ChemCatChem* **2009**, *1*, 192–208.
2. Liu, C.-j.; Ye, J.; Jiang, J.; Pan, Y. Progresses in the preparation of coke resistant Ni-based catalyst for steam and CO_2 reforming of methane. *ChemCatChem* **2011**, *3*, 529–541.
3. Hou, Z.; Gao, J.; Guo, J.; Liang, D.; Lou, H.; Zheng, X. Deactivation of Ni catalysts during methane autothermal reforming with CO_2 and O_2 in a fluidized-bed reactor. *J. Catal.* **2007**, *250*, 331–341.
4. Amin, M. H.; Mantri, K.; Newnham, J.; Tardio, J.; Bhargava, S. K. Highly stable ytterbium promoted Ni/γ-Al_2O_3 catalysts for carbon dioxide reforming of methane. *Appl. Catal., B* **2012**, *119*, 217–226.
5. García-Diéguez, M.; Pieta, I. S.; Herrera, M. C.; Larrubia, M. A.; Malpartida, I.; Alemany, L. J. Transient study of the dry reforming of methane over Pt supported on different γ-Al_2O_3. *Catal. Today* **2010**, *149*, 380–387.
6. Garcia, V.; Fernandez, J. J.; Ruiz, W.; Mondragon, F.; Moreno, A. Effect of MgO addition on the basicity of Ni/ZrO_2 and on its catalytic activity in carbon dioxide reforming of methane. *Catal. Commun.* **2009**, *11*, 240–246.
7. Zanganeh, R.; Rezaei, M.; Zamaniyan, A. Dry reforming of methane to synthesis gas on NiO-MgO nanocrystalline solid solution catalysts. *Int. J. Hydrogen Energy* **2013**, *38*, 3012–3018.
8. Pereniguez, R.; Gonzalez-delaCruz, V. M.; Caballero, A.; Holgado, J. P. $LaNiO_3$ as a precursor of Ni/La_2O_3 for CO_2 reforming of CH_4: Effect of the presence of an amorphous NiO phase. *Appl. Catal., B* **2012**, *123*, 324–332.

9. Alipour, Z.; Rezaei, M.; Meshkani, F. Effects of support modifiers on the catalytic performance of Ni/Al_2O_3 catalyst in CO_2 reforming of methane. *Fuel* **2014**, *129*, 197–203.
10. Nagaoka, K.; Seshan, K.; Aika, K.; Lercher, J. A. Carbon deposition during carbon dioxide reforming of methane - Comparison between Pt/Al_2O_3 and Pt/ZrO_2. *J. Catal.* **2001**, *197*, 34–42.
11. Zhang, Q. H.; Yan, L.; Xu, B. Q. Reforming of methane and coalbed methane over nanocomposite Ni/ZrO_2 catalyst. *Catal. Today* **2004**, *98*, 601–605.
12. Campa, M. C.; Ferraris, G.; Gazzoli, D.; Pettiti, I.; Pietrogiacomi, D. Rhodium supported on tetragonal or monoclinic ZrO_2 as catalyst for the partial oxidation of methane. *Appl. Catal., B* **2013**, *142–143*, 423–431.
13. Sato, A. G.; Volanti, D. P.; Meira, D. M.; Damyanova, S.; Longo, E.; Bueno, J. M. C. Effect of the ZrO_2 phase on the structure and behavior of supported Cu catalysts for ethanol conversion. *J. Catal.* **2013**, *307*, 1–17.
14. Bachiller-Baeza, B.; Rodriguez-Ramos, I.; Guerrero-Ruiz, A. Interaction of carbon dioxide with the surface of zirconia polymorphs. *Langmuir* **1998**, *14*, 3556–3564.
15. Pokrovski, K.; Jung, K. T.; Bell, A. T. Investigation of CO and CO_2 adsorption on tetragonal and monoclinic zirconia. *Langmuir* **2001**, *17*, 4297–4303.
16. Rezaei, M.; Alavi, S. M.; Sahebdelfar, S.; Bai, P.; Liu, X.; Yan, Z.-F. CO_2 reforming of CH4 over nanocrystalline zirconia-supported nickel catalysts. *Appl. Catal., B* **2008**, *77*, 346–354.
17. Liu, Y.; Fang, K.; Chen, J.; Sun, Y. Effect of pore size on the performance of mesoporous zirconia-supported cobalt Fischer-Tropsch catalysts. *Green Chem.* **2007**, *9*, 611–615.
18. Peterson, G. W.; Rossin, J. A.; Karwacki, C. J.; Glover, T. G. Surface chemistry and morphology of zirconia polymorphs and the influence on sulfur dioxide removal. *J. Phys. Chem. C* **2011**, *115*, 9644–9650.
19. Ghelamallah, M.; Granger, P. Impact of barium and lanthanum incorporation to supported Pt and Rh on α-Al_2O_3 in the dry reforming of methane. *Fuel* **2012**, *97*, 269–276.
20. Kim, D. H.; Sim, J. K.; Lee, J.; Seo, H. O.; Jeong, M.-G.; Kim, Y. D.; Kim, S. H. Carbon dioxide reforming of methane over mesoporous Ni/SiO_2. *Fuel* **2013**, *112*, 111–116.
21. Zhu, X.; Huo, P.; Zhang, Y.-p.; Cheng, D.-g.; Liu, C.-j. Structure and reactivity of plasma treated Ni/Al_2O_3 catalyst for CO_2 reforming of methane. *Appl. Catal., B* **2008**, *81*, 132–140.
22. Wang, N.; Shen, K.; Huang, L. H.; Yu, X. P.; Qian, W. Z.; Chu, W. Facile route for synthesizing ordered mesoporous Ni–Ce–Al oxide materials and their catalytic performance for methane dry reforming to hydrogen and syngas. *ACS Catal.* **2013**, *3*, 1638–1651.
23. Zuo, Z.-J.; Shen, C.-F.; Tan, P.-J.; Huang, W. Ni based on dual-support Mg-Al mixed oxides and SBA-15 catalysts for dry reforming of methane. *Catal. Commun.* **2013**, *41*, 132–135.

Publication Date (Web): September 11, 2015 | doi: 10.1021/bk-2015-1194.ch006

24. Tao, K.; Zhou, S.; Zhang, Q.; Kong, C.; Ma, Q.; Tsubaki, N.; Chen, L. Sol-gel auto-combustion synthesis of Ni-$Ce_xZr_{1-x}O_2$ catalysts for carbon dioxide reforming of methane. *RSC Adv.* **2013**, *3*, 22285–22294.
25. Pan, Y.-X.; Liu, C.-J.; Shi, P. Preparation and characterization of coke resistant Ni/SiO_2 catalyst for carbon dioxide reforming of methane. *J. Power Sources* **2008**, *176*, 46–53.
26. Djinovic, P.; Crnivec, I. G. O.; Erjavec, B.; Pintar, A. Influence of active metal loading and oxygen mobility on coke-free dry reforming of Ni-Co bimetallic catalysts. *Appl. Catal., B* **2012**, *125*, 259–270.
27. Serrano-Lotina, A.; Daza, L. Long-term stability test of Ni-based catalyst in carbon dioxide reforming of methane. *Appl. Catal., A* **2014**, *474*, 107–113.

Publication Date (Web): September 11, 2015 | doi: 10.1021/bk-2015-1194.ch006

Publication Date (Web): September 11, 2015 | doi: 10.1021/bk-2015-1194.ch007

Chapter 7

Key Factors on the Pressurized Tri-Reforming of Methane over Ni-SiO_2

Hua-Ping Ren, Yong-Hong Song, Zhao-Tie Liu, and Zhong-Wen Liu*

Key Laboratory of Applied Surface and Colloid Chemistry (MOE), School of Chemistry & Chemical Engineering, Shaanxi Normal University, Xi'an 710119, China

***Tel: +86-29-8153-0801. Fax: +86-29-8153-0727.**

E-mail: zwliu@snnu.edu.cn.

The effect of operating conditions, i.e., space velocity, temperature, pressure, and feed $CH_4/CO_2/H_2O/O_2$ molar ratios, on the reforming of methane with CO_2, H_2O, and O_2 (tri-reforming, TRM) was systematically investigated in a fixed-bed reactor over the Ni-SiO_2 synthesized by the complex-decomposition method by using citric acid as the complexing agent. Under different temperatures, pressures, and molar ratios of reactants, the thermodynamics equilibrium compositions of the TRM were calculated by using HSC chemistry 5.0. Irrespective of the operating conditions applied, results indicate that the Ni-SiO_2 was highly active for the TRM, in which the conversions of CH_4 and CO_2 and H_2/CO molar ratios in the products nearly reach equilibrium values. Moreover, the changes for the conversions of CH_4 and CO_2 and H_2/CO molar ratios in the products induced by varying the space velocity, temperature, pressure, and feed $CH_4/CO_2/H_2O/O_2$ molar ratios were discussed and compared with the results of the thermodynamics calculations. By simply changing the molar ratios of the feeds, the syngas with adjustable H_2/CO molar ratios between 1.0 and 3.0 was successfully obtained. Importantly, under much severe conditions of T = 750 °C, P

In Advances in CO2 Capture, Sequestration, and Conversion; He, et al.;
ACS Symposium Series; American Chemical Society: Washington, DC, 2015.

= 10.0 atm, $CH_4/CO_2/H_2O/O_2$ = 1.0/0.3/0.3/0.2, and *GHSV* = 26600 mL(CH_4)·g^{-1}·h^{-1}, the almost identical conversions of CH_4, CO_2, and the H_2/CO molar ratios to those of the thermodynamics equilibrium were kept for over 50 h. Thus, the Ni-SiO_2 is a highly active and stable catalyst for the TRM.

Introduction

The production of syngas (H_2+CO) from natural gas (methane), which is the key technology for the gas-to-liquid process, has drawn quantitative attention in recent years (*1–3*). Generally, there are three primary processes via reforming reactions to convert natural gas to syngas, i.e., steam reforming of methane (SRM, eq. 1), carbon dioxide reforming of methane (CDR, eq. 2), and catalytic partial oxidation of methane (CPOM, eq. 3) (*4*).

$$CH_4 + H_2O \rightarrow CO + 3H_2, \quad \Delta H^o_{298K} = 206 \text{ kJ/mol} \qquad (1)$$

$$CH_4 + CO_2 \rightarrow 2CO + 2H_2, \quad \Delta H_{298K} = 247 \text{ kJ/mol} \qquad (2)$$

$$CH_4 + 1/2\ O_2 \rightarrow CO + 2H_2, \quad \Delta H_{298K} = -36 \text{ kJ/mol} \qquad (3)$$

Although the SRM has successfully applied in many industrial processes, the obvious disadvantage of this process is the high energy demand due to the strong endothermic nature of the reaction (eq. 1). Moreover, the syngas with a high H_2/CO ratio of greater than 3 from the SRM process is only suitable to the synthesis of ammonia and hydrogen (*5*, *6*). In contrast to SRM, CPOM is an exothermic reaction, and has long been received considerable attention since it produces the syngas with a H_2/CO ratio of about 2.0, which well meets the requirement for the synthesis of methanol, dimethyl ether, and hydrocarbons via Fischer-Tropsch (FT) route (*7–9*). However, besides the potential explosive risk of the CPOM process, the issue of the hot spot in the catalytic bed is still a barrier for its industrialization (*9*, *10*). In the case of CDR, the principal merit is that it converts the two potent greenhouse gases (CO_2 and CH_4) into the syngas with a H_2/CO ratio of near to 1.0, which can be used as the feedstock for synthesizing valuable oxygenates and long-chain hydrocarbons (*3*, *11–13*). However, the CO_2 capture and its separation, purification, and transportation are economic barriers for the efficient utilization of CO_2 (*14*, *15*). In the catalytic aspects, the severe coke deposition and sintering of the industrially important Ni-based catalyst are still main challenges for the commercialization of CDR (*16–18*).

Combining the advantages of the three primary processes, a mixed route for the production of syngas from the reforming of methane, i.e., tri-reforming of methane (TRM), has been proposed in recent years (*3*, *19*). For the TRM, the reactions of the endothermic SRM (eq. 1) and CDR (eq. 2), and the exothermic CPOM (eq. 3) synergistically occur in one reactor. As a result, an autothermal operation characterizing the neutral energy demand may be accomplished during

Publication Date (Web): September 11, 2015 | doi: 10.1021/bk-2015-1194.ch007

In Advances in CO2 Capture, Sequestration, and Conversion; He, et al.;
ACS Symposium Series; American Chemical Society: Washington, DC, 2015.

the TRM. Moreover, the flue gas from the fired power plant is composed of CO_2, O_2, and H_2O, which is a potential candidate of the feedstock for the TRM. Indeed, it is well known that the composition of the flue gas varies depending on the operational modes of the power plant. For example, the typical volumetric composition of the flue gas from the natural gas-fired power plants is 8-10, 18-20, 2-3, and 67-72% for CO_2, H_2O, O_2, and N_2, respectively, which is different from that of the coal-fired plant, i.e., 12-14, 8-10, 3-5, and 72-77% for CO_2, H_2O, O_2, and N_2, respectively (*20*). However, the syngas with a desired H_2/CO may be achieved via adjusting the molar ratios of CO_2, H_2O, and O_2 by co-feeding the flue gas with either H_2O or O_2. When the catalytic process is concerned, the presence of H_2O and/or O_2 significantly reduces the coke deposition over the catalyst (*21*, *22*). More importantly, the TRM may largely eliminate the separation of the flue gas, which has a great economic benefit. Moreover, the outlet temperature of the flue gas is around 1000 °C, which well matches the high-temperature reaction of the tri-reforming process (*23*). Thus, the TRM by using the flue gas as a feedstock is of significantly important and promising (*23–26*).

Recently, a few studies have been concentrated on the TRM by co-feeding of H_2O, CO_2, and O_2 with different molar ratios (*8*, *9*, *27*). Considering the two facts that methane is preserved and transported under elevated pressures and the process for converting the syngas to chemicals and fuels such as FT synthesis is kinetically favored under elevated pressures, the TRM under pressurized conditions is industrially more desirable in terms of higher process efficiency (*3*, *28*). Thus, the TRM under pressurized conditions is more practical from an economical viewpoint. However, to the best of knowledge, very few works is reported in recent years (*3*).

In our previous works (*29*, *30*), the complex-decomposition method was applied to develop Ni-based catalysts for the pressurized CDR, and a highly active and stable Ni-SiO_2 was obtained by optimizing the complex agents and fuels. In this work, the Ni-SiO_2 catalyst optimized for CDR was quantitatively evaluated for the TRM under different feed $CH_4/CO_2/H_2O/O_2$ molar ratios, space velocities, reaction temperatures, and pressures. The effect of operating conditions on conversions and product compositions was revealed and compared with the calculated equilibrium data. As expected, the syngas with adjustable H_2/CO molar ratios was obtained. Importantly, the optimal Ni-SiO_2 catalyst developed for the CDR was still highly active and stable for the pressurized TRM, and near the equilibrium conversion of methane was kept for a time on stream (TOS) of 50 h without an observable decrease.

Experimental

Catalyst Preparation

The Ni-SiO_2 catalysts with a metallic nickel content of 10 wt.% was prepared by the complex-decomposition method by using nickel nitrate and tetraethoxysilane (TEOS) as the precursors of NiO and SiO_2, respectively. Firstly, the desired amount of nickel nitrate and TEOS were dissolved in ethanol. Then, the aqueous solution of citric acid as a complexing agent was added to the ethanol

In Advances in CO2 Capture, Sequestration, and Conversion; He, et al.;
ACS Symposium Series; American Chemical Society: Washington, DC, 2015.

Publication Date (Web): September 11, 2015 | doi: 10.1021/bk-2015-1194.ch007

solution until the molar ratio of citric acid to nickel plus silicon was 1.0. After this, the solvent was evaporated at 60 °C until the formation of a viscous gel, and a foam-like grey solid was obtained by burning the gel. Finally, the sample was calcined at 700 °C for 4 h leading to the Ni-SiO_2 catalyst. The more detailed procedure was described in our previous work (*29*).

Reaction Procedure

The TRM experiments were performed in a stainless steel fixed-bed reactor (i. d. = 8 mm). Prior to the reaction, the catalyst (0.15 g, 40-60 mesh) diluted with quartz sands (the volumetric ratio of quartz sands to the catalyst = 3.0) was reduced under the conditions of P = 1.0 atm, T = 700 °C, t = 2.5 h, and 50 $mL \cdot min^{-1}$ of 10% H_2/N_2. After purging with N_2, the feed gases with a desired molar ratio of CH_4 to CO_2, H_2O, and O_2 were switched, and the reaction was started under the conditions of T = 650 ~ 750 °C, P = 1.0 ~ 10.0 atm, GHSV = 15792 ~ 36840 $mL(CH_4) \cdot g^{-1} \cdot h^{-1}$, and $CH_4/CO_2/H_2O/O_2$ molar ratios between 1.0/0.5~0.1/0.5~0.1/0~0.3. The effluent products after condensing water with an ice-water trap were analysed by an on-line GC (GC-9560, Shanghai Huaai chromatographic analysis Co., Ltd) equipped with 5A and PQ capillary columns and a TCD detector.

Results and Discussion

Characteristics of Thermodynamics Equilibrium

Pressure Effects

The equilibrium conversions of CH_4, CO_2, H_2O, O_2, and H_2/CO molar ratios were calculated with HSC chemistry 5.0 under the conditions of T = 750 °C, $CH_4/CO_2/H_2O/O_2$ = 1.0/0.3/0.3/0.2, and the results under different pressures are provided in Figure 1. As shown in Figure 1, the O_2 conversion was kept at 100% with increasing the pressures from 1.0 to 10.0 atm, indicating the negligible effect of pressures on the O_2 conversion under the given temperature and system composition. In contrast, the conversions of CH_4, CO_2, and H_2O were obviously decreased with increasing the pressure from 1.0 to 10.0 atm. Moreover, the conversions of CH_4, CO_2, and H_2O were linearly decreased until the pressure of about 4.0 atm, and were leveled off when the pressure was further increased. Importantly, the conversion of CH_4 was obviously higher than those of CO_2 and H_2O. In the case of H_2/CO molar ratio, its decrease was very limited with increasing the pressure from 1.0 to 10.0 atm, indicating the pressure plays a less important role in determining the H_2/CO molar ratios.

Publication Date (Web): September 11, 2015 | doi: 10.1021/bk-2015-1194.ch007

In Advances in CO2 Capture, Sequestration, and Conversion; He, et al.;
ACS Symposium Series; American Chemical Society: Washington, DC, 2015.

Publication Date (Web): September 11, 2015 | doi: 10.1021/bk-2015-1194.ch007

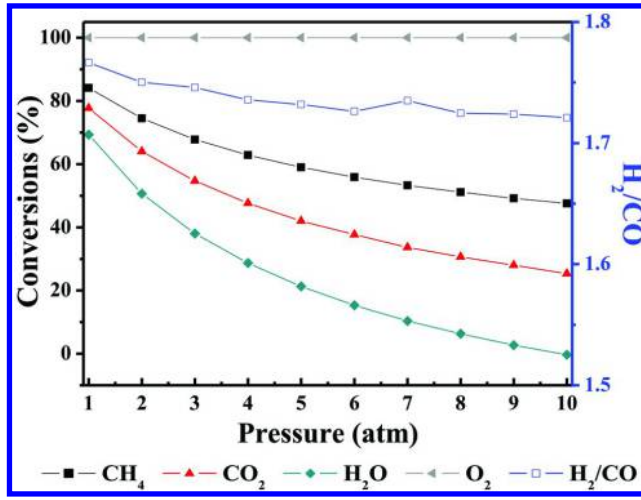

Figure 1. Effect of the pressure on equilibrium conversions and H_2/CO molar ratios under the conditions of T = 750 °C and $CH_4/CO_2/H_2O/O_2$ = 1.0/0.3/0.3/0.2.

Temperature Effects

The impact of temperature on the equilibrium conversions was calculated under the conditions of P = 1.0 atm and $CH_4/CO_2/H_2O/O_2$ = 1.0/0.3/0.3/0.2, and the results are provided in Figure 2.

The conversions of CH_4, CO_2, and H_2O were rapidly increased with increasing the temperature from 400 to 800 °C. A further increasing of the temperature leaded to slowly increased conversions, and near 100% conversions were obtained at 1000 °C. As indicated in eqs.1 and 2, both the SRM and CDR reactions are strong endothermic, leading to the increased conversions of CH_4, CO_2, and H_2O at higher temperatures. These are agreeable with the reported results (*19*, *27*). In the case of the H_2/CO molar ratio, it was sharply decreased from 11.8 to 2.1 with increasing the temperature from 400 to 600 °C, and it was around 1.8 when the temperature was further increased to 1000 °C. This indicates an important effect of the reaction temperature on the H_2/CO molar ratios at lower temperatures. It is well known that the reverse water-gas shift reaction (RWGS, $H_2 + CO_2 \rightarrow CO + H_2O$, $\Delta H°_{298K}$ = 41 kJ/mol) is endothermic (*26*). Thus, the RWGS reaction is thermodynamically favorable at higher temperatures, leading to the decrease of H_2/CO molar ratios with increasing reaction temperatures.

Publication Date (Web): September 11, 2015 | doi: 10.1021/bk-2015-1194.ch007

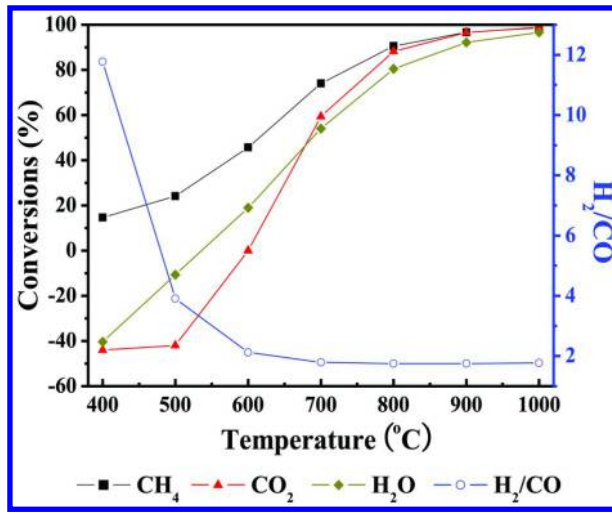

Figure 2. Effect of the temperature on equilibrium conversions and H_2/CO molar ratios under the conditions of P = 1.0 atm and $CH_4/CO_2/H_2O/O_2$ = 1.0/0.3/0.3/0.2.

Effect of System Compositions

The equilibrium conversions of CH_4, CO_2, H_2O, and H_2/CO molar ratios were calculated under the conditions of $CH_4/CO_2/H_2O/O_2$ = 1.0/0.0~0.5/0.0~0.5/0.5~0.0, T = 400~1000 °C, and P = 1.0 atm. To reveal the effect of system compositions, the molar ratio of CH_4 to (CO_2+H_2O+O_2) was kept at the stoichiometric ratio of 1.0. Moreover, the CO_2 to H_2O molar ratio was kept at 1.0 to obtain a syngas with the H_2/CO molar ratio of 2.0. As shown in Figure 3a, the CH_4 conversion was clearly increased with either increasing the O_2 content or decreasing the CO_2 and/or H_2O content, the extent of which is dependent on the temperature. Furthermore, the effect was negligible when the temperature was above 800 °C.

In the case of the CO_2 conversion, irrespective of the feed $CH_4/CO_2/H_2O/O_2$ molar ratios, it was slightly decreased with increasing the reaction temperatures from 400 to 500 °C while it was significantly increased with the further increasing of the reaction temperatures until 900 °C. The complete conversion of CO_2 was observed at 1000 °C (Figure 3b). With increasing the temperature from 400 to 800 °C, the conversion of H_2O was almost linearly increased, and 100% conversion was also obtained at 1000 °C (Figure 3c). This can be explained as follows (*31*, *32*): (1) methane was completely combusted to CO_2/H_2O; (2) The H_2O was also produced via RWCS reaction by consuming the CO_2; (3) The CDR and SRM reactions are favorable at higher temperatures while the RWGS reaction is advantageous at lower temperatures.

In the case of H_2/CO molar ratios, as shown in Figure 3d, it was sharply decreased with increasing the reaction temperature from 400 to 600 °C irrespective

of the $CH_4/CO_2/H_2O/O_2$ molar ratios. Moreover, the further increase of the reaction temperature until 1000 °C leaded to an almost constant H_2/CO molar ratio, of which is clearly dependent on the composition of CH_4, CO_2, H_2O, and O_2.

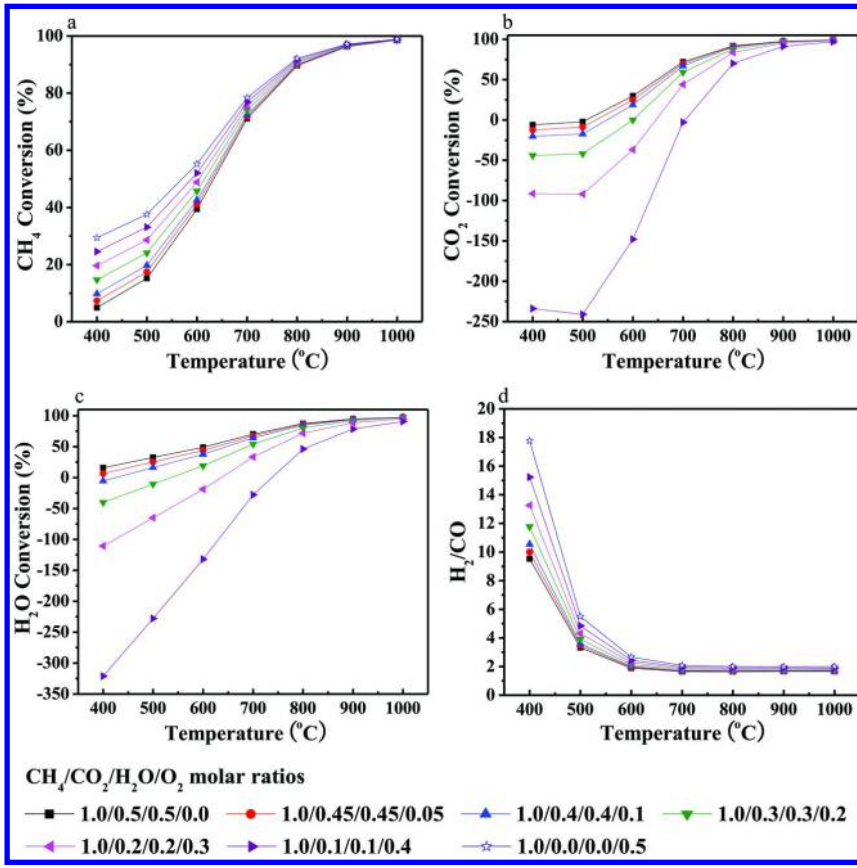

Figure 3. Equilibrium conversions of CH_4 (a), CO_2 (b), H_2O (c), and H_2/CO molar ratios (d) under P = 1.0 atm.

TRM Results over Ni-SiO_2

Effect of Space Velocity

The effect of space velocity on the TRM performance over Ni-SiO_2 was investigated under the operating conditions of T = 750 °C, P = 5.0 atm, and $CH_4/CO_2/H_2O/O_2$ = 1.0/0.4/0.4/0.1. From the results given in Figure 4, the conversions of CH_4 and CO_2 and H_2/CO molar ratio at steady state were about 62%, 43%, and 1.80 at a GHSV of 15792 mL(CH_4)·g^{-1}·h^{-1}, respectively. With increasing the GHSV from 15792 to 36840 mL(CH_4)·g^{-1}·h^{-1}, the steady-state conversions of CH_4 and CO_2 and H_2/CO molar ratio were kept almost unchanged.

In Advances in CO2 Capture, Sequestration, and Conversion; He, et al.;
ACS Symposium Series; American Chemical Society: Washington, DC, 2015.

Publication Date (Web): September 11, 2015 | doi: 10.1021/bk-2015-1194.ch007

Publication Date (Web): September 11, 2015 | doi: 10.1021/bk-2015-1194.ch007

This indicates that the Ni-SiO_2 is still highly active for TRM, which is consistent to its high activity towards CDR as reported in our previous works (*29*, *30*). Moreover, the experimental results were nearly identical to those of the calculated equilibrium data (Figure 1). Thus, the Ni-SiO_2 prepared by the complex-decomposition method is really highly active for the reforming reactions of methane even under much severe conditions of T = 750 °C and P = 5.0 atm. In the case of the catalytic stability, there was no observable decrease of the conversions within 20 h test at GHSV of 15792 mL(CH_4)·g^{-1}·h^{-1}. With the further increase of GHSV from 26600 to 36840 mL(CH_4)·g^{-1}·h^{-1}, the steady-state conversions and H_2/CO molar ratio were still unchanged. This indicates that the Ni-SiO_2 was also stable for TRM under much severe operating conditions. Thus, the Ni-SiO_2 was both active and stable for TRM.

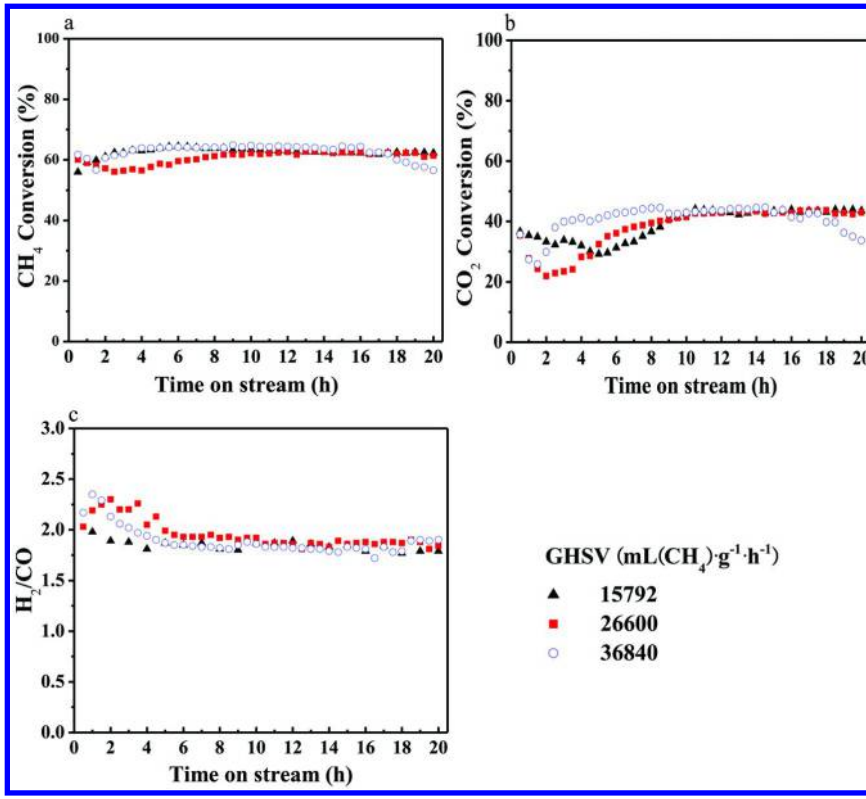

Figure 4. Effect of the space velocity on CH_4 conversion (a), CO_2 conversion (b), and H_2/CO molar ratio in the products (c) of TRM over Ni-SiO_2 under the conditions of T = 750 °C, $CH_4/CO_2/H_2O/O_2$ = 1.0/0.4/0.4/0.1, and P = 5.0 atm.

Effect of Reaction Pressure

To reveal the impact of the reaction pressures on the performance of Ni-SiO_2 for TRM, the reaction was carried out under the conditions of T = 750 °C,

In Advances in CO2 Capture, Sequestration, and Conversion; He, et al.;
ACS Symposium Series; American Chemical Society: Washington, DC, 2015.

$CH_4/CO_2/H_2O/O_2$ = 1.0/0.3/0.3/0.2, and GHSV = 26600 mL(CH_4)·g^{-1}·h^{-1}, and the results are given in Figure 5. As shown in Figure 5a, the steady-state CH_4 conversion was about 82, 61, and 50% at the pressure of 1.0, 5.0, and 10.0 atm, respectively, which is quite similar to those of the thermodynamics equilibrium (Figure 1). Thus, irrespective of the pressures, near equilibrium CH_4 conversions were obtained over Ni-SiO_2. Moreover, the steady-state CH_4 conversion was kept over 20 h without observable decrease, indicating its high stability even at elevated pressures of 10.0 atm.

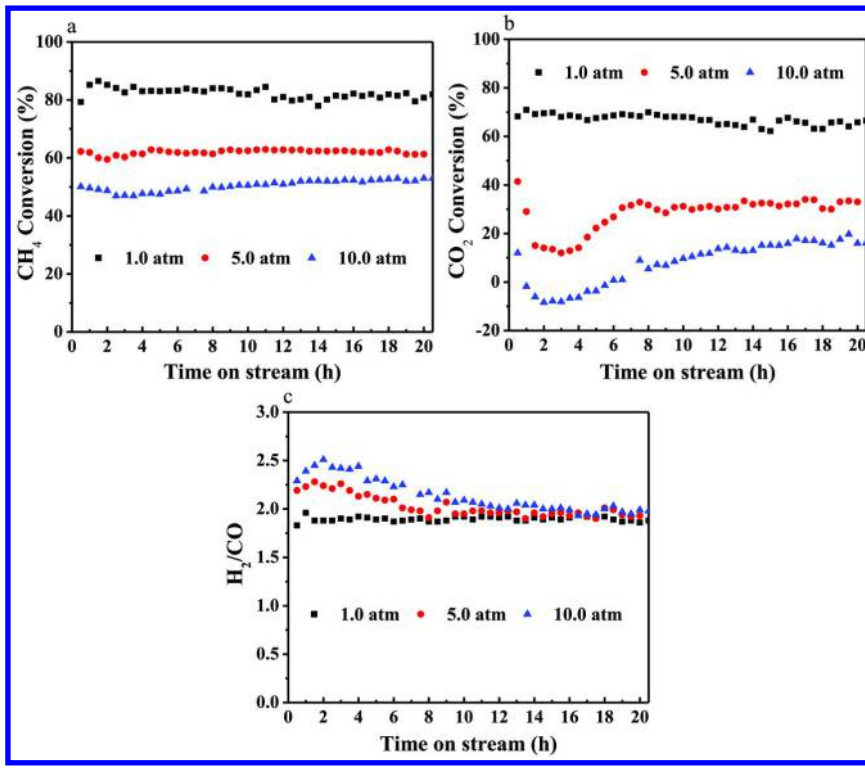

Figure 5. The time-on-stream CH_4 conversion (a), CO_2 conversion (b), and the H_2/CO molar ratio in the products (c) for TRM under the conditions of T = 750 °C, $CH_4/CO_2/H_2O/O_2$ = 1.0/0.3/0.3/0.2, GHSV = 26600 mL(CH_4)·g^{-1}·h^{-1}.

When the CO_2 conversions were concerned (Figure 5b), the most obvious observation was the fluctuation at the initial reaction stage, the extent and the time to the steady state of which are increased with increasing the pressure from 1.0 to 10.0 atm. Thus, the time required to approach the steady-state of CO_2 conversion was longer at higher pressures, indicating the fluctuated compositions of the catalytic bed at the initial stage of the reaction. In the case of the steady-state CO_2 conversion, the changing trend with increasing the pressure from 1.0 to 10.0 atm was the same to that of CH_4 conversion. However, the extent was more significant, i.e., sharply decreased from about 70% at P = 1.0 atm to about 10% at P = 10.0 atm. Moreover, the CO_2 conversion of TRM at elevated pressures

In Advances in CO2 Capture, Sequestration, and Conversion; He, et al.;
ACS Symposium Series; American Chemical Society: Washington, DC, 2015.

Publication Date (Web): September 11, 2015 | doi: 10.1021/bk-2015-1194.ch007

was significantly lower than that of the pressurized CDR (*29*, *30*). These results indicate that the reforming of CO_2 with CH_4 at a higher pressure was inhibited under the presence of O_2 and/or H_2O, which is consistent to the slightly higher steady-state H_2/CO molar ratio at 1 atm (~ 1.85) than those at 5 and 10 atm (~ 1.95, Figure 5c). This can be well explained based on the weaker oxidation ability of CO_2.

Effect of Reaction Temperature

The influence of the reaction temperature on the conversions and H_2/CO molar ratio under the conditions of $CH_4/CO_2/H_2O/O_2$ = 1.0/0.3/0.3/0.2, P = 5.0 atm, and GHSV = 26600 mL$(CH_4)\cdot g^{-1}\cdot h^{-1}$ is presented in Figure 6. The steady-state conversions of CH_4 and CO_2 and the H_2/CO molar ratio were quite stable at all of the temperatures applied. Moreover, it is clear that the conversions of CH_4 and CO_2 were obviously decreased with decreasing the reaction temperature. In contrast, the H_2/CO molar ratio was slightly increased with decreasing reaction temperatures. This suggests that the endothermic RWGS occurred very limitedly at lower temperatures, which is consistent to the equilibrium results shown in Figure 2. Importantly, after a recycle of the temperature from 750 to 650 °C, both the conversions of CH_4 and CO_2 and the H_2/CO molar ratio were fully restored, indicating the high stability of the catalyst for TRM.

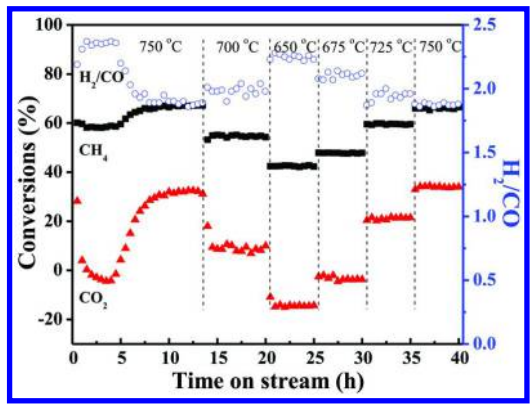

Figure 6. Effect of reaction temperature on the performance of Ni-SiO_2 for TRM under the conditions of P = 5.0 atm, $CH_4/CO_2/H_2O/O_2$ = 1.0/0.3/0.3/0.2, and GHSV = 26600 mL$(CH_4)\cdot g^{-1}\cdot h^{-1}$.

Effect of Feed Molar Ratios

The performance of Ni-SiO_2 for TRM was also carried out by changing the feed $CH_4/CO_2/H_2O/O_2$ molar ratios between 1.0/0.5~0.2/0.5~0.2/0.0~0.3, and the results are presented in Figure 7. It was observed that the variation of the CH_4 conversion was very limited irrespective of the feed compositions, which is nearly

Publication Date (Web): September 11, 2015 | doi: 10.1021/bk-2015-1194.ch007

identical to the equilibrium values under the conditions of T = 750 °C and P = 5.0 atm (Figure 3). Specifically, the CH_4 conversion was slightly increased while the CO_2 conversion was quickly decreased with increasing the O_2 content. These results are well agreeable with those of the equilibrium (Figure 3) and the reported results (*33*). Thus, simultaneous CDR and CPOM under the presence of CO_2 and O_2 in the feed occurred, and the CPOM was preferred than CDR. Considering the stoichiometric H_2/CO molar ratios of CDR (1.0) and SRM (3.0), the expected H_2/CO molar ratio between 1.0 and 3.0 can be conveniently adjusted by simply changing the feed $CO_2/O_2/H_2O$ ratios. To illustrate this, the feed with a molar ratio of CO_2 to H_2O at 1.0 was applied for producing a syngas with the H_2/CO molar ratio of 2.0. Indeed, results in Figure 7 indicate that the H_2/CO molar ratio of about 2.0 was obtained under varied feed compositions. When the results in Figure 7c were carefully examined, the H_2/CO molar ratios were slightly varied between 1.8 ~ 2.0, which can be explained as the different extents of the RWGS under varied feed compositions.

Publication Date (Web): September 11, 2015 | doi: 10.1021/bk-2015-1194.ch007

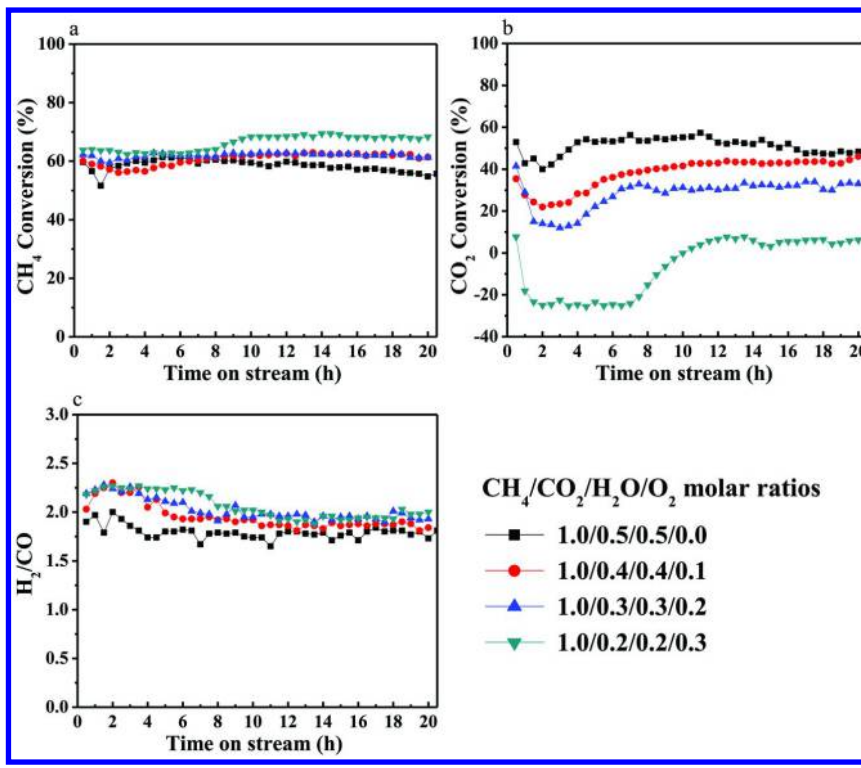

Figure 7. Effect of the feed $CH_4/CO_2/H_2O/O_2$ molar ratios on CH_4 conversion (a), CO_2 conversion (b), and H_2/CO molar ratio in the products (c) for TRM under the conditions of T = 750 °C, P = 5.0 atm, and GHSV = 26600 mL(CH_4)·g^{-1}·h^{-1}.

In Advances in CO2 Capture, Sequestration, and Conversion; He, et al.;
ACS Symposium Series; American Chemical Society: Washington, DC, 2015.

Long-Term Stability

To further confirm the stability of the Ni-SiO_2 for TRM, much severe operating conditions of T = 750 °C, P = 10.0 atm, $CH_4/CO_2/H_2O/O_2$ = 1.0/0.3/0.3/0.2, and GHSV = 26600 mL(CH_4)·g^{-1}·h^{-1} were applied for a longer TOS, and the results are given in Figure 8. Consistent to the results in Figure 5, the steady state was approached at a TOS of about 10 h. Moreover, the steady conversions of CH_4 and CO_2 and H_2/CO molar ratio were about 52%, 18%, and 2.0, respectively, which are nearly identical to the equilibrium values as shown in Figure 1. Within the TOS of 50 h, no observable decrease in conversions of CH_4 and CO_2 and H_2/CO molar ratio were found. Thus, the Ni-SiO_2 is highly active and stable for the TRM under much severe conditions with elevated pressures.

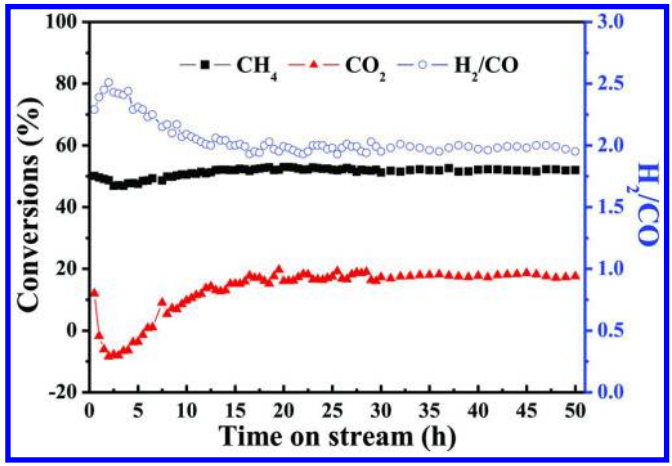

Figure 8. Long-term results of TRM over Ni-SiO_2 under the conditions of T = 750 °C, $CH_4/CO_2/H_2O/O_2$ = 1.0/0.3/0.3/0.2, GHSV = 26600 mL(CH_4)·g^{-1}·h^{-1}, and P = 10.0 atm.

Conclusions

In summary, the thermodynamics equilibrium and the kinetic behavior of the TRM over Ni-SiO_2 were systematically investigated. Irrespective of the operating conditions applied, the conversions of CH_4 and CO_2 and H_2/CO molar ratios in the products for TRM over Ni-SiO_2 almost reached the thermodynamics equilibrium values. Moreover, the syngas with a desired H_2/CO molar ratio between 1.0 and 3.0 was successfully obtained by simply adjusting the molar ratios of the feeds. Under the much severe operating conditions of *T* = 750 °C, *P* = 10.0 atm, $CH_4/CO_2/H_2O/O_2$ = 1.0/0.3/0.3/0.2, *GHSV* = 26600 mL(CH_4)·g^{-1}·h^{-1}, no observable deactivation of the Ni-SiO_2 was found for 50 h test. Thus, the highly efficient Ni-SiO_2 is very promising for the TRM.

In Advances in CO2 Capture, Sequestration, and Conversion; He, et al.;
ACS Symposium Series; American Chemical Society: Washington, DC, 2015.

Publication Date (Web): September 11, 2015 | doi: 10.1021/bk-2015-1194.ch007

Publication Date (Web): September 11, 2015 | doi: 10.1021/bk-2015-1194.ch007

Acknowledgments

The authors gratefully acknowledge the financial supports of Shaanxi Innovative Team of Key Science and Technology (2013KCT-17), the Changjiang Scholars and Innovative Research Team in University (IRT-14R33), Natural Science Foundation of Shaanxi Province (2012JZ2001), and the Fundamental Research Funds for the Central Universities (GK201305012).

References

1. Hu, Y.; Ruckenstein, E. Catalytic conversion of methane to synthesis gas by partial oxidation and CO_2 reforming. *Adv. Catal.* **2004**, *48*, 297–345.
2. Bradford, M. C. J.; Vannice, M. A. CO_2 reforming of CH_4. *Catal. Rev. Sci. Eng.* **1999**, *41*, 1–42.
3. Song, C. Global challenges and strategies for control, conversion and utilization of CO_2 for sustainable development involving energy, catalysis, adsorption and chemical processing. *Catal. Today.* **2006**, *115*, 2–32.
4. Liu, Z.-W.; Jun, K.-W.; Roh, H.-S.; Baek, S.-C.; Park, S.-E. Pulse study on the partial oxidation of methane over Ni/θ-Al_2O_3 catalyst. *J. Mol. Catal. A: Chem.* **2002**, *189*, 283–293.
5. Wang, F.; Qi, B.; Wang, G.; Li, L. Methane steam reforming: Kinetics and modeling over coating catalyst in micro-channel reactor. *Int. J. Hydrogen Energy* **2013**, *38*, 5693–5704.
6. Angeli, S. D.; Pilitsis, F. G.; Lemonidou, A. A. Methane steam reforming at low temperature: Effect of light alkanes' presence on coke formation. *Catal. Today* **2015**, *242*, 119–128.
7. Cesar, D. V.; Baldanza, M. A. S.; Henriques, C. A.; Pompeo, F.; Santori, G.; Múnera, J.; Lombardo, E.; Schmal, M.; Cornaglia, L.; Nichio, N. Stability of Ni and Rh-Ni catalysts derived from hydrotalcite-like precursors for the partial oxidation of methane. *Int. J. Hydrogen Energy* **2013**, *38*, 5616–5626.
8. Asencios, Y. J. O.; Assaf, E. M. Combination of dry reforming and partial oxidation of methane on NiO-MgO-ZrO_2 catalyst: Effect of nickel content. *Fuel Process. Technol.* **2013**, *106*, 247–252.
9. Li, B.; Xu, X.; Zhang, S. Synthesis gas production in the combined CO_2 reforming with partial oxidation of methane over Ce-promoted Ni/SiO_2 catalysts. *Int. J. Hydrogen Energy* **2013**, *38*, 890–900.
10. Guo, J.; Hou, Z.; Gao, J.; Zheng, X. Syngas production via combined oxy-CO_2 reforming of methane over Gd_2O_3-modified Ni/SiO_2 catalysts in a fluidized-bed reactor. *Fuel* **2008**, *87*, 1348–1354.
11. Fan, M.-S.; Abdullah, A. Z.; Bhatia, S. Catalytic technology for carbon dioxide reforming of methane to synthesis gas. *ChemCatChem.* **2009**, *1*, 192–208.
12. Xu, L.; Zhao, H.; Song, H.; Chou, L. Ordered mesoporous alumina supported nickel based catalysts for carbon dioxide reforming of methane. *Int. J. Hydrogen Energy* **2012**, *37*, 7497–7511.

13. Nandini, A.; Pant, K. K.; Dhingra, S. C. Kinetic study of the catalytic carbon dioxide reforming of methane to synthesis gas over Ni-K/CeO_2-Al_2O_3 catalyst. *Appl. Catal., A* **2006**, *308*, 119–127.
14. San-José-Alonso, D.; Juan-Juan, J.; Illán-Gómez, M. J.; Román-Martínez, M. C. Ni, Co and bimetallic Ni-Co catalysts for the dry reforming of methane. *Appl. Catal., A* **2009**, *371*, 54–59.
15. Wang, N.; Yu, X; Wang, Y.; Chu, W.; Liu, M. A comparison study on methane dry reforming with carbon dioxide over $LaNiO_3$ perovskite catalysts supported on mesoporous SBA-15, MCM-41 and silica carrier. *Catal. Today.* **2013**, *212*, 98–107.
16. Damyanova, S.; Pawelec, B.; Arishtirova, K.; Huerta, M. V. M.; Fierro, J. L. G. The effect of CeO_2 on the surface and catalytic properties of Pt/CeO_2-ZrO_2 catalysts for methane dry reforming. *Appl. Catal., B* **2009**, *89*, 149–159.
17. Xu, L.; Song, H.; Chou, L. Mesoporous nanocrystalline ceria-zirconia solid solutions supported nickel based catalysts for CO_2 reforming of CH_4. *Int. J. Hydrogen Energy* **2012**, *37*, 18001–18020.
18. Liu, C.-J.; Ye, J.; Jiang, J.; Pan, Y. Progresses in the preparation of coke resistant Ni-based catalyst for steam and CO_2 reforming of methane. *ChemCatChem.* **2011**, *3*, 529–541.
19. Song, C.; Pan, W. Tri-reforming of methane: A novel concept for catalytic production of industrially useful synthesis gas with desired H_2/CO ratios. *Catal. Today.* **2004**, *98*, 463–484.
20. Pan, W.; Zheng, J.; Song, C. Catalytic tri-reforming of methane using flue gas from fossil fuel-based power plants. *ACS Fuel Chemistry Division Preprints* **2002**, *47*, 262–264.
21. Zhang, Y.; Zhang, S.; Benson, T. A conceptual design by integrating dimethyl ether (DME) production with tri-reforming process for CO_2 emission reduction. *Fuel Process. Technol.* **2015**, *131*, 7–13.
22. Jahangiri, A.; Pahlavanzadeh, H.; Aghabozorg, H. Synthesis, characterization and catalytic study of Sm doped $LaNiO_3$ nanoparticles in reforming of methane with CO_2 and O_2. *Int. J. Hydrogen Energy* **2012**, *37*, 9977–9984.
23. Minutillo, M.; Perna, A. A novel approach for treatment of CO_2 from fossil fired power plants, Part A: The integrated systems ITRPP. *Int. J. Hydrogen Energy* **2009**, *34*, 4014–4020.
24. York, A. P. E.; Xiao, T.-C.; Green, M. L. H.; Claridge, J. B. Methane oxyforming for synthesis gas production. *Catal. Rev. Sci. Eng.* **2007**, *49*, 511–560.
25. Ozkara-Aydmoglu, S.; Aksoylu, A. E. CO_2 reforming of methane over Pt-Ni/Al_2O_3 catalysts: Effects of catalyst composition, and water and oxygen addition to the feed. *Int. J. Hydrogen Energy* **2011**, *36*, 2950–2959.
26. Izquierdo, U.; Barrio, V. L.; Requies, J.; Cambra, J. F.; Güemez, M. B.; Arias, P. L. Tri-reforming: A new biogas process for synthesis gas and hydrogen production. *Int. J. Hydrogen Energy* **2013**, *38*, 7623–7631.
27. Majewski, A. J.; Wood, J. Tri-reforming of methane over Ni@SiO_2 catalyst. *Int. J. Hydrogen Energy* **2014**, *39*, 12578–12585.

Publication Date (Web): September 11, 2015 | doi: 10.1021/bk-2015-1194.ch007

28. Halmanna, M.; Steinfeld, A. Fuel saving, carbon dioxide emission avoidance, and syngas production by tri-reforming of flue gases from coal- and gas-fired power stations, and by the carbothermic reduction of iron oxide. *Energy* **2006**, *31*, 3171–3185.
29. Ren, H.-P.; Hao, Q.-Q.; Wang, W.; Song, Y.-H.; Cheng, J.; Liu, Z.-W.; Liu, Z.-T.; Lu, J.; Hao, Z. High-performance Ni-SiO_2 for pressurized carbon dioxide reforming of methane. *Int. J. Hydrogen Energy* **2014**, *39*, 11592–11605.
30. Ren, H.-P.; Song, Y.-H.; Hao, Q.-Q.; Liu, Z.-W.; Wang, W.; Chen, J.-G.; Jiang, J.; Liu, Z.-T.; Hao, Z.; Lu, J. Highly active and stable Ni-SiO_2 prepared by a complex-decomposition method for pressurized carbon dioxide reforming of methane. *Ind. Eng. Chem. Res.* **2014**, *53*, 19077–19086.
31. Donazzi, A.; Beretta, A.; Groppi, G.; Forzatti, P. Catalytic partial oxidation of methane over a 4% Rh/α-Al_2O_3 catalyst. Part I: Kinetic study in annular reactor. *J. Catal.* **2008**, *255*, 241–258.
32. Donazzi, A.; Beretta, A.; Groppi, G.; Forzatti, P. Catalytic partial oxidation of methane over a 4% Rh/α-Al_2O_3 catalyst Part II: Role of CO_2 reforming. *J. Catal.* **2008**, *255*, 259–268.
33. Sun, D.; Li, X.; Ji, S.; Cao, L. Effect of O_2 and H_2O on the tri-reforming of the simulated biogas to syngas over Ni-based SBA-15 catalysts. *J. Nat. Gas Chem.* **2010**, *19*, 369–374.

Publication Date (Web): September 11, 2015 | doi: 10.1021/bk-2015-1194.ch007

Publication Date (Web): September 11, 2015 | doi: 10.1021/bk-2015-1194.ch008

Chapter 8

Ni Modified WC_x Catalysts for Methane Dry Reforming

Yali Zhang, Shaohua Zhang, Xiao Zhang, Jieshan Qiu, Limei Yu, and Chuan Shi*

Laboratory of Plasma Physical Chemistry, Dalian University of Technology, Dalian 116024, People's Republic of China
***E-mail: chuanshi@dlut.edu.cn. Tel: +86-411- 84986083.**

Ni-WC_x catalysts with different Ni/W molar ratios were prepared, and their catalytic activity for the DRM reaction at atmospheric pressure were investigated. The phase transformation of β-W_2C into α-WC was found to take place during the DRM reaction. By correlating the characterization results with activity results, Ni-WC_x was shown to be a typical bi-functional catalyst for the DRM reaction.

Introduction

Due to the increasing global demand for energy and concerns about environmental protection, the efficient production and use of clean energy has become a subject of great importance. Dry reforming of methane (DRM) is a possible route to produce syngas with high purity. One advantage of this process is that it uses CO_2, in addition to CH_4, as the feedstock, which is a potential method to utilize this greenhouse gas. The syngas produced has a H_2-to-CO ratio of 1, and the mixture can serve as the feedstock for a variety of downstream processes, such as methanol synthesis, Fischer-Tropsch synthesis or ammonia synthesis (*1–5*). In addition, it is also considered as a mean of converting solar and atomic energy into chemical energy, which is easier to store and transport (*6*, *7*).

Numerous catalysts that are based on noble or non-noble metals have been tested in the reaction (*8–11*). Among them, nickel catalysts are used industrially for both the methane steam and dry reforming reactions because of their fast turnover

In Advances in CO2 Capture, Sequestration, and Conversion; He, et al.;
ACS Symposium Series; American Chemical Society: Washington, DC, 2015.

rates, long term stability and low cost. However, they have a major drawback since nickel catalysts also catalyze carbon formation via methane decomposition and CO disproportionation, both of which lead to catalyst deactivation and plugging of the reformer tubes by carbon deposits (*12–16*).

Most of the Ni-based catalysts were supported on Al_2O_3, ZrO_2, SiO_2 or La_2O_3 components. In these catalysts, to improve the tolerance to carbon deposition, the following factors were investigated: high specific surface area, basicity, strong metal solid interaction and use of bimetallic and alloy components. Ni/Al_2O_3 and Ni/SiO_2 prepared by impregnation had high initial conversions but deactivated with time due to carbon deposition or sintering (*13*, *17*). Martha et al. (*18*) prepared a series of Ni catalysts supported on different ceramic oxides (Al_2O_3, CeO_2, La_2O_3, ZrO_2) by wet impregnation and investigated them for the CO_2 reforming of methane. They found that Ni/ZrO_2 showed excellent performance in the reaction, with high and stable catalytic activity. No deactivation was observed during the reaction period. A Ni/CeO_2 catalyst showed the highest methane conversion of all the prepared catalysts, but it evidenced signs of deactivation probably due to the presence of the "strong metal-support interaction" phenomenon. Zhang et al. (*19*) employed a Ni/La_2O_3 catalyst as well as conventional nickel-based catalysts, i.e., $Ni/\gamma\text{-}Al_2O_3$, $Ni/CaO/\gamma\text{-}Al_2O_3$, and Ni/CaO, for the DRM reaction. It was observed that, in contrast to conventional nickel-based catalysts, which exhibit continuous deactivation with time on stream, the rate of reaction over the Ni/La_2O_3 catalyst increased during the initial 2-5 h and then tended to be essentially constant with time on stream. Characterization of the catalyst indicates that the enhancement of the rate during the initial 2-5 h of reaction correlates well with increasing concentrations of $La_2O_2CO_3$ and formate species on the support. The synergetic effect between nickel and lanthanum species offer active and stable performance in the DRM reaction over the catalyst.

In recent years, transition metal carbides, especially tungsten and molybdenum carbide, have attracted much attention, owing to the fact that the carbides show catalytic properties similar to those of noble metals in a variety of reactions involving methane reforming (*20–22*). Despite the positive results and high thermal stability of these low-cost materials, the carbide catalysts deactivate rapidly due to oxidation by CO_2 at atmospheric pressure as pointed out by LaMont and Thomson (*23*). Studies of the dry reforming reaction mechanism over the group VI metal carbides have indicated that the dissociation of CO_2 is very fast, but CH_4 dissociation is rate limiting (*1*). This is in contrast to the findings for nickel catalysts (*24*). As previously reported by our group (*25–28*), Ni-modified Mo_2C catalysts exhibit higher activity and stability for CH_4/CO_2 reforming even at atmospheric pressure. The role of Ni is to dissociate CH_4, while the activation of CO_2 takes place on $\beta\text{-}Mo_2C$. By regulating the molar ratio of Ni and $\beta\text{-}Mo_2C$, there is a matching of CH_4 dissociation and CO_2 activation rates. Thus, a catalytic oxidation-recarburization cycle can be established and the deactivation due to carbon accumulation or $\beta\text{-}Mo_2C$ oxidation can be avoided.

α-WC and $\beta\text{-}Mo_2C$ show the same hexagonal crystal structure (*29*). Compared with α-WC, the oxidation of $\beta\text{-}Mo_2C$ by CO_2 takes place readily during dry reforming (*30*). This prompted us to investigate the catalytic behavior of tungsten carbide, including α-WC (hexagonal crystal structure) and $\beta\text{-}W_2C$

In Advances in CO2 Capture, Sequestration, and Conversion; He, et al.;
ACS Symposium Series; American Chemical Society: Washington, DC, 2015.

Publication Date (Web): September 11, 2015 | doi: 10.1021/bk-2015-1194.ch008

(hcp crystal structure) themselves, and metal-modified tungsten carbides for the DRM reaction. Shao et al. (*31*, *32*) reported that stable catalytic activity (80 h) was observed over bimetallic Co-W carbides at 850 °C and 3.4 bar. At 850 °C the bimetallic carbide catalyst Co_6W_6C was converted to a more stable form, containing Co, WC, and C, and this form was active and stable for the production of synthesis gas. The Co-WC catalysts were obtained by carburization of $Co(en)_3WO_4$ in CO_2-CO gas mixture. As noted by the authors, although Co_6W_6C was initially obtained, during the DRM reaction at 500-850 °C oxygen present on the surface converted Co_6W_6C into $CoWO_4$, which lead to its poor activity for the DRM reaction. However, when the reaction is performed at 850 °C or higher, the material goes through a transformation to an active phase containing Co, WC, and C as bulk phases. Once these phases are formed, the material is active, selective and stable even at lower temperatures.

In the present paper, α-WC and β-W_2C as well as Ni-modified tungsten carbides with different Ni/W molar ratios were prepared, and their catalytic activity for the DRM reaction was investigated, firstly at atmospheric pressure. The phase transformation of β-W_2C into α-WC was found to take place during the DRM reaction, and carbides with different particle sizes exhibited different abilities for CO_2 activation. Nickel was found to be stabilized in form of $Ni_{17}W_3$, which was formed during the carbonation of $NiWO_x$ in CH_4/H_2. Both of the above mentioned properties of Ni-modified WC_x rendered it an active and stable catalyst for the DRM reaction.

Publication Date (Web): September 11, 2015 | doi: 10.1021/bk-2015-1194.ch008

Experimental

Catalysts Preparation

We prepared the $NiWO_x$ precursor by stirring an aqueous solution of $(NH_4)_6H_2W_{12}O_{40}\cdot xH_2O$ and $Ni(NO_3)_2\cdot 6H_2O$ at 80 °C for 4 h. The as-obtained $NiWO_x$ was filtered out and dried at 110 °C for 12 h and calcined at 550 °C for 4 h. Then $NiWO_x$ was carburized in CH_4/H_2 (20 vol% CH_4) to Ni-WC_x following a series of temperature-programmed processes: the temperature was raised from room temperature (RT) to 300 °C in a span of 1 h, then from 300 °C to 700 °C at a rate of 1 °C/min, and subsequently kept at 700 °C for 2 h. The as-obtained Ni-WC_x was cooled down to RT in flowing CH_4/H_2 and passivated in a mixture of 1%O_2/Ar for 12 h. In a similar manner, β-W_2C was prepared by WO_3 carburization with the same temperature-programmed processes, but kept at 700 °C for 1 h. In the case of α-WC, the final temperature was 900 °C and was maintained for 2 h.

Catalyst Characterization

X-ray powder diffraction (XRD) analysis was conducted using an XRD-6000 (Shimadzu) equipment with Cu Kα radiation (λ= 0.1542 nm), operating at 40 kV and 30 mA; phase identification was achieved through comparison of XRD patterns to those of "Joint Committee on Powder Diffraction Standards (JCPDS)". Two types of scan were used to record the XRD spectra, hereby designated as

In Advances in CO2 Capture, Sequestration, and Conversion; He, et al.;
ACS Symposium Series; American Chemical Society: Washington, DC, 2015.

normal scan (2θ 6°/min, step size 2θ = 0.04°) and slow scan (2θ 0.25°/min, step size 2θ = 0.01°).

Carbon dioxide temperature-programmed oxidation (CO_2-TPO) studies were performed using a mass spectrometer (OmniStar™ Pfeiffer Vacuum, Germany). With the sample securely placed in a quartz tubular reactor, CO_2-TPO was carried out by introducing 10% CO_2/Ar (with a total flow rate of 100 ml/min) into the system while the sample temperature was raised from RT to a desired temperature at a rate of 10 °C/min. The signal intensities of CO (m/z = 28) and CO_2 (m/z = 44) were monitored.

Methane temperature-programmed surface reduction (CH_4-TPSR) studies were performed using a mass spectrometer (OmniStar™ Pfeiffer Vacuum, Germany). With the sample securely placed in a quartz tubular reactor, CH_4-TPSR profile was carried out by introducing 10% CH_4/Ar (with a total flow rate of 100 ml/min) into the system while the sample temperature was raised from RT to a desired temperature at a rate of 10 °C/min. The signal intensities of CH_4 (m/z = 15), H_2 (m/z = 2), H_2O (m/z = 18), CO (m/z = 28), and CO_2 (m/z = 44) were monitored.

Publication Date (Web): September 11, 2015 | doi: 10.1021/bk-2015-1194.ch008

Catalyst Evaluation

Catalytic tests were performed in a quartz continuous flow fixed-bed micro reactor. In each experiment, 0.2 g catalyst was packed in the reactor (secured with quartz wool) with a thermocouple inserted into the center of the catalyst bed. Before the reaction, the catalyst was activated with a hydrogen flow of 50 ml/min at 500 °C for 60 min. Next, a CH_4 and CO_2 mixture of 1:1 molar ratio was introduced into the catalyst bed at a flow rate of 30 or 60 ml/min (WHSV= 18000 or 36000 ml/g/h). The gas products were analyzed via online gas chromatography every 60 min to test the stability of the catalyst samples. Catalysts were tested under the flow of a calibrated mixed gas that comprised CH_4, CO_2 and N_2 (internal standard).

With the online GC measurements of outlet gases from the reactor (N_2, CH_4, CO_2, H_2 and CO), the conversions of CH_4 and CO_2 and the selectivity of H_2 can be determined with the following equations:

Conversion:

$$X_{CH_4} = \frac{F^{in}_{CH_4} - F^{out}_{CH_4}}{F^{in}_{CH_4}} \quad (1)$$

$$X_{CO_2} = \frac{F^{in}_{CO_2} - F^{out}_{CO_2}}{F^{in}_{CO_2}} \quad (2)$$

Selectivity of H_2:

$$S_{H_2} = \frac{F^{out}_{H_2} \cdot 2}{F^{in}_{CH_4} \cdot X_{CH_4} \cdot 4} = F_{N_2} \cdot A_{H_2} \cdot f_{H_2} / F^{in}_{CH_4} \cdot X_{CH_4} \quad (3)$$

In Advances in CO2 Capture, Sequestration, and Conversion; He, et al.;
ACS Symposium Series; American Chemical Society: Washington, DC, 2015.

Results

Physicochemical Properties of the Catalysts

Figure 1A shows the XRD patterns of the as-prepared α-WC, β-W_2C and Ni-WC_x catalysts with different Ni/W molar ratios. The diffraction peaks at 35.7°, 48.3°, 31.5°, 64.1° can be assigned to α-WC (hex crystal structure), while those at 39.6°, 38.1°, 34.5°, 61.9° assigned to β-W_2C (hcp crystal structure). Only β-W_2C could be observed in the Ni-WC_x catalyst when the Ni/W molar ratio is 0.03. The diffraction peaks of α-WC appeared until the ratio was increased to 0.16. It is noted that α-WC is obtained by carburization of WO_3 at temperatures as high as 900 °C. However, in the presence of nickel, the temperature for carburization of WO_x into WC_x decreases to 700 °C. It is apparent that the presence of nickel promotes the carburization process. It is noted that β-W_2C existed in all the Ni-modified tungsten carbide samples, α-WC being the major carbide phase except for the Ni-WC_x (Ni/W=0.03) catalyst. In addition, strong diffraction peaks due to $Ni_{17}W_3$ (2θ = 43.7°, 50.9°) are observed for the Ni-WC_x catalysts as shown in Figure 1B. As the Ni/W molar ratio increases, the $Ni_{17}W_3$ diffraction peaks become more intense, suggesting that more and more $Ni_{17}W_3$ is being formed in the bimetallic catalysts. However, metallic Ni (2θ = 44.4°, 51.8°) segregated when the content of nickel was high enough, as clearly seen for the Ni-WC_x samples with Ni/W molar ratios of 4 and 6.

The SEM patterns of the Ni-WC_x catalysts with different Ni/W molar ratios are shown in Figure 2. The α-WC sample is composed of rectangular particles. The morphology of Ni-WC_x (Ni/W=0.33) catalyst is essentially similar to that of α-WC, but the average particle size is decreased. In contrast, the Ni-WC_x (Ni/W=6) catalyst exhibites a quite different morphology from the others. Significant agglomeration is evident, which can be ascribed to the increased Ni content which is present as $Ni_{17}W_3$ and Ni, as detected in the XRD pattern (Figure 1B). Moreover, due to the increase of the Ni/W molar ratio to 6, there is less WC_x formation. Therefore, the regular particles due to the carbides could not be observed.

Publication Date (Web): September 11, 2015 | doi: 10.1021/bk-2015-1194.ch008

In Advances in CO2 Capture, Sequestration, and Conversion; He, et al.;
ACS Symposium Series; American Chemical Society: Washington, DC, 2015.

Publication Date (Web): September 11, 2015 | doi: 10.1021/bk-2015-1194.ch008

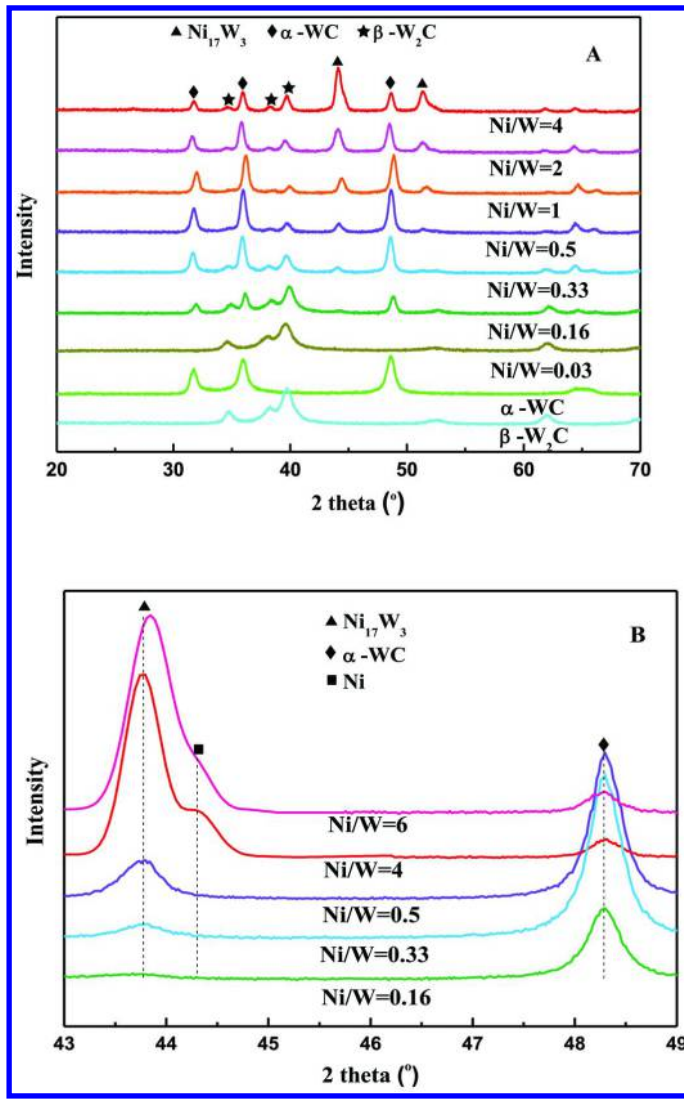

Figure 1. XRD patterns of the as-prepared α-WC, β-W_2C and Ni-WC_x catalysts with different Ni/W molar ratios: (A) normal scan of 6°/min, (B) slow scan of 0.25°/min.

In Advances in CO2 Capture, Sequestration, and Conversion; He, et al.;
ACS Symposium Series; American Chemical Society: Washington, DC, 2015.

Publication Date (Web): September 11, 2015 | doi: 10.1021/bk-2015-1194.ch008

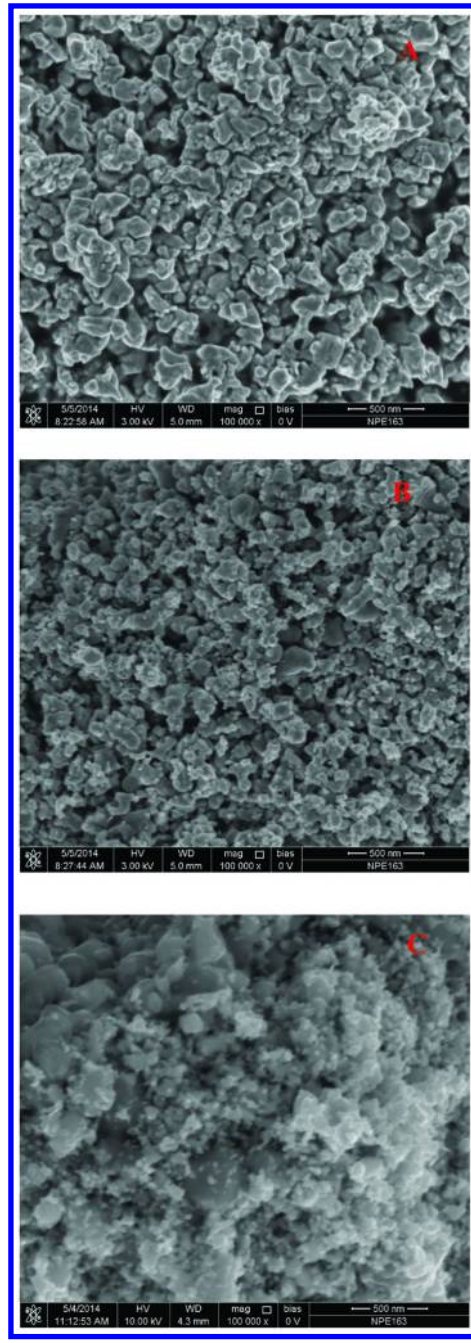

Figure 2. SEM images of Ni-WC_x catalysts with different Ni/W molar ratios: (A) α-WC, (B) Ni/W=0.33, (C) Ni/W=6.

Publication Date (Web): September 11, 2015 | doi: 10.1021/bk-2015-1194.ch008

Surface Reactions of CH_4 and CO_2 over Ni-WC_x Catalysts

Figure 3 displays the results of CH_4-TPSR performed over the Ni-WC_x catalysts with different Ni/W molar ratios in a gas stream of 10% CH_4/Ar. The CH_4 consumption peaks at temperatures around 500 °C, which are accompanied by the formation of H_2O, CO and CO_2, are the result of CH_4 interacting with the oxygen species that are formed during passivation (*27*). However, this is not observed over the Ni-WC_x (Ni/W=6) sample, indicating the disappearance of passivation layer of the carbide. This suggests that the surface of the carbide might be covered by Ni and $Ni_{17}W_3$ due to the high Ni/W ratio of 6. The consumption of CH_4 at higher temperatures, accompanied by the formation of H_2, can be ascribed to CH_4 dissociation into C* and H_2 (g). In the case of Ni-WC_x (Ni/W=0.5), the start of CH_4 dissociation is observed above 650 °C. However, with the increase of Ni/W molar ratio, the "light-off" temperature for CH_4 dissociation increases to 675 °C for Ni-WC_x (Ni/W=4) and to 705 °C for Ni-WC_x (Ni/W=6). Moreover, it is noted that the degree of CH_4 dissociation is greatly depressed over Ni-WC_x (Ni/W=6), which should be related to the increasing amount and particle size of $Ni_{17}W_3$ and Ni. This is in accordance with literature reports that the methane decomposition rate decreases with enlargment of the Ni particle size (*33*).

Figure 4 displays the CO_2-TPO profiles of the Ni-WC_x catalysts with different Ni/W molar ratios, measured in a gas stream of 10% CO_2/Ar. The insets of Figure 4 show the XRD patterns of the Ni-WC_x catalysts after 10 min exposure to CO_2 (10% CO_2/Ar) at the specified temperature. In the case of Ni-WC_x (Ni/W=0.5), two peaks are observed, one at 650 °C and the other at 850 °C. For the Ni-WC_x (Ni/W=4) sample the peaks are observed at 680 °C and 805 °C, while for Ni-WC_x (Ni/W=6) the peaks occur at 685 °C and 790 °C. According to the XRD patterns of Ni-WC_x (Ni/W=0.5) (inset of Figure 4A), tungsten carbide still remained after exposure to CO_2 at 650 °C. For the catalyst exposed to CO_2 atmosphere at 850 °C, diffraction lines corresponding to WO_2 (2θ = 25.9°, 37.0°, 52.9°, 53.9°) are detected. In other words, bulk oxidation of tungsten carbide does not occur at 850 °C, and oxidation corresponding to CO_2 consumption at 650 °C is restricted to the surface of the tungsten carbide; this may be due to the reaction between CO_2 and deposited carbon formed during carbonization. Similarly, as for Ni-WC_x (Ni/W=4) and Ni-WC_x (Ni/W=6), the CO_2 consumption peaks at lower temperature are due to the oxidation of surface carbon while the other is due to bulk oxidation of the tungsten carbide by CO_2. It should be noted that the temperature for bulk oxidation decreases with the increase of Ni/W molar ratio. As evidenced by SEM measurements, the particle size of tungsten carbide decreases with the increase of Ni/W molar ratio. Therefore, it is reasonable to conclude that when the particle size of the carbide decreases, it is more easily oxidized. This is in accordance with literature reports that both tungsten and molybdenum carbides show a decrease in oxidation of the carbide surface upon increase of the particle size (*34*).

In Advances in CO2 Capture, Sequestration, and Conversion; He, et al.;
ACS Symposium Series; American Chemical Society: Washington, DC, 2015.

Publication Date (Web): September 11, 2015 | doi: 10.1021/bk-2015-1194.ch008

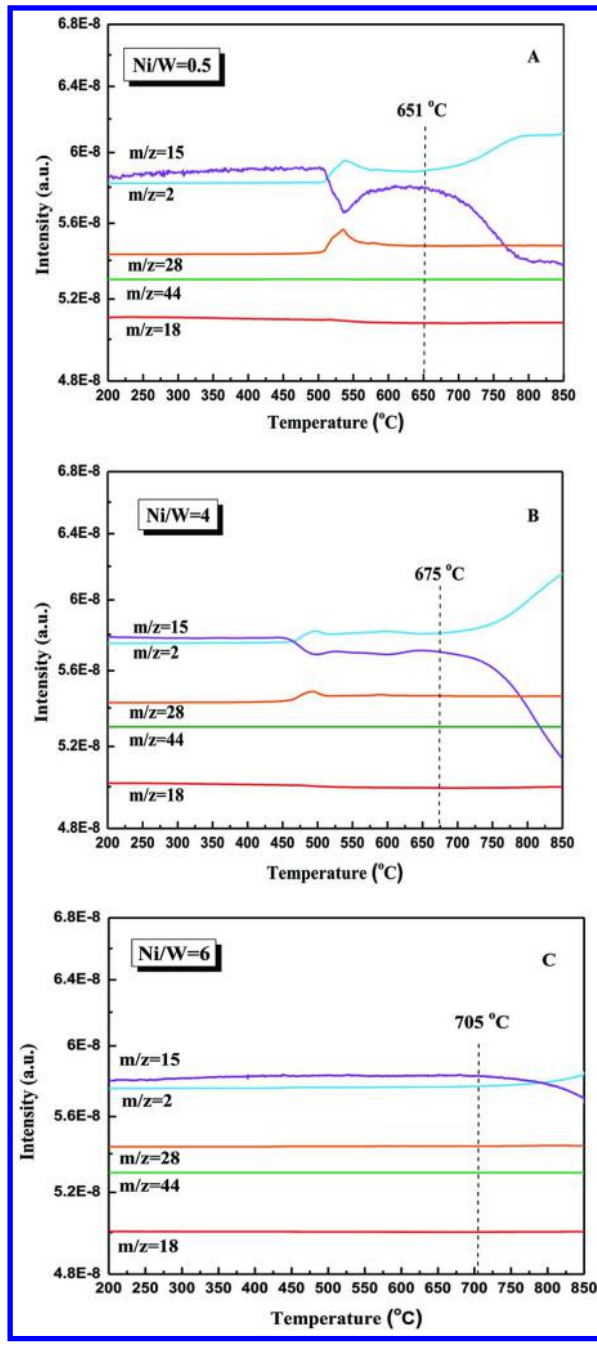

Figure 3. CH_4-TPSR profiles of Ni-WC_x catalysts with different Ni/W molar ratios: (A) Ni/W=0.5, (B) Ni/W=4, (C) Ni/W=6.

Publication Date (Web): September 11, 2015 | doi: 10.1021/bk-2015-1194.ch008

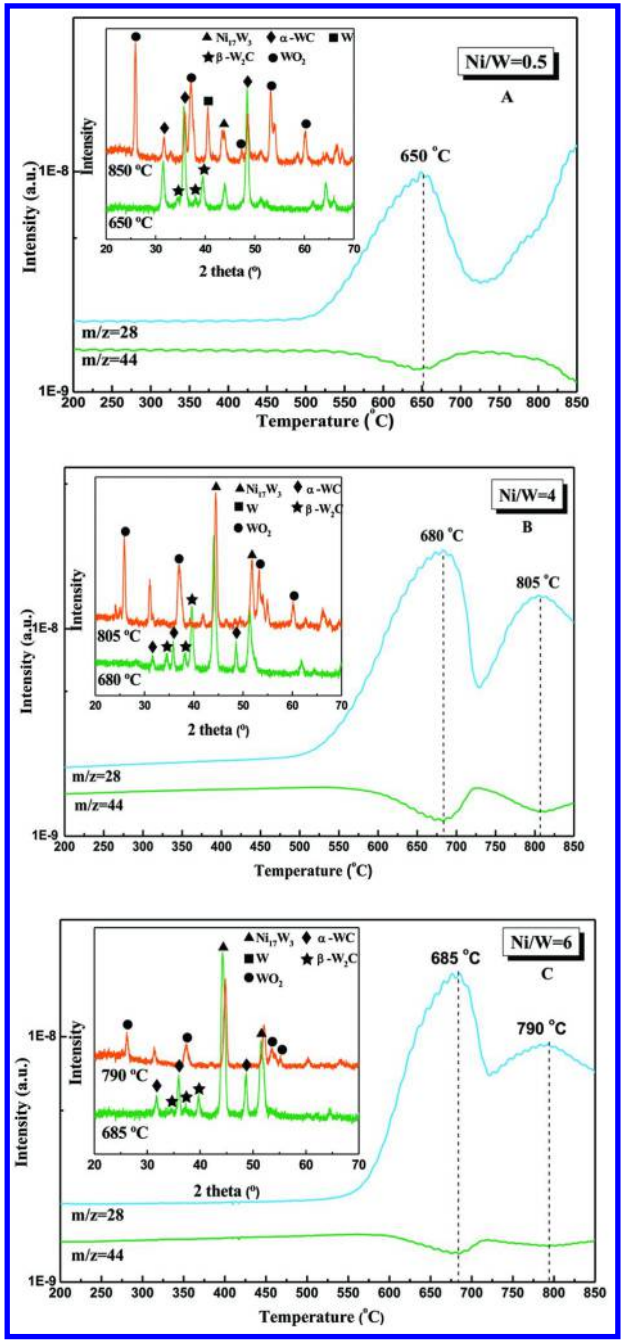

Figure 4. CO_2-TPO profiles of Ni-WC_x catalysts with different Ni/W molar ratios: (A) Ni/W=0.5, (B) Ni/W=4, (C) Ni/W=6.

Activity Measurement

The activity of Ni-WC_x catalysts with different Ni/W ratios is shown in Figure 5. It is worth noting that there is no DRM activity over the pure carbides, no matter whether it is α-WC or β-W_2C, under similar reaction conditions. Due to the low nickel content, the conversions of CH_4 are respectively 2% and 11% over the Ni-WC_x (Ni/W=0.03) and Ni-WC_x (Ni/W=0.16) catalysts. However, when the Ni/W molar ratio is increased the catalysts present very high activity, and the Ni-WC_x catalysts exhibit excellent performance over a wide range of Ni/W molar ratios from 0.33 to 6. The selectivity to H_2 is around 68% and the H_2/CO ratio is about 0.6. The results indicate that in wide Ni/W molar ratios from 0.33 to 6, the catalysts exhibit very similar initial activities for the DRM reaction.

The performance of the Ni-WC_x catalysts (Ni/W=0.5, 4, 6) as a function of time on stream is shown in Figure 6. The Ni-WC_x catalysts with Ni/W molar ratios of 0.5 and 4 show the most stable activity during the DRM reaction. On the other hand, a rapid decline of the CH_4 and CO_2 conversion was observed for the Ni-WC_x (Ni/W=6) catalyst.

Publication Date (Web): September 11, 2015 | doi: 10.1021/bk-2015-1194.ch008

In Advances in CO2 Capture, Sequestration, and Conversion; He, et al.;
ACS Symposium Series; American Chemical Society: Washington, DC, 2015.

Publication Date (Web): September 11, 2015 | doi: 10.1021/bk-2015-1194.ch008

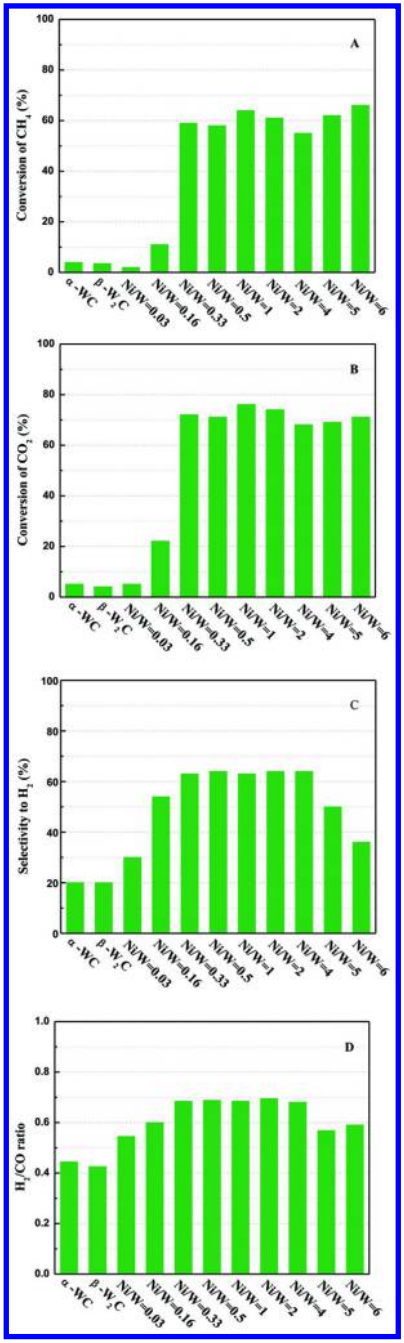

Figure 5. Catalytic activity of Ni-WC_x catalysts with different Ni/W molar ratios: (A) conversion of CH_4, (B) conversion of CO_2, (C) selectivity to H_2, (D) H_2/CO ratio (CH_4/CO_2=1, WHSV=18000 ml/g/h, 800°C, atmospheric pressure).

Publication Date (Web): September 11, 2015 | doi: 10.1021/bk-2015-1194.ch008

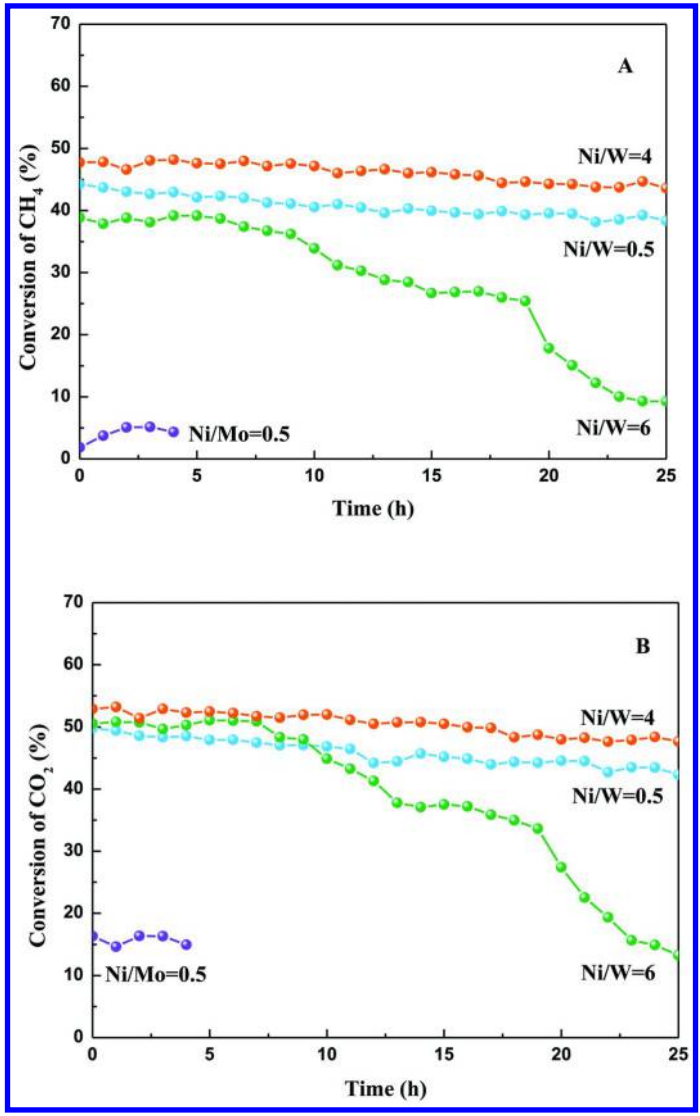

Figure 6. Effect of nickel on catalyst stability: (A) conversion of CH_4; (B) conversion of CO_2 (CH_4/CO_2=1; WHSV=36000 ml/g/h; 800°C, atmospheric pressure).

Publication Date (Web): September 11, 2015 | doi: 10.1021/bk-2015-1194.ch008

Characterization of Used Ni-WC_x Catalysts

Figure 7 shows the XRD patterns of used samples with different Ni/W molar ratios after 10 h on stream. The diffraction peaks at 35.7°, 48.3°, 31.5°, 64.1° can be assigned to α-WC, while those at 44.4°, 51.8° are assigned to $Ni_{17}W_3$. It is worth noting that the diffraction peaks of β-W_2C disappeared, and tungsten only exists as the α-WC phase.

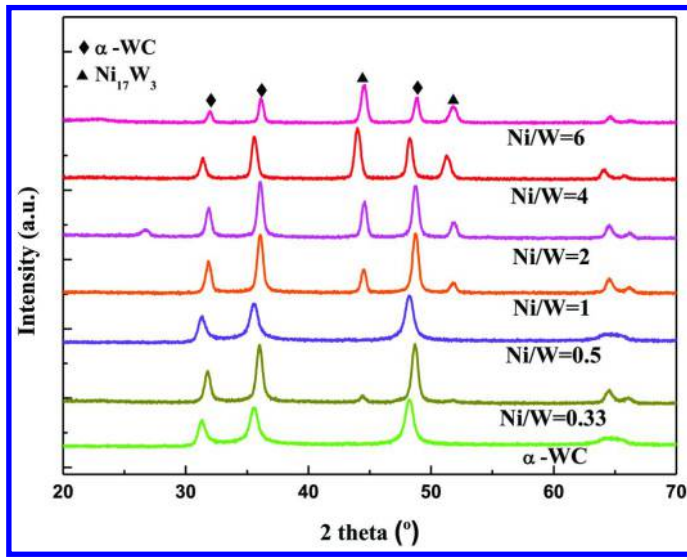

Figure 7. XRD patterns of used samples with different Ni/W molar ratios after 10 h on stream.

Figure 8A displays the XRD patterns of used samples with different Ni/W molar ratios after the stability test. The peaks corresponding to $Ni_{17}W_3$ and α-WC are still detectable. In addition, for the Ni-WC_x (Ni/W=6) catalyst there are new peaks at 25.9°, 37.0°, 52.9°, 53.9° that are attributable to WO_2, which indicates that the deactivation of the catalyst is a result of tungsten carbide bulk oxidation by CO_2. Moreover, the diffraction peaks of Ni are no longer present, and the diffraction peaks of $Ni_{17}W_3$ are shifted to a higher angle, as seen in Figure 8B; this may be a consequence of tungsten segregating to form WO_2.

Publication Date (Web): September 11, 2015 | doi: 10.1021/bk-2015-1194.ch008

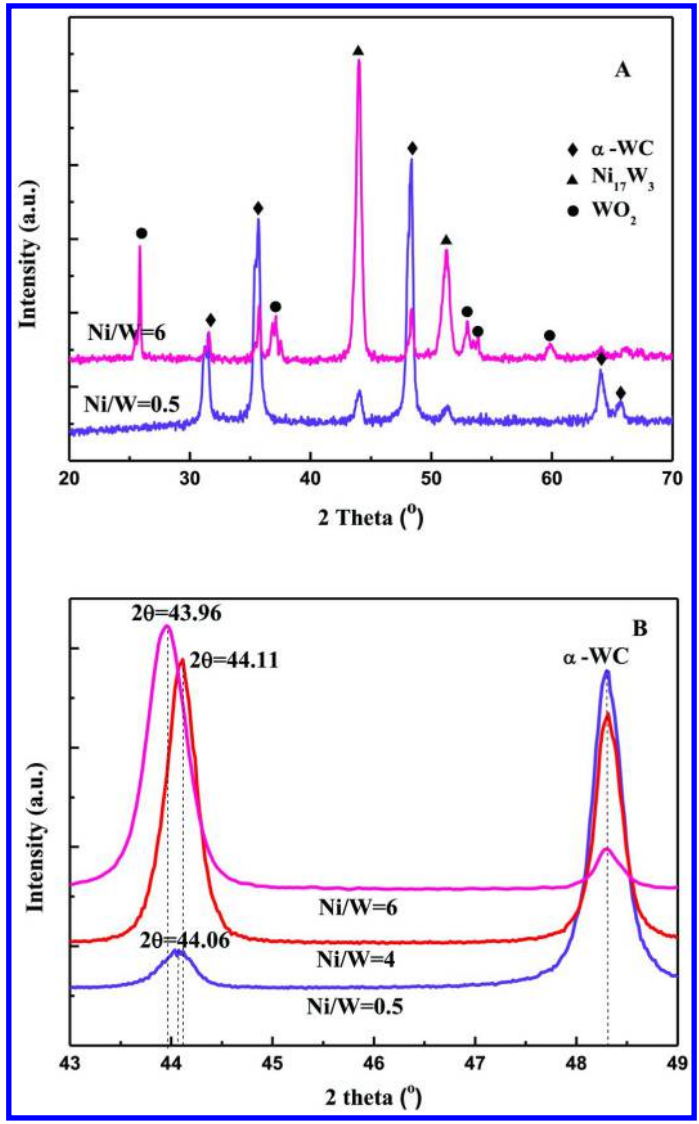

Figure 8. XRD patterns of used samples with different Ni/W molar ratios after 25 h on stream: (A) normal scan of 6°/min, (B) slow scan of 0.25°/min.

Correlations between Catalyst Microstructure and Catalytic Activity

For all of the as-prepared Ni-WC_x samples, no matter which Ni/W molar ratios is employed, the presence of mixed phases of α-WC with β-W_2C is clearly shown by XRD (Figure 1A). However, after the DRM reaction performed at 800 °C for 10 h, all of the samples display diffraction peaks ascribed to α-WC, while β-W_2C is no longer detected. These results indicate that β-W_2C was transformed into α-WC during the reaction. This is consistent with a previous report that the oxidation

In Advances in CO2 Capture, Sequestration, and Conversion; He, et al.;
ACS Symposium Series; American Chemical Society: Washington, DC, 2015.

of β-W_2C by CO_2 readily occurred during dry reforming (*1*). We propose that the transformation of β-W_2C into α-WC is due to the oxidation of β-W_2C by CO_2 during the DRM reaction, based on the following steps:

$$\beta\text{-}W_2C+3CO_2 \rightarrow WO_2+4CO+W \quad (4)$$

$$WO_2+CH_4 \rightarrow \alpha\text{-}WC+2H_2O \quad (5)$$

$$2WO_2+CH_4 \rightarrow \beta\text{-}W_2C+4H_2O \quad (6)$$

$$W+CH_4 \rightarrow \alpha\text{-}WC+2H_2 \quad (7)$$

In addition, it is found that the deactivation of the Ni-WC_x (Ni/W=6) sample is due to oxidation of the carbide into the oxide by CO_2, instead of coke deposition due to the higher Ni loading. According to the results of SEM, the more nickel the catalyst contained, the smaller the particle size of the carbide present. From the CO_2-TPO profiles, we can see that with the increase of the Ni/W molar ratios, the more easily CO_2 is activated in dry reforming. Hence, the Ni-WC_x (Ni/W=6) catalyst is deactivated due to oxidation, which is in accord with the results of XRD analysis.

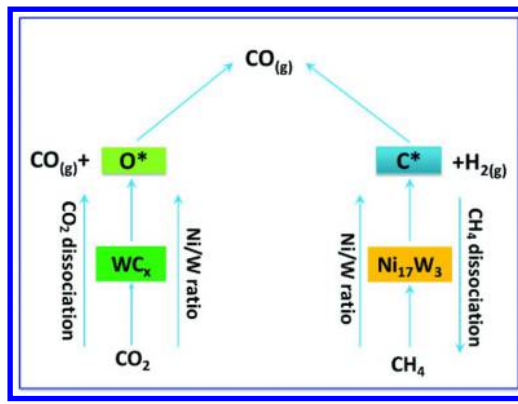

Scheme 1. Catalytic oxidation-recarburization cycle over Ni-WC_x catalyst.

Based on the results, we propose that Ni-WC_x is a bi-functional catalyst for the DRM reaction, as illustrated in Scheme 1. The dissociation of CH_4 is catalyzed by nickel, which is stabilized in form of $Ni_{17}W_3$ alloy in the present study. Simultaneously, the activation of CO_2 takes place on WC_x. With the increase of Ni/W molar ratio, the rate of CH_4 dissociation decreases, as clearly shown by CH_4-TPSR (Figure 3), while the CO_2 dissociation rate was evidently accelerated as indicated by CO_2-TPO (Figure 4). This results in the deactivation of the Ni-WC_x (Ni/W=6) catalyst at long reaction times, although the initial activity was similar to the other samples (Ni/W molar ratios from 0.33 to 5).

Publication Date (Web): September 11, 2015 | doi: 10.1021/bk-2015-1194.ch008

Conclusions

Ni-WC_x catalysts with Ni/W molar ratios ranging from 0.33 to 6 were synthesized by carburization of the corresponding oxide precursors at 700 °C. The presence of Ni was shown to accelerate the carburization and lower the temperature for carbide formation. The phase transformation of β-W_2C into α-WC took place during the DRM reaction due to the oxidation of β-W_2C by CO_2. Nickel was stabilized in the form of $Ni_{17}W_3$, which was formed during carburization of the oxide precursor in 20% CH_4/H_2. Ni-WC_x catalysts are shown to be a typical bi-functional catalyst for the DRM reaction. The dissociation of CH_4 is catalyzed by $Ni_{17}W_3$, while CO_2 activation takes place on the WC_x, which renders Ni-WC_x catalysts very active for the DRM reaction at atmospheric pressure.

Publication Date (Web): September 11, 2015 | doi: 10.1021/bk-2015-1194.ch008

Acknowledgments

We thank the National Natural Science Foundation of China for funding (Nos. 21073024 and 21373037).

References

1. Claridge, J. B.; York, A. P. E.; Brungs, A. J.; Marquez-Alvarez, C.; Sloan, J.; Tsang, S. C.; Green, M. L. H. New catalysts for the conversion of methane to synthesis gas: Molybdenum and tungsten carbide. *J. Catal.* **1998**, *180*, 85–100.
2. Wang, S. B.; Lu, G. Q. M. Effects of promoters on catalytic activity and carbon deposition of Ni/gamma-Al_2O_3 catalysts in CO_2 reforming of CH_4. *J. Chem. Technol. Biotechnol.* **2000**, *75*, 589–595.
3. Cheng, Z. X.; Wu, Q. L.; Li, J. L.; Zhu, Q. M. Effects of promoters and preparation procedures on reforming of methane with carbon dioxide over Ni/Al_2O_3 catalyst. *Catal. Today* **1996**, *30*, 147–155.
4. Khodakov, A. Y.; Chu, W.; Fongarland, P. Advances in the development of novel cobalt Fischer-Tropsch catalysts for synthesis of long-chain hydrocarbons and clean fuels. *Chem. Rev.* **2007**, *107*, 1692–744.
5. Subramani, V.; Gangwal, S. K. A review of recent literature to search for an efficient catalytic process for the conversion of syngas to ethanol. *Energy & Fuels* **2008**, *22*, 814–839.
6. Cui, Y. H.; Zhang, H. D.; Xu, H. Y.; Li, W. Z. Kinetic study of the catalytic reforming of CH_4 with CO_2 to syngas over Ni/alpha-Al_2O_3 catalyst: The effect of temperature on the reforming mechanism. *Appl. Catal., A* **2007**, *318*, 79–88.
7. Tian, L.; Zhao, X. H.; Liu, B. S.; Zhang, W. D. Preparation of an industrial Ni-based catalyst and investigation on CH_4/CO_2 reforming to syngas. *Energy Fuels* **2009**, *23*, 607–612.
8. Frusteri, F.; Arena, F.; Calogero, G.; Torre, T.; Parmaliana, A. Potassium-enhanced stability of Ni/MgO catalysts in the dry-reforming of methane. *Catal. Commun.* **2001**, *2*, 49–56.

9. Yang, M.; Papp, H. CO_2 reforming of methane to syngas over highly active and stable Pt/MgO catalysts. *Catal. Today* **2006**, *115*, 199–204.
10. Damyanova, S.; Pawelec, B.; Arishtirova, K.; Fierro, J. L. G.; Sener, C.; Dogu, T. MCM-41 supported PdNi catalysts for dry reforming of methane. *Appl. Catal., B* **2009**, *92*, 250–261.
11. Wang, H. Y.; Au, C. T. Carbon dioxide reforming of methane to syngas over SiO_2-supported rhodium catalysts. *Appl. Catal., A* **1997**, *155*, 239–252.
12. Bitter, J. H.; Seshan, K.; Lercher, J. A. Deactivation and coke accumulation during CO_2/CH_4 reforming over Pt catalysts. *J. Catal.* **1999**, *183*, 336–343.
13. Therdthianwong, S.; Siangchin, C.; Therdthianwong, A. Improvement of coke resistance of Ni/Al_2O_3 catalyst in CH_4/CO_2 reforming by ZrO_2 addition. *Fuel Process. Technol.* **2008**, *89*, 160–168.
14. Bradford, M. C. J.; Vannice, M. A. Catalytic reforming of methane with carbon dioxide over nickel catalysts .1. Catalyst characterization and activity. *Appl. Catal., A* **1996**, *142*, 73–96.
15. Laosiripojana, N.; Sutthisripok, W.; Assabumrungrat, S. Synthesis gas production from dry reforming of methane over CeO_2 doped Ni/Al_2O_3: Influence of the doping ceria on the resistance toward carbon formation. *Chem. Eng. J.* **2005**, *112*, 13–22.
16. Takanabe, K.; Nagaoka, K.; Aika, K. Improved resistance against coke deposition of titania supported cobalt and nickel bimetallic catalysts for carbon dioxide reforming of methane. *Catal. Lett.* **2005**, *102*, 153–157.
17. Pan, Y.-X.; Liu, C.-J.; Shi, P. Preparation and characterization of coke resistant Ni/SiO_2 catalyst for carbon dioxide reforming of methane. *J. Power Sources* **2008**, *176*, 46–53.
18. Barroso-Quiroga, M. M.; Castro-Luna, A. E. Catalytic activity and effect of modifiers on Ni-based catalysts for the dry reforming of methane. *Int. J. Hydrogen Energy* **2010**, *35*, 6052–6056.
19. Zhang, Z. L.; Verykios, X. E.; MacDonald, S. M.; Affrossman, S. Comparative study of carbon dioxide reforming of methane to synthesis gas over Ni/La_2O_3 and conventional nickel-based catalysts. *J. Phys. Chem.* **1996**, *100*, 744–754.
20. Hwu, H. H.; Chen, J. G. Surface chemistry of transition metal carbides. *Chem Rev* **2005**, *105*, 185–212.
21. Levy, R. B.; Boudart, M. Platinum-like behavior of tungsten carbide in surface catalysis. *Science* **1973**, *181*, 547–9.
22. York, A. P. E.; Claridge, J. B.; Brungs, A. J.; Tsang, S. C.; Green, M. L. H. Molybdenum and tungsten carbides as catalysts for the conversion of methane to synthesis gas using stoichiometric feedstocks. *Chem. Commun.* **1997**, 39–40.
23. LaMont, D. C.; Thomson, W. J. Dry reforming kinetics over a bulk molybdenum carbide catalyst. *Chem. Eng. Sci.* **2005**, *60*, 3553–3559.
24. York, A. P. E.; Suhartanto, T.; Green, M. L. H. Influence of Molybdenum and Tungsten Dopants on Nickel Catalysts for the Dry Reforming of Methane with Carbon Dioxide to Synthesis Gas. In *Natural Gas Conversion V*; Parmaliana, A.; Sanfilippo, D.; Frusteri, F.; Vaccari, A.; Arena, F., Eds.; 1998; Vol. 119, pp 777−782.

In Advances in CO2 Capture, Sequestration, and Conversion; He, et al.;
ACS Symposium Series; American Chemical Society: Washington, DC, 2015.

Publication Date (Web): September 11, 2015 | doi: 10.1021/bk-2015-1194.ch008

25. Zhang, A. J.; Zhu, A. M.; Chen, B. B.; Zhang, S. H.; Au, C. T.; Shi, C. A. In-situ synthesis of nickel modified molybdenum carbide catalyst for dry reforming of methane. *Catal. Commun.* **2011**, *12*, 803–807.
26. Shi, C.; Zhang, S. H.; Li, X. S.; Zhang, A. J.; Shi, M.; Zhu, Y. J.; Qiu, J. S.; Au, C. T. Synergism in $NiMoO_x$ precursors essential for CH_4/CO_2 dry reforming. *Catal. Today* **2014**, *233*, 46–52.
27. Guo, J.; Zhang, A. J.; Zhu, A. M.; Xu, Y.; Au, C. T.; Shi, C. A carbide catalyst effective for the dry reforming of methane at atmospheric pressure. *Advances in CO_2 Conversion and Utilization* **2010**, *1056*, 181–196.
28. Shi, C.; Zhang, A.; Li, X.; Zhang, S.; Zhu, A.; Ma, Y.; Au, C. Ni-modified Mo_2C catalysts for methane dry reforming. *Appl. Catal., A* **2012**, *431*, 164–170.
29. Brungs, A. J.; York, A. P. E.; Green, M. L. H. Comparison of the group V and VI transition metal carbides for methane dry reforming and thermodynamic prediction of their relative stabilities. *Catal. Lett.* **1999**, *57*, 65–69.
30. Shuichi Naito, M. T. Marked difference of catalytic behavior by preparation methods in CH_4 reforming with CO_2 over Mo_2C and WC catalysts. *Stud. Surf. Sci. Catal.* **2002**.
31. Shao, H. Effect of temperature on structure and performance of in-house cobalt-tungsten carbide catalyst for dry reforming of methane. *Ind. Eng. Chem. Res* **2005**, *44*, 4914–4921.
32. Shao, H.; Kugler, E. L.; Dadyburjor, D. B.; Rykov, S. A.; Chen, J. G. Correlating NEXAFS characterization of Co-W and Ni-W bimetallic carbide catalysts with reactivity for dry reforming of methane. *Appl. Catal., A* **2009**, *356*, 18–22.
33. Hou, Z.; Gao, J.; Guo, J.; Liang, D.; Lou, H.; Zheng, X. Deactivation of Ni catalysts during methane autothermal reforming with CO_2 and O_2 in a fluidized-bed reactor. *J. Catal.* **2007**, *250*, 331–341.
34. Stellwagen, D. R.; Bitter, J. H. Structure−performance relations of molybdenum- and tungsten carbide catalysts for deoxygenation. *Green Chem.* **2015**, *17*, 582–593.

Publication Date (Web): September 11, 2015 | doi: 10.1021/bk-2015-1194.ch008

Publication Date (Web): September 11, 2015 | doi: 10.1021/bk-2015-1194.ch009

Chapter 9

Selective Hydrogenation in Supercritical Carbon Dioxide Using Metal Supported Heterogeneous Catalyst

Maya Chatterjee, Takayuki Ishizaka, and Hajima Kawanami*

Micro Flow Chemistry Group,
Research Institute for Chemical Process Technology,
AIST Tohoku, 4-2-1 Nigatake, Miyagino-ku,
Sendai 983-8551, Japan
***Tel: 81 22 237 5213. Fax: 81 22 237 5388.**
E-mail: h-kawanami@aist.go.jp.

The use of supercritical carbon dioxide as a reaction medium was tested on the selective hydrogenation of different functional groups using heterogeneous catalyst. Supercritical carbon dioxide offers opportunity not only to replace conventional hazardous organic solvents but also it could improve catalytic activity and selectivity, thus, produces least waste. In this chapter, we highlighted various examples of the selective hydrogenation of different functional groups such as −C=O, −C=C, −CN and $-NO_2$. In addition, selective hydrogenation of conjugated and isolated −C=C and aromatic ring were also presented. Most of the reactions are capitalizes on (i) miscibility of the reactant gas (hydrogen) in supercritical carbon dioxide, which could enhance the reaction rate by eliminating mass transfer limitation, generally occurred in the liquid phase reaction. (ii) Enhancement of selectivity because of the tunable solvent properties arises with potentially small changes in the operating condition. (iii) Interaction with substrate: sometimes CO_2 can act as strong protective agent to prevent further hydrogenation of amine as it has tendency to interact with

In Advances in CO2 Capture, Sequestration, and Conversion; He, et al.;
ACS Symposium Series; American Chemical Society: Washington, DC, 2015.

amine to form carbamic acid. Moreover, (iv) easy product separation and (v) longer catalyst lifetime; coke formation can be prevented. We also attempted to get an insight into the molecular level interaction between substrate−Catalyst or substrate−CO_2 interaction via theoretical calculation in combination with experimental observation.

Introduction

Catalytic hydrogenation is one of the most important means of organic synthesis both in laboratory as well as in industry. The hydrogenation reaction has several advantages such as easy operation, products are often with very high yield and free from any contaminating reagents. In addition, it has broad scope and satisfactory results can be generated under a wide range of conditions (*1*). Catalytic hydrogenation can be homogeneous or heterogeneous. Here, our focus will be hydrogenation using heterogeneous catalysts, which is a classical method in the organic synthesis. Various catalysts supported or unsupported are employed for hydrogenation. Unsupported catalysts are mainly used in the laboratory whereas, supported catalysts are preferable for industrial applications. Metal catalysts are the most desirable candidates for hydrogenation, which includes Pt group of metals mainly Pt, Pd, Rh, and Ru. In addition to that Ni, Cu and Co are also established as perfect hydrogenation catalysts for different types of substrates. In recent years, Au catalysts made huge impact on the selective hydrogenation of various nitro-aromatics (*2*, *3*). This vast array of catalysts each of which may be optimal for a given reaction under operating condition such as temperature, pressure, reaction time, etc.

Since the beginning of the organic synthesis in the late 19th century, organic solvents are widely used to conduct the reaction. In particular, hydrogenation was also conducted in liquid phase using organic solvents as reaction medium. Solvent plays a critical role in the stabilization of reaction intermediates. Thus, choice of solvent is one of the significant step for a reaction to be carried out. Those conventional solvents have several issues related to toxicity, flammability and environmental hazard. Considering the ecological impact, drives the chemical research to find out more environmentally benign methods such as more efficient utilization of starting materials, reduce or eliminate waste discharge and search for green reaction medium (*4*, *5*).

The quest for green reaction medium as a replacement of volatile organic solvent is a major challenge for fundamental research in chemistry, chemical engineering and their related areas as there are multiple factors to consider (*6*). Supercritical carbon dioxide ($scCO_2$) is one of the potential alternative medium for hydrogenation. Phase diagram of CO_2 was characterized by the critical temperature= 31.0 °C, critical pressure=73.8 bar and corresponding critical density= 0.466 g/ml (*7*). This solvent provides several advantages including environmental (do not contribute to increase the VOC's level in the atmosphere), health and safety (non-toxic, non-flammable) and process benefits, which is connected to the rare occurrence of by-products owing to side reactions, absence

Publication Date (Web): September 11, 2015 | doi: 10.1021/bk-2015-1194.ch009

In Advances in CO2 Capture, Sequestration, and Conversion; He, et al.;
ACS Symposium Series; American Chemical Society: Washington, DC, 2015.

of solvent residue and facile product separation (cost-effective; related to the separation and purification steps). The most important advantage of using $scCO_2$ can arise from the complete miscibility of the reactants in the case of chemical reactions involving gasses such as H_2, O_2, N_2, etc. Furthermore, yield and selectivity of a reaction can be enhanced easily by tuning of pressure and temperature. Over the past few years, several heterogeneously catalyzed reactions have been successfully carried out in $scCO_2$, often with higher reaction rates and different product distributions, as well as high selectivity, in comparison with those in conventional organic solvents (*8*, *9*). The origin of the observed selectivity is of importance in view of the current developments on the understanding of the solvent attributes (*10–12*) and the interesting supra-molecular interactions (*13*) reported for CO_2. It has a great potential to overcome disadvantages associated with the conventional homogeneous and heterogeneous catalysts such as mass transfer limitation; frequently occur between the reactants in gas and liquid phase. The reactions in CO_2 are tuned mainly by the pressure and temperature. Chemical interaction of CO_2 with substrate or catalyst is offer an attractive potential for selectivity control (*14*, *15*).

Supported metal nanoparticles are one of the prospective heterogeneous catalysts used for various types of reaction. Mesoporous material, which was discovered by Beck *et al.* in 1992 (*16–18*) seems to be an ideal host for metal nanoparticles because of very high surface area to immobilize catalytically active species on or providing nano-size confinement inside the pore system (*19*, *20*). Mesoporous molecular sieve MCM-41 (a member of the M41S family) possesses a hexagonally arranged uniform pore structure. The important characteristics of this novel material are large BET surface area, high porosity, and controllable narrow pore size distribution. Those characteristics manifest themselves as a very promising candidate as catalyst support. Generally, the synthesis procedure of MCM-41 involves multidentate binding of the silicate oligomers to the cationic surfactant, preferential silicate polymerization in the interface region, and charge density matching between the surfactant and the silicate (*21*, *22*). Beginning with a relatively inert all-silica MCM-41, great chemical and catalytic diversity may be generated by isomorphous substitutions with trivalent cation in Si framework.

In this chapter, focus is the hydrogenation of different functional groups such as −C=O, −C=C (isolated and conjugated), $-NO_2$, −CN as well as ring hydrogenation using heterogeneous metal catalysts (Pt, Pd, Rh, Au, Ni etc.) in $scCO_2$. Different supports were used including laboratory made MCM-41 and other commercially available materials such as alumina (Al_2O_3) and activated carbon (C). Spectroscopic and diffraction techniques were used to characterize those catalysts and to interpret the catalytic performances depending on the particle size.

Publication Date (Web): September 11, 2015 | doi: 10.1021/bk-2015-1194.ch009

In Advances in CO2 Capture, Sequestration, and Conversion; He, et al.;
ACS Symposium Series; American Chemical Society: Washington, DC, 2015.

Experimental Methods

General Method Used for the Synthesis of Metal Nanoparticles Supported MCM-41

Hydrothermal synthesis of metal supported MCM-41 has been carried out as follows: Typically, sodium hydroxide and cetylytrimethylammonium bromide (CTAB) act as a template were added to de-ionized water and stirred until gets dissolved. After that, tetraethylorthosilicate (TEOS) as silica source introduced slowly under the stirring condition and continued stirring for another 1h. In the case of substitution of Si by trivalent metal, required amount of corresponding salt along with TEOS were added to the gel. For *in-situ* generation of metal nanoparticles, 1 wt. % solution of desired metal salt solution has been introduced in to the gel and again stirred for 2 h. Final gel composition was : 1 TEOS: 0.45 Na_2O: 0.12 CTAB: 118 H_2O. The gel was then autoclaved at 140 °C for 48 h and the obtained solid product was filtered, washed thoroughly with de-ionized water followed by oven drying at 60 °C. The as-synthesized material was calcined at 550 °C for 8 h in air to remove the template. Metal nanoparticles were mostly detected on the surface as well as inside the pores of mesoporous channel depending on the particle size.

Publication Date (Web): September 11, 2015 | doi: 10.1021/bk-2015-1194.ch009

Catalyst Characterization and Testing

X-ray Diffraction (XRD)

Mainly, Si MCM-41 was chosen as a support material for metal nanoparticles. Depending on the nature of the reaction, Si was substituted by B or Al to incorporate the acidic site. A typical XRD pattern of MCM-41 used as support material is shown in Figure 1. It shows low angle reflection (1 0 0) with smaller Bragg peaks for only Si. Substitution of Si by Al and B results shifting of peak position and decreased intensity depending on the Si/M (where M= B or Al) ratio used. A likely explanation is, the reduced scattering intensities of the Bragg reflections might be caused by the introduction of scattering materials into the pore (*23*). In addition, characteristic peaks of different metal ion was observed in the higher angle region ($2\theta = 30°$ to 70°). For Pd, five diffraction peaks at 2θ = 33.8, 42.0, 54.8, 60.7 and 71.4 corresponding to PdO was detected. Particle sizes, which has a significant influence on the catalytic activity can be calculated from the line broadening of higher angle XRD peaks using Scherrer's equation (*24*).

In Advances in CO2 Capture, Sequestration, and Conversion; He, et al.;
ACS Symposium Series; American Chemical Society: Washington, DC, 2015.

Publication Date (Web): September 11, 2015 | doi: 10.1021/bk-2015-1194.ch009

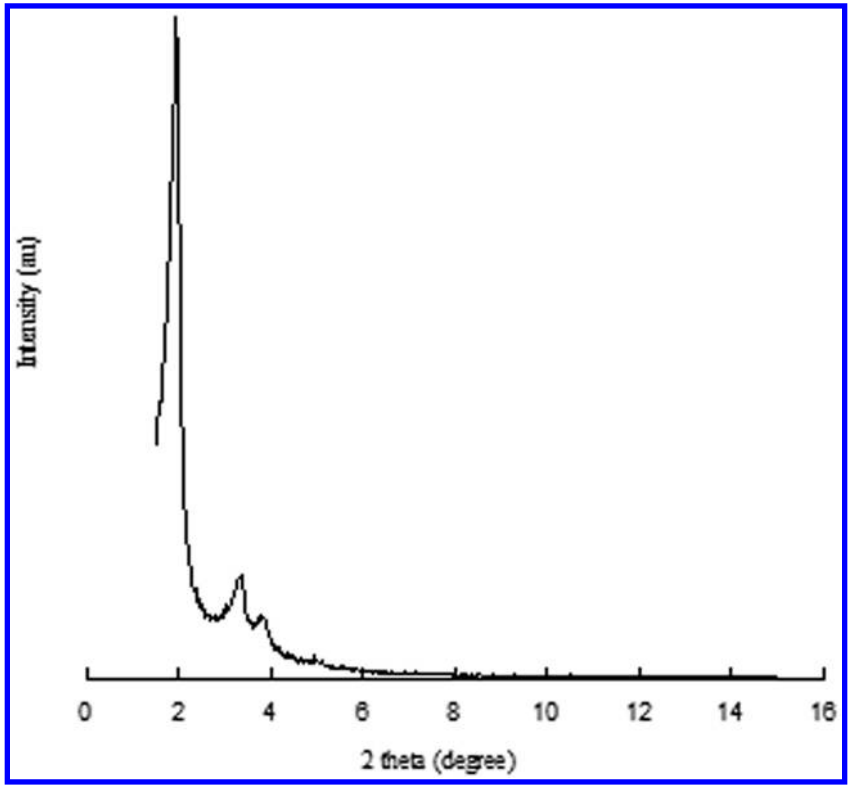

Figure 1. X-ray diffraction pattern of Si-MCM-41.

Transmission Electron Microscopy (TEM)

In order to get an insight into the structural order of the material, TEM image was recorded before and after the reaction. Figure 2a and b shows representative of the TEM images of ordered and disordered MCM-41 containing metal (Pd) nanoparticles. In most of the cases, MCM-41 maintained its structural order even after the incorporation of metal nanoparticles. However, the scenario was different when Si was substituted by B and Al. Depending on the Si/M (where M=B and Al) ratio the structural order varied. For instance, the image corresponding to Si/B= 100 exhibits the regular ordered hexagonal channel, characteristics of MCM-41 but increasing B content damaged regular order. Similarly, higher Al content (Si/Al= 8.5) material also reveals a disordered structure. TEM also focused on metal nanoparticles supported on MCM-41. In each case, particles were almost spherical in shape and distributed throughout the support matrix.

Publication Date (Web): September 11, 2015 | doi: 10.1021/bk-2015-1194.ch009

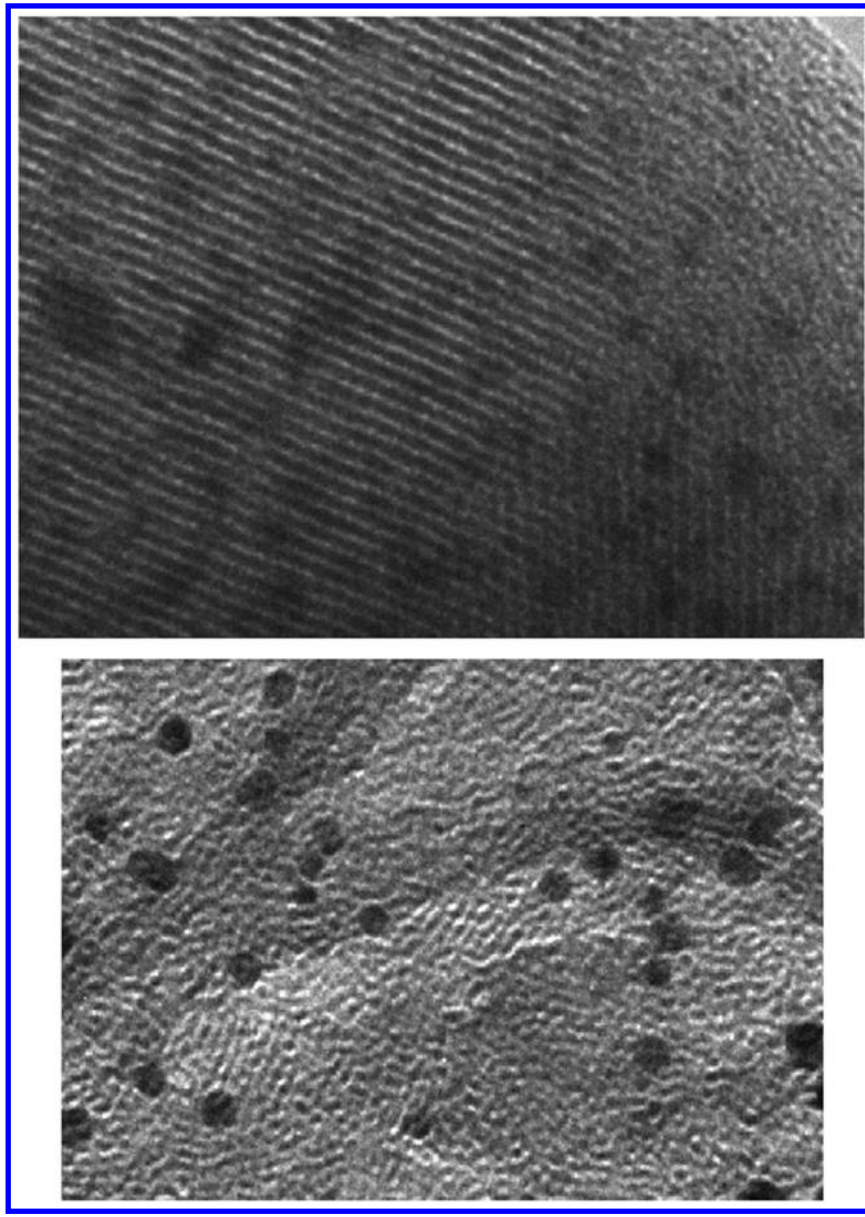

Figure 2. Sample TEM images of ordered (a) and disordered (b) metal (Pd) containing MCM-41. Scale:1.01 cm=50 nm.

Publication Date (Web): September 11, 2015 | doi: 10.1021/bk-2015-1194.ch009

Catalytic Activity

General Procedure

All the reactions were conducted in a 50 ml stainless steel batch reactor. An appropriate amount of catalyst and the reactant were introduced into the reactor and placed in an air circulating oven to maintain the desired temperature. At first hydrogen was introduced into the reactor. After that liquid CO_2 was charged using a high-pressure liquid pump (JASCO) and then compressed to the desired pressure. The reaction mixture was stirred continuously with a Teflon coated magnetic bar during the reaction. After the reaction, the reactor was placed in an ice-bath followed by the depressurization carefully. The liquid product was separated from the catalyst and identified by NMR or by GC-MS (Varian Saturn 2200). Quantitative analysis was conducted using a GC (HP 6890) equipped with capillary column and flame ionization detector. For all results reported, the selectivity was calculated by the following expression: $S_i = C_i / \sum Cp$, where C_i is the concentration of the product 'i' and $\sum Cp$ is the total concentration of the product. For comparison, 5 ml organic solvents were used in place of CO_2.

Computational Methodology

All the calculations related to the transition state were performed with Density Functional theory (DFT) (*25*) using DMol^3 (*26*, *27*) code of Accelrys Inc. BLYP exchange correlation functional (*28*, *29*) and DNP basis set (*30*). In order to consider the effect of solvent, we employed the conductor-like screening model (COSMO) salvation method within the DFT formalism as in the program DMol^3 of Accelrys Inc. (*31*). In this method, the solute molecules form a cavity within the dielectric continuum of permittivity *e* that represents the solvent. The charge distribution of the solute polarizes the dielectric medium. The response of the dielectric medium is described by the generation of screening (or polarization) charges on the cavity surface. The transition state calculations were performed using the synchronous transit methods as included in the DMol^3 module of Accelrys Inc. Complete Linear Synchronous Transit (LST)/Quadratic Synchronous Transit (QST) begins by performing an LST/Optimization calculation. The TS approximation obtained in that way is used to perform QST maximization. From that point, another conjugate gradient minimization is performed. The cycle is repeated until a stationary point is located or the number of allowed QST steps is exhausted. DMol^3 uses the nudged elastic band (NEB) method for minimum energy path calculations. The NEB method introduces a fictitious spring force that connects neighboring points on the path to ensure continuity of the path and projection of the force so that the system converges to the Minimum Energy Path (MEP), which is as well called intrinsic reaction co-ordinate if the co-ordinate system is mass weighted. We also calculated the vibration mode to identify the negative frequency to confirm the transition state.

In Advances in CO2 Capture, Sequestration, and Conversion; He, et al.;
ACS Symposium Series; American Chemical Society: Washington, DC, 2015.

Results and Discussion

Hydrogenation of different substrates were conducted in $scCO_2$ medium using heterogeneous metal catalyst supported on MCM-41 (only Si or substituted), activated carbon (C) and alumina (Al_2O_3). Depending on the substrate used we can divide them into five different categories: substrate containing (i) −C=O group, (ii) −C=C (conjugated and isolated), (iii) conjugated −C=C and −C=O (iv) −C≡N, (v) $-NO_2$ and (vi) aromatic ring hydrogenation.

(i). Selective Hydrogenation of −C=O Group

Selective hydrogenation of α, β-unsaturated aldehydes to unsaturated alcohols is a stepping-stone for the production of fine chemicals, particularly used in the fragrance and flavor industry (*32*). Selective hydrogenation of −C=O double bond is much more difficult because reaction kinetics and thermodynamics both favor hydrogenation of −C=C rather than −C=O (*33*). In general, three major products can be formed upon hydrogenation of an α, β-unsaturated aldehyde: saturated aldehyde, unsaturated alcohol (which can isomerize to saturated aldehyde), and saturated alcohol. In addition, hydrocarbons can be produced as by-products via decarbonylation and C−O bond hydrogenolysis. Several attempts were made to identify the factors that control the selectivity in the hydrogenation of unsaturated carbonyl compounds. The most studied factors are nature of the support materials (*34*, *35*), shape selectivity (*36*), electronic effect (*37*), different reaction parameters such as H_2 pressure (*38*) and solvent used as reaction medium (*39*). For this type of reaction, catalysts are generally metals supported on various materials. Different metals are used as an active component to achieve desired high conversion as well as selectivity of unsaturated alcohols and known to follow decrease in the order of Os > Ir > Pt > Ru > Rh > Pd (*40*, *41*). Furthermore, in the liquid phase hydrogenation use of solvent is necessary, which plays an important role in catalytic performance and sometimes large amount of solvents are required.

Cinnamaldehyde

To avoid the use of organic solvent, hydrogenation of cinnamaldehyde (CAL) was conducted in $scCO_2$ medium using Pt supported on MCM catalyst under a very mild reaction condition. Table 1 shows a complete set of results which revealed 96.6 % selectivity of cinnamyl alcohol (COL) at 50°C and the corresponding CO_2 and H_2 pressure were 10 and 4 MPa, respectively (*42*). An interesting CO_2 pressure dependent selectivity of COL was observed. The selectivity of COL was increased from 59 % (7 MPa) to 96.6 % (10 MPa) with pressure and then decreased significantly. A quantitative consideration of this phenomenon may be explained by the higher compressibility of $scCO_2$, around the critical point, which is responsible for the local dielectric constant being larger than the bulk area making the solvent more polar. This may affect the reactivity of C=O and hydrogenate the bond more easily because of the polarity (*43*). In order

Publication Date (Web): September 11, 2015 | doi: 10.1021/bk-2015-1194.ch009

In Advances in CO2 Capture, Sequestration, and Conversion; He, et al.;
ACS Symposium Series; American Chemical Society: Washington, DC, 2015.

to confirm the importance of CO_2, the hydrogenation of CAL was conducted in only H_2 and the conversion dropped sharply, confirming the excellent miscibility of H_2 in CO_2, which increased H_2 concentration in the reaction medium leading to the enhancement of the reaction rate. In addition, reaction temperature was also an important parameter. Along with the temperature, the conversion was increased, but the selectivity of COL passes through a maxima at 50 °C and then decreased. Instead of monometallic Pt catalyst, bimetallic Ru-Pt was also used to study the hydrogenation of CAL. Depending on the CO_2 pressure, conversion of CAL and the selectivity of COL was improved to 44.8 and 99.7 %, respectively. At a constant temperature of 50 °C the selectivity to COL roses to a maxima at around 7–7.5 MPa pressure of CO_2, and then falls off as the pressure was increased further. Oakes *et al.* also observed a significant enhancement of distereoselectivity from ~ 35 to ~ 95 % for sulfoxidation of a cysteine derivative upon varying pressure (6–18 MPa) (*44*). Now, it is well established that the density of $scCO_2$ changes with pressure. For instance, a change of pressure from 6 to 8 MPa, the density changes from 0.13 to 0.22 g ml^{-1}. Therefore, CO_2 pressure depending complete selectivity to the COL in $scCO_2$ can be appropriately related to the density of the medium. The discussion of the influence of pressure on the results obtained in the catalytic experiments presented in this study is based on the pressure-dependent properties of the reaction medium. Parameters considered here are density and (dynamic) viscosity, which affect mass transfer from the catalyst surface into the phase surrounding the catalyst particles and the solubility of reactants and products in this phase. Moreover, the nature of the metal was also an important factor behind the activity of the catalyst as lower selectivity of COL (56.5 %) was detected in the presence of Ru alone. From the characterization of the monometallic Pt catalyst, presence of metallic Pt was evident. Chemisorbed H_2 can be transferred from metallic Pt to a carbonyl group (as the surface exposed metallic Pt is more favorable for C=O adsorption), resulting in the hydrogenation of C=O, followed by formation of the unsaturated alcohol. However, compared to previous monometallic Pt catalysts (*45*), the activity and selectivity to COL was improved upon the addition of Ru. Concerning the role of Ru, it can be suggested that the more electropositive Ru transfers electron to Pt (*46*) to cause electrophilic activation to −C=O, leading to selective hydrogenation of that bond. Indeed the selectivity of COL was significantly enhanced from 38.2 to 90.2 % in $scCO_2$ medium as evident from the Table 2 (Entry 1 and 2).

Publication Date (Web): September 11, 2015 | doi: 10.1021/bk-2015-1194.ch009

Table 1. Hydrogenation of Cinnamaldehyde (CAL) in Supercritical Carbon Dioxide

Run	*Pressure (MPa)*		*Conversion (%)*	*Selectivity (%)*		
	H_2	*CO_2*		*COL*	*HCAL*	*HCOL*
1	4.0	-	3.6	45.6	39.6	14.8
2	4.0	7.0	14.6	59.5	30.3	10.2
3	4.0	8.5	21.5	78.5	13.6	7.9
4	4.0	10.0	30.8	96.6	2.5	0.9
5	4.0	12.5	33.6	77.4	17.9	4.7
			Effect of hydrogen pressure			
6	2.0	10.0	21.2	85.2	10.3	4.5
7	4.0	10.0	30.8	96.6	2.3	0.9
8	6.0	10.0	38.7	93.2	6.0	0.8

Reaction condition: catalyst= 0.1 g, substrate= 1.0 g, Time=2h, Temperature= 50 °C; COL= unsaturated alcohol, HCAL=saturated aldehyde, HCOL=saturated alcohol.

Table 2. Hydrogenation of CAL at Different CO_2 Pressure Using Ru-Pd Catalyst Supported on MCM-48

Entry	*PCO_2 (MPa)*	*Conversion (%)*	*Selectivity (%)*		
			COL	*HCAL*	*HCOL*
1	-	9.6	38.2	59.3	2.4
2	6.0	25.2	90.2	9.6	0.2
3	6.5	40.6	99.0	1.0	0.0
4	7.0	46.5	100.0	0.0	0.0
5	7.5	45.7	100.0	0.0	0.0
6	8.0	44.8	99.7	0.3	0.0
7	10.0	40.9	95.8	4.2	0.0
8	12.0	38.9	91.1	8.5	0.4
9	17.0	35.6	88.9	10.2	0.9

Reaction condition: catalyst= 0.1 g (Ru=0.18 % and Pd= 0.25 %), substrate= 1.0 g, P_{H2}= 4 MPa, Time=2h, Temperature= 50 °C.

Publication Date (Web): September 11, 2015 | doi: 10.1021/bk-2015-1194.ch009

In Advances in CO2 Capture, Sequestration, and Conversion; He, et al.;
ACS Symposium Series; American Chemical Society: Washington, DC, 2015.

Publication Date (Web): September 11, 2015 | doi: 10.1021/bk-2015-1194.ch009

Crotonaldehyde

Crotonaldehyde (CRLD) is one of the most studied α,β-unsaturated aldehydes. It boils at 101°C, thus, hydrogenation of this molecule could be performed even in the gas phase without any complications. However, undesirable secondary products such as acetal, hemiacetals are formed (*47*). In the liquid phase hydrogenation, low steric protection of olefinic bond hampered product selectivity. Hence, hydrogenation of CRLD to crotyl alcohol (CROL) is still a big challenge. Interestingly, Ag a well-documented oxidation catalyst results comparatively better selectivity to CROL (*48*, *49*) whereas Au and Pt catalysts rely on promoter or additive (*50*). We attempted the hydrogenation of CRLD in $scCO_2$ using Au/MCM-41 catalyst. The reaction was conducted under the similar condition used for CAL and the results of CO_2 pressure dependent catalytic activity are shown in Figure 3. The conversion and selectivity of CRLD shows a significant pressure dependence and the highest selectivity of CROL (90.8 %) was detected at 12 MPa of the CO_2 pressure. In addition, hydrogenation of CRLD in $scCO_2$ medium was also sensitive to the metal particle size. For instance, the selectivity to the CROL decreases from ~90 to ~50 % as the Au particle size changes from 10 nm to < 2 nm. Bailie *et al.* (*51*) studied the influence of particle size (4 nm -20 nm) on the selectivity in the Au/ZnO system and proposed that the active site for the selective hydrogenation of CRLD to CROL was associated with the presence of larger Au particle. Moreover, it is likely that, a marked change in the electronic character of nanosized Au particles occurred with the change in the particle size and the structure-sensitivity originates from a quantum-size effect (*52*).

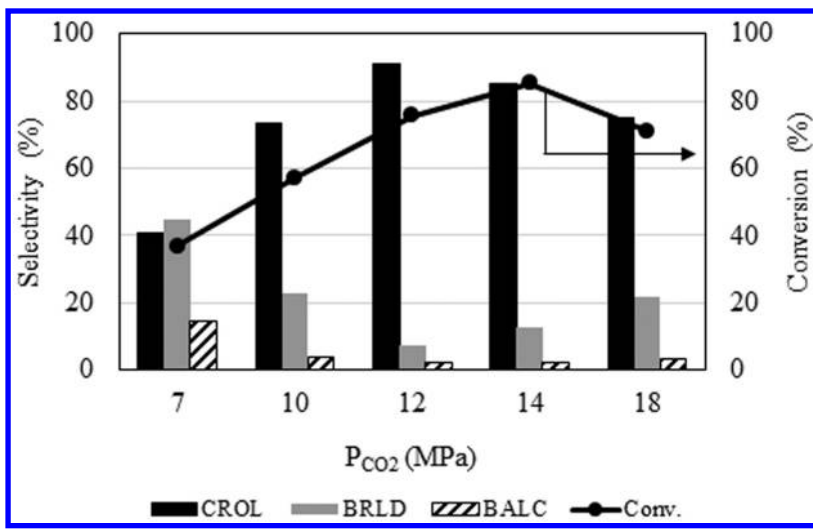

Figure 3. Effect of CO_2 pressure on the hydrogenation of crotonaldehyde (CRLD) in $scCO_2$.

In Advances in CO2 Capture, Sequestration, and Conversion; He, et al.;
ACS Symposium Series; American Chemical Society: Washington, DC, 2015.

Citral

Citral is an interesting unsaturated aldehyde mainly obtained as a mixture of *cis*- and *trans*- form and mainly used as an aroma compound. It contains an isolated −C=C along with a conjugated −C=C and −C=O bonds. The hydrogenation of conjugated −C=O leads to the formation of unsaturated alcohol in *cis*- and *trans*- form and named as nerol and geraniol, respectively. In addition, hydrogenation of −C=C yield citronellal. Moreover, the resulting unsaturated alcohol or partially saturated aldehyde can by hydrogenated at its remaining unsaturated bond to yield the partially saturated alcohol (citronellol). Furthermore, there are the possibilities of different types of side reactions such as cyclization, acetalization etc. From the previous case of CAL, we observed that the selective hydrogenation of −C=O was preferred over Pt catalysts. Thus, hydrogenation of citral was also attempted over Pt/MCM catalyst. Figure 4 shows the influence of the CO_2 pressure on the performance of the Pt catalyst at 50 °C. Under the studied reaction conditions (reaction time: 2 h, P_{H2}: 4 MPa), citral was selectively hydrogenated to the unsaturated alcohol (geraniol + nerol). With the change in CO_2 pressure from 6 to 10 MPa, the selectivity increases from ~15 to ~90 % and correlated well with the change in the density of the medium. The reaction was also studied using bimetallic Pt-Ru catalyst. Interestingly, the selectivity of the reaction shifted from unsaturated alcohol to partially saturated aldehyde (citronellal). For bimetallic Pt-Ru catalyst, the conversion and the selectivity to citronellal rises from 8 to 80 % and 70 to 90 %, respectively, with an increase in CO_2 pressure from 6 to 12 MPa, reaching a maximum at 12 MPa. It has to be mentioned that for both of the catalysts, corresponding product selectivity passes through a maximum. This phenomenon could be associated with tuning of the average distance between the solute molecules and the transition state, accompanied with the density, varies with pressure. That is, for a compressed liquid such as supercritical fluid, variation in density causes a change in chemical equilibrium and affects the activity and selectivity of a reaction (*53*). Other than CO_2, optimization of different reaction parameters such as H_2 pressure, temperature and reaction time reveled that each and individual parameter strongly influenced the product distribution. For instance, a change in the H_2 pressure enhanced the conversion because of the high solubility in $scCO_2$. Again, it could also affect the product distribution: an increase in H_2 pressure from 2 to 6 MPa, extended the selectivity of unsaturated alcohol from 5 to 33 %. Similarly, with an increase in temperature from 35 to 70 °C the conversion of citral was increased and depending on the catalyst used product distribution changes. Interestingly, for monometallic Pt catalyst the selectivity of unsaturated alcohol remain same, however, for bimetallic catalyst the selectivity increased (Table 3).

Publication Date (Web): September 11, 2015 | doi: 10.1021/bk-2015-1194.ch009

Publication Date (Web): September 11, 2015 | doi: 10.1021/bk-2015-1194.ch009

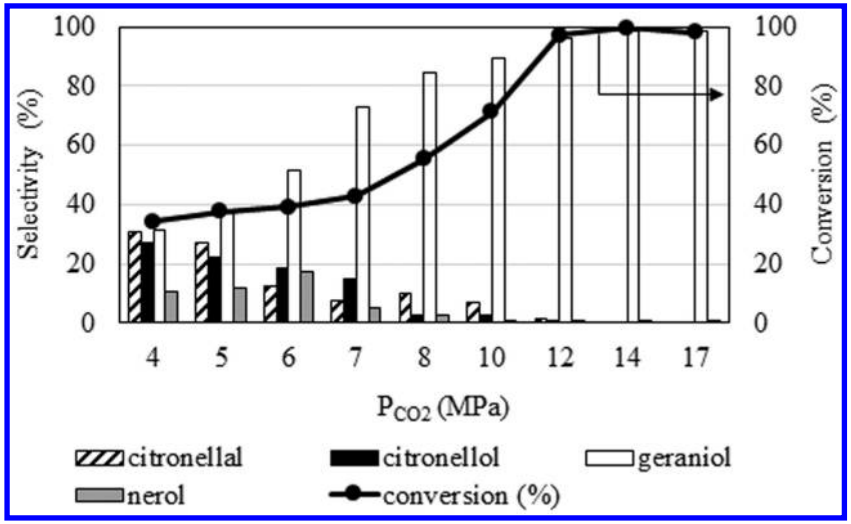

Figure 4. CO_2 pressure vs. catalytic performance of citral hydrogenation in $scCO_2$.

Table 3. Effect of Temperature on the Hydrogenation of Citral Using Pt/MCM-48[a] and Ru-Pt/MCM-48[b]

Entry	*Catalyst*	*Temp. (°C)*	*Conv. (%)*	*Selectivity (%)*		
				Citronellal	*Citronellol*	*Ger.+Nerol*
1	Pt/MCM-	35	32.7	23.2	22.8	54.0
2	48	50	71.3	2.1	7.5	90.4
3		70	75.8	1.4	10.1	88.5
4	Pt-	35	21.4	68.7	31.2	0.1
5	Ru/MCM-	50	89.8	69.8	28.3	1.9
6	48	70	91.2	66.6	10.2	23.4

Reaction condition: catalyst= 0.1 g, substrate = 1.1 g, P_{H2}= 4 MPa. Time=2h. [a] P_{CO2}= 10 MPa. [b] P_{CO2}= 12 MPa.

Comparison of the Hydrogenation of CAL, CRLD, and Citral with Organic Solvents

To confirm the significance of $scCO_2$ as reaction medium, selective hydrogenation of CAL, CRLD and citral was conducted in different organic solvents and the results are shown in Table 4. In each case marked decrease in activity and selectivity was observed compared to $scCO_2$. Hexane is considered as one of the closest solvent to $scCO_2$ in terms of dielectric constant. However,

the conversion and selectivity to corresponding alcohol of CAL (conv. = 11.2 % COL= 9.9 %), CRLD (conv. = 2.1 % COL= 5.0 %) and citral (conv. = 16.7 % ger. + ner.= 21.6 %) was dropped in hexane medium. The remarkable reduction in conversion and selectivity can be attributed to the greater mass-transfer resistances existing in the liquid phase and solvent-less conditions relative to the $scCO_2$ medium. Therefore, the enhancement of conversion and selectivity for the above-mentioned reactions must be an advantage of using $scCO_2$ as the reaction medium.

Table 4. Hydrogenation of Cinnamaldehyde (CAL), Crotonaldehyde (CRLD), and Citral in Different Organic Solvents

Substrate	*Solvent*	*Conv. (%)*	*Selectivity (%)*		
			UOL	*SALD*	*SALC*
		CAL			
	-	17.0	9.9	90.1	0.0
	hexane	11.2	25.6	57.0	17.4
	propanol	30.1	48.9	39.5	11.5
	acetone	6.6	75.7	18.6	5.6
		CRLD			
	-	3.3	9.0	91.0	0.0
	hexane	2.1	5.0	94.5	0.5
	propanol	35.6	51.5	16.3	32.2
	acetone	20.8	41.4	21	37.6
		Citral			
	-	1.3	32.2	16.3	51.5
	hexane	16.7	21.0	41.4	37.6
	propanol	89.8	1.8	79.8	18.3
	acetone				

Deactivation of Catalyst

One of the main problems in the hydrogenation of α, β-unsaturated aldehydes using heterogeneous catalysts is the formation of coke and eventually deactivation of the catalyst. Generally, deposition of coke covers catalytic active sites and plug the pore structure, which causes deactivation. The catalyst deactivation is a major issue especially in the hydrogenation of citral in organic solvents. It is mainly related to the formation of carbonaceous species (*54*) due to the decarbonylation reaction (*55–57*). For hydrogenation of citral, monometallic Pt and bimetallic

In Advances in CO2 Capture, Sequestration, and Conversion; He, et al.;
ACS Symposium Series; American Chemical Society: Washington, DC, 2015.

Publication Date (Web): September 11, 2015 | doi: 10.1021/bk-2015-1194.ch009

Ru-Pt catalyst was used. No leaching was detected by the hot filtration test and the reaction was successfully conducted for longer reaction time as well as successive runs without any decrease in the conversion and product selectivity. On the other hand, Au/MCM-41catalyst, which was used for hydrogenation of CRLD in $scCO_2$ was recycled efficiently. As Au is very susceptible of leaching, however, elemental analysis by ICP ensuring negligible amount of Au (< 0.02%) in the solution. Hence, decrease in catalytic activity by the leaching of metal ion or coke deposition can be avoided as the reaction was conducted in $scCO_2$ medium. Supercritical fluid have shown to be effective in controlling such deactivation by its extracting power (*58*, *59*). Therefore, this result highly implied the possible advantage of supercritical medium over conventional processes for the hydrogenation of different α, β-unsaturated aldehydes using heterogeneous catalysts.

Publication Date (Web): September 11, 2015 | doi: 10.1021/bk-2015-1194.ch009

(ii). Hydrogenation of −C=C (Conjugated and Isolated)

As mentioned in the previous section, hydrogenation of α, β-unsaturated aldehyde is an important reaction for synthesis of specialty and different fine chemicals. Most focused area is the selective hydrogenation of −C=O, which produces unsaturated alcohol an important building block and thermodynamically more challenging. Citarl is an interesting compound. It contains two types of −C=C conjugated and isolated. The potential products of citral hydrogenation is schematized in Scheme 1. The fully saturated aldehyde, dihydrocitronellal, is obtained by the hydrogenation of citral through citronellal. Dihydrocitronellal is more stable than citral and could enhance the citrus effect of cologne; hence it can be used in fine fragrances. Conventionally, Pd is considered as one of the effective catalysts for hydrogenation of −C=C. However, direct formation of dihydrocitronellal from citral is difficult in conventional organic solvents, required a conversion to acetal followed by the hydrolysis in acidic medium (*40*). Aramendia *et al.* observed that only the conjugated −C=C of citral was hydrogenated and producing citronellal using Pd catalyst in different solvents, either polar or non-polar (*47*). As mentioned before, one of the advantages of using CO_2 as reaction medium is the complete miscibility of H_2 in the reaction medium. Taking this advantageous point, the targeting hydrogenation of the conjugated and isolated −C=C bonds of citral was conducted in $scCO_2$. Optimization of different reaction parameters confirmed that P_{CO2}=12 MPa and P_{H2}= 4 MPa and reaction time of 2 h at 50 °C produces dihydrocitronellal with very high selectivity (100 %). To clarify the role of $scCO_2$, the reaction was conducted in different organic solvents and in the solvent-less condition. There was a striking difference in the selectivity of desired dihydrocitronellal. At the same conversion of 25 %, the selectivity for dihydrocitronellal was 100 % in $scCO_2$, whereas in the organic solvent and in the solvent-less condition ~ 73 to 90 % citronellal was obtained as the major product. Hence, from the results it could be inferred that in conventional organic solvent, only the hydrogenation conjugated −C=C bond was possible. $scCO_2$ played an interesting role to the hydrogenation of conjugated and isolated −C=C. bonds.

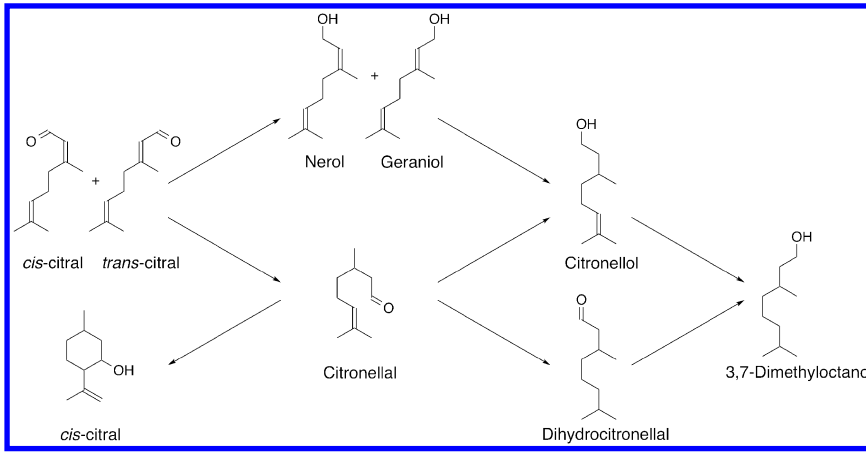

Scheme 1. Possible reaction path of citral hydrogenation.

From the above experimental study it has been observed that the adsorption geometry of the reactant and the medium has a strong impact on dictating the selectivity of the reaction. We have performed a preliminary calculation to monitor the effect of solvent on the electronic structure and geometry of the isolated citral molecule considering a gas phase, a non-polar liquid phase with a dielectric constant of 1.6 and a polar solvent with a dielectric constant 32.6 using density functional calculations with B3LYP functional and 6-311G** basis set. The geometries of the three conformers are shown in Figure 5. The dielectric constant of $scCO_2$ at our studied pressure range corresponds well to the liquid phase with a dielectric constant of 1.5 (*60*). The results show that the dielectric constant influences the geometry. The structures of the liquid phases are different from the gas phase. The conformer obtained at very low dielectric constant close to $scCO_2$ is very linear and the charges derived from Mulliken population indicate that the charge on the terminal oxygen is very high which may result in the favorable −C= C bond cleavage through an intermediate. In contrast, for the conformer in high dielectric constant medium the geometry itself shows that the cleavage of the second −C=C is improbable. Here, the charge on the terminal oxygen is positive. At this point comparing the geometries of the conformer we can foresee the favorable nature of $scCO_2$ over organic solvents in terms of dielectric constant. The calculation indicates a drastic change in geometry and thus, proposes a plausible interaction route.

Instead of MCM-41, hydrogenation of citral was also conducted on Pd containing different support materials. In each case high conversion and selectivity was detected. For instance, SiO_2, Al_2O_3 and C shows 96.0, 92.7 and 97.8 %, respectively. Irrespective of the nature of the catalyst support, very high selectivity of dihydrocitronellal (100 %) was obtained at a pressure of 12 MPa. This result might be implied to the uniqueness of the solvent properties of $scCO_2$ medium that promotes the highly selective hydrogenation of conjugated and isolated −C=C bonds under a mild reaction condition.

Publication Date (Web): September 11, 2015 | doi: 10.1021/bk-2015-1194.ch009

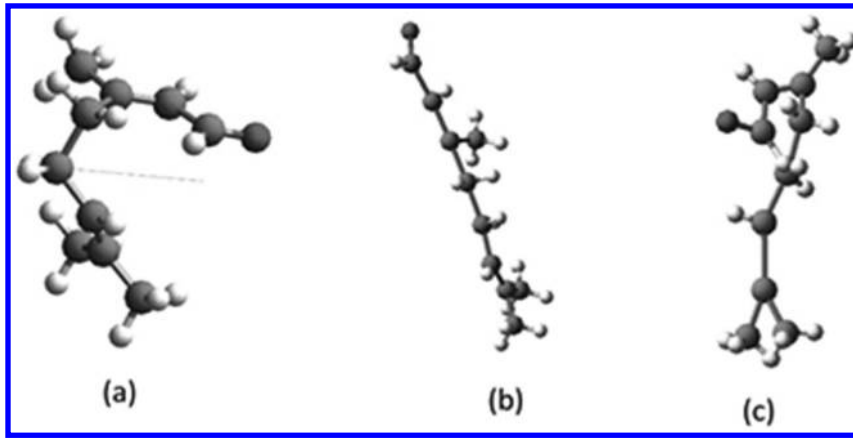

Figure 5. Three different conformation of citral (a), in hexane (b) and in methanol (c); oxygen is marked with arrow.

Instead of Pd, Ni catalyst produced an interesting relation between the oxidation state of metal and the product distribution of citral hydrogenation. Using Ni^{II} and Ni^{0} catalysts, the selectivity of products are shown in Table 5, which revealed that Ni^{II} favored the hydrogenation of −C=O, whereas, −C=C was preferred on Ni^{0}. In each case, depending on the total pressure, selectivity of the corresponding compounds were varied. For instance, a change in the pressure from 11 to 20 MPa, enhanced the selectivity of −C=O hydrogenated compound from 10.6 to 96 % over Ni^{II}. On the contrary, under the similar condition, the selectivity of citronellal (product of −C=C hydrogenation) was augmented from 55.1 to 96.8 % in the presence of Ni^{0} catalyst. This significant correlation between the product distribution and the oxidation state of metal provoked us to conduct the reaction in conventional organic solvents (Table 6). Surprisingly, the Ni^{II} catalyzed reaction did not take place at all in conventional organic solvents, whereas Ni^{0} hydrogenates −C=C selectively. For Ni^{II} the trend in catalytic activity differs widely depending on the reaction medium. In $scCO_2$, Ni^{II} is active and selective to the hydrogenation of −C=O: however, it remains inactive in the conventional organic solvents used. This drastic change in the behavior of Ni^{II} in organic solvents in comparison with that in $scCO_2$ suggested an important part of the medium. The role of solvents in catalytic processes is complicated, especially for $scCO_2$. In some cases it is inert: however in other cases CO_2 interacts with some functional groups and can thus impact on the chemical transformation (*4*). This surprising activity of the Ni^{II} catalyst provoked us to an interesting role of CO_2, since, there are physical differences between CO_2 and conventional reaction medium. The confirmation came from the activity of Ni^{II} in toluene after the addition of a very small amount of CO_2 (0.2 MPa). The activity of the Ni^{II} catalyst in the CO_2–toluene phase might also result from the CO_2- expanded properties of solvent. However, in the present case, such a contribution is insignificant, in view of the low concentration of CO_2 in the medium. Considering the entire results, it might be hypothesized that physical and chemical properties of CO_2 in association with Ni^{II} is a significant part

In Advances in CO2 Capture, Sequestration, and Conversion; He, et al.;
ACS Symposium Series; American Chemical Society: Washington, DC, 2015.

governing the product distribution. The chemical participation of the medium might also result from the direct interaction between the substrate and CO_2, which is particularly important in view of the Lewis acid–Lewis base interactions and hydrogen bonding (*61*, *62*). But, we observed that the reaction does not take place in the absence of the Ni^{II} catalyst as well as without $scCO_2$. This suggests that the observed selectivity is either due to a direct interaction between Ni^{II} and the substrate or a coupled three-body interaction operating among the catalyst, solvent, and the substrate. The possibility of Ni^{II} –substrate interaction is expectedly similar in $scCO_2$ and conventional organic solvents. Since the reaction does not take place in the conventional organic solvents studied, the possibility of a coupled substrate–catalyst–solvent interaction guiding the observed reaction and the selectivity becomes important. In other words, $scCO_2$ not only acts as a medium, but also takes part in the transition of the reactant to the product, by participating in an energetically favorable mechanism involving the substrate, catalyst and CO_2. According to the literature, CO_2 is not a non-polar solvent, but a quadrupolar solvent (*62*). There is a clear charge separation in the CO_2 molecule leaving a partial positive and negative charge towards the carbon and oxygen, respectively. It is plausible that the electron deficient Ni^{II} can attack CO_2 easily, forming a complex. The complex formation of Ni^{II} with CO_2 makes the carbon more positive, which then probably dictates the preferential hydrogenation of −C=O over −C=C. It is difficult to probe such a complex solvent participation, although there is experimental evidence reported to the formation of complexes between CO_2 and transition metal ions (*63*).

Publication Date (Web): September 11, 2015 | doi: 10.1021/bk-2015-1194.ch009

Table 5. Hydrogenation of Citral Using Ni Catalyst

Entry	*P_{Total} (MPa)*	*Conv. (%)*		*Selectivity (%)*					
				UOL		*SALD*		*SALC*	
		Ni^{II}	*Ni^0*	***Ni^{II}***	*Ni^0*	***Ni^{II}***	*Ni^0*	***Ni^{II}***	*Ni^0*
1	11	**50.5**	37.2	**10.6**	-	**50.1**	55.1	**39.3**	44.9
2	12	**52.1**	40.1	**18.2**	-	**48.9**	67.3	**32.8**	42.8
3	13	**53.5**	51.5	**40.2**	-	**41.0**	68.3	**18.8**	31.7
4	14	**60.9**	56.5	**75.0**	-	**25.0**	77.8	-	22.2
5	16	**76.5**	62.5	**87.8**	-	**12.2**	88.2	-	11.8
6	17	**80.3**	70.2	**97.3**	-	**2.8**	93.3	-	4.7
7	20	**81.2**	72.5	**96.0**	-	**4.0**	96.8	-	3.2

Reaction condition: catalyst= 0.1g, substrate= 1.1 g, total pressure = P_{H2} (4 MPa) + P_{CO2}, temperature= 70 °C, time= 2h; P_{Total}=total pressure.

In Advances in CO2 Capture, Sequestration, and Conversion; He, et al.;
ACS Symposium Series; American Chemical Society: Washington, DC, 2015.

Table 6. Hydrogenation of Citral Using Ni Catalyst in Different Organic Solvents

Entry	*Solvent*	*Product selectivity (%)*	
		Ni II	*Ni0a*
1	Hexane	No reaction	50.1
2	Propanol	No reaction	77.4
3	Ethanol	No reaction	80.6
4	Toluene	No reaction	100.0

Reaction condition: catalyst= 0.1g, substrate= 1.1 g, total pressure = P_{H2} (4 MPa) + P_{CO2}, temperature= 70 °C, time= 2h; a= citronellal.

Publication Date (Web): September 11, 2015 | doi: 10.1021/bk-2015-1194.ch009

The product distribution of a reaction is the consequence of transition state formed during the transformation. Experimentally, identification of the transition state is difficult, thus, in this context, theoretical calculation using density functional theory was performed. In the view of reported geometries for the transition metal complexes of CO_2, we have considered two different types of geometries in the present case: (A) co-ordination via O only (*64*) and (B) C-O co-ordination (*65*). However, based on energy considerations, the B-type geometries were excluded. Figure 6 presents the probable transition states obtained from the calculations, for the interaction of the Ni^{II} −CO_2 complexes of type A with the −C=O ($TSA_{C=O}$) and −C=C ($TSA_{C=C}$) bonds of citral, respectively. The calculations showed that the interactions involving the −C=O bond are more favorable than those with the –C=C bond. A comparison between the two transition state energies ($TSA_{C=O}$ and $TSA_{C=C}$) indicates that the $TSA_{C=O}$ state is energetically favored by ~25.63 kcal mol^{-1} over the $TSA_{C=C}$ state, suggesting a preferential hydrogenation of the carbonyl group. This makes the −C=O of citral more susceptible to Ni^{II}-catalyzed hydrogenation. The energy differences for the $TSA_{C=O}$ and $TSA_{C=C}$ with the corresponding products are 61.175 kcal mol^{-1} and 99.150 kcal mol^{-1}, respectively. This suggests that the low barrier height of $TSA_{C=O}$ dictates the preferential −C=O hydrogenation of citral. Thus, in the Ni^{II} catalyzed reaction there could be a possibility of the chemical participation of the medium.

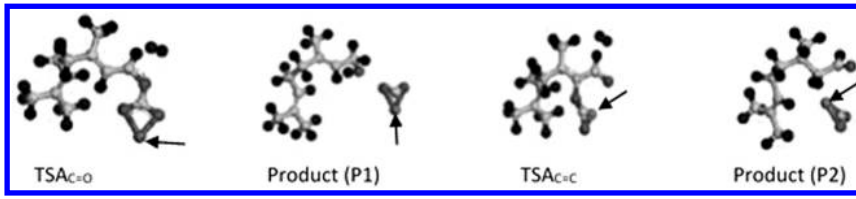

Figure 6. Interaction of citral with Ni−CO_2 complex: (A) through C=O, proposed reaction intermediates $TSA_{C=O}$ and the corresponding product (P1); (B) through C=C, proposed reaction intermediates $TSA_{C=C}$ and the corresponding product (P2) in $scCO_2$. Black=hydrogen, light grey= carbon, dark grey=oxygen and arrow represents Ni.

In Advances in CO2 Capture, Sequestration, and Conversion; He, et al.;
ACS Symposium Series; American Chemical Society: Washington, DC, 2015.

(iii). Hydrogenation of Conjugated −C=C and −C=O

The versatile role of CO_2 as reaction medium also exploited in the selective hydrogenation of 2-cyclohexenone, which contains conjugated −C=C and –C=O. Under a very mild reaction condition 2-cyclohexenone rapidly (TOF=3.1 x 10^4 h^{-1}) and specifically hydrogenated to cyclohexanone with 100 % selectivity using Pt/MCM-41 catalyst. Compared to the conventional organic solvents and the solvent-free condition, the reaction proceeds with 100 times faster reaction rate in $scCO_2$ under the same reaction condition (Table 7). Optimization of different reaction parameters suggested a temperature = 40 °C; reaction time= 10 min.; P_{H2}= 2 MPa, P_{CO2}=12 MPa was the best condition to achieve complete conversion and highest selectivity of cyclohexanone. Considering the CO_2 pressure, a density dependence performance was detected (Figure 7). In addition, solubility of H_2 in $scCO_2$ is another positive factors to achieve a significantly higher reaction rate. As mentioned before, a substantial advantage behind the hydrogenation in $scCO_2$ is particularly the high miscibility of the reacting H_2 gas and high diffusivity, which prevents mass transfer limitations. Furthermore, the temperature effect is complicated when the reaction was conducted in $scCO_2$. Fine tuning of the temperature can also changes the density of the medium and consequently the solvent strength, which have strong influence on the phase behavior as well as the chemical equilibrium and reaction rates (*66*). In the hydrogenation of 2-cyclohexenone, the effect of temperature was checked under the fixed density condition. At a fixed density of ~ 0.7 g/mL (35 °C, 10 MPa, density= 0.714 g/mL; 40 °C, 12 MPa, density= 0.719 g/mL; 45 °C, 14 MPa, density= 0.721 g/mL) (*67*), the hydrogenation of exhibited the same conversion and selectivity, but contradict with the effect of temperature at fixed pressure on conversion and selectivity. For instance, at the fixed pressure of 12 MPa, the conversion was increased from 80 to 100 % as the temperature changes from at 35 °C to 45 °C (density varies from 0.767 g/ml to 0.657 g/ml). Thus, a straight forward effect of temperature on conversion might be predicted. The same method was also applied to methyl and ethoxy substituted cyclohexenone and also acyclic ketone and the results are in Table 7. Selective hydrogenation of C=C was detected in each case and the corresponding product was obtained with very high selectivity. Although the results show reasonable reaction rate but still it is lower compared to 2-cyclohexenone as observed from the TOF (reaction rate). A decrease in TOF from 2.8 x 10^4 h^{-1} to 1.7 x 10^4 h^{-1} as the substitution changes from methyl to ethoxy group has been evident This may be attributed to the bulkiness of the substrate, which prevents easy access of the substrate molecule to the active sites of mesoporous channel and consequently the rate of the reaction decreases. However, the acyclic ketone shows larger TOF as that of the cyclohexenone (3.0 x 10^4 h^{-1}). Thus, an unusual high reaction rate due to the enhanced diffusion of the reactant at very low temperature and the mass transfer reduction were possible because of the unique properties of $scCO_2$.

Publication Date (Web): September 11, 2015 | doi: 10.1021/bk-2015-1194.ch009

In Advances in CO2 Capture, Sequestration, and Conversion; He, et al.;
ACS Symposium Series; American Chemical Society: Washington, DC, 2015.

Publication Date (Web): September 11, 2015 | doi: 10.1021/bk-2015-1194.ch009

Table 7. Hydrogenation of 2-Cyclohexenone in Different Organic Solvents and Substituted Cyclohexenone and Acyclic Ketone in $scCO_2$

Entry	*Substrate*	*Solvent*	*Conv. (%)*	*Selectivity (%)*		*TOF (h^{-1})*
				−C=C	*−C=O*	
1	2-cyclohexenone	-	15.4	87	13.0	483
2		hexane	16.6	49.7	50.3	498
3		2-propanol	10.2	90.1	9.9	352
4	3-methyl cyclohexenone	$scCO_2$	97.4	> 99.0	0.0	4603
5	3-ethoxy cyclohexenone	$scCO_2$	75.9	> 99.0	0.0	2816
6	Mesityl oxide	$scCO_2$	95.5	> 99.0	0.0	5020

Reaction condition: catalyst= 0.05 g, temperature = 40° C; Time= 10 min.; P_{H2}= 2 MPa, P_{CO2}= 12 MPa; Turnover frequency (TOF) = number of moles reacted/ moles of metal x time.

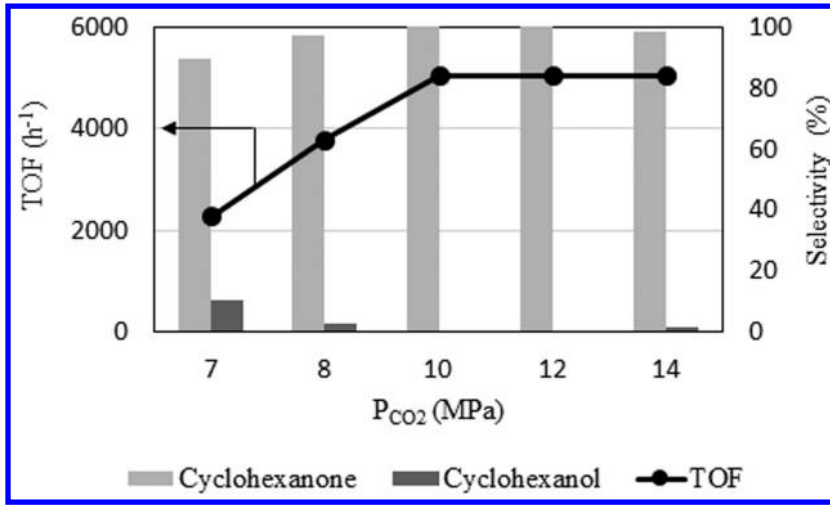

Figure 7. Role of CO_2 pressure on the catalytic hydrogenation of 2-cyclohexenone.

(iv). Hydrogenation of −CN Group

Amines are important intermediates in the synthesis of polymers, drug, dyes, agrochemicals and various fine chemicals. For example, hexamethylenediamine, a hydrogenation product of adiponitrile is a key component in the synthesis of Nylon-6, 6. Thus hydrogenation of nitrile to primary amine is highly significant. One of the main problems associated with this reaction is selectivity as imines,

In Advances in CO2 Capture, Sequestration, and Conversion; He, et al.;
ACS Symposium Series; American Chemical Society: Washington, DC, 2015.

secondary amines are often obtained as by-products. To improve the selectivity, different additives were used, which creates a waste problem, if the additives cannot be recycled, makes the process more expensive and interference on product separation.

Supercritical carbon dioxide has a great potential to overcome several disadvantages associated with the conventional homogeneous and heterogeneous catalysts. Chemical interaction of CO_2 with substrate offers an attractive potential for selectivity control (*14*). For example, amine could react with CO_2 to form carbamic acid or ammonium carbamate. It is reasonable to expect the possibility to protect the amine group, which can improve the selectivity of a reaction and prevent the catalyst deactivation. Thus, hydrogenation of benzonitrile (BN) to benzylamine (BA) was conducted in $scCO_2$ using Pd/MCM-41 catalyst without any additives (*68*).

The study was begin with the screening of catalyst under similar reaction condition targeting highest conversion and selectivity (Table 8). Results of screening presented in the Table 8 suggested that the catalytic activity of Ni, Rh and Pt was lower than Pd. Depending on the performance, Pd/MCM-41 emerged as the most suitable one among the other Pd catalysts. A comparative study was conducted between Pd/C and Pd/MCM-41. Related to CO_2 pressure, the conversion of BN changes from 64.9 to 90.2 % and 65.1 to 100 % for Pd/MCM-41 and Pd/C, respectively. However, further increase in the CO_2 pressure the conversion of BN was dropped. This scenario can be explained by visual observation of phase behavior between CO_2 and the substrate through the view cell. In the temperature considered here, the reaction mixture exists as two phase; the gas-liquid (H_2 and CO_2-substrate) phase. At low pressure region, the reactant mainly exist in the liquid phase and mass transfer limitation of H_2 causes low conversion. With increasing CO_2 pressure, the density of the medium as well as solubility of the reactants were increased and accordingly conversion of BN increased. On the other hand, excess of CO_2 at constant volume can cause dilution effect and consequently decreased the conversion. Regarding the product distribution, a strong influence of CO_2 pressure and the nature of the support used was detected. The selectivity of primary amine (BA) was changed from 64 to 90.9 %) and then decreased to 20 %, when the pressure reaches to 14 MPa due to the formation of dibenzylamine (DBA). This observation can be explained as follows: the hydrogenation of nitriles generally proposed as a combination of different steps such as conversion of nitrile to imine followed by the formation of primary amine, which is then converted to secondary amine via nucleophilic attack of primary amine with imine (Scheme 2). Considering the reaction mechanism, here we focused on two factors (i) interaction of catalyst with substrate and (ii) phase behavior. In the calcined sample of Pd/MCM-41, Pd mainly existed as Pd^{II}. So, there was a possibility that the reaction might start with an oxidative addition between BN and catalyst followed by the formation of a chemisorbed species. However, Pd^{II} can be converted to Pd^0 because of the presence of H_2 in the system. Now, from the phase behavior, at lower pressure BN mainly resides in the liquid phase. Due to mass transfer limitation, the conversion and selectivity of BA was low. Moreover, as the reaction was occurred mainly in the liquid phase, BA can readily react with imine and the secondary amine was formed.

Publication Date (Web): September 11, 2015 | doi: 10.1021/bk-2015-1194.ch009

When the pressure was increased the solubility of BN was increased in CO_2-H_2 phase and the system turned into a single phase. As a result the selectivity of BA enhanced and here lies the advantage of using CO_2 as reaction medium in the hydrogenation of nitrile to primary amine. Carbamate was easily formed through the interaction of amine with CO_2, (Figure 8), which could prevent the formation of DBA because carbamate cannot act as a nucleophile to interact with imine.

Table 8. Catalyst Screening for Hydrogenation of Benzonitrile to Benzylamine

Entry	*Catalyst*	*Conv. (%)*	*Selectivity (%)*		*TOF[a] (h^{-1})*
			BA	*DBA*	
1	Pd/C	100	0.0	100.0	2983
2	Pd/Al_2O_3	46.0	50.0	50.0	340.4
3	Pd/ MCM-41	90.2	90.9	9.1	4151
4	Pt/C	8.5	0.0	100.0	178.8
5	Pt/MCM-41	20.6	19.8	80.2	552.5
6	Rh/C	28.8	25.0	75.0	180.6
7	Rh/ Al_2O_3	21.0	22.4	77.6	291.3
8	Rh/MCM-41	5.1	25.0	75.0	42.4
9	Ni/MCM-41	15.7	37.5	62.5	5.1

Reaction conditions: catalysts =0.1 g, substrate= 1.0 g; P_{CO2}= 10 MPa, P_{H2}= 2 MPa, temperature= 50 °C, reaction time =4 h. [a] Turnover frequency (TOF) = number of moles reacted/ moles of metal x time; BA=benzylamine, DBA=dibenzylamine.

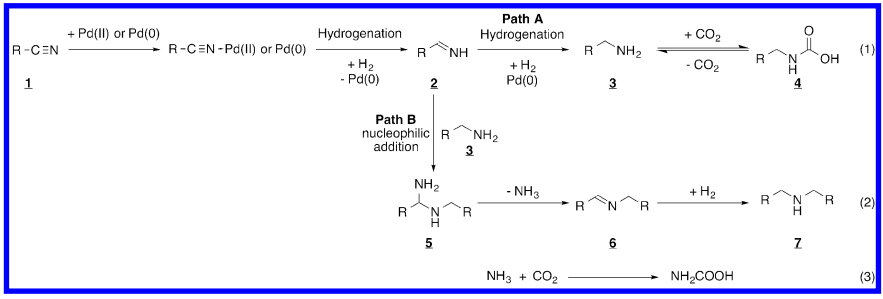

Scheme 2. Proposed reaction mechanism of benzonitrile hydrogenation; 1= nitrile, 2= intermediate, 3= Primary amine, 4= carbamate, 5= secondary amine, 6= imine.

In Advances in CO2 Capture, Sequestration, and Conversion; He, et al.;
ACS Symposium Series; American Chemical Society: Washington, DC, 2015.

Publication Date (Web): September 11, 2015 | doi: 10.1021/bk-2015-1194.ch009

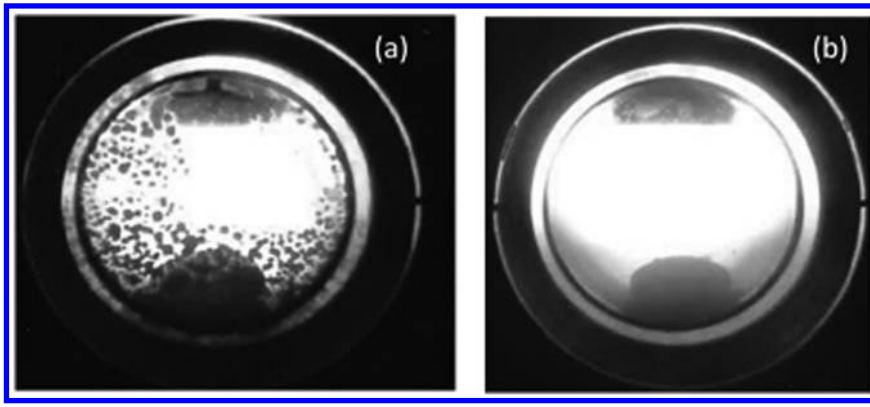

Figure 8. View cell observation of carbamic acid formation. Phase behavior study of benzylamine (a) P< 12 MPa (b) P≥ 12 MPa.

In contrast to the Pd/MCM-41, DBA was formed with very high selectivity on Pd/C catalyst. This difference in activity might be originated from the difference in the nature of the support materials. Generally, MCM-41 is less acidic than C; this acidic property could be one of the reasons behind the formation of DBA with very high selectivity of > 99 %. However, the support acidity on the hydrogenation of nitrile is a controversial issue. Some authors have claimed that acidity favors the formation of secondary amine, while other reports no effect on selectivity. According to the results of this investigation, a combined effect of CO_2 pressure and support acidity could be the possible reason behind the formation of secondary amine over Pd/C catalyst. Reaction time is an important parameter, which can provide an idea about the kinetics of the reaction as well as the stability of intermediate species on the catalyst surface. Therefore, a time course of BN hydrogenation was conducted. Apparently, the reaction on Pd/C seems faster as 74 % conversion was achieved within 2 h, which was higher compared to Pd/MCM-41 (conversion= 44 %). However, the calculation of reaction rate in terms of TOF suggested an increase of 4138 to 4151 h^{-1} with time for Pd/MCM-41, whereas, Pd/C catalyst faced a decrease of TOF from 4445 to 2983 h^{-1}. The TOF of a reaction, initially which was very high, reduces during the course of the reaction might be related to the deactivation of the catalyst. Regarding the product distribution, instead of primary amine, DBA was obtained with very high selectivity of 44.7 % over Pd/C catalyst within the reaction time of 2 h.

The optimized reaction conditions (50 °C, 4 h, P_{CO2}=10 MPa and P_{H2}=4 MPa) of BN was extended to the hydrogenation of different other substrates and the results are shown in Table 9. It exhibits that the application of Pd/MCM-41 catalyst can be extended to nitrile with different functional groups. For example, −CH_3, −Br, −OMe (Table 9; Entry 1-3) producing corresponding primary amine with high selectivity between 65 -100 %. Based on the presence of electron withdrawing and electron donating group in aromatic nitrile, a clear trend of the conversion and selectivity was clearly found. In the presence of electron donating group, the conversion was high, but selectivity to primary amine was low (Table 9; Entry

In Advances in CO2 Capture, Sequestration, and Conversion; He, et al.;
ACS Symposium Series; American Chemical Society: Washington, DC, 2015.

Publication Date (Web): September 11, 2015 | doi: 10.1021/bk-2015-1194.ch009

1 and 2). On the contrary, the situation was reverse in the presence of electron withdrawing group (Table 9; Entry 3, 4). The potential of the catalyst was also described by the hydrogenation of aliphatic nitrile (Table 9; Entry 6-8). It has to be mentioned that in comparison with the aromatic nitriles, higher temperature was needed for benzyl cyanide and 3-phenylpropionitrile (Table 9; Entry 5 and 6) to the formation of their corresponding primary amine with the selectivity of 98.3 and 80.1 %, respectively. No additive was used for any of the above-mentioned substrate to increase the yield of the primary amine.

Table 9. Hydrogenation of Benzonitrile with Different Substituents

Entry	*Substrate*	*Conv. (%)*	*Selectivity of primary amine (%)*
1	*p*-tolunitrile	89.2	82.1
2	*p* -methoxybenzonitrile	80.1	75.2
3	*p*-bromobenzonitrile	64.5	> 99.0
4	*p*-phenylbenzonitrile	61.5	> 99.0
5	Benzene isonitrile	81.5	98.3
6	Butyronitrile, 4-phenyl	94.5	80.1
7	Cyclohexanecarbonitrile	98.6	> 99.0
8	Hexanenitrile	60.5	> 99.0

Reaction condition: catalyst=0.1 g, substrate= 1.0 g, temperature = 50° C; Time= 4h.; P_{H2}= 2 MPa, P_{CO2}= 10 MPa; Entry 5 and 6; temperature=70 °C.

After the successful hydrogenation of BN, the next attempt was the hydrogenation of adiponitrile (ADN), which contains two −CN group and the selective hydrogenation of one of the −CN groups results 6-aminocapronitrile (ACN). It is used in the synthesis of caprolactum; a precursor of Nylon-6. Caprolactum is mainly produced from cyclohexanone, but this process generates a large amount of wastes and eventually increased the production cost. Thus, to minimize the waste formation, semi-hydrogenation of ADN to ACN was considered as an alternative route. However, main problem associated with this transformation is the formation of deep hydrogenated product hexamethylenediamine (HMD) along with secondary and tertiary amines. High purity of ACN generally required for nylon industry to avoid the defect in nylon thread. An attempt to achieve only ACN, hydrogenation of ADN was conducted in $scCO_2$ using noble metal supported catalysts those are generally used in the hydrogenation of nitrile. As mentioned before, formation of carbamic acid or carbamate is the advantageous part of the synthesis of amine in $scCO_2$. The interaction between sufficiently basic amine group and CO_2, the nucleophilicity of nitrogen atom is decreased and makes it less reactive in CO_2 (*69*, *70*). This criterion of CO_2 can be used as temporary protecting agent to "mask" amino group from further reaction.

In Advances in CO2 Capture, Sequestration, and Conversion; He, et al.;
ACS Symposium Series; American Chemical Society: Washington, DC, 2015.

Publication Date (Web): September 11, 2015 | doi: 10.1021/bk-2015-1194.ch009

Publication Date (Web): September 11, 2015 | doi: 10.1021/bk-2015-1194.ch009

Based on the metal ion used (Pt, Pd and Rh), supported on C and Al_2O_3, Rh was considered as one of the preferred catalysts under the working condition as Pt and Pd catalysts exhibited very poor conversion in the range of 1- 10 %. On the other hand, Rh supported on C and Al_2O_3 results 89.8 and 96.6 % conversion, respectively. Interestingly, independent to the metal catalysts used, ACN was the only product detected. Hence, targeting the highest yield of ACN, Rh/Al_2O_3 was chosen as deserved candidate for further study to optimize the reaction condition. In the first step, CO_2 pressure was optimized after conducting the reaction at various CO_2 pressure from 6 to 20 MPa. The conversion of ADN was increased from~46 to 96.6 %, with the change in pressure from 6 to 8 MPa and then started to decrease as the pressure reached above 12 MPa. The increased conversion at low CO_2 pressure is most likely attributed to the shifts of partition coefficient of the substrate in favor of the liquid phase and thus, increasing availability of substrate in the vicinity of the catalyst. On the other hand, the conversion was dropped to 20 % at very high pressure of 20 MPa. There was no effect of pressure on the product distribution; ACN was the only product through-out the pressure range studied. When the reaction was conducted in solvent-less condition the conversion was decreased to < 20 % and the product mixture contains 44 % of ACN and 55 % of HMD. Furthermore, instead of CO_2, if ethanol was introduced as reaction medium, 70 % conversion was achieved; higher than the solvent-less condition, but lower in comparison with CO_2. Similar to the solvent-less condition, 75.6 % ACN and 24.4 % HMD were detected in ethanol. From these results it could be inferred that the presence of solvent was mandatory to the formation of semi hydrogenated product ACN, but CO_2 as a solvent was the superior choice for this type of reaction. Phase behavior is one the important parameters as CO_2 has tendency to interact with amine. Figure 9 shows the images of ADN before and after the introduction of 8 MPa CO_2. A clear change was detected through the view cell. The reason behind the possible alteration is the formation of carbamic acid or carbamate through the interaction of $–NH_2$ group and CO_2. Once one nitrile group was reduced to amine, it rapidly reacts with CO_2 to produce carbamic acid and effectively removes the second nitrile group from the reaction and stops further reaction, which explains the high selectivity of ACN. Hoffer *et al.* observed that co-adsorption of two nitrile groups of the substrate is unlikely. So, one of the nitrile groups is first selectively hydrogenated to amine, and there would be an enhanced competition between dinitrile and aminonitrile for same active site because of the presence of similar group and mixture of the products might be expected (*71*).

A time dependent catalytic performance was evident for hydrogenation of ADN. The conversion of ADN was poor (~ 20 %) in the beginning, but increased up to 96.6 % as the time extended to 6 h. Unfortunately complete conversion cannot be achieved even after 24 h of reaction, which triggered to the (i) deactivation of the catalyst and (ii) competition between reactant and product for the same catalytic active site. Recycling of the catalyst for several times cut-off the possibility of deactivation. Coming to the next point, a primary study on the kinetics revealed a consistency with Langmuir-Hinshelwood law derived on the basis of reaction 1. Based on that a plot of experimental against calculated conversion (Figure 10) showing good agreement and the adsorption constant was

K_{ADN}/K_{ACN}=3.12 indicated the preferential adsorption of ADN instead of ACN as both of them competing for the same site, which explain the constant conversion after the certain period of reaction time.

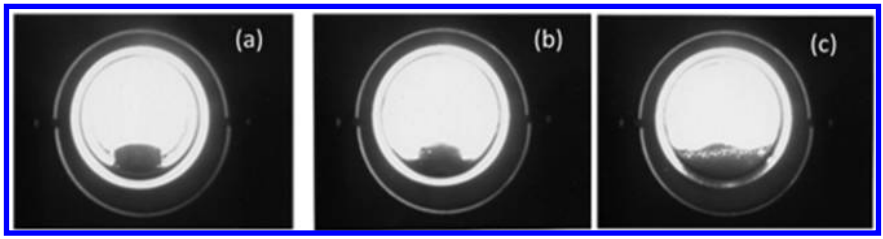

Figure 9. View cell observations of adiponitrile (ACN) in scCO₂; (a) before introduction, (b) after the incorporation of 8 MPa of CO₂ and (c) during depressurization.

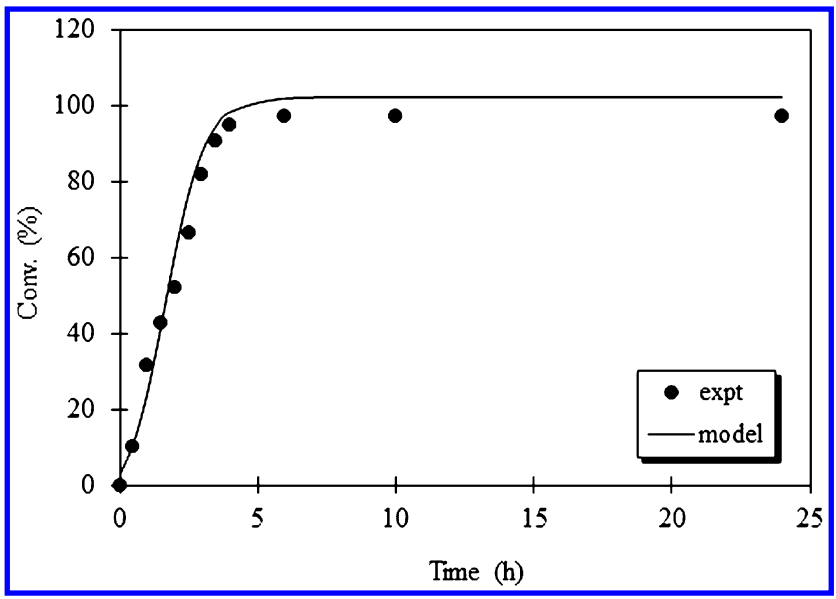

Figure 10. Plot of conversion along with time and fitted with the calculated conversion.

Publication Date (Web): September 11, 2015 | doi: 10.1021/bk-2015-1194.ch009

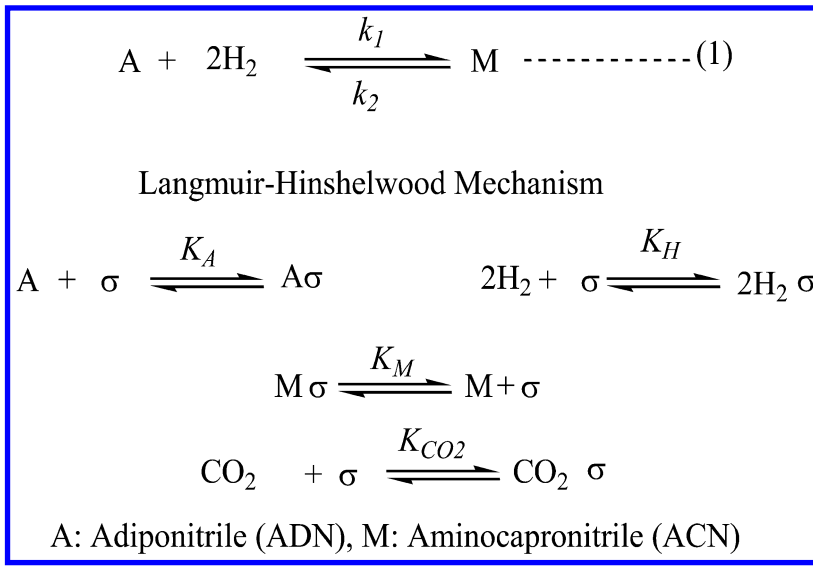

Langmuir-Hinshelwood mechanism

Rate equation is

Where, r is the rate of the reaction, k= rate constant and K=adsorption coefficient.

$$r = \frac{k\left(C_A P_H^2 - C_M / K\right)}{\left(1 + K_A C_A + K_H P_H^2 + K_M C_M + K_{CO2} P_{CO2}\right)^2}$$

$$k = k_1 K_A K_H$$

$$K = k_1 K_A K_H / k_2 K_M$$

$$\frac{dx}{dt} = \frac{k\left(P_H^{0^2}(1-x)^3 - x^2 / K\right)}{\left(1 + K_A C_A^0(1-x) + K_H P_H^{0^2}(1-x)^2 + K_M C_A^0 x + K_M C_A^0 x + K_{CO2} P_{CO2}^0\right)^2}$$

$$\frac{dx}{dt} = \frac{k_1 K_A K_H P_H^{0^2}(1-x)^3 - k_2 K_M x^2}{\left(1 + K_A C_A^0(1-x) + K_H P_H^{0^2}(1-x)^2 + K_M C_A^0 x + K_{CO2} P_{CO2}^0\right)^2}$$

There was no effect of reaction time on the selectivity was detected, and again confirmed the amine protection of CO_2.

According to the Langmuir-Hinshelwood isothermal equation, increase in H_2 pressure increases the surface concentration. Thus, an increase in pressure from 1 to 4 MPa enhanced the conversion from 28.4 to 96.6 % without changing the product selectivity and then remain constant. A change in H_2 and CO_2 pressure together keeping total pressure of 12 MPa constant (P_{CO2}/P_{H2}= 11/1, 10/2, 9/3 and 8/4) changes the conversion from 11.2 to 96.6 % attributed a positive effect of H_2 pressure.

Publication Date (Web): September 11, 2015 | doi: 10.1021/bk-2015-1194.ch009

As already described that the role of temperature is complex when the reactions are conducted in $scCO_2$ medium. In one hand, an increase in temperature could have positive effect on the reaction kinetics as defined by the transition state theory and on the other hand, change in temperature strongly influenced the physical properties of CO_2, especially the density, which might have negative effect as it affect the solubility of the reactant. Hence, it is very difficult to predict the exact reason behind the increased conversion with temperature.

After getting the satisfactory results on the selective hydrogenation of one −CN group of dinitrile compound, the method was applied to the other dinitriles such as terephthalonitriles, isophthalonitriles and phthalonitriles were subjected to hydrogenation under the similar reaction condition of ADN (P_{CO2}=8 MPa, P_{H2}= 4 MPa, temperature= 80° C, time=6 h) and the results are shown in Table 10. Depending on the position of the two $-NH_2$ groups, TOF was varied; phthalonitrile (*o*-) has lowest TOF of 570 h^{-1} as *o*-substitution was increasing the steric hindrance around the reaction centre. However, in each case corresponding aminonitrile was formed and confirmed the adsorption of only one −CN group on the active site followed by selective hydrogenation to aminonitrile.

Table 10. Hydrogenation of Different Dinitriles

Entry	*Substrate*	*Conv. (%)*	*Yield[a] (%)*	*TOF[b] (h^{-1})*
1	Terephthalonitrile	95.9	94.2	1069.6
2	Isophthalonitrile	60.1	53.1	679.2
3	Phthalonitrile	51.1	32.6	570.0

Reaction conditions: catalyst= 0.1 g, substrate=1.0g, P_{CO2}= 8 MPa P_{H2}= 4 MPa, temperature= 80 °C, reaction time= 6h. [a] =Yield of corresponding aminonitrile. [b] =Turnover frequency (TOF) = no. of moles reacted/ moles of metal x time.

(v). Hydrogenation of $-NO_2$ Group

Hydrogenation of nitrobenzene (NB) to aniline (AN) is an extremely important reaction as AN is a valuable intermediate for the synthesis of isocyanates in urethane industry. It can be also used as an accelerator, activator for rubber industry, agricultural products, pharmaceuticals and other chemical products. About 85 % of global aniline is produced from hydrogenation of NB. This reaction is extremely facile and can be easily occurred under mild reaction condition. Generally, vapor phase hydrogenation of NB was used for large scale production of aniline. Alternatively, the reaction can be conducted in liquid phase also. Different types of metals (Ni, Pt, Pd, Rh, Ru) and non-metals supported on various supports were tested. Most of the process suffers from one or more drawbacks related to the environmental concern, poor selectivity because of the formation of undesirable by-products such as nitrosobenzene, phenylhydroxylamine, azoxybenzene, azobenzene and hydrazobenzene. One of the most common way to reduce by-products as well as improved selectivity is the

In Advances in CO2 Capture, Sequestration, and Conversion; He, et al.;
ACS Symposium Series; American Chemical Society: Washington, DC, 2015.

Publication Date (Web): September 11, 2015 | doi: 10.1021/bk-2015-1194.ch009

introduction of additive, which creates a waste problem, increase production cost and reducing efficiency of the catalyst after certain runs. Hence, implementation of those processes in large scale is difficult. A solvent-free route was also introduced using Pt supported on carbon nanotube (CNT) (*72*). Although, CNT are potentially efficient support materials, still it is difficult to produce and the structures are hard to control (*73*).

In the previous section we mentioned the successful application of $scCO_2$ medium for selective hydrogenation of different functional groups and aromatic ring. In most of the cases the reaction was faster, products obtained with very high selectivity and clean product separation. According to the reported literature, high conversion of NB to AN could be readily achieved in $scCO_2$, but selectivity of AN was poor because of the formation of noticeable amount of by-products (conversion of NB = 70 %; AN selectivity = 84 %) (*74*, *75*). An improved selectivity of aniline was predicted over Ni/γ-Al_2O_3 catalyst (conv. = 68- 73 %; selectivity of aniline = > 99 %; reaction time= 50 min.), but conversion was quite low and required product separation (*76*). Main focus of this work is to find out a suitable catalyst to achieve complete conversion and selectivity of AN to avoid the separation problem. Advantageous properties of $scCO_2$ such as tunability and miscibility with reactant gases could be helpful to obtain high performance. We also tried to explore actual reaction mechanism in the presence of suitable heterogeneous catalyst. To choose a perfect catalyst, several metals supported on MCM-41 was screened under the applied condition of P_{CO2}= 12 MPa, P_{H2}= 2.5 MPa and temperature= 50 °C and reaction time=10 min. In each case metal content was ~ 1 wt. % and the particle size varied between 5 to 10 nm (Table 11). The use of MCM-41 as support material is logical because according to the reaction path, hydrogenation of NB to AN is associated with the formation of water, thus, most acceptable support should be hydrophobic like carbon (*77*)**.** However, carbon supports are not inert and therefore, sometime causes undesired by-product formation and hampers the selectivity of aniline. Hence, inert support materials with hydrophobicity are particularly preferred (*78*, *79*). Noteworthy, mesoporous MCM-41 type materials are inert and possess similar hydrophobicity to the activated carbon (*1*). All the metal used here as catalysts were not equally active under the condition used despite of the same metal content. Except Pd and Pt, all other metals showed nominal activity. As the reaction time was short, in some of the cases metal with longer induction period failed to respond. Changing the reaction condition may be advantageous for those catalysts. Additionally, initial activity is very different from the steady state. Surprisingly, independent to the metal used AN was the only product detected. Based on the catalytic efficiency, Pd was considered as most potential catalyst to obtain complete conversion and selectivity.

Different reaction parameters need to be optimized to achieve complete conversion and selectivity of AN. Figure 11 shows a CO_2 pressure dependent TOF of NB conversion, which reaches a maxima at 12 MPa of CO_2 pressure and then decreased slowly. The rate of the reaction in terms of TOF revealed that the reaction proceed with comparatively lower TOF of 7.0 x 10^4 h^{-1} when the pressure was < 12 MPa. However, highest TOF of 25.2 x 10^4 h^{-1} was attained as the pressure increased to 12 MPa, followed by a slight drop of TOF (21.7 x 10^4

In Advances in CO2 Capture, Sequestration, and Conversion; He, et al.;
ACS Symposium Series; American Chemical Society: Washington, DC, 2015.

Publication Date (Web): September 11, 2015 | doi: 10.1021/bk-2015-1194.ch009

h^{-1}) at > 12 MPa. Increased availability of the substrate with increase in pressure, TOF was reached to a very high value, but further increase in CO_2 pressure could be associated with the dilution effect and TOF dropped. The observed pressure dependent catalytic performance might be explained by the phase behavior of the system (NB−H_2−CO_2). Visual inspection showed that NB is soluble in $scCO_2$. At lower pressure, there was a separation of liquid phase observed, however, at or above 12 MPa, the system was in single phase. In fact, the difference in activity between lower and higher pressure was due to the availability of the substrates, where NB can be readily hydrogenated without any mass transfer restrictions caused by the phase border. The single phase condition was preferable to achieve high catalytic performances and it could be suggested that the complex phase behavior, which changes the concentration of NB and H_2 in various phases account for the differences in TOF.

Publication Date (Web): September 11, 2015 | doi: 10.1021/bk-2015-1194.ch009

Table 11. Catalyst Screening for Hydrogenation of NB to AN

Entry	*Catalyst*	*Conv. (%)*
1	-	0.0
2	MCM-41	0.0
3	Ni/MCM-41	0.5
4	Pd/MCM-41	100.0
5	Pt/MCM-41	83.0
6	Rh/MCM-41	1.6
7	Ru/MCM-41	0.7
8	Au/MCM-41	4.3
9	Ir/MCM-41	2.3

Reaction condition: catalysts =0.1 g, substrate= 2.0 g; P_{CO2}= 12 MPa, P_{H2}= 2.5 MPa and temperature= 50 °C and reaction time= 10 min. metal content= 1 wt. %

In another series of experiment, influence of H_2 pressure was investigated keeping other parameters fixed. The conversion was linearly increased from 20 to 100 % with the change in pressure from 0.5 to 2.5 MPa. Since, according to the Scheme 3a, 1 mole of NB required 3 moles of H_2 to produce 1 mole of AN and 2 moles of water. Hence, 0.05 moles of H_2, which corresponds to 2.5 to 3 MPa pressure at 50 °C will be required for the hydrogenation of 0.0162 mole (used in this process) of NB. At the fixed substrate concentration, if H_2 pressure was enhanced to 4 MPa or above, the reaction was much faster, but selectivity of AN dropped severely. Thus, managing H_2 pressure might be an important parameter to control the selectivity of desired AN.

In addition to the H_2 pressure, reaction temperature was another tricky parameter if the reaction conducted in $scCO_2$ because it controlled the phase topology as well as reaction kinetics. Therefore, observed change in the catalytic activity with the change in temperature was interpreted in terms of phase behavior.

In Advances in CO2 Capture, Sequestration, and Conversion; He, et al.;
ACS Symposium Series; American Chemical Society: Washington, DC, 2015.

Publication Date (Web): September 11, 2015 | doi: 10.1021/bk-2015-1194.ch009

The reaction was slow at lower temperature of 35 °C though a single phase detected between NB and CO_2-H_2. Hence, a better activity could be expected if phase behavior was only controlling factor. But the reaction affected kinetically; an increase in temperature increases the reaction rate. From the initial reaction rate, Arrhenius plot (Figure 12) was obtained with an apparent activation energy of 15 kJmol^{-1} and comparable with the liquid phase hydrogenation (*80*, *81*).

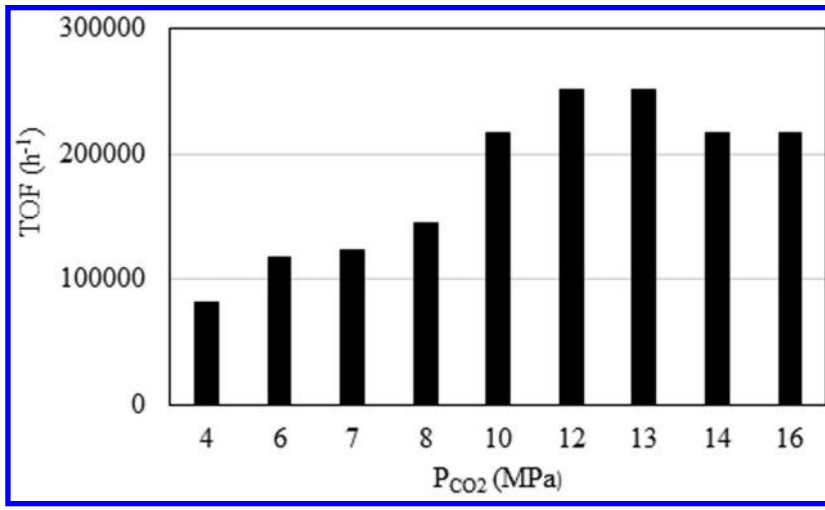

Figure 11. Effect of CO_2 pressure on the TOF of nitrobenzene (NB) to aniline (AN) hydrogenation in scCO_2.

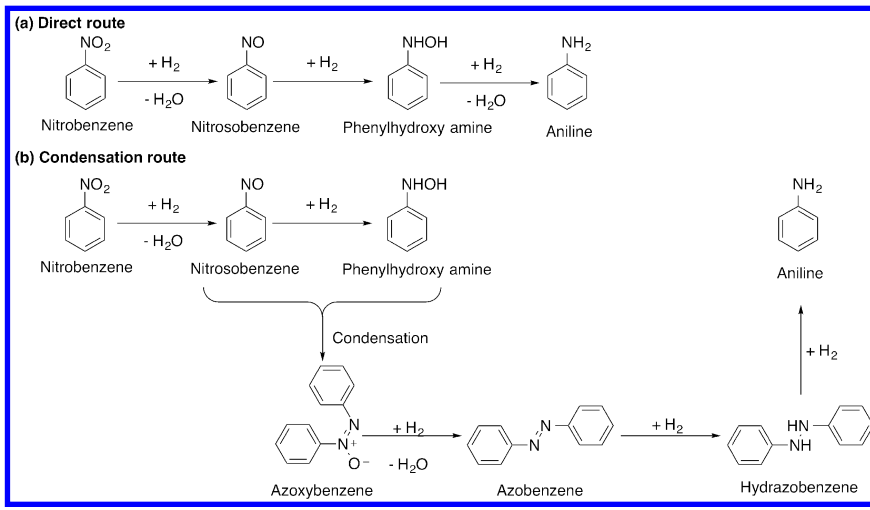

Scheme 3. Hydrogenation of nitrobenzene (NB) to aniline (AN) via (a) Direct and (b) condensation route.

In Advances in CO2 Capture, Sequestration, and Conversion; He, et al.;
ACS Symposium Series; American Chemical Society: Washington, DC, 2015.

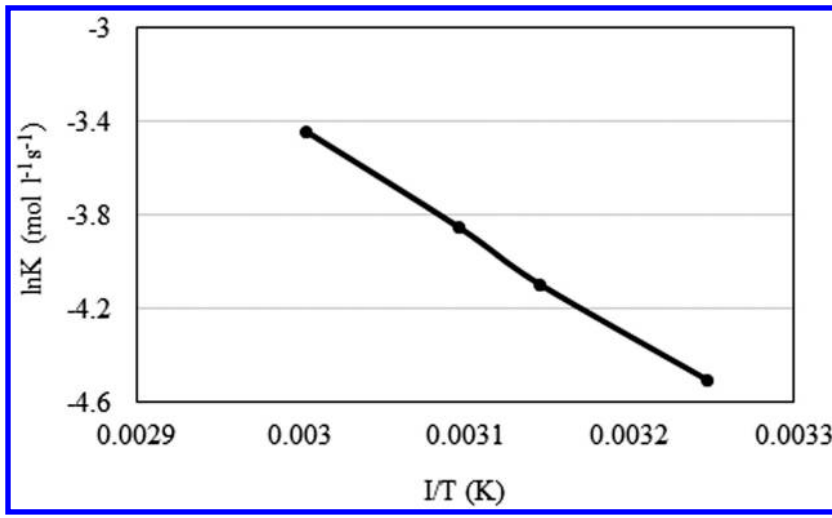

Figure 12. Arrhenius plot.

Based on the above results. the optimized reaction condition (catalysts =0.1 g, substrate= 16.2 mmol; P_{CO2}= 12 MPa, P_{H2}= 2.5 MPa and temperature= 50 °C and reaction time= 10 min) was again applied to the hydrogenation other nitro-aromatics and the results are shown in Table 12. The hydrogenation of *o- m-* and *p-* isomers of nitrotoluene producing only their corresponding amine (Entry 1-3), and the conversion decreased in the order of *p-*> *m-* > *o-* because of the steric hindrance. Following nitrotoluenes, nitroanisoles were also behaved in a similar way (Entry 4-6). In addition, successful application of the described method can also extended to dinitro compounds. For example, 2, 4, dinitrotoluene, which was hydrogenated to 2-amino 4-nitro toluene (82.0 %), and 2, 4 diaminotoluene (28.0 %) (Entry 7). Chloronitrobenzene, a representative of halogenated nitro compound also performed well to the formation of chloroaniline with the selectivity of > 90 % (Entry 8 and 9). Furthermore, the Pd/MCM-41 catalyst continued its reign to the hydrogenation of nitrobenzoic acid (Entry 10-12). In each case, independent to the conversion, only amino compounds were formed. Thus, application of Pd/MCM-41 catalyst was feasible to the hydrogenation of other nitroaromatics with different functional groups under the present reaction condition.

Mechanistically, hydrogenation of NB is a complicated reaction. Depending on the reaction condition and catalyst used the reaction path varies. There are two different routes of the hydrogenation of NB to AN: (i) direct and (ii) condensation route (Scheme 3b). To determine the reaction path under the working condition it is important to know the activity of intermediates, which sometimes provide a direct proof to the reaction mechanism. However, the reaction profile showed a direct transformation of NB to AN without any by-product or condensation products or any intermediates detected even in the shortest reaction time of 1 min. As there were no condensation products detected, only direct route can be considered. According to Haber's process, NB was converted to AN via nitrosobenzene and phenylhydroxylamine. Both of those routes (NB to nitrosobenzene and nitrosobenzene to phenylhydroxylamine) were very fast and

In Advances in CO2 Capture, Sequestration, and Conversion; He, et al.;
ACS Symposium Series; American Chemical Society: Washington, DC, 2015.

Publication Date (Web): September 11, 2015 | doi: 10.1021/bk-2015-1194.ch009

intermediates have tendency to adsorb on the catalyst support strongly. The results of the hydrogenation of nitrosobenzene and phenylhydroxylamine were compared with NB under the similar reaction condition (Figure 13). Calculation of the initial rate (TOF) of AN formation from nitrosobenzene (TOF=6264 h^{-1}) and nitrobenzene (TOF = 2.52 x 10^4 h^{-1}) provides a significant difference. The slowest rate of hydrogenation indicating that nitrosobenzene could not be the possible intermediate species involved in the AN formation. Another evidence is the reduction of initial reaction rate while the reaction was conducted in presence of nitrosobenzene because of the competitive nature of substrates. Therefore, two possible reaction paths (i) NB →AN and (ii) NB →phenylhydroxylamine → AN were predicted from the experimental results.

Publication Date (Web): September 11, 2015 | doi: 10.1021/bk-2015-1194.ch009

Table 12. Hydrogenation of Different Nitroaromatics

Entry	*Substrate*	*Conv. (%)*	*Product (%)*
1	*o*-nitrotoluene	78.5	*o*-toluidine (100)
2	*m*-nitrotoluene	89.8	*m*-toluidine (100)
3	*p*-nitrotoluene	100.0	*p*-toluidine (100)
4	*o*-nitroanisole	67.1	*o*-anisidine (100)
5	*m*-nitroanisole	80.1	*m*-anisidine (100)
6	*p*-nitroanisole	92.3	*p*-anisidine (100)
7[a]	Dinitrotoluene	66.3	Aminonitrotoluene (82)
8[b]	*m*−Chloronitrobenzene	95.5	*m*−Chloroaniline (90.2)
9[c]	*p*−Chloronitrobenzene	46.8	p−Chloroaniline (98.9)
10	*o*-nitrobenzoic acid	46.3	*o*-aminobenzoic acid (100)
11	*m*-nitrobenzoic acid	66.9	*m*-nitrobenzoic acid (100)
12	*p*-nitrobenzoic acid	90.9	*p*-aminobenzoic acid (100)

Reaction conditions: catalysts =0.1 g, substrate= 2.0 g; P_{CO2}= 12 MPa, P_{H2}= 2.5 MPa and temperature= 50 °C and reaction time= 10 min. [a] 28 % 2, 4-diaminotoluene. [b] 9.8 % aniline. [c] 1.1 % aniline.

At this point it is difficult to describe the exact consequences behind the conversion of NB to AN. To go one step further, DFT (density functional theory) studies were performed to model the adsorption of substrates, possible intermediates as well as product on catalyst surface and the results are presented in Table 13. Figure 14 depicted the adsorption geometry of each components. The calculated adsorption energy of reactant, intermediates and product follows the order of phenylhydroxylamine > NB ≈ nitrosobenzene > AN. The adsorbed molecules lies parallel to the catalyst surface. According to the results, adsorption energy of phenylhydroxylamine was very high and the strong adsorption on the catalytic surface could be predicted. On the other hand, NB and nitrosobenzene

In Advances in CO2 Capture, Sequestration, and Conversion; He, et al.;
ACS Symposium Series; American Chemical Society: Washington, DC, 2015.

has very close adsorption energy, which suggested a competitive nature of the substrate for the catalytic active site. In the next step we have calculated the energetics of each possible steps to determine the energetically preferred pathway (Table 13).

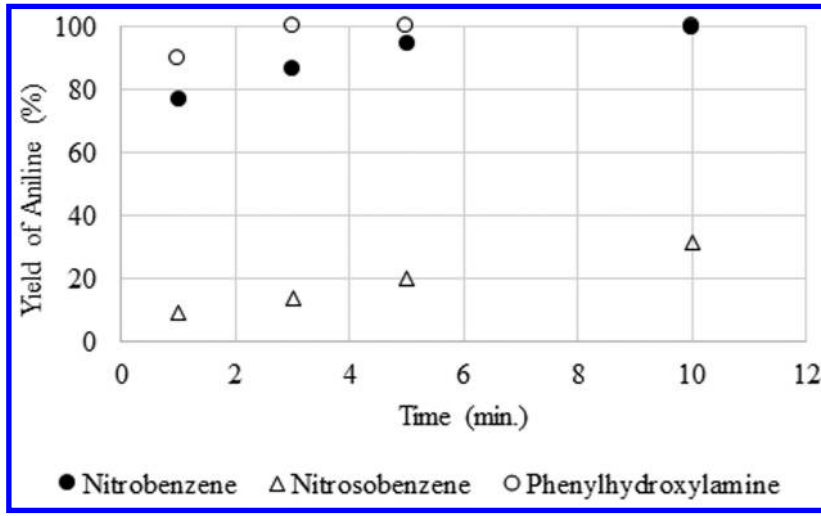

Figure 13. Comparison of the hydrogenation of nitrosobenzene and phenylhydroxylamine with nitrobenzene.

Table 13. Calculated Reaction Energies for Different Reaction Steps of NB Hydrogenation under the Studied Reaction Condition

Entry	*Reaction*	*ΔE_a react (kcal/mol)*	*ΔH_a react (kcal/mol)*
1	$C_6H_5NO_2 + H_2 \rightarrow C_6H_5NH_2 + H_2O$	19.6	-45.0
2	$C_6H_5NO_2 + H_2 \rightarrow C_6H_5NO + H_2O$	18.8	-11.0
3	$C_6H_5NO + H_2 \rightarrow C_6H_5NHOH$	10.6	+4.2
4	$C_6H_5NHOH + H_2 \rightarrow C_6H_5NH_2 + H_2O$	8.2	-55.0
5	$C_6H_5NO_2 + H_2 \rightarrow C_6H_5NHOH$	16.9	-97.0

Publication Date (Web): September 11, 2015 | doi: 10.1021/bk-2015-1194.ch009

Publication Date (Web): September 11, 2015 | doi: 10.1021/bk-2015-1194.ch009

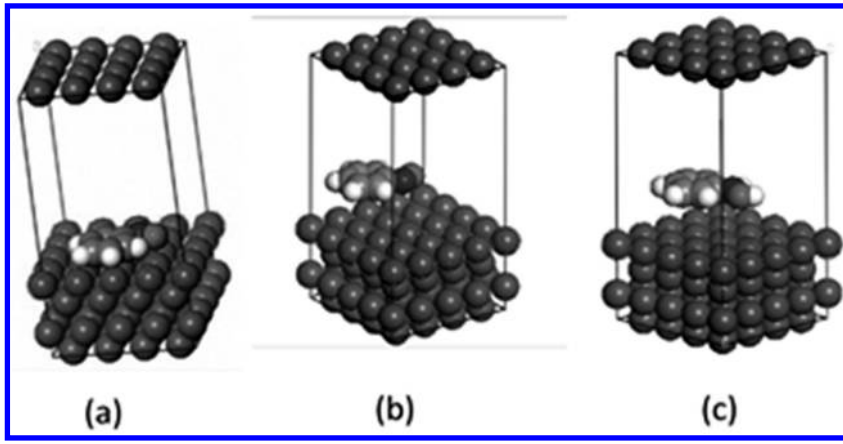

Figure 14. Adsorption geometry of (a) nitrobenzene, (b) nitrosobenzene and (c) phenylhydroxylamine.

Dihydrogen dissociation yields adsorbed H_2 and makes the surface hydrogenated. Calculations indicate that the surface reaction steps of NB to AN are highly exothermic and correspond well with the literature (*82*). The formation of phenylhydroxylamine could happen through the direct hydrogenation of NB or via nitrosobenzene. The energetic difference between the two pathways are obvious. In the former, the individual steps of NB → nitrosobenzene and nitrosobenzene → phenylhydroxylamine required to overcome activation barrier of 18.8 and 10.6 kcal/mol, respectively (Table 13; Entry 2 and 3). Interestingly, reaction step of nitrosobenzene to phenylhydroxylamine is mildly endothermic (ΔH = 4.2 kcal/mol). The high barrier along with the endothermicity makes this an unlikely path on Pd catalyst. On the contrary, phenylhydroxylamine from NB is exothermic (ΔH = - 97 kcal/mol) with activation barrier of 16.9 kcal/mol (Table 13; Entry 5), could be the effective choice as an intermediate in the hydrogenation of nitrobenzene. Furthermore, calculation shows that conversion of phenylhydroxylamine → AN possesses lowest activation barrier of 8.2 kcal/mol and could not be the rate limiting step. Therefore, instead of phenylhydroxylamine → AN, the slowest step of NB → phenylhydroxylamine is considered as the rate determining step and DFT predicted an activation barrier (16.9 kcal/mol), which is in good agreement with the experimental value of 15 kcal/mol. In an effort to understand the reaction mechanism under the studied reaction condition, experimental observation coupled with theoretical calculations provide ample evidence in favor of the reaction path of formation of aniline via phenylhydroxylamine.

After the successful application of Pd/MCM-41 to the hydrogenation of NB, the support material was modified with the substitution of boron (B), expected to modify structural properties of MCM-41. In fact great chemical and catalytic diversity might be generates by the isomorphous substitution of Si by trivalent metal ions such as B, Al, Ga etc. This type of substitution to the only Si material developed acid sites and make it more suitable to act as an acidity demanding catalyst. Borosilicate molecular sieves are mildly acidic, hence, there are fewer

studies in comparison with aluminosilicate. Here, we synthesized Pd nanoparticle supported B-MCM-41 obtained by hydrothermal method. Contrary to the Si-MCM-41, presence of B in MCM-41 might affect particle size distribution and consequently the catalytic activity. In addition mild acidic nature of the support could improve the catalytic efficiency.

Different B containing materials were synthesized by varying the ratio of Si/B from 100 to 5. The synthesized material was characterized by XRD, TEM, FTIR and TG/DTA to get an insight in to the structural diversity generated depending on the B content. XRD pattern of the calcined material shows typical low angle peak representative of MCM-41. The peak intensity was strongly dependent on the Si/B ratio and accordingly with the structural order. There was a strong correlation observed with Pd particle size and Si/B ratio; size changes from 10.9 to 22.6 nm as the ratio changes from 100 to 5 (Table 14). Because of the larger particle size, five characteristic peak of PdO at 2θ= 33.8, 42.0, 54.8, 60.7 and 71.4° were clearly visible in the XRD pattern of higher angle region, but after hydrogenation, metallic Pd was formed and a peak was detected at 2= 40.1°.

Publication Date (Web): September 11, 2015 | doi: 10.1021/bk-2015-1194.ch009

Table 14. Physical Characterization of Pd/B-MCM-41

Si/B ratio	d_{100} *(nm)*	a_0 *(nm)*	*Average Pd Particle size (nm)*	*Weight loss of template at 120- 320 °C (%)*
Only Si	4.6	5.31	-	38.6
100	4.2	4.85	10.9	35.1
25	4.1	4.73	19.5	33.4
10	4.0	4.62	21.5	30.2
5	3.8	4.38	22.6	28.5

Structural confirmation was also available from the TEM image after calcination. A regular ordered structure with hexagonal channel was only visible for higher Si/B ratio, but structural order was destroyed as the Si/B ratio became low of 5. Spherical Pd particles are detected throughout the surface. From the particle size distribution average particle sizes were determined as 12.1 and 23.1 nm for higher (100) and lower (5) Si/B ratio, respectively. These results corresponded well with the XRD measurements.

One of the primary tool to recognize the substitution of B in MCM-41is FTIR. All B containing samples developed a band at 1380 cm^{-1} and an increase in the intensity was observed with B content. However, an additional band at 940 cm^{-1} of tetrahedral B was only detected for Si/B=5. Moreover, TG/DTA analysis revealed an important information regarding the weight loss of the template based on the Si/B ratio. With increasing B content a larger part of the template was removed at high temperature as template cation bonded to the siloxy group decomposes at low temperature (*16*), which is confirmed from the analysis of only Si material (Table 14).

In Advances in CO2 Capture, Sequestration, and Conversion; He, et al.;
ACS Symposium Series; American Chemical Society: Washington, DC, 2015.

After the characterization, calcined material was subjected to the hydrogenation of NB. Interestingly the reaction was extremely fast with TOF= 5.2 x 10^5 h^{-1}. Complete conversion and 100 % selectivity to AN was achieved within the reaction time of 5 min. This reduction of reaction time compared to Pd/MCM-41 catalyst was subsequently used to optimize the reaction condition. The CO_2 and H_2 pressure as well as temperature to be varied keeping other parameters such as substrate: catalyst ratio, stirring speed and reaction time.

The optimization procedure targeted to complete conversion and selectivity was not described in detail further. About the influence of individual parameters, in general, high conversion were obtained by increasing the CO_2 pressure at constant temperature. This can be attributed to the higher substrate availability due to the increased solvent power of CO_2. Similarly, TOF was enhanced from 1.7 x 10^5 h^{-1} to 5.2 x 10^5 h^{-1} as the H_2 pressure changed from 0.5 to 2 MPa. Interestingly, maximum TOF was obtained at 2 MPa, which is lower than Pd/MCM-41. At a fixed pressure of CO_2, increase in temperature also increased the reaction rate and suggested that the kinetic effect surpasses the potential negative effect of reduced CO_2 density (*83*).

With a standard set of reaction condition, Pd/B-MCM-41 was used to the hydrogenation of different substrates containing (i) $-NO_2$ along with the electron donating and withdrawing groups, (ii) −CN and (iii) −OH group and the results are in Table 15. The hydrogenation of *o*, *m* and *p*- chloronitrobenzne converted to their corresponding amine with a very high selectivity of > 99 % and conversion follows the order of *p*-> *m*-> *o*- (Entry 1-3). Another compound such as nitroanisoles was also behaved in a similar manner (Entry 4-6) though conversion was lower than halonitroaromatics and in each case, only the nitro group was hydrogenated.

Instead of nitroaromatics, potential of Pd/B-MCM-4 once again explored through the hydrogenation of benzonitrile and phenol. It has to be mentioned that similar to nitro compounds, benzonitrile was hydrogenated to primary amine with the selectivity of 99 %, but it required reaction time of 2 h. Considering the hydrogenation of phenol (Table 12; Entry 8), where ring hydrogenation is more preferable because of presence of the –OH group (electron donating group) results cyclohexanone as the only product. The ring hydrogenation was activated by acidity of the support (*84*) due to the presence of B in the support material as confirmed by comparison with Pd/MCM-41 (only silica) catalyst under the similar reaction condition (temperature= 50 °, time = 4 h, P_{CO2}= 10 MPa, P_{H2}=4 MPa) as described previously (*85*).

Publication Date (Web): September 11, 2015 | doi: 10.1021/bk-2015-1194.ch009

Table 15. Hydrogenation of Different Substrates on Pd/B-MCM-41 in $scCO_2$

Entry	*Substrate*	*Conv. (%)*	*Product (selectivity %)*
1	*o*−Chloronitrobenzene	68.2	*o*−Chloroaniline (100)
2	*m*−Chloronitrobenzene	82.2	*m*−Chloroaniline (100)
3	*p*−Chloronitrobenzene	100	*p*−Chloroaniline (100)
4	*o*-nitroanisole	53.5	*o*-anisidine (100)
5	*m*-nitroanisole	66.9	*m*-anisidine (100)
6	*p*-nitroanisole	89.2	*p*-anisidine (100)
7[b]	Benzonitrile	60.2	Benzylamine (99.0)
8	Phenol	98.5	Cyclohexanone (100)

Reaction conditions: Entry 1-6: catalyst=0.1g, substrate= 2.0 g, P_{CO2}= 12 MPa, P_{H2}= 2 MPa, temperature = 50 °C; time= 10 min; Entry 7 catalyst=0.1g, substrate= 1.0 g, P_{CO2}= 10 MPa, P_{H2}= 2 MPa, temperature = 50 °C; time= 2h; Entry 8: catalyst=0.1g, substrate= 1.0 g, P_{CO2}= 12 MPa, P_{H2}= 4 MPa, temperature = 50 °C; time= 4h.; b= dibenzylamine = 1 %.

Publication Date (Web): September 11, 2015 | doi: 10.1021/bk-2015-1194.ch009

Why the Studied Reactions Are Faster on Pd/B-MCM-41 Compared to the Si Analogue of MCM-41?

The time profile of the conversion of NB was evaluated on two Pd/B-MCM-41 catalysts differed by Si/B ratio of 100 and 5 (Figure 15a). In each case, the reaction was comparatively fast, but complete conversion can be achieved within the shortest reaction time of 5 min. only when Si/B=5 was used. For these two catalysts, Pd particle sizes are different (Table 1). Thus, to explain these observations there are two primary factors to be considered: (i) effect of Pd particle size and (ii) B content, which controlled the structural order. It has to be mentioned that only support material was inactive and hence, catalytic activity of the metal−Containing catalysts arises unambiguously due to the presence of active metal species on the support. Generally, the variation in catalytic activity depends on the dispersion of metal. This factor is further influenced by B content of MCM-41. (i) Effect of Pd particle size: the dependence of NB hydrogenation rate on particle size is shown in Figure 15b, which indicates that the initial TOF calculated per surface Pd atom increases with the particle size. The changes in particle size from ~10 to 20 nm increased the TOF from 2.1 x 10^5 h^{-1} to 5.2 x 10^5 h^{-1}. Hence, larger Pd particles were considered to be more active than smaller one, assuming that all the particles took part in the reaction. Although there was a sharp change of TOF with particle size, it is difficult to comment on the structure sensitivity because the studied range of particle size was limited. A similar phenomenon was also reported previously in the liquid phase hydrogenation of NB in methanol over Pd/C at 50 °C (*86*).

In Advances in CO2 Capture, Sequestration, and Conversion; He, et al.;
ACS Symposium Series; American Chemical Society: Washington, DC, 2015.

(ii) B content: presence of B incorporates weak acidity on the support surface as described by many researchers and it might change catalyst morphologies such as metal dispersion, etc. We had compared the results between low B content (Si/B=100) and only Si material. The rate was comparatively higher for Si/B=100 (TOF= 3.8 x 10^5 h^{-1}) rather than only Si catalysts (TOF= 2.5 x 10^5 h^{-1}) although both of them contain Pd particles of similar size (~10 nm) and highly ordered structures. On the basis of these results it might be concluded that even in the presence of small amount of B the reaction rate was increased, which implies that weak acid sites or hydrophobicity (related to the B species) participate in the reaction process under the studied reaction condition. To check the role of support containing acid sites, the hydrogenation of NB was conducted on ~ 1% Pd containing Al and Ga-MCM-41 under the similar reaction condition as described for Pd/B-MCM-41. Generally, Al-MCM-41 possesses stronger surface acidity than its B counterpart (*87*, *88*) and the order of acid strength is Al> Ga>> B (*66*). Following the comparison of reaction rate (TOF), between Pd supported on B-MCM-41 (Si/B=10; particle size = 21.5 nm), Al-MCM-41 (Si/Al = 10; particle size = 18.9 nm) and Ga-MCM-41 (Si/Ga= 10; particle size 21.2 nm); the order is B (5.2 x 10^5 h^{-1}) > Ga (1.1 x 10^5 h^{-1}) > Al (3.6 x 10^4 h^{-1}). In each case, Pd particle size was chosen as ~ 20 nm. Thus, acidity of support could not be the responsible factor for high activity of the catalyst. Substitution of trivalent cation like B, Al and Ga modified the hydrophobic property of Si-MCM-41 and the hydrophobicity order for substituted Si surface are B> Ga> Al (*89*). Primarily, the order of hydrophobicity (prevents limited access of the substrate due to the stronger water adsorption) seems to be a possible deciding factor for higher reaction rate of Pd/B-MCM-41. However, information gathered from the TG analysis of only Si and B-MCM-41 (Si/B=100) reveals different situation as similar hydrophobicity (almost same amount of water loss) was detected for both of the materials. As mentioned before only Si and B-MCM-41 (Si/B=100) has significant difference in the reaction rate. Therefore, higher reaction rate of Pd/B-MCM-41 cannot be directly related to the hydrophobic nature of support. It might be speculated that presence of B in the support material causes an electronic interaction with Pd (*90*, *91*). This brings about an increase in the metal's electron density, causing it to interact more strongly with H_2 adsorbed on the metal surface (*92*) and the reaction rate was enhanced remarkably. A similar result was also observed during the liquid phase hydrogenation of NB over Pt supported borate catalyst (*93*).

Publication Date (Web): September 11, 2015 | doi: 10.1021/bk-2015-1194.ch009

Publication Date (Web): September 11, 2015 | doi: 10.1021/bk-2015-1194.ch009

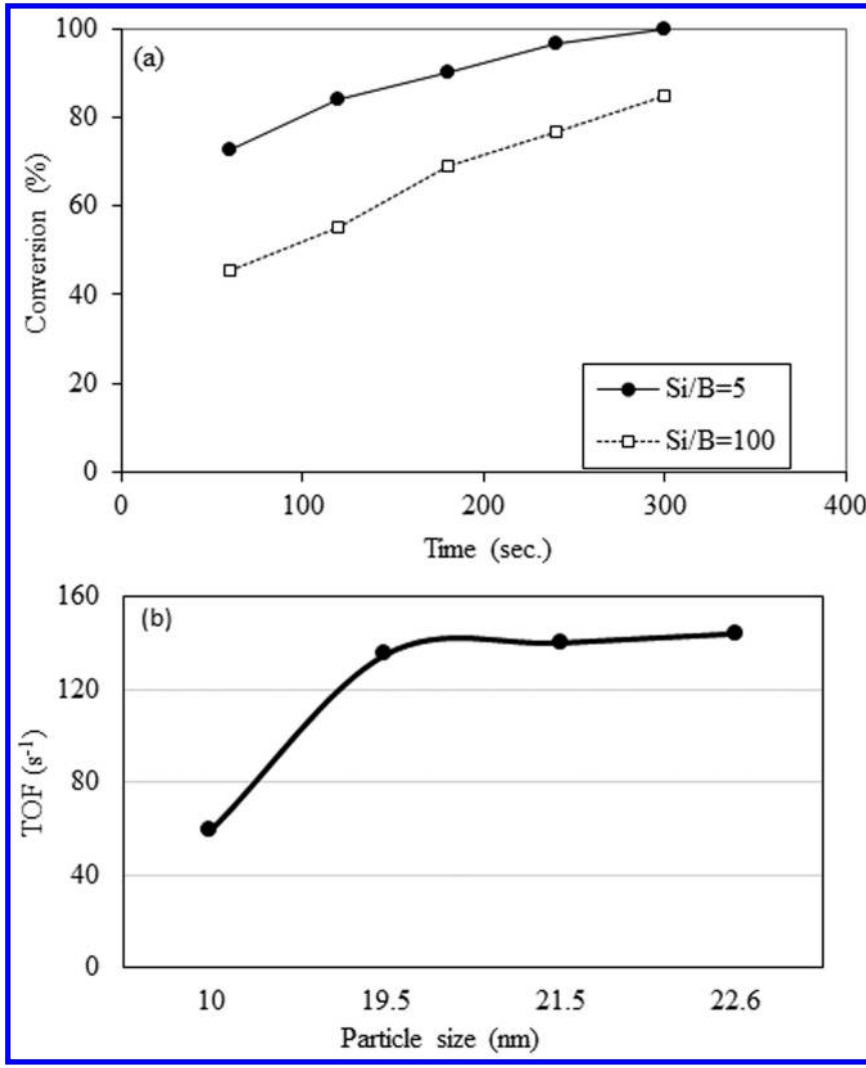

Figure 15. (a) Time profile of nitrobenzene (NB) conversion depending on Si/B ratio and (b) Pd particle size vs TOF of NB hydrogenation using Pd/B-MCM-41 catalyst.

Publication Date (Web): September 11, 2015 | doi: 10.1021/bk-2015-1194.ch009

(vi). Aromatic Ring Hydrogenation

Hydrogenation is an important industrial reaction whether a functional group or an aromatic ring. After successful application of $scCO_2$ as reaction medium for hydrogenation of different functional groups as well as protecting agent, aromatic ring hydrogenation was persuaded. In this category, aniline (AN) and phenol (PhOH) were chosen as two model compounds for hydrogenation of aromatic ring. Hydrogenation of AN to cyclohexylamine (CHA) is an important reaction as CHA is one of the most versatile intermediates from the commercial viewpoint starting from the synthesis of artificial sweeteners to natural product extraction (*94*). In general, commercial method involves (i) reductive amination of cyclohexanol and (ii) hydrogenation of aniline. However, main disadvantage associated especially with the process is the formation of large quantities of wastes because of the use of excess of NH_3 to improve the selectivity of CHA (*95–97*). Several patents were also issued describing the use of variety of metals and support materials to achieve improved selectivity of the desired CHA (*98–104*). Unfortunately, high temperature, high pressure of 35 MPa, use of additives and pressurized NH_3, become most used techniques to restrict the formation of secondary amine. For the sake of remembrance, secondary amine could be formed by the interaction between primary amine. Therefore, amine should be protected from further reaction. Thus, use of $scCO_2$ would be beneficial to achieve high selectivity of the primary amine due to the amine protection role of CO_2 (*105*).

According to the literature, noble metals are most effective choice for the hydrogenation of AN. Investigations on different metal catalysts (Pt, Pd and Rh) supported on Al_2O_3, C and MCM-41 suggested that based on the support used catalytic activity was varied. For instance, Pd supported on C, Al_2O_3 and MCM-41 producced CHA with the selectivity of 30.8, 10.3 and 100 %, respectively. Moreover, depending on the nature of the metal used as well as dispersion, catalytic performance was also different. An approximate expression was used to determine the dispersion (*106*) from particle diameter derived by Scherrer equation. The dispersion varied from 4- 10 % based on the metal and support used. For C support, the dispersion was almost same between the studied metals such as Pt (9.1 %), Pd (8.3 %) and Rh (7.9 %), but catalytic activity followed the order of Rh > Pd > Pt. On the contrary, Al_2O_3 supported catalyst are exhibited the order of Rh (95.8 %) > Pt (40.0 %) > Pd (30.0 %) and Rh (93.0 %) > Pt (61.7 %) > Pd (10.3 %) for conversion and selectivity to CHA, respectively. A significant relation between TOF and the dispersion was clearly visible from the obtained results (*105*). An increase in TOF along with the decreasing metal dispersion was evident as the support changes from Al_2O_3 to C ($TOF_{Al2O3} > TOF_C$) independent to the metal used (TOF_{Al2O3} in h^{-1}: Pd= 81.6, Pt= 110.3 and Rh= 223.3; TOF_C in h^{-1}: Pd= 50.6, Pt= 63.1 and Rh= 105.4). Among the screened catalysts Rh/ Al_2O_3 showedhighest conversion (95.8 %) and excellent selectivity of 93.8 % to CHA under the studied reaction condition (Reaction condition: catalyst=0.1 g, substrate= 0.5 g, temperature = 80° C; Time= 6 h.; P_{H2}= 4 MPa, P_{CO2}= 8 MPa). Hence, Rh/ Al_2O_3 was chosen for hydrogenation of AN to CHA. It has to be mentioned that except Rh, the catalytic performance of Pd and Pt supported on MCM-41 were poor compared to C and Al_2O_3.

In Advances in CO2 Capture, Sequestration, and Conversion; He, et al.;
ACS Symposium Series; American Chemical Society: Washington, DC, 2015.

System optimization could be important in meeting the criterion of best catalytic performances targeting high conversion and high selectivity to CHA. First parameter to be optimized was CO_2 pressure. The reaction was conducted at different pressures ranging from 6 to 14 MPa. Interestingly, lower pressure provides highest conversion of 95.8 % and decreased to 21 % as the pressure rose to 14 MPa. Phase behavior of AN, CO_2 and H_2 revealed that the system was biphasic. On the other hand, the meniscus between two phases disappeared and the single phase (AN−CO_2−H_2) was attained at or above 12 MPa. Therefore, according to the phase behavior, the highest catalytic performance was achieved in the biphasic condition. Increased conversion and selectivity in the biphasic condition is an unusual observation for hydrogenation reaction in scCO_2. However, a similar example of fast hydrogenation in a biphasic mixture containing high-pressure CO_2 was found during the conversion of pinene in scCO_2 (*107–112*). Authors interpreted their results based on the assumption that the reaction was controlled by the adsorption of substrate on the catalyst surface as the substrate is more concentrated in the liquid rich phase around the catalyst, which represents a good model of CO_2-expanded liquids as CO_2 has a tendency to add to organic liquids and the combination act as a CO_2-expanded liquid (*113*, *114*).

Considering other parameters such as H_2 pressure the effect was insignificant on the hydrogenation of aniline under the condition used as the excess of H_2 present in the system. On the other hand, the effect of reaction time was straight-forward. The conversion and the selectivity of CHA was increased with time and then reached a maxima within 6 h after that the selectivity of primary amine dropped due to the formation of secondary amine.

Another factor needs to special attention is the temperature, because it affects (i) phase behavior and (ii) formation of carbamic acid. The reaction was conducted at 35, 50, 60, 70 and 80 °C and the results are shown in Figure 16. As usual conversion of AN was low at lower temperature, but the steepness of the observed drop suggests that phase behavior rather than reaction kinetics is responsible. Visual inspection of the phases present in the system revealed that at lower temperature AN−CO_2-H_2 reside in a single phase, whereas biphasic condition belongs to the higher temperature which results very high catalytic activity. A separate experiment was conducted on the visual observation of the phase behavior of CHA at 35 °C (Figure 17), the result clearly demonstrated the deposition of solid carbamic acid through the interaction between CHA and CO_2, and this scenario continued until 60 °C. The formation of solid carbamate diminished contact between aniline and the catalyst, which inhibited the reaction rate. At the temperature of above 60 °C, solid carbamate was converted to liquid and the conversion increased sharply from 18.2 to 61 %. Temperature also played a prominent role in determining the product distribution. Concerning the selectivity, only CHA (selectivity= 100 %) was observed from 35 to 60 °C. Therefore, temperature selection for optimization was a crucial part to the AN hydrogenation in CO_2.

Publication Date (Web): September 11, 2015 | doi: 10.1021/bk-2015-1194.ch009

In Advances in CO2 Capture, Sequestration, and Conversion; He, et al.;
ACS Symposium Series; American Chemical Society: Washington, DC, 2015.

Publication Date (Web): September 11, 2015 | doi: 10.1021/bk-2015-1194.ch009

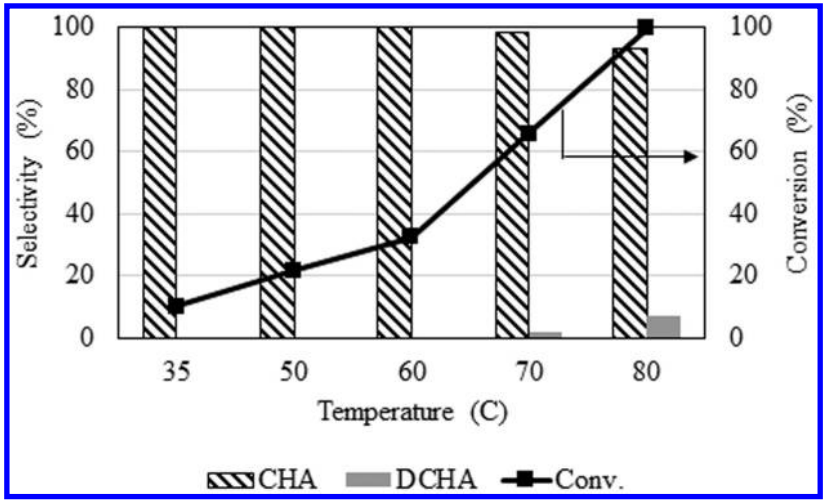

Figure 16. Effect of temperature on hydrogenation of aniline (AN) to cyclohexylamine (CHA) in $scCO_2$.

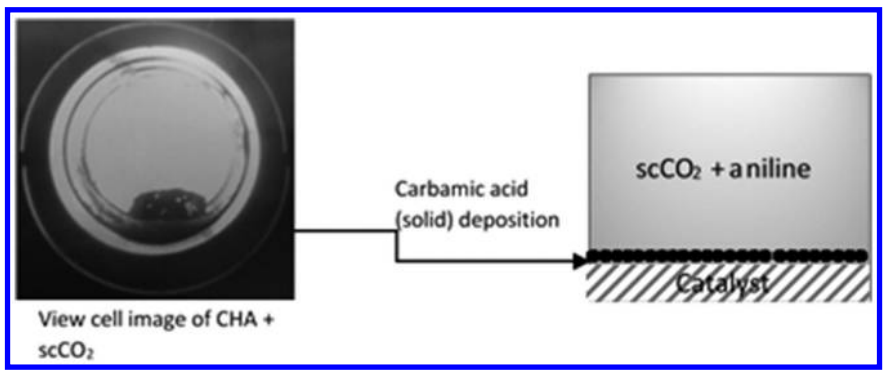

Figure 17. Visual evidence of the formation of carbamic acid via interaction between CO_2 and cyclohexylamine (CHA).

In conclusion, with the exploitation of the advantageous property of CO_2, it was possible to achieve a reasonably high conversion of AN and selectivity of CHA in $scCO_2$ medium under the optimized reaction condition. When pressurized with CO_2, AN behaved as an expanded liquid, which promoted the dissolution of H_2 and consequently the mild reaction condition for hydrogenation.

Another example is the hydrogenation of phenol (PhOH) to cyclohexanone (CHO), which is one of the key components in the synthesis of many useful materials such as caprolactam for nylon 6 and adipic acid for nylon 6, 6. General routes of CHO synthesis are (i) oxidation of cyclohexane and (ii) hydrogenation of PhOH. The oxidation route requires harsh reaction condition and generates a lot of by-products. Conversion of PhOH to CHO is a two-step process involving hydrogenation of PhOH to cyclohexanol (CHOH) followed by the dehydrogenation to CHO. There are many deficiencies exists mainly

in the dehydrogenation process such as temperature, conversion constrain due to thermodynamic equilibrium and poor H_2 utilization. A vast literature was available for hydrogenation of PhOH to CHO in gas phase (*115–119*). Depending on the reaction condition, and the nature of the metal ion used, product distribution varied. Furthermore, acidic and basic properties of the support materials is a fundamental factor. It is generally accepted that phenol adsorb on the support via aromatic ring, while metal active site adsorb H_2 and supplies to the ring via spillover mechanism (*120–126*). From the environmental viewpoint, instead of conventional organic solvents use of $scCO_2$ as reaction medium for conversion of PhOH to CHO is the most effective choice. Activated carbon (C) and carbon nano-fiber (CNF) supported Rh catalysts were used previously. Based on the reaction condition 17 % (P_{H2}=10 MPa; P_{CO2}=10 MPa) and 43 % (P_{H2}=4 MPa; P_{CO2}=12 MPa) of CHO was formed over Rh/C and Rh/CNF, respectively. To replace conventional organic solvents by $scCO_2$, it is necessary to improve the selectivity of CHO. Thus, PhOH hydrogenation was conducted on Pd/Al-MCM-41 in $scCO_2$ and the catalytic activity was compared with the Rh/Al-MCM-41. Both of the catalysts were synthesized by hydrothermal method. A primary indication of the incorporation of Pd on the mesoporous support was the difference in color between parent material (Al-MCM-41; white), and Pd/Al-MCM-41 (grey). After calcination in air, the grey colored material turned orange due to the migration of Pd^{+2} to the surface of Al-MCM-41, by reaction with SiOH groups of defect site due to insufficient substitution of Pd^{2+} ions for both Si^{4+} sites and Al^{3+} sites in the lattice of Al-MCM-41 (*127*). However, there was no such specific changes detected on Rh catalyst. In $scCO_2$, Pd/Al-MCM-41 emerged as most efficient catalyst for the transformation of PhOH to CHO. The pressure of CO_2 had significant effect on the catalytic performances. Before commenting in detail, it has to be mentioned that phase observation of PhOH−CO_2-H_2 confirmed pressure dependent solubility of PhOH and eventually a single phase was formed. Unlike AN, the hydrogenation of PhOH preferred single phase condition for high conversion and selectivity of CHO. At lower pressure of CO_2 (< 8 MPa), the product was composed of a 1:1 mixtures of CHO and cyclohexanol (CHOH), whereas CHO was the sole product at higher pressure (> 10 MPa). Hence, an optimized pressure of 12 MPa was used to accomplish high conversion (98.4 %) and selectivity of the targeted CHO (97.8 %) (Figure 18). On the contrary, no such pressure dependence were detected for Rh catalyst; in each case with the complete conversion of PHOH, CHOH was detected as the major product. Under the studied condition, the reaction took 4 h, which was faster than conventional organic solvents, might be the result of larger diffusion coefficient of the reactant in $scCO_2$ and higher miscibility of H_2 than in liquid solvents. Hence, optimization of H_2 pressure is also important criteria to achieve highest conversion and selectivity. There was an increase in PhOH conversion from 50.2 to 98.4 % and 40 to 100 % as the pressure changes from 1 to 4 MPa for Pd and Rh catalysts, respectively. Regarding the product distribution, there was a slight change in the product selectivity from 88.5 to 97.8 % for Pd/MCM-41. Interestingly, Rh catalyst showed highest selectivity of CHO (71.2 %) at lower conversion level. It could be inferred that the conversion of CHO to CHOH was fast on Rh/MCM-41.

Publication Date (Web): September 11, 2015 | doi: 10.1021/bk-2015-1194.ch009

In Advances in CO2 Capture, Sequestration, and Conversion; He, et al.;
ACS Symposium Series; American Chemical Society: Washington, DC, 2015.

Publication Date (Web): September 11, 2015 | doi: 10.1021/bk-2015-1194.ch009

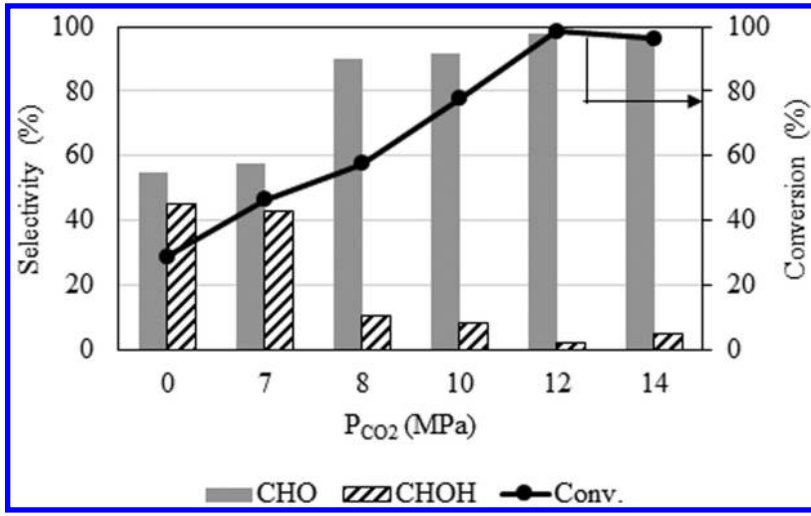

Figure 18. Hydrogenation of phenol (PhOH): Variation of CO_2 pressure.

Prior research on the hydrogenation of PhOH has established a sequential formation of CHO. The benzene ring of PhOH is partially hydrogenated to an enol, which is then isomerize rapidly to CHO, followed by further hydrogenation to CHOH. A time vs. product distribution profile of PhOH hydrogenation using Pd and Rh catalysts are shown in Figure 19. From the beginning, CHO was the major product for Pd and maintained throughout the reaction. However, for Rh, the trend was different and in the beginning CHO was formed with very high selectivity and then gradually converted to CHOH portrayed a sequential reaction scheme.

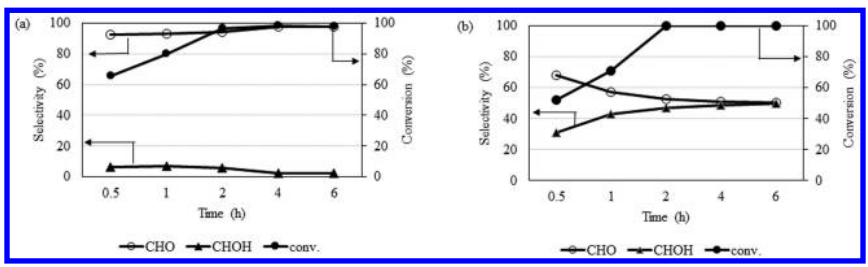

Figure 19. A time vs. product distribution profile of PhOH hydrogenation using (a) Pd and (b) Rh catalysts.

From the above-mentioned results it can be concluded that depending on the nature of the metal ion, product distribution was different. In the present system, Pd and Rh produced CHO and CHOH as the major product, respectively. As CHO was the targeted product from the PhOH hydrogenation, thus, studies continued with the Pd catalyst. A series of Pd catalysts supported on activated carbon, Al_2O_3 and MCM-41(only Si) were tested and the results are summarized in Table 16. The conversion of PhOH and the selectivity of CHO followed the order of Al-MCM-41> Al_2O_3 > MCM-41> C and Al-MCM-41> MCM-41 > Al_2O_3 > C, respectively. There was a substantial change in the catalytic performance after incorporation

of Al in MCM-41. The conversion of PhOH was increased from 20 % (only silica) to 98.4 % (Si/Al=100) and the selectivity of CHO changes from 78.4 to 97.8 %. Variation of Si/Al ratio made a strong impact on the catalytic activity (Figure 20). The promoting effect of Al could be attributed to the increase in surface acidity. It is well known that incorporation of Al to MCM-41 might serve as acid site and thus enhance the activity. PhOH molecule can adsorbs on the acidic site either by the donation of π electron of benzene ring or through the OH group, which is favorable under the present reaction condition. Figure 20 shows that the best result was obtained over Pd/AlMCM-41 of Si/Al= 100, among the catalyst of varied Si/Al ratio. It is commonly assumed that the acid sites within the molecular sieve structure are essential for enhancement of the catalytic activity (*128–130*). However, when the Al content increases with the change in Si/Al ratio from 50 to 8.5, acidity changes from 0.161 to 0.381 mmoles/g (Figure 21) and the conversion of PhOH was decreased from 80.3 to 18.5 %; higher the acidity of the support lowers the conversion of PhOH. This result can be explained by the fact that in MCM-41structure, the incorporation of Al leads to the formation of tetrahedral Al^{+3} into the framework. For high Al content, most Al are anchored on the outer surface rather than incorporated into the framework of MCM-41 (*131*) and the growing part of acid sites (tetrahedral Al^{+3}) might be neutralized by non-framework cationic Al species and block the strong acid site (*132*). In addition, increasing Al content could cause some deterioration in the pore structure as well as in the texture of the mesoporous material (*133*), which is clearly observed from the Figure 2b and harmful for the activity of the catalyst. A similar result has been obtained by Li *et al.* during the Ullmann reaction over Pd containing Al-MCM-41 catalyst (*134*). This observation is in contrast to the results of Neri *et al.* (*135*), who observed a significant decrease in the selectivity of CHO during the vapor phase hydrogenation of PhOH, with increasing acidity of the support and prefers Pd/MgO over Pd/Al_2O_3, which could be due to the difference in reaction conditions. Thus, an optimum acidity was required to obtain CHO with very high selectivity.

Publication Date (Web): September 11, 2015 | doi: 10.1021/bk-2015-1194.ch009

Table 16. Hydrogenation of PhOH Using Pd Catalysts on Various Support Materials

Entry	*Catalyst*	*Conv. (%)*	*Selectivity (%)*	
			CHO	*CHOH*
1	Pd/C	12.0	60.2	39.8
2	Pd/ Al_2O_3	46.0	70.1	29.9
3	Pd/MCM-41	20.0	86.4	13.6
4	Pd/AlMCM-41	98.4	97.8	2.2

Reaction condition: catalyst= 0.1 g, substrate = 1.0 g; temperature = 50 °C; P_{CO2}= 12 MPa, P_{H2}=4 MPa, time =4h: CHO=cyclohexanone, CHOH=cyclohexanol.

In Advances in CO2 Capture, Sequestration, and Conversion; He, et al.;
ACS Symposium Series; American Chemical Society: Washington, DC, 2015.

Publication Date (Web): September 11, 2015 | doi: 10.1021/bk-2015-1194.ch009

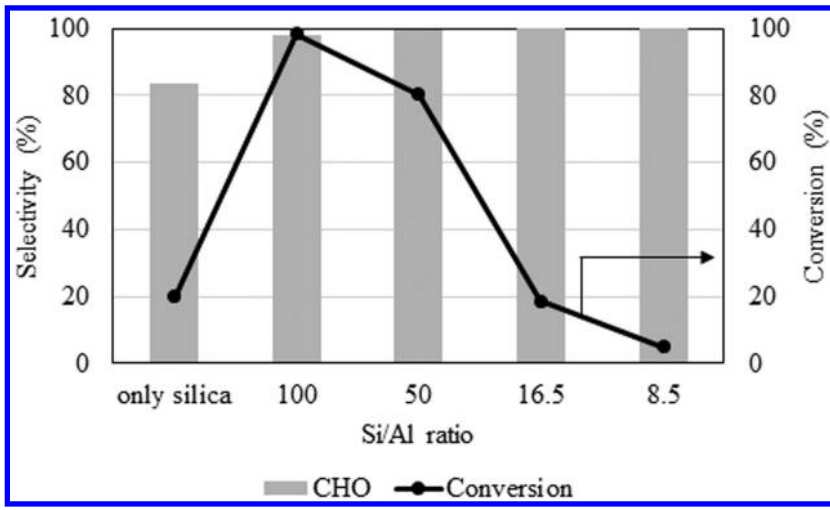

Figure 20. Effect of Si/Al ratio on the hydrogenation of PhOH.

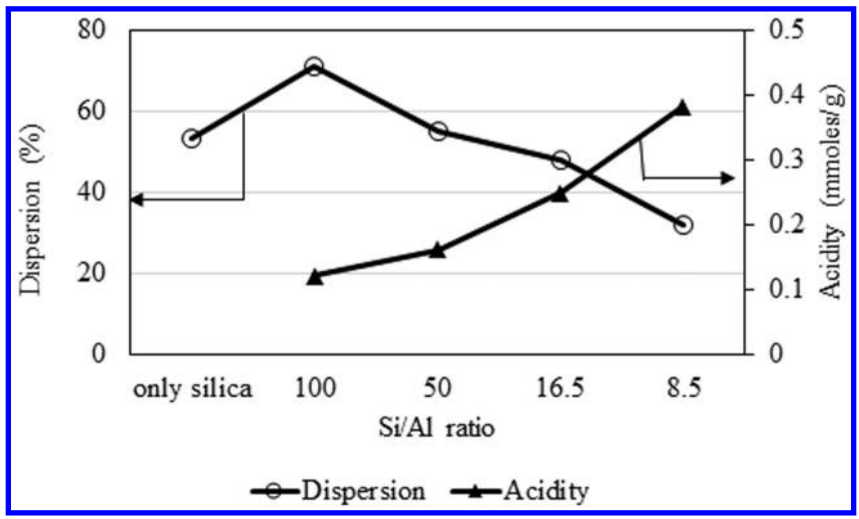

Figure 21. Effect of Si/Al ratio on dispersion of Pd particles and surface acidity.

It is well-known that depending on the Si/Al ratio metal particle size and eventually the dispersion varies, which influenced catalytic activity. Sometimes there is a correlation between product selectivity and particle size. However, in this case there was a slight modification in the selectivity of CHO from 97.8 to 100 % detected as the dispersion changes from 7.1 to 3.2 %. Hence, selectivity to CHO was structure insensitive.

Publication Date (Web): September 11, 2015 | doi: 10.1021/bk-2015-1194.ch009

A mechanistic investigation was considered on the hydrogenation of PhOH to CHO in $scCO_2$ (Scheme 4). According to the existing literature, hydrogenation of PhOH occur between adsorbed PhOH and activated H_2. The H_2 is supplied to the aromatic ring by spill-over mechanism (*136*). Depending on the acidity and basicity of support materials, PhOH can chemisorbed via two forms (i) coplanar, favor the formation of CHOH and (ii) non-planar form, which facilitates the formation of CHO. According the present results, CHO was formed exclusively when an optimum amount of Al is present in the support, which is in contrast to the described mechanism of vapor and liquid phase PhOH hydrogenation. To explain this phenomenon two possible interactions are considered: (i) catalyst-substrate and (ii) catalyst-substrate-solvent. To understand the plausible reaction routes a comparison was made between the PhOH hydrogenation in $scCO_2$ and conventional organic solvents like ethanol and hexane under the same reaction condition. Unfortunately, the conversion of PhOH in ethanol (24.7 %) and hexane (9.1 %) are extremely poor. The selectivity of CHO in ethanol (42.1 %) is strikingly low compared to the $scCO_2$ and in hexane (65.1 %). Hence, it might be confirmed that the reaction path of PhOH hydrogenation must be different in liquid phase and strongly influenced by the nature of the reaction medium. In $scCO_2$, the solubility of H_2 is higher and the increasing PhOH conversion in $scCO_2$ correlates well with the presence of high concentration of H_2 because of the larger solubility and devoid of mass transfer limitations. From the product distribution, it was evident that PhOH prefers non-planar orientation for adsorption on Pd/Al-MCM-41 rather than co-planar one as CHO was the main product. One probable explanation could be PhOH is a polar compound and its attraction towards ethanol would be stronger as the polarity of the solvent is higher. The role of solvent is crucial for hydrogenation of PHOH as well as the further hydrogenation of CHO (*137*) because CHO has tendency to interact with medium especially alcohol, and readily involved into the acetal reaction (*138*). Thus, in terms of CHO selectivity $scCO_2$ could be the better choice for PhOH hydrogenation. From the DFT calculation on the optimized geometry of PhOH in CO_2 and in ethanol it is proved that PhOH is less stable in CO_2 by ~ 8 kcal/mol (Table 17). Thus, it can be suggested that less PhOH was available to the catalyst active site in ethanol medium, as they will prefer to stay becomes solvated. So, more space will be available for co-planar adsorption on the catalyst surface. On the contrary, as $scCO_2$ is a quadropolar solvent and the interaction between solvent and substrate will be less than substrate−Catalyst. As a result, more PhOH will be attracted to the catalyst active site and eventually the concentration of PhOH over the catalyst surface will increased. Therefore, less space is available to adsorb on the catalyst surface in co-planar way. Hence it is reasonable to predict the non-planar way of adsorption of PhOH on the catalyst surface. To confirm this proposition, transition state calculation has been performed and the results are shown in Table 17. It shows that the barrier height of CHOH formation is ~19 kcal/mole less than that of CHO, which makes it as a stable product in CO_2 and hence confirmed the highest selectivity of CHO. However, it is difficult to predict the exact reaction route of phenol hydrogenation because heterogeneous catalysis in $scCO_2$ is very complicated system and the interaction of organic molecule in the channel system of molecular sieve are far from being understood completely.

In Advances in CO2 Capture, Sequestration, and Conversion; He, et al.;
ACS Symposium Series; American Chemical Society: Washington, DC, 2015.

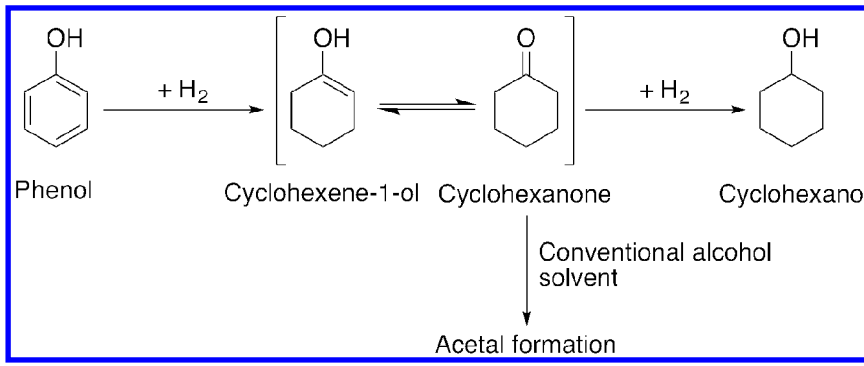

Scheme 4. Reaction path of the conversion of phenol (PhOH) to cyclohexanone (CHO).

Publication Date (Web): September 11, 2015 | doi: 10.1021/bk-2015-1194.ch009

Table 17. Total energy, Stabilization Energy of Reactant and Products in Ethanol and CO_2 Medium, and Transition State Calculation To Identify the Reaction Energy of CHO and CHOH

Molecule	*Solvent*	*Total energy (Hartree)*	*Stabilization energy (kcal/mol)*		
reactant+Pd	CO_2	-474.6736518	8.0965040747		
reactant+Pd	Ethanol	-474.6865544			
Energy of reactant (Hartree)	*Energy of CHOH (Hartree)*	*Energy of CHO (Hartree)*	*Energy for transition state (Hartree)*	*Energy of reaction (kcal/mol)*	*Feasibility of the reaction (kcal/mol)*
-474.5717	-474.7984		-474.7630	-142.274	
-474.5717		-474.8128	-474.3430	-161.301	-19.027

The optimized reaction condition was again applied to the hydrogenation of different -OH group containing aromatic compounds such as *o*- and *p*- cresol, dihydroxy benzene and naphthol. Table 18 presents the conversion and selectivity of the hydrogenation of studied derivatives. *o*- and *p*- cresol yields corresponding ketone products with very high selectivity of 77.3 and 89.1%, respectively(Table 18; Entry 1, 2). On the other hand, dihydroxybenzene (Table 18; Entry 3) was also produces ketone with 80 % selectivity. Hence, it could be suggested that the formation of ketone product was favorable under the described reaction condition. For higher selectivity of ketone, regioselective addition of H_2 to PhOH was considered, which maintain the resonance energy as much as possible and produces a series of hydrogenation intermediates. Differences in the resonance stabilization energy between transition states may play a significant role to

In Advances in CO2 Capture, Sequestration, and Conversion; He, et al.;
ACS Symposium Series; American Chemical Society: Washington, DC, 2015.

determine product selectivity. Instead of ketone products, naphthol produces only the ring hydrogenation products maintaining one benzene ring intact (Table 18; Entry 4).

Table 18. Hydrogenation of Hydroxyl Aromatic Derivatives Using Pd/MCM-41 in $scCO_2$

Entry	*Substrate*	*Conv. (%)*	*Selectivity (%)*	
			-one product	*-ol product*
1	*o*−Cresol	79.1	77.3	22.7
2	*p*−Cresol	65.6	89.1	10.1
3	Hydroquinone	30.0	79.9	20.1
4	2-naphthol	83.0	-	1, 2, 3, 4-tetrahydronaphthol (84.8) 5, 6, 7, 8-tetrahydronaphthol (5.2)

Reaction conditions: catalyst= 0.1 g, substrate = 1.0 g; temperature = 50 °C; P_{CO2}= 12 MPa, P_{H2}=4 MPa, time =4h.

A successful application of $scCO_2$ as a reaction medium was possible for hydrogenation of PhOH to CHO under a mild reaction condition. Comparison with the reaction in organic solvents, product distribution was different in $scCO_2$, suggesting a different mode of adsorption. Moreover, theoretical calculation of adsorption energy confirmed the advantage of the medium and shed some light on the reaction path of PhOH hydrogenation.

Conclusion

In conclusion, from some selected examples it can be seen that, $scCO_2$ is a potential medium to perform hydrogenation of different functional groups. Depending on the functional groups studied, CO_2 can act as a reaction medium and simultaneously a protective agent. In most of the cases, the catalytic activity and product selectivity were better than in the conventional organic solvents. Significant progress has been made in the synthesis of different types of materials using batch process; laboratory scale. However, scale-up of those processes are already underway.

In a practical term, CO_2 is an environmentally benign safe solvent and has a GRAS (generally referred as safe) status, which allow it to replace volatile organic solvents. However, to achieve commercial success with the use of CO_2 replacing conventional organic solvent it is necessary to improve fundamental knowledge about the molecular scenario behind the basic process involved. Nevertheless, the advantageous properties of $scCO_2$ as reaction medium is huge. To exploit those beneficial characteristics in a larger scale substantial research effort is needed to make a waste free and safe "green" chemical industry.

In Advances in CO2 Capture, Sequestration, and Conversion; He, et al.;
ACS Symposium Series; American Chemical Society: Washington, DC, 2015.

Publication Date (Web): September 11, 2015 | doi: 10.1021/bk-2015-1194.ch009

Publication Date (Web): September 11, 2015 | doi: 10.1021/bk-2015-1194.ch009

References

1. Raylander, P. N. In book *Catalytic Hydrogenation in Organic Synthesis*; Academic Press: New York, 1979
2. Grirrane, A.; Corma, A.; Garcia, H. Gold−Catalyzed synthesis of aromatic azo compounds from anilines and nitroaromatics. *Science* **2008**, *322*, 1661–1664.
3. Boronat, M.; Concepcion, P.; Corma, A.; Gonzalez, S.; Illas, F.; Serna, P. A molecular mechanism for the chemoselective hydrogenation of substituted nitroaromatics with nanoparticles of gold on TiO_2 catalysts: A cooperative effect between gold and the support. *J. Am. Chem. Soc.* **2007**, *129*, 16-230–16237.
4. Anastas, T.; Warnner, J. C. *Green Chemistry: Theory and Practice*; Oxford University Press: Cambridge, U.K. 2000.
5. Dum, P. A.; Wells, M.; Williams, T. *Green Chemistry in the Pharmaceutical Industry*, Wiley-VCH: Weinheim, Germany, 2010.
6. Leitner, W. Supercritical carbon dioxide as a green reaction medium for catalysis. *Acc. Chem. Res.* **2002**, *38*, 746–756.
7. McHugh, M. A.; Kruknois, V. J. In *Supercritical Fluid Extraction*, 2nd ed.; Butterworth-Heimermann: Boston, MA, 1994.
8. Fürstner, A.; Ackermann, L.; Beck, K.; Hori, H.; Koch, D.; Langeman, K.; Liebl, M.; Six, C.; Leitner, W. Olefin methathesis in supercritical carbon dioxide. *J. Am. Chem. Soc.* **2001**, *123*, 9000–9006.
9. Wittmann, K.; Wisniewski, W.; Mynott, R.; Leitner, W.; Kranemann, C. L.; Rische, T.; Eilbracht, P.; Kluwer, S.; Ernsting, J. M.; Elsevier, C. Supercritical carbon dioxide as solvent and temporary protecting group for rhodium−Catalyzed hydroaminomethylation. *J. Chem.–Eur. J.* **2001**, *7*, 4584–4589.
10. Kazarian, S. G.; Vincent, M. F.; Bright, F. V.; Liotta, C. L.; Eckert, C. A. Specific intermolecular interaction of carbon dioxide with polymers. *J. Am. Chem. Soc.* **1996**, *118*, 1729–1736.
11. Reynolds, L.; Gardecki, J. A.; Frankland, S. J. V.; Horng, M. L.; Maroncelli, M. Dipole solvation in nondipolar solvents: Experimental studies of reorganization energies and solvation dynamics. *J. Phys. Chem.* **1996**, *100*, 10337–10354.
12. Saharay, M.; Balasubramanian, S. Enhanced molecular multipole moments and solvent structure in supercritical carbon dioxide. *Chem. Phys. Chem.* **2004**, *5*, 1442–1445.
13. Rudkevich, D. M. Emerging supramolecular chemistry of gasses. *Angew. Chem., Int. Ed.* **2004**, *43*, 558–571.
14. Leitner, W. *Angew. Chem.* **1995**, *107*, 2391. Leitner, W. Carbon dioxide as a raw material- the synthesis of formic acid and its derivatives from CO_2. *Angew. Chem., Int. Ed.* **1995**, *34*, 2207–2221.
15. Chatterjee, M.; Chatterjee, A.; Raveendran, P.; Ikushima, Y. Hydrogenation of citral in supercritical CO_2 using a heterogeneous Ni (II) catalyst. *Green Chem.* **2006**, *8*, 445–449.

16. Beck, J. S.; Vartuli, J. C.; Roth, W. J.; Leonowicz, M. E.; Kresge, C. T.; Schmitt, K. D.; Chu, C. T.-W; Olson, D. H.; Sheppard, E. W.; McCullen, S. C.; Higgins, J. B.; Schlenker, J. L. A new family of mesoporous molecular sieves prepared with liquid−Crystal template. *J. Am. Chem. Soc.* **1992**, *114*, 10834–10843.
17. Köhn, R.; Förba, M. Nanoparticles of 3d transition metal oxides in mesoporous MCM-48 silica host structures: Synthesis and characterization. *Catal. Today* **2001**, *68*, 227–236.
18. Morey, M.; Davidson, A.; Eckert, H.; Stucky, G. D. Pseudotetrahedral O3/2V=0 centers immobilized on the walls of a mesoporous, cubic MCM-48 support: Preparation, characterization, and reactivity toward water as investigated by V-51 NMR and UV-vis spectroscopies. *Chem. Mater.* **1996**, *8*, 486–492.
19. Sonwane, C. G.; Bhatia, S. K. Structural characterization of MCM-41 over a wide range of length scales. *Langmuir* **1999**, *15*, 2809–2816.
20. Antonelli, D.; Ying, J. Y. Mesoporous materials. *Curr. Opin. Colloid Interface Sci.* **1996**, *1*, 523–529.
21. Sayari, A.; Yang, Y. Highly ordered MCM-41 silica prepared in the presence of decyltrimethylammonium bromide. *J. Phys. Chem. B* **2000**, *104*, 4835–4839.
22. Corma, A. Preparation and catalytic properties of new mesoporous materials. *Top. Catal.* **1997**, *4*, 249–260.
23. Mokaya, R.; Jones, W. Grafting of Al on purely siliceous mesoporous molecular sieves. *Phys. Chem. Chem. Phys.* **1999**, *1*, 207–213.
24. Klug, H. P.; Alexander, L. E. *X-ray Diffraction Procedures for Polycrystalline Amorphous Materials*, 2nd ed.; Wiley: New York, 1974.
25. Kohn, W.; Sham, L. J. Self−Consistent equations including exchange and correlation effects. *Phys. Rev. A* **1965**, *140*, A1133.
26. Delley, B. An all-electron numerical method for solving the local density functional for polyatomic molecules. *J. Chem. Phys.* **1990**, *92*, 508–517.
27. Delley, B. Analytic energy derivatives in the numerical local-density-functional approach. *J. Chem. Phys.* **1991**, *94*, 7245–7250.
28. Delley, B. From molecules to solids with the DMol3 approach. *J. Chem. Phys.* **2000**, *113*, 7756–7764.
29. Delley, B. Fast calculation of electrostatics in crystals and large molecules. *J. Phys. Chem.* **1996**, *100*, 6107–6110.
30. Klamt, A.; Schüürmann, G. J. COSMO: A new approach to dielectric screening in solvents with explicit expressions for the screening energy and its gradient. *Chem. Soc. Perkin Trans.* **1993**, *2*, 799–805.
31. Becke, A. D. A multicenter numerical integration scheme for polyatomic molecules. *J. Chem. Phys.* **1988**, *88*, 2547–2553.
32. Augustine, R. L. In *Heterogeneous Catalysis in Organic Synthesis*; Dekker: New York, 1995.
33. Bond, G. C. *Catalysis of Metals*, Academic Press: London, 1962.
34. Vannice, M. K.; Sen, B. Metal supports effect on the intramolecular selectivity of crotonaldehyde hydrogenation over platinum. *J. Catal.* **1989**, *115*, 65–78.

35. Piqueras, C. M.; Gutierrez, V.; Vega, D. A.; Volpe, M. A. Selective hydrogenation of cinnamaldehyde in supercritical CO_2 over Pt/SiO_2 and $Pt/HS{-}CeO_2$; An insight about the role of carbonyl interaction with supercritical CO_2 or with ceria support sites in cinnamyl alcohol selectivity. *Appl. Catal., A* **2013**, *467*, 253–260.
36. Gallezot, P.; Blanc, B.; Barthomeuf, D.; da Silva, M. I. P. Selective hydrogenation of cinnamaldehyde controlled by host-guest interactions in beta zeolite. *Stud. Surf. Sci. Catal.* **1994**, *84*, 1433–1439.
37. Gallezot, P.; Giroir-Fender, A.; Richard, D. Chemoselectivity in cinnamaldehyde hydrogenation induced by shape selective effects in Pt-Y-zeolite catalysts. *Catal. Lett.* **1990**, *4*, 169–174.
38. Sokolskii, D. V.; Anisimova, N. V.; Zharmagambetova, A. K.; Ualikhanova, A. Effect of hydrogen pressure on the selectivity of 2-butene-1-al hydrogenation. *React. Kinet. Catal. Lett.* **1981**, *17*, 419–421.
39. Neri, G.; Mercadante, L.; Donato, A.; Visco, A. M.; Galvagno, S. Influence of Ru precursor support and solvent in the citral hydrogenation over ruthenium catalyst. *Catal. Lett.* **1994**, *29*, 379–386.
40. Gallezot, P.; Richard, D. Selective hydrogenation of alpha beta unsaturated aldehydes. *Catal. Rev.: Sci. Eng.* **1998**, *40*, 81–126.
41. Delbecq, F.; Sautet, P. Competitive C=C and C=O hydrogenation of alpha beta unsaturated aldehydes on Pt and Pd surfaces in relation with the selectivity of hydrogenation reactions: A theoretical approach. *J. Catal.* **1995**, *152*, 217–236.
42. Chatterjee, M.; Ikushima, Y.; Zhao, F-Y. Highly efficient hydrogenation of cinnamaldehyde by Pt-MCM-48 in supercritical carbon dioxide. *Catal. Lett.* **2002**, *82*, 141–144.
43. Vergunst, Th.; Kaptejin, F.; Moulijin, J. A. Kinetics of cinnamaldehyde hydrogenation−Concentration dependent selectivity. *Catal. Today* **2001**, *66*, 381–387.
44. Oakes, R. S.; Clifford, A. A.; Bartle, K. D.; Pett, M. T.; Rayner, C. M. Sulfur oxidation in supercritical carbon dioxide: dramatic pressure dependant enhancement of diastereoselectivity for sulfoxidation of cysteine derivatives. *Chem. Commun.* **1999**, 247–248.
45. Bhanage, B. M.; Ikushima, Y.; Shirai, M.; Arai, M. The selective formation of unsaturated alcohols by hydrogenation of alpha,beta-unsaturated aldehydes in supercritical carbon dioxide using unpromoted Pt/Al_2O_3 catalyst. *Catal. Lett.* **1999**, *62*, 175–177.
46. Richard, D.; Couves, J.; Thomas, J. M. Structural and electronic properties of finely- divided supported Pt group metals and bimetals. *Faraday Discuss.* **1991**, *92*, 109–119.
47. Aramendia, M.; Boreau, V.; Jimenez, C.; Marinas, J.; Porras, A.; Urbano, F. Selective liquid phase hydrogenation of citral over supported palladium. *J. Catal.* **1997**, *172*, 46–54.
48. Nagase, Y.; Muramatu, H.; Sato, T. Selective hydrogenation of crotonaldehyde to crotyl alcohol on $AgMnO_2/Al_2O_3$-5 $AlPO_4$ catalysts. *Chem. Lett.* **1988**, 1695–1698.

Publication Date (Web): September 11, 2015 | doi: 10.1021/bk-2015-1194.ch009

49. Claus, P.; Hofmeister, H. Electron microscopy and catalytic study of silver catalysts: Structure sensitivity of the hydrogenation of crotonaldehyde. *J. Phys. Chem. B* **1999**, *103*, 2766–2775.
50. Hidalgo−Carrillo, J.; Marinas, A.; Marinas, J. M.; Delgado, J. J.; Raya-Miranda, R.; Urbano, F. J. Water as solvent in the liquid-phase selective hydrogenation ofcrotonaldehyde to crotyl alcohol over Pt/ZnO: A factorial design approach. *Appl. Catal,. B* **2014**, *154-155*, 369–378.
51. Bailie, J. E.; Abdullah, H. A.; Anderson, J. A.; Rochester, C. H.; Richardson, N. V.; Hodge, N.; Zhang, J. G.; Burrows, A.; Kiely, C. J.; Hutchings, G. Hydrogenation of but-2-enal over supported Au/ZnO catalysts. *J. Phys. Chem. Chem. Phys.* **2001**, *3*, 4113–4121.
52. Schimpf, S.; Lucas, M.; Mohr, C.; Rodemerck, U.; Brükner, A.; Radnik, J.; Hofmeister, H.; Claus, P. Supported gold nanoparticles: In-depth catalyst characterization and application in hydrogenation and oxidation reactions. *Catal. Today* **2002**, *72*, 63–78.
53. Clifford, A. A.; Pople, K.; Gaskill, W. J.; Bartle, K. D.; C., M. Potential tuning and reaction control in the Diels-Alder reaction between cyclopentadiene and methyl acrylate in supercritical carbon dioxide. *J. Chem. Soc. Faraday Trans.* **1998**, *94*, 1451–1456.
54. Shekhar, R.; Barteau, M. A. Decarbonylation and hydrogenation reactions of allyl alcohol and acrolein on Pd (1 1 0). *Surf. Sci.* **1994**, *319*, 298–314. Gallezot, P.; Fendler, A. G.; Richard, D. *Chemical Industry (Catalysis of Organic Reactions)* **1992**, *47*.
55. Houtman, C. J.; Barteau, M. A. Divergent pathways of acetaldehyde and Rh decarbonyaltion on Rh (1 1 1) surface. *J. Catal.* **1991**, *130*, 528–546.
56. Davis, J. L.; Barteau, M. A. Polymerization and decarbonylation reactions of aldehyde on the Pd (1 1 1) surface. *J. Am. Chem. Soc.* **1989**, *111*, 1782–1792.
57. Wagray, A.; Blackmond, D. G. Infrared spectroscopic studies of the adsorption and reaction of 3-methyl-2-butenal over alkali-promoted ruthenium/silica catalysts. *J. Phys. Chem.* **1993**, *97*, 6002–6006.
58. Tiltscher, H.; Hofmann, H. Trends in high pressure reaction engineering. *Chem. Eng. Sci.* **1987**, *42*, 959–977.
59. Arai, M.; Nishiyama, Y.; Ikushima, Y. Optical absorption of fine gold particles in supercritical carbon dioxide for the characterization of solvent properties. *J. Supercrit. Fluids* **1998**, *13*, 149–153.
60. Baiker, A. Supercritical Fluids in heterogeneous catalysis. *Chem. Rev.* **1999**, *99*, 453–473.
61. Raveendran, P.; Wallen, S. L. Cooperative C-H center dot center dot center dot O hydrogen bonding in CO_2-Lewis base complexes: Implications for solvation in supercritical CO_2. *J. Am. Chem. Soc.* **2002**, *124*, 12590–12599.
62. Raveendran, P.; Ikushima, Y; Wallen, S. L. Polar attributes of supercritical carbon dioxide. *Acc. Chem. Res.* **2005**, *38*, 478–485.
63. Mascetti, J.; Galan, F.; Papai, I. Carbon dioxide interaction with metal atoms: matrix isolation spectroscopic study and DFT calculations. *Coord. Chem. Rev.* **1999**, *190*, 557–576.

Publication Date (Web): September 11, 2015 | doi: 10.1021/bk-2015-1194.ch009

64. Mebel, A. M.; Hwang, D.-Y. Theoretical study on the reaction mechanism of nickel atoms with carbon dioxide. *J. Phys. Chem. A* **2000**, *104*, 11622–11627.
65. Leitner, W. The coordination chemistry of carbon dioxide and its relevance for catalysis: A critical study. *Coord. Chem. Rev.* **1996**, *153*, 257–284.
66. Furstner, A.; Koch, D.; Langemann, K.; Leitner, W.; Six, C. Olefin metathesis in compressed carbon dioxide. *Angew. Chem., Int. Ed.* **1997**, *36*, 2466–2469.
67. The density data of supercritical carbon dioxide are from the NIST Chemistry Web Book.
68. Chatterjee, M.; Kawanami, H.; Sato, M.; Ishizaka, T.; Yokoyama, T.; Suzuki, T. Hydrogenation of nitrile in supercritical carbon dioxide: A tunable approach to amine selectivity. *Green Chem.* **2010**, *12*, 87–93.
69. Xie, X.; Liotta, C. L.; Eckert, C. A. CO_2-protected amine formation from nitrile and imine hydrogenation in gas-expanded liquids. *Ind. Eng. Chem. Res.* **2004**, *43*, 7907–7911.
70. Hyde, J.; Licence, R.; Carter, P. D.; Poliakoff, M. Continues catalytic reactions in supercritical fluids. *Appl. Catal.* **2001**, *222*, 119–131.
71. Hoffer, B. W.; Moulijn, J. A. Hydrogenation of dinitriles on Raney-type Ni catalysts: Kinetic and mechanistic aspects. *Appl. Catal., A* **2009**, *352*, 193–201.
72. Sun, Z.; Zhao, Y.; Xie, Y.; Tao, R.; Zhang, H.; Huang, C.; Liu, Z. The solvent-free selective hydrogenation of nitrobenzene to aniline: an unexpected catalytic activity of ultrafine Pt nanoparticles deposited on carbon nanotubes. *Green Chem.* **2010**, *12*, 1007–1011.
73. Serp, P.; Corrias, M.; Kalck, P. Carbon nanotubes and nanofibers in catalysis. *Appl. Catal., A* **2003**, *253*, 337–358.
74. Zhao, F.; Zhang, R.; Chatterjee, M.; Ikushima, Y.; Arai, M. Hydrogenation of nitrobenzene with supported transition metal catalysts in supercritical carbon dioxide. *Adv. Synth. Catal.* **2004**, *346*, 661–668.
75. Zhao, F.; Ikushima, Y.; Arai, M. Hydrogenation of nitrobenzene with supported platinum catalysts in supercritical carbon dioxide: Effects of pressure, solvent, and metal particle size. *J. Catal.* **2004**, *224*, 479–483.
76. Meng, X.; Cheng, H.; Akiyama, Y.; Hao, Y.; Qiao, W.; Yu, Y.; Zhao, F.; Fujita, S.; Arai, M. Selective hydrogenation of nitrobenzene to aniline in dense phase carbon dioxide over Ni/gamma-Al_2O_3: Significance of molecular interactions. *J. Catal.* **2009**, *264*, 1–10.
77. Birkenstock U.; Lachmann, B.; Metten, J.; Schmidt, H. U.S. Patent 4265834, 1981.
78. Zhao, X. S.; Ma, Q.; Lu, G. Q. VOC removal: Comparison of MCM-41 with hydrophobic zeolites and activated carbon. *Energy Fuels* **1998**, *12*, 1051.
79. Gläser, R.; Roesky, R.; Boger, T.; Eigenberger, G.; Ernst, S.; Weitkamp, J. Probing the hydrophobic properties of MCM-41-type materials by the hydrophobicity index. *Stud. Surf. Sci. Catal.* **1997**, *105*, 695.
80. Chapuzet, J. M.; Lasia, A.; Lessard J. In *Electrocatalysis*, 1st ed.; Lipkowski, J., Ross, P. N., Eds.; Wiley-VCH: New York, 1998, Vol. 2, pp 10−20.

Publication Date (Web): September 11, 2015 | doi: 10.1021/bk-2015-1194.ch009

81. Metcalfe, A.; Rowden, M. N. Hydrogenation of nitrobenzene over palladium-silver catalysts. *J. Catal.* **1971**, *22*, 30–38.
82. Obraztsova, I. L.; Eremenko, N. K.; Velyakine, Y. N. Reaction kinetics of nitrobenzene hydrogenation on a palladium catalyst supported on nanodiamonds. *Kinet. Catal.* **2008**, *40*, 401–406.
83. Burgemeister, K.; Francio, G.; Gego, V. H.; Greiner, L.; Hugo, H.; Leitner, W. Inverted supercritical carbon dioxide/aqueous biphasic media for rhodium−Catalyzed hydrogenation reactions. *Chem. Eur. J.* **2007**, *15*, 2798–2804.
84. Liu, H. Z.; Jiang, T.; Han, B. X.; Liang, S. G.; Zhou, Y. X. Selective phenol hydrogenation to cyclohexanone over a dual supported Pd-Lewis acid catalyst. *Science* **2009**, *326*, 1250–1252.
85. Chatterjee, M.; Kawanami, H.; Sato, M.; Chatterjee, A.; Yokoyama, T.; Suzuki, T. Hydrogenation of phenol in supercritical carbon dioxide catalyzed by palladium supported on Al-MCM-41: A facile route for one-pot cyclohexanone formation. *Adv. Synth. Catal.* **2009**, *351*, 1912–1924.
86. Gelder, E. A.; Jackson, S. D.; Lok, C. M. A study of nitrobenzene hydrogenation over palladium/carbon catalysts. *Catal. Lett.* **2002**, *84*, 205–208.
87. Chu, C. T.-W.; Kuehl, G. H.; Lago, R. M.; Chang, C. D. Isomorphous substitution in zeolite frameworks: II. Catalytic properties of [B] ZSM-5. *J. Catal.* **1985**, *93*, 451–458.
88. Adjdir, M.; Ali-Dahmane, T.; Weidler, P. G. The structural comparison between Al-MCM-41 and B-MCM-41. *C. R. Chim.* **2009**, *12*, 793–800.
89. Kosslick, H.; Lische, G.; Landmesser, H.; Parlitz, B.; Storek, W.; Fricke, R. Acidity and catalytic behavior of substituted MCM-48. *J. Catal.* **1998**, *176*, 102–114.
90. Serrano, D. P.; Calleja, G.; Botas, J. A.; Gutierrez, F. J. Adsorption and hydrophobic properties of mesostructured MCM-41 and SBA-15 materials for volatile organic compound removal. *Ind. Chem. Eng. Res.* **2004**, *43*, 7010–7018.
91. Zhang, L. P.; Wu, P.; Sullivan, M. B. Hydrogen adsorption on Rh, Ni and Pd functionalized single-walled boron nitride nanotube. *J. Phys. Chem. C* **2011**, *115*, 4289–4296.
92. Chen, Y. W.; Li, C. Liquid phase hydrogenation of cyclohexene over Pt/aluminum borate catalyst. *Catal. Lett.* **1992**, *13*, 359–361.
93. Chen, G-X.; Zhang, J-M.; Wang, D-D.; Xu, K-W. First-principles study of palladium atom adsorption on the boron- or nitrogen-doped carbon nanotubes. *Phys. B* **2009**, 4173–4177.
94. Li, C.; Chen, Y. W.; Wang, W. J. Nitrobenzene hydrogenation over aluminum borate- supported platinum catalyst. *Appl. Catal., A* **1994**, *119*, 185–194.
95. Vishwanathan, V.; Sajjad, S. M.; Narayanan, S. Gas phase aniline hydrogenation over supported rhodium alumina catalyst. *Indian J. Chem. A* **1991**, *30*, 679–681.
96. Narayanan, S.; Unnikrishnan, R.; Vishwanathan, V. Nickel-alumina prepared by constant and varying pH method: Evaluation by hydrogen-oxygen chemisorption and aniline hydrogenation. *Appl. Catal.* **1995**, *129*, 9–19.

Publication Date (Web): September 11, 2015 | doi: 10.1021/bk-2015-1194.ch009

97. Mink, G.; Horvath, L. Hydrogenation of aniline to cyclohexylamine on NaOH-promoted or lanthana supported nickel. *React. Kinet. Catal. Lett.* **1998**, *65*, 59–65.
98. Immel, O.; Schwarz, H. H.; Thiel, R. DE Patent 3,801,755, 1989, Bayer AG.
99. Irgang, M.; Wambach, L. DE Patent 4,207,314, 1993, BASF AG.;
100. Darsow, G.; Immel, O.; Petruck, G.; Waldmann, H.; Petruch, G. M. European Patent 50,126, 1992, Bayer AG.
101. Ruetter, H.; Ruehl, T.; Breitscheidel, B.; Henkelmann, J.; Henne, A.; Wettling, T. DE Patent 19,533,718, 1997, BASF AG.
102. Buysch, H. J.; Darsow, G.; Immel, O.; Langer, R. WO Patent 9,815,351, 1998, Bayer AG.
103. Darsow, G.; Langer, R. DE Patent 19,754,571 1999 to Bayer AG.
104. Naramoto, I. Kiyuma, T. U.S. Patent 4,914,239, 1990, New Japan Chemical Co., Ltd.
105. Chatterjee, M.; Sato, M.; Kawanami, H.; Ishizaka, T.; Yokoyama, T.; Suzuki, T. Hydrogenation of aniline to cyclohexylamine in supercritical carbon dioxide: significance of phase behavior. *Appl. Catal., A* **2011**, *396*, 186–193.
106. Boudart, M.; Djega-Mariadassou, G. In *Kinetics of Heterogeneous Catalytic Reactions*; Princeton University Press: Princeton, NJ, 1984.
107. Hitzler, G.; Small, F. R.; Ross, S. K.; Poliakoff, M. Selective catalytic hydrogenation of organic compounds in supercritical fluids as a continuous process. *Org. Process Res. Dev.* **1998**, *2*, 137–146.
108. Chouchi, D.; Gourgouillon, D.; Courel, M.; Vital, J.; Nunes da Ponte, M. The influence of phase behavior on reactions at supercritical conditions: The hydrogenation of alpha-pinene. *Ind. Eng. Chem. Res.* **2001**, *40*, 2551–2554.
109. Milewska, A.; Banet Osuna, A. M.; Fonseca, I. M.; Nunes da Ponte, M. Biphasic hydrogenation of alpha-pinene in high-pressure carbon dioxide. *Green Chem.* **2005**, *7*, 726–732.
110. Bogel-Lukasik, E.; Bogel-Lukasik, R.; Kriaa, K.; Fonseca, I.; Tarasenko, Y. A.; Nunes da Ponte, M. Limonene hydrogenation in high-pressure CO_2: Effect of hydrogen pressure. *J. Supercrit. Fluid* **2008**, *45*, 225–230.
111. Devetta, L.; Giovanzana, A.; Canu, P.; Bertucco, A.; Minder, B. J. Kinetic experiments and modeling of a three-phase catalytic hydrogenation reaction in supercritical CO_2. *Catal. Today* **1999**, *48*, 337–345.
112. Bertucco, A.; Canu, P.; Devetta, L.; Zwahlen, A. G. Catalytic hydrogenation in supercritical CO_2: Kinetic measurements in a gradientless internal-recycle reactor. *Ind. Eng. Chem. Res.* **1997**, *36*, 2626–2633.
113. Akien, G. R.; Poliakoff, M. A critical look at reactions in class I and II gas-expanded liquids using CO_2 and other gases. *Green Chem.* **2009**, *11*, 1083–1100.
114. Lazzaroni, M. J.; Bush, D.; Brown, J. S.; Eckert, C. A. High-pressure vapor-liquid equilibria of some carbon dioxide plus organic binary systems. *J. Chem. Eng. Data* **2005**, *50*, 60–65.
115. Narayanan, S.; Krishna, K. Highly active hydrotalcite supported palladium catalyst for selective synthesis of cyclohexanone from phenol. *Appl. Catal., A* **1996**, *147*, L253–L258.

In Advances in CO2 Capture, Sequestration, and Conversion; He, et al.;
ACS Symposium Series; American Chemical Society: Washington, DC, 2015.

Publication Date (Web): September 11, 2015 | doi: 10.1021/bk-2015-1194.ch009

116. Mahata, N.; Vishwanathan, V. Gas phase hydrogenation of phenol over supported palladium catalysts. *Catal. Today* **1999**, *49*, 65–69.
117. Shore, S. G.; Ding, E; Park, C.; Keane, M. A. Vapor phase hydrogenation of phenol over silica supported Pd and Pd-Yb catalysts. *Catal. Commun.* **2002**, *3*, 77–84.
118. Talukdar, A. K.; Bhattacharyya, K. G.; Sivasanker, S. Hydrogenation of phenol over supported platinum and palladium catalysts. *Appl. Catal., A* **1993**, *96*, 229–239.
119. Itoh, N.; Xu, W.−C. Selective hydrogenation of phenol to cyclohexanone using palladium based membrane as catalysts. *Appl. Catal., A* **1993**, *107*, 83–100.
120. Srinivas, S. T.; Lakshmi, L. J.; Rao, P. K. Selectivity dependence on the alloying elements of carbon supported Pt-alloy catalysts in the hydrogenation of phenol. *Appl. Catal., A* **1994**, *110*, 167–172.
121. Srinivas, S. T.; P., K. Rao, Highly selective Pt−Cr/C alloy catalysts for single-step vapor phase hydrogenation of phenol to give cyclohexanone. *J. Chem. Soc. Chem. Commun* **1993**, 33–34.
122. Zhuang, L.; Li, H.; Dai, W.; Qiao, M. Liquid phase hydrogenation of phenol to cyclohexenone over a Pd-La-B amorphous catalyst. *Chem. Lett.* **2003**, *32*, 1072–1073.
123. Higashijima, M.; Nishimura, S. Studies concerning the factors affecting the formation of cyclohexanone intermediates in the catalytic hydrogenation of phenol. 2. Effects of alcoholic solvents on the formation of cyclohexanones in the hydrogenation of phenol over Pd−C catalysts. *Bull. Chem. Soc. Jpn.* **1992**, *64*, 2955–2999.
124. Xiang, Y.; Ma, L.; Lu, C.; Zhang, Q.; Li, X. Aqueous system for the improved hydrogenation of phenol and its derivatives. *Green Chem.* **2008**, *10*, 939–943.
125. Rode, C. V.; Joshi, U. D.; Sato, O.; Shirai, M. Catalytic ring hydrogenation of phenol under supercritical carbon dioxide. *Chem. Commun.* **2003**, 1960–1961.
126. Wang, W.; Zhao, F.; Fujita, S.; Arai, M. Hydrogenation of phenol in $scCO_2$ over carbon nanofiber supported Rh catalyst. *Catal. Commun* **2008**, *9*, 362–368.
127. Kawabata, T.; Atake, I.; Ohishi, Y.; Shishido, T.; Tian, Y.; Takaki, K.; Takehira, K. Liquid phase catalytic hydrodechlorination of aryl chlorides over Pd–Al-MCM-41 catalyst. *Appl. Catal., B* **2006**, *66*, 151–160.
128. Jayamurthy, M.; Vasudevan, S. Temperature Programmed Surface Reaction studies of the methanol to gasoline (MTG) conversion over ZSM-5. *Phys. Chem.* **1995**, *99*, 1521–1527.
129. Haase, F.; Sauer, J. Interaction of methanol with Bronsted acid sites of zeolite catalysts: An ab-initio study. *J. Am. Chem. Soc.* **1995**, *117*, 3780–3799.
130. Blaszkowski, S. R.; van Santen, R. A. Density-functional theory calculations of the activation of methanol by a Bronsted zeolite. *J. Phys. Chem.* **1995**, *99*, 11728–11738.

Publication Date (Web): September 11, 2015 | doi: 10.1021/bk-2015-1194.ch009

131. Ryong, R.; Chang, H. K.; Howe, R. F. Imaging the distribution of framework aluminum in mesoporous molecular sieve MCM-41. *Chem. Mater.* **1997**, *9*, 1607–1613.
132. Busio, K.; Janchen, J.; van Hooff, J. H. C. Aluminium incorporation in MCM-41 mesoporous molecular sieves. *Microporous Mater.* **1995**, *5*, 211.
133. Michalik, J.; Brown, D.; Yu, J. S.; Danilczuk, M.; Kim, J. Y.; Kevan, L. Conduction electron paramagnetic resonance of metal nanoparticles in AlMCM-41 aluminosilica mesoporous molecular sieves. *Phys. Chem. Chem. Phys.* **2001**, *3*, 1705–1708.
134. Li, H.; Chen, J.; Wan, Y.; Chai, W.; Zhang, F.; Lu, Y. Aqueous medium Ullmann reaction over a novel Pd/Ph-Al-MCM-41 as a new route of clean organic synthesis. *Green Chem.* **2007**, *9*, 273–280.
135. Neri, G.; Visco, A. M.; Donato, A.; Milone, C.; Malentacchi, M.; Gubitosa, G. Hydrogenation of phenol to cyclohexanone over palladium and alkali-dopped palladium catalysts. *Appl. Catal., A* **1994**, *110*, 49–59.
136. Chen, Y. Z.; Liaw, C. W.; Lee, L. I. Selective hydrogenation of phenol to cyclohexanone over palladium supported on calcined Mg/Al hydrotalcite. *Appl. Catal., A* **1999**, *177*, 1–8.
137. Feng, G.; Liu, Z.; Chen, P.; Lou, H. Influence of solvent on upgrading of phenolic compounds in pyrolysis bio-oil. *RSC Adv.* **2014**, *4*, 49924–49929.
138. He, J.; Zhao, C.; Lercher, J. A. Impact of solvent for individual steps of phenol hydrodeoxygenation with Pd/C and ZSM-5 as catalysts. *J. Catal.* **2014**, *309*, 362–375.

Publication Date (Web): September 11, 2015 | doi: 10.1021/bk-2015-1194.ch009

Publication Date (Web): September 11, 2015 | doi: 10.1021/bk-2015-1194.ch010

Chapter 10

Hydrazine as a New and Facile Hydrogen Source for Hydrothermal Reduction of CO_2 to Formic Acid

Guodong Yao, Feiyan Chen, Hua Zhang, Runtian He, and Fangming Jin*

School of Environmental Science and Engineering, State Key Lab of Metal Matrix Composites, Shanghai Jiao Tong University, 800 Dongchuan Road, Shanghai 200240, China
***E-mail: fmjin@sjtu.edu.cn**

Reduction of CO_2 into value-added chemicals has attracted considerable attention as an important method to reduce greenhouse gas emissions and also to alleviate the current dependence on fossil fuels. Traditional reducing agent for CO_2 reduction relies on gaseous hydrogen from high-pressure cylinder, which meets storage and transportation problem. Moreover, the thermodynamical stability of gaseous hydrogen results in the demand of high reactive catalyst, mainly involving noble-metal complexes. Thus, new safe and facile hydrogen source is needed urgently. Hydrous hydrazine, which possesses high hydrogen capacity (7.9%), is regarded as a promising liquid hydrogen storage material. Herein, hydrous hydrazine was employed as a in-situ hydrogen source for reduction of CO_2 under hydrothermal conditions. A 50% yield of formic acid with 99% selectivity was achieved by using a common Ni powder catalyst. The proposed method is facile and environment-friendly because it requires neither elaborately prepared catalysts, nor high-purity hydrogen and hydrogen storage.

In Advances in CO2 Capture, Sequestration, and Conversion; He, et al.;
ACS Symposium Series; American Chemical Society: Washington, DC, 2015.

Publication Date (Web): September 11, 2015 | doi: 10.1021/bk-2015-1194.ch010

Introduction

The earth's sustainable development is threatened by the global warming, which mainly caused by the sharply rising level of atmospheric CO_2. The massive emission of CO_2 is predominantly from the combustion of fossil fuels by anthropogenic activities owing to economic growth and industrial development. Therefore, reduction of CO_2 emission is urgently needed. On the other hand, CO_2 acts as an available renewable carbon source due to its advantages of being nontoxic, abundant, and economical. Simple carbon capture and storage is wasteful for carbon resource and one of the most promising methods is the utilization of the CO_2 as a carbon source to produce valuable chemicals. Recently, reduction of CO_2 into chemicals has attracted considerable attention as an key method to reduce greenhouse gas emissions and also to alleviate the current dependence on fossil fuels (*1–3*). In the past several decades, many promising methods for CO_2 reduction into chemicals have been proposed (*4–7*). Among these approaches, the photochemical reduction of CO_2 is regarded as a high potential method, but its efficiency is too low to apply in industry at present, and costly catalysts or complex catalysts are needed (*8*). The hydrogenation of CO_2 with gaseous H_2 is currently considered to be the most commercially feasible process. However, high-pressure hydrogen used in this method meets storage and transportation problem. Moreover, due to the thermodynamical stability of gaseous hydrogen and CO_2, its hydrogenation is always associated with the finding or synthesis of highly reactive catalysts, mainly involving nobel-metal (Ir, Ru, Rh, etc) complexes (*9–13*). Thus, developing a novel method for the hydrogenation of CO_2 with a safe and facile hydrogen source and a simple catalyst is urgently required.

Hydrous hydrazine ($N_2H_4{\cdot}H_2O$) contains 7.9% hydrogen and is therefore proposed as a promising indirect liquid hydrogen storage material. Recently, several studies on hydrogen production by the catalytic decomposition of $N_2H_4{\cdot}H_2O$ have been reported (*14–17*). However, to the best of our knowledge, there has been no report of CO_2 reduction with $N_2H_4{\cdot}H_2O$ as an in-situ hydrogen source.

Hydrothermal reaction, which the Earth has used in its fossil fuel formation during the carbon cycle, is receiving increasing attention due to the unique inherent properties of high temperature water (HTW) that include a fewer and weaker hydrogen bonds, a high ion product (K_w) and a low dielectric constant (*18*). Thus, some reactions that hardly proceed at low temperatures can occur in HTW (*19*). Recently, there is also an increasing interest in CO_2 reduction under hydrothermal conditions. For example, our group and others have demonstrated the reduction of CO_2 into value-added chemicals using metals as the reductant without expensive or complex catalysts in HTW (*20–23*). We found in-situ hydrogen possesses higher reactivity than gaseous hydrogen (*20*). Moreover, HTW facilitates CO_2 activation and improve the reaction rate. Thus, there is a possibility for efficient reduction of CO_2 into chemicals by using $N_2H_4{\cdot}H_2O$ as a hydrogen source together with a simple catalyst in HTW (Scheme 1).

In Advances in CO2 Capture, Sequestration, and Conversion; He, et al.;
ACS Symposium Series; American Chemical Society: Washington, DC, 2015.

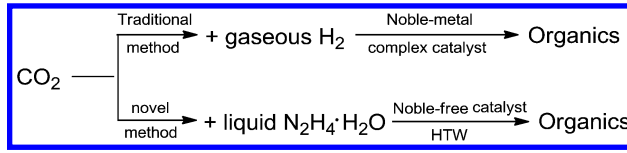

Scheme 1. Reduction of CO_2 into value-added chemicals.

Herein, we focused our attention on the use of hydrothermal reaction for the hydrogenation of CO_2 into chemicals, such as formic acid, by employing $N_2H_4 \cdot H_2O$ as an in-situ liquid hydrogen source with a simple catalyst, such as Ni powder.

Experimental

Materials

$NaHCO_3$ was used as a CO_2 source in order to simplify the experiments. Furthermore, salts containing HCO_3^- are products formed by Carbon Capture and Storage (CCS) technology. $NaHCO_3$, $N_2H_4 \cdot H_2O$ (85%), and Ni (200 mesh) were purchased from Sinopharm Chemical Reagent Co., Ltd. Formic acid (98%) was ordered from Sigma-Aldrich. Gaseous H_2 (≥99.999%) was obtained from Shanghai Poly-Gas Technology Co., Ltd. All reagents were used as test materials without further purification. Formic acid and gaseous H_2 were employed for the quantitative analysis of liquid and gaseous products, respectively.

Product Analyses

The HPLC analysis of liquid products was performed on Agilent 1260 serials equipped with UV-vis detector. Two Shodex RSpak KC-811columnswere used in series. The solvent was 2 mM $HClO_4$ with a flow rate of 1.0 mL·min^{-1}. Liquid samples also were analyzed by GC-MS on an Aglient7890AGC system equipped with a 5975C inert MSD. The samples were separated by an HP-INNOWax capillary column (diamension: 30 m × 250 μm × 0.25 μm) using helium as a carrier gas. Gaseous samples were analyzed using HP-5890 Series II GC-TCD system equipped with an HP-INNOWax packing column. Solid samples were characterized by XRD on Shimadzu XRD-6100 equipment and XPS on ESCALab 250Xi.

Considering that the real product should be formate due to the alkalinity of hydrazine solution, the formate yield, which was defined as the mole ratio of carbon in formate to carbon in $NaHCO_3$ (Scheme 2) and mean value of three times experiments are adopted. The relative errors of these data are less than 5% and standard deviations are less than 0.9.

$$\text{Yield (\%)} = \frac{C \text{ in formate (mmol)}}{C \text{ in initial } NaHCO_3 \text{ (mmol)}} \times 100\%$$

Scheme 2. The definition of formate yield.

In Advances in CO2 Capture, Sequestration, and Conversion; He, et al.;
ACS Symposium Series; American Chemical Society: Washington, DC, 2015.

Publication Date (Web): September 11, 2015 | doi: 10.1021/bk-2015-1194.ch010

Publication Date (Web): September 11, 2015 | doi: 10.1021/bk-2015-1194.ch010

General Procedure for the Synthesis of Formate from $NaHCO_3$

All experiments were conducted in a batch reactor (3/8 in. diameter, 1 mm wall thickness, and 120 mm length) made of SUS 316 alloys with an internal volume of 5.7 mL. In a typical procedure, the 2235 μL water mixture of test materials with 0.5 M $NaHCO_3$, 5 M $N_2H_4 \cdot H_2O$ (85%, 900 μL), and 3.135 mmol Ni were added into the reactor, and then the sealed reactor was put into the salt bath that had been preheated to desired temperature. The salt bath can offer a fast heat-up time of about 15 s from 20 °C to 300 °C. The reactor was shaken horizontally in the salt bath until the desired reaction time was complete. After the reaction, the reactor was taken out of the salt bath and put into a cold water bath to quench the reaction (Figure 1). The reaction time was defined as the time that the reactor was kept in the salt bath.Water filling was defined as the ratio of the volume of the solution, including added $N_2H_4 \cdot H_2O$ and deionized water, to the inner volume (5.7 mL) of the reactor. After cooling off, liquid sample was collected and filtered with 0.45 μm filter membrane. Solid sample washed with deionized water and ethanol several times and dried in air for analysis.

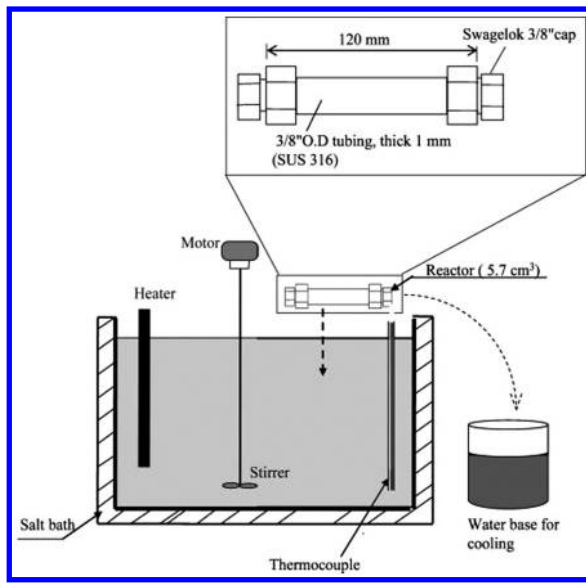

Figure 1. Schematic of batch reactor system.

Results and Discussion

Examination of the Possibility of $NaHCO_3$ Reduction with $N_2H_4 \cdot H_2O$

Initially, to test the possibility of hydrogenation of $NaHCO_3$ into chemicals with $N_2H_4 \cdot H_2O$, experiments with $N_2H_4 \cdot H_2O$ and $NaHCO_3$ were carried out at 300 °C. 300 °C was selected because our previous studies have shown that 300 °C was the optimal temperature for conversion of $NaHCO_3$ to chemicals (*24*,

25). Analyses of the liquid samples with GC-MS and HPLC showed that the major product was formic acid (Figure 2&3). No formation of formic acid was observed in the absence of $N_2H_4 \cdot H_2O$ (Table1, entry 1). These results showed that $NaHCO_3$ was selectively reduced into formic acid and that $N_2H_4 \cdot H_2O$ acts as the reductant. Considering that the real product should be formate due to the alkalinity of $N_2H_4 \cdot H_2O$, the formate yield, which was defined as the percentage of formate to the initial amount of $NaHCO_3$ based on carbon balance, was used to assess $NaHCO_3$ reduction in this study. As shown in Table 1, a formate yield of 18% was obtained (entry 2).

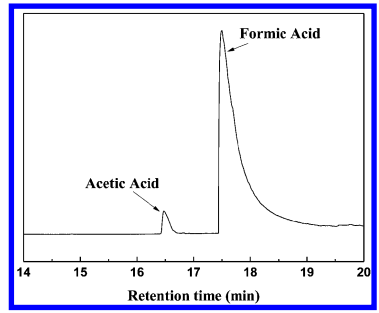

Figure 2. GC-MS chromatogram of liquid products.

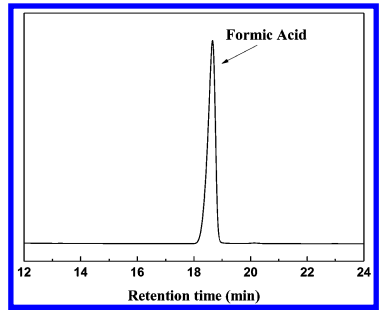

Figure 3. HPLC chromatogram of liquid products.

Although $NaHCO_3$ can be reduced into formate without the addition of a catalyst, the formate yield was only 18%. To improve the yield of formate, some metals were screened for active catalysts to enhance the yield of formate. As shown in Table 1, among the metals chosed, only Ni promote the yield of formate (entry 4). XRD analyses of the solid residues after the reactions showed that Ni still existed in the zero-valence form of the metal (Figure 4), indicating that Ni acts as a catalyst in the reduction of $NaHCO_3$ into formate with $N_2H_4 \cdot H_2O$.

Publication Date (Web): September 11, 2015 | doi: 10.1021/bk-2015-1194.ch010

Publication Date (Web): September 11, 2015 | doi: 10.1021/bk-2015-1194.ch010

Table 1. Yields of Formate from Reduction of $NaHCO_3$ by $N_2H_4 \cdot H_2O$ with Different Catalysts[a]

Entry	*Reducing agent*	*Catalyst*	*Yield (%)* [b]
1	-	-	0
2	$N_2H_4 \cdot H_2O$	-	18
3	-	Ni	1
4	$N_2H_4 \cdot H_2O$	Ni	23
5	$N_2H_4 \cdot H_2O$	Cu	9
6	$N_2H_4 \cdot H_2O$	Fe	13
7	$N_2H_4 \cdot H_2O$	Co	3
8	$N_2H_4 \cdot H_2O$	Al-Ni	4
9	$N_2H_4 \cdot H_2O$	WC	6

[a] Reaction conditions: 0.5 M $NaHCO_3$; 2 M $N_2H_4 \cdot H_2O$; 4 mmol Ni; 35% water filling; 120 min; 300 °C. [b] The formate yield is defined as the percentage of formate to initial $NaHCO_3$ based on the carbon balance.

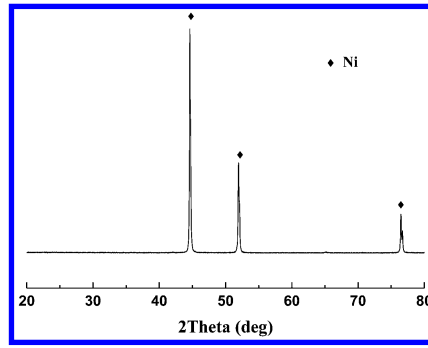

Figure 4. XRD patterns of solid products after the reaction ($NaHCO_3$: 0.5 M; $N_2H_4 \cdot H_2O$: 2 M; Ni: 4 mmol; water filling: 35%; time: 120 min; temp.: 300 °C).

Effects of Reaction Conditions on the Yield of Formate

Subsequently, a series of experiments were conducted over a wide range of conditions by varying the concentration of reactants, water filling, reaction temperature and reaction time in order to study the reaction features and then design the optimal synthetic conditions for a high yield of formate. The effect of the Ni amount was studied firstly. As shown in Figure 5, the formate yield increased to 27% with 2 mmol Ni. However, the formate yield decreased when the amount of Ni further increased to 3 mmol. The reason of decrease in the formate yield with over 2 mmol of Ni is most likely due to the conversion of formate into CH_4, which was confirmed by the TCD analysis that CH_4 was detected with 3 mmol of Ni. Ni plays an catalytic role in the hydrogenation reaction of $NaHCO_3$ to formate and formate to CH_4.

In Advances in CO2 Capture, Sequestration, and Conversion; He, et al.;
ACS Symposium Series; American Chemical Society: Washington, DC, 2015.

Publication Date (Web): September 11, 2015 | doi: 10.1021/bk-2015-1194.ch010

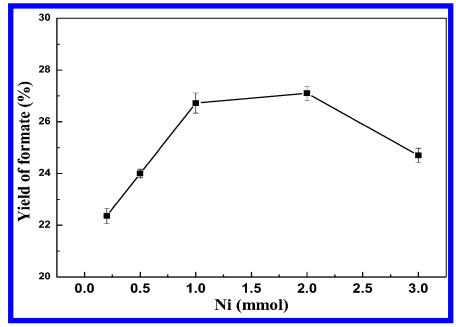

Figure 5. Effect of the amount of Ni on the yields of formate ($NaHCO_3$: 0.5 M; $N_2H_4{\cdot}H_2O$: 2M; water filling: 35%; time: 120 min; temp.: 300 °C).

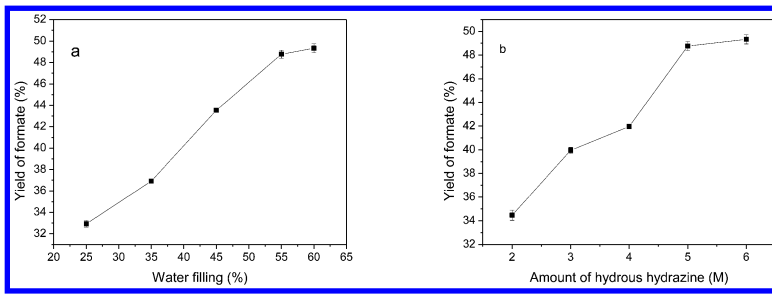

Figure 6. Effects of water filling (a) and the amount of $N_2H_4{\cdot}H_2O$ (b) on the yields of formate (time: 60 min; temp.: 300 °C.).

Generally, the pressure of the reaction reactor should have a strong effect on the yield of formate. The influence of the pressure was investigated by changing water filling in a batch reactor. As shown in Figure 6(a), the increase in the water filling/pressure is favorable for $NaHCO_3$ reduction into formate, and the yield of formate remarkably increased to 50% as the water filling increased to 60%. A possible reason for the increase of formate yield with an increase of water filling is that more hydrogen was dissolved in the water under a higher pressure, which facilitates the reaction of H_2 with $NaHCO_3$. Considering that the similar yield of formate with 55% and 60% water filling, the following experiments were conducted with 55% water filling. More $N_2H_4{\cdot}H_2O$ should also be favorable for $NaHCO_3$ reduction but not for cost. Thus, to obtain an optimized amount of $N_2H_4{\cdot}H_2O$ (or ratio of $N_2H_4{\cdot}H_2O$ to $NaHCO_3$), the effect of the amount of $N_2H_4{\cdot}H_2O$ was investigated with a fixed amount of $NaHCO_3$ (0.5 M). As shown in Figure 6(b), the yield of formate increased greatly with an increase in the concentration of $N_2H_4{\cdot}H_2O$, however, as the concentration of $N_2H_4{\cdot}H_2O$ further increased to 6 M, the formate yield remained stable.

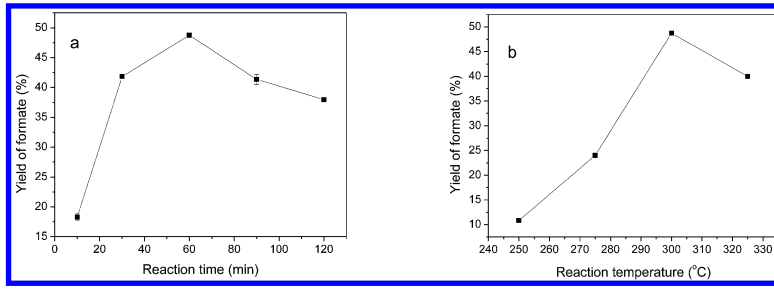

Figure 7. Effects of reaction time (a) and temperature (b) on the yields of formate ($N_2H_4{\cdot}H_2O$: 5 M; water filling: 55%).

Publication Date (Web): September 11, 2015 | doi: 10.1021/bk-2015-1194.ch010

Then, the effects of reaction time and temperature on the yield of formate were further investigated at the optimal conditions obtained above. As shown in Figure 7(a), the formate yield increased first and then decreased with prolonging the reaction time, and the highest yield was obtained after 60 min. A possible reason for the decrease in the formate yield with a longer time than 60 min is that Ni can promote the methane formation through hydrogenation of formate, leading to the decomposition of formate. For the effect of temperature, as shown in Figure 7(b), the formate yield drastically increased as the reaction temperature increased from 250 to 300 °C and reached a maximum at 300 °C. The observed decrease in the formate yield at temperatures above 300 °C could also be caused by the decomposition of the formate.

The organic carbon in the liquid samples was also determined by TOC analysis, and the amount of carbon in the formate was roughly equal to the total carbon in the samples, which indicates that the product of the hydrogenation of $NaHCO_3$ was almost formate. The main by-product, acetic acid, is only 0.4%, that is, the selectivity of the production of formate was approximately 99%.

Examination of the Stability of Ni and the Effect of Reactor Wall

The catalyst stability is key for application in practice. Thus, the stability of Ni catalyst was examined in the experiments. As shown in Figure 8, although a certain decrease in the yield of formate was observed in the 2nd cycle, further obvious decrease was not observed, indicating that Ni can maintain the activity after 2nd cycle. The specific surface area of the Ni powder was measured by BET, which showed that the specific surface area of Ni decreased from 2290 m^2/kg before the reaction to 2196 m^2/kg after the first time reaction. This phenomenon may partly explain the decrease in the formate yield. Moreover, to assess the leaching of the Ni and other main compositions (Fe, Mn) of the SUS316 reactor wall, the ion concentration of Ni, as well as Fe and Mn in the solution after the reactions were measured by ICP. Small amount of these ions was found in the liquid sample with Ni at 2.126 ppm, Fe at 0.5366 ppm, and Mn at 0.1642 ppm, respectively. This result indicates that the leaching concentration of these metals was very low. To further investigate the possible catalytic activity of Fe or Mn

from the reactor wall, control experiments were conducted without Fe or Mn and with a 10^4-fold concentration of Fe or Mn ions as the values detected by ICP. The results are comparable, indicating the effect of leaching Fe and Mn on the yield of formate is negligible.

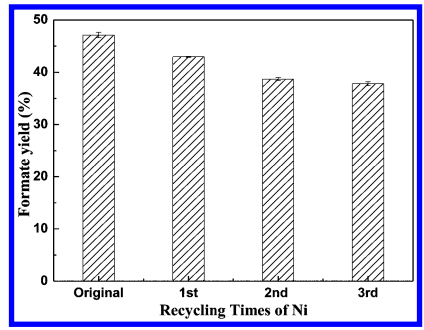

Figure 8. Effect of reused Ni on the yields of formate ($NaHCO_3$: 0.5 M; $N_2H_4{\cdot}H_2O$: 5 M; Ni: 3.135 mmol; water filling: 55%; time: 60 min; temp.: 300 °C).

Possible Mechanism of $NaHCO_3$ Reduction into Formate with $N_2H_4{\cdot}H_2O$

Generally, the decomposition of N_2H_4 takes place by two typical reaction routes: $N_2H_4 \rightarrow N_2\ (g) + 2H_2\ (g)$ and $3N_2H_4 \rightarrow 4NH_3 + N_2\ (g)$, and the ways of decomposition can be explained by Scheme 3.

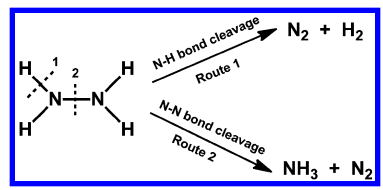

Scheme 3. Decomposition ways of $N_2H_4{\cdot}H_2O$.

To investigate the main route of N_2H_4 decomposition in this study, reactions with only $N_2H_4{\cdot}H_2O$ in the presence and absence of Ni were conducted. Analyses of the gaseous samples with TCD showed that the amounts of both H_2 and total gas were much higher in the presence of Ni compared to those in the absence of Ni. These results indicate that Ni can improve the decomposition of N_2H_4 to H_2 and N_2 by N-H bond cleavage (Route 1), while avoiding the undesired decomposition of N_2H_4 to ammonia (NH_3) (Route 2). Similar results were reported in H_2 production from N_2H_4, in which Raney Ni and Ni-based bimetallic catalysts, such as Ni-Rh, Ni-Ir and Ni-Pt, were used (*17*). Obviously, in this study, a common Ni powder can selectively decompose N_2H_4 into H_2, most likely because HTW can activate the Ni catalyst surface and make the H in N_2H_4 more easily adsorbed onto the Ni, followed by N-H bond cleavage and the formation of H_2. The results also illuminate the low yield of formate with metals except Ni in Table 1. These metals

Publication Date (Web): September 11, 2015 | doi: 10.1021/bk-2015-1194.ch010

Publication Date (Web): September 11, 2015 | doi: 10.1021/bk-2015-1194.ch010

are favorable for decomposition of hydrous hydrazine to NH_3 instead of H_2. Thus, hydrogenation of $NaHCO_3$ is difficult to proceed. On the other hand, some metals like Cu and Co can promote the formate decomposition, leading to the decrease of formate yield. Then, an experiment with $NaHCO_3$ and ammonia ($NH_3 \cdot H_2O$) was conducted to examine whether $NaHCO_3$ can be reduced by ammonia. The result showed that almost no formation of formate was observed, indicating that the formation of formate should be contributed to the hydrogen from N_2H_4 rather than NH_3. Furthermore, an experiment without Ni at the optimum condition (300 °C, 55% water filling, 5 M $N_2H_4 \cdot H_2O$) was conducted and the yield of formate was 15%, which is much lower than that with 3.135 mmol Ni (49% yield). The result indicated the catalytic role of Ni again. To study whether the surface of Ni can be oxidised in HTW and then affect the catalyst activity of Ni, XPS of the Ni before and after the reaction were measured. As shown in Figure 9(a), peak 1 at 852.6 eV, peak 2 at 853.58 eV and peak 3 at 855.38 are characteristic peaks of metallic Ni $2p_{3/2}$, Ni^{2+} $2p_{3/2}$ in NiO and Ni^{2+} $2p_{3/2}$ in $Ni(OH)_2$, respectively. Peaks 4, 5, 6, 7 and 8 are accompanying peaks. The results showed that a trace of $Ni(OH)_2$ and NiO on Ni surface before the reaction. XPS spectra of Ni after the reaction was shown in Figure 9(b), peak 1 at 852.6 eV and peak 2 at 855.78 eV are characteristic peaks of metallic Ni $2p_{3/2}$ and Ni^{2+} $2p_{3/2}$ in $Ni(OH)_2$, respectively. Peaks 3, 4, 5, 6, 7 are accompanying peaks. The results showed that a trace of $Ni(OH)_2$ on Ni surface after the reaction. However, reactions with $Ni(OH)_2$ or NiO showed that the formate yield was much lower than that without Ni, only 8% and 7% with $Ni(OH)_2$ and NiO, respectively. These results suggest that Ni, rather NiO or $Ni(OH)_2$, acts as a catalyst in the $NaHCO_3$ reduction with $N_2H_4 \cdot H_2O$. This phenomenon likely occurs because Ni^{2+} is reduced into Ni (0) by $N_2H_4 \cdot H_2O$, which was supported by the fact that Ni (0) was observed in the reaction with NiO or $Ni(OH)_2$ in the presence of $N_2H_4 \cdot H_2O$ (Figure 10).

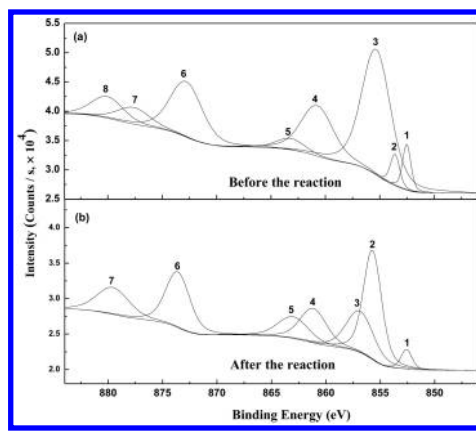

Figure 9. XPS spectra of Ni $2p_{3/2}$ from Ni metal before (a) and after (b) the reaction.

In Advances in CO2 Capture, Sequestration, and Conversion; He, et al.;
ACS Symposium Series; American Chemical Society: Washington, DC, 2015.

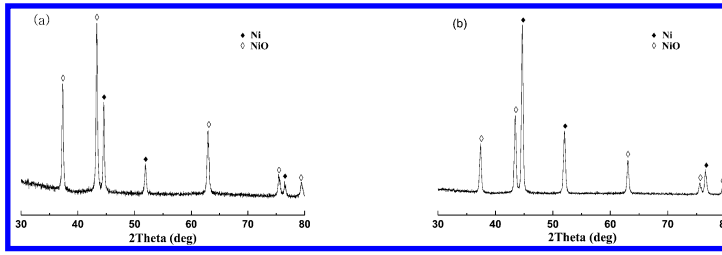

Figure 10. XRD patterns of solid products after the reaction with Ni(OH) (a) or NiO (b) ($NaHCO_3$: 0.5 M; $N_2H_4{\cdot}H_2O$: 5 M; $Ni(OH)_2$/NiO: 3.135 mmol; water filling: 55%; time: 60 min; temp.: 300 °C.).

Publication Date (Web): September 11, 2015 | doi: 10.1021/bk-2015-1194.ch010

After understanding the catalytic activity of Ni for decomposing N_2H_4 into H_2, next important question is whether the formed hydrogen reacts with CO_2 or HCO_3^-. To solve this question, reactions with gaseous CO_2 instead of $NaHCO_3$ were conducted. As a result, the yield of formate was only 1%, indicating that the hydrogenation can be considered to occur mainly with HCO_3^- rather than CO_2. The low formic acid with CO_2 is most likely due to low dissolution of CO_2 in water. Increasing the initial pH of the solution should lead to an increase in the dissolved CO_2 in water. Our previous study (*20*). indicated the yield of formate increased with the increase in the initial pH from 8 to 14. In this study, we have not investigated the effect of pH on formate yield because hydrous hydrazine was already strong base. Furthermore, to explore the difference between the activity of the in-situ hydrogen from $N_2H_4{\cdot}H_2O$ and gaseous hydrogen, an experiment with gaseous hydrogen as the hydrogen source instead of $N_2H_4{\cdot}H_2O$ was conducted. Only 2% yield of formate was obtained. Although further evidence is needed, present results suggests in-situ hydrogen formed from $N_2H_4{\cdot}H_2O$ may act as a higher activity than the gaseous hydrogen in $NaHCO_3$ reduction into formic acid.

Based on the above results, a possible mechanism was proposed as shown in Scheme 4. First, the H proton of $N_2H_4{\cdot}H_2O$ is adsorbed onto the Ni surface and the $N_2H_4{\cdot}H_2O$ prefers the cleavage of the N-H bond, leading to H_2 formation. Subsequently, the in-situ generated H_2 is also adsorbed onto the Ni surface and is activated by Ni. Furthermore, the active H attacks the carbon of C=O, followed by the hydroxyl group of HCO_3^- leaving. Finally, formate was obtained together with H_2O, which was formed by the combination of another active H of H_2 and leaving hydroxyl group of HCO_3^-.

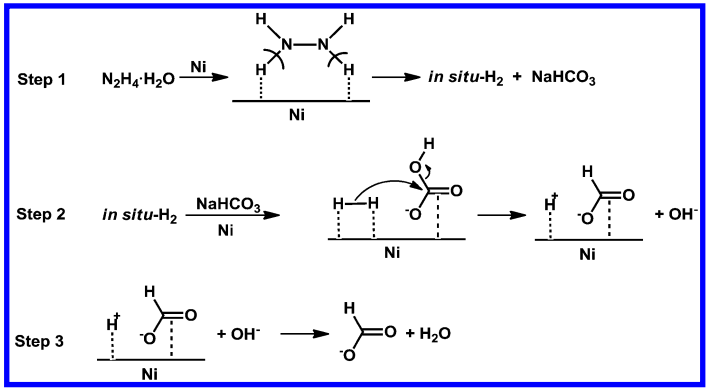

Scheme 4. Proposed mechanism of reduction of HCO_3^- into formate with $N_2H_4{\cdot}H_2O$ over Ni.

Conclusions

A novel efficient method for selective reduction of $NaHCO_3$ into formate by using $N_2H_4{\cdot}H_2O$ over a common Ni powder in HTW was proposed. Nearly 99% selectivity and approximately 50% yield of formate were achieved. The results indicates $N_2H_4{\cdot}H_2O$ is an excellent in-situ hydrogen source for CO_2 reduction. High catalytic activity of common Ni powder may involve in the unique properties of HTW because this reaction hardly proceed at low temperatures. This approach provides a facile method for reduction of CO_2 into value-added chemicals.

Acknowledgments

The authors thank the financial support of the National Natural Science Foundation of China (No. 21277091 & 51472159), the State Key Program of National Natural Science Foundation of China (No. 21436007), Key Basic Research Projects of Science and Technology Commission of Shanghai (No. 14JC1403100) and China Postdoctoral Science Foundation (No. 2013 M541520).

References

1. Aresta, M.; Dibenedetto, A. Utilisation of CO_2 as a chemical feedstock: Opportunities and challenges. *Dalton Trans.* **2007**, *28*, 2975–2992.
2. Song, C. S. Global challenges and strategies for control, conversion and utilization of CO_2 for sustainable development involving energy, catalysis, adsorption and chemical processing. *Catal. Today* **2006**, *115*, 2–32.
3. Hu, Y. H.; Huo, Y. Fast and exothermic reaction of CO_2 and Li_3N into C-N-containing solid materials. *J. Phys. Chem. A* **2011**, *115*, 11678–11681.
4. Tsai, J. C.; Nicholas, K. M. Rhodium-catalyzed hydrogenation of carbon-dioxide to formic-acid. *J. Am. Chem. Soc.* **1992**, *114*, 5117–5124.
5. Yu, K. M. K.; Curcic, I.; Gabriel, J.; Tsang, S. C. E. Recent advances in CO_2 capture and utilization. *ChemSusChem* **2008**, *1*, 893–899.

In Advances in CO2 Capture, Sequestration, and Conversion; He, et al.;
ACS Symposium Series; American Chemical Society: Washington, DC, 2015.

Publication Date (Web): September 11, 2015 | doi: 10.1021/bk-2015-1194.ch010

6. Centi, G.; Perathoner, S. Opportunities and prospects in the chemical recycling of carbon dioxide to fuels. *Catal. Today* **2009**, *148*, 191–205.
7. Takeda, H.; Koizumi, H.; Okamoto, K.; Ishitani, O. Photocatalytic CO_2 reduction using a Mn complex as a catalyst. *Chem. Commun.* **2014**, *50*, 1491–1493.
8. Usubharatana, P.; McMartin, D.; Veawab, A.; Tontiwachwuthikul, P. Photocatalytic process for CO_2 emission reduction from industrial flue gas streams. *Ind. Eng. Chem. Res.* **2006**, *45*, 2558–2568.
9. Tai, C. C.; Pitts, J.; Linehan, J. C.; Main, A. D.; Munshi, P.; Jessop, P. G. In situ formation of ruthenium catalysts for the homogeneous hydrogenation of carbon dioxide. *Inorg. Chem.* **2002**, *41*, 1606–1614.
10. Munshi, P.; Main, A. D.; Linehan, J. C.; Tai, C. C.; Jessop, P. G. Hydrogenation of carbon dioxide catalyzed by ruthenium trimethylphosphine complexes: The accelerating effect of certain alcohols and amines. *J. Am. Chem. Soc.* **2002**, *124*, 7963–7971.
11. Jessop, P. G.; Hsiao, Y.; Ikariya, T.; Noyori, R. Homogeneous catalysis in supercritical fluids: Hydrogenation of supercritical carbon dioxide to formic acid, alkyl formates, and formamides. *J. Am. Chem. Soc.* **1996**, *118*, 344–355.
12. Zhou, X.; Qu, J.; Xu, F.; Hu, J.; Foord, J. S.; Zeng, Z.; Hong, X.; Tsang, S. C. E. Shape selective plate-form Ga_2O_3 with strong metal-support interaction to overlying Pd for hydrogenation of CO_2 to CH_3OH. *Chem. Commun.* **2013**, *49*, 1747–1749.
13. Ogo, S.; Kabe, R.; Hayashi, H.; Harada, R.; Fukuzumi, S. Mechanistic investigation of CO_2 hydrogenation by Ru(II) and Ir(III) aqua complexes under acidic conditions: two catalytic systems differing in the nature of the rate determining step. *Dalton Trans.* **2006**, *39*, 4657–4663.
14. Gkizis, P. L.; Stratakis, M.; Lykakis, I. N. Catalytic activation of hydrazine hydrate by gold nanoparticles: Chemoselective reduction of nitro compounds into amines. *Catal. Commun.* **2013**, *36*, 48–51.
15. Singh, S. K.; Singh, A. K.; Aranishi, K.; Xu, Q. Noble-metal-free bimetallic nanoparticle-catalyzed selective hydrogen generation from hydrous hydrazine for chemical hydrogen storage. *J. Am. Chem. Soc.* **2011**, *133*, 19638–19641.
16. He, L.; Huang, Y.; Wang, A.; Wang, X.; Chen, X.; Jose Delgado, J.; Zhang, T. A noble-metal-gree catalyst derived from Ni-Al hydrotalcite for hydrogen generation from N_2H_4 center dot H2O decomposition. *Angew. Chem. Int. Ed.* **2012**, *51*, 6191–6194.
17. He, L.; Huang, Y.; Liu, X. Y.; Li, L.; Wang, A.; Wang, X.; Mou, C.-Y.; Zhang, T. Structural and catalytic properties of supported Ni-Ir alloy catalysts for H_2 generation via hydrous hydrazine decomposition. *Appl. Catal., B* **2014**, *147*, 779–788.
18. Savage, P. E.; Akiya, N. Roles of water for chemical reactions in high-temperature water. *Chem. Rev.* **2002**, *102*, 2725–2750.
19. Akiya, N.; Savage, P. E. Kinetics and mechanism of cyclohexanol dehydration in high-temperature water. *Ind. Eng. Chem. Res.* **2001**, *40*, 1822–1831.

Publication Date (Web): September 11, 2015 | doi: 10.1021/bk-2015-1194.ch010

20. Jin, F.; Zeng, X.; Liu, J.; Jin, Y.; Wang, L.; Zhong, H.; Yao, G.; Huo, Z. Highly efficient and autocatalytic H_2O dissociation for CO_2 reduction into formic acid with zinc. *Sci. Rep.* **2014**, 4.
21. Takahashi, H.; Liu, L. H.; Yashiro, Y.; Ioku, K.; Bignall, G.; Yamasaki, N.; Kori, T. CO_2 reduction using hydrothermal method for the selective formation of organic compounds. *J. Mater. Sci.* **2006**, *41*, 1585–1589.
22. Tian, G.; He, C.; Chen, Y.; Yuan, H.-M.; Liu, Z.-W.; Shi, Z.; Feng, S.-H. Hydrothermal reactions from carbon dioxide to phenol. *ChemSusChem* **2010**, *3*, 323–324.
23. He, C.; Tian, G.; Liu, Z.; Feng, S. A mild hydrothermal route to fix carbon dioxide to simple carboxylic acids. *Org. Lett.* **2010**, *12*, 649–651.
24. Shen, Z.; Zhang, Y. L.; Jin, F. M. The alcohol-mediated reduction of CO_2 and $NaHCO_3$ into formate: A hydrogen transfer reduction of $NaHCO_3$ with glycerine under alkaline hydrothermal conditions. *RSC Adv.* **2012**, *2*, 797–801.
25. Liu, J.; Zeng, X.; Cheng, M.; Yun, J.; Li, Q.; Jing, Z.; Jin, F. Reduction of formic acid to methanol under hydrothermal conditions in the presence of Cu and Zn. *Bioresour. Technol.* **2012**, *114*, 658–662.

Publication Date (Web): September 11, 2015 | doi: 10.1021/bk-2015-1194.ch010

Publication Date (Web): September 11, 2015 | doi: 10.1021/bk-2015-1194.ch011

Chapter 11

RuBisCO-Inspired Biomimetic Approaches to Reversible CO_2 Capture from Air

Metal Dependence of the H_2O/CO_2 Replacement Penalty

Rainer Glaser*

Department of Chemistry, University of Missouri, Columbia, Missouri 65211, and Institute of Chemistry, Chinese Academy of Sciences, Beijing 100190, China
***E-mail: glaserr@missouri.edu**

The highly endergonic exchange of a Mg^{2+}-coordinated H_2O by CO_2 is an essential feature of rubisco thermochemistry because this H_2O/CO_2 replacement penalty ensures the overall reversibility of the CO_2 capture reaction. While the active site of rubisco employs Mg^{2+} catalysis, rubisco-inspired biomimetic approaches to CO_2 capture from air may involve alternatives to Mg^{2+}. To guide the search for alternatives, we studied the metal dependence of the H_2O/CO_2 exchange reaction $CO_2 + H_2O{\cdot}ML_2 \leftrightarrows OCO{\cdot}ML_2 + H_2O$ for $M^{2+} = Mg^{2+}$, Ca^{2+}, Zn^{2+} (closed-shell, class 1) and $M^{2+} = Cu^{2+}$, Ni^{2+}, Co^{2+}, and Fe^{2+} (open-shell, class 2) at the MP2(full)/6-31G* level. The results suggest that Ca^{2+}, Zn^{2+}, Cu^{2+}, and Co^{2+} are excellent candidates as magnesium alternatives.

In Advances in CO2 Capture, Sequestration, and Conversion; He, et al.;
ACS Symposium Series; American Chemical Society: Washington, DC, 2015.

Publication Date (Web): September 11, 2015 | doi: 10.1021/bk-2015-1194.ch011

Introduction

CO_2 scrubbing involves the capture of CO_2 from air by a substrate, the release of CO_2 from the substrate and its collection, and the long-term CO_2 sequestration. Global Research Technologies (GRT) first demonstrated CO_2 capture from air with the ACCESS™ system in 2007 (*1*), CO_2 capture from the air is the pertinent tool to address CO_2 emissions from distributed sources (*2*, *3*), and, most importantly, CO_2 capture from the air is the method of last resort to combat excessive atmospheric CO_2 concentrations (*4*, *5*). CO_2 scrubbing relies on chemical systems for reversible CO_2 capture and usually involve carbamic acid formation; i.e., CO_2 reaction with amines (*6–8*), polyamine-based solid adsorbents (*9*), alkylamine-appended metalorganic framework (*10–12*), or diamine-appended metal-organic frameworks (*13*). Alternatives to amine-based capture systems also have been explored and these include, for example, polyethylene glycol promoted CO_2 chemistry (*14*). The success of any CO_2 capture system relies on the thermochemistry and the kinetics of the CO_2 capture reaction. The thermochemistry of the CO_2 capture reaction must ensure the effective capture as well as the possibility for the subsequent CO_2 release. The kinetics of the CO_2 capture reaction must be such that both the capture and the release of CO_2 are not hindered too much by their activation barriers. Biomimetic CO_2 capture systems are of special interest because they hold promise to meet both the thermodynamic and the kinetic requirements for reversible CO_2 capture. For example, bio-CO_2 capture in carbonic anhydrase II from *Chlorella vulgaris* has been characterized (*15*). It is our goal to develop rubisco-based biomimetic systems for reversible CO_2 capture from air and the general strategy has been described (*16*). Our designs of the chemical CO_2 capture and release systems (CCR) are informed by the understanding of the binding of *the activator* CO_2 ($^{A}CO_2$) in rubisco.

Rubisco (ribulose 1,5-bisphosphate carboxylase/oxygenase, RuBisCO) catalyzes the addition of CO_2 and water to RuBP (d-ribulose 1,5-bisphosphate) in the photosynthetic carbon assimilation via the Calvin-Bassham-Benson cycle and results in two molecules of 3-PGA (3-phospho-d-glycerate) and 0.5 O_2 (*17–19*). The carboxylation reaction competes with photorespiration, that is, the fixing of molecular O_2 by its addition to RuBP to form one equivalent of 3-PGA and one equivalent of phosphoglycolate. Nearly all carbohydrate production in the biosphere depends on rubisco catalysis and rubisco is the most abundant protein on Earth. Many photosynthetic organisms contain form I rubisco (*20*) which is comprised of eight large (L) and eight small (S) subunits and the crystal structure of *Spinacia oleracea* (*21*, *22*) provided an early example of a hexa-decameric rubisco (*23*). Form II rubisco lacks small subunits, generally occurs as L_2, and is exemplified by the bacterial rubisco of *Rhodospirillum rubrum* (*24*). We focus on form I rubisco and this form also occurs in algae including the green algae *Chlamydomonas reinhardtii* (*25*) and the red algae *Galdieria sulphuraria* (*26*).

In Advances in CO2 Capture, Sequestration, and Conversion; He, et al.;
ACS Symposium Series; American Chemical Society: Washington, DC, 2015.

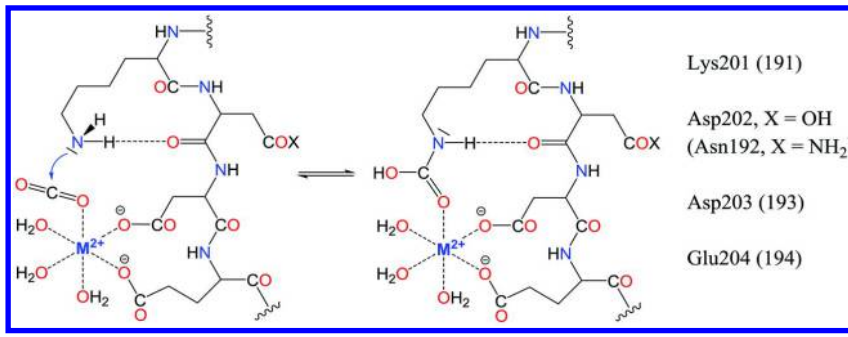

Scheme 1. Activation of RuBisCO by N-carbamic acid formation with $^{A}CO_2$. Residue numbers refer to the structures of activated RuBisCO in Spinacia oleracea (21, 22) and Rhodospirillum rubrum ((24), data in parentheses).

Hartmann and Harpel (*27*) and Lorimer et al. (*28*) discussed the mechanism of rubisco catalysis. To exhibit both the carboxylase and oxygenase activities, rubisco must be activated by carbamylation of active-site lysine (Lys) with an activator CO_2 ($^{A}CO_2$). The carbamate formed is stabilized both by complexation to Mg^{2+} and by NH···OC hydrogen-bonding (Scheme 1). Rubisco activase (*29*) causes the release of RuBP from unactivated rubisco so that the carbamylation of the lysine by $^{A}CO_2$ can occur. Theoretical studies of the carboxylation and oxygenation reactions of a model system (CH_3COCH_2OH in place of RuBP; Mg^{2+} coordinated by two formate anions as models for Asp203 and Glu204; $H_2N–CO_2^-$ as carbamate model of Lys201) have been reported (*30*, *31*).

$$CO_2(g) + ML_2(g) \leftrightarrows [CO_2 \cdot ML_2](g) \quad (R7)$$
$$H_2O(g) + ML_2(g) \leftrightarrows [H_2O \cdot ML_2](g) \quad (R9)$$
$$CO_2(g) + [H_2O \cdot ML_2](g) \leftrightarrows [CO_2 \cdot ML_2)](g) + H_2O(g) \quad (R10 = R7 - R9)$$

In the context of our studies of heterocumulenes (*32–34*) and of nucleophilic additions to heterocumulenes (*35–37*), we recently analyzed the thermochemistry of a rubisco-based small molecule model of the formation of *N*-methylcarbamic acid (NMCA) by addition of methylamine (CH_3NH_2) to CO_2 considering substrate and product stabilization by an active-side carbonyl model and complexation by a model metal complex ML_2 (*16*). The model system is described by 14 reactions, the reactions R1 - R14 will be reviewed below, and the thermochemistry was determined at the B3LYP/6-31G* level for the natural case of magnesium $M^{2+} = Mg^{2+}$. Importantly, the complexation of CO_2 to the metal cation M^{2+} requires the replacement a water molecule and our analysis showed that this H_2O/CO_2 replacement is an essential feature of rubisco thermochemistry. The exchange of a ligand water by a CO_2 molecule (reaction R10) is highly endergonic with ΔG_{298}(R10) = 15.7 kcal/mol (*16*, *38*), and this H_2O/CO_2 replacement penalty is required to lower the overall exergonicity of the CO_2 capture reaction and to allow overall reversibility. While rubisco employs Mg^{2+} catalysis, one may consider other metals in rubisco-inspired biomimetic approaches to CO_2 capture. As a first step in that direction, we studied the metal dependence of the H_2O/CO_2 replacement penalty for the metal cations $M^{2+} = Mg^{2+}$, Ca^{2+}, Zn^{2+}, Cu^{2+}, Ni^{2+},

Publication Date (Web): September 11, 2015 | doi: 10.1021/bk-2015-1194.ch011

Co^{2+}, and Fe^{2+}. Here we report on the geometries of the metal formates ML_2 and their electronic structures, on the conformations of the $H_2O{\cdot}ML_2$ and $OCO{\cdot}ML_2$ adducts, and on the thermochemistry of reactions R7, R9 and R10.

The present study employs second-order Møller-Plesset perturbation theory (MP2) at the MP2(full)/6-31G* level while the earlier work employed density functional theory (DFT) at the B3LYP/6-31G* level (*16*). Technical aspects of the MP2 computations and especially of the 6-31G* basis sets for the metals will be described below, and here we want to briefly address the major conceptual difference between the approaches. In Hartree-Fock self-consistent field (HF-SCF) theory, each orbital is optimized considering the average electron density of all the other electrons until the iterative process reaches self-consistency. Post-HF electronic structure theory deals with the fact that electrons actually move in ways to avoid each other as much as possible to minimize electron-electron repulsion, that is, the motion of each electron is correlated with the motions of all the other electrons (rather than each electron moving in the field of the average electron density of the other electrons). In post-HF theories, it is common to distinguish between dynamical and non-dynamical (or static) electron correlations. The dynamical correlations of the electrons' motions minimize electron-electron repulsion and especially improve the motions (i.e., the orbitals) of opposite spin electrons. Static correlations become important when only a small gap separates low-lying excited states from the electronic ground state. In such cases one electron configuration may not suffice to describe the wave function. The common DFT approach accounts only for short-range dynamical correlations and neglects static correlations. However, dispersion interactions require long-range dynamical correlations and van der Waals interactions (a.k.a., London interactions or dispersion interactions) are known to affect the accuracy of the reaction thermochemistry of larger systems. To capture dispersion interactions one can perform DFT calculations with empirical London dispersion corrections ((*39*), DFT-D methods) or one may employ correlation interaction (CI) methods. The CI methods are advantageous because they do not only account for dispersion but also for static electron correlations. Møller-Plesset perturbation theory (MPPT) is a powerful approxi-mation to CI theory and methods development has especially focused on second-order Møller-Plesset perturbation theory (MP2, (*40*)). With a view to the incor-poration of dispersion interactions, one may employ DFT-D or MP2 methods. We chose to employ the MP2 method in the present study because this method also accounts for non-dynamical correlations and this type of electron correlation becomes important in situations with low-lying empty orbitals (i.e., metal d-orbitals) and weak dative bond formation.

Small Molecule RuBisCO Model

Reaction R1 is the formation of *N*-methylcarbamic acid (NMCA, H_3C—NH—CO—OH) by addition of methylamine to CO_2 in the gas phase (*g*). Three effects of the environment need to be considered in the active site of rubisco (Scheme 1) and these are (A) the stabilization of the product by hydrogen-bonding between NMCA and a model carbonyl compound, (B) the complexation of

In Advances in CO2 Capture, Sequestration, and Conversion; He, et al.;
ACS Symposium Series; American Chemical Society: Washington, DC, 2015.

Publication Date (Web): September 11, 2015 | doi: 10.1021/bk-2015-1194.ch011

NMCA by a model metal complex ML_2, and (C) the forced replacement of ligand water by CO_2 at the metal center. We describe the thermochemistry of small molecule model systems {CO2, RNH2, (A/K), MgL_2} by a system of 14 reactions, R1 - R14, and the case for magnesium ($M^{2+} = Mg^{2+}$) has been analyzed (*16*).

$$CO_2(g) + CH_3NH_2(g) \leftrightarrows \text{NMCA} \quad \text{(R1)}$$

Reaction R2 describes the association of NMCA with a model carbonyl compound (aldehyde A or ketone K) to the aggregate NMCA·(A/K). The presence of the carbonyl compound also may stabilize the amine substrate prior to the addition reaction in the aggregate CH_3NH_2·(A/K) as described by reaction R3. The combined effects of substrate and product stabilization by the carbonyl compound are reflected in reaction R4, the addition of CO_2 to a carbonyl-aggregated methylamine to form carbonyl-aggregated NMCA. The thermo-chemistry of reaction R4 is a function of reactions R1 - R3: R4 = R1 + R2 - R3.

$$\text{NMCA}(g) + (\text{A/K})(g) \leftrightarrows [\text{NMCA}\cdot(\text{A/K})](g) \quad \text{(R2)}$$
$$CH_3NH_2(g) + (\text{A/K})(g) \leftrightarrows [CH_3NH_2\cdot(\text{A/K})](g) \quad \text{(R3)}$$
$$[CH_3NH_2\cdot(\text{A/K})](g) + CO_2(g) \leftrightarrows [\text{NMCA}\cdot(\text{A/K})](g) \quad \text{(R4)}$$

The model metal complex is neutral ML_2 where L is a singly charged anion, and here we use metal(II) formate ($L = HCO_2^-$). Reaction R5 describes the association of NMCA with the formate ML_2 to form the complex NMCA·MgL_2. The metal formate will not only stabilize the addition product NMCA, but it also has the potential to stabilize the CO_2 substrate prior to its addition reaction. Reaction R7 describes the association of the CO_2 with MgL_2 to form the pre-reaction substrate aggregate OCO·ML_2. The combined effects of CO_2 substrate stabilization and of NMCA product stabilization by the model metal complex are reflected in reaction R8, the addition of methylamine to an M^{2+}-complexed CO_2 molecule to form the M^{2+}-complexed NMCA. The thermochemistry of reaction R8 depends on reactions R1, R5, and R7: R8 = R1 + R5 - R7 and with R6 = R1 + R5 one obtains R8 = R6 - R7.

$$\text{NMCA}(g) + ML_2(g) \leftrightarrows [\text{NMCA}\cdot ML_2](g) \quad \text{(R5)}$$
$$CO_2(g) + CH_3NH_2(g) + ML_2(g) \leftrightarrows [\text{NMCA}\cdot ML_2](g) \quad \text{(R6)}$$
$$CO_2(g) + ML_2(g) \leftrightarrows [CO_2\cdot ML_2](g) \quad \text{(R7)}$$
$$[CO_2\cdot ML_2](g) + CH_3NH_2(g) \leftrightarrows [\text{NMCA}\cdot ML_2](g) \quad \text{(R8)}$$

Prior to the addition reaction, the substrates methylamine and CO_2 and their future binding sites, the model carbonyl compound and the model metal complex, all will be interacting with their respective environments as best as possible. We have shown that the interactions of one water molecule with CH_3NH_2, a carbonyl, or CO_2 all are relatively weak whereas the complexation of ML_2 by water (reaction R9) stands out dramatically for $M^{2+} = Mg^{2+}$ (*16*).

$$H_2O(g) + ML_2(g) \leftrightarrows [H_2O\cdot ML_2](g) \quad \text{(R9)}$$
$$CO_2(g) + [H_2O\cdot ML_2](g) \leftrightarrows [CO_2\cdot ML_2)](g) + H_2O(g) \quad \text{(R10)}$$
$$[H_2O\cdot ML_2](g) + CO_2(g) + CH_3NH_2(g) \leftrightarrows [\text{NMCA}\cdot ML_2](g) + H_2O(g) \quad \text{(R11)}$$

Publication Date (Web): September 11, 2015 | doi: 10.1021/bk-2015-1194.ch011

The association of one water molecule with magnesium formate, reaction R9, is highly exothermic (ΔH_{298}(R9) = -20.7 kcal/mol) and the reaction also is significantly exergonic (ΔG_{298}(R9) = -12.0 kcal/mol) at the B3LYP/6-31G* level (*16*). On the other hand, CO_2 binding is weak and, hence, the exchange of a ligand water by a CO_2 molecule, reaction R10 (R10 = R7 - R9) is significantly endothermic with ΔH_{298}(R10) = 16.4 kcal/mol and endergonic with ΔG_{298}(R10) = 15.7 kcal/mol (*38*) at the B3LYP/6-31G* level (*16*). Therefore, a reasonable model of the M^{2+}-catalyzed NMCA formation must consider the forced replacement of ligand water by CO_2. Accounting for reaction R10 converts reaction R8 to reaction R11: R11 = R8 + R10.

$$[NMCA{\cdot}ML_2](g) + (A/K)(g) \leftrightarrows [(A/K){\cdot}NMCA{\cdot}ML_2](g) \quad (R12)$$

$$[H_2O{\cdot}ML_2](g) + CO_2(g) + CH_3NH_2(g) + (A/K)(g) \leftrightarrows [(A/K){\cdot}NMCA{\cdot}ML_2](g) + H_2O(g) \quad (R13)$$

$$[H_2O{\cdot}ML_2](g) + CO_2(g) + [CH_3NH_2{\cdot}(A/K)](g) \leftrightarrows [(A/K){\cdot}NMCA{\cdot}ML_2](g) + H_2O(g) \quad (R14)$$

The combined effects of the product stabilization by effects (A) - (C) can now be considered. The model systems (A/K)·NMCA·ML_2 is constructed by addition a carbonyl (aldehyde or ketone) to the appropriate metal formate complexes NMCA·ML_2 (reaction R12). Combination of R11 and R12 results in reaction R13 (R13 = R11 + R12), and considering the aggregation between the substrate methylamine and the carbonyl model (reaction R3) one obtains reaction R14; R14 = R13 - R3 = R11 + R12 - R3. Reaction R14 models the capture of CO_2 and the addition of the M^{2+}-complexed CO_2 to a pre-positioned, carbonyl-aggregated methylamine CH_3NH_2·(A/K) to form the M^{2+}-complexed and carbonyl-aggregated NMCA, (A/K)·NMCA·ML_2.

Computational Methods

Theoretical Level and Potential Energy Surface Analysis.

Computations were performed at the MP2(full)/6-31G* level of ab initio quantum theory, that is, second-order Møller-Plesset perturbation theory (*41–43*) was employed with the inclusion of all electrons in the active space. Structures were optimized completely using redundant internal coordinates (*44*) and vibrational frequencies were computed analytically for stationary structures to determine the thermochemical properties.

Solvation influences the electronic energy of molecular systems because of the mutual polarizations between solute and solvent and solvation also manifests itself in the molecular thermochemistry. One can consider solvation effects in several ways and these include the explicit inclusion of solvent molecules in the model system, the application of continuum solvation models (*45*), or a combination of both approaches (*46*). Within each approach one may select various levels of sophistication beginning with the computation of solvation corrections to the energies of gas-phase structures, via the optimization of structures within the solvation model, and on to the determination of optimized structures and their thermochemical properties with the solvation model. In the

In Advances in CO2 Capture, Sequestration, and Conversion; He, et al.;
ACS Symposium Series; American Chemical Society: Washington, DC, 2015.

Publication Date (Web): September 11, 2015 | doi: 10.1021/bk-2015-1194.ch011

present study, we consider the two most important solvent effects. First, we are studying the metal dependence of the H_2O/CO_2 replacement penalty with explicit consideration of the water molecule which is replaced by CO_2 as ligand of the ML_2 complex. Second, we are accounting for the fact that translational entropies in solution are much smaller than the value computed for free or solvated molecules in the gas phase (vide infra). This approach will provide meaningful results about the metal dependence of the H_2O/CO_2 replacement penalty and further refinements may include additional corrections for bulk solvation.

Basis Sets

Publication Date (Web): September 11, 2015 | doi: 10.1021/bk-2015-1194.ch011

In Pople's nomenclature, the 6-31G* basis set describes the atomic orbitals (AOs) of H, C, and O in the usual fashion (*47*). Hydrogen atoms are described by a "31G" basis set, that is, by two s-type basis functions which are comprised of 3 or 1 primitive Gaussian functions, respectively. The so-called first-row atoms C and O are described by the 6-31G* basis set, that is, the core 1s AO is described by one basis function comprised of 6 primitive Gaussian functions ("6G" part for the core), and each of the 2s and 2p valence AOs is described by two basis functions comprised of 3 and 1 primitive Gaussian functions, respectively. The Pople basis sets are particularly efficient because s- and p-basis functions in the same sp-shell use primitives with the same exponents. The star in the notation indicates that one set of d-type polarization functions was added to the basis sets of C and O atoms. These polarization functions allow the p-orbitals to deviate from perfect rotational symmetry to better account for polarization in the molecule.

The 6-31G* basis set for magnesium (*48*) really is a 66-31G* basis set: the 1s core-AO is described by one s-type basis function, and each one of the 2s and 2p core-AOs, respectively, is described by one s- or p-type basis function, respectively, and all of them are comprised of 6 primitive Gaussian functions. The electrons in the valence shell of magnesium (3s, 3p) are described with a split sp-shell and a set of d-functions is added to allow for polarization (0.175).

In analogy, the 6-31G* basis set for calcium (*48*) really is a 666-31G* basis set: Three core shells (s, sp, sp), a split-valence 31G description of the 4s and 4p atomic orbitals, and one set of d-type polarization functions (0.216).

The 6-31G* basis sets for the transition metals (*48*) build on the 666-31G basis set of calcium: Three core shells (s, sp, sp; 6G) and a split-valence 31G description of the 4s and 4p AOs. However, the 3d orbitals now are part of the valence shell and they are described by a 31G basis set, that is, with two sets of d-type basis functions. These d-type basis functions also help to polarize the 4s and 4p orbitals. In addition, one set of f-type polarization functions is added to allow for more flexibility of the d-orbitals (f-exponents, Zn – Fe: 0.8).

The calculations employed sets of 6 Cartesian d-type orbitals (6D) which were later combined to sets of 5 spherical d-orbitals and one additional s-type basis function. Sets of seven pure f-functions were used throughout (7F).

Publication Date (Web): September 11, 2015 | doi: 10.1021/bk-2015-1194.ch011

Molecular Entropies

While molecular entropies for vibrational and rotational motions in solution can be approximated well by gas phase computations (*49*), the translational entropy is greatly reduced in solution relative to the value computed for the free molecules in the gas phase (*50–52*). Wertz (*53*) derived an equation that relates the entropy of solvation ΔS_{sol} to the gas-phase entropy S_{gas} at 25 °C and 1 atm via $\Delta S_{sol} = -0.46 \cdot (\Delta S_{gas} - 14.3)$. We employ the Wertz equation to compute the translational molecular entropy in solution via $S_{tr,W} = S_{tr,gas} + S_{tr,sol} = 0.54 \cdot S_{tr} + 6.578$, and we then use the corrected molecular entropy $S_W = S_{vib,gas} + S_{rot,gas} + S_{tr,W} = S_{gas} + S_{tr,sol}$ instead of the directly computed molecular entropy S to compute free enthalpies.

Total Energies and Thermochemistry

The most pertinent results of the potential energy surface analysis at the MP2(full)/6-31G* level are summarized in Table 1 and the data include total energies E(MP2(full)/6-31G*), vibrational zero-point energies (ZPE) and thermal energies (TE), and molecular entropies (S). The molecular entropy includes contributions from vibrational, rotational and translational motions, $S = S_{vib} + S_{rot} + S_{tr}$. The computed molecular transla-tional entropy (S_{tr}) also is listed together with a corrected total molecular entropy (S_W) which accounts for the reduced translational entropy in solution.

Table 1. Total Energies and Thermochemical Data

Molecule	*E(MP2)*[a]	*ZPE*[b]	*TE*[c]	*S*[d]	S_{tr}[e]	S_W[f]
H_2O	-76.19924	13.5	15.3	45.1	34.6	35.8
CO_2	-188.11836	7.3	8.9	51.2	37.3	40.6
Diformate, ML_2						
Mg^{2+}, tetra	-577.15278	30.8	35.5	86.5	40.1	74.7
Ca^{2+}, tetra	-1054.28288	29.9	35.0	92.5	40.5	80.4
Zn^{2+}, tetra	-2155.28461	30.7	35.4	87.5	41.0	75.2
Cu^{2+}, square	-2016.45207	30.9	35.5	87.5	41.0	75.2
Ni^{2+}, square	-1884.35764	31.7	35.9	81.9	40.9	69.7
Co^{2+}, square	-1758.90937	31.7	35.9	83.4	40.9	71.1
Fe^{2+}, square	-1639.88556	30.8	35.5	86.8	40.9	74.6
Hydrate, $L_2M \cdot OH_2$						
Mg^{2+}, tbpy-HB2ax	-653.39401	46.3	52.9	101.5	40.6	89.5
Ca^{2+}, tbpy-HB1ax	-1130.52277	45.4	52.4	107.3	40.9	95.1
Zn^{2+}, tbpy-HB2ax	-2231.52231	46.3	52.9	101.8	41.3	89.3

Continued on next page.

In Advances in CO2 Capture, Sequestration, and Conversion; He, et al.;
ACS Symposium Series; American Chemical Society: Washington, DC, 2015.

Table 1. (Continued). Total Energies and Thermochemical Data

Molecule	*E(MP2)*[a]	*ZPE*[b]	*TE*[c]	*S*[d]	S_{tr}[e]	S_W[f]
Cu^{2+}, spy-HB2a	-2092.68542	46.6	53.0	101.3	41.3	88.8
Ni^{2+}, spy-HB2a	-1960.57769	47.0	53.2	96.9	41.2	84.5
Co^{2+}, spy-HB2a	-1835.14561	47.1	53.3	97.8	41.6	85.4
Fe^{2+}, spy-HB2a	-1716.16992	47.7	53.6	93.7	41.2	81.3
Cu^{2+}, spy-HB2b	-2092.68428	46.1	52.8	104.6	41.3	92.1
Ni^{2+}, spy-HB2b	-1960.57747	46.4	53.0	102.7	41.2	90.3
Co^{2+}, spy-HB2b	-1835.14594	46.9	53.8	98.7	41.6	86.3
Fe^{2+}, spy-HB2b	-1716.17001	47.6	53.5	94.6	41.2	82.2
CO_2-Agg, $L_2M{\cdot}OCO$						
Mg^{2+}, tbpy-INA1ax	-765.28614	38.7	45.9	110.0	41.1	97.7
Ca^{2+}, tbpy-INA1ax	-1242.41900	37.8	45.4	116.8	41.4	104.3
Zn^{2+}, tbpy-INA1ax	-2343.41681	38.5	45.8	112.6	41.8	99.9
Cu^{2+}, spy-INA2	-2204.58715	38.8	45.9	112.7	41.7	100.1
Ni^{2+}, spy-INA2	-2072.48821	39.5	46.3	107.1	41.7	94.6
Co^{2+}, spy-INA1	-1947.04467	39.1	46.0	110.4	41.7	97.9
Fe^{2+}, spy-INA2, s	-1828.06284	39.6	46.2	103.8	41.6	91.2
Fe^{2+}, spy-INA2, l	-1828.03511	39.4	46.3	109.4	41.6	96.9

[a] Total energy E(MP2(full)/6-31G*), in atomic units. [b] Vibrational zero-point energy (ZPE) in kcal/mol. [c] Thermal energy (TE) in kcal/mol. [d] Molecular entropy (S) in cal/(K·mol). [e] Molecular translational entropy (S_{tr}) in cal/(K·mol) as computed. [f] Total molecular entropy (S_W) in cal/(K·mol) based on reduced translational entropy.

Computations were performed with Gaussian09 (*54*) on various platforms including the *Lewis* cluster system of the University of Missouri Bioinformatics Consortium (*55*).

Molecular Structures

The structures naturally fall into two classes (Scheme 2). The formates of magnesium, calcium, and zinc feature quasi-tetrahedral coordination (qt) of the metal ion (closed-shell systems), and they are clearly distinct from the (nearly) square planar (spl) coordination modes of the formates of copper, nickel, cobalt and iron (unfilled d-shells). The H_2O and CO_2 adducts of the formates ML_2 reflect the structural distinctions of the formates and also fall into two classes.

The optimized structures of the formates ML_2 of M = Mg, Ca, and Zn are shown in the left column of Figure 1, and the structures of the formates of M = Cu, Ni, Co and Fe are shown in Figure 2. The structures of their $D{\cdot}ML_2$ complexes of the closed-shell systems are included in Figure 1 and the others are shown in

In Advances in CO2 Capture, Sequestration, and Conversion; He, et al.;
ACS Symposium Series; American Chemical Society: Washington, DC, 2015.

Publication Date (Web): September 11, 2015 | doi: 10.1021/bk-2015-1194.ch011

Figures 3 - 5. Major structural parameters are given in the captions of Figures 1 and 2 for the formates, in Table 2 for the hydrates, and in Table 3 for the CO_2 complexes. Complete Cartesian coordinates of all stationary structures can be obtained via email from the author.

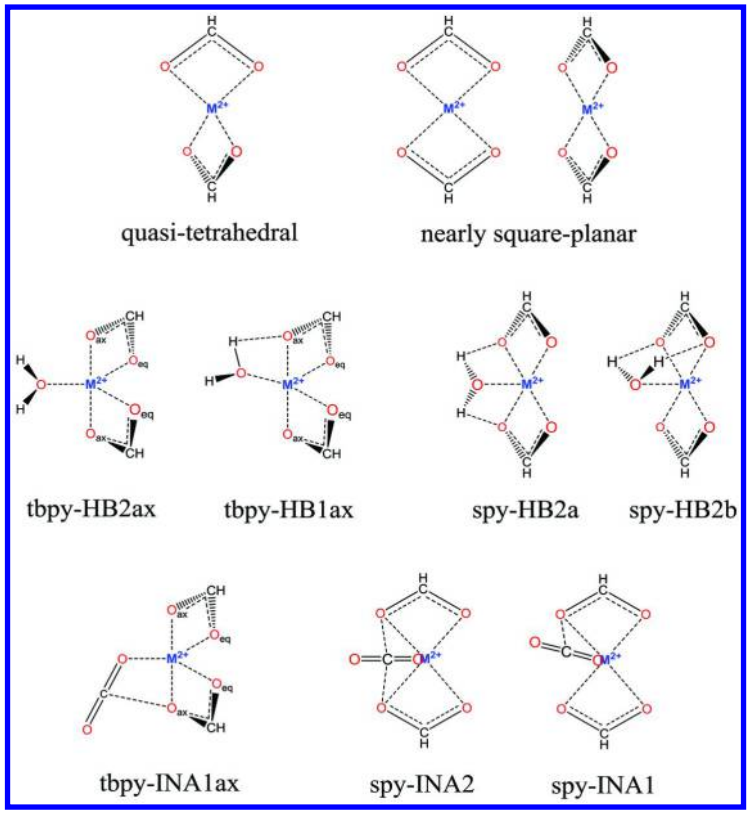

Scheme 2. Geometries of the formates ML_2 (top) and of their complexes $H_2O{\cdot}ML_2$ (center) and $OCO{\cdot}ML_2$ (bottom). The formates of the closed-shell systems with M = Mg, Ca, and Zn (class 1) feature quasi-tetrahedral structures (qt) while the formates of the open-shell systems with M = Cu, Ni, Co, and Fe (class 2) feature square-pyramidal structures (spy). The $D{\cdot}ML_2$ complexes of the closed-shell systems adopt trigonal-bipyramidal structures (tbpy) while the complexes of the open-shell systems prefer square-pyramidal structures (spy). Conformational aspects are discussed in the text.

The distances $d(M\cdots O)$between M^{2+} and a ligand O atom in the formates ML_2 (Figures 1 and 2) roughly parallel M^{2+} ion sizes (*56*); M^{2+} = Mg^{2+} (86 pm), Ca^{2+} (114 pm), Zn^{2+} (88 pm), Cu^{2+} (87 pm), Ni^{2+} (83 pm), Co^{2+} (79 pm), and Fe^{2+} (75 pm). The Ca^{2+} ion is much larger than Mg^{2+}, Zn^{2+} ion is the best match for Mg^{2+}, and the ions in class 2 allow for a systematic decrease in M^{2+} size.

In Advances in CO2 Capture, Sequestration, and Conversion; He, et al.;
ACS Symposium Series; American Chemical Society: Washington, DC, 2015.

Publication Date (Web): September 11, 2015 | doi: 10.1021/bk-2015-1194.ch011

The additional coordination of one donor ligand D to a tetrahedral formate results in trigonal bipyramidal structures (tbpy) in which one formate O-atom of each ligand occupies an axial position (O_{ax}) while the second O-atom of each formate occupies an equatorial position (O_{eq}). The additional ligand D occupies an equatorial position. The addition of donor ligand D to a (nearly) square-planar formate results in (nearly) square-pyramidal structures (spy) in which the additional ligand occupies the unique axial position. These main structural motives are further distinguished depending on the orientation of the ligand D.

Publication Date (Web): September 11, 2015 | doi: 10.1021/bk-2015-1194.ch011

Table 2. Major Structural Parameters of Hydrates $H_2O \cdot ML_2$[a-d]

Mol.	*d(M…O)*	*Đ(OCO)*	*d(M…D)*	*Other*
MgL_2	2.098 & 2.063	122.2	2.064	Đ(O_{ax}-M-D) 89.11 *d*(H…O_{ax}) 2.862
CaL_2	2.446 & 2.384 2.396 & 2.382	124.3 124.5	2.403	Đ(O_{ax}-M-D) 67.53 *d*(H…O_{ax}) 2.065
ZnL_2	2.113 & 1.999	121.8	2.055	Đ(O_{ax}-M-D) 85.63 *d*(H…O_{ax}) 2.699
CuL_2 HB2a	1.970 & 2.016	120.3	2.182	Đ(O-M-D) 84.77 *d*(H…O) 2.470
CuL_2 HB2b	1.986 & 2.002 1.984 & 1.972	120.5 120.3	2.169	Đ(O-M-D) 91.61 *d*(H…O) 2.836, 3.159
NiL_2 HB2a	1.908 & 1.879	118.1	2.396	Đ(O-M-D) 80.66 *d*(H…O) 2.396
NiL_2 HB2b	1.893 & 1.895 1.884 & 1.885	118.3 118.1	2.325	Đ(O-M-D) 94.95 *d*(H…O) 3.229, 3.045
CoL_2 HB2a	1.961 & 1.943	119.1	2.149	Đ(O-M-D) 86.45 *d*(H…O) 2.502
CoL_2 HB2b	1.954 & 1.955 1.939 & 1.941	119.3 119.1	2.133	Đ(O-M-D) 92.67 *d*(H…O) 2.872, 2.855
FeL_2 HB2a	1.995 & 1.983	119.5	1.971	Đ(O-M-D) 87.36 *d*(H…O) 2.411
FeL_2 HB2b	1.992 & 1.994 1.974 & 1.976	119.7 119.5	1.969	Đ(O-M-D) 91.42 *d*(H…O) 2.663, 2.672

[a] *d*(M···O)and Đ(OCO) values in one row refer to the same formate. [b] Class 1 systems: In each row, the *d*(M···O)values refer to O_{ax} and O_{eq}, respectively. Data for the formate more engaged in HB are listed first. HB contacts refer to the closer O_{ax}. [c] Class 2, HB2a systems: The first *d*(M···O)value as well as the Đ(O-M-D) and *d*(H···O) values refer to the formate-O with the HB contact. [d] Class 2, HB2b systems: *d*(M···O)and Đ(OCO) values in the first row refer to the formate more engaged in HB contacts. The Đ(O-M-D) value and the first *d*(H···O) value refer to the formate-O with the best HB contact.

Table 3. Major Structural Parameters of CO_2-Aggregates $OCO{\cdot}ML_2$[a-d]

Mol.	*d*(M···O)	Đ(OCO)	*d*(M···D)	*Other*
MgL_2	2.101 & 2.055 2.068 & 2.048	121.9 121.9	2.210	Đ(M-O-C) 124.35 Đ(O-M-O-C) -2.03 *d*(INA) 2.830
CaL_2	2.405 & 2.383 2.374 & 2.372	124.2 124.3	2.551	Đ(M-O-C) 125.53 Đ(O-M-O-C) 1.08 *d*(INA) 2.826
ZnL_2	2.073 & 2.014 2.043 & 2.009	121.1 121.2	2.234	Đ(M-O-C) 125.82 Đ(O-M-O-C) 0.36 *d*(INA) 2.808
CuL_2	1.975 & 1.963	119.9	2.319	Đ(M-O-C) 113.84 Đ(O_f-M-O) 85.86 *d*(INA) 3.110
NiL_2	1.880 & 1.875	117.7	2.527	Đ(M-O-C) 103.56 Đ(O_f-M-O) 82.91 *d*(INA) 2.991
CoL_2	1.966 & 1.961 1.957 & 1.958	119.2 119.2	2.236	Đ(M-O-C) 115.11 Đ(O_f-M-O) 86.93 *d*(INA) 3.010 & 3.238
FeL_2 short	1.973 & 1.977	119.2	2.027	Đ(M-O-C) 114.78 Đ(O_f-M-O) 89.91 *d*(INA) 3.002
FeL_2 long	1.911 & 1.909	117.9	2.745	Đ(M-O-C) 106.42 Đ(O_f-M-O) 78.16 *d*(INA) 3.110

[a] For all CO_2 aggregates: *d*(M···O) and Đ(OCO) values in one row refer to the same formate. [b] In the absence of C_s-symmetry, data in the first row refer to the formate closer to CO_2. [c] Đ(M-O-C) is the angle between the (M···D)dative bond and OCO. [d] Đ(O_f-M-O) is the angle between and CO_2-O and the (M···O_f) dative bond of the formate-O involved in INA. [e] *d*(INA) is the distance between the CO_2-C and the closest formate-O.

In the hydrate complexes (D = OH_2) of class 1 systems (Figure 1, center column), there exists the possibility for hydrogen bonding between the ligand water and one or two proximate formate O-atoms (Scheme 2). In the $H_2O{\cdot}CaL_2$ complex, the ligand water is placed to optimized one H-bond to one axial formate-O (HB1ax) with a short contact of 2.065 Å, while the $H_2O{\cdot}ML_2$ complexes with M = Mg, Zn feature two equivalent HB-contacts to the two axial formate-O atoms (HB2ax) which are much longer (> 2.65 Å).

In the carbon dioxide complexes (D = OCO) of class 1 systems (Figure 1, right column), there exists the possibility for incipient nucleophilic attack (INA) interaction (*57*, *58*) between the electrophilic C-atom and one or two proximate formate O-atoms. In the $OCO{\cdot}ML_2$ complexes with M = Mg, Ca, Zn, the ligand CO_2 is placed to optimize one INA to one axial formate-O (tbpy-INA1ax) and allows the proximate nucleophilic formate-O to approach the electrophilic CO_2-carbon to a distance of *d*(INA) ≈ 2.80 - 2.83 Å (Table 3).

In Advances in CO2 Capture, Sequestration, and Conversion; He, et al.;
ACS Symposium Series; American Chemical Society: Washington, DC, 2015.

Publication Date (Web): September 11, 2015 | doi: 10.1021/bk-2015-1194.ch011

Publication Date (Web): September 11, 2015 | doi: 10.1021/bk-2015-1194.ch011

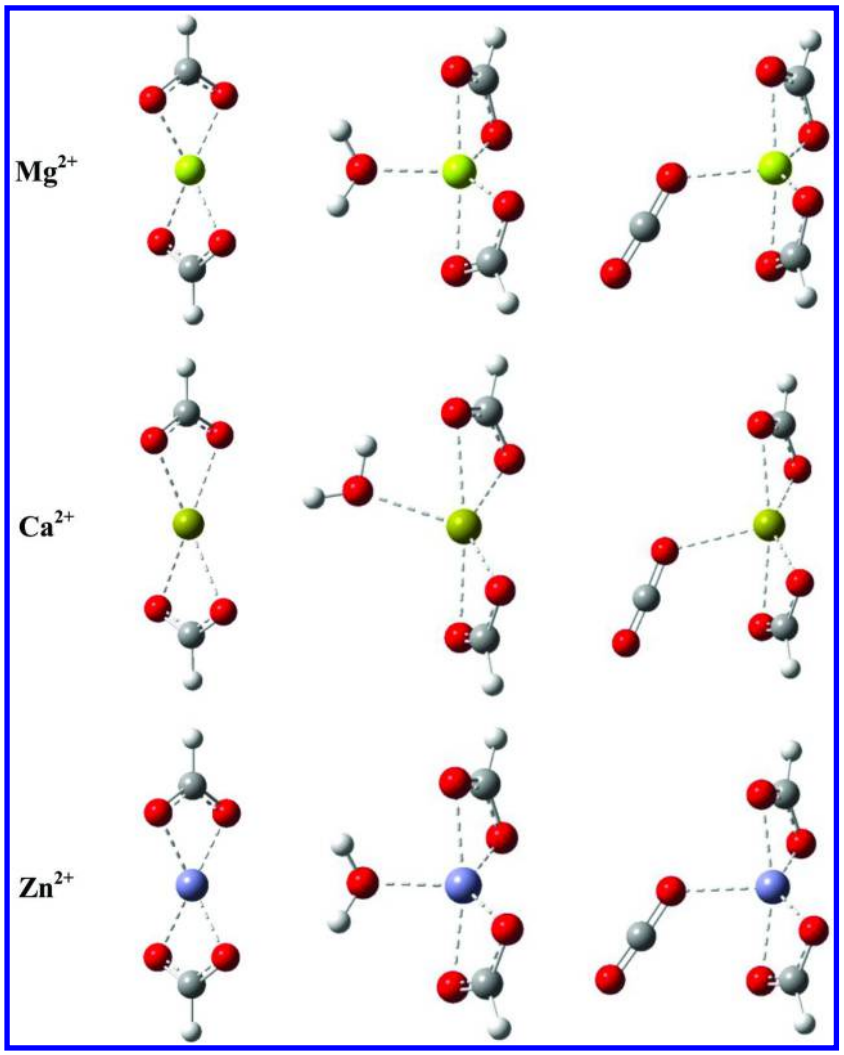

Figure 1. Optimized structures of the metal formates ML_2 (left) and of complexes $D{\cdot}ML_2$ formed with water (center) and CO_2 (right) with M^{2+} = Mg^{2+}, Ca^{2+}, and Zn^{2+}. Structural parameters d(M···O) and Ð(OCO) of formates ML_2: Mg^{2+}: 2.044 Å, 121.8°; Ca^{2+}: 2.366 Å, 124.2°; and Zn^{2+}: 2.007 Å, 120.9°.

In the hydrate complexes (D = OH_2) of the open-shell systems in class 2, the water molecule can be oriented in such a way that water forms one HB contact with each ligand (HB2a) and such structures correspond to minima for every formate of this type (Figure 3). Alternatively, the ligand water can be oriented to engage preferentially with one of the ligand (HB2b) and such structures also correspond to minima for every formate (Figure 4). The HB2b structures allow for a somewhat closer approach of water to the metal center. Irrespective of the specific type of HB

In Advances in CO2 Capture, Sequestration, and Conversion; He, et al.;
ACS Symposium Series; American Chemical Society: Washington, DC, 2015.

contact, the d(M···O)distances are markedly longer for the class 2 ions than for the closed-shell systems. Note especially that the *d*(M···O)distance in the $H_2O{\cdot}NiL_2$ complex is almost as long as that in $H_2O{\cdot}CaL_2$.

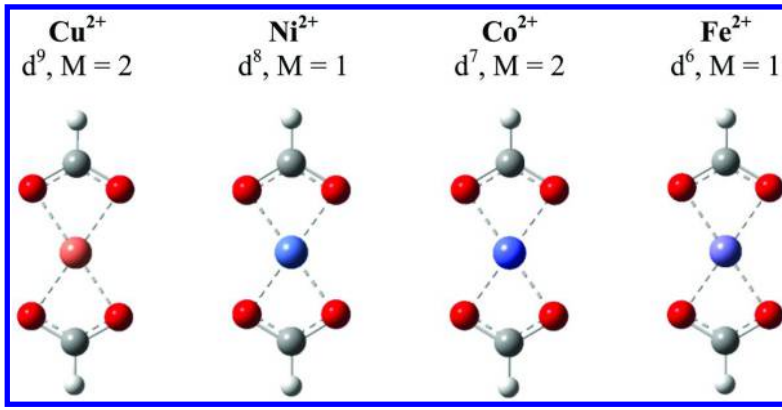

Figure 2. Optimized structures of the metal formates ML_2 of the open-shell systems with M^{2+} = Cu^{2+}, Ni^{2+}, Co^{2+}, and Fe^{2+}. Structural parameters d(M···O) and Ð(OCO) of formates ML_2: Cu^{2+}: 1.959 Å, 119.6°; Ni^{2+}: 1.871 Å, 117.4°; Co^{2+}: 1.895 Å, 117.8°; and Fe^{2+}: 1.943 Å, 118.8°.

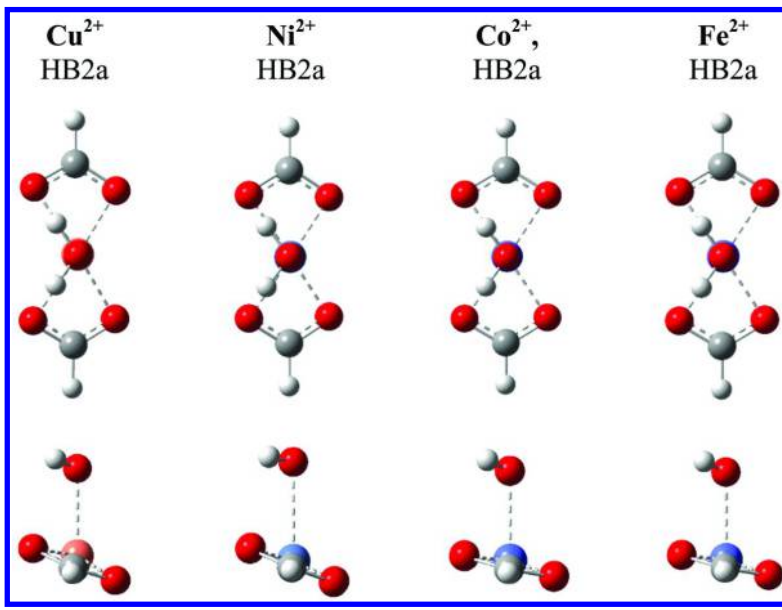

Figure 3. Optimized structures of the hydrate complexes $D{\cdot}ML_2$ of the open-shell systems with M^{2+} = Cu^{2+}, Ni^{2+}, Co^{2+}, and Fe^{2+}. HB2a complexes are viewed down the $H_2O{\cdots}M$ bonding line (top row) and from the side (second row).

In Advances in CO2 Capture, Sequestration, and Conversion; He, et al.;
ACS Symposium Series; American Chemical Society: Washington, DC, 2015.

Publication Date (Web): September 11, 2015 | doi: 10.1021/bk-2015-1194.ch011

Publication Date (Web): September 11, 2015 | doi: 10.1021/bk-2015-1194.ch011

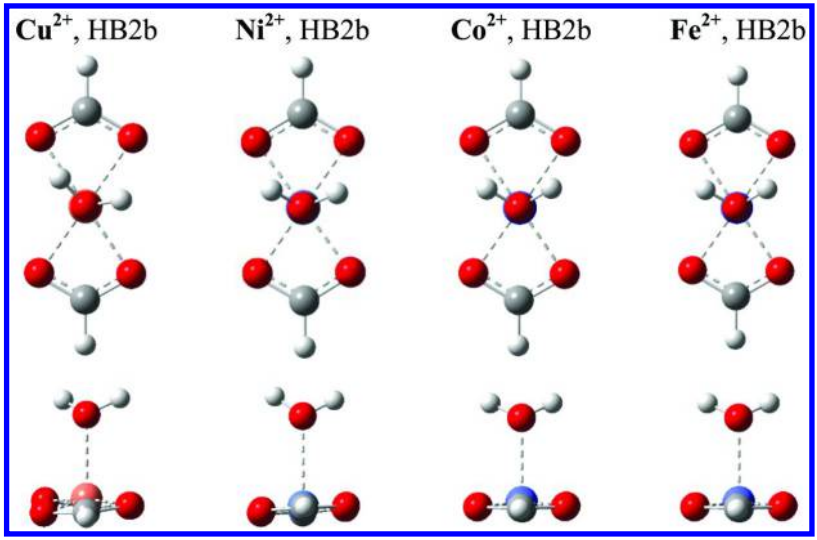

Figure 4. Optimized structures of the hydrate complexes D·ML$_2$ of the open-shell systems with M^{2+} = Cu^{2+}, Ni^{2+}, Co^{2+}, and Fe^{2+}. HB2b complexes are viewed down the H$_2$O···M bonding line (top row) and from the side (second row).

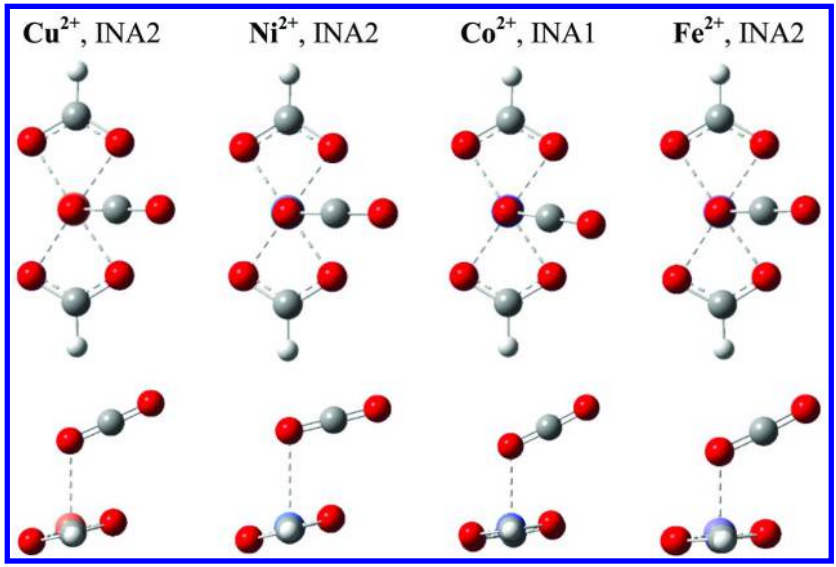

Figure 5. Optimized structures of the CO$_2$ complexes D·ML$_2$ of the open-shell systems with M^{2+} = Cu^{2+}, Ni^{2+}, Co^{2+}, and Fe^{2+}. The complexes are viewed down the OCO···M bonding line (top row) and from the side (second row).

In the class 2 systems, the $OCO{\cdot}ML_2$ complexes (Figure 5) with M = Cu, Ni, and Fe feature double INA involving one O-atom of each formate (spy-INA2), while the $OCO{\cdot}CoL_2$ complex prefers a structure with one stronger INA contact (spy-INA1). The contacts d(INA) ≈ 3.0 - 3.1 Å are slightly longer than for class 1 ions (Table 4).

The geometries indicate that H_2O is a much better donor compared to CO_2 and this is true for all metal ions. The d(M···O)distances are about 0.16±0.02 Å shorter for $H_2O{\cdot}ML_2$ than for $OCO{\cdot}ML_2$ for the class 1 metal ions and the same is true for Cu^{2+} and Ni^{2+} (Tables 3 and 4). However, this difference is reduced to 0.10 Å and 0.06 Å for Co^{2+} and Fe^{2+}, respectively.

Binding Energies and H_2O/CO_2 Replacement Penalty

Relative and reaction energies computed at the MP2(full)/6-31G* level are summarized in Table 4, and Figures 6 (ΔE, ΔH_{298}) and 7 (ΔG_{298}, ΔG_W) illustrate the cost of replacement (in kcal/mol) of water by CO_2 in complexes (R10) and binding energies of ML_2 with water (R9) and CO_2 (R7).

Theoretical Level Dependency

The B3LYP/6-31G* data for Mg^{2+} (*16*) are included in Table 4 for comparison. The MP2(full)/6-31G* data of the present study indicate stronger binding for water (ΔH_{298}(R9) = -24.1 kcal/mol) and CO_2 (ΔH_{298}(R7) = -7.9 kcal/mol) than at the B3LYP/6-31G* level, but the enthalpy of the exchange reaction (ΔH_{298}(R10) = 16.2 kcal/mol) is just about the same as the value computed at the DFT level. The enthalpy differences at the two levels account for all but 0.24 kcal/mol of the differences between the ΔG_{298}(R7) and ΔG_{298}(R9) values computed at the two levels, and it accounts essentially for all of the difference between the ΔG_{298}(R10) values computed at the DFT (15.7 kcal/mol) and MP2 (15.5 kcal/mol) levels.

Wertz Correction of Molecular Translational Entropy

The comparison of the DFT and MP2 data for the Mg^{2+} systems suggests that both theoretical levels provide rather similar thermochemical parameters, which is encouraging. The thermochemical parameters are computed for the gas phase and we pointed out above that molecular entropies for vibrational and rotational motions in solution can be approximated well by gas phase computations while translational entropies are significantly reduced in solution relative to the free molecules in the gas phase. Hence, we employed the Wertz equation (*53*) to compute the translational molecular entropy in solution via $S_{tr,W} = 0.54{\cdot}S_{tr} + 6.578$ and we employed the corrected molecular entropy $S_W = S_{vib,gas} + S_{rot,gas} + S_{tr,W}$ (Table 1) in the computation of the ΔG_W values (Table 4).

Publication Date (Web): September 11, 2015 | doi: 10.1021/bk-2015-1194.ch011

Publication Date (Web): September 11, 2015 | doi: 10.1021/bk-2015-1194.ch011

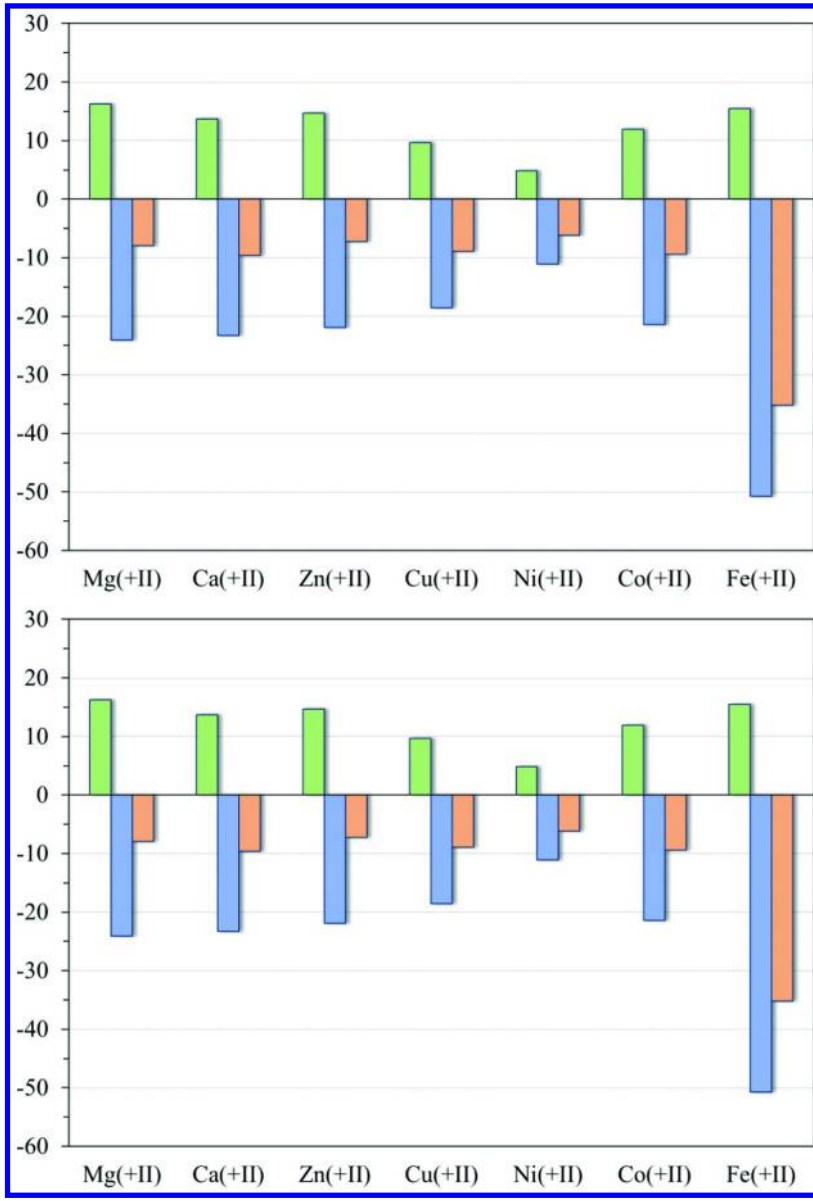

Figure 6. Cost of replacement (in kcal/mol) of water by carbon dioxide in complexes D·ML_2 (left column, green online) and binding energies of ML_2 with water (center column, blue online) and CO_2 (right column, red online). Top: ΔE. Bottom: ΔH_{298}.

In Advances in CO2 Capture, Sequestration, and Conversion; He, et al.;
ACS Symposium Series; American Chemical Society: Washington, DC, 2015.

Publication Date (Web): September 11, 2015 | doi: 10.1021/bk-2015-1194.ch011

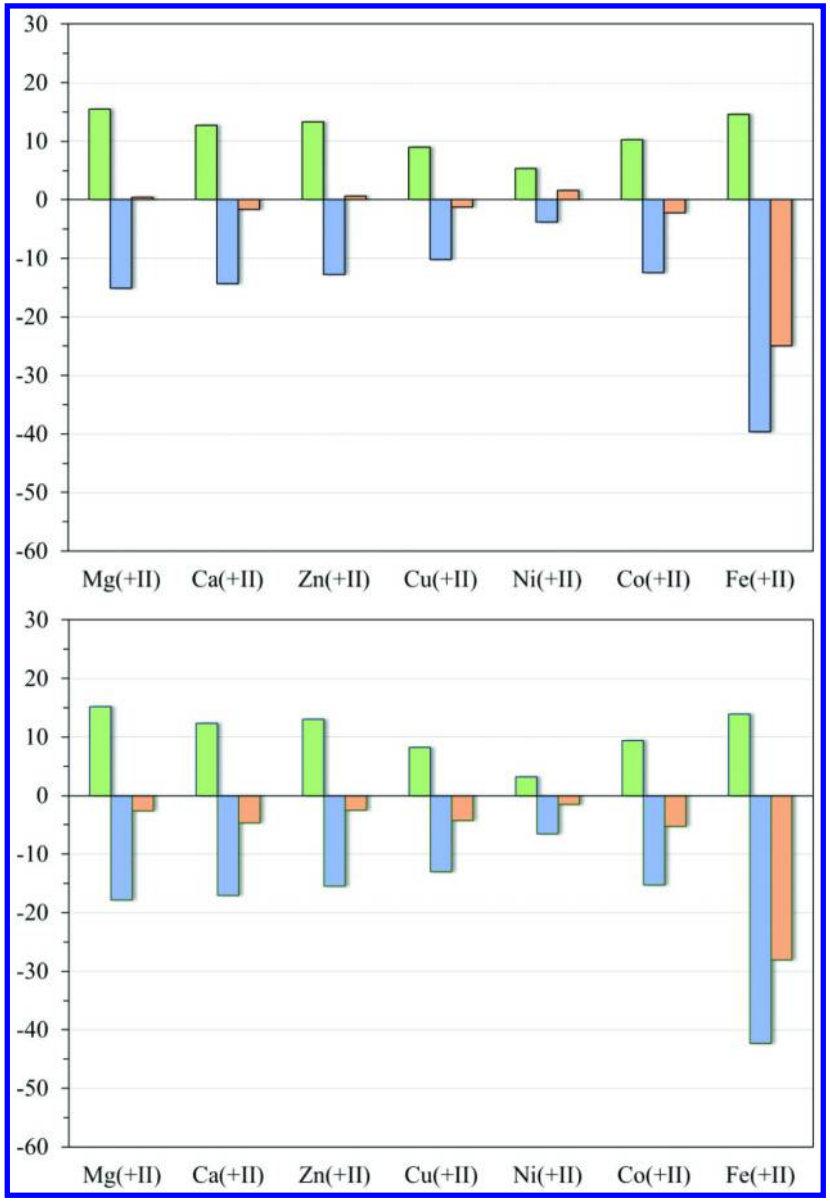

Figure 7. Cost of replacement (in kcal/mol) of water by carbon dioxide in complexes D·ML_2 (left column, green online) and binding energies of ML_2 with water (center column, blue online) and CO_2 (right column, red online). Top: ΔG_{298}. Bottom: ΔG_W.

In Advances in CO2 Capture, Sequestration, and Conversion; He, et al.;
ACS Symposium Series; American Chemical Society: Washington, DC, 2015.

Table 4. Relative and Reaction Energies[a]

Parameter	ΔE^b	$\Delta H_0{}^c$	ΔH^d	ΔG^e	$\Delta G_W{}^f$
HB2a *vs.* **HB2b**					
Cu(+II)	-0.72	-0.29	-0.54	0.45	0.45
Ni(+II)	-0.14	0.44	0.09	1.83	1.83
Co(+II)	0.21	0.38	0.29	0.56	0.56
Fe(+II)	0.06	0.19	0.12	0.40	0.40
R10: $L_2M{\cdot}OH_2$ (HB2b) + $CO_2 \leftrightarrows L_2M{\cdot}OCO + H_2O$					
Mg(+II)[g]	16.47	15.95	16.42	15.69[h]	
Mg(+II)	16.93	15.57	16.23	15.52	15.23
Ca(+II)	14.36	12.96	13.70	12.69	12.39
Zn(+II)	15.45	13.93	14.73	13.31	13.00
Cu(+II)	10.20	9.08	9.63	9.02	8.27
Ni(+II)	5.26	4.55	4.90	5.39	3.25
Co(+II)	12.79	11.18	11.97	10.28	9.41
Fe(+II)	16.50	14.75	15.52	14.60	13.89
R7: $L_2M + CO_2 \leftrightarrows L_2M{\cdot}OCO$					
Mg(+II)[g]	-6.52	-5.01	-4.33	3.72[h]	
Mg(+II)	-9.41	-8.72	-7.89	0.39	-2.63
Ca(+II)	-11.15	-10.52	-9.63	-1.61	-4.64
Zn(+II)	-8.68	-8.12	-7.20	0.60	-2.45
Cu(+II)	-10.49	-9.85	-8.96	-1.22	-4.27
Ni(+II)	-7.66	-7.15	-6.18	1.57	-1.48
Co(+II)	-10.63	-10.48	-9.40	-2.22	-5.26
Fe(+II)	-36.97	-35.44	-35.19	-24.99	-28.03
R9: $L_2M + H_2O \leftrightarrows L_2M{\cdot}OH_2$ (HB2b)					
Mg(+II)*g*	-22.99	-20.96	-20.74	-11.99	
Mg(+II)	-26.35	-24.30	-24.12	-15.13	-17.86
Ca(+II)	-25.51	-23.48	-23.33	-14.30	-17.03
Zn(+II)	-24.14	-22.05	-21.92	-12.71	-15.45
Cu(+II)	-20.68	-18.93	-18.60	-10.24	-12.98
Ni(+II)	-12.92	-11.69	-11.07	-3.82	-6.56

Continued on next page.

Publication Date (Web): September 11, 2015 | doi: 10.1021/bk-2015-1194.ch011

Table 4. (Continued). Relative and Reaction Energies[a]

Parameter	ΔE^b	$\Delta H_0{}^c$	ΔH^d	ΔG^e	$\Delta G_W{}^f$
Co(+II)	-23.42	-21.66	-21.38	-12.50	-15.23
Fe(+II)	-53.47	-50.19	-50.71	-39.59	-42.32

[a] All values in kcal/mol. [b] Relative or reaction energy, ΔE, computed using total energies. [c] Relative or reaction enthalpy at absolute zero Kelvin, $\Delta H_0 = \Delta E + \Delta(\mathrm{ZPE})$. [d] Relative or reaction enthalpy at standard conditions (298.15 Kelvin), $\Delta H = \Delta E + \Delta(\mathrm{TE})$. [e] Relative or reaction free enthalpy at standard conditions (298.15 Kelvin), $\Delta G = \Delta H - T\Delta(S)$. [f] Relative or reaction free enthalpy at standard conditions (298.15 Kelvin) with Wertz correction for translational entropy, $\Delta G_W = \Delta H - T\Delta(S_W)$. [g] B3LYP/6-31G*, ref. (*16*). [h] $S(CO_2) = 51.17$ cal/(mol·K) at B3LYP/6-31G* and was listed erroneously in ref. (*16*) as $S(CO_2) = 39.63$ cal/(mol·K).

Publication Date (Web): September 11, 2015 | doi: 10.1021/bk-2015-1194.ch011

If molecular translational entropy is reduced in solution, then any association reaction in solution will suffer less of an entropy penalty compared to the association reaction in the gas phase; $\Delta G_W < \Delta G_{298}$. This is borne out by the ΔG_W values for the formations of the $OCO{\cdot}ML_2$ complexes ($\Delta G_{298} - \Delta G_W \approx 3.04$ kcal/mol) and of the $H_2O{\cdot}ML_2$ complexes ($\Delta G_{298} - \Delta G_W \approx 2.74$ kcal/mol). Note in particular that the CO_2 complexes are predicted to be bound in solution: $\Delta G_W(\mathrm{R7}) < 0$ for all of the cases studied (Figure 7).

Conformational Preference Energy of $H_2O{\cdot}ML_2$ Complexes

We optimized the $H_2O{\cdot}ML_2$ complexes of the class 2 systems with two conformations about the H_2O-M axis, HB2a and HB2b. On the potential energy surface, the HB2a conformation is preferred for Cu^{2+} and Ni^{2+} while the HB2b conformation is preferred for Co^{2+} and Fe^{2+}. Thermal energies and molecular entropies provide advantages to the HB2b conformation, the free enthalpies ΔG all show a small preference for HB2b, and rotation about the H_2O-M axis is essentially free. Reactions R9 and R10 have been evaluated using the HB2b structures.

Alternatives to Magnesium

The major reason for the exergonicity of the CO_2 capture reaction with rubisco mimics is the coordination of the carbamic acid adduct to the metal cation (R5). The overall exergonicity of the CO_2 capture reaction is moderated by the H_2O/CO_2 replacement penalty (R10) which allows for overall reversibility. The most important parameter of the present study clearly is $\Delta G_W(\mathrm{R10})$; it needs to be positive and of significant magnitude. In addition, it is advantageous if the water binding is not too strong; $|\Delta G_W(\mathrm{R9})|$ should be relatively small because the reaction rate constant for the dehydration is inversely proportional to the strength of the water binding.

Among all of the metals studied, magnesium shows the highest $\Delta G_W(\mathrm{R10})$ value. Iron shows the second highest H_2O/CO_2 replacement penalty, but the very high water affinity is a disadvantage for iron(II). The data show that the

closed-shell systems calcium and zinc are excellent candidates to serve as potential magnesium alternatives. The data further suggest that the open-shell transition metal ions copper(II) and cobalt(II) might be possible magnesium alternatives.

Reaction Free Enthalpies and Equilibrium Concentrations

We computed reaction free enthalpies ΔG (also referred to as Gibbs free energies) and these values provide the equilibrium constants K_i via the familiar equation $\Delta G_i = -RT \cdot ln(K_i)$, or equivalently $K_i = exp(-\Delta G_i/RT)$, where ΔG_i is the free enthalpy of reaction i, R is the gas constant, and T is the absolute temperature. With Chicone, we recently described mathematical methods for the determination of steady-state concentrations of all species in multiequilibria systems using the traditional equilibrium approach or with the dynamical approach (*59*). The dynamical approach to the equilibrium problem involves the formulation of the kinetic rate equations for each species using general mass action kinetics theory, which together constitute a nonlinear system of ordinary differential equations (ODEs). The equilibrium concentrations are determined by evolving the initial concentrations via this dynamical system to their steady state (*59*).

Every equilibrium reaction is described by two reaction rate constants, one reaction rate constant k_f for the forward reaction and one reaction rate constant k_b for the backward reaction. These reaction rate constants are related via the equilibrium constant K via $K = k_f/k_b$. If the equilibrium constants K_i are specified for a multiequilibria system and one is interested in the determination of the concentrations of all species *at equilibrium*, then one can freely choose in each case either the forward or backward reaction rate constant and use the equation $K_i = k_{f,i}/k_{b,i}$ to determine the other. Hence, with the reaction free enthalpies ΔG_i reported here and some elemental knowledge of computing software (i.e., *Mathematica*, (*60*)), the fast and accurate computation of all equilibrium concentrations is feasible for any given set of initial conditions. On the other hand, if one is interested in the transient *kinetics of reaching the equilibrium*, then it no longer suffices to know only the ratios of the forward and backward reactions (i.e., the equilibrium constants) and one must also know one of the reaction rate constants for each elemental reaction (*59*). We are in the process of computing the actication barriers for the M^{2+}-catalyzed carbamylation reactions for simulations of the transient kinetics.

Electronic Structures and Spin Density Distributions of Formate Complexes of Open-Shell Systems

Molecular orbitals (MOs) with significant d-orbital involvement are shown in Figures 8 and 9, respectively, for iron formate, FeL_2 (d^6) and nickel formate, NiL_2 (d^8), respectively. The description of atomic orbital (AO) components of the MOs assumes that the molecules lie in the xy plane with the CH bonds aligned with the x-axis.

In Advances in CO2 Capture, Sequestration, and Conversion; He, et al.;
ACS Symposium Series; American Chemical Society: Washington, DC, 2015.

Publication Date (Web): September 11, 2015 | doi: 10.1021/bk-2015-1194.ch011

In the quasi spl-coordination, the lobes of the d(xy) orbital are oriented toward the O atoms of the formate ligands and d(xy) is the highest-lying d-orbital because of electron-electron repulsion. The lobes of the d(yz) orbital are in the plane that is perpendicular to the molecular plane and mirrors the two ligands. The d(xy) orbital is singly occupied in CuL_2 and it is left empty in NiL_2, CoL_2 and FeL_2. The d(yz) orbital is doubly occupied in CuL_2 and NiL_2, it is singly occupied in CoL_2, and it is left empty in FeL_2. The MO analysis helps to understand the spin density distributions of CoL_2 and CuL_2 (Figure 10).

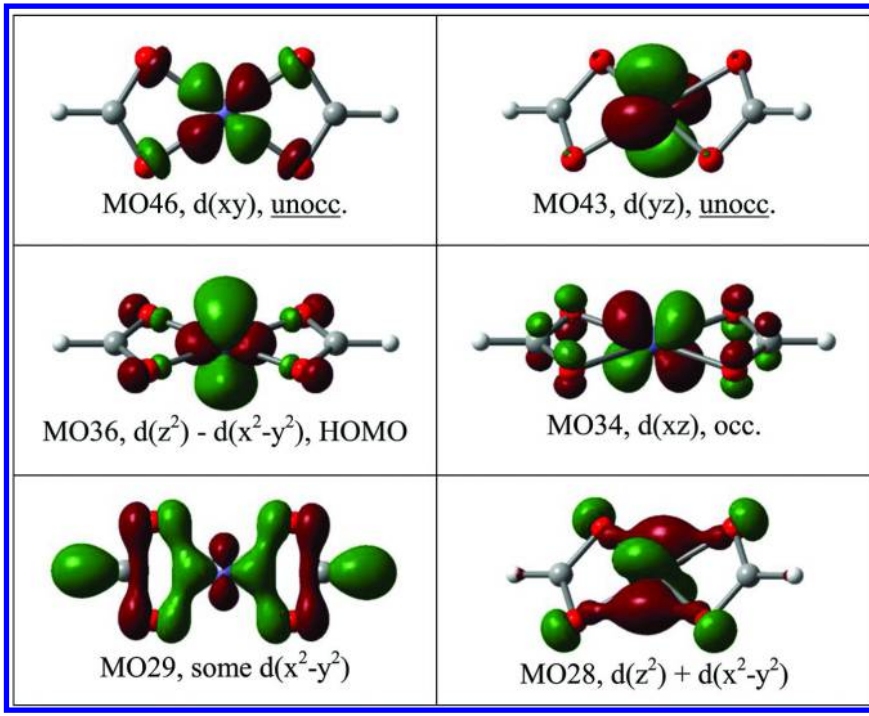

Figure 8. Selected MOs of iron formate, FeL_2 with significant d-orbital involvement. The description of AO components of the MOs assumes that the molecule lies in the xy plane with the CH bonds aligned with the x-axis.

For CoL_2, one might expect single-occupation of the $d(z^2)$ MO because it is above the d(yz) MO in NiL_2. Nevertheless, CoL_2 features single-occupation of the d(yz) orbital as is evidenced by the α-spin density in a d(yz)-shaped region around the cobalt center. The α-spin density is largely localized at the Co-center with only minor spin polarization in the basins of the formate O atoms. Large α-spin density accumulation at the M^{2+} center might lead to spin-polarization of a coordinating CO_2 and influence its reactivity.

Publication Date (Web): September 11, 2015 | doi: 10.1021/bk-2015-1194.ch011

On the other hand, the spin density distribution of CuL_2 is more complex. The SOMO of CuL_2 involves the d(xy)-MO as expected, but the excess α-spin density clearly is not localized in the d(xy)-shaped region around the copper center. For CuL_2, the MO analysis merely provides a starting point to think about the spin density and the actual spin density distribution shows large transfers of α-spin density from a d(xy)-shaped region around copper toward the formate O-atoms.

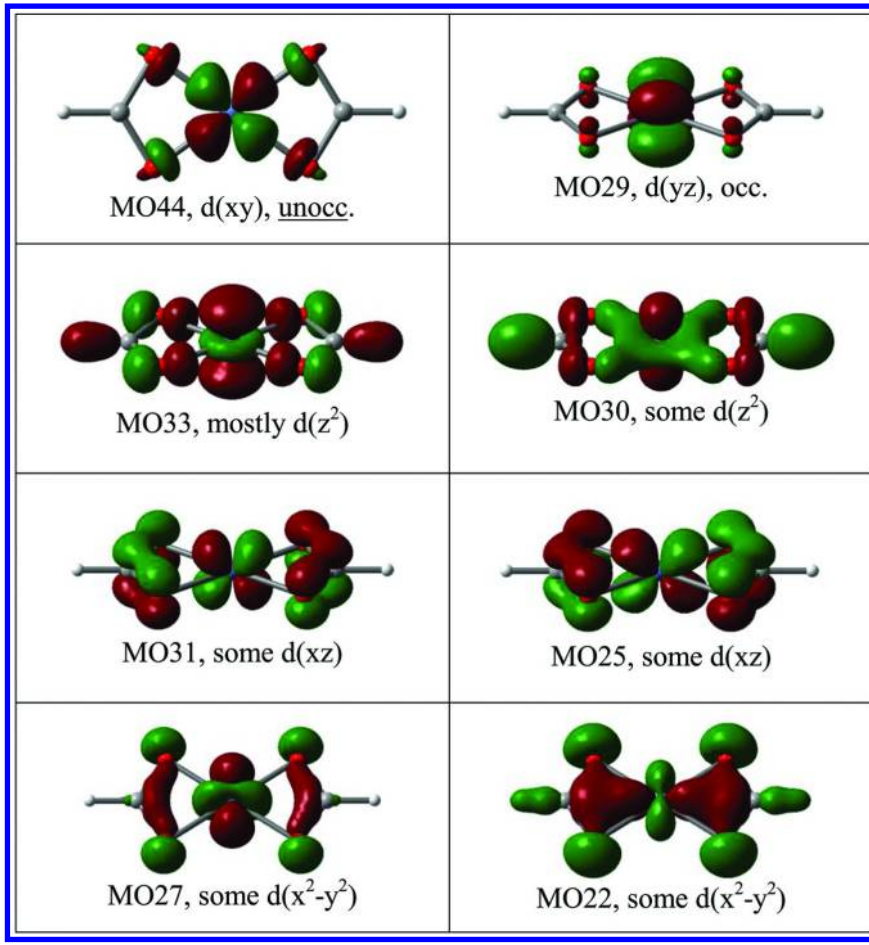

Figure 9. Selected MOs of nickel formate, NiL_2 with significant d-orbital involvement. The description of AO components of the MOs assumes that the molecule lies in the xy plane with the CH bonds aligned with the x-axis.

Publication Date (Web): September 11, 2015 | doi: 10.1021/bk-2015-1194.ch011

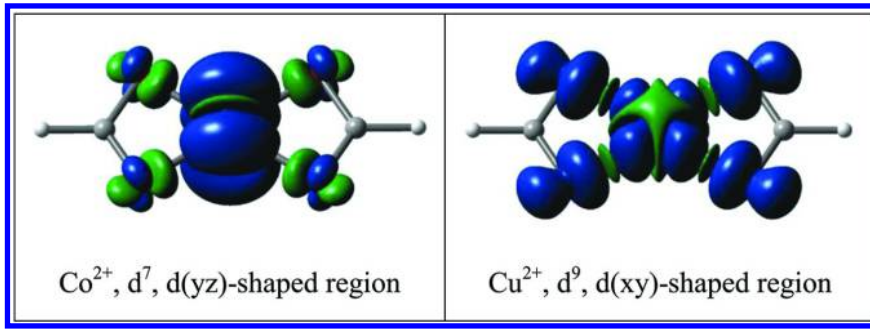

Figure 10. Spin density distributions of the formates CuL_2 and CoL_2 in their doublet states. The complete UMP2/6-31G spin densities are shown for an isodensity value of 0.001 e/au³; α-spin density is shown in dark grey (blue online) and β-spin density regions in light grey (green online). The description of d-type AO components assumes that the molecules lie in the xy plane with the CH bonds aligned with the x-axis.*

Publication Date (Web): September 11, 2015 | doi: 10.1021/bk-2015-1194.ch011

Conclusions

The equilibrium $CO_2 + H_2O{\cdot}ML_2 \leftrightarrows OCO{\cdot}ML_2 + H_2O$ lies very much on the left side: Water is great donor ligand, CO_2 is a comparatively poor donor ligand, and the H_2O/CO_2 exchange reaction is significantly endergonic for $M^{2+} = Mg^{2+}$ (ΔG_W = 15.2 kcal/mol). How can a reaction with such a large H_2O/CO_2 replacement penalty be nature's key to reversible CO_2 capture? Well, the "capture" reaction is only one side of the coin and the "release" reaction is just as important for "reversibility". Rubisco's $^ACO_2$ binding is reversible because of the large H_2O/CO_2 replacement penalty and this advantage of reversibility comes at the tolerable disadvantage of slow CO_2 loading. The equilibrium reaction $CO_2 + H_2O{\cdot}ML_2 \leftrightarrows OCO{\cdot}ML_2 + H_2O$ may go back and forth many times, but an $OCO{\cdot}ML_2$ aggregate must eventually lead to CO_2 capture because only CO_2 can react with the lysine's amino group and because the carbamic acid complex $(RNH)(HO)C{=}O{\cdot}ML_2$ is bound much more strongly than CO_2 and also more strongly than H_2O. Water does not prevent CO_2 capture, it only slows it down, and more importantly, it is only for the sake of water that CO_2 release is feasible.

The enzyme rubisco employs magnesium and Mg^{2+} exhibits the highest H_2O/CO_2 replacement penalty among the metal ions studied here. The results show that the closed-shell systems Ca^{2+} and Zn^{2+} are excellent candidates for magnesium alternatives. The theoretical analysis further suggests that the open-shell transition metal ions Co^{2+} and Cu^{2+} also are interesting targets in the search for magnesium alternatives with similar size and comparable binding energies, and Co^{2+} is particularly interesting from a mechanistic perspective. The cobalt ion's spin density is localized at the Co^{2+}-center and may lead to spin-polarization of coordinating O=C=O or (RNH)(HO)C=O and influence their reactivities.

In Advances in CO2 Capture, Sequestration, and Conversion; He, et al.;
ACS Symposium Series; American Chemical Society: Washington, DC, 2015.

Publication Date (Web): September 11, 2015 | doi: 10.1021/bk-2015-1194.ch011

Acknowledgments

The author thanks the Chinese Academy of Sciences for the award of a Visiting Professorship for Senior International Scientists 2014 and Professor Wen-Hua Sun for being a most generous host. Part of the manuscript was written while the author was a Guest Professor in the College of Chemistry and Materials Science, Northwest University, Xi'an.

References

1. *First Successful Demonstration of Carbon Dioxide Air Capture Technology Achieved*; Earth Institute, Columbia University, April 25, 2007. physorg.com/news96732819.html (accessed February 27, 2015).
2. Keith, D. W.; Ha-Duong, M.; Stolaroff, J. K. Climate strategy with CO_2 capture from the air. *Clim. Change* **2006**, *74*, 17–45.
3. Socolow, R.; Desmond, M.; Aines, R.; Blackstock, J.; Bolland, O.; Kaarsberg, T.; Lewis, N.; Mazzotti, M.; Pfeffer, A.; Sawyer, K.; Siirola, J.; Smit, B.; Wilcox, J. *Direct Air Capture of CO_2 with Chemicals: A Technology Assessment for the APS Panel on Public Affairs*. American Physical Society, Washington, DC, June 1, 2011. http://www.aps.org/policy/reports/assessments/upload/dac2011.pdf (accessed February 27, 2015).
4. Zeman, F. S.; Lackner, K. S. Capturing carbon dioxide directly from the atmosphere. *World Resources Rev.* **2004**, *16*, 62–68.
5. Lackner, K. S.; Brennan, S. Envisioning carbon capture and storage: Expanded possibilities due to air capture, leakage insurance, and C-14 monitoring. *Clim. Change* **2009**, *96*, 357–378.
6. Sun, Z.; Fan, M.; Argyle, M. Supported monoethanolamine for CO_2 separation. *Ind. Eng. Chem. Res.* **2011**, *50*, 11343–11349.
7. Kuntz, J.; Aroonwilas, A. Performance of spray column for CO_2 capture application. *Ind. Eng. Chem. Res.* **2008**, *47*, 145–153.
8. Idem, R.; Wilson, M.; Tontiwachwuthikul, P.; Chakma, A.; Veawab, A.; Aroonwilas, A.; Gelowitz, D. Pilot plant studies of the CO_2 capture performance of aqueous MEA and mixed MEA/MDEA solvents at the University of Regina CO_2 capture technology development plant and the Boundary Dam CO_2 capture demonstration plant. *Ind. Eng. Chem. Res.* **2006**, *45*, 2414–2420.
9. Goeppert, A.; Czaun, M.; May, R. B.; Prakash, G. K. S.; Olah, G. A.; Narayanan, S. R. Carbon dioxide capture from the air using a polyamine based regenerable solid adsorbent. *J. Am. Chem. Soc.* **2011**, *133*, 20164–20167.
10. McDonald, T.; Lee, W. R.; Mason, J. A.; Wiers, B. M.; Hong, C. S.; Long, J. R. Capture of carbon dioxide from air and flue gas in the alkylamine-appended metal-organic framework mmen-Mg_2(dobpdc). *J. Am. Chem. Soc.* **2012**, *134*, 7056–7065.

11. Sumida, K.; Rogow, D. L.; Mason, J. A.; McDonald, T. M.; Bloch, E. D.; Herm, Z. R.; Bae, T.-H.; Long, J. R. Carbon dioxide capture in metal-organic frameworks. *Chem. Rev.* **2012**, *112*, 724–781.
12. Poloni, R.; Smit, B.; Neaton, J. B. Ligand-assisted enhancement of CO_2 capture in metal-organic frameworks. *J. Am. Chem. Soc.* **2012**, *134*, 6714–6719.
13. McDonald, T. M.; Mason, J. A.; Kong, X.; Bloch, E. D.; Gygi, D.; Dani, A.; Crocella, V.; Giordanino, F.; Odoh, S. O.; Drisdell, W. S.; Vlaisavljevich, B.; Dzubak, A. L.; Poloni, R.; Schnell, S. K.; Planas, N.; Lee, K.; Pascal, T.; Wan, L. F.; Prendergast, D.; Neaton, J. B.; Smit, B.; Kortright, J. B.; Gagliardi, L.; Bordiga, S.; Reimer, J. A.; Long, J. R. Cooperative insertion of CO_2 in diamine-appended metal-organic frameworks. *Nature* **2015**, *519*, 303–319.
14. Yang, Z.-Z.; Song, Q.-W.; He, L.-N. *Capture and Utilization of Carbon Dioxide with Poly-Ethylene Glycol, SpringerBriefs in Molecular Science*; Springer: New York, 2012.
15. Li, L.; Fu, M.-L.; Zhao, Y.-H.; Zhu, Y.-T. Characterization of carbonic anhydrase II from *Chlorella vulgaris* in bio-CO_2 capture. *Environ. Sci. Pollut. Res.* **2012**, *19*, 4227–4232.
16. Glaser, R.; Castello-Blindt, P. O.; Yin, J. Biomimetic Approaches to Reversible CO_2 Capture fom Air. *N*-Methylcarbaminic Acid Formation in Rubisco-Inspired Models. In *New and Future Developments in Catalysis. Activation of Carbon Dioxide*; Suib, S. L., Ed.; Elsevier Publishers: Amsterdam, The Netherlands, 2013; Chapter 17; pp 501−534.
17. Shively, J. M.; Van Keulen, G.; Meijer, W. G. Something about almost nothing: CO_2 fixation in chemautotrophs. *Ann. Rev. Microbiol.* **1998**, *52*, 191–230.
18. Kusian, B.; Bowien, B. Organization and regulation of cbb CO_2 assimilation genes in autotrophic bacter. *FEMS Microbiol. Rev.* **1997**, *21*, 135–155.
19. Hugler, M.; Sievert, S. M. Beyond the Calvin cycle: autotrophic carbon fixation in the ocean. *Ann. Rev. Marine Sci.* **2011**, *3*, 89–261.
20. Mueller-Cajar, O.; Badger, M. R. New roads lead to Rubisco in archaebacterial. *BioEssays* **2007**, *29*, 722–724.
21. Taylor, T. C.; Andersson, I. Structure of a product complex of spinach ribulose-1,5-bisphosphate carboxylase/oxygenase. *Biochemistry* **1997**, *36*, 4041–4046PDB 1AUS.
22. Taylor, T. C.; Andersson, I. Structural transitions during activation and ligand binding in hexadecameric Rubisco inferred from the crystal structure of the activated unliganded spinach enzyme. *Nat. Struct. Biol.* **1996**, *3*, 95–101.
23. Gutteridge, S.; Newman, J.; Herrmann, C.; Rhoades, D. The crystal structures of Rubisco and opportunities for manipulating photosynthesis. *J. Exp. Botany* **1995**, *46*, 1261–1267.
24. Lundqvist, T.; Schneider, G. Crystal Structure of the ternary complex of ribulose-1,5-bisphosphate carboxylase, magnesium(II) and activator carbon dioxide at 2.3 Å resolution. *Biochemistry* **1991**, *30*, 904–908PDB 2RUS.
25. Mizohata, E.; Matsumura, H.; Okano, Y.; Kumei, M.; Takuma, H.; Onodera, J.; Kato, K.; Shibata, N.; Inoue, T.; Yokota, A.; Kai, Y. Crystal

Publication Date (Web): September 11, 2015 | doi: 10.1021/bk-2015-1194.ch011

structure of activated ribulose-15-bisphosphate carboxylase/oxygenase from green alga Chlamydomonas reinhardtii complexed with 2-carboxyarabinitol-15-bisphosphate. *J. Mol. Biol.* **2002**, *316*, 679–691.
26. Baranowski, M.; Stec, B. Crystallization and characterization of Galdieria sulphuraria Rubisco in two crystal forms: structural phase transition observed in P21 crystal form. *Intl. J. Mol. Sci.* **2007**, *8*, 1039–1051.
27. Hartman, F. C.; Harpel, M. R. Structure, function, regulation, and assembly of D-ribulose-1,5-bisphosphate carboxylase/oxygenase. *Annu. Rev. Biochem.* **1994**, *63*, 197–234.
28. Cleland, W. W.; Andrews, T. J.; Gutteridge, S.; Hartman, F. C.; Lorimer, G. H. Mechanism of Rubisco: the carbamate as general base. *Chem. Rev.* **1998**, *98*, 549–561.
29. Portis, A. R.; Li, C.; Wang, D.; Salvucci, M. E. Regulation of Rubisco activase and its interaction with Rubisco. *J. Exp. Botany* **2008**, *59*, 1597–1604.
30. Tapia, O.; Fidder, H.; Safont, V. S.; Oliva, M.; Andrés, J. Enzyme catalysis: transition structures and quantum dynamical aspects: Modeling Rubisco's oxygenation and carboxylation mechanisms. *Int. J. Quant. Chem.* **2002**, *88*, 154–166.
31. Oliva, M.; Safont, V. S.; Andres, J.; Tapia, O. Transition structures for D-Ribulose-1,5-bisphosphate carboxylase/oxygenase-catalyzed oxygenation chemistry: Role of carbamylated lysine in a model magnesium coordination sphere. *J. Phys. Chem. A* **2001**, *105*, 4726–4736.
32. Glaser, R.; Wu, Z.; Lewis, M. A higher level ab initio quantum-mechanical study of the quadrupole moment tensor components of carbon dioxide. *J. Mol. Struct.* **2000**, *556*, 131–141.
33. Glaser, R.; Lewis, M.; Wu, Z. Theoretical study of the quadrupolarity of carbodiimide. *J. Phys. Chem. A* **2002**, *106*, 7950–7957.
34. Lewis, M.; Wu, Z.; Glaser, R. Polarizabilities of carbon dioxide and carbodiimide. Assessment of theoretical model dependencies on dipole polarizabilities and dipole polarizability anisotropies. *J. Phys. Chem. A* **2000**, *104*, 11355–11361.
35. Lewis, M.; Glaser, R. Synergism of catalysis and reaction center rehybridization. A novel mode of catalysis in the hydrolysis of carbon dioxide. *J. Phys. Chem. A* **2003**, *107*, 6814–6818.
36. Lewis, M.; Glaser, R. Synergism of catalysis and reaction center rehybridization. An ab initio study of the hydrolysis of the parent carbodiimide. *J. Am. Chem. Soc.* **1998**, *120*, 8541–8542.
37. Lewis, M.; Glaser, R. Synergism of catalysis and reaction center rehybridization in nucleophilic additions to cumulenes: The one-, two- and three-water hydrolyses of carbodiimide and methyleneimine. *Chem. Eur. J.* **2002**, *8*, 1934–1944.
38. This value was given erroneously as 12.3 kcal/mol in ref. 16; see discussion of Table 4 and footnote (h) of Table 4.
39. Grimme, S. Density functional theory with London dispersion corrections. *WIREs Comput. Mol. Sci.* **2011**, *1*, 211–228.

Publication Date (Web): September 11, 2015 | doi: 10.1021/bk-2015-1194.ch011

40. Cremer, D. Møller-Plesset perturbation theory: from small molecule methods to methods for thousands of atoms. *WIREs Comput. Mol. Sci* **2011**, *1*, 509–530.
41. Møller, C.; Plesset, M. S. Note on an approximation treatment for many-electron systems. *Phys. Rev.* **1934**, *46*, 618–622.
42. Frisch, M. J.; Head-Gordon, M.; Pople, J. A. Semi-direct algorithms for the MP2 energy and gradient. *Chem. Phys. Lett.* **1990**, *166*, 281–289.
43. Head-Gordon, M.; Head-Gordon, T. Analytic MP2 frequencies without fifth order storage: Theory and application to bifurcated hydrogen bonds in the water hexamer. *Chem. Phys. Lett.* **1994**, *220*, 122–128.
44. Peng, C.; Ayala, P. Y.; Schlegel, H. B.; Frisch, M. J. Using redundant internal coordinates to optimize equilibrium geometries and transition states. *J. Comp. Chem.* **1996**, *17*, 49–56.
45. Tomasi, J.; Mennucci, B.; Cammi, R. Quantum mechanical continuum solvation models. *Chem. Rev.* **2005**, *105*, 2999–3093.
46. Da Silva, E. F.; Svendsena, H. F.; Merz, K. M. Explicitly representing the solvation shell in continuum solvent calculations. *J. Phys. Chem. A* **2009**, *113*, 6404–6409.
47. Francl, M. M.; Petro, W. J.; Hehre, Q. J.; Binkley, J. S.; Gordon, M. S.; DeFrees, D. J.; Pople, J. A. Self-consistent molecular orbital methods. 23. A polarization-type basis set for 2nd-row elements. *J. Chem. Phys.* **1982**, *77*, 3654–3665.
48. Rassolov, V. A.; Pople, J. A.; Ratner, M. A.; Windus, T. L. 6-31G* Basis set for atoms K through Zn. *J. Chem. Phys.* **1998**, *109*, 1223–1229.
49. Murray, C. W.; Verdonk, M. L. The consequences of translational and rotational entropy lost by small molecules on binding to proteins. *J. Comp.-Aided Mol. Des.* **2002**, *16*, 741–753.
50. Mammen, M.; Shakhnovich, E. I.; Deutch, J. M.; Whitesides, G. M. Estimating the entropic cost of self-assembly of multiparticle hydrogen-bonded aggregates based on the cyanuric acid-melamine lattice. *J. Org. Chem.* **1998**, *63*, 3821–3830.
51. Murphy, K. P.; Xie, D.; Thompson, K. S.; Amzel, L. M.; Freire, E. Entropy in biological binding processes: Estimation of translational entropy loss. *Proteins: Structure, Function, and Genetics* **1994**, *18*, 63–67.
52. Finkelstein, A. V.; Janin, J. The price of lost freedom: entropy of bimolecular complex formation. *Protein Eng.* **1989**, *3*, 1–3.
53. Wertz, D. H. Relationship between the gas-phase entropies of molecules and their entropies of solvation in water and 1-octanol. *J. Am. Chem. Soc.* **1980**, *102*, 5316–5322.
54. Frisch, M. J.; Trucks, G. W.; Schlegel, H. B.; Scuseria, G. E.; Robb, M. A.; Cheeseman, J. R.; Scalmani, G.; Barone, V.; Mennucci, B.; Petersson, G. A.; Nakatsuji, H.; Caricato, M.; Li, C.; Hratchian, H. P.; Izmaylov, A. F.; Bloino, J.; Zheng, G.; Sonnenberg, J. L.; Hada, M.; Ehara, M.; Toyota, K.; Fukuda, R.; Hasegawa, J.; Ishida, M.; Nakajima, T.; Honda, Y.; Kitao, O.; Nakai, H.; Vreven, T.; Montgomery, J. A., Jr.; Peralta, J. E.; Ogliaro, F.; Bearpark, M.; Heyd, J. J.; Brothers, E.; Kudin, K. N.; Staroverov, V. N.; Keith, T.; Kobayashi, R.; Normand, J.; Raghavachari, K.; Rendell, A.; Burant, J. C.;

Publication Date (Web): September 11, 2015 | doi: 10.1021/bk-2015-1194.ch011

Iyengar, S. S.; Tomasi, J.; Cossi, M.; Rega, N.; Millam, J. M.; Klene, M.; Knox, J. E.; Cross, J. B.; Bakken, V.; Adamo, C.; Jaramillo, J.; Gomperts, R.; Stratmann, R. E.; Yazyev, O.; Austin, A. J.; Cammi, R.; Pomelli, C.; Ochterski, J. W.; Martin, R. L.; Morokuma, K.; Zakrzewski, V. G.; Voth, G. A.; Salvador, P.; Dannenberg, J. J.; Dapprich, S.; Daniels, A. D.; Farkas, O.; Foresman, J. B.; Ortiz, J. V.; Cioslowski, J.; Fox, D. J. *Gaussian 09, Revision D.01*; Gaussian, Inc.: Wallingford, CT, 2013.

55. University of Missouri Bioinformatics Consortium. http://umbc.rnet.missouri.edu (accessed February 28, 2015).
56. Winter, M. *WebElements Periodic Table: The Periodic Table on the Web*. http://www.webelements.com (accessed February 28, 2015).
57. Glaser, R.; Horan, C.; Nelson, E.; Hall, M. K. Incipient nucleophilic attack as a probe for the electronic structure of diazonium ions. An analysis of neighboring group interactions in ß-carboxyvinyldiazonium ions. *J. Org. Chem.* **1992**, *57*, 215–228.
58. Glaser, R.; Horan, C. J. Interpretation of neighboring group interactions in crystal structures. A solid state and quantum-chemical study of incipient nucleophilic attack in 2-diazonium benzoic acid and its benzoate. *Can. J. Chem.* **1996**, *74*, 1200–1214.
59. Glaser, R. E.; Delarosa, M. A.; Salau, A. O.; Chicone, C. Dynamical approach to multi-equilibria problems for mixtures of acids and their conjugated bases. *J. Chem. Educ.* **2014**, *91*, 1009–1016.
60. Mathematica. Wolfram Research. http://www.wolfram.com/mathematica/ (accessed April 17, 2015).

Publication Date (Web): September 11, 2015 | doi: 10.1021/bk-2015-1194.ch011

Publication Date (Web): September 11, 2015 | doi: 10.1021/bk-2015-1194.ch012

Chapter 12

Carbonation of Silicate Minerals and Industrial Wastes and Their Potential Use as Sustainable Construction Materials

Greeshma Gadikota,[1,2] Kyle Fricker,[1] Sung-Hwan Jang,[3] and Ah-Hyung Alissa Park*[,1,2]

[1]Department of Earth and Environmental Engineering, Lenfest Center for Sustainable Energy, Columbia University in the City of New York, New York 10027, United States
[2]Department of Chemical Engineering, Columbia University in the City of New York, New York, New York 10027, United States
[3]Department of Civil Engineering and Engineering Mechanics, Columbia University in the City of New York, New York, New York 10027, United States
***Phone: +1 212 854 8989. Fax: +1 212-854-7081.**
E-mail: ap2622@columbia.edu

One of the permanent methods to store anthropogenic CO_2 is to convert it into thermodynamically stable mineral carbonates. Depending on the reaction pathways and the reaction conditions such as temperature, partial pressure of CO_2, composition and concentration of the reaction fluid and reactants, different phases of magnesium and calcium carbonates can be formed with tuned chemistry and structures. Naturally occurring silicate minerals such as olivine (Mg_2SiO_4), serpentine ($Mg_3(OH)_4(Si_3O_5)$) and wollastonite ($CaSiO_3$) as well as alkaline industrial wastes can be used to capture and store CO_2. Furthermore, the tailored formation of carbonates and their by-products such as silica would allow their utilization in various applications including construction materials. Some studies have shown that the mechanical strength of construction materials can be sustained or even improved with the addition of carbonated materials

In Advances in CO2 Capture, Sequestration, and Conversion; He, et al.;
ACS Symposium Series; American Chemical Society: Washington, DC, 2015.

and Si-rich by-products. This chapter introduces different carbonation pathways and the chemical and physical properties of carbonation products for the application in construction materials.

Introduction

A rapid increase in the CO_2 concentrations in the atmosphere over the past century has significant environmental and ecological implications such as inverted weather patterns and ocean acidification. As shown in Figure 1, the largest contributors to increasing CO_2 emissions are power generation at 79%, followed by the emission from the cement production, refineries, iron and steel manufacturing, and petrochemical production which account for 7, 6, 5, and 3% of the global CO_2 emissions, respectively (*1*, *2*). The CO_2 footprint from power generation is primarily from the combustion of fossil fuels, while the calcination of limestone is responsible for the large fraction of the CO_2 emissions from the cement industry. Thus, considerable CO_2 emissions from the cement industry could be reduced by limiting the uses of raw materials or processes that result in the significant CO_2 emissions (*3*).

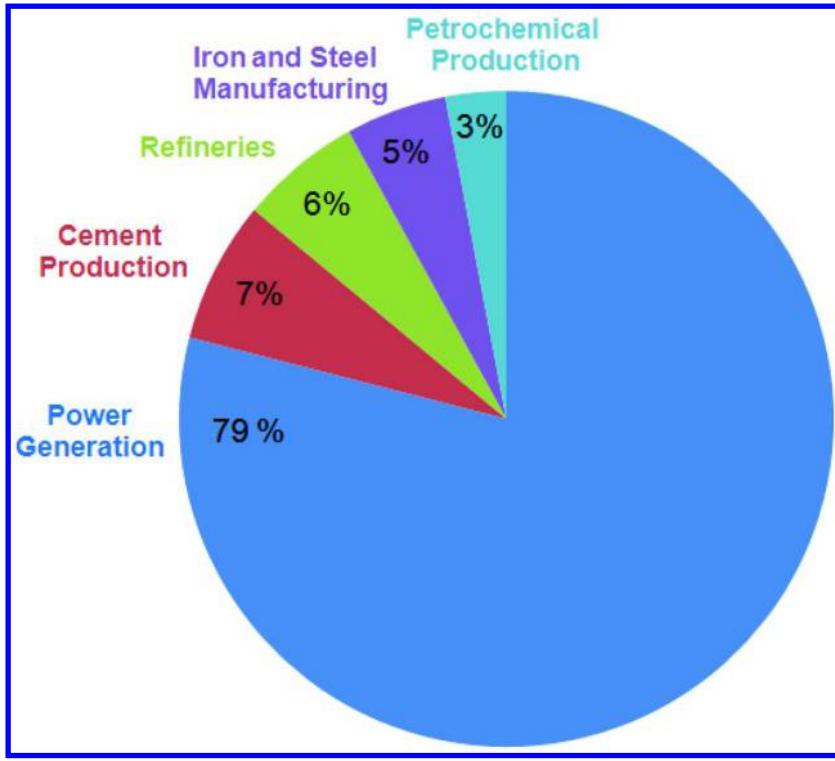

Figure 1. Contribution of various industrial activities to the global CO_2 emission. (data from ref (1, 2)).

In Advances in CO2 Capture, Sequestration, and Conversion; He, et al.;
ACS Symposium Series; American Chemical Society: Washington, DC, 2015.

Publication Date (Web): September 11, 2015 | doi: 10.1021/bk-2015-1194.ch012

Publication Date (Web): September 11, 2015 | doi: 10.1021/bk-2015-1194.ch012

In the past few decades, various CO_2 capture, utilization, and storage (CCUS) technologies have been developed to reduce carbon emissions and limit atmospheric CO_2 concentration. One of the methods to permanently store CO_2 is by converting gaseous CO_2 into solid carbonates via a process also known as carbon mineralization. This particular technology has been proposed to offset the large CO_2 emission from the cement and construction industries by utilizing the products and by-products of the carbon mineralization process as construction materials. The carbon mineralization process can be performed using both Ca- and Mg-bearing minerals and industrial wastes including waste cement and lime kiln dust. The key factors to consider for the use of engineered carbonates as construction materials would include compressive and mechanical strengths, as well as long-term environmental safety and the net CO_2 reduction.

Most of the carbon mineralization technologies have been developed by mimicking the natural weathering process of silicate minerals. As Ca- and Mg-bearing minerals such as wollastonite ($CaSiO_3$), olivine (Mg_2SiO_4) and serpentine ($Mg_3(OH)_4(Si_3O_5)$) react with CO_2, they form calcium or magnesium carbonates, which are environmentally benign, thermodynamically stable, and insoluble in water (*4*). One of the primary advantages of carbon mineralization using silicate minerals and rocks, is that more than 10,000-1,000,000 Gt of total carbon can be stored as carbonates, which do not require long-term monitoring and formation of carbonates is exothermally favored (*5*). In addition, a fraction of the carbonated products and by-products of the carbon mineralization process (e.g., silica) can also be used as value-added materials in various applications ranging from paper fillers to construction materials. The extent of their utilization would be limited by the size of each application market, which is generally significantly smaller than the amount of carbon to be sequestered. Their use as construction materials is particularly interesting since, as discussed earlier, the cement and construction industries are one of the large emitters of CO_2, and thus, any CO_2 captured and utilized along with their own wastes would reduce the overall carbon footprint of those industries. Studies have shown that replacing 10% of building materials with minerals carbonated with anthropogenic CO_2 is expected to reduce CO_2 emissions by 1.6 Gt/year (*6*).

Industrial wastes that have a potential to mineralize CO_2 include fly ash, cement kiln dust, and steel slag and they have a significant amount of calcium and/or magnesium contents. Often these alkaline wastes are co-generated with CO_2 as in the cement production process. Figure 2 represents the annual CO_2 emissions from specific industrial sectors in 2002 and the amounts of their co-generated industrial wastes in the United States. The CO_2 emission from power generation was the highest at 2068 million metric tons/year followed by CO_2 emissions related to iron and steel, mining, cement, and aluminum production at 115, 99, 83, and 57 million metric tons/year, respectively (*7*, *8*). The corresponding industrial wastes co-produced with power generation, iron and steel production, cement, and aluminum production were fly ash (131 MT/year), steel slag (9 MT/year), cement kiln dust (14 MT/year), and red mud (3 MT/year) (*7*, *9–11*). Carbonation of these industrial wastes can not only capture anthropogenic CO_2 in solid carbonate forms, but also neutralize these highly alkaline wastes so that they can be safely disposed or utilized. However, as shown

In Advances in CO2 Capture, Sequestration, and Conversion; He, et al.;
ACS Symposium Series; American Chemical Society: Washington, DC, 2015.

in Figure 2, there is a mismatch of scales of CO_2 emission and the generation of alkaline wastes. Therefore, the overall carbon storage potential of industrial wastes is not as large as silicate minerals. About 200-300 Mt of CO_2 can be stored using industrial alkaline wastes annually in the world (*5*). Nevertheless, the carbon mineralization technology offers an option of reducing the carbon footprint, reusing the wastes, and reducing the alkalinity of the solid wastes in these energy and carbon intensive industries.

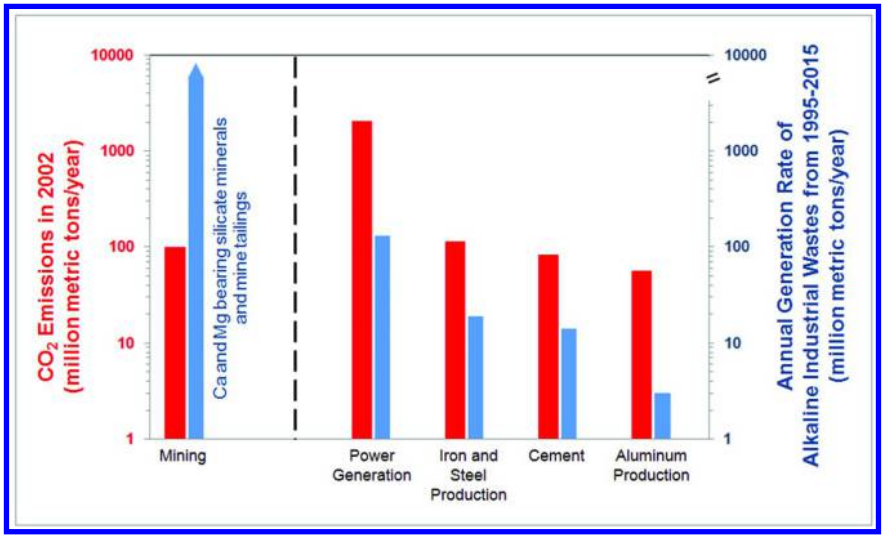

Figure 2. Annual emission rate of CO_2 produced from each industrial sector (7) and corresponding co-generated alkaline industrial wastes (7, 9–11).

The industrial wastes have a wide range of calcium and magnesium contents. The calcium contents in fly ash, cement kiln dust, steel slag, and red mud are in the range of 9~34%, 22~31%, 27~39%, and 1~6%, respectively, whereas their magnesium contents are 0~7%, 0~1.3%, 1~5% and negligible amount, respectively (*12*). These values are significantly lower than the Ca and Mg contents in silicate minerals which are generally more than 30%. On the other hand, the alkaline industrial wastes are generally significantly more reactive than silicate minerals and possess higher surface areas.

Industrial wastes such as fly ash are already being used as construction materials (*13–15*), and more carbonated forms of the alkaline industrial wastes are being introduced as alternatives to construction materials produced using freshly mined materials. Studies have shown that alkaline industrial wastes converted into carbonates could be used in cement based materials (*16*). It has also been reported that the carbonation of alkaline industrial wastes lead to the immobilization of toxic heavy metals such as chromium in solid wastes making them safer for the environment (*17*). However, this is dependent on the chemical conditions and the speciation of the specific metals concerned.

In addition to the above mentioned alkaline industrial wastes, calcium and magnesium bearing mine tailings are another industrial source of calcium and

In Advances in CO2 Capture, Sequestration, and Conversion; He, et al.;
ACS Symposium Series; American Chemical Society: Washington, DC, 2015.

Publication Date (Web): September 11, 2015 | doi: 10.1021/bk-2015-1194.ch012

magnesium for carbon sequestration, and as shown in Figure 2, the scale of mine tailings is orders of magnitudes greater than that of alkaline industrial wastes. Mg-bearing minerals such as serpentine ($(Mg,Fe)_3(OH)_4(Si_3O_5)$) and olivine ($(Mg,Fe)_2SiO_4$) are often mined for nickel (0.2~2% in ores) and large tailing deposits of these materials already exist around the world (*12*). Thus, mine tailings have been included in the subsequent discussion as a potential carbon mineralization feedstock.

A number of process schemes have been proposed for carbon mineralization. An ex-situ carbon mineralization with the proposed production of value-added materials is represented in Figure 3. One of the great advantages of the ex-situ carbon mineralization technology is that the chemical compositions (e.g., hydration degree) and physical properties (e.g., particle size and particle size distribution, morphological structures like surface area and pore sizes) of the carbonated materials, as well as reaction by-products, can be tuned for each proposed application (i.e., construction materials, fillers) (*12*, *18–23*). In this chapter, the carbonation of silicate minerals, their by-products such as silica and industrial wastes will be discussed in terms of the tailored formations of the products and by-products, including precipitated magnesium carbonate, precipitated calcium carbonate and silica while considering their subsequent use as construction materials.

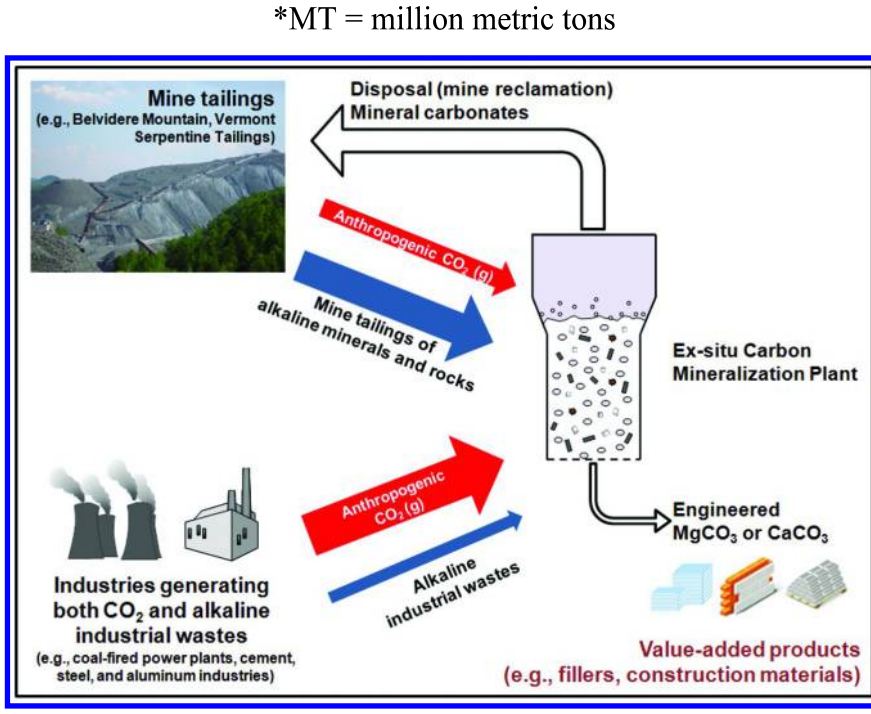

Figure 3. Carbon mineralization scheme for converting alkaline materials such as Ca and Mg-bearing minerals and industrial wastes to Ca and Mg-carbonates for disposal and use as value-added products.

In Advances in CO2 Capture, Sequestration, and Conversion; He, et al.;
ACS Symposium Series; American Chemical Society: Washington, DC, 2015.

Publication Date (Web): September 11, 2015 | doi: 10.1021/bk-2015-1194.ch012

Conventional Cement Production

The global cement production is about 1.7 x 10^9 tons/year, which makes concrete one of the most extensively used materials around the world (*3*). Unfortunately, the production of concrete results in CO_2 emissions of 0.2 tons per 1 m^3 of cement or 0.08 tons per ton of concrete (*3*). The primary reason for the high CO_2 emissions is the extensive use of limestone (mostly $CaCO_3$) to produce portland cement clinker, whose principal component is alite (impure Ca_3SiO_5), as represented by the following reaction:

$$3CaCO_{3(s)} + SiO_{2(s)} \rightarrow Ca_3SiO_{5(s)} + 3CO_{2(g)} \quad \text{(Rx. 1)}$$

Publication Date (Web): September 11, 2015 | doi: 10.1021/bk-2015-1194.ch012

For every ton of alite that is produced, 579 kg of CO_2 is released. In addition, the enthalpy of this reaction is +416 kJ/mol (at 20 °C), which implies that 1.83 GJ of energy is needed to produce 1 ton of alite. The energy requirement would further increase if the feedstock is low in quality. The reaction temperatures are as high as 1400 °C to provide sufficient rates (*3*). Thus, the combustion of fossil fuels to generate the high temperatures needed for the production of Portland cement clinker is also responsible for high CO_2 emissions.

Given this backdrop, systematic efforts are being undertaken to develop alternative materials for cement production. Some of the new and newly repurposed materials are proposed and used as pozzolanic materials, which do not inherently possess cementitious properties but acquire these properties in the presence of other phases such as calcium hydroxide. Pozzolanic materials have been widely investigated due to their ability to improve the durability and the mechanical strength of cementitious-based composites. Some of the materials such as Ca- and Mg-bearing minerals and rocks with hydroxides, silica, and fly ash have been studied as potential pozzolanic materials. For example, forsterite (Mg_2SiO_4) and periclase (MgO) obtained from the heat treatment of asbestos (*24*) and Ordinary Portland Cement (OPC) containing 35% limestone paste (*25*), have been proposed as additives in cement. The following sections provide a detailed overview of the production of potential pozzolanic materials via carbon mineralization and how their synthesis can be tailored to achieve desired chemical and structural properties.

Carbonation Chemistry of Mg- and Ca-Bearing Materials

The conversion of Ca- and Mg-bearing silicate minerals to carbonates was first proposed by Seifritz (1990) (*26*), and then shown to be feasible by Lackner et al., (1995) (*27*). The reactions of wollastonite, olivine and serpentine with CO_2 are exothermic and occur in nature as evidenced in carbonate veins in geologic formations. Unfortunately, the rates of direct gas-solid reactions between Ca- and Mg-bearing minerals and gaseous CO_2 have been found to be very slow in various experimental studies (*28*). Thus, most of the carbon mineralization technologies are operated in an aqueous mode with the following reactions:

In Advances in CO2 Capture, Sequestration, and Conversion; He, et al.;
ACS Symposium Series; American Chemical Society: Washington, DC, 2015.

Carbonation of Mg-Bearing Minerals (e.g., Olivine (Rx. 2) and e.g., Serpentine (Rx. 3)):

$$Mg_2SiO_{4(s)} + 2CO_{2(g)} + 2H_2O_{(aq)} \rightarrow 2MgCO_3 + (SiO_{2(s)} \times 2H_2O_{(aq)}) \quad \text{(Rx. 2)}$$

$$Mg_3Si_2O_5(OH)_{4(s)} + 3CO_{2(g)} + 2H_2O_{(aq)} \rightarrow 3MgCO_3 + 2(SiO_{2(s)} \times 2H_2O_{(aq)}) \quad \text{(Rx. 3)}$$

Carbonation of Ca-Bearing Minerals (e.g., Wollastonite):

$$CaSiO_{3(s)} + CO_{2(g)} + 2H_2O_{(aq)} \rightarrow CaCO_{3(s)} + (SiO_{2(s)} \times 2H_2O_{(aq)}) \quad \text{(Rx. 4)}$$

The aqueous carbonation of minerals can be performed via a single-step process (also known as the direct carbonation process), where mineral and CO_2 dissolution as well as the precipitation of carbonates occur in the same reactor. Another mode of the aqueous carbon mineralization is a two-step process (also known as a pH swing process). In both cases, there are a number of reaction parameters such as pH, ionic strength, slurry concentration, reaction temperatures, CO_2 partial pressures, and chemical additives which would impact the overall reaction rate as well as the rate determining step. Thus, those parameters should be carefully considered for the design of any carbon mineralization process using silicate minerals or alkaline wastes.

One of the main drawbacks of the single-step carbon mineralization would be the impurity of the carbonated materials. While the capital and operating costs of the single-step process could be lower than the two-step process, the single-step direct carbonation does not allow the production of high purity products (e.g., carbonates) and by-products (e.g., high surface area silica). Another challenge with direct aqueous carbonation is that various reaction steps such as CO_2 hydration, mineral dissolution, and formation of carbonates, all occur simultaneously, while they are favored at different reaction conditions (e.g., temperature and pH). The addition of a pH buffer such as $NaHCO_3$ which maintains the pH in the range of 6-7, has been found to be effective in aiding the single-step conversion of silicates minerals into carbonates (*18*, *29*, *30*) but the use of the carbonated materials would still be limited to fewer applications due to the low purity of the final products.

In contrast, the two-step carbon mineralization process that decouples the reaction steps of CO_2 hydration, mineral dissolution, and formation of carbonates, is expected to be more effective in aiding the production of high purity calcium carbonate, magnesium carbonate, and by-products since each step can be performed under optimized reaction conditions. In some cases, the CO_2 hydration and mineral dissolution steps can be combined.

Publication Date (Web): September 11, 2015 | doi: 10.1021/bk-2015-1194.ch012

The decoupled reactions are represented below.

Hydration of CO_2:

$$CO_{2(g)} + H_2O_{(aq)} <-> H_2CO_{3(aq)} <-> H^+_{(aq)} + HCO_3^-{}_{(aq)} \quad \text{(Rx. 5)}$$

$$HCO_3^-{}_{(aq)} <-> CO_3^{2-}{}_{(aq)} + H^+_{(aq)} \quad \text{(Rx. 6)}$$

Dissolution of Mg-Bearing Minerals (e.g., Forsterite (Rx. 8) and Serpentine (Rx. 9)):

$$Mg_2SiO_{4(s)} + 4H^+_{(aq)} -> 2Mg^{2+}_{(aq)} + (SiO_{2(s)} \times 2H_2O_{(aq)}) \quad \text{(Rx. 7)}$$

$$Mg_3Si_2O_5(OH)_{4(s)} + 6H^+_{(aq)} -> 3Mg^{2+}_{(aq)} + (2SiO_{2(s)} \times 5H_2O_{(aq)}) \quad \text{(Rx. 8)}$$

Dissolution of Ca-Bearing Minerals (e.g., Wollastonite):

$$CaSiO_{3(s)} + 2H^+_{(aq)} -> Ca^{2+}_{(aq)} + (SiO_{2(s)} \times H_2O_{(aq)}) \quad \text{(Rx. 9)}$$

Formation of Carbonates:

$$Mg^{2+}_{(aq)} + CO_3^{2-}{}_{(aq)} -> MgCO_{3(s)} \quad \text{(Rx. 10)}$$

$$Ca^{2+}_{(aq)} + CO_3^{2-}{}_{(aq)} -> CaCO_{3(s)} \quad \text{(Rx. 11)}$$

The reactions that are favored at a lower temperature are CO_2 hydration, while mineral dissolution and carbonation formation are favored at higher temperatures. In addition, the dissolution of minerals is favored at lower pH conditions (pH < 5), while the formation of carbonate ions in solution leading to mineral carbonation is favored at higher pH conditions (pH > 8). Therefore, various studies have proposed the use of this "pH-swing" concept to produce high purity calcium carbonate or magnesium carbonate, silica, and other potential by-products (*5*, *21*). It has also been reported that weak organic chelating agents such as oxalate

Publication Date (Web): September 11, 2015 | doi: 10.1021/bk-2015-1194.ch012

and acetate can bind to silicate minerals and destabilize the Mg-O and Ca-O bonds leading to enhanced mineral dissolution rates. The reaction temperature also impacts the chemistry of carbonate phases being formed, particularly for Mg-carbonates. Generally, more hydrated phases (e.g., $(Mg_5(CO_3)_4(OH)_2 \cdot 4H_2O)$ and $MgCO_3 \cdot 3H_2O$) are formed at lower temperatures (< 120 °C). In this chapter, the chemistries and morphologies of various magnesium and calcium carbonates are discussed. The precursors for forming magnesium and calcium carbonates as discussed in this chapter are magnesium and calcium silicate minerals. The relative natural abundance of magnesium silicate minerals compared to calcium silicate minerals is the reason for exploring magnesium carbonates in addition to calcium carbonates (*31*).

Publication Date (Web): September 11, 2015 | doi: 10.1021/bk-2015-1194.ch012

Production of Carbonates with Controlled Physical and Chemical Properties and Other Solid By-Products

Magnesium Carbonates

Precipitated Magnesium Carbonates (PMCs), which comprise anhydrous magnesite ($MgCO_3$) and hydrated magnesium carbonates like hydromagnesite ($Mg_5(CO_3)_4(OH)_2 \cdot 4H_2O$) and nesquehonite ($MgCO_3 \cdot 3H_2O$), are used in many industries such as pharmaceuticals, cosmetics, and rubber, and as precursors for other Mg-based chemicals (*32*). $MgCO_3$ is the most desirable carbonate species from a carbon storage perspective due to its omission of an added hydroxide group and water molecule mass, the efficient stoichiometric utilization of Mg, and the lowest solubility compared to other hydrated magnesium carbonate phases (*33–37*). From a construction material standpoint, the morphologies of the various magnesium carbonate phases may be more relevant.

Mg-Bearing Construction Materials

One of the challenges of using conventional Portland cement is the approximate ton of CO_2 that is produced per ton of Portland cement produced. One of the benefits associated with using Mg-based cements is that the kilns for calcining $MgCO_3$ can operate at lower temperatures (~650 °C), compared to temperatures greater than 1000 °C needed for $CaCO_3$ calcination. The lower temperature requirement would significantly reduce the corresponding CO_2 emissions. Another advantage of Mg-based cements is that MgO or $Mg(OH)_2$ has lower alkalinity compared to CaO or $Ca(OH)_2$. It is known that fresh concrete reacts with CO_2 over time to form carbonate crystals, and excess $CaCO_3$ crystal formation has been reported to reduce mechanical strength (*38*). Thus, less reactive Mg-bearing materials in cements would be better for the long-term strength of the cement. Furthermore, $MgCO_3$ crystals are stronger than $CaCO_3$ potentially adding to the mechanical strength of the cement (*38*).

The use of Mg-based cements does face challenges. $MgCO_3$ deposits are not as abundant as limestone reserves, and the reactivity of $Mg(OH)_2$ with pozzolans may be slower (*3*). While the lower calcination temperature of $MgCO_3$ may

In Advances in CO2 Capture, Sequestration, and Conversion; He, et al.;
ACS Symposium Series; American Chemical Society: Washington, DC, 2015.

result in lower energy requirements and hence lower CO_2 emissions compared to $CaCO_3$, the CO_2 emissions cannot be entirely avoided. Recently, various sources of Mg-based materials including industrial wastes have been studied, and the use of $MgCO_3$ as (non-reacting) filler materials to enhance the mechanical strength of cement has been investigated. The following section presents the synthesis of Precipitated Magnesium Carbonates (PMC) with controlled physical and chemical properties for various applications.

Synthesis of Magnesium Carbonates

Magnesium carbonates are formed via an ionic reaction (Rx. 10) between Mg^{2+} leached out from minerals or industrial wastes and carbonate ions formed as gaseous CO_2 dissolved into the aqueous phase. As discussed earlier, anhydrous form of magnesium carbonate – magnesite ($MgCO_3$) - is preferred for carbon storage, but in terms of the use of PMC as construction materials, other phases of Mg-carbonates could be used depending on the scale and the applications. The precipitation of hydrated magnesium carbonate species such as $MgCO_3 \cdot 3H_2O$ and $Mg_5(CO_3)_4(OH)_2 \cdot 4H_2O$ is driven by the highly hydrated character of Mg^{2+} ions (*34*, *39*, *40*). Moreover, the Oswald rule of stages suggests that the formation of more stable phases, $MgCO_3$ in this case, is likely to be preceded by the appearance of less thermodynamically stable phases such as $MgCO_3 \cdot 3H_2O$ (*41*).

While $MgCO_3 \cdot 3H_2O$ is formed at ambient temperature and pressure conditions (*34*, *42–45*), the composition can be changed to $Mg_5(CO_3)_4(OH)_2 \cdot 4H_2O$ as the temperature is increased to 55-60 °C (*32*, *44*) or the pH is raised to > 8.5 (*44*). The transformation of hydrated magnesium carbonates such as $Mg_5(CO_3)_4(OH)_2 \cdot 4H_2O$ or $MgCO_3 \cdot 3H_2O$ to anhydrous $MgCO_3$ is quite complex, and it can occur via dehydration (shrinkage of the hydrated species) or progressive dissolution and precipitation of the specie (*34*). Davies and Bubela (1973) (*42*) proposed that the transition from $MgCO_3 \cdot 3H_2O$ to $Mg_5(CO_3)_4(OH)_2 \cdot 4H_2O$ proceeds via dehydration of an intermediate with a similar composition to less common, $Mg_5(CO_3)_4(OH)_2 \cdot 5H_2O$ (dypingite). Lanas and Alvarez (2004) (*46*) showed that shorter heating times at temperatures ≥ 115 °C allowed the conversion of $MgCO_3 \cdot 3H_2O$ to $Mg_5(CO_3)_4(OH)_2 \cdot 4H_2O$, while longer heating times resulted in the formation of amorphous magnesium carbonate.

Generally, high reaction temperatures and high CO_2 pressures, as well as high salinity have shown to enhance the transition from hydrated to anhydrous magnesium carbonates in aqueous systems (*34*, *40*, *47*, *48*). Hänchen et al., (2008) (*34*) reported that even at a relatively high reaction temperature (120 °C), $MgCO_3$ was initially formed along with hydrated carbonate species such as $MgCO_3 \cdot 3H_2O$ and ($Mg_5(CO_3)_4(OH)_2 \cdot 4H_2O$). The hydrated species were subsequently transformed to $MgCO_3$ as reaction proceeded further (~ 5 hours). Others observed that at higher reaction temperatures (~150 °C), only $MgCO_3$ were observed in the product phase (*36*, *47*, *49*).

These studies on the formation of magnesium carbonates are typically carried out in hydrothermal batch systems using a variety of magnesium precursors including $MgCl_2 \cdot 6H_2O$ (*34*, *50–55*), $Mg(HCO_3)_2$ (*42*, *56*), $Mg(NO_3)_2$ (*44*, *57*, *58*),

In Advances in CO2 Capture, Sequestration, and Conversion; He, et al.;
ACS Symposium Series; American Chemical Society: Washington, DC, 2015.

Publication Date (Web): September 11, 2015 | doi: 10.1021/bk-2015-1194.ch012

$Mg(OH)_2$ (*20*, *32*, *37*, *59–64*), and Mg-bearing silicate minerals (*18*, *29*, *30*, *65*). The carbon source for these studies also vary from CO_2(g), Na_2CO_3, $(NH_4)_2CO_3$, HCO_3^-, K_2CO_3, to urea (CH_4N_2O).

Seeded Formation of Precipitated Magnesium Carbonates

Various methods have been proposed and tested to stimulate $MgCO_3$ growth at generally unfavorable reaction conditions. Reducing the activity of water by adding salts (*33*) or polymers (*66*), increasing the ionic strength (*34*, *40*), and longer reaction times (*34*, *62*) have been shown to be effective in producing $MgCO_3$. Slow nucleation steps were circumvented by seeding systems with $MgCO_3$ to accelerate the precipitation of $MgCO_3$ (*65*). Additionally, Swanson et al., (2014) (*48*) found the use of $MgCO_3$ seed particles to direct the precipitation of carbonates to produce $MgCO_3$ at 150 °C and 15 atm CO_2, where the unseeded tests produced $Mg_5(CO_3)_4(OH)_2{\cdot}4H_2O$. Hövelmann et al., (2012) (*67*) also observed carbonate growth with AFM and found that the carbonates to grow up and not across a $Mg(OH)_2$ surface. The growth of carbonate on the magnesium carbonate phase instead of magnesium hydroxide was explained by self-adhesion and linear phase misfit between hydroxide and carbonate.

Morphologies of Precipitated Magnesium Carbonates

The most common magnesium carbonate phases reported in literature, $MgCO_3{\cdot}3H_2O$, $Mg_5(CO_3)_4(OH)_2{\cdot}4H_2O$ and $MgCO_3$, are represented in Figure 4. The materials shown in the SEM images were synthesized by reacting aqueous $Mg(OH)_2$ and CO_2 at different temperatures, which favor the formation of particular carbonate phases. As shown in Figure 4, the morphological diversity among magnesium carbonate phases is clearly apparent and matches the previously reported structures (given as references): needle-shaped $MgCO_3{\cdot}3H_2O$ (*55*), sheet and rosette-shaped $Mg_5(CO_3)_4(OH)_2{\cdot}4H_2O$ (*33*), and crystalline cubic shape $MgCO_3$ (*68*). While these distinct phase morphologies provide general guidelines for the controlling the morphologies of magnesium carbonate products, some have reported that both sheet-like and needle-shaped morphologies for $MgCO_3{\cdot}3H_2O$ can be co-synthesized (*55*).

In addition to the morphological structure, the particle size distribution of precipitated magnesium carbonates can also be tuned. Increasing the reaction (aging) time was shown to increase the particle size (*22*, *67*). The samples analyzed after longer reaction or aging periods had much more distinct and clearly delineated morphological features compared to the fresh samples (*22*).

Publication Date (Web): September 11, 2015 | doi: 10.1021/bk-2015-1194.ch012

Publication Date (Web): September 11, 2015 | doi: 10.1021/bk-2015-1194.ch012

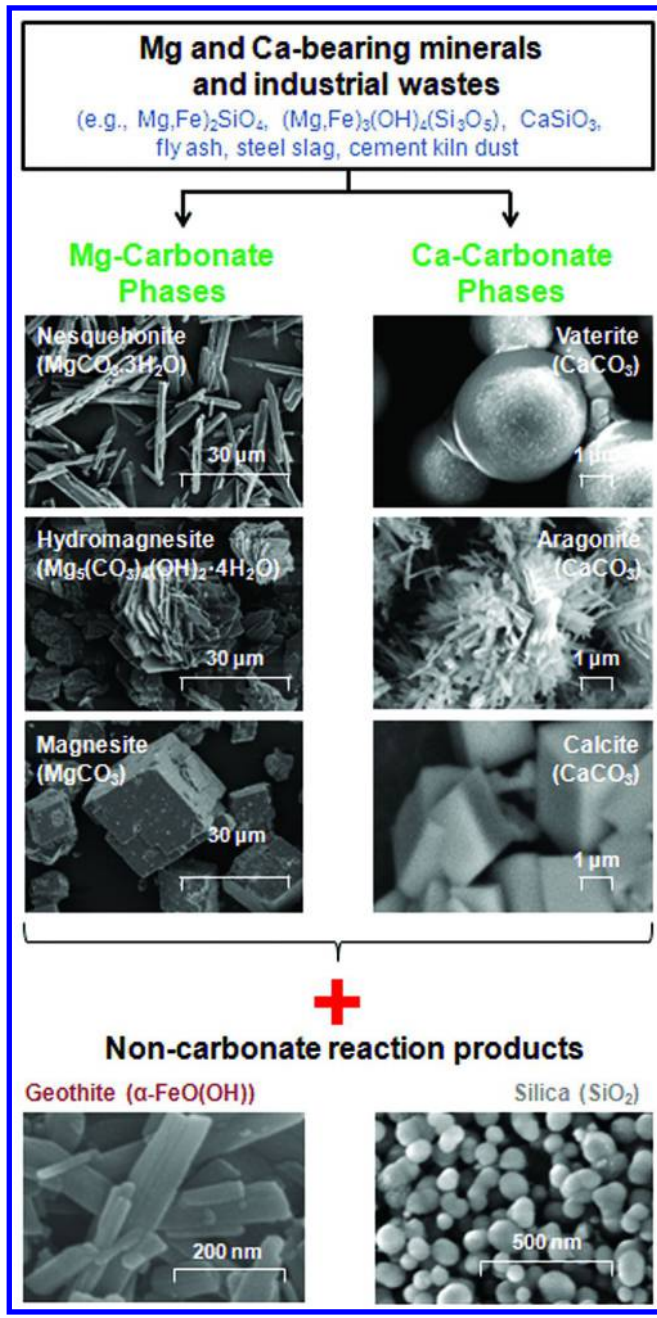

Figure 4. Products and by-products from the carbonation of Mg-bearing minerals (e.g., serpentine and olivine) and Ca-bearing minerals (e.g., wollastonite): various phases of Mg- and Ca-carbonate phases and non-carbonate by-products such as silica. (SEM image adapted from reference (137). Copyright 2009, ACS) and geothite (SEM image adapted from reference (138). Copyright 2005, ACS).

Calcium Carbonates

Precipitated Calcium Carbonate (PCC) has a wide range of industrial applications ranging from coatings to paper fillers and pigments (*69*). In the United States, the production of limestone including dolomite was to the order of 781 million tons in 2012 (*70*) and the global production of limestone is set to increase to 5.7 billion metric tons by 2020 (*71*). As discussed earlier, limestone is mined to produce lime via calcination which is used in Portland cement or directly used as filler materials. The increasing production of limestone and the associated CO_2 emissions from calcination are expected to increase over time.

Ca-Bearing Construction Materials

The utilization of limestone filler in concrete is a common practice in European countries. As limestone ($CaCO_3$) replaces ordinary Portland Cement (OPC), the economics, as well as the environmental impacts, could be positively improved. If the cementations composite containing limestone can perform as well as the one with only OPC, the cement usage and its associated CO_2 emissions can be significantly reduced leading to the conservation of fossil fuels and mineral resources (*72*). Most Portland cement specifications allow the inclusion of limestone up to 5% (*73*, *74*). Beyond that, Portland limestone cements are categorized based on the percentage of limestone added to the cement, generally ranging from 5% to 35%. The European Standard (EN 197-1-2000) also identified four different types of Portland-Limestone Cements (PLC) that contain 6-20% (types II/A-L and II/A-LL) and 21-35% limestone types (II/B-L and II/B-LL) (*74*).

The performance of limestone addition to Portland cement has been widely studied. It has been reported that limestone improves the hydration rate of the cement compounds and consequently shows high compressive strength at an early age up to 28 days or longer (*75*, *76*), although a drop in cement strength has been suggested at above 20% limestone inclusion. The limestone reacts with the alumina phases of cement to form hydrated calcium phases such as calcium monocarboaluminate hydrate ($3CaO.Al_2O_3.CaCO_3.nH_2O$, n~11 at room temperatures). Limestone also acts as the crystallization nucleus for the precipitation of calcium hydroxide (CH), resulting in an increase in the rate of hydration of silicates, a change in the composition of the calcium silicate hydrate (C-S-H) system, and a better development of the microstructure of the cementitious composite (*77*, *78*).

Other advantages of using limestone as a filler material, is better packing of cement granular skeleton and larger dispersion of cement grains. Increased cement strength is attributed to a denser microstructure of the composite through the filler effect, reducing a void volume of the composite. The strength of concrete containing limestone is affected by the quality of limestone, and particle size distribution of limestone (*79*). It is reported that addition of limestone up to 5% would increase strength at early age due to its particle packing effect

Publication Date (Web): September 11, 2015 | doi: 10.1021/bk-2015-1194.ch012

In Advances in CO2 Capture, Sequestration, and Conversion; He, et al.;
ACS Symposium Series; American Chemical Society: Washington, DC, 2015.

(*80*). Limestone addition produces a more desirable particle size distribution and improved particle packing when mixing with OPC (*81*).

While the use of ground limestone without any chemical treatment would be most economical, from a morphological standpoint, however, it would be interesting to investigate the effects of using $CaCO_3$ with different morphological structures on the mechanical strength of cement. Unlike magnesium carbonates, calcium carbonates has been extensively studied including the formation of $CaCO_3$ from the carbon mineralization process starting with Ca-rich minerals and industrial wastes such as wollastonite and fly ash as represented in Figure 4.

Synthesis of Calcium Carbonates

$CaCO_3$ can exist as three distinct crystalline structures, which are calcite (rhombohedral), aragonite (spiky/orthorhombic), and vaterite (plate-like/ hexagonal) (Figure 4). However, polycrystal and football-shapes for calcite, rosette for aragonite, and sphreulite, and lettuce-shapes for vaterite have also been reported (*82*). Calcite is the most thermally stable structure, while vaterite is most unstable (*83*). Other metastable phases of calcium carbonate: monohydrocalcite ($CaCO_3 \cdot H_2O$), and ikaite ($CaCO_3 \cdot 6H_2O$), do exist but they are generally not found in carbonate products due to their highly unstable nature (*84*, *85*). The crystallization behaviors of $CaCO_3$ in different structures have been extensively studied in the past due to its importance not only in the industrial systems, but also in the ecological systems (e.g., shells and bonds of many animals (*86–89*)) as well. Understanding the crystal structures and the reaction conditions that result in their formations would be important for determining how they can be utilized as construction materials.

Most of the studies in this area have been focused on the synthesis of $CaCO_3$ phases from Ca-bearing solutions derived from minerals and industrial wastes rich in calcium. It has been demonstrated that it is possible to achieve a high level of control on the synthesis of calcium carbonate crystals with tuned morphological structures. Colfen (2003) (*90*) reviewed various approaches to control the crystal structure of $CaCO_3$ during its synthesis. The use of additives (e.g., polymers), fluid composition and concentration, solution pH, temperature, and degree of Ca saturation were found to affect the phases of $CaCO_3$ formed (*82*, *91–93*). Polymers tested include double-hydrophilic block copolymers (DHBCs) (*94*, *95*) and amino acids (*96*, *97*).

The morphology of $CaCO_3$ can also be controlled via self-assembled (*98*) and Langmuir (*99*) monolayer depositions. The growth of $CaCO_3$ on gold nanoparticles (*100*) and bio-based solid matrixes (e.g., cellulose, chitosan, and chitin in the presence of acidic macromolecules such as poly-acrylic acid (*101*) have been reported with different crystal structures. Other unconventional substrates such as decalcified egg membrane and Nylon 66 fibers were also used to grow $CaCO_3$ (*102*). The addition of ethanol to the carbonation system also influenced the crystalline structure of produced $CaCO_3$ (*103*), while in some cases, the presence of competing ions (e.g., Mg^{2+}) inhibited the formation of calcium carbonate (*104–106*). As with the synthesis of precipitated magnesium carbonate

Publication Date (Web): September 11, 2015 | doi: 10.1021/bk-2015-1194.ch012

(PMC), a highly precise control over $CaCO_3$ morphology was also reported using seed crystals (*107*). The following sections describe various synthesis routes for three $CaCO_3$ phases.

The formation of plate-like vaterite, which is most unstable among $CaCO_3$ phases, has been reported in cross-linked gelatin films containing peptides such as poly-L-aspartate and poly-L-glutamate (*108*). In an alternative route, Li et al., (2002) (*109*) proposed the synthesis of pure vaterite by mixing $CaCl_2$ and urea (CO_3^{2-} donor) in the presence of solvents such as ethylene glycol, 1, 2-propanediol and glycerol at temperatures in the range of 80-190 °C. Han et al., (2005) (*110*) observed that increasing the flow rate of CO_2 bubbled through a $CaCl_2$ solution resulted in the preferential formation of vaterite. Due to its metastable characteristic, vaterite can quickly transform to other forms of $CaCO_3$.

The crystallization of spiky aragonite has found to be favored at higher pH conditions (> 13.5) and with longer reaction times compared to vaterite (*111*). Kitano et al., (1962) (*112*) showed that pure aragonite could be prepared at around 25 °C by slowing the removal of CO_2 from a solution containing $Ca(HCO_3)_2$ and $MgCl_2$. Like vaterite, the formation of aragonite is also challenged by its metastable nature. Depending on the temperature and pH, aragonite readily transforms into calcite within a day (*113*, *114*). Interestingly, stable aragonite with mechanical stability and strength has been observed in nature and when it is formed with complex structures is exemplified in the nacre of pearls (*115*). Unique biomimetic pathways have been shown to use macromolecules (e.g., polymers and protein) to induce the formation of stable aragonite structures as shells (*116–119*). Other alternatives for synthesizing aragonite include using ultrasonic irradiation of $Ca(HCO_3)_2$ (*120*), reverse surfactant microemulsions (*121*), self-assembled monolayers as substrates (*122*), and vapor diffusion of CO_2 into a solution of $CaCl_2$ mixed with particles of a hydrophilic block copolymer (*123*).

Calcite is the most stable crystal structure of $CaCO_3$ and it is rhombohedral as shown in Figure 4. A number of studies have shown that the solution pH and temperature have the most significant effects on altering the phases of calcium carbonate (*82*, *83*). Under ambient condition, the optimal pH conditions for forming calcite, aragonite and vaterite are pH >12, pH ~11 and pH <10, respectively (*82*). Calcite can be formed directly from a Ca-rich solution or indirectly using metastable $CaCO_3$. An increase in reaction time leads to the preferential formation of calcite over the other phases (i.e., vaterite and aragonite) (*83*). As the reaction temperature increases, the production of aragonite becomes favored if pH <11 and at pH > 11, calcite is formed as the main product (*83*). Orthophosphate ions in solution favor calcite formation, while aragonite and calcite formations are favored in the presence of magnesium and manganese ions (*82*).

Silica (Non-Carbonate By-Product)

Many of previously discussed approaches for the production of magnesium and calcium carbonates involve silicate minerals or industrial wastes that contain a significant fraction of silica (e.g., steel slags). Thus, one of the major by-products

In Advances in CO2 Capture, Sequestration, and Conversion; He, et al.;
ACS Symposium Series; American Chemical Society: Washington, DC, 2015.

Publication Date (Web): September 11, 2015 | doi: 10.1021/bk-2015-1194.ch012

of these processes is Si-bearing materials. High surface area silica is produced as Mg and/or Ca are leached out from the silicate minerals such as olivine, serpentine and wollastonite under low pH conditions. The resulting silica can be further ground to achieve the same fineness as silica fume, which are widely used in the cement industry. Traditionally, silica fume is one of the by-products generated in electric arc furnaces that produce silicon and ferrosilicon alloys (*124*). High purity quartz silicon is converted to SiO_2 vapor at a high temperature (2000 °C), and it is subsequently oxidized and condensed resulting in non-crystalline silica particles (*125*). Silica fume is a very fine powder with spherical shape, which is about 100 times smaller than the size of cement. Particle size of silica fume ranges from 0.1 and 0.2 μm and is highly pozzolanic in nature because silica fume contains about 90 wt.% of non-crystalline silica with high surface area (13,000 – 30,000 m^2/kg) (*126*).

Many have reported that the mechanical strength of construction materials can be improved with the addition of silica fume since it reacts with $Ca(OH)_2$ resulting in an increase in bond strength between hydrated cement materials and sand as well as changes the pore distribution of cementitious composite (*127–130*). Sobolev (2004) (*131*) observed the maximum compressive strength of 91 MPa at 10% silica fume replacement of cement for high performance concrete. By adding silica fume, pore alteration can also improve the durability of concrete. For example, the diffusion of chloride ion into concrete is reduced with an increase in the silica fume content in cement (*132–134*). Silica fume has also been used to compensate for the reduction in the compressive strength of mortar when high compositions of limestone are used (*135*). The use of limestone-silica fume Portland cement mortars were also found to increase sulfate resistance of the construction materials (*136*). Various by-products of magnesium and calcium silicates such as silica (*137*) and geothite (*138*) can be produced in various carbonation processes discussed earlier (Figure 4). Silica-bearing by-products (or wastes) in particular have a great potential to be used in construction materials with lower environmental impacts.

Publication Date (Web): September 11, 2015 | doi: 10.1021/bk-2015-1194.ch012

Use of Low Grade Industrial Wastes in Construction Materials

Various wastes can be carbonated and utilized as discussed in Bertos et al., (2004) (*16*). Some of the most common alkaline industrial wastes include blast furnace slag, stainless steel slag, MSWI ash, cement kiln dust, air pollution control residues, coal fly ash to list a few. However, the effectiveness of using these wastes is dependent on the chemical and morphological properties they impart to the cement. For example, greater alkalinity, high content of Ca and higher Ca:Si ratio result in a greater extent of carbonation (*139*, *140*). The presence of organics, anions (e.g., chloride, sulfate, and nitrate), heavy metals (e.g., Pb, Cd, and Ni), and phases such as ettringite ($Ca_6Al_2(SO_4)_3(OH)_{12}\cdot 26H_2O$) that decompose to form gypsum, carbonate, and alumina gel in the presence of CO_2 affect the long-term mechanical strength of cement (*141*). The effect of water is also important to consider. While excess initial free water occupies the pore space and hinders CO_2 diffusion which lowers strength development, some water is needed to aid the carbonation reaction. Morphological features such as greater microporosity of the hydrated products aid better carbonation, and materials with less surface area

need less water for optimum carbonation (*142*). Higher gas permeability of the cementitious materials aids CO_2 diffusion thereby facilitating carbonation (*16*).

Some of the abundant industrial wastes such as fly ash and steel slags are of particular interest for their use as construction materials. Some of those materials are interesting because they also have carbon capture and storage potential based on their alkaline contents. According to Cement and Concrete Terminology from ACI Committee 226, fly ash is defined as "the finely divided residue resulting from the combustion of ground or powdered coal, which is transported from the firebox through the boiler by flue gases" (*143*). The particle size of fly ash varies from less than 1 μm to more than 100 μm, and the surface area of fly ash is typically 300 – 500 m^2/kg. The bulk density can also vary from 540 to 860 kg/m^3, and the relative density of fly ash is between 1.9 and 2.8. The exact compositions of fly ash differ depending on the source of coal, but all fly ashes include large amount of silica (SiO_2) and lime (CaO) as major constituents. Minor phases include alumina, iron, magnesium, sulfur, and sodium. Fly ash can be classified as Class F or Class C (*144*). Class F has low calcium (< 10% CaO) with around 5% carbon, whereas Class C is high calcium fly ash with less than 2% carbon (*145*).

Fly ash can be used to replace cement up to 25-35 wt.% of the total construction material based on its workability, which is a measure of the ease of homogeneous compaction of the construction material (*146*). Studies have shown that fly ash significantly improves the mechanical properties of concrete due to its pozzolanic reaction (*147*, *148*), particularly in the long run if the concrete is kept moist (*149–151*). Studies have reported that the natural uptake of CO_2 in fly ash concrete forms $CaCO_3$ over time (*13–15*). Alternatively, the industrial wastes with high Ca and Mg contents can be carbonated prior to be used as construction materials. Another interesting property of fly ash in cement is that it acts as lubricating balls when mixed with cementitious materials because it has a high content of micro beads providing enhanced workability and the ability to be compacted (*152*). One of the technical challenges of using industrial wastes such as fly ash is the lack of consistency in the composition of the material to produce carbonated construction materials of consistent quality. Another environmental challenge is the presence of heavy metals such as Ni and Cr and how they may be immobilized or mobilized in construction materials.

Other major industrial wastes in the United States which contain calcium and could be used as construction materials are cement kiln dust and steel slag (*12*). As discussed earlier, all of these alkaline industrial wastes can offset the carbon emission from its own process (e.g., fly ash in a power plant and steel slags in a steel manufacturing plant). However, their scales do not match their CO_2 emissions. Thus, the carbon capture and storage potentials of these industrial materials are limited. But in terms of both carbon and solid wastes management perspectives, this approach of treating industrial wastes with anthropogenic CO_2 and using them in construction materials is a positive step towards the environmental sustainability.

Publication Date (Web): September 11, 2015 | doi: 10.1021/bk-2015-1194.ch012

In Advances in CO2 Capture, Sequestration, and Conversion; He, et al.;
ACS Symposium Series; American Chemical Society: Washington, DC, 2015.

Effects of Carbonated Stainless Steel Slags and Carbon Mineralization By-Product in Construction Materials

To further investigate the concept of adding carbonated industrial wastes and other solid additives to the construction materials, the mechanical strength of construction materials in the presence of silica-rich materials and carbonated stainless steel slag (cSSS) were examined. Silica (SiO_2), which is a by-product of the carbon mineralization process, was chosen to determine if it would have the same beneficial effects in enhancing the mechanical strength of construction materials as silica fume. Stainless steel slag (SSS) was studied since it usually contains more than 20 wt% of free lime (CaO) and silica, which both are known to enhance the binding of cement and improve the mechanical strength of the material.

In this study, silica and carbonated stainless steel slag were prepared using two different methods. Silica was obtained by dissolving serpentine in 1.5 liters of 70% HNO_3 at 80 °C for 96 hours. The solution was then filtered and the filtrate was collected and analyzed using the Inductively Coupled Plasma - Atomic Emission Spectroscopy in order to determine the extraction extent of Mg. The solid product rich in SiO_2 was cleaned using de-ionized water and dried at 70 °C for 48 hours. Carbonated stainless steel slag was prepared by reacting SSS with CO_2 at 30 °C in a solution of 1.0 M $NaHCO_3$. The reaction was performed at ambient pressure with a CO_2 flow rate of 0.25 scfm, while stirring at 200 rpm for 12 hours. Next, the cementitious composite was prepared by replacing cement with silica derived from serpentine to constitute 20% of the total binder content. In case of cSSS, the cement was prepared with cSSS to constitute 10% of the total binder content. The water to cementitious material ratio was kept at 0.5 for both cases. The raw materials were mixed in a mortar mixer for 3 min, casted into the plastic cubic molds, and subsequently compacted by a tamping rod. All specimens were removed from the molds after 24 hours and cured in water at room temperature until performing the compressive strength tests (3, 7, and 28 days). The compressive strength of each cement mortar was measured while applying the load at a rate of 150 N/s.

As shown in Figure 5, after 28 days, the compressive strengths of construction materials containing SiO_2-rich by-product and cSSS (51 and 42 MPa, respectively) were substantially greater than that of the control case prepared without any additives (34 MPa). Since both SiO_2-rich materials and cSSS do not contain reactive components, the enhanced compressive strengths should have been due to the filler effect which reduced the void space in the cementitious composite. The compressive or mechanical strength of composite containing SiO_2-rch by-product was significantly increased with the curing age (from 3, 7, to 28 days), whereas that of composite containing cSSS relatively leveled off after 10 days. These two additives also changed the hydration behaviors of cementitious composites, which implied that changes occurred in the heat flow and binding behaviors of these materials.

Publication Date (Web): September 11, 2015 | doi: 10.1021/bk-2015-1194.ch012

In Advances in CO2 Capture, Sequestration, and Conversion; He, et al.;
ACS Symposium Series; American Chemical Society: Washington, DC, 2015.

Publication Date (Web): September 11, 2015 | doi: 10.1021/bk-2015-1194.ch012

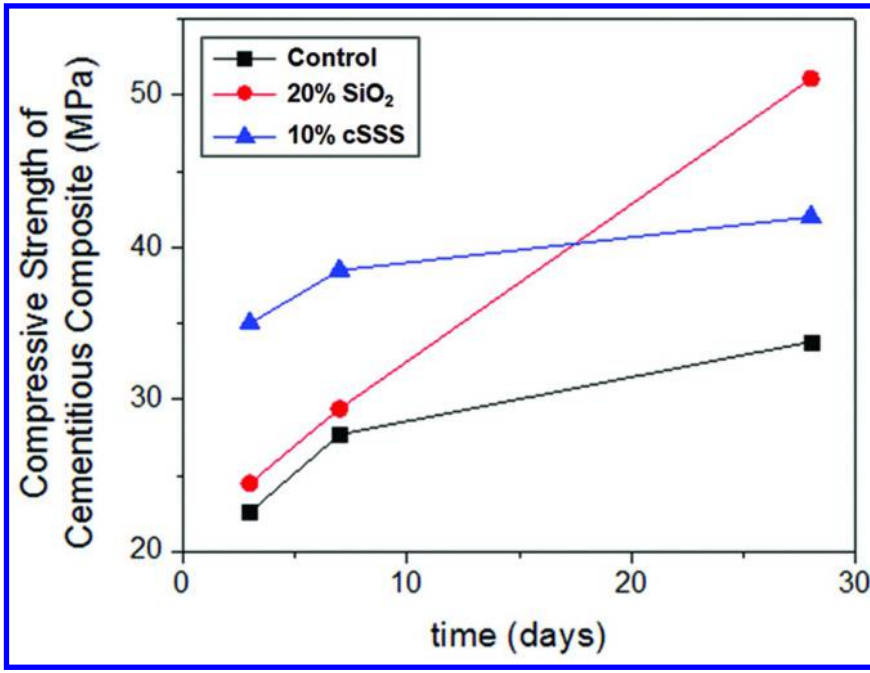

Figure 5. Compressive strengths of cementitious composites prepared with no additives (control case), 20% Si-rich materials and 10% carbonated stainless steel slag (cSSS).

Conclusions

A number of options exist for the reduction of industrial CO_2 emissions. Among those, the use of industrial wastes in carbon capture and storage is attractive because it allows for the simultaneous management of CO_2 and solid wastes. The carbonation of alkaline industrial wastes mimics the natural weathering of silicate minerals which can also be performed in an ex-situ mode at industrial scales. The carbonated materials can either safely store carbon permanently, or be used in various applications including construction materials as discussed in this chapter. The complex chemistry and morphological structures when naturally occurring calcium and magnesium bearing minerals and industrial wastes are carbonated and by-products such as silica are produced are important to consider. More importantly, how these materials impact the mechanical strength and durability of the construction material prior to full implementation needs to be investigated. The impacts of impurities in these additives on the integrity of cement are also important to consider.

Publication Date (Web): September 11, 2015 | doi: 10.1021/bk-2015-1194.ch012

References

1. Metz, B., Ed.; *Carbon Dioxide Capture and Storage: Special Report of the Intergovernmental Panel on Climate Change*; Cambridge University Press: Cambridge, U.K., 2005.
2. Hendriks, C.; van der Waart, A. S.; Byers, C.; Phylipsen, D.; Voogt, M.; Hofman, Y. *Building the Cost Curves for CO_2 Storage, Part 1: Sources of CO_2, PH4/9*; 2002, IEA-GHG: Utrecht, The Netherlands.
3. Gartner, E. Industrially interesting approaches to "low-CO_2" cements. *Cem. Concr. Res.* **2004**, *34*, 1489–1498.
4. Lackner, K. S. Carbonate chemistry for sequestering fossil carbon. *Annu. Rev. Energy Environ.* **2002**, *27*, 193–232.
5. Sanna, A.; Hall, M. R.; Maroto-Valer, M. Post-processing pathways in carbon capture and storage by mineral carbonation (CCSM) towards the introduction of carbon neutral materials. *Energy Environ. Sci.* **2012**, *5*, 7781.
6. Sridhar, N.; Hill, D. *Electrochemical Conversion of CO_2 - Opportunities and Challenges, Research and Innovation - Position Paper 07-2011*; 2011.
7. EPA. *Quantifying Greenhouse Gas Emissions from Key Industrial Sectors in the United States*, 2008. http://www.epa.gov/sectors/pdf/greenhouse-report.pdf (accessed on July 8, 2015).
8. EIA. *Energy Explained*, 2013. http://www.eia.gov/energyexplained/index.cfm (accessed on May 15, 2014).
9. Johnson, J. W. The Foul Side of "Clean Coal.". *Chem. Eng. News* **2009**, *87*, 44–47.
10. U.S. Department of Transportation. *User Guidelines for Waste and Byproduct Materials in Pavement Construction - Publication Number: FHWA-RD-97-148*; 2012.
11. Slag Cement Association. *Avoided "Waste" (Disposal, Energy, and Emissions)*. http://www.slagcement.org/Sustainability/disposal.html (accessed on July 8, 2015).
12. Gadikota, G.; Park, A-H. A. Accelerated carbonation of Ca- and Mg-bearing minerals and industrial wastes using CO_2 In *Carbon Dioxide Utilization: Closing the Carbon Cycle*; Styring, P., Quadrelli, A., Eds.; Elsevier, 2014.
13. Atiş, C. D. Accelerated carbonation and testing of concrete made with fly ash. *Constr. Build. Mater.* **2003**, *17*, 147–152.
14. Sakai, E.; Miyahara, S.; Ohsawa, S.; Lee, S. H.; Daimon, M. Hydration of fly ash cement. *Cem. Concr. Res.* **2005**, *35*, 1135–1140.
15. Thomas, M. D. A.; Matthews, J. D. Carbonation of fly ash concrete. *Mag. Concr. Res.* **1992**, *44*, 217–228.
16. Bertos, M. F.; Simons, S. J. R.; Hills, C. D.; Carey, P. J. A review of accelerated carbonation technology in the treatment of cement-based materials and sequestration of CO_2. *J. Hazard. Mater.* **2004**, *112*, 193–205.
17. Baciocchi, R.; Costa, G.; Di Bartolomeo, E.; Polettini, A.; Pomi, R. CO_2 sequestration by direct gas-solid carbonation of air pollution control (APC) residues. *Waste Manage.* **2009**, *29*, 2994–3003.
18. Gadikota, G.; Matter, J.; Kelemen, P.; Park, A. H. A. Chemical and morphological changes during olivine carbonation for CO_2 storage in the

presence of NaCl and $NaHCO_3$. *Phys. Chem. Chem. Phys.* **2014**, *16*, 4679–4693.
19. Gadikota, G.; Swanson, E. J.; Zhao, H.; Park, A.-H. A. Experimental design and data analysis for accurate estimation of reaction kinetics and conversion for carbon mineralization. *Ind. Eng. Chem. Res.* **2014**, *53*, 6664–6676.
20. Park, A. A.; Jadhav, R.; Fan, L. CO_2 mineral sequestration: chemically enhanced aqueous carbonation of serpentine. *Can. J. Chem. Eng.* **2003**, *81*, 885–890.
21. Park, A.-H. A.; Fan, L.-S. CO_2 mineral sequestration: physically activated dissolution of serpentine and pH swing process. *Chem. Eng. Sci.* **2004**, *59*, 5241–5247.
22. Zhao, H.; Dadap, N.; Park, A.-H. A. Tailored Synthesis of Precipitated Magnesium Carbonates As Carbon-Neutral Filler Materials during Carbon Mineral Sequestration. In *The 13th International Conference on Fluidization - New Paradigm in Fluidization*; 2010, pp 821−828.
23. Zhao, H.; Park, Y.; Lee, D. H.; Park, A.-H. A. Tuning the dissolution kinetics of wollastonite via chelating agents for CO_2 sequestration with integrated synthesis of precipitated calcium carbonates. *Phys. Chem. Chem. Phys.* **2013**, *15*, 15185–15192.
24. Viani, A.; Gualtieri, A. F. Preparation of magnesium phosphate cement by recycling the product of thermal transformation of asbestos containing wastes. *Cem. Concr. Res.* **2014**, *58*, 56–66.
25. Hartshorn, S. A.; Sharp, J. H.; Swamy, R. N. Thaumasite formation in Portland-limestone cement pastes. *Cem. Concr. Res.* **1999**, *29*, 1331–1340.
26. Seifritz, W. CO_2 disposal by means of silicates. *Nature* **1990**, *345*, 486.
27. Lackner, K. S.; Wendt, C. H.; Butt, D. P.; Joyce, E. L., Jr; Sharp, D. H. Carbon dioxide disposal in carbonate minerals. *Energy* **1995**, *20*, 1153–1170.
28. Veetil, S. P.; Pasquier, L. C.; Blais, J. F.; Cecchi, E.; Kentish, S.; Mercier, G. Direct gas–solid carbonation of serpentinite residues in the absence and presence of water vapor: a feasibility study for carbon dioxide sequestration. *Environ. Sci. Pollut. Res.* **2015**, 1–10.
29. Gerdemann, S. J.; O'Connor, W. K.; Dahlin, D. C.; Penner, L. R.; Rush, H. Ex situ aqueous mineral carbonation. *Environ. Sci. Technol.* **2007**, *41*, 2587–2593.
30. O'Connor, W. K.; Dahlin, D. C.; Rush, G. E.; Gerdemann, S. J.; Nilsen, D. N. *Final Report: Aqueous Mineral Carbonation: DOE/ARC-TR-04-002*; 2004.
31. Brent, G. F.; Petrie, J. G. CO_2 Sequestration by Mineral Carbonation in the Australian Context. In *Chemeca 2008: Towards a Sustainable Australasia*; 2008, pp 1273−1283.
32. Christ, C. L.; Hostetle, P. B. Studies in system $MgO–SiO_2–CO_2–H_2O$. 2. Activity-product constant of magnesite. *Am. J. Sci.* **1970**, *268*, 439–453.
33. Hänchen, M.; Prigiobbe, V.; Baciocchi, R.; Mazzotti, M. Precipitation in the Mg−carbonate system—effects of temperature and CO_2 pressure. *Chem. Eng. Sci.* **2008**, *63*, 1012–1028.
34. Kittrick, J. A.; Peryea, F. J. Determination of the Gibbs free energy of formation of magnesite by solubility methods. *Soil Sci. Soc. Am. J.* **1986**, *50*, 243–247.

In Advances in CO2 Capture, Sequestration, and Conversion; He, et al.;
ACS Symposium Series; American Chemical Society: Washington, DC, 2015.

Publication Date (Web): September 11, 2015 | doi: 10.1021/bk-2015-1194.ch012

35. Krupka, K. M.; Cantrell, K. J.; McGrail, B. P. *Thermodynamic Data for Geochemical Modeling of Carbonate Reactions Associated with CO_2 Sequestration – Literature Review: PNNL - 19766*; 2010.
36. Schaef, H. T.; Windisch, C. F.; McGrail, B. P.; Martin, P. F.; Rosso, K. M. Brucite [$Mg(OH)_2$] carbonation in wet supercritical CO_2: an in situ high pressure X-ray diffraction study. *Geochim. Cosmochim. Acta* **2011**, *75*, 7458–7471.
37. Pearce, F. Green foundations. *New Sci.* **2002**, 39–40.
38. Deelman, J. C. Breaking Ostwald's rule. *Chemie Der Erde-Geochemistry* **2001**, *61*, 224–235.
39. Sayles, F. L.; Fyfe, W. S. Crystallization of magnesite from aqueous solution. *Geochim. Cosmochim. Acta* **1973**, *37*, 87–99.
40. Mullin, J. W. *Crystallization*, third ed.; Butterworth-Heinemann: Oxford, 1993.
41. Davies, P. J.; Bubela, B. The transformation of nesquehonite into hydromagnesite. *Chem. Geol.* **1973**, *12*, 289–300.
42. Langmuir, D. Stability of carbonates in the system. *J. Geol.* **1965**, 730–754.
43. Zhang, Z.; Zheng, Y.; Ni, Y.; Liu, Z.; Chen, J.; Liang, X. Temperature- and pH-dependent morphology and FT-IR analysis of magnesium carbonate hydrates. *J. Phys. Chem. B* **2006**, *110*, 12969–12973.
44. Zhao, L.; Sang, L.; Chen, J.; Ji, J.; Teng, H. H. Aqueous carbonation of natural brucite: relevance to CO_2 sequestration. *Environ. Sci. Technol.* **2009**, *44*, 406–411.
45. Botha, A.; Strydom, C. A. Preparation of a magnesium hydroxy carbonate from magnesium hydroxide. *Hydrometallurgy* **2001**, *62*, 175–183.
46. Lanas, J.; Alvarez, J. I. Dolomitic lime: thermal decomposition of nesquehonite. *Thermochim. Acta* **2004**, *421*, 123–132.
47. Fricker, K. J.; Park, A.-H. A. Investigation of the different carbonate phases and their formation kinetics during $Mg(OH)_2$ slurry carbonation. *Ind. Eng. Chem. Res.* **2014**, *53*, 18170–18179.
48. Swanson, E. J.; Fricker, K. J.; Sun, M.; Park, A.-H. A. Directed precipitation of hydrated and anhydrous magnesium carbonates for carbon storage. *Phys. Chem. Chem. Phys.* **2014**, *16*, 23440–23450.
49. Fricker, K. J.; Park, A.-H. A. Effect of H_2O on $Mg(OH)_2$ carbonation pathways for combined CO_2 capture and storage. *Chem. Eng. Sci.* **2013**, *100*, 332–341.
50. Ballirano, P.; De Vito, C.; Ferrini, V.; Mignardi, S. The thermal behaviour and structural stability of nesquehonite, $MgCO_3 \cdot 3H_2O$, evaluated by in situ laboratory parallel-beam X-ray powder diffraction: New constraints on CO_2 sequestration within minerals. *J. Hazard. Mater.* **2010**, *178*, 522–528.
51. Cheng, W.; Li, Z. Precipitation of nesquehonite from homogeneous supersaturated solutions. *Cryst. Res. Technol.* **2009**, *44*, 937–947.
52. Cheng, W.; Li, Z. Controlled supersaturation precipitation of hydromagnesite for the $MgCl_2$– Na_2CO_3 system at elevated temperatures: chemical modeling and experiment. *Ind. Eng. Chem. Res.* **2010**, *49*, 1964–1974.

Publication Date (Web): September 11, 2015 | doi: 10.1021/bk-2015-1194.ch012

53. Dong, M.; Cheng, W.; Li, Z.; Demopoulos, G. P. Solubility and stability of nesquehonite ($MgCO_3 \cdot 3H_2O$) in NaCl, KCl, $MgCl_2$, and NH_4Cl solutions. *J. Chem. Eng. Data* **2008**, *53*, 2586–2593.
54. Ferrini, V.; De Vito, C.; Mignardi, S. Synthesis of nesquehonite by reaction of gaseous CO_2 with Mg chloride solution: its potential role in the sequestration of carbon dioxide. *J. Hazard. Mater.* **2009**, *168*, 832–837.
55. Kloprogge, J. T.; Martens, W. N.; Nothdurft, L.; Duong, L. V.; Webb, G. E. Low temperature synthesis and characterization of nesquehonite. *J. Mater. Sci. Lett.* **2003**, *22*, 825–829.
56. Ming, D. W.; Franklin, W. T. Synthesis and characterization of lansfordite and nesquehonite. *Soil Sci. Soc. Am. J.* **1985**, *49*, 1303–1308.
57. Sutradhar, N.; Sinhamahapatra, A.; Pahari, S. K.; Pal, P.; Bajaj, H. C.; Mukhopadhyay, I.; Panda, A. B. Controlled synthesis of different morphologies of MgO and their use as solid base catalysts. *J. Phys. Chem. C* **2011**, *115*, 12308–12316.
58. Vágvölgyi, V.; Hales, M.; Frost, R. L.; Locke, A.; Kristóf, J.; Horváth, E. Conventional and controlled rate thermal analysis of nesquehonite $Mg(HCO_3)(OH) \cdot 2(H_2O)$. *J. Therm. Anal. Calorim.* **2008**, *94*, 523–528.
59. Harrison, A. L.; Power, I. M.; Dipple, G. M. Accelerated carbonation of brucite in mine tailings for carbon sequestration. *Environ. Sci. Technol.* **2013**, *47*, 126–134.
60. Hopkinson, L.; Kristova, P.; Rutt, K.; Cressey, G. Phase transitions in the system $MgO–CO_2–H_2O$ during CO_2 degassing of Mg-bearing solutions. *Geochim. Cosmochim. Acta* **2012**, *76*, 1–13.
61. Mitsuhashi, K.; Tagami, N.; Tanabe, K.; Ohkubo, T.; Sakai, H.; Koishi, M.; Abe, M. Synthesis of microtubes with a surface of "house of cards" structure via needlelike particles and control of their pore size. *Langmuir* **2005**, *21*, 3659–3663.
62. Smithson, G. L.; Bakhshi, N. N. Kinetics and mechanism of carbonation of magnesium oxide slurries. *Ind. Eng. Chem. Process Des. Dev.* **1973**, *12*, 99–106.
63. Xiong, Y.; Lord, A. S. Experimental investigations of the reaction path in the $MgO–CO_2–H_2O$ system in solutions with various ionic strengths, and their applications to nuclear waste isolation. *Appl. Geochemistry* **2008**, *23*, 1634–1659.
64. Zhao, L.; Sang, L.; Chen, J.; Ji, J.; Teng, H. H. Aqueous carbonation of natural brucite: relevance to CO_2 sequestration. *Environ. Sci. Technol.* **2009**, *44*, 406–411.
65. Giammar, D. E.; Bruant, R. G.; Peters, C. A. Forsterite dissolution and magnesite precipitation at conditions relevant for deep saline aquifer storage and sequestration of carbon dioxide. *Chem. Geol.* **2005**, *217*, 257–276.
66. Sandengen, K.; Jøsang, L. O.; Kaasa, B. Simple method for synthesis of magnesite ($MgCO_3$). *Ind. Eng. Chem. Res.* **2008**, *47*, 1002–1004.
67. Hövelmann, J.; Putnis, C. V; Ruiz-Agudo, E.; Austrheim, H. Direct nanoscale observations of CO_2 sequestration during brucite [$Mg(OH)_2$] dissolution. *Environ. Sci. Technol.* **2012**, *46*, 5253–5260.

Publication Date (Web): September 11, 2015 | doi: 10.1021/bk-2015-1194.ch012

68. Saldi, G. D.; Jordan, G.; Schott, J.; Oelkers, E. H. Magnesite growth rates as a function of temperature and saturation state. *Geochim. Cosmochim. Acta* **2009**, *73*, 5646–5657.
69. *Specialty Minerals - Mineral Technologies. What is PCC - Precipitated Calcium Carbonate?*. http://www.mineralstech.com/Pages/SMI/Precipitated-Calcium-Carbonate-%28PCC%29.aspx (accessed on July 8, 2015)
70. Willett, J. C. *2013 Minerals Year Book: Crushed Stone*, 2015. http://minerals.usgs.gov/minerals/pubs/commodity/stone_crushed/myb1-2013-stonc.pdf (accessed on June 14, 2015).
71. Global Industry Analysts, 2014. *Limestone - A Global Strategic Business Report*; San Jose, CA, 2014.
72. Bonavetti, V.; Donza, H.; Menendez, G.; Cabrera, O.; Irassar, E. F. Limestone filler cement in low w/c concrete: A rational use of energy. *Cem. Concr. Res.* **2003**, *33*, 865–871.
73. ASTM C. *Standard Specification for Portland Cement*; American Society for Testing and Materials: Philadelphia, PA, 2004.
74. Hooton, R. D.; Nokken, M.; Thomas, M. D. A. Portland-limestone cement: state-of-the- art report and gap analysis for CSA A 3000. *Cem. Assoc. Canada. Univ. Toronto.* **2007**.
75. Lothenbach, B.; Le Saout, G.; Gallucci, E.; Scrivener, K. Influence of limestone on the hydration of Portland cements. *Cem. Concr. Res.* **2008**, *38*, 848–860.
76. Ramachandran, V. S.; Zhang, C. M. Dependence of fineness of calcium-carbonate on the hydration behavior of tricalcium silicate. *Durab. Build. Mater.* **1986**, *4*, 45–66.
77. Heikal, M.; El-Didamony, H.; Morsy, M. S. Limestone-filled pozzolanic cement. *Cem. Concr. Res.* **2000**, *30*, 1827–1834.
78. Vuk, T.; Tinta, V.; Gabrovsek, R.; Kaucic, V. The effects of limestone addition, clinker type and fineness on properties of Portland cement. *Cem. Concr. Res.* **2001**, *31*, 135–139.
79. Sun, H. F.; Hohl, B.; Cao, Y. Z.; Handwerker, C.; Rushing, T. S.; Cummins, T. K.; Weiss, J. Jet mill grinding of portland cement, limestone, and fly ash: Impact on particle size, hydration rate, and strength. *Cem. Concr. Compos.* **2013**, *44*, 41–49.
80. Sprung, S.; Siebel, E. Assessment of the suitability of limestone for producing portland limestone cement (Pkz). *Zement-Kalk-Gips* **1991**, *44*, 1–11.
81. Cyr, M.; Lawrence, P.; Ringot, E. Efficiency of mineral admixtures in mortars: quantification of the physical and chemical effects of fine admixtures in relation with compressive strength. *Cem. Concr. Res.* **2006**, *36*, 264–277.
82. Tai, C. Y.; Chen, F. B. Polymorphism of $CaCO_3$ precipitated in a constant-composition environment. *AIChE J.* **1998**, *44*, 1790–1798.
83. Nebel, H.; Epple, M. Continuous preparation of calcite, aragonite and vaterite, and of magnesium-substituted amorphous calcium carbonate (Mg-ACC). *Zeitschrift für Anorg. und Allg. Chemie* **2008**, *634*, 1439–1443.

Publication Date (Web): September 11, 2015 | doi: 10.1021/bk-2015-1194.ch012

84. Coleyshaw, E. E.; Crump, G.; Griffith, W. P. Vibrational spectra of the hydrated carbonate minerals ikaite , monohydrocalcite , lansfordite and nesquehonite. *Spectrochim. Acta Part A* **2003**, *59*, 2231–2239.
85. Hesse, K. F.; Kueppers, H.; Suess, E. Refinement of the structure of ikaite, ($CaCO_3 \cdot 6H_2O$). *Zeitschrift für Krist.* **1983**, *163*, 227–231.
86. Baeuerlein, E.; Behrens, P.; Epple, M. *Handbook of Biomineralisation*; Weinheim: Wiley-VCH, 2007.
87. Lowenstam, H. A.; Weiner, S. *On Biomineralization*; Oxford University Press: New York, 1989.
88. Mann, S. *Biomineralization*; Oxford University Press: Oxford, U.K., 2001.
89. Meldrum, F. C. Calcium carbonate in biomineralisation and biomimetic chemistry. *Int. Mater. Rev.* **2003**, *48*, 187–224.
90. Colfen, H. Precipitation of carbonates : recent progress in controlled production of complex shapes. *Curr. Opin. Colloid Interface Sci.* **2003**, *8*, 23–31.
91. Lakshminarayanan, R.; Valiyaveettil, S.; Loy, G. L. Selective nucleation of calcium carbonate polymorphs: role of surface functionalization and poly (vinyl alcohol) additive. *Cryst. Growth Des.* **2003**, *3*, 953–958.
92. Li, M.; Mann, S. Emergent nanostructures: water-induced mesoscale transformation of surfactant-stabilized amorphous calcium carbonate nanoparticles in reverse microemulsions. *Adv. Funct. Mater.* **2002**, *12*, 773–779.
93. Park, H. K.; Lee, I.; Kim, K. Controlled growth of calcium carbonate by poly (ethylenimine) at the air/water interface. *Chem. Commun.* **2004**, *1*, 24–25.
94. Cölfen, H.; Antonietti, M. Crystal design of calcium carbonate microparticles using double-hydrophilic block copolymers. *Langmuir* **1998**, *14*, 582–589.
95. Yu, S. H.; Cölfen, H. Bio-inspired crystal morphogenesis by hydrophilic polymers. *J. Mater. Chem.* **2004**, *14*, 2124–2147.
96. Kitamura, M. J. Controlling factor of polymorphism in crystallization process. *Cryst. Growth* **2002**, *237-239*, 2205–2214.
97. Manolia, F.; Kanakisa, J.; Malkajb, P.; Dalasa, E. The effect of aminoacids on the crystal growth of calcium carbonate. *J. Cryst. Growth* **2002**, *236*, 363–370.
98. Küther, J.; Seshadri, R.; Knoll, W.; Tremel, W. Templated growth of calcite, vaterite and aragonite crystals onself-assembled monolayers of substituted alkylthiols on gold. *J. Mater. Chem.* **1998**, *8*, 641–650.
99. Loste, E.; Díaz-Martí, E.; Zarbakhsh, A.; Meldrum, F. C. Study of calcium carbonate precipitation under a series of fatty acid Langmuir monolayers using Brewster angle microscopy. *Langmuir* **2003**, *19*, 2830–2837.
100. Lee, I.; Han, S. W.; Choi, H. J.; Kim, K. Nanoparticle-directed crystallization of calcium carbonate. *Adv. Mater.* **2001**, *13*, 1617.
101. Hosoda, N.; Kato, T. Thin-film formation of calcium carbonate crystals: effects of functional groups of matrix polymers. *Chem. Mater.* **2001**, *13*, 688–693.
102. Ajikumar, P. K.; Lakshminarayanan, R.; Valiyaveettil, S. Controlled deposition of thin films of calcium carbonate on natural and synthetic templates. *Cryst. Growth Des.* **2004**, *4*, 331–335.

Publication Date (Web): September 11, 2015 | doi: 10.1021/bk-2015-1194.ch012

103. Chen, S.-F.; Yu, S.-H.; Jiang, J.; Li, F.; Liu, Y. Polymorph discrimination of $CaCO_3$ mineral in an ethanol/water solution: formation of complex vaterite superstructures and aragonite rods. *Chem. Biol.* **2006**, *18*, 115–122.
104. Kitamura, M. Crystallization and transformation mechanism of calcium carbonate polymorphs and the effect of magnesium ion. *J. Colloid Interface Sci.* **2001**, *236*, 318–327.
105. Loste, E.; Wilson, R. M.; Seshadri, R.; Meldrum, F. C. The role of magnesium in stabilising amorphous calcium carbonate and controlling calcite morphologies. *J. Cryst. Growth* **2003**, *254*, 206–218.
106. Raz, S.; Weiner, S.; Addadi, L. Formation of high-magnesian calcites via an amorphous precursor phase: possible biological implications. *Adv. Mater.* **2000**, *12*, 38–42.
107. Donnet, M.; Bowen, P.; Jongen, N.; Lemaître, J.; Hofmann, H. Use of seeds to control precipitation of calcium carbonate and determination of seed nature. *Langmuir* **2005**, *21*, 100–108.
108. Falini, G.; Fermani, S.; Gazzano, M.; Ripamonti, A. Oriented crystallization of vaterite in collagenous matrices. *Chem. A Eur. J.* **1998**, *4*, 1048–1052.
109. Li, Q.; Ding, Y.; Li, F.; Xie, B.; Qian, Y. Solvothermal growth of vaterite in the presence of ethylene glycol, 1,2-propanediol and glycerin. *J. Cryst. Growth* **2002**, *236*, 357–362.
110. Han, Y. S.; Hadiko, G.; Fuji, M.; Takahashi, M. Effect of flow rate and CO_2 content on the phase and morphology of $CaCO_3$ prepared by bubbling method. *J. Cryst. Growth* **2005**, *276*, 541–548.
111. Kitamura, M.; Konno, H.; Yasui, A.; Masuoka, H. Controlling factors and mechanism of reactive crystallization of calcium carbonate polymorphs from calcium hydroxide suspensions. *J. Cryst. Growth* **2002**, *236*, 323–332.
112. Kitano, Y.; Park, K.; Hood, D. W. Pure aragonite synthesis. *J. Geophys. Res.* **1962**, *67*, 4873–4874.
113. Richter, A.; Petzold, D.; Hofmann, H.; Ullrich, B. Production, properties and application of calcium carbonate powders. 3. Investigations to the transition of vaterite and aragonite in aqueous systems. *Chem. Tech.* **1996**, *48*, 271–275.
114. Zhou, G. T.; Zheng, Y. F. Chemical synthesis of $CaCO_3$ minerals at low temperatures and implication for mechanism of polymorphic transition. *Neues Jahrb. für Mineral.* **2001**, 323–343.
115. Nassif, N.; Pinna, N.; Gehrke, N.; Antonietti, M.; Jäger, C.; Cölfen, H. Amorphous layer around aragonite platelets in nacre. *Proc. Natl. Acad. Sci. U. S. A.* **2005**, *102*, 12653–12655.
116. Belcher, A. M.; Wu, X. H.; Christensen, R. J.; Hansma, P. K.; Stucky, G. D.; Morse, D. E. Control of crystal phase switching and orientation by soluble mollusc-shell proteins. *Nature* **1996**, *381*, 56–58.
117. Falini, G.; Albeck, S.; Weiner, S.; Addadi, L. Control of aragonite or calcite polymorphism by mollusk shell macromolecules. *Science* **1996**, *271*, 67–69.
118. Heywood, B. R.; Mann, S. Molecular construction of oriented inorganic materials: controlled nucleation of calcite and aragonite under compressed Langmuir monolayers. *Chem. Mater.* **1994**, *6*, 311–318.

Publication Date (Web): September 11, 2015 | doi: 10.1021/bk-2015-1194.ch012

119. Litvin, A. L.; Valiyaveettil, S.; Kaplan, D. L.; Mann, S. Template-directed synthesis of aragonite under supramolecular hydrogen-bonded langmuir monolayers. *Adv. Mater.* **1997**, *9*, 124–127.
120. Zhou, G. T.; Yu, J. C.; Wang, X. C.; Zhang, L. Z. Sonochemical synthesis of aragonite-type calcium carbonate with different morphologies. *New J. Chem.* **2004**, *28*, 1027–1031.
121. Li, M.; Lebeau, B.; Mann, S. Synthesis of aragonite nanofilament networks by mesoscale self-assembly and transformation in reverse microemulsions. *Adv. Mater.* **2003**, *15*, 2032–2035.
122. Küther, J.; Nelles, G.; Seshadri, R.; Schaub, M.; Butt, H. J.; Tremel, W. Templated crystallisation of calcium and strontium carbonates on centred rectangular self-assembled monolayer substrates. *Chem. Eur. J.* **1998**, *4*, 1834–1842.
123. Nassif, N.; Gehrke, N.; Pinna, N.; Shirshova, N.; Tauer, K.; Antonietti, M.; Cölfen, H. Synthesis of stable aragonite superstructures by a biomimetic crystallization pathway. *Angew. Chem., Int. Ed. Engl.* **2005**, *44*, 6004–6009.
124. Malhotra, V. M.; Carette, G. G. Silica fume. *Concr. Constr.* **1982**, *27*, 443–446.
125. Siddique, R.; Chahal, N. Use of silicon and ferrosilicon industry by-products (silica fume) in cement paste and mortar. *Cem. Concr. Compos.* **2011**, *55*, 739–744.
126. Shanmugapriya, T.; Uma, R. N. Experimental investigation on silica fume as partial replacement of cement in high performance concrete. *Int. J. Eng. Sci.* **2013**, *2*, 40–45.
127. Huang, C. Y.; Feldman, R. F. Influence of silica fume on the microstructural development in cement mortars. *Cem. Concr. Res.* **1985**, *15*, 285–294.
128. Mazloom, M.; Ramezanianpour, A. A.; Brooks, J. J. Effect of silica fume on mechanical properties of high-strength concrete. *Cem. Concr. Compos.* **2004**, *26*, 347–357.
129. Rao, G. A. Influence of silica fume on long-term strength of mortars containing different aggregate fractions. *Cem. Concr. Res.* **2001**, *31*, 7–12.
130. Toutanji, H. A.; Elkorchi, T. The Influence of silica fume on the compressive strength of cement paste and mortar. *Cem. Concr. Res.* **1995**, *25*, 1591–1602.
131. Sobolev, K. The development of a new method for the proportioning of high-performance concrete mixtures. *Cem. Concr. Compos.* **2004**, *26*, 901–907.
132. Chung, D. D. L. Review: Improving cement-based materials by using silica fume. *J. Mater. Sci.* **2002**, *37*, 673–682.
133. Rasheeduzzafar, S. S. A.; Algahtani, A. S. Reinforcement corrosion-resisting characteristics of silica-fume blended-cement concrete. *Aci Mater. J.* **1992**, *89*, 337–344.
134. Soroushian, P.; Mirza, F.; Alhozaimy, A. Permeability characteristics of polypropylene fiber-reinforced concrete. *ACI Mater. J.* **1995**, *92*, 291–295.
135. Sezer, G. I. Compressive strength and sulfate resistance of limestone and/or silica fume mortars. *Constr. Build. Mater.* **2012**, *26*, 613–618.
136. Zelić, J.; Krstulović, R.; Tkalčec, E.; Krolo, P. Durability of the hydrated limestone-silica fume Portland cement mortars under sulphate attack. *Cem. Concr. Res.* **1999**, *29*, 819–826.

In Advances in CO2 Capture, Sequestration, and Conversion; He, et al.;
ACS Symposium Series; American Chemical Society: Washington, DC, 2015.

137. Bernecker, A.; Wieneke, R.; Riedel, R.; Seibt, M.; Geyer, A.; Steinem, C. Tailored synthetic polyamines for controlled biomimetic silica formation. *J. Am. Chem. Soc.* **2009**, *132*, 1023–1031.
138. Zhang, J.; Stanforth, R. Slow adsorption reaction between arsenic species and goethite (α-FeOOH): diffusion or heterogeneous surface reaction control. *Langmuir* **2005**, *21*, 2895–2901.
139. Johnson, D. C *Accelerated Carbonation of Waste Calcium Silicate Materials*, 2000, SCI Lecture Papers Series.
140. Hills, C. D.; Sweeney, R. E. H.; Buenfeld, N. R. Microstructural study of carbonated cement-solidified synthetic heavy metal waste. *Waste Manage.* **1999**, *19*, 325.
141. Lange, L. C.; Hills, C. D.; Poole, A. B. The effect of accelerated carbonation on the properties of cement-solidified waste forms. *Waste Manage.* **1996**, *16*, 749.
142. Johannesson, B.; Utgenannt, P. Microstructural changes caused by carbonation of cement mortar. *Cem. Concr. Res.* **2001**, *31*, 925–931.
143. ACI Committee 226. Use of Fly Ash in Concrete. *ACI Mater. J., ACI 226.3R* **1987**, 381–409(Title No. 84-M39).
144. ASTM C204. Test Method for Fineness of Portland Cement by Air Permeability Apparatus. In *Annual Book of ASTM Standards*; West Conshohocken, PA, 1994.
145. McKerall, W. C.; Ledbetter, W. B.; Teague, D. J. *Analysis of Fly Ashes Produced in Texas*; College Station, Texas, 1982, No. FHWA/TX-81/21 Intrm Rpt.
146. Kou, S. C.; Poon, C. S.; Chan, D. Influence of fly ash as cement replacement on the properties of recycled aggregate concrete. *J. Mater. Civ. Eng.* **2007**, *19*, 709–717.
147. Jain, J. A.; Neithalath, N. Chloride transport in fly ash and glass powder modified concretes - Influence of test methods on microstructure. *Cem. Concr. Compos.* **2010**, *32*, 148–156.
148. Uysal, M.; Akyuncu, V. Durability performance of concrete incorporating Class F and Class C fly ashes. *Constr. Build. Mater.* **2012**, *34*, 170–178.
149. Stuart, K. D.; Anderson, D. A.; Cady, P. D. Compressive strength studies on portland cement mortars containing fly ash and superplasticizer. *Cem. Concr. Res.* **1980**, *10*, 823–832.
150. Chindaprasirt, P.; Jaturapitakkul, C.; Sinsiri, T. Effect of fly ash fineness on compressive strength and pore size of blended cement paste. *Cem. Concr. Compos.* **2005**, *27*, 425–428.
151. Turkel, S. Long-term compressive strength and some other properties of controlled low strength materials made with pozzolanic cement and Class C fly ash. *J. Hazard. Mater.* **2006**, *137*, 261–266.
152. Paya, J.; Monzo, J.; Borrachero, M. V.; Peris-Mora, E.; Gonzalez-Lopez, E. Mechanical treatment of fly ashes. 2. Particle morphologies in ground fly ashes (GFA) and workability of GFA-cement mortars. *Cem. Concr. Res.* **1996**, *26*, 225–235.

Publication Date (Web): September 11, 2015 | doi: 10.1021/bk-2015-1194.ch012

Publication Date (Web): September 11, 2015 | doi: 10.1021/bk-2015-1194.ch013

Chapter 13

Utilization of Rice Husk in the CO_2-Recycling Gasification System for the Effective Implementation of Bioenergy with Carbon Capture and Storage (BECCS) Technology

Bayu Prabowo,[*,1] Muhammad Aziz,[2] Kentaro Umeki,[3] Mi Yan,[1] Herri Susanto,[4] and Kunio Yoshikawa[5]

[1]Institute of Energy and Power Engineering, Zhejiang University of Technology, Hangzhou, Zhejiang 310014, China
[2]Solutions Research Laboratory, Tokyo Institute of Technology, 2-12-1 Ookayama, Meguro-ku, Tokyo 152-8550, Japan
[3]Division of Energy Science, Luleå University of Technology, 971 87 Luleå, Sweden
[4]Department of Chemical Engineering, Institut Teknologi Bandung, Bandung 40132, Indonesia
[5]Department of Environmental Science and Technology, Tokyo Institute of Technology, Yokohama, Kanagawa 226-8503, Japan
[*]E-mail: 2847728511@qq.com; bayu.prabowo85@gmail.com

A biomass gasification system with CO_2-recycling was developed and examined using the thermal equilibrium model. Performance comparison was conducted against the conventional air gasification system. Sensitivity analyses were performed by varying the gasifier temperature from 750 °C to 950 °C and testing three kinds of rice husk as feedstock: As harvested, naturally dried, or torrefied. The proposed system produced 7.5 % higher efficiency than the conventional air gasification. Moreover, the system exhausted 302 g-CO_2/kWh lower emission and in the form of high purity of CO_2 stream that is favorable for sequestration process. The recycled CO_2 from the gas turbine acted as an effective heat source for the gasifier as well as gasifying agent. The positive effect of CO_2-recycling was more prominent at the lower gasifier temperature. The utilization of high quality feedstock, i.e.

In Advances in CO2 Capture, Sequestration, and Conversion; He, et al.;
ACS Symposium Series; American Chemical Society: Washington, DC, 2015.

low moisture content and low O/C ratio, was favorable for optimizing the effect of CO_2-recycling on the system efficiency. Under the examined conditions, the optimum conditions for gaining the highest system efficiency, 39.4%, were a gasifier temperature of 850 °C with CO_2 recycling ratio of 0.87 and the torrefied feedstock. Application of carbon capture and storage process to the system at the optimum condition resulted in 1.75 kg-CO_2/kg-dry-biomass negative carbon intensity with merely 6.5% efficiency penalty. These results show that the CO_2-recycling gasification system is promising for effectively applying BECCS concept.

Publication Date (Web): September 11, 2015 | doi: 10.1021/bk-2015-1194.ch013

Introduction

In terms of carbon neutrality of biomass, bioenergy can be further driven to carbon-negative by reducing the release of carbon emission from the conversion process to the atmosphere. This concept can be realized by integrating the carbon capture and storage (CCS) process to the biomass-to-energy conversion system, so called bioenergy with carbon capture and storage (BECCS). BECCS offers a unique opportunity for the net removal of atmospheric CO_2 while at the same time fulfilling energy requirements. However as a relatively new emerging concept, BECCS still has large gaps to the implementation. One of the biggest challenge arises from the scale contradiction between the biomass conversion system that in many cases is required to be small (*1*, *2*) and the CCS sub-system that is merely feasible for the relatively large scale and multicomponent process. The balance between these factors is largely unexplored (*1*).

In this study we recognized the potential utilization of biomass CO_2 gasification as a compatible method for supporting the implementation of BECCS. It is related to the fact that CO_2 could react with carbon in biomass through Boudouard's reaction. By this feature, the high yield of producer gas yield, that might lead to high thermal effciciency, could be expected while on the other the producer gas of this process would be mainly consisted of CO and CO_2 (*3*, *4*). Combustion of the producer gas with O_2 will result in a high purity of CO_2 stream that can be sequestrated in a simple process and/or recycled back to the gasifier as gasifying agent. Studies regarding the potential implementation of CO_2 gasification had been frequently conducted (*3–6*). The promising performances also had been shown in some proposed comprehensive systems of CO_2 gasification (including energy conversion units and CO_2 cycle) (*7*, *8*). However, only limited number of research works examined the potential of CO_2 gasification for supporting the application of CCS. Moreover, all of those studies were performed with coal feedstock. Walker et al. (*9*) developed the dry gasification oxy-combustion (DGOC) power cycle. In the system, the recycled flue gas (61 % CO_2 and 32 % H_2O) was utilized in the high pressure O_2 blown gasification and boiler (6 atm.). A 34.2 % system efficiency after CCS was obtained in DGOC that is 4.9 % higher than the oxy-combustion-based CCS technology. Oki et al. (*10*) investigated the CO_2 recycle in the pressurized

In Advances in CO2 Capture, Sequestration, and Conversion; He, et al.;
ACS Symposium Series; American Chemical Society: Washington, DC, 2015.

oxygen blown-Integrated Gasification Combined Cycle (oxy-IGCC) with coal. The proposed system successfully obtained more than 40 % thermal efficiency after CO_2 sequestration.

To the best of our knowledge, CO_2 gasification systems with biomass and especially with the complementary CCS sub-system have hardly been examined. The optimum operating parameters of the biomass system might differ from those of the coal system since the feedstock properties are significantly different. In addition, small and distributed conversion is common for processing biomass. Therefore, system modifications and/or simplifications might be required for the biomass-fed CO_2 gasification systems.

Publication Date (Web): September 11, 2015 | doi: 10.1021/bk-2015-1194.ch013

CO_2-Recycling Gasification System

In order to examine the feasibility of biomass CO_2 gasification as an effective method for implementing BECCS concept, a biomass-based CO_2-recycling gasification system was developed in this study. Compared with the systems established in the previous works (*9*, *10*), some simplifications are proposed: the first simplification consists in the performance of the atmospheric pressure gasification process; the second simplification involves the omission of the steam turbine component for optimal utilization of hot gas turbine flue gas as heat source for the gasifier and as gasifying agent.

Description of the System

Figure 1 shows the scheme of the proposed CO_2-recycling biomass gasification system. Compared to the conventional air blown gasification system, shown in Figure 2, the main improvement of the CO_2-recycling biomass gasification system is the recycle of high temperature flue gas from the gas turbine, which mainly consisted of CO_2, to the gasifier (stream 16 Figure 1) and to the gas turbine cycle (stream 15 Figure 1). To the gasifier, the recycled CO_2 was aimed to be the heat source and gasifying agent in addition to the supplied O_2. It is expected to improve heat recovery and producer gas yield compared with the merely flue gas heat recovery in the air gasification system (stream 9 Figure 2). The Boudouard's reaction (Eq. 1) and the reverse water gas shift reaction (the reverse of Eq. 2) were expected to be the dominant reactions in CO_2 gasifier. Hence, the produced CO and the unconverted CO_2 would be the major composition in the producer gas (stream 2 Figure 1). Combustion of the CO_2-diluted producer gas with oxygen would exhaust high concentration of CO_2, over than 98 % mass, and small amount of water vapor. Thus, it can be recycled in the next process cycle (stream 12 Figure 1). The un-recycled part of the flue gas would go to the CO_2 capture process (stream CO2OUT Figure 1).

$$C + CO_2 \rightarrow 2CO \qquad \Delta H = 171.1\,kJ/mol \qquad (1)$$

$$CO + H_2O \leftrightarrow CO_2 + H_2 \qquad \Delta H = -41.1\,kJ/mol \qquad (2)$$

In Advances in CO2 Capture, Sequestration, and Conversion; He, et al.;
ACS Symposium Series; American Chemical Society: Washington, DC, 2015.

To the gas turbine cycle, the recycled CO_2 was aimed to be the producer gas diluent for controlling the turbine inlet temperature (TIT). It is also expected to improve heat recovery from the flue to the compressed gas (steam 13 to stream 9 in Figure 1) compared with that in air gasification system (stream 8 to stream AIRC1 in Figure 2) where N_2 is the major diluent. This improvement could be expected since CO_2 has lower specific heat capacity and heat capacity ratio than N_2. Three heat exchangers were attached for recovering the heat from the recycled part of the flue gas to the turbine cycle (HX1 Figure 1) and from the producer gas (HX2 and HX3 in Figure 2). In contrast, only two heat exchangers were attachable in air gasification system (HX1 and HX2 in Figure 2) due to the limited existence of significant temperature gradients between the streams.

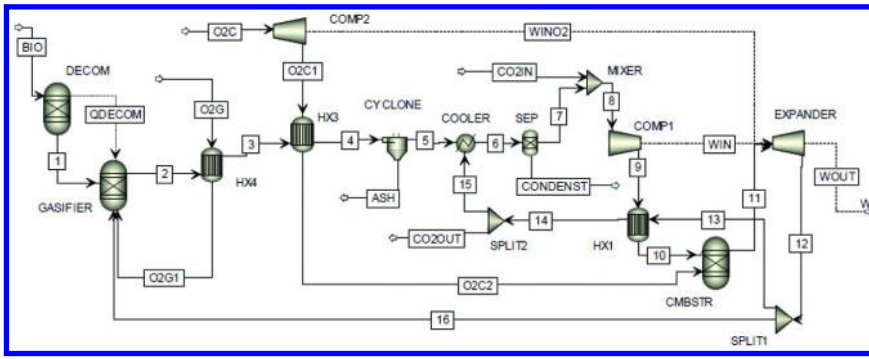

Figure 1. Scheme of the CO_2-recycling biomass gasification system.

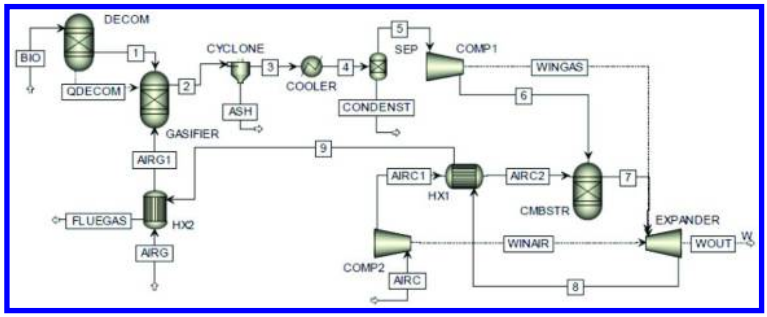

Figure 2. Scheme of the conventional biomass air gasification system.

As shown in Figure 1, CO_2 inlet (stream CO2IN) was installed for supplying CO_2 at the initial stage and will be closed later during the process cycle. CO_2 supplied would be sustained during the cycle since the system is net CO_2 generating. However during the operation cycles in this study, the CO_2 inlet tube was continuously operated to supply the producer gas diluent instead of splitting some of the flue gas back to the system by activating SPLIT2 block. This is since the utilized simulation model cannot accommodate the change of the operating mode. Therefore, the net CO_2 output of the system, which will subsequently go to the CCS process, was calculated as a difference between the CO_2 output (stream CO2OUT) and the CO_2 input (stream CO2IN).

In Advances in CO2 Capture, Sequestration, and Conversion; He, et al.;
ACS Symposium Series; American Chemical Society: Washington, DC, 2015.

Publication Date (Web): September 11, 2015 | doi: 10.1021/bk-2015-1194.ch013

Process Modelling Methodology

Aspen Plus software was utilized for developing the system and simulating its behavior and performance. The process simulation was performed based on the mass and energy balance and chemical equilibrium. The following assumptions were applied: (1) Chemical reactions reached the equilibrium condition (kinetic and physical limitations were neglected), (2) all gases were following the ideal gas properties, and (3) no pressure and temperature drop inside the components and during the transportation between components. The basic parameters of the involved components in the CO_2-recycling biomass gasification system were set as follow:

Publication Date (Web): September 11, 2015 | doi: 10.1021/bk-2015-1194.ch013

Material and Streams

Three kinds of rice husk were tested as feedstock: As harvested, naturally dried, or torrefied . Rice husk is chosen as a feedstock model since it is abundant in Indonesia, the place where the BECCS is promising to be implemented due to the availability of biomass resource and geological storage for CO_2 (*11*). The ultimate and proximate composition of the samples, shown in Table 1, was taken from the previous research (*12*). The moisture content of the as harvested rice husk was adjusted to 25 % to simulate the husk harvested at the rainy season. The feed rate was fixed at 100 kg-wet-biomass/h to simulate the small and distributed power generation system. All of the material and stream from the outside of process were in ambient condition (28 °C, 1 atm.). The streams in the process were in the atmospheric pressure and the possible lowest temperature was 40 °C (after COOLER block). Heating value of the feedstock is calculated based on Boie correlation.

The gasifier component was simulated using the RGibbs reactor model. Syngas composition—consisted of residual C, H_2, CO, CO_2, H_2O, N_2, O_2, NO, NO_2, benzene, toluene, and phenol—and the temperature were calculated based on the minimization of the Gibbs free energy. Prior to the gasifier, a block for decomposition (DECOM block) is required when we used biomass as a feedstock since biomass is a non-conventional component in Aspen Plus. Decomposition block was simulated using RYield where the feedstock was converted into its components including carbon, H_2, O_2, H_2O, and N_2. The yield distribution was specified based on the feedstock's ultimate analysis using a FORTRAN statement in Calculator block. The elements and heat generated from decomposition process were then going into the gasifier block.

The direct gasifier type was applied in this study so that the heat source mainly came from the feedstock partial oxidation. Oxygen supply to the gasifier was set as a dependent variable to maintain the gasifier at the target temperature, 750-950 °C, by setting the design specification and the manipulated variable limit in Design Spec block. During the analysis of this study, oxygen supply is expressed in the mole ratio of its supplied amount to the required oxygen for the stoichiometric combustion of the feedstock (Eq. 3) and termed as 'Equivalence ratio' (E/R). The efficiency of the gasifier is calculated as the low heating value (LHV)-based ratio

In Advances in CO2 Capture, Sequestration, and Conversion; He, et al.;
ACS Symposium Series; American Chemical Society: Washington, DC, 2015.

of the energy of the producer gas to the energy of the biomass supplied in one process cycle, shown in Eq. 4. $\dot{m}$ is the mass flow rate while *p* subscript refer to producer gas and *b* subscript refers to biomass.

Table 1. Proximate and Ultimate Analysis Results of Rice Husk (*12*)

	As harvested	*Naturally dried*	*Torrefied*
Proximate analysis (%wt.)[a]			
VM	59.7	73.2	61.9
FC	7.6	9.3	22.3
Ash	7.8	9.6	13.2
MC	25.0	8.0	2.7
Ultimate analysis (%wt.)[b]			
C	48.0	48.0	55.3
H	4.8	4.8	5.3
O (by difference)	46.5	46.5	38.5
N	0.7	0.7	0.8

[a] wet base , [b] dry, ash-free base

$$\text{Equivalence ratio (E/R)} = \frac{\text{O}_2 \text{ supply } (mol/s)}{\text{O}_2 \text{ for stoichiometric combustion } (mol/s)} \quad (3)$$

$$\text{Gasifier efficiency (\%)} = \frac{LHV_p(MJ/kg_p) \times \dot{m}_p(kg_p/s)}{LHV_b(MJ/kg_b) \times \dot{m}_b(kg_b/s)} \quad (4)$$

Gas Turbine

The gas turbine was simulated as an arrangement of a compressor, a combustor, a turbine/expander, and a heat exchanger. The parameter setting of each component is shown in Table 2. The combustor was also simulated using RGibbs, so that the combustion products were calculated based on the minimization of the Gibbs free energy. Oxygen supply to combustor was specified to be in the exact amount for stoichiometric combustion of producer gas by specifying another FORTRAN statement in Calculator block. For the purpose of maintaining combustor at the targeted temperature, 1100 °C, CO_2 supply to

In Advances in CO2 Capture, Sequestration, and Conversion; He, et al.;
ACS Symposium Series; American Chemical Society: Washington, DC, 2015.

Publication Date (Web): September 11, 2015 | doi: 10.1021/bk-2015-1194.ch013

the compressor as a producer gas diluent was set as a dependent variable and manipulated by using Design Spec block specification. Since there is no heat loss in the system, TIT was assumed to be the same as the combustor temperature. For the purpose of maintaining turbine exit temperature (TET) at the targeted temperature, 1000 °C, pressure ratio of the compressors were set as a dependent variable and manipulated by using another Design Spec block specification.

Table 2. Gas Turbine Parameter Setting

Component	*Parameter*	*Basic setting*
Compressor	Isentropic efficiency (*13*)	72 %
Turbine/Expander	Inlet temperature (*14*, *15*)	1100 °C
	Exit temperature	1000 °C
	Isentropic efficiency (*13*)	80 %
Heat exchanger	Minimum temperature approach	20 °C

$$\text{Gas turbine efficiency}\,(\%) = \frac{(W_t - W_{c,\,p})(MJ/s)}{LHV_p(MJ/kg_p) \times \dot{m}_p(kg_p/s)} \tag{5}$$

The specification of TET to 1000 °C is based on the optimization of the gas turbine efficiency with the applied TIT of 1100 °C at the various pressure ratios, shown in Figure 3. The gas turbine efficiency is calculated as the ratio of the net of the work produced by the gas turbine (subtraction of the turbine work, W_t and the compressor work for the producer gas, $W_{c,\,p}$) to the LHV-based energy of the producer gas (LHV_p), shown in Eq. 5. As shown in Figure 3, the peak of gas turbine efficiency occurred at the pressure ratio range of around 1.9 to 2.7, obtained under the applied TET of 1000 °C to 950 °C. The occurrence of the efficiency peak at certain pressure ratio is typical in regenerated gas turbine and has been reported in some previous works (*16*, *17*). This peak is the result of the optimization between the increase of compressor work input and turbine/expander work output as the pressure ratio increased. However, the obtained optimum range of pressure ratio at 1.9 to 2.7 might not be generally applicable and merely specific for the turbine condition examined in this study. 1000 °C is specified to be the applied TET instead of the lower temperatures in optimum pressure ratio range since some portion of the flue gas would be utilized as heat source for the gasifier without any additional preheating process.

Publication Date (Web): September 11, 2015 | doi: 10.1021/bk-2015-1194.ch013

In Advances in CO2 Capture, Sequestration, and Conversion; He, et al.;
ACS Symposium Series; American Chemical Society: Washington, DC, 2015.

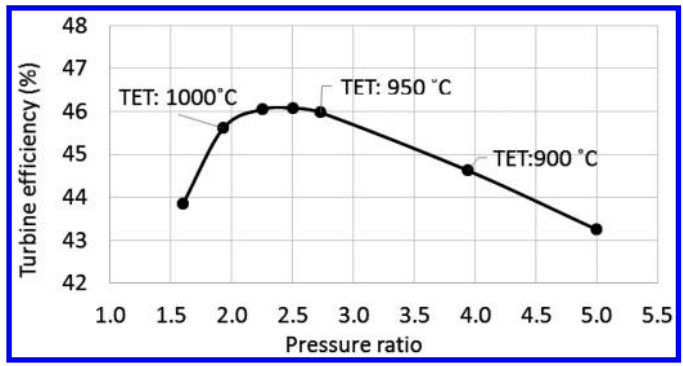

Figure 3. Effect of pressure ratio on the gas turbine efficiency.

Publication Date (Web): September 11, 2015 | doi: 10.1021/bk-2015-1194.ch013

Other Auxiliary Components, Operating Variable, and Process Parameter

The other installed auxiliary components, refer to Figure 1, are two heat exchangers (HX2 and HX3), an oxygen compressor (COMP2), a cyclone (CYCLONE), a gas cooler (COOLER), a liquid separator (SEP), a gas mixer (MIXER), and two gas splitters (SPLIT1 and SPLIT2). The parameter setting of heat exchangers and the compressor were the same as those that were attached in the gas turbine. The cyclone and liquid separators separated all of ash and liquid from the producer gas stream, respectively. The gas cooler outlet temperature was set to 40 °C. In order to simplify the system, the air separation unit was not simulated and the oxygen supply is assumed to come independently from the outside of the system (i.e. oxygen tank or cylinders). The energy requirement of oxygen supply was assumed to be 0.576 MJ/kg-O_2 as taken from the reference (*18*).

The term "CO_2 recycling ratio" used hereafter in this manuscript refers to the amount of recycled CO_2 to the gasifier relative to the amount of carbon in biomass in one process cycle, shown in Eq. 6. This is used since one of the main objectives of this study is to find the optimum amount of recycled CO_2 to the gasifier and since CO_2 recycled to the gas turbine cycle is a dependent variable of TIT. The overall system efficiency, Eq.7, is calculated as the ratio of the net of the work produced by the gas turbine (including the work of the O_2 compressor, W_{c,O_2}) and the energies of the supplied biomass and for supplying O_2 (multiplication of O_2 energy cost, E_{O_2},0.576 MJ/kg-O_2, with the mass flow rate of O_2, $\dot{m}_{O_2}$).

$$\text{CO}_2\text{ recycling ratio} = \frac{\text{CO}_2\text{ recycled to gasifier}\left(mol/s\right)}{\text{C in biomass}\left(mol/kg_b\right)\times \dot{m}_b\left(kg_b/s\right)} \tag{6}$$

$$\text{System efficiency (\%)} = \frac{\left(W_t - W_{c,p} - W_{c,O_2}\right)\left(MJ/s\right)}{LHV_b\left(\frac{MJ}{kg_b}\right)\times \dot{m}_b\left(\frac{kg_b}{s}\right) + E_{O_2}\left(\frac{MJ}{kg_{O_2}}\right)\times \dot{m}_{O_2}\left(\frac{kg_{O_2}}{s}\right)} \tag{7}$$

In Advances in CO2 Capture, Sequestration, and Conversion; He, et al.;
ACS Symposium Series; American Chemical Society: Washington, DC, 2015.

Publication Date (Web): September 11, 2015 | doi: 10.1021/bk-2015-1194.ch013

Analysis of Validity

The validity analysis of this system was partially performed on the gasifier component by comparing the results of the simulation with those of the experiment of mesquite fuel gasification with CO_2-O_2 mixtures (*19*). The gasifier, which is controlled by several chemical reactions and heat equilibriums, is a highly complex sub-system compared with the other components that are mostly controlled by spontaneous irreversible reaction (combustion in gas turbine) and/or physical reactions (heat transfer, compression, expansion and separation). Therefore, the validity of the gasifier is expected to well represent the validity of the overall system.

Table 3. Comparison of the Producer Gas Composition Obtained from Experiment and Simulation

	Run 1		*Run 2*		*Run 3*	
E/R	0.27		0.31		0.37	
CO_2/C	1.07		1.24		1.47	
Gas composition (%)	Exp.	Sim.	Exp.	Sim.	Exp.	Sim.
H_2	4.0	15.6	5.0	16.5	5.0	16.0
CO	24.0	24.3	24.0	25.7	32.0	27.3
CO_2	70.0	54.5	69.0	54.9	60.0	56.3
CH_4	2.0	5.6	2.0	2.9	2.0	0.4
Average RMS error	5.5		5.0		3.7	

The experimental result data were interpreted from graph (*19*). Experimental runs 1 and 2 were performed once, run 3 was repeated.

Table 3 shows the comparison of the producer gas composition obtained in the experiment and in the simulation. CO_2/C is calculated in the same method as CO_2 recycling ratio, Eq. 6. Thermal equilibrium model can generally predict the result of gasification under CO_2-O_2 atmosphere with the average of root mean square (RMS) error of around 3.7 – 5.5. The deviations might imply that equilibrium state was hardly achieved in the experiment. In addition, the overestimation of H_2 was consistently observed in the simulation results. It might be related to the employment of an updraft gasifier type in the experiment. In the updraft gasifier, some extent of moisture content, which is one of the H_2 precursor, might be excluded from the equilibrium reaction system. This also might shifts the equilibrium condition. The moisture exclusion is owing to the combination of the upward direction of the product gas flow and the upper-end position of drying sequence in the gasifier. Results of some previous research suggest that equilibrium model was more suitable for simulating the downdraft gasifier (*20*, *21*). That is since all the product gas was forced toward equilibrium state in the reduction zone before leaving the gasifier. Therefore, results with better agreement with our simulation can be expected from downdraft gasifier

In Advances in CO2 Capture, Sequestration, and Conversion; He, et al.;
ACS Symposium Series; American Chemical Society: Washington, DC, 2015.

experiment. Vice versa, our gasifier simulation might be suitable for predicting the case where downdraft gasifier is employed. Validation with downdraft gasifier experiment is hardly performed at present due to the nonexistence of the report of downdraft CO_2-O_2 gasification experiment to the best of our knowledge.

Performance Comparison of the CO_2-Recycling Biomass Gasification System and the Conventional Biomass Air Gasification System

To examine the potential advantages of CO_2-recycling biomass gasification system, performance comparison was conducted against the conventional air gasification system. Naturally dried rice husk was used as a model feedstock since its properties, e.g. elemental composition, moisture content, etc., can generally represent those of the most typical biomass. Table 4 shows the comparison of the optimum operating condition and the performace of each system. For the CO_2-recycling biomass gasification system, 850 °C gasifier temperature along with 1000 °C TET were found as the optimum operating conditions. The assessment of these optimum conditions will be described in the following section. For the conventional air gasification system, 750 °C gasifier temperature was considered as the optimum condition as suggested in the reference (*22*). Gas turbine was specified to have 900 °C TET, associated with 2.3 pressure ratio, in order to obtain the highest efficiency.

The proposed system produced 7.5 % higher efficiency than the conventional air gasification over the examined conditions. This is resulted by the higher efficiencies of the gasifier and the turbine gas as CO_2 were introduced in those components. In the gasifier, the CO_2 recirculation to the component allow better heat recovery and provide more producer gas precursor than the merely flue gas heat recovery in the air gasification system. In the gas turbine, the usage of CO_2 as a diluent allow better heat recovery from the flue gas to the compressed gas than that of when N_2 is utilized. Hence under the certain applied TIT, a high amount of the diluent flow, which resulted in a high work output, is allowable for the CO_2 diluted fuel gas compared to that of N_2 diluted fuel gas.

The CO_2-recycling gasification system exhausted 302 g-CO_2/kWh lower CO_2 emission than the conventional air gasification over the examined conditions. Moreover, unlike those of the air gasification, the exhaust gas of the CO_2-recycling gasification system was in the form of high purity CO_2 (over than CO_2 98 % mass) which is favorable for the sequestration process. Hence considering the carbon-neutral property of biomass, the attachment of CO_2 sequestration process to this proposed system would realize the concept of BECCS and carbon-negative power plant. If the sequestration is applied, the system would potentially have the negative carbon intensity up to 1.57 kg-CO_2/kg-dry-biomass. Up to 7.0 % efficiency penalty might be required for total CO_2 sequestration. The efficiency penalty was considering the pressurizing process for underground CO_2 injection, 150 atm. The penalty should be less if only transporting is considered. Despite the efficiency penalty, the system efficiency of the CO_2-recycling gasification with CCS is still higher than that of the air gasification without CCS. Moreover, the

Publication Date (Web): September 11, 2015 | doi: 10.1021/bk-2015-1194.ch013

In Advances in CO2 Capture, Sequestration, and Conversion; He, et al.;
ACS Symposium Series; American Chemical Society: Washington, DC, 2015.

air gasification system might require higher energy penalty due to the complexity of the applicable CCS techniques. Therefore, the proposed CO_2-recycling gasification system might be an effective method for applying BECCS concept.

Table 4. Comparison of the Operating Condition and the Performance between the Conventional Air Gasification System and the CO_2-Recycling Gasification System

Comparison item	*Conventional air gasification*	*CO_2-recycling gasification*
Operating condition		
Gasifier temperature (°C)	750	850
Equivalence ratio	0.34	0.30
CO_2 recycling ratio (mole CO_2/mole C)	-	0.75
TIT (°C)	1100	1100
TET (°C)	900	1000
Gas Turbine pressure ratio	2.34	1.93
Performance		
Gasifier efficiency (%)	80.8	87.6
Gas turbine efficiency (%)	37.4	45.4
System efficiency without CCS (%)	30.3	37.8
CO_2 emission (gCO_2/kWh)	1286.6	984.7
System efficiency with CCS (%)	-	30.8

Publication Date (Web): September 11, 2015 | doi: 10.1021/bk-2015-1194.ch013

Sensitivity Analysis

Effect of the CO_2-Recycling Ratio on the Operating Variable and the Thermal Efficiency of the System at Various Gasifier Temperature

Sensitivity analysis was performed to investigate the behavior of the main components and performance of the total system as a function of the amount of CO_2 recycled to the gasifier under various conditions. The first part of sensitivity analysis was conducted by by varying the gasifier temperature to 750 , 850, and 950 °C. Naturally dried rice husk was used as a model feedstock. All material stream described in this section refer to Figure 1.

Figure 4 shows the effect of the CO_2 recycling ratio on the gasifier efficiency and the required equivalence ratio (E/R) to maintain the gasifier at the target temperatures of 750, 850 and 950 °C. As previously mentioned, the recycled CO_2 was obtained from the outlet of turbine/expander component at 1000 °C and no preheating process was applied. The increased portion of the recycled CO_2 into the gasifier resulted in a lower required E/R at the gasifier temperature of 750 °C

In Advances in CO2 Capture, Sequestration, and Conversion; He, et al.;
ACS Symposium Series; American Chemical Society: Washington, DC, 2015.

and 850 °C. The more significant trend shown at the lower gasifier temperature. These implied that the recycled CO_2 from gas turbine acted as an effective heat source and supplied some heat demand in the gasifier. Consequently, the less extent of the feedstock oxidation was required to provide the heat for maintaining the target temperature as the increase of CO_2 recycling ratio. Meanwhile, despite the higher CO_2 supply temperature than the target temperature, an increasing trend of E/R against the increase CO_2 recycling ratio was observed at the gasifier temperature of 950 °C. The increase might imply the significant progress of the endothermic reactions (Boudouard's reactions, Eq. 1, and the reverse water gas shift reaction, the reverse of Eq. 2). The reactions increased the heat demand and subsequently the extent of the feedstock oxidation required to maintain the gasifier at this target temperature.

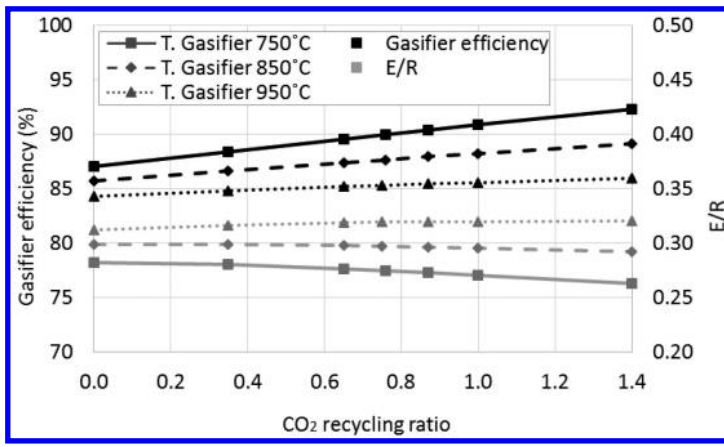

Figure 4. Effect of the CO_2 recycling ratio on the required equivalence ratio and the gasifier efficiency at various gasifier temperatures.

The CO_2 recycling ratio positively affected the gasifier efficiency at all gasifier temperatures, with the more significant increase shown at the lower temperature. At the gasifier temperatures of 750 °C and 850 °C, the gasifier efficiency increase as CO_2 recycling ratio increased was strongly correlated with the reduced E/R. While at the gasifier temperature of 950 °C, the increase implied that the producer gas energy increased due to the enhancement of the Boudouard's and water gas shift reactions was more than the producer gas energy reduced by the increase of the oxidized part of the feedstock.

Figure 5 shows the gas turbine efficiency of the CO_2-recycling gasification as a function of the CO_2 recycling ratio under the various gasifier temperature setting. The gas turbine efficiency at all gasifier temperatures remained constant under the CO_2 recycling ratio below 0.75 and then significantly decreased as the CO_2 recycling ratio was increased. The decrease was related to the significant reduction of the exchanged heat from the flue gas recycled toward the turbine cycle (stream 13) to the compressed gas (stream 9) when the recycled portion of flue

Publication Date (Web): September 11, 2015 | doi: 10.1021/bk-2015-1194.ch013

gas toward the gasifier (stream 16) increased over the CO_2 recycling ratio of 0.75. Under the CO_2 recycling ratio below 0.75, the minimum temperature approach (the pinch temperature) applied between the hot inlet (flue gas, stream 13) and the cold outlet (compressed gas, stream 10) temperatures which allowed a maximum heat transfer to the cold stream. Meanwhile under the CO_2 recycling ratio of 0.75 and above, the minimum temperature approach applied between the hot outlet (stream 14) and the cold inlet (stream 9) temperatures. The temperature setting of the gasifier slightly increased the gas turbine efficiency under the CO_2 recycling ratio of 0.75 and below. This is expected because the producer gases produced in high temperature had low energy content as is indicated by the low gasifier efficiencies (Figure 4).

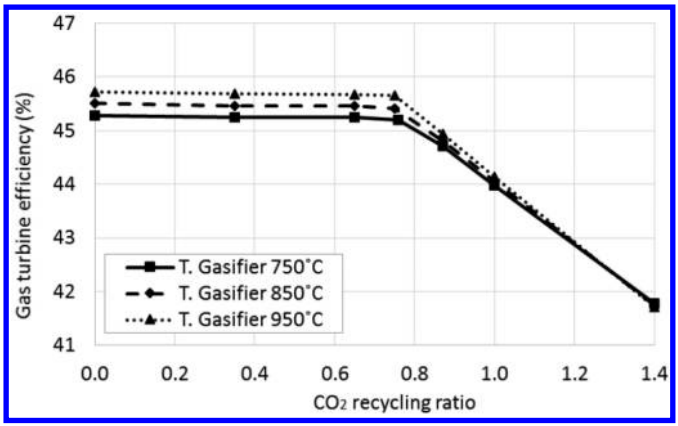

Figure 5. Effect of the CO_2 recycling ratio the gas turbine efficiency at various gasifier temperatures.

Figure 6 shows the overall efficiency of the CO_2-recycling gasification system as a function of the CO_2 recycling ratio under the various gasifier temperature settings. The combination of the increase of the gasifier efficiency, the relatively constant energy for providing O_2, and the decrease of the gas turbine efficiency as the CO_2 recycling ratio increase, resulted in the peak of the system efficiency under the CO_2 recycling ratio of 0.75 at all gasifier temperatures. At the gasifier temperature of 750 °C, the peak of system efficiency, 38.59 %, was 1.2 % higher than that of O_2 gasification-based power generation system (0 CO_2 recycling ratio). At the gasifier temperatures of 850 °C and 950 °C, the peak of system efficiency were down to 37.8 % and 37.0 %, and those were merely 0.8 % and 0.4 % higher than those of O_2 gasification-based power generation system, respectively.

From the thermal equilibrium analysis, it is found that the gasifier temperature as low as 750 °C was essential for this CO_2-recycling gasification system since CO_2 recycle at this condition produced a significant positive trend of the system efficiency. However a problem might occur from the kinetic limitation of the CO_2-char reaction (Eq. 1) that is highly endothermic and slow. Our previous research (*3*) indicated that 750 °C might be too low for expecting the optimum performance of CO_2 gasification. Other research also has shown that catalyst is required to have

Publication Date (Web): September 11, 2015 | doi: 10.1021/bk-2015-1194.ch013

the CO_2 gasification performance close to the equilibrium prediction at 750 °C (*6*). Hence in this first part of study, 850 °C gasifier temperature with 0.75 CO_2 recycling ratio might be the optimum condition for operating the CO_2-recycling gasification system.

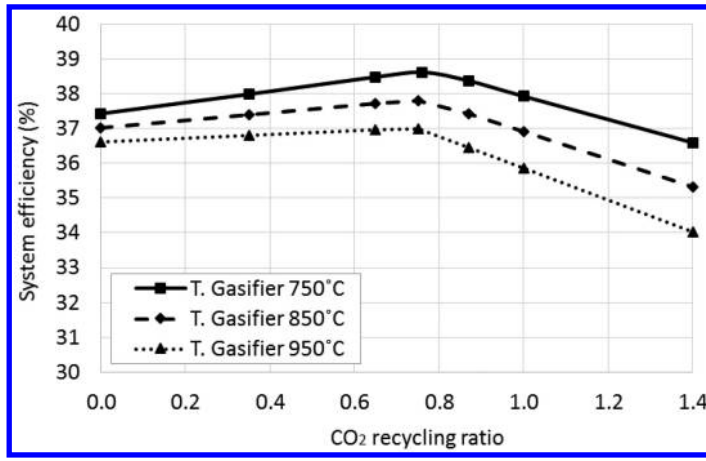

Figure 6. Effect of the CO_2 recycling ratio on the overall system efficiency at various gasifier temperatures.

Effect of the CO_2-Recycling Ratio on the Operating Variable and the Thermal Efficiency of the System over Various Feedstock with Different Properties

Further study was performed to examine the behavior and performance of the proposed system over various feedstock quality. The gasifier temperature was set at 850 °C. Rice husk underwent three types of pretreatment: as harvested, naturally dried, and torrefied, were tested as the feedstock model. As harvested rice husk represent the low quality fuel which has relatively high moisture, 25 % (wet base), and high O/C ratio, 0.97 (dry base). Naturally dried rice husk represent the typical biomass feedstock which has relatively low moisture content, 8 %, but high O/C ratio, 0.97. Torrefied rice husk with its low moisture, 2.7 %, and low O/C ratio, 0.70, represents the high quality feedstock. The properties of the torrefied sample is reported to be obtained from the torrefaction process at 250 °C for 1 h (*13*).

Figure 7 shows the overall efficiency of the CO_2-recycling gasification system as a function of the CO_2 recycling ratio over the various feedstock. The torrefied rice husk produced highest system efficiency followed by naturally dried and then as harvested sample at each CO_2 recycling ratio. This implied that the moisture content of the feedstock is strongly influenced the performance of the gasifier and eventually the total system. Moisture content reduction decreased the heat requirement for evaporation so that lower extent of feedstock oxidation is required. Therefore, the required E/R for torrefied rice husk, 0.28, is the lowest among the other samples (0.29 - 0.30 for naturally dried rice husk and 0.34 - 0.35 for as harvested rice husk). The elimination of water molecule from the gasifier also

Publication Date (Web): September 11, 2015 | doi: 10.1021/bk-2015-1194.ch013

In Advances in CO2 Capture, Sequestration, and Conversion; He, et al.;
ACS Symposium Series; American Chemical Society: Washington, DC, 2015.

allowed the CO_2 involved endothermic reactions (Eq. 1 and the reverse of Eq. 2) to occur in the greater extent and subsequently increase the energy content of the producer gas. Therefore, the net CO_2 yield in gasification for torrefied rice husk, 0.16 - -0.32 kg-CO_2/kg-dry-biomass, is the lowest among the other samples over the examined range of CO_2 recycling ratio shown in Figure 7 (0.37 - -0.05 kg-CO_2/kg-dry-biomass for naturally dried sample and 0.65 - 0.25 kg-CO_2/kg-dry-biomass for as harvested sample).

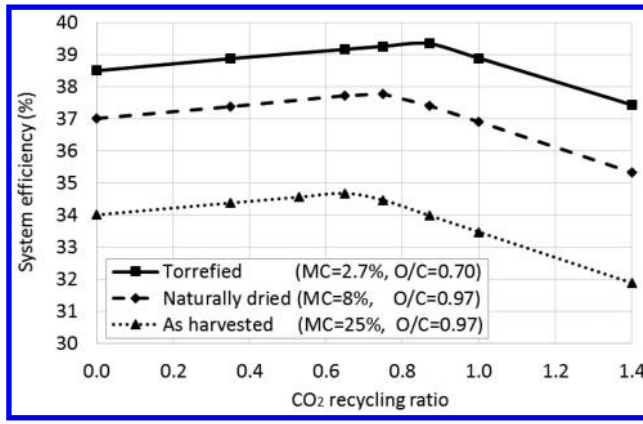

Figure 7. Effect of the CO_2 recycling ratio on the overall system efficiency over various feedstock.

As also shown in Figure 7, the positive effect of CO_2 recycling ratio on the system efficiency is more significant in the system with higher quality feedstock. With the torrefied sample, the optimum CO_2 recycle occurred at the ratio of 0.87 and it produced the highest peak of system efficiency in this study, 39.4%. It increased the system efficiency around 0.9 % from O_2 gasification-based power generation system (0 CO_2 recycling ratio). The optimum ratios and their impacts were smaller over the naturally dried sample and moreover as harvested sample. The increase of the ratio for the optimum CO_2 recycle was related to the increase of the amount of the exhaust gas produced from producer gas combustion (stream 12). As the feedstock with lower moisture content and O/C ratio was supplied, the syngas content on the producer gas increased and so the amount of O_2 required for its stoichiometric combustion. Higher amount of exhaust gas allowed the more of its portion to be recycled to the gasifier (stream 16) without reducing the amount of heat transferred to the compressed gas (stream 9). In view of this occurrence, the more significant effect of CO_2 recycle on the system efficiency can be expected for the feedstock with higher carbon content such as coal or biomass char. Upon the application of sequestration process, the system with torrefied feedstock would potentially have the negative carbon intensity up to 1.75 kg-CO_2/kg-dry-biomass with the final efficiency of 32.9% (6.5% penalty). The values are higher than in those of the system with naturally dried feedstock that were 1.57 kg-CO_2/kg-dry-biomass with the final efficiency of 30.8% (7% penalty).

Publication Date (Web): September 11, 2015 | doi: 10.1021/bk-2015-1194.ch013

Conclusion

A biomass-fed power system utilizing CO_2 recycled to the gasifier and the gas turbine cycle was proposed and analyzed using the thermal equilibrium model. The proposed system produced 7.5 % higher efficiency and exhausted 302 g-CO_2/kWh lower CO_2 emission than the conventional air gasification. In addition, the exhausted CO_2 stream was of high purity and suitable for sequestration or further utilization. The recycled CO_2 from the gas turbine acted as an effective heat source for the gasifier as well as gasifying agent. The positive effect on the system efficiency was more prominent at the lower gasifier temperature. The utilization of high quality feedstock, i.e. low moisture content and low O/C ratio, was favorable for optimizing the effect of CO_2-recycling. Peaks of system efficiency were observed under all examined condition at the CO_2 recycling ratio range of 0.65-0.87. The highest peak, 39.4%, was obtain with torrefied ruch husk under the gasifier temperature of 850 °C and CO_2 recycling ratio of 0.87. Application of CCS to the system at the optimum condition resulted in 1.75 kg-CO_2/kg-dry-biomass negative carbon intensity with merely 6.5% efficiency penalty. These results imply that the CO_2-recycling gasification system is promising for effectively applying BECCS concept.

Publication Date (Web): September 11, 2015 | doi: 10.1021/bk-2015-1194.ch013

Acknowledgments

This work was supported by the National Natural Science Foundation (Grant No. 51406182) and Talented Young Scientists Program (INA-14-003) – People's Republic of China.

References

1. Obersteiner, M.; Karlsson, H. Prestudy of BECCS Bio-Energy with Carbon Capture and Storage. *MISTRA (Online)*, June 2011. http://www.mistra.org/download/18.6ab10bcb1382e9868e9442/1378682263448/Prestudybeccs.pdf (accessed April 1, 2015).
2. Ruan, R.; Chen, P.; Hemmingsen, R.; Morey, V.; Tiffany, D. Size Matters: Small Distributed Biomass Energy Production Systems for Economic Viability. *Int. J. Agric. Biol. Eng.* **2008**, *1*, 64–68.
3. Prabowo, B.; Umeki, K.; Yan, M.; Nakamura, M. R.; Castaldi, M. J.; Yoshikawa, K. CO_2-Steam Mixture for Direct and Indirect Gasification of Rice Straw in a Downdraft Gasifier: Laboratory-Scale Experiments and Performance Prediction. *Appl. Energy* **2014**, *113*, 670–679.
4. Renganathan, T.; Yadav, M. V.; Pushpavanam, S.; Voolapalli, R. K.; Cho, Y. S. CO_2 Utilization for Gasification of Carbonaceous Feedstocks: A Thermodynamic Analysis. *Chem. Eng. Sci.* **2012**, *83*, 159–170.
5. Garcia, L.; Salvador, M. L.; Arauzo, J.; Bilbao, R. CO_2 as a Gasifying Agent for Gas Production from Pine Sawdust at Low Temperatures Using a Ni/Al Coprecipitated Catalyst. *Fuel Process. Technol.* **2001**, *69*, 157–174.

6. Irfan, M. F.; Usman, M. R.; Kusakabe, K. Coal Gasification in CO_2 Atmosphere and Its Kinetics since 1948: A Brief Review. *Energy* **2011**, *36*, 12–40.
7. Bermúdez, J. M.; Ruisánchez, E.; Arenillas, A.; Moreno, A. H.; Menéndez, J. A. New Concept for Energy Storage: Microwave-Induced Carbon Gasification with CO_2. *Energy Convers. Manage.* **2014**, *78*, 559–564.
8. Castaldi, M. J.; Dooher, J. P. Investigation into a Catalytically Controlled Reaction Gasifier (CCRG) for Coal to Hydrogen. *Int. J. Hydrogen Energy* **2007**, *32*, 4170–4179.
9. Walker, M. E.; Abbasian, J.; Chmielewski, D. J.; Castaldi, M. J. Dry Gasification Oxy-Combustion Power Cycle. *Energy Fuels* **2011**, *25*, 2258–2266.
10. Oki, Y.; Inumaru, J.; Hara, S.; Kobayashi, M.; Watanabe, H.; Umemoto, S.; Makino, H. Development of Oxy-Fuel IGCC System with CO_2 Recirculation for CO_2 Capture. *Energy Procedia* **2011**, *4*, 1066–1073.
11. Kraxner, F.; Fuss, S.; Leduc, S.; Aoki, K.; Wicaksono, A.; Yowargana, P.; Heidug, W.; Best, D. *A Geographically Explicit Analysis of BECCS Potential in Indonesia. The 32th International Energy Workshop 2013*, International Energy Agency, Paris, France, June 19−21, 2013.
12. Kuo, P. C.; Wu, W.; Chen, W. H. Gasification Performances of Raw and Torrefied Biomass in a Downdraft Fixed Bed Gasifier Using Thermodynamic Analysis. *Fuel* **2014**, *117*, 1231–1241.
13. Soares, C. *Microturbines: Applications for Distributed Energy Systems*; Butterworth-Heinemann: Oxford, 2011.
14. Doty, D. F. *Phase I Development of an Advanced, Intercooled, Ceramic Gas Microturbine*, Unsolicited Proposal Submitted to the U.S Department of Energy, 2002. http://dotynmr.com/download/pubs/2003_Doty_DOE_CGMT.pdf (accessed April 1, 2015).
15. Takehara, I.; Tatsumi, T.; Ichikawa, Y. Summary of CGT302 Ceramic Gas Turbine Research and Development Program. *J. Eng. Gas Turbines Power* **2002**, *124*, 627–635.
16. Haseli, Y. Optimization of a Regenerative Brayton Cycle by Maximization of a Newly Defined Second Law Efficiency. *Energy Convers. Manage.* **2013**, *68*, 133–140.
17. Haseli, I.; Dincer, G. F.; Naterer, G. F. Thermodynamic Modeling of a Gas Turbine Cycle Combined with a Solid Oxide Fuel Cell. *Int. J. Hydrogen Energy* **2008**, *33*, 5811–5822.
18. Tranier, J. P.; Dubettier, R.; Darde, A.; Perrin, N. Air Separation, Flue Gas Compression and Purification Units for Oxy-Coal Combustion Systems. *Energy Procedia* **2011**, *4*, 966–971.
19. Chen, W.; Thanapal, S. S.; Annamalai, K.; Ansley, R. J.; Mirik, M. Updraft Gasification of Mesquite Fuel Using Air/Steam and CO_2/O_2 Mixtures. *Energy Fuels* **2013**, *27*, 7460–7469.
20. Sharma, A. K. Equilibrium Modeling of Global Reduction Reactions for a Downdraft (Biomass) Gasifier. *Energy Convers. Manage.* **2008**, *49*, 832–842.

Publication Date (Web): September 11, 2015 | doi: 10.1021/bk-2015-1194.ch013

21. Zainal, Z. A.; Ali, R.; Lean, C. H.; Seetharamu, K. N. Prediction of Performance of a Downdraft Gasifier Using Equilibrium Modeling for Different Biomass Materials. *Energy Convers. Manage.* **2001**, *42*, 1499–1515.
22. Reed, T.; Das, A. *Handbook of Biomass Downdraft Gasifier Engine Systems*. The Biomass Energy Foundation Press: Golden, CO, 1988.

Publication Date (Web): September 11, 2015 | doi: 10.1021/bk-2015-1194.ch013

Publication Date (Web): September 11, 2015 | doi: 10.1021/bk-2015-1194.ch014

Chapter 14

Recent Advances in CO_2 Capture by Functionalized Ionic Liquids

Mingguang Pan and Congmin Wang*

Department of Chemistry, ZJU-NHU United R&D Center, Zhejiang University, Hangzhou 310027, P. R. China
***E-mail: chewcm@zju.edu.cn**

CO_2 capture and storage (CCS) receives wordwide attention because the rising emission of CO_2 from fossil fuels is threatening economies, environments, and human health. Ionic liquids address new opportunities for carbon capture because of their promising and unique properties, such as negligible vapor pressures, high thermal stabilities, excellent CO_2 solubilities, and tunable properties. In this review, we summerized the recent advances in the chemisorption of CO_2 using functionalized ionic liquids. It is of great importance to tune the anion structures, including amino acid anions, azole anions, and phenol anions because the anion moieties of ionic liquids usually play a dominant role in the absorption performance of CO_2. Strategies for efficient CO_2 capture, energy-saving release, and rapid absorption kinetics are present. The absorption mechanism was studied through a combination of spectroscopic investigation, and theoretical calculation. The recent developments in carbon capture by non-amino anion-functionalized ionic liquids present limitless potential to enhance the absorption performance of CO_2. Some new concepts, such as multiple site cooperative interactions, the effect of enthalpy, and phase-change ionic liquids, open a door for improving CO_2 capture by tuning the specific structure of the ionic liquid.

In Advances in CO2 Capture, Sequestration, and Conversion; He, et al.;
ACS Symposium Series; American Chemical Society: Washington, DC, 2015.

Publication Date (Web): September 11, 2015 | doi: 10.1021/bk-2015-1194.ch014

Introduction

Emissions of CO_2 from the consumption of fossil fuels have received worldwide attention due to the effects of CO_2 on climate change as a major greenhouse gas (*1–4*). Myriad efforts have been dedicated to one challenging environmental objective—CO_2 capture and storage (CCS) (*5*, *6*). The traditional method for CO_2 capture is chemcial absorption by aqueous amine solutions (*7*, *8*). This liquid-based method with numerous advantages, e.g., high reactivity, low cost, and good absorption capacity, gained in popularity in industry (*9*). However, some serious inherent drawbacks including solvent loss, coorosion, and high energy demand for regeneration, limit the use of this amine-based technology (*10*). Various novel materials and technologies are emerged and developed for efficient, revesible, economical CO_2 capture from the burning of fossil fuels. Metal-organic frameworks (MOFs) are crystalline and porous materials, in which metal centres can coordinate with the intended organic linkers, but also with solvent molecules (*11*). Subsequent activation by removal of the solvent molecules creates unsaturated 'open' metal sites for CO_2 adsorption (*12–17*). Zeolites, crystalline and porous aluminosilicates, have the avarage pore sizes with a conventional value of 9-10 nm, giving advantage of a strong affinity for CO_2 but difficult to regenerate and very sensitive to the presence of water in the flue gas (*18–22*). Membranes with intrinsic porosity exhibit excellent CO_2 permeation performance with low energy requirements relative to conventional amine absorber/desorber columns (*23–27*). Ionic liquids (ILs) offer a new opportunity for developing novel capture systems that are capable of reversibly capturing CO_2 in high capacity, because of their unique properties, such as negligible vapor pressures, high thermal stabilities, excellent CO_2 solubilities, and tunable properties (*28–38*).

Room temperature ionic liquids (RTILs), which are composed entirely of ions and are liquids under ambient conditions, provide unlimited potential to address the challenge of developing novel capture methods. A great deal of experimental and theretical studies on the solubility of CO_2 in the ILs focus on understanding and increasing the physical solubility of CO_2 (*39–51*). Even with these improvements, it is clear that the CO_2 capacity of the ILs for physical dissolution at low partial pressures of CO_2 from post-combustion flue gas is too low to develop a reasonable separation process based on physical solubility. Therefore, the design of functionalized ILs for chemical absorption of CO_2 is highly desirable. The Davis group (*52*) reported the first example of CO_2 chemisorption by an IL that tethered with an amine group on an imidazolium cation in 2002; their work presented that 0.5 moles of CO_2 was captured per mole of IL under ambient pressure (Table 1, entry 1). One of the disadvantages of this method was its low absorption kinetics as a result of the relatively high viscosity of the IL during the absorption of CO_2 (*52*, *53*). Nevertheless, after that, ionic liquid once again became a hot research area as a promising absorbent for CO_2 capture. Some strategies utilizing other functionalized ILs such as amino acid-based ILs (*54*, *55*), azole-based ILs (*56*), and phenol-based ILs (*57*) with improved properties were developed. Some significant progresses in the capture of CO_2 by the ILs have been achieved (*58–69*). Noble and coworkers have explored

In Advances in CO2 Capture, Sequestration, and Conversion; He, et al.;
ACS Symposium Series; American Chemical Society: Washington, DC, 2015.

the use of room temperature ionic liquids (RTILs) in absorptive and membrane technologies for CO_2 capture (*58*, *60*, *70*). Atilhan *et al.* (*67*) reviewed the use of the ILs as alternative fluids for CO_2 capture and natural gas sweetening. Recently, it received increasing attention in CO_2 chemisorption by functionalized ILs. It was demonstrated by Dai that a 1:1 mixture of a superbase and an alcohol-containing task-specific ionic liquids (TSILs) can serve as a non-volatile CO_2 capture solvent (*71*). Brennecke and coworkers studied CO_2 solubility in several commonly used ILs and concluded that the anion plays a dominant role in CO_2 solubility (*72*, *73*). Subsequently, they proposed a new concept for postcombustion CO_2 capture technology that uses phase-change ionic liquids (PCILs) (*74*). Rogers demonstrated chemisorption of CO_2 in 1,3-dialkylimidazolium acetate ionic liquids (e.g., 1-ethyl-3-methyl-imidazoliumacetate ([C_2mim][OAc]), Scheme 1), and evidenced the presence of an unstable N-heterocyclic carbene in a relatively stable IL based on single crystal X-ray diffraction analysis (*75*). Currently, Dai *et al*. establish a facile synthetic strategy to fabricate a porous liquid containing empty cavity by surface engineering of hollow structures with ionic liquid species (*76*). In their work, the ether groups in the supported ionic liquids enhance the gas solubility and selectivity towards CO_2 and the presence of the empty cavities improve gas separation. Therefore, it is of great importance to design the strategies for improving CO_2 capture performance by tuning the structures of ILs.

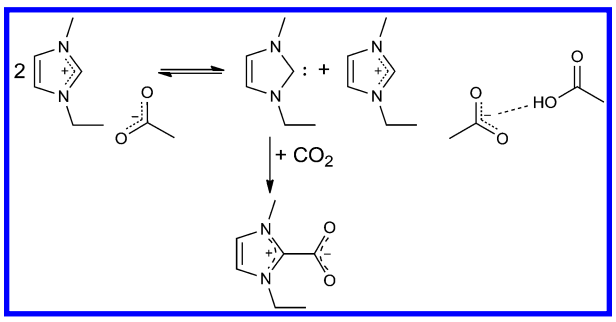

Scheme 1. Proposed reaction of CO_2 and [C_2mim][OAc].

This perspective review focuses on recent advances and strategies in CO_2 capture by functionalized ILs. Herein, we present the strategies for high CO_2 capacity, energy-saving demand, and rapid absorption kinetics. It is entirely feasible to achieved desirable carbon dioxide capture with both high capacity and low energy penalty by carefully designing suitable structures of ILs. CO_2 absorption by different functionalized ILs was explained and investigated at the molecular level through a combination of experiments, spectroscopic methods, and theoretical calculations. Finally, the future directions and prospects for CO_2 capture by designs of functionalized ILs are put forward. There is still a long way to go in order to fully understand the reasons behind some interesting absorption behaviours.

In Advances in CO2 Capture, Sequestration, and Conversion; He, et al.;
ACS Symposium Series; American Chemical Society: Washington, DC, 2015.

Publication Date (Web): September 11, 2015 | doi: 10.1021/bk-2015-1194.ch014

Strategies for Efficient CO_2 Capture

One of the most important features of any CO_2 absorbent is its absorption capacity. An amine group was first projected onto the cation by Davis (*52*) to form the amino-functionalized IL, which reacts with CO_2 in a carbamate mechanism similar to the aqueous amine system, as shown in Scheme 2. This process is atom inefficient because one captured CO_2 molecule require two amines. Subsequently, some other amino-functionalized ILs, such as sulfone anions with ammonium cations were explored for CO_2 capture (*77*). However, all these systems were considered atom inefficient to produce a 1:2 stoichiometry. How to enhance the absorption capacity of gasous CO_2 by tunable designs of the structures of ILs?

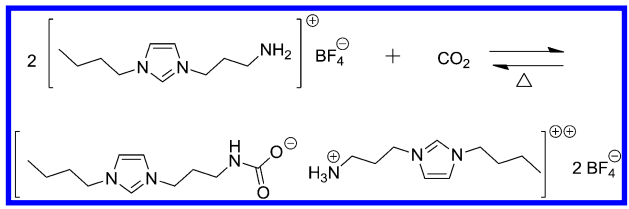

Scheme 2. Reaction mechanism of amino-functionalized IL and CO_2.

Attaching an Amine Group to the Anion

Zhang *et al*. (*55*) employed amino acids as the anion moieties to fabricate amino acid-based ILs. The CO_2 absorption of the ILs supported on porous SiO_2 is fast and reversible with a captured amount of 0.6 mole of CO_2 per mole of IL (Table 2, entires 1-3), resulting from the reaction mechanism of two amine groups with one CO_2. Wang *et al*. (*78*) developed a strategy for improving CO_2 capture through entropic effect by tuning the geometric construction of anion-functionalized ionic liquids with the amino group at the para or ortho position (Table 1, entries 2-5). Brennecke and co-workers (*79*) reported CO_2 absorption with enhanced capacity by phosphonium-based amino acid ILs in a 1:1 stoichiometry (Table 1, entries 6-7), achieving higher molar capacities than cation-functionalized ILs or even aqueous amine absorbents.

Theoretical caculations at the B3LYP/6-31G ++ (d, p) level were carried out on isolated prolinate and methioninate anions binding with CO_2 in a 1:1 stoichiometry, as shown in Scheme 3. The net energies for the formation of the prolinate and methioninate complexes are -71 and -55 kJ mol^{-1}, respectively, which are in good agreement with the experimental values (-80 kJ mol^{-1} and -64 kJ mol^{-1}) measured using calorimetry. The ab initio calculations indicated that tethering the amine to the cation favored the formation of carbamate salt, reflecting the electrostatic stability of the zwitterions, leading to a poor efficient absorption capacity (one mole of CO_2 per two moles of IL), while an equimolar CO_2 capture was achieved when tethering the amine to the anion favored the carbamic acid, indicating the instability of the product dianion. The equimolar reaction mechanisms of CO_2 with $[P_{66614}][Pro]$ and $[P_{66614}][Met]$ were further confirmed by FT-IR spectroscopy. For example, the prolinate N-H stretch at 3290

In Advances in CO2 Capture, Sequestration, and Conversion; He, et al.;
ACS Symposium Series; American Chemical Society: Washington, DC, 2015.

Publication Date (Web): September 11, 2015 | doi: 10.1021/bk-2015-1194.ch014

cm^{-1} disappears, no ammonium bands emerged, and a new band centered at 1689 cm^{-1}, belonging to the new COOH moiety formed from the reaction of CO_2 and [P_{66614}][Pro] (*79*).

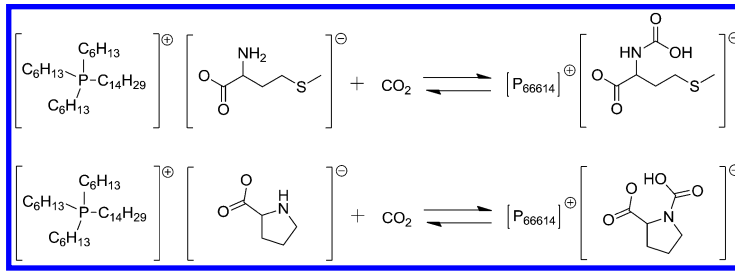

Scheme 3. Reaction schematics of CO_2 with [P_{66614}][Met] (top) and [P_{66614}][Pro] (bottom).

To further increase the absorption capacity, Brennecke (*73*) selected anions of naturally occurring amino acids containing an additional amine group (e.g. lysine, asparaginate, glutaminate) and trihexyl(tetradecyl)phosphonium cations to fabricate functionalized ILs (Table 1, entries 8-14). For example, The CO_2 capacity approached to 1.4 mol CO_2 per mol IL by trihexyl(tetradecyl)phosphonium lysinate ([P_{66614}][Lys]) at room temperature at 1 bar CO_2. Recently, to gain insight of these amine-functionalized amino acid-based ionic liquids as absorbents for CO_2, Riisager (*80*) studied the effect of cation on the absorption capacity of CO_2. Thus, trihexyl(tetradecyl)phosphonium cation ([P_{66614}]) was replaced by trihexyl(tetradecyl)ammonium cation ([N_{66614}]). An absorption capacity of up to 2.1 mol CO_2 per mol of IL was achieved by [N_{66614}][Lys] at ambient temperature under 1 bar of CO_2. They proposed that the [P_{66614}][Lys]-CO_2 and [N_{66614}][Lys]-CO_2 adducts are comprised of two different anion structures (Scheme 4). However, the dramatic increase in viscosity of an amino acid IL would make the practical application for postcombustion CO_2 capture quite challenging.

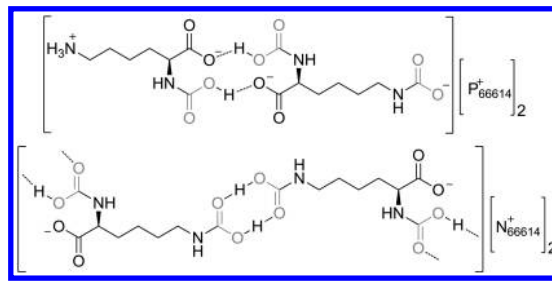

Scheme 4. Proposed structures of the anions in the [P_{66614}][Lys]–CO_2 and [N_{66614}][Lys]–CO_2 adducts (CO_2 groups highlighted in gray color).

In Advances in CO2 Capture, Sequestration, and Conversion; He, et al.;
ACS Symposium Series; American Chemical Society: Washington, DC, 2015.

Publication Date (Web): September 11, 2015 | doi: 10.1021/bk-2015-1194.ch014

Publication Date (Web): September 11, 2015 | doi: 10.1021/bk-2015-1194.ch014

Attaching Amine Groups to Both the Cation and the Anion

To improve the CO_2 absorption efficiency, more amino groups were modified into both the cation and anion moieties of an IL thanks to its facile structure tunability. From this point of view, dual amino-functionalized ILs including an amine-based cation and an amino acid anion were synthesized and developed to enhance the absorption capacity of CO_2 (Table 2, entries 7-10). Zhang *et al*. (*81*) investigated a series of dual amino-functionalized phosphonium ILs, (3-aminopropyl) tributylphosphonium amino acid salts ([aP_{4443}][AA]) as shown in Scheme 5 for the capture of CO_2. Supported absoprtion of CO_2 by [aP_{4443}][AA] ILs on porous SiO_2 was performed to accelerate the absorption rate, which can overcome the high viscosities of these ILs so that it takes only 80 min to complete the CO_2 absorption. Due to the dual-amino functionalization of ILs, both the cation and the anion parts were able to capture CO_2, resulting to an equimolar CO_2 absorption by [aP_{4443}][Gly] and [aP_{4443}][Ala].

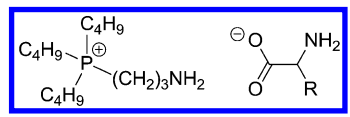

Scheme 5. Structure.of the dual amino-functionalized phosphonium ILs ([aP4443][AA]). [AA]⁻ = [Ala]⁻, [Arg]⁻, [Asn]⁻, [Asp]⁻, [Cys]⁻, [Gln]⁻, [Glu]⁻, [Gly]⁻, [His]⁻, [Ile]⁻, [Leu]⁻, [Lys]⁻, [Met]⁻, [Phe]⁻, [Pro]⁻, [Ser]⁻, [Thr]⁻, [Trp]⁻, [Tyr]⁻ and [Val]⁻.

The theoretical absorption capacity should be about 1.5 moles of CO_2 per mole of IL for dual-amino functionalized ILs because one amine-tethered anion and two amino-tethered cations can catch one CO_2 molecule, respectively. Mu *et al*. (*82*) gave one reason why the absorption capacity could not reach 1.5 moles of CO_2 per mole of IL as the $R\text{-}N^+H_2COO^-$ formed between the amine tethered anion and CO_2 was not enough stable, and can react with another amine to form $R\text{-}NHCOO^-$, leading to the absorption capacity not good as expected with the value of about 1 mole of CO_2 per mole of IL.

Multidentate Cation Coordination

The traditional technology for CO_2 capture was based on aqueous alkanolamine systems, which have some intrinsic drawbacks, including solvent loss, degradation, and high energy consumption for regeneration. Thus, Wang *et al*. (*83*) present a new method using tunable alkanolamine-based ILs (Table 1, entries 46-50) through multidentate cation coordination between alkanolamine and Li^+ for efficient CO_2 capture, eliminating both intensive synthesis of traditional functionalized ILs and the volatility of alkanolamine. For example, [Li(DOBA)][Tf_2N] (DOBA, 2,2'-(ethylenedioxy) bis(ethylamine)) shows a high absorption capacity of 0.90 mole CO_2 per mole IL in the presence of two amine groups in this IL.

Highly efficient CO_2 absorption was realized through the formation of zwitterionic adducts, He *et al*. (*84*) adopt a similar strategy making use

of multidentate cation coordination between Li^+ and an organic base to enhance CO_2-philicity. As an example, the CO_2 capacity of the neutral ligand $PEG_{150}MeBu_2N$ was highly increased from 0.10 to 0.66 (mol CO_2 per mol base) through the formation of zwitterionic complexes stabilized by Li^+.

Incorporating Non-Amino Groups into the Anion

It is in common that amino-functionalized ILs were designed for CO_2 capture making use of the reaction of the amine in the cation or anion with CO_2. Whether can we develop novel non-amino contaning ILs for enhancing the chemisorption of CO_2? Dai and coworkers (*85*) offered a strategy for equimolar CO_2 capture by employing non-amino groups as the anion parts. Treatment of a superbase with weak proton donors such as imidazole, fluorinated alcohol, pyrolidinone, and phenol, affords a series superbase-derived protic ionic liquids (Scheme 6). The superbase plays a vital role as a stronge proton acceptor to deprotonate the weak proton donors directly, providing a thermodynamic driving force for the reaction of the reactive protic ILs with CO_2. An equimolar absorption amount of CO_2 was successfully achieved in this system under atmospheric pressure, where a gravimetric capacity was up to more than 16% (Table 1, entries 15-20). The tunable anion provides the different driving forces for the reaction with CO_2 and affects the absorption amount. Fixing [MTBDH] as the cation, the absorption capacities of [TFE], [Im], and [PhO] anion were 1.13, 1.03, and 0.49 moles of CO_2 per mole of IL, respectively.

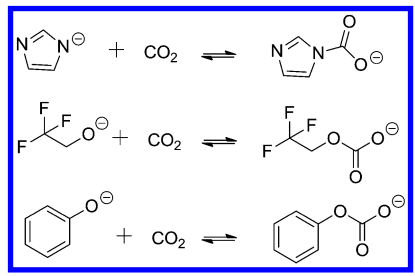

Scheme 6. Reaction mechanism of non-amino anion-functionalized protic ILs and CO_2.

To gain insight into the mechanism of CO_2 absorption by these non-amino anion-functionalized protic ILs, they computed the gas-phase energetics according to the reactions in Scheme 4 at the B3LYP/TZVP level of theory and obtained changes of energy at -116.8, -85.2, and -41.7 kJ mol^{-1} for TFE^-, Im^-, and PhO^-, respectively, which are in agreement with the variations of CO_2 absorption capacity. Furthermore, the equimolar reaction mechnism of CO_2 with [MTBDH][Im] was confirmed by NMR and IR spectroscopy. For exmple, after CO_2 bubbling, a new band observed at 1696.4 cm^{-1} would be assigned to carbamate stretches (*86*, *87*).

In Advances in CO2 Capture, Sequestration, and Conversion; He, et al.;
ACS Symposium Series; American Chemical Society: Washington, DC, 2015.

Publication Date (Web): September 11, 2015 | doi: 10.1021/bk-2015-1194.ch014

Publication Date (Web): September 11, 2015 | doi: 10.1021/bk-2015-1194.ch014

Multiple-Site Cooperative Interactions

In the past decades, great endeavors have been devoted to the capture of CO_2 in 1:1 stoichiometry by the ILs. Whether a new method for capturing CO_2 in more than 1:1 stoichiometry can be achieved? Wang *et al*. (*88*, *89*) first demonstrate that it can achieve an extremely high capacity of up to 1.60 mol of CO_2 per mol of IL in the presence of multiple-site cooperative interactions (Scheme 7), which was originated from the π-electron delocalization in the pydrine ring. In their work, the pyridine-containing anion-functionalized ionic liquids (Table 1, entries 51-55) were selected for significant improvements in CO_2 capture.

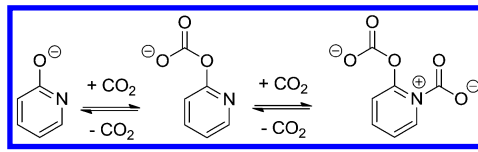

Scheme 7. The plausible mechanism of CO_2 absorption by [P_{66614}][2-Op] through multiple-site cooperative interactions.

The existence of multiple site cooperative interactions was fully evidenced by experimental results, quantum-chemical calculations, spectroscopic investigations, and calorimetric data. In detail, The absorption capacities of [P_{66614}][PhO] and pyridine are 0.85 and 0.013 (mol CO_2 per mol IL), respectively. While, CO_2 capacities of the hydroxypyridine anion-containing ILs, Such as [P_{66614}][2-Op], are significantly higher than the combination of that by phenolate IL and that by pyridine. The Mulliken atomic charges of the nitrogen atom in [P_{66614}][2-Op], [P_{66614}][3-Op], and [P_{66614}][4-Op] are -0.323, -0.235, and -0.285, respectively, far above that in pyridine (-0.161), illustrating the negative charge of the O atom was delocalized to the N atom. The multiple site interaction of [P_{66614}][2-Op] with CO_2 was further investigated by ^{13}C NMR and FTIR spectroscopy (Figure 1). After the uptake of CO_2, two new peaks appeared in IR spectra at 1670 cm^{-1} and 1650 cm^{-1}, which were assigned to the asymmetrial stretching vibrations of carboxylate ion in N-CO_2 interaction and O-CO_2 interaction, respectively. Two new signals in the ^{13}C NMR spectra at 159.3 ppm and 166.6 ppm emerged after the absorption of CO_2, and further confirmed the formation of carbonate and carbamate carbonyl carbon. Furthermore, The appearances of two exothermic peaks in the calorimetry after the capture of CO_2 by [2-Op] also evidenced the presence of multiple-site interactions (N-CO_2 interaction and O-CO_2 interaction) in the hydroxypyridine anion. In situ IR spectroscopy with two-dimensional correlation analysis revealed that the change of the peak at 1586 cm^{-1} and 1650 cm^{-1} preceded 1670 cm^{-1}, suggesting the O atom superior to the N atom binds CO_2 first.

In Advances in CO2 Capture, Sequestration, and Conversion; He, et al.;
ACS Symposium Series; American Chemical Society: Washington, DC, 2015.

Inspired by this work, a new method for enhancing the CO_2 capacity by introducing a carbonyl group into the anion (Table 1, entries 56-61) was subsequently developed by Wang *et al*. (*90*). Thus, an extremely high capacity of up to 1.24 mol CO_2 per mol IL resulted from lewis acid-base and cooperative C-H···Ohydrogen bonding interactions.

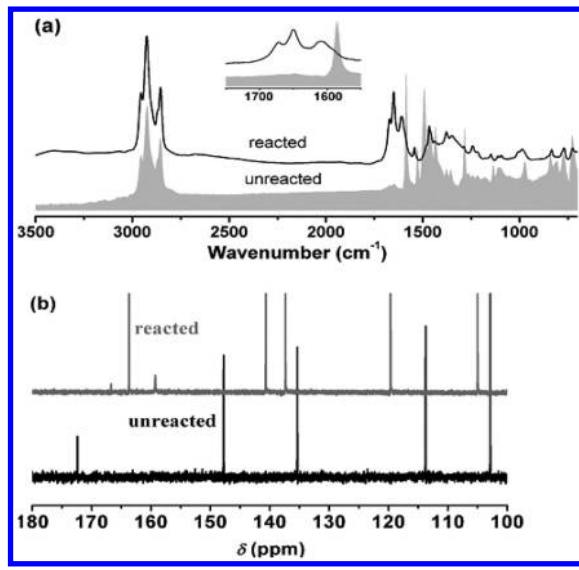

Figure 1. a) IR and b) ^{13}C NMR spectra of pyridine containing anion-functionalized IL $[P_{66614}][2\text{-Op}]$ before and after CO_2 capture.

Publication Date (Web): September 11, 2015 | doi: 10.1021/bk-2015-1194.ch014

Stetric Hindrance

In amino-containing ILs systems, the formation of carbamate salt usually leads to the atom inefficiency for the CO_2 capture. Stetric hindrance provides an effective idea to make the formed carbamic acid more stable than the ammonium carbamate, resulting in equimolar absorption and improved ease of desorption. He *et al*. (*72*) selected sodium *N*-alkglycinates and alaninates with PEG as a suitable solvent to design a steric hindrance-controlled absorbent for CO_2 absorption, realizing a high CO_2 capacity of up to 1:1 stoichiometry.

Publication Date (Web): September 11, 2015 | doi: 10.1021/bk-2015-1194.ch014

Table 1. CO_2 Chemisorption by Different Functionalized Ionic Liquids

Entry	*Ionic liquid*	*Temperature (°C)*	*Time (min)*	*Absorption capacity (mol mol^{-1})*	*ΔH^b (kJ mol^{-1})*	*Reference*
1	[Apmim][BF_4]	22	180	~0.5	—[c]	(*52*)
2	[P_{66614}][*p*-AA]	30	—[a]	0.94	(-41)	(*78*)
3	[P_{66614}][*o*-AA]	30	—[a]	0.60	(-56)	(*78*)
4	[P_{66614}][*p*-ANA]	30	—[a]	0.78	(-54)	(*78*)
5	[P_{66614}][*o*-ANA]	30	—[a]	0.56	(-60)	(*78*)
6	[P_{66614}][Met]	25	—[a]	~0.8	-64	(*79*)
7	[P_{66614}][Pro]	25	—[a]	~0.9	-80	(*79*)
8	[P_{66614}][Tau]	25	—[a]	0.8	—[c]	(*73*)
9	[P_{66614}][Gly]	25	—[a]	1.26	—[c]	(*73*)
10	[P_{66614}][Ala]	25	—[a]	0.66	—[c]	(*73*)
11	[P_{66614}][Sar]	25	—[a]	0.91	—[c]	(*73*)
12	[P_{66614}][Ile]	25	—[a]	0.97	—[c]	(*73*)
13	[P_{66614}][Pro]	25	—[a]	0.88	—[c]	(*73*)
14	[P_{66614}][Met]	25	—[a]	0.88	—[c]	(*73*)
15	[MTBDH][TFE]	23	10	1.13	-116.8	(*85*)
16	[MTBDH][TFPA]	23	60	0.93	—[c]	(*85*)
17	[MTBDH][Im]	23	30	1.03	-85.2	(*85*)

Publication Date (Web): September 11, 2015 | doi: 10.1021/bk-2015-1194.ch014

Entry	*Ionic liquid*	*Temperature (°C)*	*Time (min)*	*Absorption capacity (mol mol^{-1})*	*ΔH^b (kJ mol^{-1})*	*Reference*
18	[(P_2Et)H][Im]	23	10	0.96	-85.2	(*85*)
19	[MTBDH][Pyrr]	23	30	0.86	—[c]	(*85*)
20	[MTBDH][PhO]	23	30	0.49	-41.7	(*85*)
21	[P_{66614}][Pyr]	23	20	1.02	-91	(*56*)
22	[P_{66614}][Im]	23	20	1	-89.9	(*56*)
23	[P_{66614}][Ind]	23	20	0.98	-63.1	(*56*)
24	[P_{66614}][Triz]	23	20	0.95	-56.4	(*56*)
25	[P_{66614}][Bentriz]	23	20	0.17	-37.2	(*56*)
26	[P_{66614}][Tetz]	23	20	0.08	-19.1	(*56*)
27	[P_{66614}][Oxa]	23	20	0.91	-69.8	(*56*)
28	[P_{66614}][PhO]	23	20	0.5	-46.7	(*56*)
29	[P_{66614}][4-Me-PhO]	30	30	0.91	-49.2	(*57*)
30	[P_{66614}][4-MeO-PhO]	30	30	0.92	-51.4	(*57*)
31	[P_{66614}][4-H-PhO]	30	30	0.85	-46.8	(*57*)
32	[P_{66614}][4-Cl-PhO]	30	30	0.82	-38.1	(*57*)
33	[P_{66614}][4-CF_3-PhO]	30	30	0.61	-22.4	(*57*)
34	[P_{66614}][4-NO_2-PhO]	30	30	0.3	-17.1	(*57*)

Continued on next page.

Publication Date (Web): September 11, 2015 | doi: 10.1021/bk-2015-1194.ch014

Table 1. (Continued). CO_2 Chemisorption by Different Functionalized Ionic Liquids

Entry	*Ionic liquid*	*Temperature (°C)*	*Time (min)*	*Absorption capacity (mol mol^{-1})*	*ΔH^b (kJ mol^{-1})*	*Reference*
35	[P_{66614}][3-Cl-PhO]	30	30	0.72	-31.4	(*57*)
36	[P_{66614}][2-Cl-PhO]	30	30	0.67	-27.6	(*57*)
37	[P_{66614}][2,4-Cl-PhO]	30	30	0.48	-29.5	(*57*)
38	[P_{66614}][2,4,6-Cl-PhO]	30	30	0.07	-19	(*57*)
39	[P_{66614}][3-NMe_2-PhO]	30	30	0.94	-42.9	(*57*)
40	[P_{66614}][1-Naph]	30	30	0.89	-27.9	(*57*)
41	[P_{66614}][2-Naph]	30	30	0.86	-32.3	(*57*)
42	[P_{66614}][2-CN-Pyr]	22	—[a]	~0.9	-43	(*54*)
43	[P_{66614}][3-CF_3-Pyr]	22	—[a]	~0.9	-46	(*54*)
44	[Aemim][Tau]	30	—[a]	~0.9	—[c]	(*54*)
45	[Choline][Pro]	35	240	~0.5	—[c]	(*96*)
46	[Li(EA)][Tf_2N]	40	60	0.54	—[c]	(*83*)
47	[Li(DEA)][Tf_2N]	40	60	0.52	—[c]	(*83*)
48	[Li(AEE)][Tf_2N]	40	60	0.55	—[c]	(*83*)
49	[Li(HDA)][Tf_2N]	40	60	0.88	—[c]	(*83*)
50	[Li(DOBA)][Tf_2N]	40	60	0.9	—[c]	(*83*)
51	[P_{66614}][2-Op]	20	—[a]	1.58	—[c]	(*89*)

Publication Date (Web): September 11, 2015 | doi: 10.1021/bk-2015-1194.ch014

Entry	*Ionic liquid*	*Temperature (°C)*	*Time (min)*	*Absorption capacity (mol mol^{-1})*	*ΔH^b (kJ mol^{-1})*	*Reference*
52	$[P_{66614}][4\text{-Op}]$	20	—[a]	1.49	—[c]	(*89*)
53	$[P_{66614}][3\text{-Op}]$	20	—[a]	1.38	—[c]	(*89*)
(*54*)	$[P_{66614}][3\text{-OMe}_3\text{-2-Op}]$	20	—[a]	1.65	—[c]	(*89*)
55	$[P_{66614}][4\text{-ABI}]$	20	—[a]	1.6	—[c]	(*89*)
(*56*)	$[P_{66614}][4\text{-CHO-PhO}]$	30	—[a]	1.01	—[c]	(*90*)
(*57*)	$[P_{66614}][4\text{-EF-PhO}]$	30	—[a]	1.03	—[c]	(*90*)
58	$[P_{66614}][4\text{-Kt-PhO}]$	30	—[a]	1.04	—[c]	(*90*)
59	$[P_{66614}][4\text{-CHO-Im}]$	30	—[a]	1.24	—[c]	(*90*)
60	$[P_{66614}][4,5\text{-2EF-Im}]$	30	—[a]	0.85	—[c]	(*90*)
61	$[\text{Im-EA}][Tf_2N]$	30	—[a]	0.06	—[c]	(*90*)

[a] Absorption time is not mentioned in the literature. [b] Absorption enthalpy is calculated by DFT method, values given in brackets are obtained using the van't Hoff equation. [c] Absorption enthalpy is not mentioned in the literature

Publication Date (Web): September 11, 2015 | doi: 10.1021/bk-2015-1194.ch014

Strategies for Energy-Saving Release

For traditional amino-functionalized ILs, the enthalpy of CO_2 absorption is about 80 kJ mol^{-1} (*59*), which require a huge amount of energy for regeneration. It is an urgent task to design attractive sorbent materials that can capture CO_2 in an efficient and energy-saving manner. Non amino-functionalized ionic liquids are endowed this mission, because their physicochemical properties can be easily tuned by changing the structures of cation and anion. Herein, we present some representative works for reducing the absorption energy of CO_2.

Tuning the Basicity of the Anion

It is realized that the anion part plays a dominant role in determining the chemisorption capacity of CO_2. Therefore, Wang *et al.* (*56*) designed a series of non amino-functionalized ILs such as azole-based ILs to tune the enthalpy of CO_2 chemisorption due to the various basicities of the anion moieties with p*K*a values in DMSO ranging from 19.8 to 8.2. Quantum chemical calculations showed the enthalpy of CO_2 absorption decreaed from 91.0 to 19.1 kJ mol^{-1} in accordance with the decreasing trend of the p*K*a value of the anion in DMSO (Figure 2), resulting in an energy-saving requirement during regeneration, shown in Table 1, entries 21-28. There is a quantitative relationship between the enthalpy of CO_2 absorption and the p*K*a value, indicating that the enthalpy of CO_2 absorption can be quantified by tuning the basicity of the ILs, which is helpful to future design for CO_2 capture.

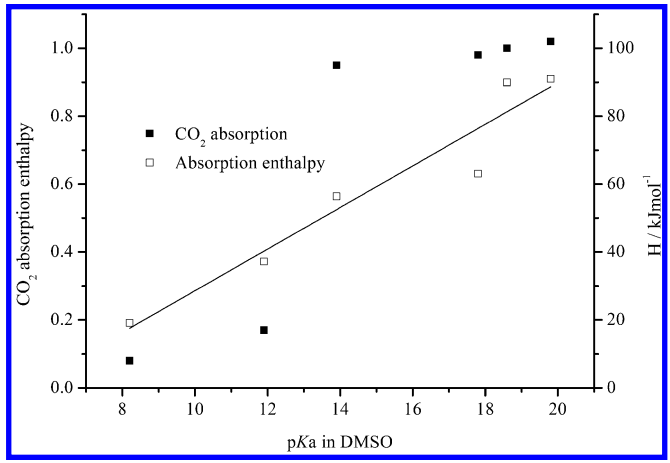

Figure 2. The relationship between CO_2 absorption capacity (■), absorption enthalpy (△H, □), and the pKa value of the anion in DMSO. The linear relationship between △H and the pKa of anion in DMSO is shown: $R^2 = 0.930$.

Thermal gravimetric analysis (TGA) was an effective calorimetric methodology to evaluate the release capability of CO_2. The results reveal that the desorption of CO_2 is more facile when the basicity of the IL decreases, which is in accord with the change trend of the enthalpy of absorption. Furthermore, the absorption capacity of the IL was tuned by the basicity of the IL, for

example, among the mentioned ILs, $[P_{66614}][Tetz]$ has the smallest amount of CO_2 absorption due to its weakest basicity with the p*K*a value of 8.2 in DMSO. While, $[P_{66614}][Pyr]$ captures CO_2 up to 1.02 mol per mol IL, which agrees well with its robustest basicity in DMSO with p*K*a value of 19.8. Therefore, the enthalpy of CO_2 absorption and absorption capacity can be adjusted by tuning the basicity of the ILs, suggesting that it is promising to achieve both efficient CO_2 capture and energy-saving release.

NMR and IR spectroscopy further confirmed the chemisorption of CO_2 in these azole-based ionic liquid systems. The formation of a liquid carbamate via reaction with CO_2 results in an equimolar CO_2 absorption. For exmple, compared with fresh IL $[P_{66614}][Triz]$, a new peak formed at 1736 cm^{-1} upon the uptake of CO_2, attributable to a carbamate (C=O) stretch. Similarly, after the absorption of CO_2, a signal at 160.7 ppm appears in ^{13}C NMR spectrum, which can be assigned to carbamate carbonyl carbon.

Publication Date (Web): September 11, 2015 | doi: 10.1021/bk-2015-1194.ch014

Tuning the Substituent of the Anion

The substituent effect of the anion works on the absorption capacity of CO_2 because the enthalpy of CO_2 absorption can be tuned by the substituent of the anion-functionalized ILs. Wang *et al.* (*57*) designed a series of substituent-containing phenolic ILs to investigated the chemisorption of carbon dioxide. It was found that the enthalpy of CO_2 absorption significantly depended on the electron-withdrawing ability, position, and number of the substituted group in the anion of these phenolic ILs (Table 1, entries 29-41). The results showed that the stronger the electron-withdrawing ability of the substituent on the anion, the lower the enthalpy of CO_2 absorption as well as CO_2 absorption capacity. Moreover, the increasing numbers of the electron-with-drawing substituent result in the decreasing absorption enthalpy and capacity of CO_2.

The interactions between CO_2 and these phenolic ILs were studied by IR and NMR spectroscopy to support the experimental results. During the chemisorption of CO_2, reaction with CO_2 affords a liquid carbonate salt. For example, a new band at 1617 cm^{-1} in the IR spectrum and a new peak at 161 ppm in the ^{13}C NMR spectrum of $[P_{66614}][4\text{-Cl-PhO}]\text{-}CO_2$ upon CO_2 absorption strongly evidenced the formation of the carbonate salt. To gain insight into the effect of substituents on the phenolic anion on the enthalpy of CO_2 absorption, the Mulliken atomic charge of the oxygen atom in such substituted phenolic anions was calculated at the B3LYP/6-31++G (p, d) level. The results showed that the decrease of charge on the oxygen atom lead to the decrease of absorption enthalpy as a result of a weaker interaction between the chemical binding site and the acidic CO_2. Thus, the interaction strength of the binding site in the anion with CO_2 was tuned by the substituent, which is useful for designing ILs with low energy requirements during the regeneration.

Brennecke and coworkers (*54*) reported a similar work on the CO_2 capture by a class of functionalized ILs with substituted aprotic heterocyclic anions such as trihexyl(tetradecyl)phosphonium 2-cyanopyrrolide ($[P_{66614}][2\text{-CN-Pyr}]$), as seen in Table 1, entries 42-43. Likewise, the reaction enthalpy of CO_2 absorption was

modulated by altering the substituent on the anion, indicating energy demands during the desorption process could be properly regulated and controlled.

Phase-Change Ionic Liquids (PCILs)

It is true that the chemical tunability of ILs provides innumerable opportunities to achieve desirable CO_2 capture and energy-saving release. It still needs a strong impulsion to reduce the energy consumption during the regeneration. Phase-change ionic liquids (PCILs), which are solid salts at normal flue gas processing temperatures, react with CO_2 to form liquid PCIL-CO_2 complexes, whose melting points are sufficiently lower than those of the pure PCILs.

Brenneckes *et al.* (*74*) discovered a series of phase-change ionic liquids based on aprotic heterocyclic anions (AHAs) (Scheme 8). Utilizing this unique phase transition ability, it can be anticipated that a postcombustion CO_2 capture with PCILs has the potential to require less parastitic energy, because phase-change that the liquid complex changes back to a solid releases heat, reducing the added energy for regeneration.

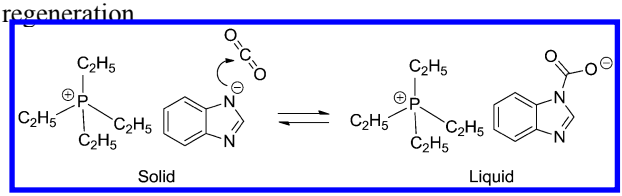

Scheme 8. Schematic of [P_{2222}][BnIm]-CO_2 reaction.

Strategies for Rapid Absorption Kinetics

Despite great advances have been obtained by amino-functionalized ILs for CO_2 capture, there is still enormous room for enhancing the development of efficient CO_2 capture and storage. For example, the formation of intermolecular hydrogen bonding dramatically increased the visicity of the amino-functionalized IL systems by up to two orders of magnitude, resulting to slow absorption rate. Another remarkable disadvantage is that it always requires a huge amount of energy to strip the chemisorbed CO_2 during the regeneration. Thus, the question, how to reduce the visicity and improve absorption rate, appears relevant. Many groups have already realized the importance of this point. With the aid of a molecular dynamics simulation method, Maginn *et al.* (*91*) explained the dramatic increase in viscosity, which is due to the formation of strong and densely hydrogen-bonded networks between the zwitterions and dication species formed after the uptake of CO_2 by the amino-based cation. Despite some progresses have been achieved to avoid the formation of carbamate salt through tethering the amine to the anion (*73*, *92*), the viscosity only can be mitigated to a limited degree. Thus, Non-amino anion-functionalized ILs in the absence of hydrogen bonding networks received particular attention for CO_2 capture in the recent years. Therefore, in this case, we summarize the general strategies to reduce the viscosity and improve the absorption kinetics during the absorption of CO_2 by functionalized ILs.

Publication Date (Web): September 11, 2015 | doi: 10.1021/bk-2015-1194.ch014

In Advances in CO2 Capture, Sequestration, and Conversion; He, et al.;
ACS Symposium Series; American Chemical Society: Washington, DC, 2015.

Publication Date (Web): September 11, 2015 | doi: 10.1021/bk-2015-1194.ch014

Table 2. CO_2 Chemisorption by Ionic Liquid-Based Mixtures

Entry	*System*	*Ratio*[a]	*Absorption T (°C)*	*Absorption time (min)*	*CO_2 capacity (mol mol^{-1})*	*Reference*
1	$[P_{4444}][Gly]$-SiO_2	—[b]	—[c]	100	~0.6	(*55*)
2	$[P_{4444}][Ala]$-SiO_2	—[b]	—[c]	100	~0.65	(*55*)
3	$[P_{4444}][\beta\text{-Ala}]$-$SiO_2$	—[b]	—[c]	100	~0.6	(*55*)
4	$[Hmim][Tf_2N]$-MEA	1 : 1	40	25	~0.5	(*93*)
5	$[EmimOH][Tf_2N]$-DEA	1 : 1	40	25	~0.3	(*93*)
6	[Choline][Pro]-PEG200	1 : 1	35	50	~0.61	(*96*)
7	$[AP_{4443}][Gly]$-SiO_2	—[b]	—[c]	80	~1.2	(*81*)
8	$[AP_{4443}][Ala]$-SiO_2	—[b]	—[c]	80	~1.15	(*81*)
9	$[AP_{4443}][Val]$-SiO_2	—[b]	—[c]	80	~1.1	(*81*)
10	$[AP_{4443}][Lau]$-SiO_2	—[b]	—[c]	80	~1.08	(*81*)
11	$[Im_{21}OH][Tf_2N]$-DBU	1 : 1	20	30	1.04	(*71*)
12	$[Im_{21}OH][Tf_2N]$-DBU	1.2 :1	20	30	1.11	(*71*)
13	$[N_{ip,211}OH][Tf_2N]$-DBU	1 : 1	20	30	1.02	(*71*)
14	$[Im_{21}OH][Tf_2N]$-MTBD	1 : 1	20	30	1.02	(*71*)
15	$[Im_{21}OH][Tf_2N]$-BEMP	1 : 1	20	60	0.81	(*71*)
16	$[Bmim][Tf_2N]$-DBU	1 : 1	23	30	0.99	(*97*)

Continued on next page.

Publication Date (Web): September 11, 2015 | doi: 10.1021/bk-2015-1194.ch014

Table 2. (Continued). CO_2 Chemisorption by Ionic Liquid-Based Mixtures

Entry	*System*	*Ratio*[a]	*Absorption T (°C)*	*Absorption time (min)*	*CO_2 capacity (mol mol^{-1})*	*Reference*
17	[Bmim][BF_4]-DBU	1 : 1	23	90	0.80	(*97*)
18	[Emim][BF_4]-DBU	1 : 1	23	30	0.93	(*97*)
19	[Bmim][BF_6]-DBU	1 : 1	23	60	0.75	(*97*)
20	[Bmim][Tf_2N]-MTBD	1 : 1	23	30	1.08	(*97*)
21	[Pdmim][Tf_2N]-DBU	1 : 1	23	30	0.64	(*97*)
22	[Bmim][Tf_2N]-EtP_2	1 : 1	23	30	1.00	(*97*)

[a] The molar ratio of the ionic liquids mixture. [b] The ratio is not mentioned in the literature. [c] Absorption temperature is not mentioned in the literature.

Publication Date (Web): September 11, 2015 | doi: 10.1021/bk-2015-1194.ch014

Eliminating the Intermolecular Hydrogen Bonds

To avoid the formation of hydrogen bonds, Wang and coworkers (*56*) provided a class of non-amino anion-functionalized ILs such as azole-based ILs for CO_2 capture (Table 1, entries 21-28). An important feature of these azole-based ILs is that the chemisorption kinetic of CO_2 is rapid (Figure 3). It can be seen that the absorption was almost complete in the first 10 min with a faster rate than that by conventional amino-functionalized ILs. The absorption rate by the ILs may result from the differences of viscosity during the CO_2 absorption. Contrary to the dramatic increase in the viscosity during the absorption of CO_2 by amino-functionalized ILs, there is no obvious change of viscosity in the absence of hydrogen bonding networks upon CO_2 capture by non-amino azole-based ILs. As examples, the viscosites of $[P_{66614}][Pyr]$ and $[P_{66614}][Im]$ varied only from 245.4 to 555.1 cP and 810.4 to 648.7 cP respectively after the uptake of CO_2. Similarly, the viscosites of substituted phenol-based and pyrrolide-based ILs changed little during the absorption of CO_2 in the absence of hydrogen bonding networks, which resulted in rapid absorption kinetics.

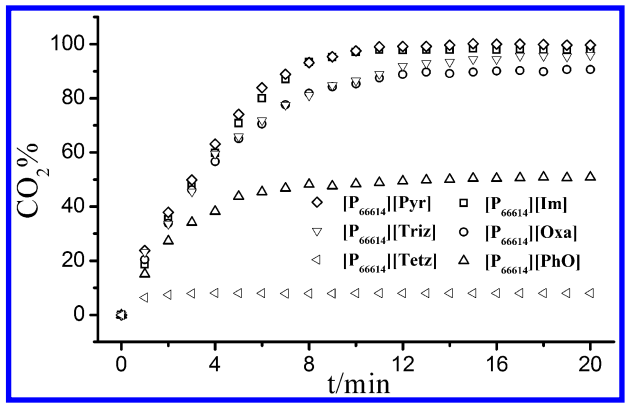

Figure 3. Rapid CO_2 absorption by some non-amino anion-functionalized ILs: ◇ $[P_{66614}][Pyr]$, □ $[P_{66614}][Im]$, ▽ $[P_{66614}][Triz]$, ○ $[P_{66614}][Oxa]$, ◁ $[P_{66614}][Tetz]$, △ $[P_{66614}][PhO]$.

Mixed Solutions Based on ILs

Considering the disadvantages of amine-functionalized ILs, such as high viscosity, multi-step synthesis, and no cost-competition with commodity chemicals, Noble *et al.* (*93*) reported an industrially attractive and unprecedented method for rapid and reversible capture of 1 mol CO_2 per 2 moles amine by using organic amine/RTIL solutions (Table 2, entries 4-5). The RTILs with desirable properties, i.e., nonvolatility, enhanced CO_2 solubility, and lower heat capacities, were mixed with commercial amines to capture CO_2, which offered significant advantages, including increased energy efficiency. The absorption reaction was rapid and complete after 25 min because RTILs with Tf_2N anions have relatively low viscosities, and the insoluble amine-carbamate

precipitate helps to drive the capture reaction. Taking advantage of the significant performance of functionalized ILs in the uptake of CO_2. Li and coworkers (*94*) realized that mixing functionalized ILs with N-methyldiethanolamine (MDEA) solution is a good way to improve the efficiency of ILs in the absorption of CO_2. Thus, $[N_{1111}][Gly]$, $[N_{2222}][Gly]$, $[N_{1111}][Lys]$, $[N_{2222}][Lys]$ was selected for CO_2 absorption due to their extremely high solubility in water. The mixture of functionalized ILs and MDEA aqueous solution greatly increased the absorption rate of CO_2 because plenty of MDEA deprotonate the formed zwitterions. In addition, Chen *et al*. (*95*) reported that hydrogen bonding between protonated monoethanolamine and chloride ion can benefit the CO_2 capture in hydroxyl imidazolium based ionic liquids and monoethanolamine mixture. Recently, Wang *et al*. (*83*) presented a new strategy for CO_2 chemisorption by a class of tunable alkanolamine-based IL. The formation of the multidentate coordination interactions between alkanolamine and alkali metallic ions in a quasi-aza-crown ether fashion results to the high capacity and rapid kinetics of CO_2 absorption by tuning the chelation of the alkali metal salt.

To deal with the high viscosity of amino-functionalzied ILs and solvent loss during the capture of CO_2, the Han group (*96*) employed another strategy by mixing an amino-functionalized IL (2-hydroxyehtyl-trimethyl-ammonium 2-pyrrolidine carboxylic acid salt, [Choline][Pro]) and polyethylene (PEG 200) as shown in Table 2, entry 6. Addition of PEG 200 in the IL enhanced the absorption rate of CO_2 significantly. PEG 200 acts as a solvent to decrease the viscosity of the system upon CO_2 capture, which is kinetically beneficial for the absorption of CO_2.

Mixtures of an amidine with an alcohol, alkylamine, or amino alcohol have been reported for the capture of CO_2. The associated key problem of these methods is the volatility of their molecular constituents. To overcome loss of the absorbents, Dai and coworkers (*71*) proposed an integrated strategy with an equimolar mixture of a hydroxyl-functionalized IL as a proton donor and a superbase as a proton acceptor, which was capable of rapid and reversible capture of about 1 mol CO_2 per mol IL (Table 2, entries 11-15). Furthermore, they also present another method for CO_2 capture to avoid the use of volatile alcohol or amine by the mixture of imidazolium ILs and a superbase (Table 2, entries 16-22) (*97*). Similarly, it also reach rapid and equimolar absorption of CO_2 in these systems.

Effect of Water

Due to the inescapability of water in postcombustion CO_2, a great deal of researches emerged and developed to investigate the effect of water on CO_2 capture. It has been found that adding water into ionic liquids results to a dramatically decreased viscosity. The effect of water content on the capacity of CO_2 for a series of amine-functionalized ionic liquids with tetra-alkylphosphonium cations was studied. As a result, the presence of water reduces the viscosity of both pure IL samples and CO_2-complexed IL samples and causes a slight decrease in CO_2 molar capacity, presumably due to reprotonation of the anion (*98*, *99*). Recently, Brennecke (*100*) investigated the effect of water on aprotic heterocyclic anion-functionalized ILs for CO_2 capture. In contrast to the previous

In Advances in CO2 Capture, Sequestration, and Conversion; He, et al.;
ACS Symposium Series; American Chemical Society: Washington, DC, 2015.

Publication Date (Web): September 11, 2015 | doi: 10.1021/bk-2015-1194.ch014

works, water improve the solubility of CO_2 in trihexyl(tetradecyl)phosphonium 2-cyano-pyrrolide [P_{66614}][2-CNPyr] and significantly altered the slope of the isotherm. The enhanced CO_2 solubility may result from the formation of bicarbonate and changes in the activity of the IL-CO_2 complex upon addition of water. Briefly, in one word, a certain amount of water into the pure ILs decreases the viscosity, which is favorable for rapid absorption kinetics.

Supported Functionalized ILs

How to find out a solution to eliminate the high viscosity of functionalized ILs, Zhang *et al*. (*81*) investigated the absorption of CO_2 by amino-functionalized ILs supported on porous silica gel. These ILs contain amino acid anions and tetrabutylphosphonium cations (Table 2, entries 1-3). They found that fast and reversible CO_2 absorption was achieved by this method when compared with bubbling CO_2 into the bulk of the ionic liquid. The large surface of silica gel provides a significant improvement of the absorption rate of CO_2.

Supported IL membranes play a crucial role in gas separation and significantly save the operational cost. Undoubtedly, this method avoids the question of the high viscosity during CO_2 separation. Hanioka (*101*) reported a supported liquid membrane (SLM) based on a task-specific ionic liquid to achieve the selective and facilitated CO_2 separation from the CO_2/CH_4 gas mixture. The prepared SLM facilitated by the amine-terminated ionic liquid exhibited high selectivity and high permeability for CO_2 transport through the membrane because CH_4 permeation only depends on simple physical transport. Subsequently, it was reported that a supported ionic liquid membrane (the amino-functionalized ILs [$H_2NC_3H_6$mim][Tf_2N] in a cross-linked nylon-66 polymeric support) separated CO_2 from H_2 with a high permeability and selectivity even at elevated temperatures (*102*). Furthermore, supported liquid membranes incorporating amino acid ionic liquids remarkably facilitated CO_2 permeation under dry and low humid conditions (*103*).

Conclusions and Outlook

In summary, by taking advantage of their unique properties, including negligible vapor pressures, high thermal stabilities, excellent CO_2 solubilities, and tunable properties, ionic liquids offer new opportunities for CO_2 capture and storage, especially after Davis first reported a task-specific ionic liquid for CO_2 capture. Considering the limited CO_2 solubility of physical absorption, this review focuses on the chemical absorption of CO_2 by functionalized ionic liquids. Despite great progress has been achieved in improving the chemisorption of CO_2 by functionalized ionic liquids, it still remains challenging to design a new strategy by tuning the structure of the ionic liquid for high absorption capacity of CO_2, energy-saving demand during the regeneration, decreased visicosity upon the uptake of CO_2, and rapid absorption rate. In view of the dramatic increases in the viscosities of amino-functionalized ionic liquids upon CO_2 uptake, supported ionic liquids and non-amino anion-functionalized ionic

In Advances in CO2 Capture, Sequestration, and Conversion; He, et al.;
ACS Symposium Series; American Chemical Society: Washington, DC, 2015.

Publication Date (Web): September 11, 2015 | doi: 10.1021/bk-2015-1194.ch014

liquids are highly desirable and promising for industrial applications in carbon capture. The interactions between ionic liquid and CO_2 should be investigated in depth, which are the reasons for some interesting and abnormal phenomena of CO_2 absorption. Multi-cooperative interactions provide countless opportunities to improve the absorption performance of CO_2 in an atom-efficient manner. Furthermore, the physicochemical property changes (e.g. polarity, basicity, and viscosity) of ionic liquids upon CO_2 absorption present unlimited potential as switchable solvents. The CO_2 loaded ionic liquid possesses sufficient thermal stability by tuning the structure of the ionic liquid to allow the conversion of CO_2 to value-added chemicals or materials (*104*). Ionic liquids as efficient catalysts, react with CO_2 to form liquid carbonate, carbamate, or phenolate salts, which might render the chemical transformation under mild reaction conditions via activation of CO_2 (*105*). The prosperous development of ionic liquids for CO_2 capture can not live without the unremitting efforts of chemists. Great endeavors should be devoted to seeking the new breakthough of ionic liquids for CO_2 capture. We hope that new strategies and concepts can be introduced into ionic liquids for CO_2 capture, facilitating an indepth understanding of the interactions between ionic liquids and CO_2.

Publication Date (Web): September 11, 2015 | doi: 10.1021/bk-2015-1194.ch014

Acknowledgments

The National Key Basic Research Program of China (2015CB251401), the National Natural Science Foundation of China (No.21176205, No.21322602, No.J1210042), the Zhejiang Provincial Natural Science Foundation of China (R12BL06002), the Program for Zhejiang Leading Team of S&T Innovation (2011R50007), and the Fundamental Research Funds of the Central Universities are greatly acknowledged for their generous financial support.

References

1. Figueroa, J. D.; Fout, T.; Plasynski, S.; McIlvried, H.; Srivastava, R. D. Advances in CO_2 capture technology—the U.S. department of energy's carbon sequestration program. *Int. J. Greenhouse Gas Control* **2008**, *2*, 9–20.
2. Canadell, J. G.; Quéré, C. L.; Paupach, M. R.; Field, C. B.; Buitenhuis, E. T.; Ciais, P.; Conway, T. J.; Gillett, N. P.; Houghton, R. A.; Marland, G. Contributions to accelerating atmospheric CO_2 growth from economic activity, carbon intensity, and efficiency of natural sinks. *Proc. Natl. Acad. Sci. U. S. A.* **2007**, *104*, 18866–18870.
3. Hasib-ur-Rahman, M.; Siaj, M.; Larachi, F. Ionic liquids for CO_2 capture—development and progress. *Chem. Eng. Process* **2010**, *49*, 313–322.
4. Pan, Y. X.; Kuai, P. Y.; Liu, Y.; Ge, Q. F.; Liu, C. J. Promotion effects of Ga_2O_3 on CO_2 adsorption and conversion over a SiO_2-supported Ni catalyst. *Energy Environ. Sci.* **2010**, *3*, 1322–1325.

5. Yu, K. M. K.; Curcic, I.; Gabriel, J.; Tsang, S. C. E. Recent advances in CO_2 capture and utilization. *ChemSusChem* **2008**, *1*, 893–899.
6. Wang, W.; Wang, S. P.; Ma, X. B.; Gong, J. L. Recent advances in catalytic hydrogenation of carbon dioxide. *Chem. Soc. Rev.* **2011**, *40*, 3703–3727.
7. Rochelle, G. T. Amine scrubbing for CO_2 Capture. *Science* **2009**, *325*, 1652–1654.
8. Han, B.; Zhou, C. G.; Wu, J. P.; Tempel, D. J.; Cheng, H. S. Understanding CO_2 capture mechanisms in aqueous monoethanolamine via first principles simulations. *J. Phys. Chem. Lett.* **2011**, *2*, 522–526.
9. McCann, N.; Madaeder, M.; Attalla, M. Simulation of enthalpy and capacity of CO_2 absorption by aqueous amine systems. *Ind. Eng. Chem. Res.* **2008**, *47*, 2002–2009.
10. Heldebrant, D. J.; Yonker, C. R.; Jessop, P. G.; Phan, L. Organic liquid CO_2 capture agents with high gravimetric CO_2 capacity. *Energy Environ. Sci.* **2008**, *1*, 487–493.
11. Dzubak, A. L.; Lin, L.-C.; Kim, J.; Swisher, J. A.; Poloni, R.; Maximoff, N. S.; Smitt, B; Gagliardi, L. *Ab initio* carbon capture in open-site metal–organic frameworks. *Nat. Chem.* **2012**, *4*, 810–816.
12. Morris, W.; Doonan, C. J.; Furukawa, H.; Banerjee, R.; Yaghi, O. M. Crystals as molecules: Postsynthesis covalent functionalization of zeolitic imidazolate frameworks. *J. Am. Chem. Soc.* **2008**, *130*, 12626–12627.
13. Plaza, M. G.; Pevida, C.; Arias, B.; Casal, M. D.; Martin, C. F.; Fermoso, J.; Rubiera, F.; Pis, J. J. Different approaches for the development of low-cost CO_2 adsorbents. *J. Environ. Eng.* **2009**, *135*, 426–432.
14. Kitagawa, S.; Matsuda, R. Chemistry of coordination space of porous coordination polymers. *Coord. Chem. Rev.* **2007**, *251*, 2490–2509.
15. Ferey, G. Hybrid porous solids: past, present, future. *Chem. Soc. Rev.* **2008**, *37*, 191–214.
16. Wang, Z. Q.; Cohen, S. M. Postsynthetic modification of metal–organic frameworks. *Chem. Soc. Rev.* **2009**, *38*, 1315–1329.
17. Liu, J.; Thallapally, P. K.; McGrail, B. P.; Brown, D. R.; Liu, J. Progress in adsorption-based CO_2 capture by metal–organic frameworks. *Chem. Soc. Rev.* **2012**, *41*, 2308–2322.
18. Zukal, A.; Dominguez, I.; Mayerová, J.; Cejka, J. Functionalization of delaminated zeolite ITQ-6 for the adsorption of carbon dioxide. *Langmuir* **2009**, *25*, 10314–10321.
19. Nachtigall, P.; Grajciar, L.; Perez-Pariente, J.; Pinar, A. B.; Zukal, A.; Cejka, J. Control of CO_2 adsorption heats by the Al distribution in FER zeolites. *Phys. Chem. Chem. Phys.* **2012**, *14*, 1117–1120.
20. Lozinska, M. M.; Mangano, E.; Mowat, J. P.; Shepherd, A. M.; Howe, R. F.; Thompson, S. P.; Parker, J. E.; Brandani, S.; Wright, P. A. Understanding carbon dioxide adsorption on univalent cation forms of the flexible zeolite Rho at conditions relevant to carbon capture from flue gases. *J. Am. Chem. Soc.* **2012**, *134*, 17628–17642.
21. Loganathan, S.; Tikmani, M.; Ghoshal, A. K. Novel pore-expanded MCM-41 for CO_2 capture: synthesis and characterization. *Langmuir* **2013**, *29*, 3491.

Publication Date (Web): September 11, 2015 | doi: 10.1021/bk-2015-1194.ch014

22. Wang, J. Y.; Huang, L.; Yang, R. Y.; Zhang, Z.; Wu, J. W.; Gao, Y. S.; Wang, Q.; O'Hare, D.; Zhong, Z. Y. Recent advances in solid sorbents for CO_2 capture and new development trends. *Energy Environ. Sci.* **2014**, *7*, 3478–3518.
23. Gin, D. L.; Noble, R. D. Designing the next generation of chemical separation membranes. *Science* **2011**, *332*, 674–676.
24. D'Alessandro, D. M.; Smit, B.; Long, J. R. Carbon dioxide capture: Prospects for new materials. *Angew. Chem., Int. Ed.* **2010**, *49*, 6058–6082.
25. Ho, M. T.; Leamon, G.; Allinson, G. W.; Wiley, D. E. Economics of CO_2 and mixed gas geosequestration of flue gas using gas separation membranes. *Ind. Eng. Chem. Res.* **2006**, *45*, 2546–2552.
26. Powell, C. E.; Qiao, G. G. Polymeric CO_2/N_2 gas separation membranes for the capture of carbon dioxide from power plant flue gases. *J. Membr. Sci.* **2006**, *279*, 1–49.
27. Yave, W.; Car, A.; Funari, S. S.; Nunes, S. P.; Peinemann, K. V. CO_2-philic polymer membrane with extremely high separation performance. *Macromolecules* **2010**, *43*, 326–333.
28. Dupont, J.; de Souza, R. F.; Suarez, P. A. Z. Ionic liquid (molten salt) phase organometallic catalysis. *Chem. Rev.* **2002**, *102*, 3667–3691.
29. Wasserscheid, P.; Keim, W. Ionic liquids—new "solutions" for transition metal catalysis. *Angew. Chem., Int. Ed.* **2000**, *39*, 3772–3789.
30. Huang, J. F.; Luo, H. M.; Liang, C. D.; Sun, I. W.; Baker, G. A.; Dai, S. Hydrophobic brønsted acid−base ionic liquids based on PAMAM dendrimers with high proton conductivity and blue photoluminescence. *J. Am. Chem. Soc.* **2005**, *127*, 12784–12785.
31. Huang, J. F.; Luo, H. M.; Dai, S. A new strategy for synthesis of novel classes of room-temperature ionic liquids based on complexation reaction of cations. *J. Electrochem. Soc.* **2006**, *153*, J9–J13.
32. Greaves, T. L.; Drummond, C. J. Protic ionic liquids: Properties and applications. *Chem. Rev.* **2008**, *108*, 206–237.
33. Wu, W. Z.; Han, B. X.; Gao, H. X.; Liu, Z. M.; Jiang, T.; Huang, J. Desulfurization of flue gas: SO_2 absorption by an ionic liquid. *Angew. Chem., Int. Ed.* **2004**, *43*, 2415–2417.
34. Tempel, D. J.; Henderson, P. B.; Brzozowski, J. R.; Pearlstein, R. M.; Cheng, H. S. High gas storage capacities for ionic liquids through chemical complexation. *J. Am. Chem. Soc.* **2008**, *130*, 400–401.
35. Fukumoto, K.; Yoshizawa, M.; Ohno, H. Room temperature ionic liquids from 20 natural amino acids. *J. Am. Chem. Soc.* **2005**, *127*, 2398–2399.
36. Earle, M. J.; Esperanca, J.; Gilea, M. A.; Lopes, J. N. C.; Rebelo, L. P. N.; Magee, J. W.; Seddon, K. R.; Widegren, J. A. The distillation and volatility of ionic liquids. *Nature* **2006**, *439*, 831–834.
37. Wang, C. M.; Guo, L. P.; Li, H. R.; Wang, Y.; Weng, J. Y.; Wu, L. H. Preparation of simple ammonium ionic liquids and their application in the cracking of dialkoxypropanes. *Green Chem* **2006**, *8*, 603–607.
38. Wang, C. M.; Zhao, W. J.; Li, H. R.; Guo, L. P. Solvent-free synthesis of unsaturated ketones by the Saucy–Marbet reaction using simple ammonium ionic liquid as a catalyst. *Green Chem* **2009**, *11*, 843–847.

In Advances in CO2 Capture, Sequestration, and Conversion; He, et al.;
ACS Symposium Series; American Chemical Society: Washington, DC, 2015.

39. Anderson, J. L.; Dixon, J. K.; Brennecke, J. F. Solubility of CO_2, CH_4, C_2H_6, C_2H_4, O_2, and N_2 in 1-hexyl-3-methylpyridinium bis(trifluoromethylsulfonyl)imide: Comparison to other ionic liquids. *Acc. Chem. Res.* **2007**, *40*, 1208–1216.
40. Baltus, R. E.; Culbertson, B. H.; Dai, S.; Luo, H. M.; DePaoli, D. W. Low-pressure solubility of carbon dioxide in room-temperature ionic liquids measured with a quartz crystal microbalance. *J. Phys. Chem. B* **2004**, *108*, 721–727.
41. Bara, J. E.; Gabriel, C. J.; Carlisle, T. K.; Camper, D. E.; Finotello, A.; Gin, D. L.; Noble, R. D. Gas separations in fluoroalkyl-functionalized room-temperature ionic liquids using supported liquid membranes. *Chem. Eng. J.* **2009**, *147*, 43–50.
42. Perez-Blanco, M. E.; Maginn, E. J. Molecular dynamics simulations of carbon dioxide and water at an ionic liquid interface. *J. Phys. Chem. B* **2011**, *115*, 10488–10499.
43. Zhang, X. C.; Liu, Z. P.; Wang, W. C. Screening of ionic liquids to capture CO_2 by COSMO-RS and experiments. *AICHE J.* **2008**, *54*, 2717–2728.
44. Huang, X. H.; Margulis, C. J.; Li, Y. H.; Berne, B. J. Why is the partial molar volume of CO_2 so small when dissolved in a room temperature ionic liquid? Structure and dynamics of CO_2 dissolved in [$Bmim^+$] [$PF6^-$]. *J. Am. Chem. Soc.* **2005**, *127*, 17842–17851.
45. Zhang, X. C.; Huo, F.; Liu, Z. P.; Wang, W. C.; Shi, W.; Maginn, E. J. Absorption of CO_2 in the ionic liquid 1-n-hexyl-3-methylimidazolium tris(pentafluoroethyl)trifluorophosphate ([hmim][FEP]): A molecular view by computer simulations. *J. Phys. Chem. B* **2009**, *113*, 7591–7598.
46. Finotello, A.; Bara, J. E.; Narayan, S.; Camper, D.; Noble, R. D. Ideal gas solubilities and solubility selectivities in a binary mixture of room-temperature ionic liquids. *J. Phys. Chem. B* **2008**, *112*, 2335–2339.
47. Carlisle, T. K.; Bara, J. E.; Gabriel, C. J.; Noble, R. D.; Gin, D. L. Interpretation of CO_2 solubility and selectivity in nitrile-functionalized room-temperature ionic liquids using a group contribution approach. *Ind. Eng. Chem. Res.* **2008**, *47*, 7005–7012.
48. Muldoon, M. J.; Aki, S.; Anderson, J. L.; Dixon, J. K.; Brennecke, J. F. Improving carbon dioxide solubility in ionic liquids. *J. Phys. Chem. B* **2007**, *111*, 9001–9009.
49. Bara, J. E.; Gabriel, C. J.; Lessmann, S.; Carlisle, T. K.; Finotello, A.; Gin, D. L.; Noble, R. D. Enhanced CO_2 separation selectivity in oligo(ethylene glycol) functionalized room-temperature ionic liquids. *Ind. Eng. Chem. Res.* **2007**, *46*, 5380–5386.
50. Cadena, C.; Anthony, J. L.; Shah, J. K.; Morrow, T. I.; Brennecke, J. F.; Maginn, E. J. Why is CO_2 so soluble in imidazolium-based ionic liquids? *J. Am. Chem. Soc.* **2004**, *126*, 5300–5308.
51. Wang, Y.; Wang, C. M.; Zhang, L. Q.; Li, H. R. Difference for SO_2 and CO_2 in TGML ionic liquids: A theoretical investigation. *Phys. Chem. Chem. Phys.* **2008**, *10*, 5976–5982.
52. Bates, E. D.; Mayton, R. D.; Ntai, I.; Davis, J. H. CO_2 capture by a task-specific ionic liquid. *J. Am. Chem. Soc.* **2002**, *124*, 926–927.

Publication Date (Web): September 11, 2015 | doi: 10.1021/bk-2015-1194.ch014

53. Li, X. Y.; Hou, M. Q.; Zhang, Z. F.; Han, B. X.; Yang, G. Y.; Wang, X. L.; Zou, L. Z. Absorption of CO_2 by ionic liquid/polyethyleneglycol mixture and the thermodynamic parameters. *Green Chem.* **2008**, *10*, 879–884.
54. Gurkan, B.; Goodrich, B. F.; Mindrup, E. M.; Ficke, L. E.; Massel, M.; Seo, S.; Senftle, T. P.; Wu, H.; Glaser, M. F.; Shah, J. K.; Maginn, E. J.; Brennecke, J. F.; Schneider, W. F. Molecular design of high capacity, low viscosity, chemically tunable ionic liquids for CO_2 capture. *J. Phys. Chem. Lett.* **2010**, *1*, 3494–3499.
55. Zhang, J. M.; Zhang, S. J.; Dong, K.; Zhang, Y. Q.; Shen, Y. Q.; Lv, X. M. Supported absorption of CO_2 by tetrabutylphosphonium amino acid ionic liquids. *Chem.-Eur. J.* **2006**, *12*, 4021–4026.
56. Wang, C. M.; Luo, X. Y.; Luo, H. M.; Jiang, D. E.; Li, H. R.; Dai, S. Tuning the basicity of ionic liquids for equimolar CO_2 capture. *Angew. Chem., Int. Ed.* **2011**, *50* (21), 4918–4922.
57. Wang, C. M.; Luo, H. M.; Li, H. R.; Zhu, X.; Yu, B.; Dai, S. Tuning the physicochemical properties of diverse phenolic ionic liquids for equimolar CO_2 capture by the substituent on the anion. *Chem.-Eur. J.* **2012**, *18*, 2153–2160.
58. Bara, J. E.; Camper, D. E.; Gin, D. L.; Noble, R. D. Room-temperature ionic liquids and composite materials: Platform technologies for CO_2 capture. *Acc. Chem. Res.* **2010**, *43*, 152–159.
59. Huang, J. H.; Ruther, T. Why are ionic liquids attractive for CO_2 absorption? An overview. *Aust. J. Chem.* **2009**, *62*, 298–308.
60. Bara, J. E.; Carlisle, T. K.; Gabriel, C. J.; Camper, D.; Finotello, A.; Gin, D. L.; Noble, R. D. Guide to CO_2 separations in imidazolium-based room-temperature ionic liquids. *Ind. Eng. Chem. Res.* **2009**, *48*, 2739–2751.
61. Zhang, X. P.; Zhang, X. C.; Dong, H. F.; Zhao, Z. J.; Zhang, S. J.; Huang, Y. Carbon capture with ionic liquids: overview and progress. *Energy Environ. Sci.* **2012**, *5*, 6668–6681.
62. Shannon, M. S.; Bara, J. E. Reactive and reversible ionic liquids for CO_2 capture and acid gas removal. *Sep. Sci. Technol.* **2012**, *47*, 178–188.
63. Zhao, Z. J.; Dong, H. F.; Zhang, X. P. The research progress of CO_2 capture with ionic liquids. *Chin. J. Chem. Eng.* **2010**, *20*, 120–129.
64. Zhou, L. Y.; Fan, J.; Wang, J. J. Capture of CO_2 by ionic liquids. *Prog. Chem.* **2011**, *23*, 2269–2275.
65. Favre, E. Membrane processes and postcombustion carbon dioxide capture: Challenges and prospects. *Chem. Eng. J.* **2011**, *171*, 782–793.
66. Rees, N. V.; Compton, R. G. Electrochemical CO_2 sequestration in ionic liquids; a perspective. *Energy Environ. Sci.* **2011**, *4*, 403–408.
67. Karadas, F.; Atilhan, M.; Aparicio, S. Review on the use of ionic liquids (ILs) as alternative fluids for CO_2 capture and natural gas sweetening. *Energy Fuels* **2010**, *24*, 5817–5828.
68. Blasucci, V. M.; Hart, R.; Pollet, P.; Liotta, C. L.; Eckert, C. A. Reversible ionic liquids designed for facile separations. *Fluid Phase Equilib.* **2011**, *294*, 1–6.

69. Mac Dowell, N.; Florin, N.; Buchard, A.; Hallett, J.; Galindo, A.; Jackson, G.; Adjiman, C. S.; Williams, C. K.; Shah, N.; Fennell, P. An overview of CO_2 capture technologies. *Energy Environ. Sci.* **2010**, *3*, 1645–1669.
70. Noble, R. D.; Gin, D. L. Perspective on ionic liquids and ionic liquid membranes. *J. Membr. Sci.* **2011**, *369*, 1–4.
71. Wang, C. M.; Mahurin, S. M.; Luo, H. M.; Baker, G. A.; Li, H. R.; Dai, S. Equimolar CO_2 capture by imidazolium-based ionic liquids and superbase systems. *Green Chem.* **2010**, *12*, 870–874.
72. Mejía, I.; Kathleen, S.; Canales, R.; Brennecke, J. F. On the high-pressure solubilities of carbon dioxide in several ionic liquids. *J. Chem. Eng. Data.* **2013**, *58*, 2642–2653.
73. Goodrich, B. F.; de la Fuente, J. C.; Gurkan, B. E.; Zadigian, D. J.; Price, E. A.; Huang, Y.; Brennecke, J. F. Experimental measurements of amine-functionalized anion-tethered ionic liquids with carbon dioxide. *Ind. Eng. Chem. Res.* **2011**, *50*, 111–118.
74. Seo, S.; Simoni, L. D.; Ma, M.; DeSilva, M. A.; Huang, Y.; Stadtherr, M. A.; Brennecke, J. F. Phase-change ionic liquids for postcombustion CO_2 capture. *Energy Fuels* **2014**, *28*, 5968–5877.
75. Gurau, G.; Rodríguez, H.; Kelley, S. P.; Janiczek, P.; Kalb, R. S.; Rogers, R. D. Demonstration of chemisorption of carbon dioxide in 1,3-dialkylimidazolium acetate ionic liquids. *Angew. Chem., Int. Ed.* **2011**, *50*, 12024–12026.
76. Zhang, J. S.; Chai, S.-H.; Qiao, Z.-A.; Mahurin, S. N.; Chen, J. H.; Fang, Y. X.; Wan, S.; Nelson, K.; Zhang, P. F.; Dai, S. Porous liquids: a promising Class of media for gas separation. *Angew. Chem., Int. Ed.* **2015**, *54*, 932–936.
77. Soutullo, M. D.; Odom, C. I.; Wicker, B. F.; Henderson, C. N.; Stenson, A. C.; Davis, J. H. Reversible CO_2 capture by unexpected plastic-, resin-, and gel-like ionic soft materials discovered during the combi-click generation of a TSIL library. *Chem. Mater.* **2007**, *19*, 3581–3583.
78. Luo, X. Y.; Ding, F.; Lin, W. J.; Qi, Y. Q.; Li, H. R.; Wang, C. M. Efficient and energy-saving CO_2 capture through the entropic effect induced by the intermolecular hydrogen bonding in anion-functionalized ionic liquids. *J. Phys. Chem. Lett.* **2014**, *5*, 381–386.
79. Gurkan, B. E.; de la Fuente, J. C.; Mindrup, E. M.; Ficke, L. E.; Goodrich, B. F.; Price, E. A.; Schneider, W. F.; Brennecke, J. F. Equimolar CO_2 absorption by anion-functionalized ionic liquids. *J. Am. Chem. Soc.* **2010**, *132*, 2116–2117.
80. Saravanamurugan, S.; Kunov-Kruse, A. J.; Fehrmann, R.; Riisager, A. Amine-functionalized amino acid-based ionic liquids as efficient and high-capacity absorbents for CO_2. *ChemSusChem* **2014**, *7*, 897–902.
81. Zhang, Y. Q.; Zhang, S. J.; Lu, X. M.; Zhou, Q.; Fan, W.; Zhang, X. P. Dual amino-functionalised phosphonium ionic liquids for CO_2 Capture. *Chem. –Eur. J.* **2009**, *15*, 3003–3011.

82. Xue, Z. M.; Zhang, Z. F.; Han, J.; Chen, Y.; Mu, T. C. Carbon dioxide capture by a dual amino ionic liquid with amino-functionalized imidazolium cation and taurine anion. *Int. J. Greenhouse Gas Control* **2011**, *5*, 628–633.
83. Wang, C. M.; Guo, Y.; Zhu, X.; Cui, G. K.; Li, H. R.; Dai, S. Highly efficient CO_2 capture by tunable alkanolamine-based ionic liquids with multidentate cation coordination. *Chem. Commun.* **2012**, *48*, 6526–6528.
84. Yang, Z. Z.; He, L. N. Efficient CO_2 capture by tertiary amine-functionalized ionic liquids through Li^+-stabilized zwitterionic adduct formation. *Beilstein J. Org. Chem.* **2014**, *10*, 1959–1966.
85. Wang, C. M.; Luo, H. M.; Jiang, D.; Li, H. R.; Dai, S. Carbon dioxide capture by superbase-derived protic ionic liquids. *Angew. Chem. Int. Ed.* **2010**, *49*, 5978–5981.
86. Jessop, P. G.; Heldebrant, D. J.; Li, X. W.; Eckert, C. A.; Liotta, C. L. Green chemistry: Reversible nonpolar-to-polar solvent. *Nature* **2005**, *436*, 1102–1102.
87. Phan, L.; Chiu, D.; Heldebrant, D. J.; Huttenhower, H.; John, E.; Li, X. Y.; Pollet, P.; Wang, R. Y.; Eckert, C. A.; Liotta, C. L.; Jessop, P. G. Switchable solvents consisting of amidine/alcohol or guanidine/alcohol mixtures. *Ind. Eng. Chem. Res.* **2008**, *47*, 539–545.
88. Wang, C. M.; Cui, G. K.; Luo, X. Y.; Xu, Y. J.; Li, H. R.; Dai, S. Highly efficient and reversible SO_2 capture by tunable azole-based ionic liquids through multiple-site chemical absorption. *J. Am. Chem. Soc.* **2012**, *133*, 11916–11919.
89. Luo, X. Y.; Guo, Y.; Ding, F.; Zhao, H. Q.; Cui, G. K.; Li, H. R.; Wang, C. M. Significant improvements in CO_2 capture by pyridine-containing anion-functionalized ionic liquids through multiple-site cooperative interactions. *Angew. Chem., Int. Ed.* **2014**, *53*, 7053–7057.
90. Ding, F.; He, X.; Luo, X. Y.; Lin, W. J.; Chen, K. H.; Li, H. R.; Wang, C. M. Highly efficient CO_2 capture by carbonylcontaining ionic liquids through Lewis acid–base and cooperative C-H···O hydrogen bonding interaction strengthened by the anion. *Chem. Commun.* **2014**, *50*, 15041–15044.
91. Gutowski, K. E.; Maginn, E. J. Amine-functionalized task-specific ionic liquids: A mechanistic explanation for the dramatic increase in viscosity upon complexation with CO_2 from molecular simulation. *J. Am. Chem. Soc.* **2008**, *130*, 14690–14704.
92. Liu, A. H.; Ma, R.; Song, C.; Yang, Z. Z.; Yu, A.; Cai, Y.; He, L. N.; Zhao, Y. N.; Yu, B.; Song, Q. Equimolar CO_2 capture by N-substituted amino acid salts and subsequent conversion. *Angew. Chem., Int. Ed.* **2012**, *51*, 11306–11310.
93. Camper, D.; Bara, J. E.; Gin, D. L.; Noble, R. D. Room-temperature ionic liquid−amine solutions: Tunable solvents for efficient and reversible capture of CO_2. *Ind. Eng. Chem. Res.* **2008**, *47*, 8496–8498.
94. Zhang, F.; Fang, C.-G.; Wu, Y.-T.; Wang, Y.-T.; Li, A.-M.; Zhang, Z.-B. Absorption of CO_2 in the aqueous solutions of functionalized ionic liquids and MDEA. *Chem. Eng. J.* **2010**, *160*, 691–697.
95. Huang, Q.; Li, Y.; Jin, X. B.; Zhao, D.; Chen, G. Z. Chloride ion enhanced thermal stability of carbon dioxide captured by monoethanolamine in

Publication Date (Web): September 11, 2015 | doi: 10.1021/bk-2015-1194.ch014

hydroxyl imidazolium based ionic liquids. *Energy Environ. Sci.* **2011**, *4*, 2125–2133.
96. Li, X. Y.; Hou, M. Q.; Zhang, Z. F.; Han, B. X.; Zhang, G. Y.; Wang, X. L.; Zou, L. Z. Absorption of CO_2 by ionic liquid/polyethylene glycol mixture and the thermodynamic parameters. *Green Chem.* **2008**, *10*, 879–884.
97. Wang, C. M.; Luo, H. M.; Luo, X. Y.; Li, H. R.; Dai, S. Equimolar CO_2 capture by imidazolium-based ionic liquids and superbase systems. *Green Chem.* **2010**, *12*, 2019–2023.
98. Goodrich, B. F.; de la Fuente, J. C.; Gurka, B. E.; Lopez, Z. K.; Price, E. A.; Huang, Y.; Brennecke, J. F. Effect of water and temperature on absorption of CO_2 by amine-functionalized anion-tethered ionic liquids. *J. Phys. Chem. B* **2011**, *115*, 9140–9150.
99. McDonald, J. L.; Sykora, R. E.; Hixon, P.; Mirjafari, A.; Davis, J. H. Impact of water on CO_2 capture by amino acid ionic liquids. *Environ. Chem. Lett.* **2014**, *12*, 201–208.
100. Seo, S.; Guzman, M. Q.; DeSilva, M. A.; Lee, T. B.; Huang, Y.; Goodrich, B. F.; Schneider, W. F.; Brennecke, J. F. Chemically tunable ionic liquids with aprotic heterocyclic anion (AHA) for CO_2 Capture. *J. Phys. Chem. B* **2014**, *118*, 5740–5751.
101. Hanioka, S.; Maruyama, T.; Sotani, T.; Teramoto, M.; Matsuyama, H.; Nakashima, K.; Hanaki, M.; Kubota, F.; Goto, M. CO_2 separation facilitated by task-specific ionic liquids using a supported liquid membrane. *J. Membr. Sci.* **2008**, *314*, 1–4.
102. Myers, C.; Pennline, H.; Luebke, D.; Ilconich, J.; Dixon, J. K.; Maginn, E. J.; Brennecke, J. F. High temperature separation of carbon dioxide/hydrogen mixtures using facilitated supported ionic liquid membranes. *J. Membr. Sci.* **2008**, *322*, 28–31.
103. Kasahara, S.; Kamio, E. J.; Ishigami, T.; Matsuyama, H. Amino acid ionic liquid-based facilitated transport membranes for CO_2 separation. *Chem. Commun.* **2012**, *48*, 6903–6905.
104. Rosen, B. A.; Khojin, A. S.; Thorson, M. R.; Zhu, W.; Whipple, D. T.; Kenis, P. J. A.; Masel, R. I. Ionic liquid–mediated selective conversion of CO_2 to CO at low overpotentials. *Science* **2011**, *334*, 643–644.
105. Zhao, Y. F.; Yu, B.; Yang, Z. Z.; Zhang, H. Y.; Hao, L. D.; Gao, X.; Liu, Z. M. A protic ionic liquid catalyzes CO_2 conversion at atmospheric pressure and room temperature: Synthesis of quinazoline-2,4(1*H*,3*H*)-diones. *Angew. Chem., Int. Ed.* **2014**, *53*, 5922–5925.

Publication Date (Web): September 11, 2015 | doi: 10.1021/bk-2015-1194.ch014

Subject Index

Publication Date (Web): September 11, 2015 | doi: 10.1021/bk-2015-1194.ix002

In Advances in CO2 Capture, Sequestration, and Conversion; He, et al.;
ACS Symposium Series; American Chemical Society: Washington, DC, 2015.

In Advances in CO2 Capture, Sequestration, and Conversion; He, et al.;
ACS Symposium Series; American Chemical Society: Washington, DC, 2015.

M

In Advances in CO2 Capture, Sequestration, and Conversion; He, et al.;
ACS Symposium Series; American Chemical Society: Washington, DC, 2015.

Publication Date (Web): September 11, 2015 | doi: 10.1021/bk-2015-1194.ix002

Publication Date (Web): September 11, 2015 | doi: 10.1021/bk-2015-1194.ix002

Q

R

S

T

In Advances in CO2 Capture, Sequestration, and Conversion; He, et al.;
ACS Symposium Series; American Chemical Society: Washington, DC, 2015.

Z

Publication Date (Web): September 11, 2015 | doi: 10.1021/bk-2015-1194.ix002

In Advances in CO2 Capture, Sequestration, and Conversion; He, et al.;
ACS Symposium Series; American Chemical Society: Washington, DC, 2015.